Uncertainty analysis of biological systems: towards a digital twin of the human heart

Ph.D. Candidate:

Giulio Del Corso[(1)]

1- Gran Sasso Science Institute (GSSI)

Advisors:

Francesco Viola[(1)]

Roberto Verzicco[(1,2,3)]

2- Università di Roma "Tor Vergata", Roma, Italy

3- University of Twente, Enschede, The Netherlands

Referees:

Alessio Gizzi[(4)]

Gianluca Iaccarino[(5)]

4- Università di Roma Campus Bio-Medico, Roma, Italy

5- Stanford University, Stanford, USA

GRAN SASSO SCIENCE INSTITUTE
SCHOOL OF ADVANCED STUDIES
Scuola Universitaria Superiore

Publication year - 2022

The best scientists and explorers have the attributes of kids.
They ask questions and have a sense of wonder.

SYLVIA EARLE

Abstract

The human heart has always been a challenge for doctors and scientists with its amazing complexity and individual variability. Owing to recent decades increase in computational power, it has been possible to develop in-silico duplicates of reality that greatly extend the possible analyses. However, such models have a main limitation: their results do not directly account for individual variability. Uncertainty Quantification (UQ) methodologies integrate elements of probability theory and statistics with machine learning techniques to investigate how uncertainties and variability impact model dynamics. In this manuscript, starting with a simplified cardiac duplicate comprising only the left chambers, UQ methodologies were applied to investigate the most relevant uncertain quantities and guide the subsequent optimisation of the model. According to the analyses performed, the activation of a healthy heart is totally dominated by fast conduction pathways (Purkinje network, internodal bundles, etc.) and fibers orientation. The model was therefore updated to account for these structures, in particular the Purkinje Network extending into the ventricles and the double orientation of ventricular fibers. In addition, fundamental elements of cardiac dynamics were included, such as the orientation of muscle fibres for both atria and ventricles, four realistic chambers, and differentiated cell models to characterise the action potentials of different parts of the heart. Importantly, this advanced cardiac model has been designed to account for a parametric variation of geometrical and physical quantities, which is essential for running UQ analyses.

The flexibility of UQ techniques also allowed several partnerships with medical groups. The methodologies of classical statistics, integrated with metamodelling techniques, allowed the analysis of gastroenterological diseases. Furthermore, global sensitivity analyses coupled with Monte Carlo methods enabled studies on teaching neonatal resuscitation procedures to medical residents. These works highlighted the main challenge of UQ analyses: in applicative contexts, particularly medical ones, the information available to the investigator is limited, therefore the results are potentially biased or even incorrect. To address the necessity to perform UQ analyses even with incomplete/wrong information, we developed techniques to perform correlation analyses for error-affected databases and defined a robustness index for global sensitivity analyses (Nested UQ).

Contents

Chapter 1

Introduction

The complexity of natural phenomena has always fascinated scientists who, with the tools of their times, have attempted to investigate them. Despite for centuries they have been mainly investigated experimentally, in modern times we increasingly rely on digital simulacra of reality. The latter, also called in-silico models, are tools that integrate two different components: a mathematical description of the phenomenon and, when necessary, a numerical method to solve it. The *model* consists of a system of equations that describes the problem in a simplified way, focusing only on those components that the experimenter believes may play a fundamental role. These equations can admit an analytical solution but, in most of the cases, the latter must be solved approximately using a proper *numerical method* implemented in a computing machine.

Making a digital duplicate of the problem at study is therefore a complex task that requires in-depth knowledge of very different areas, raging from Numerical Analysis, to Physics and Computer Science. Often only a multidisciplinary team can efficiently manage the various stages of model development. Regardless of these difficulties, this is the decade of the digital revolution: the flourishing research into efficient numerical methods [1, 2, 3] and the staggering increase in available computing power [4, 5] have opened the way to applications that could not be tackled just a few years ago. Virtual models allow several applications, encompassing cultural heritage preservation through image reconstruction to fluid dynamics investigation of sea waves and biological phenomena. Although different in their objectives and methodologies, all these applications are characterised by a modelling process and a numerical resolution phase using an efficient software. In addition, they aim to create a digital twin of reality to be used as a predictive tool other than an experiment. As an example, a reconstruction procedures of the three-dimensional (3D) model of buildings, can be applied to the study of cultural heritage. A detailed 3D reconstruction of churches or monuments can be useful for educational purposes and even as a reference for subsequent restoration work. While classical methodologies are based on measurements and CAD reconstruction, or requires a complete scan of the object

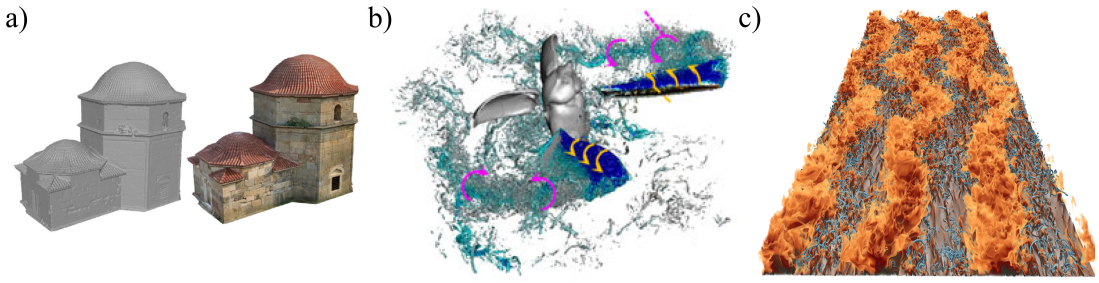

Figure 1.1: Examples of numerical model and applications: Panel a): reconstruction from photos of Ottoman church. Panel b): flow around a flapping rhinoceros beetle. Panel c): thermal structures rising from the heated plate.

with *ad hoc* equipment, a modern approach is the reconstruction of quality 3D models using collections of unordered photos representing a scene from different viewpoints. Despite the limitations of these new approaches (which require very good lighting conditions and are computationally burdensome), very promising results include the reconstruction of entire complex buildings from standard photos (in this case an Ottoman church located in the region of Xanthi, Greece, Figure 1.1a) without the need of labelling or mapping the relative position of each image [6]. The reconstructed 3D model can be used in various applications that are not limited to buildings. In a much different context, a numerical study of a flapping rhinoceros beetle in hovering flight (Figure 1.1b) [7] made it possible to investigate the flow around the wings, differentiating the hovering phase from the initial thrust phase, and to propose a simplified model with an excellent match with the more complex one. Furthermore, the study of animal flight can be an inspiration for the next generation of flying robots. Also the details of the thermal convection of a heat-hedged wall can be analysed from a numerical point of view [8] (Figure 1.1c). This investigation of the different states (buoyancy dominated, transitional, and shear dominated regime) with their respective flows allows to deeply understand the heat transfer dynamic.

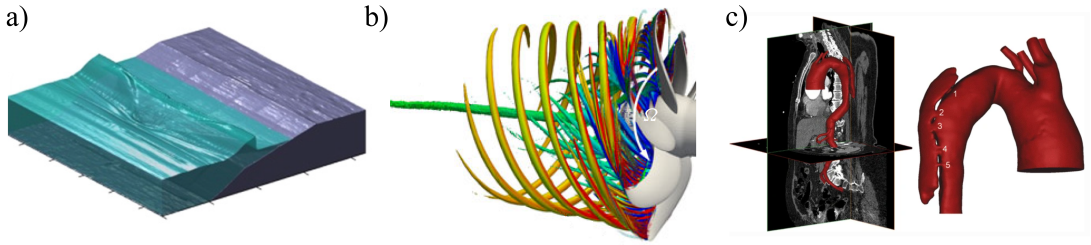

Figure 1.2: Examples of numerical model and applications: Panel a): solitary wave breaking against a reef. Panel b): hub vortex at the leading edge of a hydrofoil. Panel c): study of aortic dissection.

In the field of numerical simulations, fluid dynamics ones are relatively recent due to the high computational cost required to solve them. One of the most

interesting numerical experiment it is certainly the study of sea waves [9], for which the shape and evolution of the wave is dependent on the characteristics of the seabed and the coastline (shown in Figure 1.2a). Certain reef conformations may reduce the risk of destructive waves while others, on the contrary, may amplify their effects, making preliminary simulations a powerful tool for preventing serious long-term effects. Numerical trials can also allow a detailed view of the properties of a physical/engineering system. Indeed, simulations allow the vortex dynamics generated by the propeller to be resolved and can be used to increase the efficiency of the propeller itself (reducing resistance and noise) [10] (Figure 1.1b).

Among the various applications, one of the most fascinating is the modelling of biological phenomena. As an example, by reconstructing the aorta on the basis of medical images, it is possible to investigate problems of aortic dissection (AoD) [11], in which a tear occurs in the inner layer of the artery. The pressure exerted by the blood on the tear causes the inner and middle layers to dissect (split). The study of hemodynamics and the stress exerted on the aortic wall is therefore an important step towards in-silico duplicates that can be used for early and correct diagnosis. Undeniably, the human body fascinates precisely because of its complexity and several models have been proposed over the years to investigate both physiological and pathological functioning of brain [12], bones [13], or even the growth of tumours [14]. Models have made it possible to investigate both physiological and pathological functions, allowing a more detailed understanding of the phenomena.

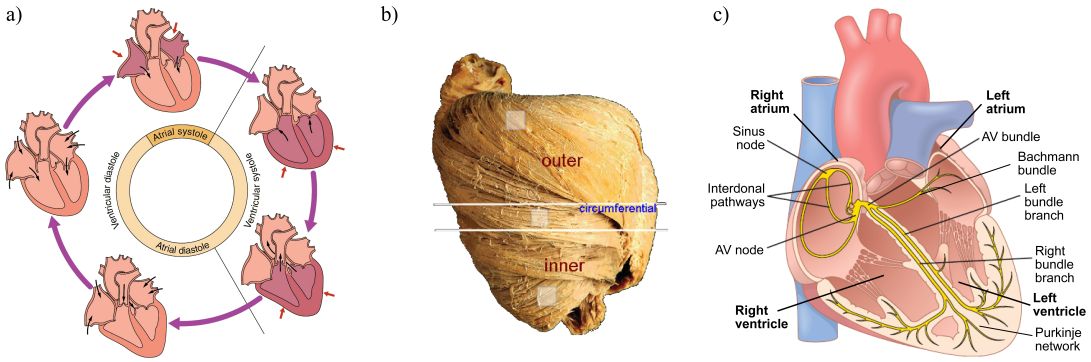

Figure 1.3: Panel a) shows the cardiac cycle: starting from the atrial systole (the blood is pumped from the atria to the ventricles) is followed by the atrial diastole (the ventricles contract expelling the blood into the circulatory system). The muscles of the four chambers relax (Atrial and Ventricular diastole) to allow a new contraction cycle. Panel b) illustrates the complex orientation of the ventricle fibers, slightly different from the inner (counterclockwise) to the outer part (clockwise) [15]. A sketch of the fast electrical conduction network of the heart is shown in panel c) [16]. These include the sinoatrial node in the right atrium, the internodal pathways that carry the signal up to the AV node and, finally, the Purkinje network that uniformly activates the ventricles.

One of the organs that has most captivated scientists' interest is undoubtedly the heart. Since the fourth century BC, Aristotélēs defined it as the most important organ of the body because, together with the brain, "are the main governing powers of life" [17] and in the second century A.D., Galenus investigated the complex fibrous structures that composed it [18]. Until the Renaissance, however, the details of cardiac rhythm and function remained largely unknown. It was the studies of Andrés de Laguna and Leonardo da Vinci that investigated the valves, introducing the idea of alternating rhythms between the atria and ventricles and, above all, took the first steps towards correctly identifying the chambers [19]. A comprehensive insight on the heart functioning (with the division of the ventricular chambers and the correct interpretation of the phases of systole and diastole) was only achieved in the 17^{th} century, by William Harvey [20]. Since then, new methods of studying the organ's behaviour in-vivo (using electrocardiography, ultrasound or magnetic resonance imaging) have allowed a real revolution in the progress of medical research and modelling.

The heart is the organ responsible for pumping blood in the systemic and pulmonary circulation. Mainly consisting of a particular type of muscle tissue, the myocardium. This muscle contracts at a variable rate (60-70 acts/minute) so as to ensure proper oxygenation of the entire body both at rest and under fatigue. Anatomically, the heart is composed of four chambers, two atria and two ventricles, capable in their contraction of pumping the blood to the farthest points of the organism (see Figure 1.3c). These chambers are connected in pairs: the left atrium to the left ventricle and the right atrium to the right ventricle. The atrioventricular connection is controlled by two valves (mitral and tricuspid valves) whose closure prevents blood from re-entering the atrium. The blood flow then exits the ventricles (through the aorta and pulmonary artery) where two more valves (aortic and pulmonary valves) prevent reflux back into the ventricles (see Figure 1.3). The ventricular blood pressure exerted by the blood is so intense that, in order to prevent the valves from subverting, they are attached to muscles at the base of the ventricle (known as the papillary muscles) by strong cords of tendon (chordae tendinae). The muscle that forms the walls of the atrium and ventricles consists of specialised cells (fibers) capable of contracting in only one direction. The orientation of these fibers plays a crucial role in how the contraction occurs, in particular the ventricle is formed by two different bands of overlapping fibers oriented at an angle of 60 degrees (outer counterclockwise, inner clockwise and a circumferential median layer) so that the combined force produces an effective bottom-up ventricular contraction [21], see Figure 1.3b. The orientation of the fibers is not only influenced by individual's characteristics, but is also dependent on the state of health, the level of physical training and, finally, trauma (e.g. heart attacks) suffered that leave the tissue with a reduced capacity to contract.

Importantly, the periodic contraction and relaxation of the cardiac muscle is governed by the cardiac electrophysiology system (Figure 1.3c. The heart activation signal initiates in a specialised structure in the right atrium called the sinoatrial node (SA-node). The latter, appropriately controlled by the sympa-

thetic and parasympathetic systems, induces electrical signals in the surrounding tissue at a fixed rate (typically in the order of 60 Hz at rest, with marked differences depending on training status, age, size, and gender). These signals travel through the muscle fibers at speeds of the order of 0.5 - 1 m/s [16, 22], occurring along the fibers direction in order to ensure fast and uniform activation of the atrium, the signal travels through specialised fibers bundles (internodal bundles: Anterior, Thorel and Wenckebach bundles) which carry the signal at higher speed (1.54 m/s [23, 24, 22]) to both the right atrium and, via Bachmann's bundle, to the left atrium. These internodal pathways join at the base of the right atrium a second specialised structure called the atrioventricular node (AV-node), see Figure 1.3c. The latter slows down the signal by more than 100 ms. The reason for this slowdown is that the propagation of the signal in the atrium triggers the contraction of the underlying muscle, which takes longer to actually push blood from the atria to the ventricles. The AV-node therefore serves to ensure a minimum physiological delay for blood to be pumped from the atria to the ventricles. At the end of this phase the atria are contracted and the ventricles are ready to be activated. Similar to the atria, the ventricles are endowed with a fast conduction system, the signal descends from the AV node through a structure called the His bundle which splits the signal into a plethora of fine, very high speed (4 m/s [16]) fibers called the Purkinje network which activates the entire base of the ventricle, the papillary muscles (contracting the chordae tendinae to hold the valves) and finally the wall of the ventricular myocardium, allowing blood to be pumped in pulmonary and systemic circulation. The muscle tissues then begin to decontract in preparation for the next cycle (which occurs at about 70 beats per minute for more than 3 billion heart beats/lifetime [25]).

Importantly, each of the cardiac components described above is characterised by marked individual variety. As an example, the mean atrial volume of a healthy man may be up to 15% higher than that of a woman of the same age, and also the variability between individuals of the same sex is such that it is not difficult to find individuals with volumetric differences of more than 65% [26, 27]. Even the heart rate, which at rest is between 60 and 70 beats per minute, can vary between two healthy individuals by more than 20% [25], not to mention differences in cardiac geometry, or the positioning and even the number of papillary muscles with corresponding chordae tendineae [28]. This uncertainty is compounded by local variability in fibers orientation and electrical conductivity which, despite minor differences, can have a major impact on cardiac dynamics [29].

All these examples are sources of uncertainties for the numerical model, and such intrinsic variability of the input parameters can only be described by an appropriate probability distribution. Choosing a particular set of parameters corresponds to a choice of the experimenter (e.g. setting ventricle size to a certain volume or conductivity to a fixed value). The limit of making a choice is that the model is no longer representative of the entire population but, conversely, only describes a specific individual, leading to biased or even unrealistic results. This bottleneck makes the work of refining a mathematical model seem pointless: it is counterproductive to develop more efficient model or a more pre-

cise numerical method when the impact of the variability of the parameters is so great that it cancels out any possible gain. Consequently, a growing body of literature deals with measuring/calibrating uncertainties in physical and engineering models. Once detailed information on the variability of the inputs has been obtained, this can be supplemented with a suitable methodology to extend a classical deterministic analysis (i.e. with fixed parameters and no model uncertainties).

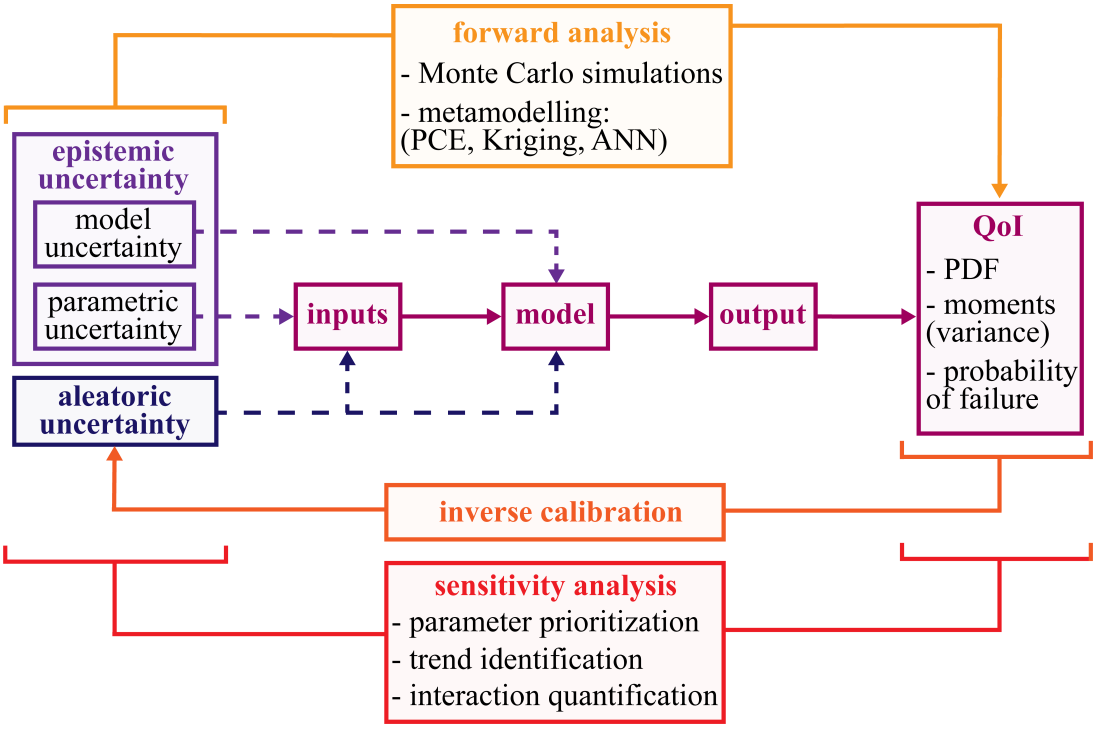

Figure 1.4: Outline of an uncertainty quantification (UQ) analysis. Uncertainties (epistemic and aleatoric) affect both the inputs of a model (e.g. the initial conditions of a system of differential equations) and the parameters that influence the dynamics. From the output of the model, quantities of interest (QoI) are extracted. The description of QoI as a function of input uncertainties is called forward analysis. Conversely, calibrating variability on the basis of known information on QoI is known as an inverse problem. The impact that the variability of each uncertainty has on the QoI is called sensitivity analysis and can be decisive for parameter prioritisation, trend identification and interaction quantification.

Uncertainty quantification (UQ) is a branch of mathematics that deals in a structured way with analysing the effect of uncertainties on a computational model. Working with variability and unknown data, UQ is part of the broader field of statistics. However, where normal statistical analyses are forced to deal with data coming from the complexity of the real world, UQ operates mainly with in-silico models. Consequently, the parameters of the study are fully defined by the experimenter, who may use ad-hoc techniques not possible in canonical statistical analysis (e.g. use an efficient sampling strategy to produce an opti-

mal study population). With reference to Figure 1.4, each UQ analysis can be schematised as follows: the model, typically an in-silico duplicate of reality, links like a black box the inputs to the outputs of the problem. The inputs are any parameters influencing the model solutions such as initial or boundary conditions, while the outputs are the response of the model for the given combination of inputs. However, to handle the complexity of the outputs, relevant scalar values called quantities of interest (QoI) are extracted from them. Referring to the cardiac model, the output of the model is the entire dynamics of the heart (the vector field of fluid velocity, the activation map of the electrophysiology, etc.). Examples of the corresponding quantities of interest, selected on the basis of medical interest, are the activation time of the atria and ventricles or the percentage of blood leaving the ventricles each time they fully contract (i.e. the ejection fraction).

Given the model and the QoIs, the key component of an UQ analysis to add are the uncertainties. These can be summarised in two macro-categories: epistemic uncertainties and random/aleatoric uncertainties. The former are given by individual variability, unknown information and incorrect measurements. These are uncertainties that could be avoided if the experimenter had complete knowledge of the data. Conversely, aleatoric ones are those that are intrinsically random. For instance, a simulation involving the roll of a die will always have a completely random component. Both these uncertainties are described by means of appropriate probability distribution (e.g, Normal, LogNormal, Uniform, etc.). These distributions are not known a priori and a detailed data collection campaign is necessary to obtain information about them. The raw data thus collected must then be processed to see which of the different distributions best approximates the dataset. The numerous ad-hoc techniques for calibration, such as Bayesian calibration or maximum likelihood estimation methods, then lead to the selection of an optimal approximating one. The fitting between this distribution and the data finally requires the use of special goodness of fit tests (e.g. Shapiro-Wilk, Kolmogorov-Smirnov, etc.) to further assess the goodness of the choice as the calibration of the appropriate distribution is a fundamental step in any UQ analysis. An incorrect choice of input distributions can affect the entire analysis, leading to inaccurate or even false results.

Once the three blocks of an UQ analysis have been defined (model, QoI, and uncertainties), the methodology to be applied depends on the following research questions, see Figure 1.4.

How does the uncertainty of the inputs propagate on the QoI?

This is called the direct/forward problem and can be solved using a direct approach. In order to understand how the inputs (described by an opportune probability distribution) propagate to the QoI it is sufficient to sample their values from the corresponding distributions (Monte Carlo method). For each sampled set of values (one for each input), the model it is evaluated to obtain the corresponding QoI. By repeating this procedure several (thousands) times, the QoI distribution can be recovered, answering the research question. This brute force approach can be modified to be more efficient in terms of model

evaluations and, thus, simulation time required. Proper sampling strategies (like Latin Hypercube sampling, quasi-Monte Carlo or Markov chain Monte Carlo [30]) can greatly reduce the number of simulations needed to obtain the result. These techniques must be used wisely, as improper use can be counterproductive (e.g. quasi-Monte Carlo approaches are much slower in the case of a large number of parameters).

If the research question is more specific convergence can be further increased. As an example, the interest is often only in determining the probability that the QoI exceeds a certain threshold. This happens in all those cases where the value of the QoI, as long as it remains within ranges, is not relevant while exceeding a limit value can lead to catastrophic consequences. Examples are the temperature inside a nuclear power plant reactor or the cornering speed of a train. There are several methodologies that can answer this question using only a few simulations, like Subset simulations [31, 32], Asymptotic Sampling [33] or importance sampling. All these techniques attempt to explore the input space not randomly but by targeting sampling on those combinations that cause the QoI to exceed the threshold.

Which input distributions may have generated a certain QoI distribution?

In the so-called inverse calibration the investigator has data on QoI and wants to find the most likely input distributions that could have generated them. Using a Bayesian approach, inverse calibration methods are based on reconstructing the input distribution from an a-priori hypothesis (e.g. assuming that the input follows a normal distribution with a fixed mean and variance). After each simulation performed for a given input combination, this hypothesis is updated to better match the new information [34]. By repeating this procedure a sufficient number of times, the input distribution becomes stable, so each new simulation makes a minor change and the method is said to have reached convergence. The distribution of inputs thus obtained is the most likely to have generated that particular output, these values can be used for future analysis or to check whether the model is realistic in describing the input-output relationship. Despite their importance, applications of inverse calibration are less frequent than for forward analysis as these techniques are very onerous in terms of the simulations to be performed.

Which inputs are the most relevant for the model dynamics?

Determining which of the inputs is most influential is often a crucial issue in UQ analyses. In fact, distinguishing between relevant and unimportant parameters allows not only for better understanding of how the model works, but also to identify the inputs that can be neglected in subsequent analyses. Reduce the input space dimension (i.e. model reduction) it is relevant because most of the UQ techniques are more efficient when the dimensionality of the inputs is reduced. Furthermore, a large number of inputs implies the use of models with more degrees of freedom and, consequently, more prone to overfitting risks. This question is the most complex in terms of the choices to be made by the experimenter as the results are strongly dependent on the assumptions on the input space. Moreover, the methodologies used to address is are computation-

ally expensive in terms of the number of simulations to be performed. Several techniques have been developed to handle these difficulties. The latter can be subdivided in two broad families: screening techniques (as Morris method [35] or One-At-Time analysis) which allow with a low computational cost to obtain an initial insight into input-output relevance, and sensitivity analysis (as Saltelli's algorithm [36] or Glen and Isaacs method [37]) which also consider the combined effect of the inputs and allow a more complete understanding of the phenomenon. However, the proper design of the study and the correct interpretation of the results remains a frequent problem. Indeed, a survey by Saltelli showed that most of the sensitivity analyses carried out even on highly-cited papers are of poor methodological quality [38].

Although the techniques developed in last decades greatly reduce the number of simulations needed to tackle the proposed problems, in many applications this is not sufficient. In fact, the computational cost of solving the model is often so high that even a simple forward problem is almost impossible to be solved accurately. A modern idea to solve this bottleneck is the use of surrogate models, also called metamodels. The latter are an integration of the flourishing machine learning research into uncertainty quantification problems. The idea is to reduce the computational burden of the simulations to be performed by training a simpler model, a surrogate to be used instead of the original one. The most basic example of a metamodel is the linear regression of a complex phenomenon. For example, if we realise that when the input varies, the QoI returned by the model is approximately double the value supplied, we can emulate the behaviour of the model with a simple linear relationship $y = 2 \cdot x$. This regression line is obviously an extreme simplification of the underlying model as it does not attempt to mimic its complexity but only to return the input/QoI relationship which is very often simple. The choice of the appropriate metamodel is strongly dependent on the problem, whether it is a classical machine learning model (multi-linear models, polynomial regression, General Linear model), based on artificial neural networks (ANN) or defined ad-hoc for UQ analysis (Gaussian process regression/Kriging [39], Polynomial Chaos Expansion [40]). The advantage of using metamodels is their ability to model the problem even with small input dataset and the negligible computational cost with respect to the aforementioned standard direct approach. Consequently, when the original problem is too expensive, a reduced sampling of the input spaces can be generated and an appropriate metamodel trained on that data. The metamodel is then used instead of the original model, whether it is a forward, inverse or sensitivity analysis problem. Simulations using the surrogate model can be performed almost in real time. Consequently, all the techniques described above can be applied at low computational cost obtaining the same UQ if the metamodel is well trained (as discussed in Chapter 1). Owing to increased computational power, efficient techniques and, above all, the use of metamodels, UQ analyses can be applied to problems that were almost impossible to be solved until a few years ago.

In particular, the availability of these new UQ methodologies opens the way to unexplored possibilities in cardiac modelling. The in-silico heart models available

are indeed highly detailed, often with data extrapolated from medical analyses and the number of parameters controlling them is so large that a systematic study of the effect and variability of cardiac inputs is almost impossible with standard methods. Therefore, the aim of this thesis is to develop cardiac models that take into account the variability between individuals through UQ analysis and to derive a complete digital twin of the human heart to be used for medical application. In order to achieve such an ambitious goal, choices have to be made: which components of the heart can be simplified and which ones need to be described in detail? The UQ techniques described above, in particular sensitivity analyses, can provide the necessary answers. The *fil rouge* of this thesis is thus an iteration between two different research step: a modelling part, in which the model is updated by adding new components, and a model reduction one in which a sensitivity analysis defines the roadmap for the next modelling step. The result of this work was the development, from a simplified model with a single atrial and ventricular chamber, of an advanced in-silico duplicate of a whole human heart. The latter, not only includes the four chambers, the fast conduction system, a realistic orientation of the muscle fibres and the fluid-structure interaction between the heart wall and the blood but, above all, it is highly parametric, adaptable to the individual patient, and suitable for subsequent UQ analyses.

A brief outline of the uncertainty quantification techniques used within this thesis are presented in Chapter 2. In particular, the choice of input distributions based on appropriate calibration techniques and Shannon's entropy theory is discussed. The methodologies for performing forward analyses are then given, both in the case of error propagation and for determining the probability of exceeding a fixed threshold. The different sampling techniques (Monte Carlo, Latin Hypercube, quasi-Monte Carlo, etc.) are discussed with respect to their different convergence speed and usage hypothesis. The most common indices and optimal sampling methods for screening techniques, local and global sensitivity analyses are then presented, with particular reference to variance based sensitivity analysis. In particular, the different cross-validation methodologies for the detection of under/overfitting problems are presented.

In Chapter 3, a first UQ analysis of the human heart is presented. Starting from the original cardiac model, developed by [41], comprising of a single (left) ventricular chamber, we described an adaptive methodology to apply a metamodelling technique to the problem. The chosen metamodel, specifically an adaptive sparse Polynomial Chaos Expansion, allows to investigate which of the source of uncertainties play a major role on the electrical activation of the ventricle. This simplified model also allows direct control simulations to be carried out to verify the effectiveness of the metamodel for cardiac electrophysiology before applying it to more complete ones. This analysis confirmed the goodness of the use of polynomial chaos expansions as metamodels for the electrophysiology problems under consideration, in particular the proposed adaptive methodology for the choice of the hyper-parameters proved useful and effective. Furthermore, of all the parameters under examination, those of geometry and electrical conductivity have the greatest impact on the dynamics. This analysis, therefore, highlights

the need to focus subsequent modelling efforts on the geometric components of the model and on those structures capable of rapidly conveying the electrical signal through the tissue.

The electrophysiology model is therefore extended to the whole heart, including the fast conduction networks, as described in Chapter 3. In particular, the atrial (internodal bundles, Bachmann bundle) and ventricular (AV node, His bundle, bundle branches, and Purkinje network) fast conduction structures are also modelled in order to replicate proper physiological activation. Even the differences between the action potential response of the atria and ventricles are modelled, using different mathematical descriptions of cell properties (Courtemanche, Stewart and ten Tusscher-Panfilov cellular models). Furthermore, all the structures (the positions of fast conduction bundles, cell model parameters, etc.), are defined as a parametric variations of a reference model and the cardiac electrophysiology model is thus designed for UQ analyses. This realistic and highly parametric model of cardiac electrophysiology is GPU accelerated, allowing fast simulations of the entire cardiac electrophysiology.

The new electrical model allows unprecedented UQ analysis of cardiac electrophysiology. However, the number of uncertain parameters, greatly increased and multiple sensitivity analyses are needed to determine the relevant input quantities. Chapter 5, therefore, studies in detail the atrial uncertainty and its effect on ventricular quantities of interest. A sensitivity analysis based on the previously introduced adaptive technique it is used to determine which among internodal pathways positioning, conductivity and some parameters of the atrial cell model impacts most some relevant QoI (Bachmann bundle and AV node activation times). The results confirm that almost all atrial parameters do not influence the healthy activation of the ventricle. Electrical conductivity and AV-node delay are dominant over the entire dynamics. As a consequence, subsequent cardiac electrophysiology analyses can separate the two components (atrial and ventricular), drastically reducing the number of simulations needed to carry out the studies.

However, the complete electrophysiology model alone can not tackle research question related to the hemodynamics and the tissue dynamics. In Chapter 6 is presented a complete heart model that integrates the electrophysiology model with a fluid-structure solver capable of describing blood flow in detail. The high parameterization combined with an efficient GPU implementation provides an ideal model for future uncertainty quantification analyses.

The application of these UQ techniques has shown that the main difficulty in the study of complex models lies in a proper calibration of the uncertainties under investigation. Indeed, the available literature provides disagreeing data, the variation of which can lead to radically different results of the analyses. In Chapter 7, therefore, a technique that combines a Forward analysis with a Monte Carlo method to define a stability index for correlation tests is presented . In fact, in medical practice, measurement errors are often neglected in correlation analyses with the consequent risk, for small datasets, of having false results. We therefore propose an index that assesses the stability to perturbations (given by

measurement errors) of the dataset to strengthen classical correlation tests. Instead, in Chapter 8, a method based on metamodelling is proposed, in order to carry out nested sensitivity analyses. An uncertainty on the uncertainty itself is considered and an algorithmic procedure is introduced to determine whether this variability may affect the analysis performed.

UQ methodologies arise from an integration of numerical analysis, computer science, and classical statistics. In the course of the research work carried out on cardiac problems, we encountered several medical institutions willing to collaborate. Although many of the problems were solvable using classical statistical techniques, the results of these collaborations are briefly reported in Chapter 9 and 10. In particular, the DIANA-Game project was developed from a collaboration with the Unità professionale Centro di Formazione e Simulazione Neonatale (Centro NINA)- Azienda Ospedaliero Universitaria Pisana (AOUP). DIANA is software for teaching neonatal resuscitation procedures that exploits the ability of computer games to instruct in an effective and entertaining way. This software was subjected to a rigorous evaluation of its effectiveness, which included written tests and a group of students undergoing intensive traditional teaching. The validation of this approach, using stratified sampling validated by Monte Carlo methods, laid the foundation for further developments in on-web and augmented reality forms. Similarly, a collaboration with the Unità di Gastroenterologia Universitaria Pisana resulted in a project for the early diagnosis of esophagitis. The result of the study is that, thanks to certain non-invasive analyses, it is possible to discriminate more serious pathologies from less serious ones with very high precision, providing precise and rapid diagnoses before proceeding to further investigations. The ROC (Receiver Operating Characteristic) curve analyses performed provided the basis for further studies based on the search for the optimal predictive metamodel, determined by means of a Monte Carlo strategy on the hyperparameters that characterise it.

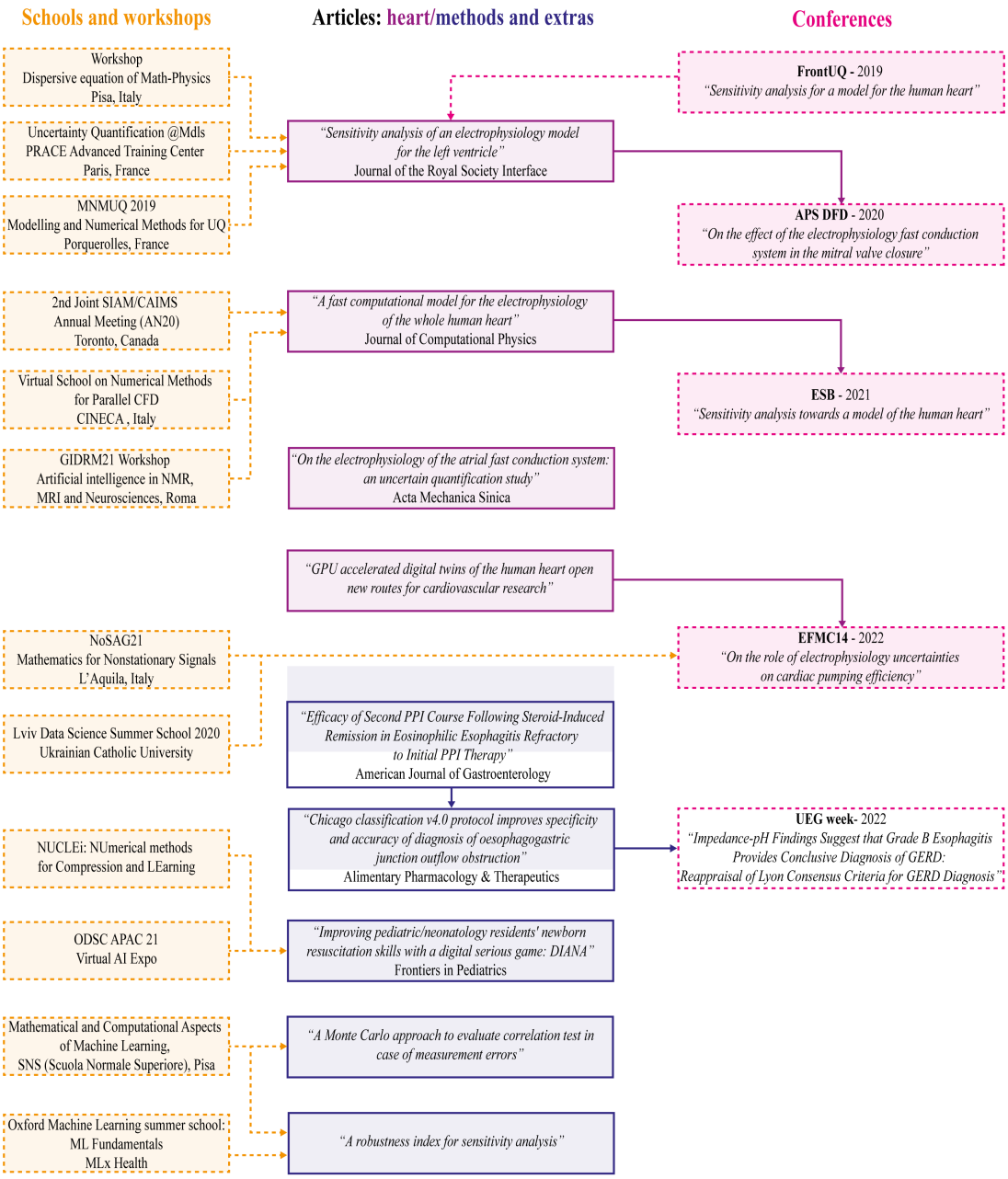

Figure 1.5: Graphical abstract of school/workshops (in orange), articles (in purple), and conferences (in pink) leading to the development of this thesis.

Chapter 2

Uncertainty Quantification

What is the UQ?

Uncertainty quantification (UQ) is a field of applied mathematics that investigates the relationships between inputs and outputs of a model affected by uncertainties.

UQ is a recent science emerged from the integration of statistical techniques and probability theory with numerical analysis and computer science. Indeed, it was only after the mid-90s that risk analyses were no longer conducted exclusively with statistical methodologies but rather integrating underlying physical models. [42]. Similarly, it is within the last few decades that engineering sciences have begun to add random variability to models to improve their predictive capabilities. By replacing deterministic models with their stochastic counterparts, it is feasible to integrate the uncertainties of the variables into the model, enriching the predictions made with confidence intervals on the actual goodness of the result. A consequence of the relative youth of this science, unlike other established mathematical fields (e.g. Algebra, Geometry, and even Numerical Analysis) is that there is still not a unified theory of UQ, just as there are no theoretical results on many UQ techniques that unequivocally determine which one is preferable.

As a science that is still not mature and originates from the well-established field of mathematical statistics, UQ is often referred to as a sub-sector of probability theory or as a complex form of error analysis. However, within the last year UQ developed as a novel branch of applied mathematics that is rooted in a solid mathematical foundation and developed by means of numerical analysis techniques, relying on tools proper to computer science (efficient software implementation, machine learning). Despite an important advanced mathematics base that makes it less accessible to practitioners, UQ has the characteristics of an applied science. The UQ methods are always aimed at solving applicative problems (risk analysis, probability estimation, variability calibration, Bayesian

optimisation) and cannot disregard efficient implementation.

With reference to Figure 1.4, a canonical mathematical model is made of a d-dimensional vector X which given as input to a model M, returns a family of outputs $M(X)$. These d outputs are often too complex (in terms of quantity of data and difficulty of interpretation), so scalar quantities of interest (QoI) $g(X) := \text{QoI}\,(M(X))$ are extracted from them. Evaluate a model means fix all the values of the vector X, apply the model M and then analyse the quantity of interest $f(X)$ obtained. However, by performing this single simulation, the result thus obtained is hardly generalizable. In fact, some of the input variables may have a high variation due to a lack of knowledge (e.g. the parameters of cardiac cell models are often selected by calibration on other observable quantities to obtain a realistic result) or an intrinsic variability of a characteristic (no two human hearts have the same atrioventricular volumes). From a methodological point of view, the problem can be extended straightforwardly: the input variables and quantities of interest determined are replaced by their probabilistic counterparts, a proper multivariate random variable.

Remark 1. *Considering the cardiac model as an example, the vector X has a dimension of hundreds of values, ranging from macroscopic characteristics (volume of the chambers, electrical conductivity, extension of the fast conduction fibres) to microscopic ones (parameters of the cellular patterns, local orientation of the muscle fibers). The M model is the mathematical description of the heart associated with the corresponding numerical solver. The output is the time-varying description of the electrical, muscular, and blood flow activation profile. From the latter, simple scalar quantities of high medical interest are extracted, such as ejection fraction, chamber activation time and signal propagation uniformity.*

The variability that is incorporated in the input vector X may have different sources. The first type encountered in UQ problems is *epistemic uncertainty*. This is the uncertainty given by the experimenter's lack of knowledge of a given quantity, which is then described by a probabilistic distribution whose estimate is based on real data. This randomness can be measurement error (the precision of an instrument), individual variability or even the unreliability of the model itself. It is common to find a further subdivision of the epistemic uncertainty into *parametric uncertainty* (the uncertainty on the inputs /parameters of the study) and *model uncertainty* (the uncertainty given by the lack of trust in the mathematical model itself). A different type of variability is *aleatoric uncertainty*, which does not depend on differences between individuals or measurement errors, but is instead a random element that can vary with each model evaluation. As an example, if the the result depends on a random step (e.g. the roll of a die, a random market fluctuation) this is an aleatoric uncertainty.

It exists several kinds of UQ analysis. The first family of problems is called *forward analysis* and investigates how variability of inputs propagates to outputs. This can be further subdivided in *forward propagation* (given the inputs distribution, find the QoI distribution), the *reliability/certification problem* (find the probability that a given event occurs, typically used to assess the risk of failure

of an engineering system) and the *prediction problem* (find the maximum subsets of the QoI values for a prescribed probability). Other techniques are devoted to solve *inverse problem*, i.e. to identify the distribution of inputs that might have generated a family of available outputs. Finally, the *sensitivity analysis* consists in identifying the parameters that mostly influence the model. A natural consequence of sensitivity analysis is a *model reduction* of the problem, that is limiting further studies to only relevant variables to reduce the computational burden of the analysis [42].

Therefore, this chapter offers a guide through the different UQ techniques. With no pretence of completeness, this is a handbook of techniques with annotated bibliographical references useful for applications. In particular, it was decided to neglect intrusive UQ techniques (e.g. stochastic Galerkin, theory of stochastic PDEs) that require substantial modifications of the problem under investigation to be applied. Instead, the focus of the chapter is on efficient black-box methodologies (based on metamodelling and machine learning techniques) as they are of immediate utility for even the most disparate problems. First, input spaces are presented, discussing the copula formalism for modelling non-complex relations between variables, Shannon's information theory, and techniques for sampling arbitrary distributions. Afterwards, different space sampling methodologies (Monte Carlo, Latin Hypercube, low discrepancy sequences etc.) are discussed. Indeed, proper sampling allows UQ analysis with a small number of simulations and can provide a good dataset for training metamodels. Sensitivity analysis techniques for model reduction are then presented, distinguishing between local techniques (limited input information) and global techniques (detailed information). Metamodelling techniques are then treated in the last part of the chapter, such as Polynomial Chaos Expansion and Gaussian process regression (Kriging). An outline of the symbols used in this chapter is given in Table 2.1.

Symbol	**Name**	**Description**
$X = (X_1, \cdots, X_d)$	Input vector	Is a d-dimensional random variable that has real values in most UQ applications. φ_X is the probability density function of X.
$Y = g(X)$	QoI vector	Is a one-dimensional (real-valued) random variable. It is obtained as the propagation of input X through g. The function g is the composition of the model M and the QoI extraction.
$F_i(x) = \mathbb{P}(X_i \leq x)$ $\mathcal{C}$	Marginals Copula	F_i is the marginal distribution of the input X_i. $\mathcal{C}$ is the copula describing the multivariate relationship.
$\mathcal{H}$	Shannon entropy	Is the Shannon entropy of a discrete/continuous random variable.
$(\mathcal{X}, \mathcal{Y})$ $\{(x^{(i)}, y^{(i)})\}_{i=1}^n$	Dataset	$\mathcal{X} = \{x^{(i)}\}_{i=1}^n$ is a sample of the input space. Each value is a d-dimensional vector: $x^{(i)} = (x_1^{(i)}, \cdots, x_d^{(i)})$. $\mathcal{Y} = g(\mathcal{X}) = \{y^{(i)}\}_{i=1}^n$ is the corresponding model QoI.

Table 2.1: Outline of the symbols used in the chapter.

2.1 Input vector

Underlying all uncertainty quantification analyses is the distribution of input spaces. Formally, an input is a random vector $X = (X_1, \cdots, X_d)$ for which each element X_i corresponds to a certain uncertain quantity (e.g. a model parameter, an initial condition). This vector in most of the application it is real valued and the distribution of X is often considered a distribution with density:

$$\mathbb{P}(X \in A) = \int_A \varphi_{(X_1,\cdots,X_d)}(x_1, \cdots, x_d)dx_1 \cdots dx_d = \int_A \varphi_X(x)dx \tag{2.1}$$

with $\varphi_X(x)$ its probability density function and x a value of $\mathbb{R}^d$.

On the other hand discrete distributions are described by their probability mass function. In case the input space includes both continuous and discrete variables, it is possible to define models that take both components into account. The variable X is therefore characterised by a multidimensional distribution. Except in some specific cases (e.g. Multivariate Normal distribution), multidimensional distributions are difficult to describe as there are complex relationships between the variables that do not always follow parametric rules. Therefore, one relies on the copula theorem to break down the description of X into that of its marginal distributions (1-dimensional) and an appropriate function, called a copula, that describes their relationship. These marginals are often approximated by families of known distributions (Gaussian, Uniform, LogNormal, Exponential) in order to guarantee useful theoretical properties and to simplify subsequent analyses.

Remark 2 (Correct input distribution)**.** *The choice of a correct input distribution is crucial: an erroneous decision propagates through the study leading to totally unreliable results in both forward analysis (wrong estimates of probability of events) and sensitivity analysis (model reduction on quantities incorrectly assumed to be more important). The steps of choosing, calibrating, and verifying distributions are therefore necessary in any uncertainty quantification analysis. In the event of insufficient information, the study should be discontinued and reduced to those techniques that do not require input space distributions (local sensitivity analysis).*

2.1.1 Copula formalism

The copula formalism is based on Sklar's theorem, which states that any multivariate joint distribution (with continuous marginal CDFs) can be written in terms of univariate marginal distribution functions and a copula (which is a proper multivariate cumulative distribution function) describing the dependency structure between the variables [43, 44].

Given a d-dimensional random vector $X = (X_1, \cdots, X_d)$ with continuous marginals ($F_i(x) = \mathbb{P}(X_i \leq x)$), by applying the universality of the uniform theorem (see § 2.1.3) to each component, the random vector

$$(\mathcal{U}_1, \cdots, \mathcal{U}_d) = (F_1(X_1), \cdots, F_d(X_d))$$

has marginals that are uniformly distributed on the interval $[0, 1]$. The copula of $X = (X_1, \cdots, X_d)$ is the joint cumulative distribution function (CDF) of $(\mathcal{U}_1, \cdots, \mathcal{U}_d)$:

$$\begin{aligned}\mathcal{C}(u_1, \cdots, u_d) :=& \mathbb{P}\left(U_1 \leq u_1, \cdots, U_d \leq u_d\right) \\ =& \mathbb{P}\left(X_1 \leq F_1^{-1}(u_1), \cdots, X_d \leq F_d^{-1}(u_d)\right)\end{aligned}$$

Definition 1. *$C : [0, 1]^d \to [0, 1]$ is a d-dimensional **copula**, if $\mathcal{C}$ is a joint cumulative distribution of a d-dimensional random vector on the unit cube $[0, 1]^d$ with uniform marginals.*

Theorem 1 (Sklar)**.** *Every multivariate cumulative distribution function*

$$CDF(x_1, \cdots, x_d) = \mathbb{P}\left(X_1 \leq x_1, \cdots, X_d \leq x_d\right)$$

of a random vector $(X_1, \cdots, X_d)$ can be expressed in terms of its marginals $F_i(x_i) = \mathbb{P}\left(X_i \leq x_i\right)$ and a copula $\mathcal{C}$:

$$CDF(x_1, \cdots, x_d) = \mathcal{C}(F_1(x_1), \cdots, F_d(x_d))$$

and the copula is unique if the marginals F_i are continuous.

This formalism makes it possible to work with arbitrary multivariate joint distributions. However, calibrating the copula appropriately can be a challenging task because as the size of the input space grows, an increasing amount of data is required to identify it correctly. Thus, simplifying assumptions are often made about the copula (i.e. it is assumed to have a known, parametric distribution) and only its parameters are calibrated. In addition, appropriate choices of copula (e.g. Gaussian copula or Elliptical copula) allows easy sampling strategies from the multidimensional distribution [45, 46].

There are several strategies for calibrating the marginals and the copula. A canonical approach is the two-steps calibration: the marginals are approximated by empirical distributions, the copula parameters are then estimated by maximum likelihood [47]. More complex alternative approaches instead exploit the joint estimation of copula and marginals [48, 49].

In UQ applications, the copula itself can be effected by uncertainties that can be included in the study. In addition, it may be interesting to investigate how a higher/lower correlation between variables (described by the copula parameters) may influence the analysis. In such cases, one exploits the corollary of Sklar's theorem that guarantees the existence of a d-dimensional distribution once the copula and marginals are fixed. The parameters of the copula then become additional uncertain quantities of the study.

Corollary 1 (Converse)**.** *Given a copula $\mathcal{C} : [0, 1]^d \to [0, 1]$ and marginals $F_i(x)$, then $\mathcal{C}(F_1(x_1), \cdots, F_d(x_d))$ defines a d-dimensional cumulative distribution function with marginal distributions $F_i(x)$.*

The main advantage of writing a multivariate distribution using a copula and marginals is the possibility of using the Nataf transformation [45]. This transformation, in its standard version, only works for Gaussian copula [46]. Its generalised version works instead for arbitrary elliptical copulas [50]. Referring to Lebrun et al [50] for details, the Nataf transformation is an isoprobabilistic transformation that maps the random vector X with a complex distribution into the random vector $\mathcal{U}$ which follows the standard representative distribution of the copula of X. In the case of Gaussian copula, in particular, the generalized Nataf isoprobabilistc transformation maps the physical space of the probabilistic input data into the standard space, where all the variables are independent and follow the same normal distribution with zero mean and unit variance

An appropriate choice of a copula (Gaussian or more generally elliptic) thus allows to define a space that, by means of the Nataf transformation, is always reducible to a random vector with independent components. UQ techniques requiring the independence of vectors are therefore always applicable.

Remark 3 (QoI)**.** *The quantity of interest also has a probabilistic interpretation. In application contexts, however, the QoI is typically a one-dimensional Y random variable, so its description can do without the multidimensional formalism and copula.*

2.1.2 Shannon entropy

In several practical applications, especially in the medical field, the UQ scientist does not have databases on which to calibrate the distribution of inputs. In these cases, an alternative strategy for choosing distributions must be defined on the basis of information available from the literature.

Shannon's theory provides a method for choosing the optimal distribution given prior information. The basis of this theory is the definition of the entropy of a random variable.

Definition 2. *Given a discrete random variable X, with possible outcomes $e_1, \cdots, e_k$, the **Shannon entropy** [51] of X is defined as:*

$$\mathcal{H}(X) = \mathbb{E}\left[-\log_b \mathbb{P}(X)\right] = -\sum_{i=1}^{k} \mathbb{P}(e_i) \log_b \mathbb{P}(e_i) \tag{2.2}$$

*Given a random variable X with probability density function φ_X whose support is $\mathcal{S}$, the **differential entropy** (or continuous entropy) [52] is defined as:*

$$\mathcal{H}(X) := -\iint_{\mathcal{S}} \varphi_X(x) \log_b \varphi_X(x) dx \tag{2.3}$$

where the base of the logarithm b can be chosen freely. Common choices include $b = 2$ or $b = e$.

Based on this definition of entropy, one can state the principle of maximum entropy: *the probability distribution which best represents the current state of*

knowledge is the one with largest entropy. According to this principle, the distribution with the largest entropy should be chosen as the least informative default.

Definition 3. *A **maximum entropy probability distribution** has entropy that is at least as great as that of all other members of a specified class of probability distributions.*

Given testable information (a statement about the probability distribution whose truth or falsity is well-defined), the maximum entropy procedure consists of seeking the probability distribution which maximizes information entropy, subject to the constraints of the information. In particular, if only the mean and variance of a distribution are known to the experimenter, the corresponding maximum entropy function is precisely the Gaussian distribution.

Remark 4 (Gaussian is the right choice)**.** *Shannon's entropy theory is one of the reasons why Gaussian distributions are so common in applications, especially in medicine. With the sample sizes typical of medical studies, it is only possible to accurately estimate the mean and variance and not the higher order moments. With these two values fixed, the distribution that maximises entropy is precisely the Gaussian. The other two reasons for the choice of this distribution in medical analyses are: its good theoretical properties and the fact that many quantities are defined as the average of analyses performed.*

The maximum entropy distributions for multiple application cases are shown in Table 2.2. For many of the reported distributions, once the constraints and support are fixed, there is an analytical formula for the parameters of the distribution (Uniform, Bernoulli, Normal). In general, however, especially when working with truncated distributions, an analytical formula does not necessarily exist. To determine the parameters of the maximum entropy distribution, one possibility is to solve the associated differential system [53]. However, in the case of one-dimensional distributions, a brute-force approach is always possible, where one searches in the parameter space for the set of values that minimises the distance of the constraints with the imposed constraints.

2.1.3 Generating the pseudo-random sample

The input sampling procedure needed for the UQ analysis, is based on a pseudo-random number generator for arbitrary distributions. However, sampling software typically generates pseudo-random sequences from some commonly used distributions (e.g. Gaussian, Uniform, LogNormal, Exponential), rather than arbitrary distribution resulting from the problem at study. In this case, different sampling strategies should be used, such as the Inverse Transform Sampling (ITS) and the Acceptance Rejection method (AR) which are briefly presented here. Modern alternatives exist to generate these numbers in shorter time compared to ITS or AR (e.g. slice sampling [54], rejection sampling [55]) or from larger input sizes (to handle the curse of dimensionality, e.g. Metropolis-Hastings sampling [56]). However, in UQ analyses, the evaluation of the model is typically much more time-consuming than the time required to generate the sampling.

Constraints	**Support**	**Distribution**
	$[a, b]$	Uniform
$\mathbb{E}[X] = p$	$\{0, 1\}$	Bernoulli
$\mathbb{E}[X] = \frac{1}{p}$	$\mathbb{N} \setminus \{0\}$	Geometric
$\mathbb{E}[X] = \frac{1}{\lambda}$	$[0, \infty)$	Exponential
$\mathbb{E}[\lvert X - b \rvert] = \mu$	$(-\infty, \infty)$	Laplace
$\mathbb{E}[X] = \mu$ $\mathbb{E}[(X - \mu)^2] = \sigma^2$	$(-\infty, \infty)$	Normal
$\mathbb{E}[X] = \mu_T$ $\mathbb{E}[(X - \mu_T)^2] = \sigma_T^2$	$[a, b]$	Truncated Normal
$\mathbb{E}[\log(X)] = \mu$ $\mathbb{E}[(\log(X) - \mu)^2] = \sigma^2$	$(0, \infty)$	LogNormal

Table 2.2: Maximum entropy distributions for different constraints on both statistical moments and support. The parameters of the distributions can be obtained by means of an analytical formula in some cases and as solutions to minimisation problems otherwise. Where p is the parameter of the Bernoulli/Geometric distribution, λ the rate parameter of the Exponential distribution, μ and μ_T are the mean/truncated mean of the Laplace, Normal, LogNormal and Trucated normal distributions while σ, σ_T their standard deviation.

Inverse Transform Sampling

Inverse transform sampling/inversion sampling is a method for generating a sample from any *one-dimensional* probability distribution. Given a real-valued one-dimensional random variable X admitting a density $\varphi_X(x)$, its cumulative distribution function satisfies:

$$F_X(x) := \mathbb{P}(X \leq x) = \int_{-\infty}^{x} \varphi_X(t)dt \tag{2.4}$$

The Inverse Transform Sampling method samples from the distribution of X relying on the universality of the uniform theorem.

Theorem 2 (Universality of the uniform)**.** *Given a continuous one-dimensional random variable X and its cumulative distribution function $F_X(x)$. Then the variable $Y = F_X(X)$ has a standard uniform distribution.*

As a consequence, if Y is a variable with a standard uniform distribution, $F_X^{-1}(Y)$ has the same distribution as X. Formally, the Inverse Transform Sampling algorithm is the following:

1. Generate n samples $\{y^{(i)}\}_{i=1}^n$ from the uniform distribution $\mathcal{U}([0, 1])$ with a standard pseudo-random generator.
2. Invert the CDF analytically or numerically: $F_X \to F_X^{-1}$
3. Apply the inverse CDF to the sample:

$$\{x^{(i)}\}_{i=1}^n := \{F_X^{-1}(y^{(i)})\}_{i=1}^n$$

4. $\{x^{(i)}\}_{i=1}^{n}$ is a sample of the original distribution.

Remark 5. *If the input vector is considered to consist of d mutually independent one-dimensional variables, this method allows the d-multidimensional input vector X to be sampled by generating each one-dimensional component independently.*

The main drawback of this method is that $F_X(x)$ must be obtained for the distribution being sampled. Not all distributions admit an explicit formulation for the CDF which, once calculated, must be inverted (analytically or numerically) to apply the algorithm. An error in the approximation of the inverse propagates to the sample and gives potentially erroneous results. Despite its simplicity, this method requires more computing time than other approaches to obtain a sample and does not generalize to multiple dimensions [55, 57, 58].

One technique to improve the standard inverse transform sampling method is to use a polynomial approximation based on Chebyshev polynomials [59]. Assuming a bounded support $[a, b]$ of the density $\varphi_X(x)$ (if the interval or the support is not limited, is sufficient to take $[a, b]$ such that $\int_a^b \varphi_X(x)dx \sim 1$), the density can be written as $\varphi_X(x) = \frac{f(x)}{\int_a^b f(x)dx}$. The idea is to replace f with its polynomial approximation:

$$\tilde{f}(x) = \sum_{k=0}^{m} \alpha_k \mathcal{T}_k \left(\frac{2(x-a)}{b-a} - 1 \right) \tag{2.5}$$

where $\mathcal{T}_k(x) := \cos k \cos^{-1} x$ is the k^{th} Chebyshev polynomial, and $\alpha_k \in \mathbb{R}$ are the expansion coefficients, which can be calculated with $\mathcal{O}(m \log m)$ operations by a fast cosine transform [60]. Using the polynomial approximation, the approximated CDF is:

$$\begin{aligned} &\tilde{F}(x) \approx F(x) := \int_a^x f(t)dt \\ &\tilde{F}(x) = \sum_{k=0}^{m} \alpha_k \int_a^x \mathcal{T}_k \left(\frac{2(t-a)}{b-a} - 1 \right) dt = \sum_{k=0}^{m} \beta_k \mathcal{T}_k \left(2\frac{x-a}{b-a} - 1 \right) \\ &\tilde{F}_X(x) := \frac{\tilde{F}(x)}{\tilde{F}(b)} \end{aligned} \tag{2.6}$$

where β_k can be derived with $\mathcal{O}(m)$ operations and $\tilde{F}_X(x)$ is normalized to obtain the approximated CDF of the density $\varphi_X(x)$. The normalization also guarantees that $\tilde{F}_X(x)$ is a CDF.

Instead of inverting the CDF, the values $\{x^{(i)}\}_{i=1}^{n}$ are obtained throughout bisection from the root-finding problem:

$$\{\tilde{F}_X(x^{(i)})\}_{i=1}^{n} = \{y^{(i)}\}_{i=1}^{n} \tag{2.7}$$

This approach is faster and less prone to inversion error than canonical inverse sampling transformation for each class of probability distribution that can be numerically approximated and evaluated [59].

Acceptance-Rejection method

Acceptance-rejection method [61, 62] allows to sample from a distribution without inverting the CDF. This method is therefore more robust compared to inverse transform sampling (if there is no analytical formula for $F_X^{-1}(x)$). Furthermore, it can be applied to multidimensional distributions.

Given the continuous random variable X with density $\varphi_X(x)$, $x \in \mathbb{R}$ and suppose that exists another auxiliary density $\delta(x)$ and a constant $c \geq 1$ such that:

$$\varphi_X(x) \leq c \cdot \delta(x) \quad \forall x \in \mathbb{R}^d \tag{2.8}$$

Moreover, assume that the auxiliary density $\delta(x)$ is easier to sample (e.g. a uniform distribution on the support of $\varphi_X(x)$). As a remark, the minimum value of the constant is $c = \sup_x \left(\frac{\varphi_X(x)}{\delta(x)}\right)$

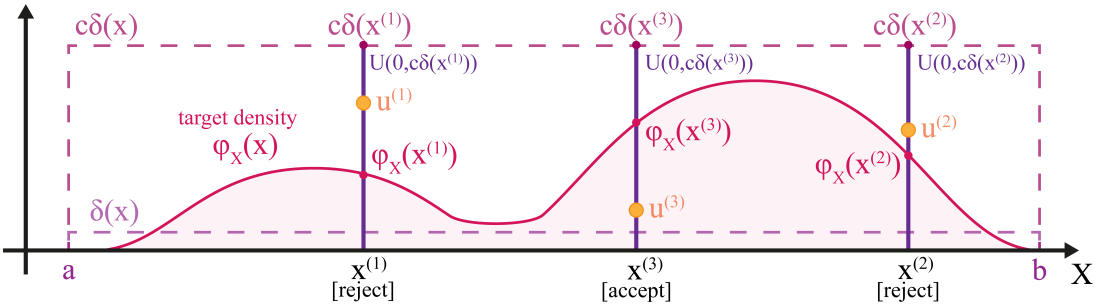

Figure 2.1: Example of one-dimensional acceptance-rejection method for target density $\varphi_X(x)$ with an auxiliary density $\delta(x) \sim \mathcal{U}([a, b])$. A value $x^{(1)}$ is sampled accordingly to $\delta(x)$, the corresponding uniform distribution $\mathcal{U}\left([0, c \cdot \delta(x^{(1)})\right)$ is sampled obtaining the value $u^{(1)}$. The latter is compared with $\varphi_X(x^{(1)})$ and since $u^{(1)} > \varphi_X(x^{(1)})$ is rejected. Similarly, the second sampled point $x^{(2)}$ is rejected. However, the third point $x^{(3)}$ satisfies $u^{(3)} < \varphi_X(x^{(3)})$, and therefore $x^{(3)}$ is accepted as a value sampled from $\varphi_X(x)$.

With reference to Figure 2.1, the algorithm is the following:

1. Generate a sample x^* from the auxiliary density $\delta(x)$.
2. Generate a sample u^* from the uniform distribution $\mathcal{U}([0, c \cdot \delta(x^*)])$.
3. Check if $u^{(*)} \leq \varphi(x^*)$:

True: x^* can be considered a sample from the density $\varphi(x^*)$. End the algorithm

False: Return to step 1.

The convergence of the algorithm is guaranteed by the fact that the conditional distribution of the variable X with density $\delta(x)$, given that the event $\{\mathcal{U}([0, c \cdot \delta(X)]) \leq \varphi(X)\}$ is the CDF $F_X(x)$ of the target distribution [63, 61].

However, this algorithm can be costly. Indeed, first the distribution $\delta(x)$ has to be sampled, then $\mathcal{U}([0, c \cdot \delta(x)])$ must be sampled as well, and finally the value obtained is compared against $\varphi_X(x)$. If the value u^* is higher than $\varphi_X(x^*)$ the point is rejected and the method has to restart. Therefore, it is straightforward that the smaller the distance between the original density $\varphi_X(x)$ and $\delta(x)$, the less evaluation has to be carried out before a positive result is obtained. Uniform auxiliary distributions are easy to implement but do not always give the best result because their shape is different from several empirical distributions. However, any distribution from which one already knows how to sample can be chosen as an auxiliary function.

Remark 6 (How many iterations?)**.** *The algorithm presented at every iteration determines whether to return the value obtained or to restart the procedure. The aim is to determine on average how many times it rejects the result before returning the correct value. Consider the random variable N which counts how many iterations of the algorithm are required. This random variable has a geometric distribution (e.g. $\mathbb{P}(N = n) = (1 - p)^{n-1}p$) with success probability $p = \mathbb{P}\left(\mathcal{U}([0, c \cdot \delta(x)]) \leq \varphi_X(x)\right)$. It holds that $p = \frac{1}{c}$ and therefore the average number of iterations is [63]:*

$$\mathbb{E}[N] = \frac{1}{p} = c$$

2.2 Forward analysis

Forward analysis investigates how uncertainty in the inputs propagates through the model to the outputs and, consequently, to the quantities of interest. Among the various UQ problems (input calibration, sensitivity analysis, inverse UQ), this problem is the less complex to solve since the resolution is based on the well-known integration methodologies. Indeed, with reference to Figure 2.2, of the quantities of interest, mainly the statistical moments (mean, variance, skewness) or the probability of an event (e.g. that the QoI exceeds a certain threshold) are studied. Respectively, these can be written using the *law of the unconscious statistician* [64] as the following integrals:

$$\begin{aligned} \mu(g) &= \int_{\Omega} g(x)\varphi_X(x)dx \\ \sigma^2(g) &= \int_{\Omega} \left(g^2(x) - \mu(g)^2\right)\varphi_X(x)dx \\ \mathbb{P}(g(x) \in \mathcal{S}) &= \int_{\Omega} \mathbf{1}_{\{g(x)\in\mathcal{S}\}}\varphi_X(x)dx \\ \mathbb{P}(g(x) \geq \mathrm{t}) &= \int_{\Omega} \mathbf{1}_{\{g(x)\geq \mathrm{t}\}}\varphi_X(x)dx \end{aligned} \tag{2.9}$$

where $\varphi_X(x)$ is the density function of the input, $\Omega \subseteq \mathbb{R}^d$ is its support, $g(x) : \mathcal{D} \subseteq \mathbb{R}^d \to y \in \mathbb{R}$ is the model, $\mathcal{S} \subseteq \mathbb{R}$ is a possible set of outcomes, t is a threshold, and $\mathbf{1}$ is the indicator function.

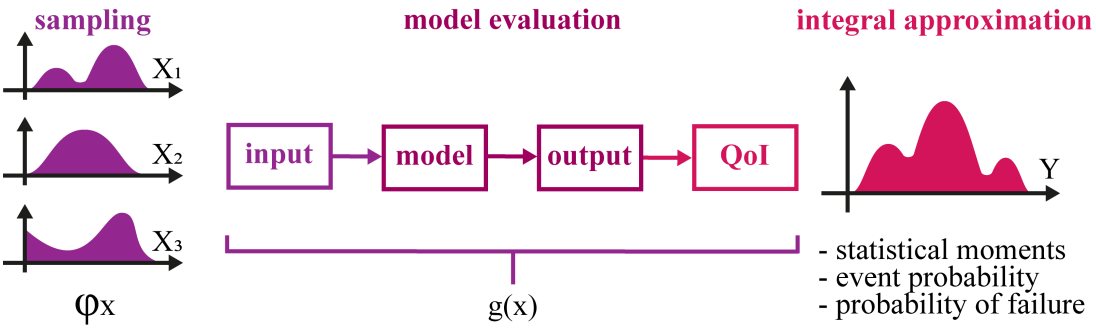

Figure 2.2: Sketch of the forward analysis. The input distribution with joint density $\varphi_X(x)$ is sampled. The values are evaluated by the model and a QoI is extracted from the outputs, obtaining for each sample x the corresponding $g(x)$. The latter is studied using integral approximation of QoI statistical moments (mean, variance, skewness), percentiles, event probability and probability of failure.

These integrals can be calculated using a Monte Carlo approach [65], which consists of the following procedure:

- The input space X is sampled n times according to its probability distri-

bution $\varphi_X(x)$ obtaining n d-dimensional inputs:

$$\{x^{(i)}\}_{i=1}^n := \{(x_1^{(i)}, \cdots, x_d^{(i)})\}_{i=1}^n$$

- The model $g(x)$ it is evaluated for each $\{x^{(i)}\}_{i=1}^n$, obtaining $\{g(x^{(i)})\}_{i=1}^n$. This step, in UQ applications, is the computational bottleneck.
- The integrals to be calculated are replaced by their estimators.

Remark 7 (standard MC integration)**.** *The standard MC integration aims to solve an integral $\int_\Omega f(x)dx$. This is the same as using an uniform distribution $\varphi_X(x)$. In this elementary case, therefore, we can sample directly from Ω uniformly and apply straightforward the estimator. In the general case in which we want to approximate $\int_\Omega f(x)\varphi_X(x)dx$ and, therefore, the input must be sampled from the more complex input space with density $\varphi_X(x)$. This can be done with several techniques, including the acceptance-rejection method [62, 61].*

2.2.1 Efficient sampling strategies

The sampling strategy of the input space can greatly influence the speed of convergence. Classical quadrature formulae (like the Gaussian quadrature rule) are capable of approximating an integral with a few points but suffer from the curse of dimensionality. Indeed, as the size of the input space increases they become less and less efficient. Furthermore, many of the integration methods are not extensible, meaning that if one wants to increase the accuracy, it is necessary to redefine the sampling to be calculated from scratches.

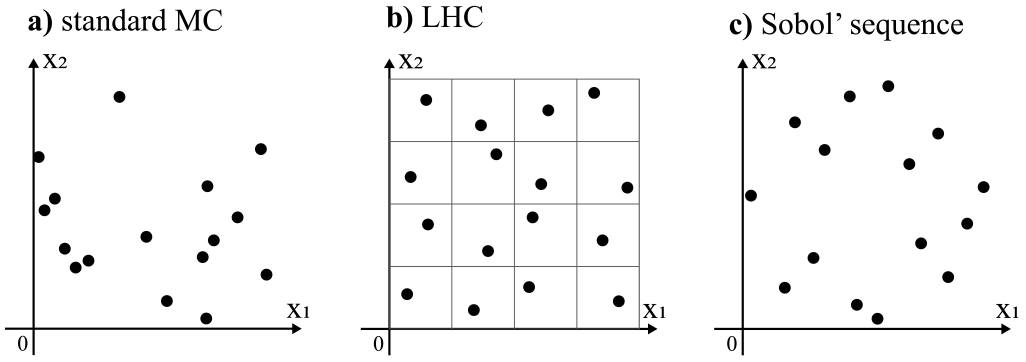

Figure 2.3: Examples of three different sampling strategies applied to a $d = 2$ input space of uniform random variables. Standard MC (Panel a) does not prevent clustering, while both Latin HyperCube Sampling (Panel b) and Sobol' low discrepancy sequence (Panel c), produce a more homogeneous distribution that better fills the input space.

An alternative to grid-based methods are the aforementioned **Monte Carlo (MC) integration rules**. With reference to Figure 2.3, MC methods are highly

dependent on the clustering of the input data. If the sampling points are too close together, they do not add enough new information and integration requires additional values.

Standard Monte-Carlo

The methodologies for calculating integrals based on random sampling are all variants of the Monte Carlo (MC) method.

Suppose we want to approximate a multidimensional integral:

$$I(f) := \int_{\Omega} f(x)\varphi_X(x)dx \tag{2.10}$$

This can be interpreted as the expectation of a function $f(x)$, where X is the random variable with density $\varphi_X(x)$ and Ω its support. For UQ applications, $f(x)$ is some function of the model QoI $g(x)$. When calculating the mean of the QoI, it holds $f(x) = g(x)$. Otherwise, when calculating the probability of exceeding a threshold t: $f(x) = \mathbf{1}_{\{g(x)\geq \mathrm{t}\}}$

In order to simplify the notation and conform to the typical terminology of MC techniques, an isoprobabilistic transformation can be used to reduce the integral calculation to:

$$I(f) := \int_{\mathbb{I}^d} f(x)dx \tag{2.11}$$

where the domain is the unit cube $\mathbb{I}^d = [0,1]^d$ and the variables are uniformly distributed.

Definition 4. *The **Monte Carlo quadrature formula** is based on the probabilistic interpretation of the integral. Given a sequence $\{x_i\}_{i=1}^n$ sampled from the input space X, the empirical approximation is:*

$$I_n(f) = \frac{1}{n}\sum_{i=1}^{n} f(x^{(i)}) \approx I(f)$$

which is unbiased (i.e. $\mathbb{E}[I_n(f)] = I(f)$) and convergent according to the strong law of large numbers:

$$\lim_{n\to\infty} I_n(f) \to I(f) \tag{2.12}$$

The corresponding MC integration error is defined as:

$$\varepsilon_n(f) = I(f) - I_n(f) \tag{2.13}$$

The Central Limit Theorem (CLT) describes the behaviour of this error.

Theorem 3 (Convergence)**.** *For n large:*

$$\lim_{n\to\infty} \mathbb{P}\left(a < \frac{\sqrt{n}}{\sigma}\varepsilon_n < b\right) = \mathbb{P}(a < \mathcal{N}(0,1) < b) \implies \varepsilon_n(f) \approx \frac{\sigma}{\sqrt{n}}\mathcal{N}(0,1)$$

where $\mathcal{N}(0,1)$ is a standard normal distribution and σ^* is the (unknown) standard deviation of f. As a consequence, the MC integration error is:

$$\varepsilon_n(f) = \mathcal{O}\left(\sigma\frac{1}{\sqrt{n}}\right) \approx \mathcal{O}\left(\frac{1}{\sqrt{n}}\right)$$

The reported theorem is an asymptotic estimate for the calculation of any integral quantity. When working with a small sample size, this estimate is therefore no longer reliable. In addition, in the case of specific problems (e.g. when one wants to estimate the average QoI or calculate the probability of an event) a much more precise estimates can be obtained without asymptotic Gaussian approximation [66].

Remark 8 (Sample size)**.** *Using the CLT, the number of points n to ensure an error of size at most ε with confidence level c is:*

$$n = \frac{\sigma^2 s(c)}{\varepsilon^2}$$

with $s(c)$ the confidence function for a normal variable: $c = \int_{-s(c)}^{s(c)} \frac{1}{\sqrt{2\pi}} e^{-x^2/2} dx$. In practice the variance σ^2 is unknown and difficult to estimate. A few points can be used to get an estimate of the variance and use it to produce the right sampling dimension.

The Monte Carlo method is therefore capable of approximating any integral (at arbitrary dimensions) and the speed of convergence does not depend directly on the size of the input space. The drawback of this methodology is that the speed of convergence is very slow. Structured grid exhibits stronger convergence properties (but dependent on dimension), for example a k^{th}-order quadrature rule has a convergence rate of $\mathcal{O}\left(n^{-k/d}\right)$ on a d-dimensional space, and thus MC is better if $\frac{k}{d} < \frac{1}{2} \implies d > 2k$.

Variance reduction methods

The MC method converges with a speed dependent on the sample size and the standard deviation σ of the function $f(x)$ to be integrated. Therefore, variance reduction methods modify the integral to reduce the σ and thus speed up convergence (e.g. an elementary approach may be to divide the integral into a sum of several sub-integrals, whose σ is much smaller).

Among the variance reduction methods, **stratification** is an efficient approach that combines the benefits of a grid based rule with those fully random [30]. The idea is to divide the input domain into regions of equal size and calculate the integral over each part. In this way, the total variance is the sum of the contributions and is therefore less than/equal to the original one σ^2. Furthermore, this technique avoids the clustering of points.

Formally, to approximate $\int_\Omega f(x)\varphi_X(x)dx$:

1. Split the integration region Ω into m pieces $\{\Omega_k\}_{k=1}^m$ such that:

$$\Omega = \bigcup_{k=1}^{m} \Omega_k$$

2. In each sub-region $\{\Omega_k\}_{k=1}^m$, sample n_k points $\{x^{(i,k)}\}_{i=1}^{n_k}$ using the sub-region density:
$$\varphi_{X,k}(x) = \frac{\varphi_X(x)}{\int_{\Omega_k} \varphi_X(x)dx}$$
where $\varphi_X(x)$ is the original density.

3. The **stratified quadrature formula** is:
$$I_n(f) = \sum_{k=1}^{m} \int_{\Omega_k} \varphi_X(x)dx \cdot \left(\frac{1}{n_k} \sum_{i=1}^{n_k} f\left(x^{(i,k)}\right) \right)$$
with $n = \sum_{k=1}^m n_k$.

The corresponding integration error is:

$$\begin{aligned}
\varepsilon_n(f) := I(f) - I_n(f) &= \sum_{k=1}^{m} \varepsilon_k(f) \\
\varepsilon_k(f) &\approx \frac{\overline{\varphi}_{X,k}}{\sqrt{n_k}} \left(\int_{\Omega_k} (f(x) - \overline{f}_k)^2 \varphi_{X,k}(x)dx \right)^{1/2} = \sqrt{\frac{\overline{\varphi}_{X,k}}{n_k}} \sigma_k \\
\overline{\varphi}_{X,k} &:= \int_{\Omega_k} \varphi(x)dx \\
\sigma_k &:= \left(\int_{\Omega_k} (f(x) - \overline{f}_k)^2 \varphi_X(x)dx \right)^{1/2} \\
\overline{f}_k &:= \int_{\Omega_k} f(x) \frac{\varphi_X(x)}{\overline{\varphi}_{X,k}} dx
\end{aligned}$$

If the number of points n_k is proportional to the weight Ω_k, the set is called balanced. Formally: $\{n_k\}_{k=1}^m$is balanced $\iff \frac{\overline{\varphi}_{X,k}}{n_k} = \frac{1}{m}\ \forall k \in \{1, \cdots, m\}$

Theorem 4. *Stratification always lower the integration error if the distribution of points is balanced.*

The error for balanced stratified quadrature is:

$$\begin{aligned}
\varepsilon_n &\approx \frac{\sigma_s}{\sqrt{n}} \\
\sigma_s^2 &:= \sum_{k=1}^{m} \sigma_k^2
\end{aligned}$$

According to Theorem 4, stratification is always a better choice than standard MC. Furthermore, stratification can be combined with other variance reduction methods or even quasi-random approaches to additionally accelerate convergence. However, domain splitting and sub-sampling can be computationally burdensome and, in some cases, reduce the number of simulations to convergence but increase the time required for calculation (e.g. when using MC methods to calculate almost real time multi-dimensional integrals). However,

the cost of sampling in UQ problems is negligible compared to that of simulations. Therefore, stratification is always a better choice compared to pure MC for UQ applications.

The selection of the number of n_k points and choosing the subdivision into regions originates several different stratification methodologies. The most basic approach is the **Latin HyperCube** (LHC) sampling [67], where the input space is subdivided in m regions of the same weight and sample an equal number of points from each of them (balance condition). This approach outperforms standard MC and substantially reduces clustering phenomena [68].

Remark 9 (LHC drawback)**.** *A limitation of the LHC approach is that it cannot be extended once sampling has been carried out. More advanced methods, such as the replicated LHC, retain the advantages of the LHC and allow it to be extended a posteriori [69].*

Halting criterion for MC and LHC

We recall that in a UQ analysis each sampling point corresponds to a model evaluation and, thus, solving a numerical simulation. In applications, only a certain number of simulations can be run, depending on the available computing capacity. The convergence rates of the sampling method hence determines which problems are affordable and which are not. Once the simulations have been carried out, the accuracy of the result obtained is analysed. If this is not sufficient, it is necessary to extend the sample size efficiently (i.e. without repeating the simulations already carried out).

The standard MC method allows an elementary extension of the sample size, as it is sufficient to add new points sampled from the input distribution. Among the variance reduction methods, some allows easy extension of the sample size to improve precision (such as the use of antithetic variables), while others requires careful modifications (such as the LHC, which can be extended in the form of replicated Latin HyperCubes [70]). Quasi-random methods, on the other hand, are much more complex to extend (and evaluate).

Convergence indicators are necessary in order to assess whether sampling should be extended.

Remark 10 (standard sampling convergence for mean/variance)**.** *When only the mean/variance of the targeted outcome is relevant, thanks to the CLT the mean/variance on the targeted outcome divided by the current number of runs—can be used as a convergence criterion [71] (i.e.* $\left(\frac{\mu}{n}\right)$, $\left(\frac{\sigma}{n}\right)$*):*

A general-purpose strategy to assess sampling convergence and eventually halt the simulation is based on a 'sample-splitting' bootstrap method [72] to compute the internal standard deviation. Given the integral $I(f) := \int_{\mathcal{D}} f(x)\varphi_X(x)dx$ [73]:

1. A sample $\{x^{(i)}\}_{i=1}^n$ is obtained from the input space based on the joint distribution $\varphi_X(x)$ of X.

2. The n outcomes are randomly split into m subgroups. For each subgroup the estimate for the integral is obtained: $\{I^{(j)}(f)\}_{j=1}^{m}$.

3. The internal single-n-run-set based accuracy indicators are [69]:

$$std\,(I(f)) = \frac{\sigma_m(\{I^{(j)}(f)\}_{j=1}^{m})}{\sqrt{m}}$$

   where $std\,(I(f))$ is the internal deviation estimator and $\sigma_m(\{I^{(j)}(f)\}_{j=1}^{m})$ is the internal standard deviation of the m values.

4. If the internal deviation estimator is not small enough, add further points to the sample and iterate.

If the internal deviation between subgroups is high, it means that there are marked subdivision-dependent differences. Consequently, it means that the sample size n is not yet large enough for a homogeneous description of the space. As a remark, the internal standard deviations no longer indicate the actual deviations from the reference solutions (sampling convergence). Instead they should be considered as an indicator of the order of magnitude for the accuracy of Monte Carlo results.

Remark 11 (standard internal standard deviation)**.** *For a single n-run set, internal standard deviations for the mean and variance can be derived directly from statistical theory:*

$$\begin{aligned} std(\mu) &= \sigma\sqrt{\frac{1}{n}} \\ std(\sigma) &= \frac{\sigma}{2}\sqrt{\frac{2}{n-1} + \frac{k}{n}} \end{aligned} \tag{2.14}$$

where n is the number of runs, k the excess kurtosis of the n-run analysis, and std are the expected internal standard deviations on μ and σ. σ and k are computed on the n-dimensional sample. These formulae are used in several commercial software [73].

Quasi-random low discrepancy sequences

Quasi-random sequences are a deterministic alternative to random or pseudo-random ones. These sequences are designed to provide better uniformity and hence faster convergence for quadrature formulas [30]. The drawbacks of these high-speed techniques include: implementation difficulty, a high time to generate the sample, and a convergence speed dependent on the dimensionality of the integral (curse of dimensionality). Low discrepancy sequences are based on the definition of discrepancy, Hardy-Krause variation and the Koksma-Hlawka theorem.

Definition 5. *For a sequence of n points $\{x^{(i)}\}_{i=1}^n$ in the unit cube I^d, define:*

$$R_n(J) = \frac{1}{n}\#\{x^{(i)} \in J\} - m(J)$$

for any subset J of $\mathbb{I}^d$ (i.e. is the MC quadrature error in measuring the volume of J). Restrict J to the rectangular set (and thus can be written as $J(x, y)$ using x, y antipodal vertices), call E the subset of all these rectangular sets. Now can be defined the L^∞ discrepancy as:

$$D_n = \sup_{J \in E} |R_n(J)|$$

The counterpart with one vertex fixed at 0 (subset E^*) is:

$$D_n^* = \sup_{J \in E^*} |R_n(J)|$$

Remark 12 (MC discrepancy)**.** *The MC has an expected discrepancy of [74]:*

$$D_n^* = \mathcal{O}\left(\frac{\log\log n}{\sqrt{n}}\right)$$

Definition 6. *The **Hardy-Krause variation** of a single variable function is defined as:*

$$V[f] = \int_0^1 \left|\frac{df}{dt}\right| dt$$

In d dimensions, the variation is defined (recursively) as:

$$V[f] = \int_{I^d} \left|\frac{\partial^d f}{\partial t_1 \cdots \partial t_d}\right| dt_1 \cdots dt_d + \sum_{i=1}^{d} V[f_1^{(i)}]$$

in which $f_1^{(i)}$ is the restriction of the function f to the boundary $x_i = 1$.

Theorem 5 (Koksma-Hlawka inequality)**.** *For any sequence $\{x_i\}_{i=1}^n$ and any function f with bounded variation, the integration error ε_n is bounded as:*

$$\varepsilon_n(f) \leq V[f] \cdot D_n^*$$

This bound is a worst-case upper bound (instead of the probabilistic bound given by the root mean square error of standard MC) and it depends not only on the function f we are integrating, but also on the choice of sequence. Indeed, exist many type of quasi-random low-discrepancy sequence with different D_n^* values.

Definition 7. *An infinite sequence $\{x^{(i)}\}_{i=1}^n$ is uniformly distributed if*

$$\lim_{n\to\infty} D_n^* = 0$$

Definition 8. *An uniformly distributed sequence is a* ***low discrepancy sequence*** *if*

$$D_n^* \leq c(d)\frac{(\log n)^{k(d)}}{n}$$

in which $c(d)$ and $k(d)$ are constants that are independent of n but may be dependent on the dimension d.

Remark 13 (MC discrepancy)**.** *The MC has an expected discrepancy of [74]:*

$$D_n^* = \mathcal{O}\left(\frac{\log\log n}{\sqrt{n}}\right)$$

Examples of quasi-random sequences are: Van der Corput, Halton, Inverse Halton, Haselgrove, Faure, Sobol', Niederreiter and Owen [30]. For Halton, Inverse Halton, and Sobol' sequence, it holds:

$$D_n^* = \mathcal{O}\left(\frac{(\log n)^d}{n}\right) \tag{2.15}$$

where d is the input space size. The Koksma-Hlawka inequality and discrepancy bounds for a quasi-random sequence together imply that quasi-Monte Carlo quadrature converges much faster than standard Monte Carlo quadrature:

$$\varepsilon_n(f) \leq \mathcal{O}\left(\frac{(\log n)^d}{n}\right) \tag{2.16}$$

For very large n the dominant term is the denominator and therefore QMC converge speed is approximately $\mathcal{O}\left(\frac{1}{n}\right)$. However, the dominant term is the denominator only if $n > 2^d$. Therefore, the speed is much greater for spaces with low dimensionality but deteriorates for higher d. The dependence on $V[f]$ also means that for discontinuous functions the behaviour is even worse.

It should be emphasized that the Koksma-Hlawka inequality is a worst-case upper bound. Therefore, in several applications the convergence speed is much faster (e.g. approximately $\mathcal{O}\left(\frac{1}{n^\alpha}\right)$ with $\alpha \in [1/2, 1]$ [74]) even for $n < 2^d$.

Comparison between strategies

In summary, the convergence rate for order k grid-based quadrature method is $\mathcal{O}\left(\frac{1}{n^{k/d}}\right)$ while standard MC convergence rate is $\mathcal{O}\left(\frac{1}{\sqrt{n}}\right)$. Whereas for low dimensionality (e.g. $d \leq 5$) grid-based quadrature totally outperforms MC methods, for higher d the MC approach is the only viable.

The low MC convergence speed depends on a multiplier $\sigma(f)$, which is function of the variance of the integrand function. This multiplier can be reduced using a variance reduction method (e.g. antithetic variables, stratification, LHC sampling). Variance reduction methods can be even combined. The convergence speed is always faster than standard MC.

Alternatively, it is possible to use quasi-random/quasi-Monte Carlo methods (Halton, Sobol' low discrepancy sequences), which change the convergence speed to $\mathcal{O}\left(\frac{(\log n)^{k(d)}}{n}\right)$ where $k(d)$ is function of the input dimension. Despite again including a dimensionality dependency, in applications QMC methods outperform the standard MC even for high dimensionality ($d \in [10, 20]$). QMC methods can be combined with variance reduction methodologies to further accelerate convergence.

Remark 14 (MC or variance reduction + QMC?)**.** *QMC methodologies almost always perform better than the standard MC [74]. The drawbacks to their use are mainly the difficulty of calculating the sampling elements and, above all, the time required to generate the sample. However, in UQ applications, the latter is negligible compared to the resolution time of the model. Therefore, variance reduction + QMC methods are always preferable to standard MC.*

In several applications, the integrand function f only depends on a few important input variables (in the sense of an ANOVA decomposition, see [74]). For functions f that depend on only a few relevant inputs, QMC outperforms standard MC, whereas there is no relevant gain when using LHC. If all inputs are relevant but there are only low-order interactions, both QMC and LHC perform better than standard MC. However, if there are no relevant subsets of input variables and there are high-order interactions between the variables, QMC, LH and MC perform similarly [74].

2.2.2 Rare event estimation

One of the applications of forward UQ analysis is to estimate a probability of an event (e.g. determine the probability that the UQ exceeds a certain threshold or has values in specified ranges). As an example, in the study of a hydraulic system, the quantity of interest could be the pressure on the pipe wall at designated points. An event to be studied is whether the pressure exceeds a breaking threshold value leading to damage to the system.

The sampling techniques described allow the calculation of these probabilities, but lose efficiency when events become rare. An event is said to be rare if it has a probability $\leq 10^{-3}$. For several industrial safety analysis, a rare event has a probability even $\leq 10^{-8}$.

The study of rare events is difficult to approach with the MC methodologies discussed above. Indeed, consider the problem of calculating the following integral:

$$\mathbb{P}(\mathcal{S}) := \int_{\Omega} \mathbf{1}_{\{f(x)\in\mathcal{S}\}} \varphi_X(x) dx \tag{2.17}$$

where $\Omega \subseteq \mathbb{R}^d$ is the support of the density $\varphi_X(x)$, and $\mathbf{1}_{\{f(x)\in\mathcal{S}\}}$ is the indicator function of $\mathcal{S}$.

The integration error for an MC estimate of a probability (i.e. $\mathbb{P}(\mathcal{S}) = p_0$) is:

$$\varepsilon_n = \mathcal{O}\left(\sqrt{\frac{1-p_0}{p_0 n}}\right) \sim \mathcal{O}\left(\frac{1}{\sqrt{p_0 n}}\right) \tag{2.18}$$

for $p_0 \ll 1$ [66].

As a rule of thumb, to estimate an event of probability p_0 with a fixed level of accuracy δ, the total number of samples needed is $n = \frac{1}{p_0 \delta^2}$. This estimation is very expensive, indeed, for an accuracy of 1% and an event of probability 10^{-4}, $n = 10^8$ simulations are needed. There are numerous techniques (e.g. importance sampling [75], subset simulation [31, 32], directional simulation [76], line sampling [77], Asymptotic Sampling [33]) for the study of rare events, whose choice depends on the problem under investigation. In this section, Subset Simulation is briefly discussed for its high flexibility and applicability to UQ problems.

Remark 15 (Independence and Gaussian hypothesis)**.** *Most techniques assume that the input variables are i.i.d. (independent and identically distributed) Gaussian variables. It is always possible to reduce to these assumptions through an appropriate isoprobabilistic transformation [78].*

Subset Simulation

Subset Simulation, which has been studied in the mathematical literature under the terms Sequential Monte Carlo and Generalized Splitting, expresses $\mathbb{P}(\mathcal{S})$ as a product of conditional probabilities that are significantly larger than $\mathbb{P}(\mathcal{S})$. Formally, the event $\mathcal{S}$ is written as an intersection of nested intermediate events:

$$\begin{array}{l} \mathcal{S} = \cap_{j=1}^{m} \mathcal{F}_j \\ \mathcal{S} = \mathcal{S}_m \subset \cdots \subset \mathcal{S}_1 \end{array} \implies \mathbb{P}(\mathcal{S}) = \mathbb{P}(\cap_{j=1}^{m} \mathcal{F}_j) = \mathbb{P}(\mathcal{S}_1) \prod_{j=2}^{m} \mathbb{P}(\mathcal{S}_j | \mathcal{S}_{j-1}) \tag{2.19}$$

If the event $\mathcal{S}$ an be described as $\mathcal{S} := \{g(x) \leq y^*\}$, the intermediates become $\mathcal{S}_j := \{g(x) \leq y_j\}$ such that $y_1 > \cdots > y_m = y^*$.

The intermediate failure events are selected such that the conditional probabilities $\mathbb{P}(\mathcal{S}_j|\mathcal{S}_{j-1})$ are large (e.g. $\gg \mathbb{P}(\mathcal{S})$), thus requiring a reduced number of simulation to be calculated. Each element of the product is calculated for a certain number of samples before starting to evaluate the next one.

The probability $\mathbb{P}(\mathcal{S}_1)$ is computed by application of crude MC. For estimating the conditional probabilities $\mathbb{P}(\mathcal{S}_j|\mathcal{S}_{j-1})$ one needs to generate samples from conditional PDFs $\varphi(x|\mathcal{S}_{j-1})$. Generation of i.i.d. samples from $\varphi\left(x|\mathcal{S}_{j-1}\right)$ can be achieved by application of acceptance-rejection method [62, 61]. However, this approach is inefficient for events $\mathcal{S}_j$ close to actual failure event since the acceptance probability is proportional to $\mathbb{P}(\mathcal{S}_j)$. A more efficient method is a modified Metropolis algorithm (MMA) [31] which belongs to Markov Chain Monte Carlo methods [79]. Once the estimates of the probabilities of the intermediate events have been obtained, the overall estimator is simply their product.

Remark 16 (Drawbacks)**.** *Similar to all techniques for estimating rare events, Subset Simulation has several drawbacks. Mainly, the estimation obtained is affected by bias even when conditional probabilities are estimated with i.i.d. samples, due to the adaptive estimation of intermediate failure events. Furthermore, it is possible to construct counterexamples demonstrating the convergence of the subset simulation to an incorrect probability [80, 81]. However, it should be emphasized that the bias of* $\mathcal{O}(n^{-1})$ *is negligible compared to the coefficient of variation of the probability estimate [32] and that in most of the applications the Subset simulation converges to the true probability.*

Despite the limitations, Subset Simulation is incomparably faster than the standard MC for estimating rare events. Defined the relative efficiency as the ratio between the number of samples for a standard MC (n_{MC}) and a Subset Simulation (n_{SS}) with the same estimator covariance, it holds [78, 82]:

$$\frac{n_{MC}}{n_{SS}} = \frac{p_0 \left(\ln p_0^{-1}\right)^r}{(1+\gamma)(1-p_0)\mathbb{P}\left(\mathcal{F}\right)\left(\ln \mathbb{P}\left(\mathcal{F}\right)^{-1}\right)^r} \approx \frac{0.03 \cdot \mathbb{P}\left(\mathcal{F}\right)^{-1}}{\left(\log_{10} \mathbb{P}\left(\mathcal{F}\right)^{-1}\right)^2} \tag{2.20}$$

where a numerical good approximation is $r \sim 2, \gamma \sim 3, p_0 \sim 0.1$ [31, 80]. As an example, for $\mathbb{P}\left(\mathcal{F}\right) = 10^{-6}$, subset simulation requires only 1/800 of the simulation of a standard MC approach.

2.3 Sensitivity analysis

Introduction

Sensitivity analysis (SA) investigates which uncertain parameters have the greatest impact on the problem dynamics. Formally, is "*the study of how the uncertainty in the output of a model (numerical or otherwise) can be apportioned to different sources of uncertainty in the model input*" [83]. SAs provide detailed information on the model under examination with regard to:

- **Understand the dynamics:** SA makes it possible to understand which variables are the most relevant in the dynamics. Combining what has been discovered numerically with an expert commentary on the significance of the relationships identified can lead to fundamental discoveries about the phenomenon investigated.

- **Model Reduction:** The most frequent application of sensitivity analyses is the resulting model reduction. Having determined that only a subset k of the d input variables has an effect on the quantity of interest, it allows all those $d - k$ secondary variables to be set to their nominal values in subsequent analyses. This reduction in input space mitigates the effect of curse of dimensionality and therefore decreases the number of simulations required for the follow-up studies.

- **Future developments:** To improve the model, it will be necessary to develop and refine only those aspects related to the most relevant variables first.

Sensitivity analysis pivotal importance is widely acknowledged, and they are required in national and international guidelines in the context of impact assessment (e.g. European Commission, 2009; Office of Management and Budget, 2006; U.S. Environmental Protection Agency (EPA), 2009).

It should be emphasized that in an ideal context (comprehensive information on input distributions and a low computational cost of simulations) a model reduction is superfluous. However, working with limited computational resources or computationally expensive numerical models, it was seen in the previous sections how almost all the techniques discussed suffer from the curse of dimensionality. Therefore, reducing the analysis to only the most important input variables allows more accurate results to be obtained with a reduced number of simulations. However, sensitivity analyses suffer from an additional difficulty compared to Forward UQ: there is no unambiguous way to define the impact of a variable on the model. Consequently, there is no one sensitivity index but, rather, families of different indices investigating different aspects of the input-output interaction.

In a recent systematic review [38] by one of the founders of the modern UQ, Saltelli found that more than 40% of the sensitivity analyses performed start from

wrong assumptions or are methodologically poor. Sensitivity analyses require a careful set of choices and tests of assumptions on the input-output relationship in order to be correctly applied. With reference to Figure 2.4, first it must be determined whether detailed information on the input distributions is available or not. In the first case, a global sensitivity analysis can be carried out. Otherwise, it is necessary to limit the analysis to a local one. A preliminary graphical analysis (by means of scatter-plots and cobweb-plots) on the available data can identify useful relationships to investigate.

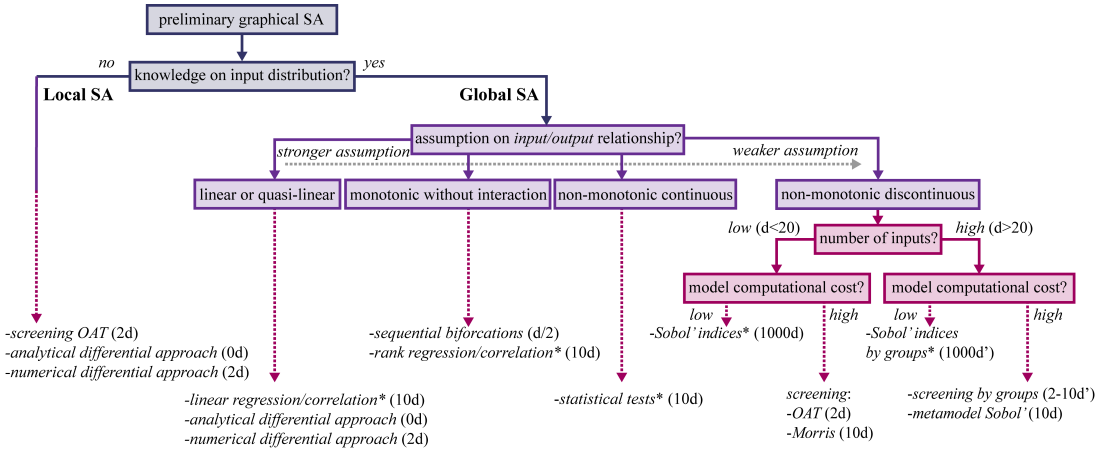

Figure 2.4: Algorithmic chart for selecting the appropriate technique/index to perform a sensitivity analysis, partially based on [84, 85]. In particular, in the case of reduced information on the input, it is necessary to perform a simple local SA that can only be generalised to the global case under assumptions of linearity. Global SA are distinguished according to the assumptions (less or more restrictive) on the input-output relationship.* indicates variance-based SA. In brackets is the expected number of simulations with respect to the d dimension of the input space. d' is the number of groups of input variables.

Local sensitivity analyses assume that there is no reliable information on the distributions of the input space. The indices and associated techniques are therefore limited to exploring a neighbourhood of the nominal values of the model in order to gain insight into the most relevant quantities. These techniques require an extremely limited number of simulations and are hence used in a computationally onerous context with limited information. The most commonly used local SA is the OAT (one-at-a-time) analysis, which alters parameters around mean values, and differential SA, based on analytical or numerical estimation of partial derivatives. Local SA requires few assumptions and a low number of simulations, but the results can only be generalised to the entire space in the case of a linear input-output relationship.

When detailed information on the input space, described by a proper multi-dimensional distribution, is available, then a **global sensitivity analyses** can be applied. By exploring not only the neighbourhood of the nominal value but the entire input space (appropriately weighted for its probability measures), the

global sensitivity analysis addresses the following question: *which of the inputs, considered across the entire spectrum of their possible variations, impacts the dynamics the most?* Answering this question is definitively more valuable than running a simple local SA. These analyses are much more computationally expensive. However, less costly indices and strategies can be exploited when additional assumption on the input-output relationship can be mad (see Figure 2.4 for details). Importantly, it should be remarked that an incorrect assumption on the input distributions propagates through the analysis contaminating the results of the analysis.

In the case of very expensive models, it is possible to apply **screening strategies** (such as OAT analyses or Morris method) to obtain a preliminary SA. These techniques, either in their local version (i.e. OAT screening) or global version (i.e. OAT or Morris method) allow with a very small number of simulations to obtain a first insight into the dynamics of the model. This is especially useful when there are too many input parameters d compared to the simulations that can be performed. Using this screening analysis, a model reduction is performed to reduce the dimensionality d of the problem so that more advanced techniques can be used. Alternatively, it is possible to exploit metamodels trained on reduced datasets in order to still be able to study complex indices such as Sobol' sensitivity indices, as detailed in Section 2.4.

2.3.1 Graphical SA

A powerful SA screening tool for both local and global analyses is the graphical investigation of the properties of the input-output relationships. In particular, two of the most widely used ones are scatter-plots and the cobweb-plot.

With reference to Figure 2.4a,b,c, the scatter-plots show pairs of values for two variables on a plane. From the relationship described by the points, it is possible to identify variables with a reduced effect (cloud of points, as in panel c), to detect a linear relationship (panel a), or to determine the presence of non-linear ones that necessitate the use of appropriate non local methodologies (panel b).

Scatter-plots, however, do not capture some interaction effects between inputs. In fact, they are the two-variable projection of a d-dimensional problem that cannot be represented graphically in its entirety. Another useful tool is the cobweb plot [86]. This graph connects the values of each variable (shown on vertical axes) by straight lines. Highlighting a subset of the QoI with a different colour allows complex relationships between the variables to be identified. With reference to Figure 2.4d, for instance, it can be seen that the high values of the Y-QoI correspond to large values of the variable X_1 and low ones for the variable X_2.

2.3.2 Local SA

If there is no information on the input distributions available to the experimenter, the only methodologically correct approach is to carry out local sensi-

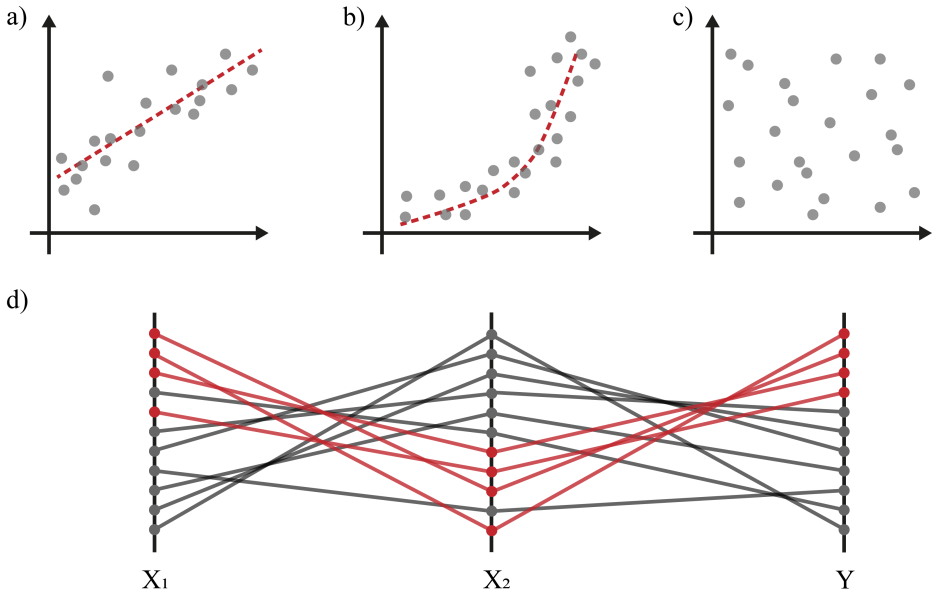

Figure 2.5: Examples of scatter-plots determining a linear (a) and a non linear (b) relationship. Panel b shows a cloud of points that can predict a reduced effect of the variable on the output. Panel d presents a cobweb plot that highlights higher values of Y and proves that they corresponds to larger X_1 values coupled with lower X_2 ones.

tivity analyses [87]. The latter derive their name from the fact that the variables under investigation are only locally perturbed around their nominal values. Local sensitivity analyses will be treated very briefly, as they provide less precise results than the corresponding global analyses. In addition, cardiac problems, and more generally biomedical problems, have a vast literature at their disposal for correctly estimating input distributions.

Differential approach

The gold standard for local sensitivity analyses is the direct method (also called Differential Sensitivity Analysis, or Differential Approach). The inputs are fixed at their nominal values and the partial derivatives of the QoI $Y = g(X)$ are calculated for each input parameter. The corresponding slope, eventually normalised by the ratio of the parameter to remove the effects of units, is called the **ranking index** and is used as an estimate of importance of the variables. These derivatives can be calculated analytically for many application problems (either by direct derivation or by the adjoint method [88]). Alternatively, it is also possible to obtain the derivatives numerically and apply this method for (smooth) black-box input-output relations. The main drawback of the direct method, like most local techniques, concerns the non-generalizability of the result in the absence of a linear input-output relationship.

One-At-Time SA

An alternative to direct methods for SA are one-at-a-time (OAT) methods, which exploit the input space varying one parameter at time while fixing the others to their nominal value. This kind of exploration neglects any kind of interaction among variables and, therefore, the results obtained are valid for small perturbations and generalizable only in the case of linear models. For the sake of completeness, two of the most commonly used OAT indices are listed here [87].

The **OAT Sensitivity Measure** can be calculate with just two model f evaluations for each input (i.e. a total of $2d$). For each input X_i with nominal value μ_i, is chosen a value p_i equal to a percentage of the mean ($\pm 5\%\mu_i, \pm 10\%\mu_i$) or, if more detailed information on the input distribution is is available, as $\pm\sigma_i$. The index is calculated as the ratio of the highest to the lowest variation:

$$\mathrm{SM}_i = \frac{g\left((\mu_1, \cdots, \mu_i, \cdots, \mu_d) + (0, \cdots, p_i, \cdots, 0)\right)}{g\left((\mu_1, \cdots, \mu_i, \cdots, \mu_d) - (0, \cdots, p_i, \cdots, 0)\right)} \tag{2.21}$$

An alternative index is the **OAT Sensitivity Index**, similarly defined as the percentage difference in output from its minimum to its maximum perturbation:

$$\begin{aligned}
\mathrm{SI}_i &= \frac{M_i - m_i}{m_i} \cdot 100 \\
M_i &= f\left((\mu_1, \cdots, \mu_i, \cdots, \mu_d) + (0, \cdots, p_i, \cdots, 0)\right) \\
m_i &= f\left((\mu_1, \cdots, \mu_i, \cdots, \mu_d) - (0, \cdots, p_i, \cdots, 0)\right)
\end{aligned}$$

The OAT techniques can be substituted in most of the application with better ones (e.g. Morris method) and should be avoided where possible [89, 90]. Indeed, the results of the OAT neglect interactions and cannot be generalised to the whole space without strong assumptions of model linearity.

2.3.3 Global Sensitivity Analysis

Local SA methods are extremely limited in their applications as they can not span. Furthermore, many of the local methods are based on very strong assumptions about the input-output relationship (e.g. linearity/monotonicity) that are not found in practice. An extension of local methods are the **global sensitivity analyses**, so called because they consider the entire range of variation of the input [91]. As shown in Figure 2.4, there are numerous global SA techniques with more or less strong assumptions on the input-output relationship.

It should be recalled that in the absence of information on input distributions, it is not methodologically correct to define arbitrary ranges of variation and label the sensitivity analysis performed as global. In such cases it is better to run a local SA.

Linear regression

If an approximately linear relationship between input and output is present, elementary sensitivity indices can be defined. Given an n-dimensional sampling of space and the corresponding model evaluations

$$(\mathcal{X}, \mathcal{Y}) := \{x^{(i)}, y^{(i)}\}_{i=1}^{n} = \{(x_1^{(i)}, \cdots, x_d^{(i)}), y^{(i)}\}_{i=1}^{n}$$

it is first necessary to check linear assumptions. This can be done with the **coefficient of determination** R^2 and the **predictivity coefficient** Q^2. First it is defined a $m-$size test set:

$$(\mathcal{X}^p, \mathcal{Y}^p) := \{(x_1^{(i),p}, \cdots, x_d^{(i),p}), y^{(i),p}\}_{i=1}^{m}$$

which is an arbitrary subset extracted from the original set $(\mathcal{X}, \mathcal{Y})$. Then, $\hat{y}$ is the linear model approximation that associate each input $(x_1, \cdots, x_d)$ to a corresponding output. This linear approximation is trained on the remaining set once that the test set is extracted.

Definition 9. *The predictivity coefficient is is defined as:*

$$Q^2 = 1 - \frac{\sum_{i=1}^{m} \left(y^{(i),p} - \hat{y}\left(x_1^{(i),p}, \cdots, x_d^{(i),p}\right)\right)^2}{\sum_{i=1}^{m} \left(y^{(i),p} - \mathbb{E}\left[y^p\right]\right)^2}$$

The value of Q^2 corresponds to the percentage of output variability explained by the linear regression model. If $Q^2 \sim 1$ the linear hypothesis can be assumed. Otherwise, if $Q^2 < 1$, other SA methodologies should be used.

Once the linear relationship has been verified, it is possible to define several sensitivity measures.

The first possible measure is based on the strength of the linear relationship among an input variable X_j and the output, which can be quantified by the **Pearson correlation coefficient**:

$$\rho_j := \rho\left(X_j, Y\right) = \frac{\sum_{i=1}^{n} \left(x_j^{(i)} - \mathbb{E}\left[X_j\right]\right)\left(y^{(i)} - \mathbb{E}\left[Y\right]\right)}{\sqrt{\sum_{i=1}^{n} \left(x_j^{(i)} - \mathbb{E}\left[X_j\right]\right)^2} \sqrt{\sum_{i=1}^{n} \left(y^{(i)} - \mathbb{E}\left[Y\right]\right)^2}}$$

where values close to 1 or -1 describe a strong linear correlation, while $\rho_j \approx 0$ means an essentially null (linear) effect of X_j on Y. Consequently, the variables are ordered with respect to the absolute value of Pearson's coefficient. It should be emphasised that if linearity assumptions are improperly accepted, this index may return a value of 0 even in the presence of a strong non-linear relationship between X_j and Y, leading to a misclassification of the importance of the variables.

Sometimes it is relevant to consider not only the strength of the linear relationship but the regression coefficients among the variables X_j and Y. The **Standard Regression Coefficient** is therefore defined as:

$$\mathrm{SRC}_j = \alpha_j \sqrt{\frac{\mathrm{var}\left[X_j\right]}{\mathrm{var}\left[Y\right]}}$$

where α_j is the linear regression coefficient associated to X_j. As a remark, under the linear assumption, if the input variables are independent, each SRC_j^2 expresses the part of output variance explained by the input X_j. Higher values correspond to a greater amount of explained variance and, therefore, more important input variables.

Remark 17 (Efficient sampling)**.** *An efficient sampling strategy as the one described in the previous section can greatly reduce the amount of model evaluation required to correctly estimate these coefficients [67].*

Rank regression

If the linear assumptions are not fulfilled but a monotonic input/output relationship still exists, both the Pearson correlation coefficient and the Standard regression coefficient can be used by applying a rank transformation [92]. The latter substitutes each value of the sample $\{(x_1^{(i)}, \cdots, x_d^{(i)}), y^{(i)}\}_{i=1}^n$ with the corresponding rank (the relative position of the variable: 1 for the first, 2 for the second).

The monotonic hypothesis is tested by computing the predictivity coefficient Q^2 on the rank transformed sample. Similarly, the **Spearman correlation coefficient** and the **Standardized Rank Regression Coefficient** are defined as the Pearson correlation coefficient and the Standard regression coefficient of the rank transformed sample.

As a remark, these indices implicitly assume that there are no interactions between the input variables. This can be verified using a preliminary screening analysis such as the Morris method, see § 2.3.3. In case of interactions, more complex global SA methods should be preferred.

Statistical tests

If linear or monotonic relationships between input and output have not been confirmed, it is possible to use the results of certain statistical tests as sensitivity

measures. These indices, although requiring less restrictive assumptions, often lack quantitative interpretation [85].

Statistical testing based SA [93] starts from a n-dimensional sampling of the input space and the corresponding model evaluations

$$(\mathcal{X}, \mathcal{Y}) := \{(x_1^{(i)}, \cdots, x_d^{(i)}), y^{(i)} = g(x^{(i)})\}_{i=1}^{n}$$

To obtain a sensitivity measure for a given input variable X_j, the sample is subdivided into m sub-samples (for small dataset: $m = 2$):

$$\begin{aligned} \mathcal{SS}_1^j &:= \{(x_1^{(i_1)}, \cdots, x_j^{(i_1)}, \cdots, x_d^{(i_1)}), y^{(i_1)}\}_{i=1}^{n_1} \\ &\vdots \\ \mathcal{SS}_m^j &:= \{(x_1^{(i_m)}, \cdots, x_j^{(i_m)}, \cdots, x_d^{(i_m)}), y^{(i_m)}\}_{i=1}^{n_m} \end{aligned} \tag{2.22}$$

such that each sub-sample corresponds to an equiprobable stratum to the respect of the variable X_j:

$$\mathbb{P}_{X_j}(\mathcal{SS}_1^j) = \cdots = \mathbb{P}_{X_j}(\mathcal{SS}_m^j) \tag{2.23}$$

A statistical test of homogeneity of population is therefore applied to the sub-samples and a value $\mathcal{T}$ derived from the statistic of the population is used as a measure of sensitivity:

$$I_j = \mathcal{T}\left(\mathcal{SS}_1^j, \cdots, \mathcal{SS}_m^j\right) \tag{2.24}$$

The variables are ordered with respect to the measures I_j. Several statistical tests of homogeneity of population (including χ^2-test, Fisher test, Kruskal-Wallis test [94]) can be applied to calculate I_j, whereas parametric tests such as the t-test can also be applied to compare sub-samples. However, these tests are based on strong assumptions about the distribution of the variable which are often not fulfilled. In such cases, non-parametric alternatives should be preferred [93] as they are based on the ranks of both input and output vectors, thus providing an appropriate and strong tool for tackling sensitivity analysis problems [95]. A detailed description of the tests is reported in the textbook of Conover [96], while Saltelli and Marivoet [93] make a comparison of several alternatives on a common test function.

Remark 18 (Same ranking?)**.** *Having introduced numerous sensitivity indices, it is natural to ask whether these provide similar results when classifying important variables. While variance-based indices return similar results as the number of simulations increases, different indices focus on distinct aspects of the input-output relationship and thus, in general, do not necessarily return the same important variables [93].*

ANOVA decomposition and Sobol' indices

The measures of importance discussed so far do not investigate the relationship between variables (e.g. is there a combination of variable 1 and 2 that

impacts dynamics the most?). This *analysis of interaction* can be achieved with the most general of the sensitivity indices described in this section, the **Sobol' index**. The latter not only provides precise insight into the relationships between variables, but can also be calculated under the least restrictive of the proposed assumptions: *the input-output relationship can admit interactions and does not even have to be continuous*. The drawback of this index is its high computational cost compared to the other methodologies discussed.

Let us consider the model $Y = g(X)$, $X = (X_1, \cdots, X_d)$ and Y an univariate response. Assuming that X_i are independently and uniformly distributed within the unit hypercube $[0,1]^d$, $g(X)$ may be decomposed (ANOVA-HDMR decomposition of the QoI f [97]) as:

$$Y = g_0 + \sum_{i=1}^{d} g_i(X_i) + \sum_{i<j}^{d} g_{ij}(X_i, X_j) + \cdots + g_{12\cdots,d}(X_1, \cdots, X_d) \tag{2.25}$$

The assumption of independence and the choice of the domain $[0,1]^d$ is not restrictive, as each model can be appropriately transformed to satisfy these hypotheses by using an isoprobabilistic transformation [46]. This representation, is unique under the assumption [98]:

$$\begin{gathered}\int_0^1 g_{i_1,\cdots i_n}\left(X_{i_1}, \ldots, X_{i_n}\right) dX_{i_k} = 0 \\ 1 \leq k \leq s,\ \{i_1, \ldots, i_s\} \subseteq \{1, \ldots, d\}\end{gathered}$$

As a consequence, summands are orthogonal with each other:

$$\mathbb{E}\left[g_{\mathcal{A}}(X_{\mathcal{A}}) g_{\mathcal{B}}(X_{\mathcal{B}})\right] = 0 \quad \forall \mathcal{A}, \mathcal{B} \subseteq \{1, \cdots, d\} \quad \mathcal{A} \neq \mathcal{B} \tag{2.26}$$

and therefore it is possible to define a recurrent formula to calculate the terms of the decomposition:

$$\begin{aligned} g_0 &= \mathbb{E}[f(X)] \\ g_i(X_i) &= \mathbb{E}[f(X)|X_i] - g_0 \\ g_{ij}(X_i, X_j) &= \mathbb{E}[f(X)|X_i, X_j] - g_i - g_j - g_0 \\ &\vdots \end{aligned}$$

From this formula follows the names of these coefficients: g_i are the **main effect** of X_i, g_{ij} are the **second order interaction** of X_i, X_j, and so on. The given decomposition combined with the orthogonality property leads to the **functional ANOVA decomposition** [99] of the model:

$$\begin{aligned} \operatorname{Var}[Y] &= \operatorname{Var}\left[g_0 + \sum_{i=1}^{d} g_i\left(X_i\right) + \sum_{i<j}^{d} g_{ij}\left(X_i, X_j\right) + \cdots + g_{12..d}(X)\right] \\ &= \sum_{i=1}^{d} V_i + \sum_{i<j}^{d} V_{ij} + \cdots + V_{12\cdots d} \end{aligned} \tag{2.27}$$

where:

$$\begin{aligned} V_i &:= \mathrm{Var}\left[\mathbb{E}\left[Y|X_i\right]\right] \\ V_{ij} &:= \mathrm{Var}\left[\mathbb{E}\left[Y|X_i, X_j\right]\right] - V_i - V_j \\ V_{ijk} &:= \mathrm{Var}\left[\mathbb{E}\left[Y|X_i, X_j, X_k\right]\right] - V_{ij} - V_{ik} - V_{jk} - V_i - V_j - V_k \\ &\vdots \end{aligned} \tag{2.28}$$

Definition 10. *The **Sobol' indices** [100] are defined as :*

$$\begin{aligned} \mathcal{S}_i &:= \frac{V_i}{Var[Y]} \\ \mathcal{S}_{ij} &:= \frac{V_{ij}}{Var[Y]} \\ &\vdots \\ \mathcal{S}_{\mathcal{D}} &:= \frac{V_{\mathcal{D}}}{Var[Y]} \end{aligned} \tag{2.29}$$

*where $\mathcal{D} \subseteq \{1, \cdots, d\}$ is an arbitrary subset of the inputs. The first order indices are also called **importance measures** or **main effect indices**.*

These indices have a strong intuitive meaning, representing the amount of variance of Y that is due to the given input or input combination. As a remark, V_i is the contribution of varying X_i but averaged over other variations in input space. The $\mathrm{Var}\left[Y\right]$ standardization is provided to give a fractional response and implies that:

$$\sum_{i=1}^{d} \mathcal{S}_i + \sum_{i<j}^{d} \mathcal{S}_{ij} + \cdots + \mathcal{S}_{12\cdots d} = 1 \tag{2.30}$$

The main advantages of Sobol' indices include: high interpretability, the capability to deal with non-linear/non-monotonic and even discontinuous responses, and the possibility of describing the effect of interactions in non-additive system.

Remark 19 (Linear regression model)**.** *If the model is linear, it holds:*

$$\mathcal{S}_i = SRC_i^2 := \alpha_i \sqrt{\frac{Var[X_i]}{Var[Y]}}$$

where SRC is the standard regression coefficient. Therefore the Sobol' SA leads to the same analysis of standard linear SA.

These indices can also be used to quantify the degree of interactions. Indeed, the amount of perturbation of the output caused by interactions is given by:

$$\mathrm{Interaction}(f) := 1 - \sum_{i=1}^{d} \mathcal{S}_i \tag{2.31}$$

Sobol' indices defined in this way, however, do not provide information on the contribution of a variable X_i taking into account all interactions with other variables. An extension of classical Sobol' indices, are the total order Sobol' indices [101].

Definition 11. *The **total order Sobol' indices** (also called **total indices** or **total effects** are defined as:*

$$\mathcal{S}_i^T := \sum_{\mathcal{D}\ s.t\ i\in\mathcal{D}} \mathcal{S}_{\mathcal{D}} \tag{2.32}$$

This is the measure of the contribution to the output variance of X_i including all variance alterations caused by its interactions of any order with any other input variables. Total order indices can be calculated directly without first having to evaluate all terms in the sum. In practice, when d is large, only the main effects and the total effects are computed, to provide both a description of the behaviour of each variable alone and its combined effect with the others.

There are different strategies for calculating Sobol' indices. The classical approach involves calculating each index $\mathcal{S}_D$ by a direct Monte Carlo method. In particular, an efficient technique for calculating first-order indices is the Sobol' algorithm [100]. More efficient sampling strategies can be used to speed up convergence even by a factor of 10 (such as the LHC or quasi-Monte Carlo) [102]. However, it should be noted that the number of indices 2^d-1 grows exponentially with the number d of dimensions. Consequently, in most applications, indices of order greater than two should not be estimated. A particularly efficient algorithm for calculating first order indices and simultaneously total order ones is Saltelli's algorithm [103]. The direct procedure of Saltelli to calculate the indices is the following:

1. Generate two independent sample matrices of n rows and d columns A, B. Each row is a random sample of the input space.

2. Define further d matrices $\{A_B^i\}_{i=1}^d$ matrices with d columns and n rows. These matrices are the original A one with the i^{th} column of A_B^i equal to the i^{th} column of B.

3. Evaluate the model f for A, B, and all the $\{A_B^i\}_{i=1}^d$. This leads to a total of $n + n + n \cdot d = n \cdot (2 + d)$ model evaluations.

4. The estimator for first and total indices are:

$$\mathcal{S}_i \approx \frac{1}{n}\sum_{j=1}^{n} f(B)_j \left(f(A_B^i)_j - f(A)_j\right)$$
$$\mathcal{S}_i^T \approx \frac{1}{2n}\sum_{j=1}^{n} \left(f(A)_j - f(A_B^i)_j\right)^2$$

This method is particularly efficient as it requires only $N \cdot (d+2)$ simulations to obtain both first order indices and total ones. However, as it is defined, it is

not trivial to extend the sampling in case the required precision on the indices is not attained. Furthermore, the algorithm can be modified to calculate second order indices as well, but is much less efficient.

Remark 20 (Why is my index negative?)**.** *In practical applications, it may happen that the calculated indices do not respect the theoretical properties expected. It is indeed crucial to be aware that approximation error may produce incorrect results or even lead to errors in the ordering of variables with respect to their importance. Indices should therefore always be presented with their confidence intervals to assess the reliability of the results.*

For pure Monte Carlo approach (including Saltelli's algorithm) the confidence intervals relies on the asymptotic behaviours of the estimators [104]. Alternatives include random repetition confidence intervals [105] and bootstrap methods [106].

There are other strategies for calculating Sobol' indices: Mauntz formula is useful for estimating small indices [107], while the Janon-Monod one [104] can efficiently approximate large first-order indices. Jansen's method [108] is an alternative to Saltelli's algorithm for calculating total order indices. A strategy widely used in the literature is the FAST method [109]. Although this method is efficient for calculating first-order indices and total order indices [110], it is known that this method is slow, unstable and, above all, biased when the number of inputs is larger than 10 [111, 85].

Remark 21 (Surrogate models)**.** *A very efficient family of methods to overcome the computational bottleneck and calculate* ***all*** *Sobol' indices (not only first and total order) is the use of a surrogate model. With a reduced dataset, the model f is approximated with a surrogate one $\tilde{f}$ of low computational cost. Indices are then derived from analytical formulas (e.g. in the case of PCE or Kriging) or by directly evaluating $\tilde{f}$. These methods, however, suffer from the curse of dimensionality. High dimensional input spaces therefore require the use of direct methods such as Saltelli's algorithm.*

Screening global SA: OAT

Despite the discussed limitations of OAT techniques, in some practical contexts (d-dimensionality of hundreds/thousands) it is still useful to have this screening tool available. In addition to the SM and SI indices already presented, two other OAT variants applicable when the input distribution is known are the OAT Importance Index and the Relative Deviation method [87].

The most elementary between the variance-based sensitivity analysis is based on the **OAT Importance Index**. To calculate this index, each input variable X_i is sampled keeping all the other variables fixed at their nominal value (e.g. the mean). The sample thus obtained

$$\{\tilde{x}_i^{(j)}\}_{j=1}^n := \{(\mu_1, \cdots, x_i^{(j)}, \cdots, \mu_d)\}_{j=1}^n$$

is evaluated using the model f. The index it is defined as the ratio between the input variance and the output variance:

$$\mathrm{II}_i := \frac{\mathrm{Var}[g(X_i)]}{\mathrm{Var}[X_i]} \approx \frac{\mathrm{Var}\left[\{g\left(\tilde{x}_i^{(j)}\right)\}_{j=1}^n\right]}{\mathrm{Var}\left[\{\tilde{x}_i^{(j)}\}_{j=1}^n\right]} \tag{2.33}$$

Exploiting a similar approach to that of the Importance Index, it is possible to define the **Relative Deviation index**. The latter is defined as the ratio of the standard deviation of the output to its mean (similar to the coefficient of variation):

$$\mathrm{RD}_i := \frac{\sigma\left[g(X_i)\right]}{\mu\left[g(X_i)\right]} \approx \frac{\sigma\left[\{g\left(\tilde{x}_i^{(j)}\right)\}_{j=1}^n\right]}{\mu\left[\{g\left(\tilde{x}_i^{(j)}\right)\}_{j=1}^n\right]}$$

This index is the gold standard for OAT sensitivity analysis if many evaluations may be afforded for each variable.

Screening: Morris method

OAT analyses are a screening technique with severe limitations because the results completely neglect interactions between variables. However, there is a family of techniques (global screening techniques) that investigate the entire input space (global analysis) at a low computational cost to provide preliminary insight into the most relevant variables.

Among these techniques, one of the best in terms of detailed information retrieved is the **Morris method** [35], presented here using Campolongo's extension [112].

The algorithm of Morris method is the following:

1. It is defined a set of starting values $\{x^{(j)}\}_{j=1}^r$ accordingly to the d dimensional input distribution. It is prescribed a step-size Δ_s.

2. Define the starting value $x^{(j,0)} := x^{(j)}$. For $i = 1$ to d:

   (a) The value $x(j, i-1)$ is modified by adding a perturbation Δ_s in the i^{th} direction of the input space (OAT respect to the i^{th} input variable):

   $$x^{(j,i)} = x^{(j,i-1)} + \Delta_s \cdot e_{\hat{i}} \tag{2.34}$$

   (b) The **Elementary effect** is computed as:

   $$E_j^{(i)} := \frac{g\left(x^{(j,i)}\right) - g\left(x^{(j,i-1)}\right)}{\Delta_s} \tag{2.35}$$

Therefore, each initial element is perturbed d times, one in each direction, randomly exploring the space around that initial value. This leads to a total of $r(d+1)$ runs of the model.

Remark 22. *A good parameter value is r between 4 and 10 [113].*

Since the order of the displacements is random as are the choices of initial points, this method investigates the entire space in a very complete manner. For each input space direction $i \in [1, d]$, the obtained set of $\{E_j^{(i)}\}_{j=1}^r$ follows an unknown distribution $E^{(i)}$, which is used to define the corresponding sensitivity indices: the *mean of the elementary effects*:

$$\mu^{(i)} = \mathbb{E}[E^{(i)}] \approx \frac{1}{r} \sum_{j=1}^{r} E_j^{(i)} \tag{2.36}$$

the *mean of the absolute value of the elementary effects*:

$$\mu_*^{(i)} = \mathbb{E}[|E^{(i)}|] \approx \frac{1}{r} \sum_{j=1}^{r} |E_j^{(i)}| \tag{2.37}$$

and the *standard deviation of the elementary effects*:

$$\sigma^{(i)} = \sigma[E^{(i)}] \approx \sqrt{\frac{1}{r} \sum_{j=1}^{r} \left(E_j^{(i)} - \mu^{(i)}\right)^2} \tag{2.38}$$

The value $\mu_*^{(i)}$ is a measure of influence of the i^{th} input on the output. Larger values correspond to a more important input variable. The standard deviation $\sigma^{(i)}$ is a measure of non-linear and/or interaction effects of the i^{th} input. If $\sigma^{(i)}$ is small, means that every starting value $\{X_j\}_{j=1}^r$, once perturbed in the i^{th} directions, leads to a similar modification. Consequently, a small difference among these values leads to a lower $\sigma^{(i)}$ and therefore suggests a linear relationship between input and output. Viceversa, a large $\sigma^{(i)}$ implies a non-linear relationship or an interaction with at least one other variable.

Remark 23 (Classical Morris)**.** *The Classical Morris method uses $\mu^{(i)}$ instead of $\mu_*^{(i)}$. Campolongo proves that the absolute mean value can improve the classical results [112].*

The method of Morris allows to classify the inputs in three groups:

- Inputs i having *negligible effects*: low value of $\mu_*^{(i)}$.
- Inputs i having *large linear effects without interactions*: high value of $\mu_*^{(i)}$ and low value of $\sigma^{(i)}$.
- Inputs i having *large non-linear and/or interaction effects*: high values of $\mu_*^{(i)}$ and $\sigma^{(i)}$.

Other screening techniques

The Morris method is one of the most costly among the screening techniques. When the number of evaluations has to be smaller or equal than the input space (e.g. $n \leq d$) this technique can not be applied. Such extreme cases must be addressed by appropriate methodologies, not discussed in detail here for the sake of brevity. If $n \sim d$, a classical **Factorial Fractional Design** can be used [114], whereas if $n < d$ two possibilities are the **Supersaturated design** [115] or **Sequential Bifurcation Method** [116]. However, in some applications can happen that $n \ll d$ (e.g. having an input space of dimensionality 100 with a maximum of 10 simulation to run). One of the few techniques to address this problem is based on partitioning the input space (with the number of partitions $d' \ll d$, such that $d' \sim n$) and then applying **Screening by groups** methodologies [117].

Remark 24 (The efficiency of surrogate models)**.** *The use of a properly validated surrogate model avoids the computational bottleneck of an onerous model. For particularly expensive model evaluation cases, a surrogate model can succeed in returning very precise estimates of complex indices (Sobol') using few tens of simulations. Nevertheless, surrogate models still suffer from the curse of dimensionality and thus cannot be used for spaces with large d dimension.*

2.4 Surrogate models

The number of evaluations of the original model $y = g(x)$ required to apply the UQ methodologies is the main bottleneck of computational resources and time. Each evaluation corresponds to an experiment or a resolution of the numerical model, that may even take several days (e.g. the heart model developed in this thesis requires over 15 hours on a GPU unit V100).

An elegant solution to overcome this limitation is to use a surrogate model (also called metamodel). The latter is an approximation of the real problem based on the data available to the experimenter. Formally, given the original model $y = g(x)$ and a set of pairs $(\mathcal{X}, \mathcal{Y}) := \{(x^{(i)}, y^{(i)} = g(x^{(i)}))\}_{i=1}^{N}$ called the training set, the surrogate model $y = \overline{g}(x)$ is defined on the basis of assumptions made by the experimenter (e.g. the presence of a polynomial relationship between input and output) to minimise an appropriate distance between the surrogate model predictions and the known information, $\|\overline{g}(x) - g(x)\|$.

The idea behind the use of the surrogate model is that instead of querying the original model $g(x)$ for a given input x^* not belonging to the training set, the approximation provided by $\overline{g}(x^*)$ is exploited. If this surrogate is well trained and the underlying assumptions are valid, the calculated prediction will be similar to that obtained using the original model (i.e. $\overline{g}(x^*) \approx g(x^*)$).

Remark 25 (Linear regression model)**.** *The most basic example of a surrogate model is the linear model* $y = \overline{g}(x) = \alpha \cdot x$*. The assumptions underlying the choice of this metamodel are that there is only one input variable* x*, one output variable* y *and that the relationship between the two is approximately linear. Once a training dataset (e.g.* $\{(1,1),(2,4.3),(3,5.6)\}$*) is fixed, the line that best approximates these three points is chosen, in this case* $y = 1.95 \cdot x$ *. If we want to make a prediction on a new* $x^* = 4$ *value, we can use the chosen straight line as an approximation of the real problem:* $y = 7.8 = 1.95 \cdot 4$*.*

The assumptions underlying the choice of the model are crucial, one must therefore choose the appropriate surrogate for the problem under investigation. Simple surrogates include the linear model [118],its extension to account for multivariate input variables (general linear model, GLM) [119] and the multivariate logistic regression model [120] which estimates the probability of an event (output) occurrence given the inputs. These surrogates are easy to interpret, but are often too basic to describe more complex UQ questions. Conversely, in recent times, much more sophisticated models have emerged that are capable of describing a wider family of problems. Examples of these metamodels are artificial neural networks (ANN) [121] and in particular their variants explicitly developed for probabilistic interpretation such as Bayesian neural networks [122] and variational autoencoders [123].

The use of a surrogate model for UQ analysis thus involves the choice of a model, a training phase on a suitably generated sample (e.g. using the qMC techniques discussed) and a validation phase to check whether it is predictive. The surrogate model can be then applied in place of the original model to run

forward and sensitivity analysis, performing hundreds of thousands of evaluations of $\overline{G}(x)$ almost in real time.

Although any suitably validated metamodel can be used to fit the dynamics of the original model, there are a number of surrogate families which have been properly designed for UQ. Such approaches often provide analytical formulas for calculating sensitivity indices and allow the necessary information to be extracted efficiently already with a very small number of samples. The two most used surrogate models for UQ are Polynomial Chaos Expansion (PCE) [124, 125] and Gaussian process regression (also known as Kriging) [126, 127]. The first provides an analytical formula for Sobol' indices. The surrogate is a multivariate probabilistic polynomial expansion and therefore it is easy to interpret the model's choices by analysing the polynomial coefficients. The second provides a method for estimating the error of the metamodel itself, which can be used to implement an adaptive methodology for extending the training dataset.

Remark 26 (Surrogate models or direct approach?)**.** *The use of a surrogate model adds a further source of error to the UQ procedure. Therefore, where possible, direct methodologies are preferred, as they are more stable and less prone to error. However, in applications where only a few hundred (or even tens) of simulations are possible, surrogate models remain the only viable strategy.*

2.4.1 Training

After choosing a metamodel, it is necessary to train it on the available data (the training set). In fact, each surrogate is dependent on several parameters that must be calibrated to fit the problem. Good calibration means that the metamodel can be used as a low-cost substitute for the original model. In the case of a linear metamodel $y = m \cdot x + q$, for instance, the two parameters to be calibrated are m and q.

Identifying the optimal parameters is a complex problem and is highly dependent on the chosen metamodel. For linear models there are closed formulas while for more complex polynomial models there are iterative methods, and in the case of feedforward Neural Networks, backpropagation algorithms are used. However, underlying all these methodologies, there is the idea of minimising a distance between the predictions of the model $g(x)$ and the chosen metamodel $\overline{g}(x)$. This distance, discussed in the next section, is often a mean square error calculated over the entire training set.

2.4.2 Validation

Given a trained surrogate model, is fundamental to set up a control phase to validate the results, see Figure 2.6.

Remark 27 (Training)**.** *In many applications, the experimenter is forced to work with a pre-existing training dataset. However, in the design phase of the experiment, the training dataset can be defined wisely in order to maximise the*

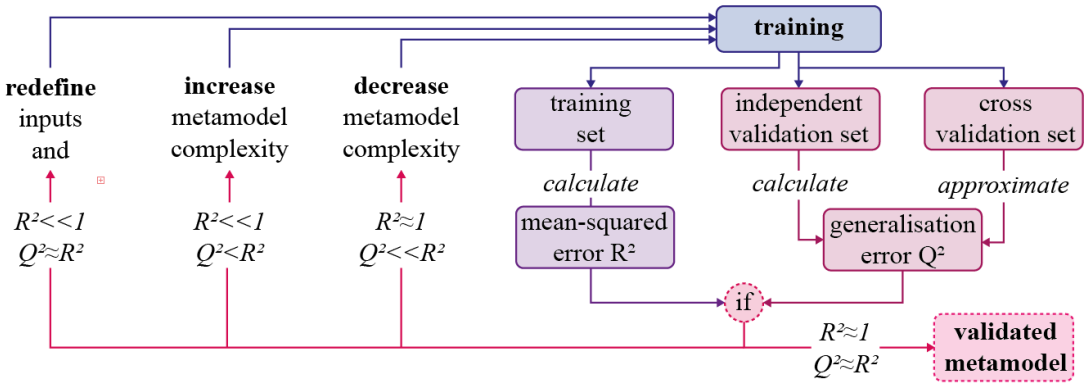

Figure 2.6: Training and validation sketch of a metamodel. After the training phase, the model is evaluated using the mean-squared error R^2 and the generalisation error Q^2. High values of both parameters ensure good predictive ability. Low values of both, on the other hand, mean that the experimental design is not adequate.

information obtained from a small number of simulations. The techniques presented in Section 2.2 are therefore applicable not only for direct methods but also for the definition of an efficient training set.

Testing error - R^2 accuracy estimator

The first validation to be performed when using the metamodel is to determine its ability to replicate results of the original model on the training dataset. A metamodel has, indeed, to provide the correct inputs/outputs relationship for the cases used for its training to be a good surrogate.

Definition 12. *An estimator of the error committed by using a metamodel instead of the original model is the mean-square error (MSE) or generalisation error:*

$$MSE = \mathbb{E}\left[(g - \overline{g})^2\right]$$

Definition 13. *MSE can be approximated using the training dataset* $\{x^{(i)}, G(x^{(i)})\}_{i=1}^n$

$$MSE \approx Err_{training} = \frac{1}{n}\sum_{i=1}^{n}\left(g(x^{(i)}) - \overline{g}(x^{(i)})\right)^2$$

Definition 14. *The R^2 estimator (also called coefficient of determination in regression analysis), it is defined as:*

$$R^2 = 1 - \frac{MSE}{Var[g]} \approx 1 - \frac{\sum_{i=1}^{n}\left(g(x^{(i)}) - \overline{g}(x^{(i)})\right)^2}{\sum_{i=1}^{n}\left(g(x^{(i)}) - \frac{1}{n}\sum_{j=1}^{n} g(x^{(j)})\right)^2}$$

where $\{x^{(i)}, g(x^{(i)})\}_{i=1}^n$ *is the training set.*

The index thus defined ranges from zero (no predictive ability on the training dataset) to 1 (perfect match on the training dataset). However, the risk of overfitting should also be assessed in order to validate the metamodel.

Remark 28 (Polynomial example and Runge's phenomenon)**.** *As an example, consider a training dataset of dimension n and an interpolating polynomial on the given points. As the degree of the polynomial increases, the approximation on those points will become progressively better (until a polynomial of degree n perfectly approximates all n points). In that case, the index R^2 will be equal to 1 but the model will be poorly able to generalise the results as it will fluctuate between the points in the training dataset.*

Q^2 accuracy estimator

To determine the capability of a predictive model outside the training set, evaluation is performed on a new independent dataset called the validation set $\{x^{(i)}, g(x^{(i)})\}_{i=1}^m$ [128].

Definition 15. *The MSE estimator of the error committed by using a metamodel can be computed on the validation set $\{x^{(i)}, g(x^{(i)})\}_{i=1}^m$*

$$MSE \approx Err_{test} = \frac{1}{m}\sum_{i=1}^{m}\left(g(x^{(i)}) - \overline{g}(x^{(i)})\right)^2$$

Definition 16. *The Q^2 estimator it is defined as:*

$$Q^2 = 1 - \frac{MSE}{Var[g]} \approx 1 - \frac{\sum_{i=1}^m \left(g(x^{(i)}) - \overline{g}(x^{(i)})\right)^2}{\sum_{i=1}^m \left(g(x^{(i)}) - \frac{1}{m}\sum_{j=1}^m g(x^{(j)})\right)^2}$$

where $\{x^{(i)}, g(x^{(i)})\}_{i=1}^m$ is the validation set.

An increase in the complexity of the metamodel leads to a monotonic increase in the R^2 index. However, the index Q^2 is initially increasing and then begins to decrease when the metamodel starts to over-fit the original model. When training a metamodel, the quantity to be controlled is therefore the difference between R^2 and Q^2 (generalisation gap, [129]). In conclusion, a low R^2 index and a low Q^2 means insufficient input to perform a regression. A large difference between $R^2 \approx 1$ and $Q^2 \ll 1$ implying that the metamodel has been over-adapted to the training dataset (overfitting) [128], while a high R^2 and a high Q^2 means a good metamodel [129].

Remark 29 ($R^2 = Q^2 < 1$ is a good metamodel?)**.** *Regardless of the computational complexity of the metamodel, there is the possibility that the indices do not exceed a certain threshold (e.g. $Q^2 \approx R^2 \approx 70\%$). In these cases, it means that the input variables are not sufficient, regardless of its complexity, to predict the quantity of interest or that the size of the training set needs to be increased. In these cases, the best metamodel will be the one for which the R^2 index is maximal and the Q^2 index is coincident (same prediction on training and test set).*

Cross-validation

In some situations, the training set must also be used as a test set. This is necessary when the evaluation of the original model is very expensive and therefore the number of available simulations is low and it is not possible to build two independent sets. Such approach is also used for optimizing the hyper-parameters of the metamodel itself (e.g. LAR-methods to produce the coefficient of the PCE metamodel [130]).

The main idea of **cross-validation** is to split the original training set in a new training set and a test set, compute the error (Equation 15) and repeat for different combination of training and test sets. Average these obtained errors and use the value to investigate the goodness of the metamodel.

K-fold cross-validation error estimate is obtained applying the following procedure [131]:

- Split the original set $(\mathcal{X}, \mathcal{Y} = g(\mathcal{X}))$ into K mutually exclusive sub-samples $(\mathcal{X}_1, \mathcal{Y}_1 = g(\mathcal{X}_1)), \cdots, (\mathcal{X}_K, \mathcal{Y}_K = g(\mathcal{X}_k))$ with similar size.
- One of the sub-sample $(\mathcal{X}_i, \mathcal{Y}_i)$ is selected and the corresponding error is computed:
$$Err^{(i)} = \frac{1}{|\mathcal{X}_i|} \sum_{x^{(j)} \in \mathcal{X}_i} \left(g(x^{(j)}) - \overline{g}(x^{(j)}) \right)^2$$
- Repeat on each subset $i \in \{1, \cdots, K\}$.
- The **K-fold cross-validation error estimate** is the average:
$$Err_{\text{K-fold}} = \frac{1}{K} \sum_{i=1}^{K} Err^{(i)}$$

Definition 17. *The $Q^2_{K\text{-}fold}$ index it is defined as:*

$$Q^2_{K\text{-}fold} \approx 1 - \frac{Err_{K\text{-}fold}}{Var[g]}$$

The **Jack-knife cross-validation error estimate** (or Leave-One-Out, LOO) is a powerful K-fold strategy with $K = n$. This method requires a large number of training sessions of the metamodel but provides precise validation of the ability to generalise [132]. The Err_{LOO} and Q^2_{LOO} are defined as in the standard K-fold cross validation.

Remark 30. *Some metamodelling strategies (like the PCE expansion) admit a closed formula for calculating Q^2_{LOO} [130].*

Remark 31 (Hyperparameters optimization)**.** *Two data sets are sufficient to train and evaluate a metamodel: the training set and the test set. The training set, obtained with an efficient sampling strategy (e.g. LHC, quasi-MC), provides*

the metamodel with the information to be trained correctly. Conversely, the test set is a completely independent dataset that is used to ensure the goodness of the metamodel on data that was not used for training. However, if a hyper-parameter optimisation procedure is to be performed, it is necessary to have a dataset other than the test set. This dataset is called the validation set. In the optimal case, therefore, the metamodel is trained on the training set, providing an index R^2. A first value $Q^2_{validation}$ is then computed on the validation set. The hyper-parameters of the metamodel are chosen to maximise these two indices. The metamodel is finally evaluated on the test set (Q^2) to determine its reliability. In the case of small datasets, cross validation procedures can be used to extract test/validation sets from the original pool.

2.4.3 Polynomial Chaos Expansion

Among the surrogate models developed specifically for UQ, Polynomial Chaos Expansions (PCE) are among the most widely used. Based on a mathematical theory well developed since the 1800s, this method is based on the decomposition of the chosen quantity of interest by an appropriate polynomial basis. Given the multidimensional space of the inputs, the joint distribution of the variables is estimated. The latter describes the probability of having a given input vector. The polynomial basis is then chosen such that the elements are mutually orthonormal with respect to the input distributions [133]. The surrogate model is therefore a standard polynomial approximation of the output variable but, being defined on the basis of a probabilistic space, allows an analytical derivations of the sensitivity indices.

PCEs are an effective metamodel for performing sensitivity analyses, in particular for moderate dimensionality ($d < 10$) of the input space and for small datasets, they outperform direct methods [125].

Remark 32. *The charming name Polynomial Chaos Expansion dates back to Wiener (1838), who used it in the context of Hermite expansion for constructing a physical theory of chaos [124]. Ghanem and Spanos (1991) used the PCE representation to develop the Stochastic Finite Element Method [134]. Xiu and Karniadakis (2002) have greatly expanded the applications by employing different polynomial basis [135]. More recently, Sudret and Blatman (2008) described the currently most widely used form of PCE, providing an adaptive method to reduce the risk of overfitting [40, 130]. Given the historical motivation for the name, the term "spectral expansion" is often preferred in UQ contexts.*

Mathematical setup

Given the computational model $g : \mathcal{D}_X \subset \mathbb{R}^d \to \mathbb{R}$, the uncertainty of the input parameters is modeled by a random vector $X = (X_1, \cdots, X_d)$ prescribed by joint probability density function $\varphi_X(x)$, and the QoI $Y = g(X)$ which is obtained by propagating the uncertainty on X through g [136].

Remark 33. *Assuming that Y has finite variance (i.e. it belongs to Hilbert space of second order random variable), it admits the following spectral representation:*

$$Y = \sum_{j=0}^{\infty} c_j B_j \tag{2.39}$$

where $\{B_j\}_{j=1}^{\infty}$ is a basis of the Hilbert space and $\{c_j\}_{j=1}^{\infty}$ are the coefficients of the expansion [136].

The assumption on the variance of Y is physically meaningful in UQ applications. However, the theorem is not constructive and we have to make a choice on the basis B_j and define an algorithmic approach to find the coefficients c_j. Polynomial Chaos Expansions define an appropriate B_j base of multivariate orthonormal polynomials in the input vector X.

PCE basis

We want to define a basis of the Hilbert space which is orthonormal to the respect of the input X distribution [133] . Under the assumption that the input variables $(X_1, \cdots, X_d)$ are statistically independent (which can be obtained through the use of a Nataf transformation [46]), the joint input PDF $\varphi_X(x)$ is the product of d marginal distributions:

$$\varphi_X(x) = \prod_{i=1}^{d} \varphi_{X_i}(x_i) \tag{2.40}$$

where φ_{X_i} is the distribution of the i^{th} input variable.

The first step is to define the inner product for each variable X_i and for any $\phi_1, \phi_2 : \mathcal{D}_{X_i} \to \mathbb{R}$ as:

$$\langle \phi_1, \phi_2 \rangle_i := \mathbb{E}[\phi_1(X_i)\phi_2(X_i)] = \int_{\mathcal{D}_{X_i}} \phi_1(x)\phi_2(x)\varphi_{X_i}(x)dx \tag{2.41}$$

where $\mathcal{D}_{X_i}$ is the support of X_i. Having defined an inner product, we can construct a corresponding family of orthogonal polynomial $\{P_k^{(i)}, k \in \mathbb{N}\}$ through the use Gram-Schmidt orthogonalization procedure [137]. There is one family of polynomials for each input variable X_i. These *univariate* orthonormal polynomials provide the elements to define with a tensor product construction a family of *multivariate* orthonormal polynomials.

Definition 18. *Given a multi-index $\alpha = (\alpha_1, \cdots, \alpha_d), \alpha_i \in \mathbb{N}$ and the family of the univariate orthonormal polynomial $\{P_k^{(i)}, k \in \mathbb{N}\}_{i=1}^{d}$, the associated multivariate polynomial can be defined as*

$$\Psi_\alpha(x) := \prod_{i=1}^{d} P_{\alpha_i}^{(i)}(x_i) \tag{2.42}$$

As a remark, the choice of a multi-index with all but one null entry identifies the polynomials of that specific entry. This family is also orthonormal, as it follows from the definition of the inner product:

$$\mathbb{E}[\Psi_\alpha(X), \Psi_\beta(X)] := \int_{\mathcal{D}_X} \Psi_\alpha(x)\Psi_\beta(x)\varphi_X(x)dx = \delta_{\alpha\beta} \tag{2.43}$$

with α and β two multi-indices and $\delta_{\alpha\beta}$ the Kronecker delta.

Theorem 6. *The set of all multivariate polynomials Ψ_α in the input random vector X forms a basis of the Hilbert space [136].*

Consequently, $Y = G(X)$ admits the following spectral representation:

$$Y = \sum_{\alpha \in \mathbb{N}^d} c_\alpha \Psi_\alpha(X) \tag{2.44}$$

that is the so called **Polynomial Chaos Expansion** (PCE).

Orthonormal polynomials

Given a random variable X_i, the univariate orthonormal polynomials $\{P_k^{(i)}(x)\}_{k=0}^{\infty}$ can always be constructed through the use Gram-Schmidt orthogonalization procedure [137]. The latter can be applied to arbitrary input distribution but for most standard distributions, there is an analytical formula for the corresponding univariate orthonormal polynomials, as summarised in the Table 2.3

Type of variable	**Distribution**	**Orthonormal polynomials**
Uniform $\mathcal{U}[(-1,1)]$	$1_{[-1,1]}(x)/2$	Legendre $P_k(x)/\sqrt{\frac{1}{2k+1}}$
Gaussian $\mathcal{N}(0,1)$	$\frac{1}{\sqrt{2}}e^{-x^2/2}$	Hermite $He_k(x)/\sqrt{k!}$
Gamma $\Gamma(\alpha, \lambda = 1)$	$x^\alpha e^{-x} 1_{\mathbb{R}^+}(x)$	Laguerre $L_k^\alpha(x)/\sqrt{\frac{\Gamma(k+\alpha+1)}{k!}}$

Table 2.3: Standard distribution and related orthonormal polynomials, as reported in [138]. Further details on orthonormal polynomial families can be found in Bini [137]. Orthonormal polynomials for arbitrary distributions can be calculated using the Gram-Schmidt orthogonalization.

In practice, most of the random variable are not in the normalized forms reported in Table 2.3 (e.g. an input random variable X_i with uniform distribution $\mathcal{U}[(3,7)]$). In these cases, an isoprobabilistic transformation can turn the variable into a standard distribution.

The construction of the multivariate orthonormal families requires the independence of the random variables X_i. This assumption is often unrealistic as the input distribution has to be described by a proper copula which models the relationship within the single marginals. However, if the input vector X is defined by a set of marginals and a Gaussian copula, it can be transformed into a set of independent standard normal variables using the Nataf transform [46].

Remark 34 (Unknown random variables: PCE yes or not?)**.** *The input distribution must always be calibrated on real data. If the calibration is performed incorrectly, the results of the PCE are unpredictable. Indeed, although it is always possible to calibrate the coefficients of the PCE on the basis of the training set, the analytical formulae for calculating sensitivity indices are based on the assumption that the polynomials are orthonormal with respect to the real input distribution. Therefore, when input information is partial, it is better to use other methodologies (e.g. local sensitivity analysis, direct methods, other metamodels).*

Enumeration rule

The PCE is an infinite series which describes the output distribution $Y = G(X)$. The latter has to be truncated in order to get a finite approximation which can be used in practical applications. The truncation strategy it is based (i) on how to enumerate the element of the multivariate basis and (ii) on how many terms of the basis have to be retained [130].

Definition 19. *An enumeration strategy is an enumeration functions $\tau : \mathbb{N} \to \mathbb{N}^d$, which creates a one-to-one mapping between an integer j and a multi-index α of the d-multivariate polynomials.*

Most of the enumeration strategies for the multivariate polynomials are based on the definition of the total degree of a multivariate polynomial.

Definition 20. *The total degree of a multivariate polynomial Ψ_α is:*

$$\|\Psi_\alpha\| := \sum_{i=1}^{d} \alpha_i$$

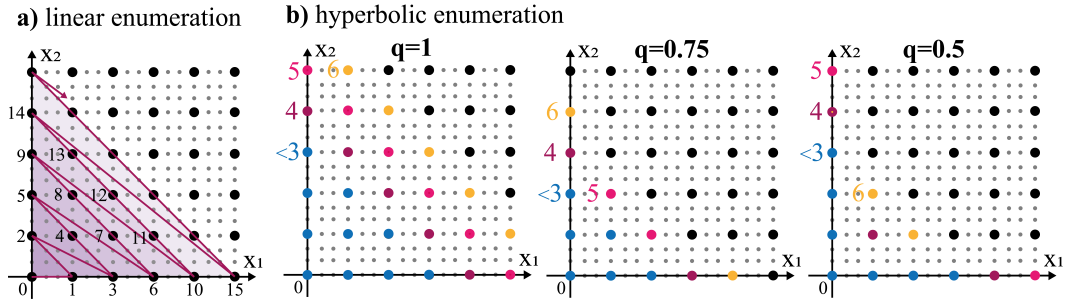

Figure 2.7: Example of linear (a) and hyperbolic (b) enumeration strategy in the case of two variables. Note how the hyperbolic enumeration in the case $q = 1$ is coincident with the linear enumeration (in each of the strata the normal linear enumeration is applied). As q decreases, the shape of the strata becomes increasingly hyperbolic, i.e. elements with a low number of interactions are numbered first.

With reference to Figure 2.7a), the **standard (linear) enumeration strategy** is defined as the lexicographical order with a constraint of increasing total

degree (e.g. for a two dimensional multi-index $(0,0) < (0,1) < (1,0) < (2,0) < (1,1,) < \cdots$).

The *sparsity-of-effects principle* states that most models are governed by their main effects (i.e. the effect of one single input variable on the QoI) and lower order interactions. The enumeration strategy defines the order in which the coefficients of the multivariate polynomial are considered. Therefore, a linear enumeration strategy investigates many high-level interactions between the variables and is in contrast with the sparsity-of-effects principle.

Definition 21. *For any $q \in (0,1]$, the q-hyperbolic quasi-norm of a multi-index α it is defined as:*

$$\|\alpha\|_q := \left(\sum_{i=1}^{d} \alpha_i^q\right)^{\frac{1}{q}} \tag{2.45}$$

With reference to Figure 2.7b), the hyperbolic enumeration strategy it is based on the partition of $\mathbb{N}^d$ into strata $(\Delta_n)_{n\in\mathbb{N}}$. The enumeration it is obtained by sorting the elements of the stratum Δ_n in ascending order of the q-norm.

Definition 22. *The **partition based on the total degree** defines the strata as*

$$\begin{cases} \Delta_0 = \{0\} \\ \Delta_n = \{\alpha \in \mathbb{N}^d : n-1 < \|\alpha\|_q \leq n\} \end{cases} \tag{2.46}$$

The hyperbolic norms penalize the indices associated with high-order interactions. Setting $q = 1$ leads to the standard linear enumeration strategy. When q ¡ 1, the retained basis are located under an hyperbola, hence the name hyperbolic enumeration strategy.

In some applications, we want to prioritise one variable over another. As an example, using an approximating polynomial of high degree with respect to input x_1 and a simple interpolating line for input x_2. In such cases, a rule can be defined that weights the different input spaces differently.

Definition 23. *For any $q \in (0,1]$ and $\omega \in \mathbb{R}_+^d$, the ω, q-anisotropic hyperbolic quasi-norm of a multi-index α it is defined as:*

$$\|\alpha\|_{\omega,q} := \left(\sum_{i=1}^{d} \omega_i \alpha_i^q\right)^{\frac{1}{q}} \tag{2.47}$$

As a remark, highest weights correspond to input variables with lower order interactions.

Truncation strategy

Having defined an enumeration strategy, we want to choose where to truncate the polynomial expansion (i.e. define the set of multi-indices $\mathcal{A} \subseteq \mathbb{N}^d$ that describe the chosen coefficients of the PCE). Several truncation methods exist, but the most common is the **standard truncation scheme**.

Once a maximum value p has been fixed, all the coefficients of the expansions such that $\|\alpha\| \leq p$ are maintained:

$$\mathcal{A} = \mathcal{A}^{d,p} := \{\alpha \in \mathbb{N}^d : \|\alpha\| \leq p\} \tag{2.48}$$

The chosen norm can be either the standard one or alternatives (e.g. hyperbolic, anisotropic hyperbolic) and thus can be applied to each of the enumeration rules discussed. This choice, although intuitive, leads to maintaining in the case of linear enumeration a number of coefficients that grows approximately exponentially in the size of the input space:

$$\text{card}(\mathcal{A}^{p,d}) = \binom{d+p}{p} = \frac{(d+p)!}{d!p!}$$

An increase in the number of coefficients leads to an increase in the sample size of the training set. Indeed, the latter must be larger than the number of unknowns $\text{card}\,\mathcal{A}$ for the problem to be well-posed. As a rule of thumb, a sufficient size of the training set is $\approx$ 2-3 $\times$ $\text{card}\,(\mathcal{A})$ [130]. This problem is called the **curse of dimensionality** and is the main limitation to using PCE (and other metamodelling strategies) for input spaces with high dimensionality. The use of a hyperbolic norm not only reduces the number of coefficients but also focuses the metamodel on low interactions between variables.

Alternatives to the standard truncation scheme are sequential strategies. These strategies circumvent the curse of dimensionality starting with a small number of coefficients and increasing this set according to a certain rule, thus extending the base progressively up to a maximum number of coefficients.

The **standard sequential strategy** starts from the term Ψ_0 of the PCE. Once a maximum base size has been set, the elements of the base are progressively added according to the chosen enumeration strategy. Base extension is interrupted when a number of points equal to the chosen maximum base size have been added or a certain convergence criterion has been reached (e.g. MSE error below a fixed threshold).

Another sequential method is the **cleansing strategy**. In this case we start with a number of coefficients (chosen in accordance with the enumeration strategy) equal to the maximum base size. The metamodel is trained on the training set and all the unimportant coefficients are identified, i.e. c_* such that $c_* \leq \varepsilon \cdot \max_i \|c_i\|$ where $\varepsilon \approx 10^{-4}$. The identified coefficients are removed from the base and an equal number is added following the chosen enumeration strategy. This process iterates until convergence. More complex sequential strategies can add the next basic element using efficient methodologies. Examples are the

adaptive sparse PCE based on Least Angle Regression [139] or the sparse high order FEM [140].

Once the set of coefficients has been defined $\alpha \subset \mathbb{N}^d$, the truncated PCE is defined as:

$$\hat{Y} = \sum_{\alpha \in \mathcal{A}} \hat{c}_\alpha \Psi_\alpha(X) \tag{2.49}$$

Training strategy

To find the optimal values of $\hat{c}_\alpha$, the metamodel must be trained. There are many methods for training the PCE that fall into two families: methods that impose limitations on the choice of training dataset (i.e., the sample must be chosen accordingly to the chosen methodologies) and methodologies that can exploit arbitrary sampling sets (and thus can be expanded if the training set has to be redefined). To the first type of methods belong intrusive methods such as stochastic finite element [141] or those based on the orthonormal properties of the basis and exploiting efficient sampling (collocation methods). These strategies, although capable of obtaining accurate results with a limited sample size, often do not allow the extension of a pre-existing dataset. New analyses thus require redefining the sample from scratches and re-performing all simulations. In practical applications, the possibility of extending the dataset is crucial. Therefore, one of the most widely used non-intrusive methods for PCE training is the choice of the coefficients of the expansion as those values that minimise the MSE (**least-square minimization problem**).

Formally, as detailed in [142, 143], the real model can be described using the truncated series and a residual:

$$Y = g(X) = \overline{g}(X) + \varepsilon = \sum_{\alpha \in \mathcal{A}} \hat{c}_\alpha \Psi_\alpha(X) + \varepsilon \tag{2.50}$$

The least-square minimization method consists in finding the set of coefficients $\mathcal{C} = \{\hat{c}_\alpha, \alpha \in \mathcal{A}\}$ which minimizes the mean square error:

$$\begin{aligned} \mathcal{C} &= \arg\min_{\hat{c}_\alpha} \mathbb{E}[\varepsilon^2] \\ \mathbb{E}[\varepsilon^2] &:= \mathbb{E}\left[(g(X) - \overline{g}(X))^2\right] \approx \frac{1}{n} \sum_{i=1}^{n} \left(g(x^{(i)}) - \sum_{\alpha \in \mathcal{A}} \hat{c}_\alpha \Psi_\alpha(x^{(i)}) \right)^2 \end{aligned} \tag{2.51}$$

where $(\mathcal{X}, \mathcal{Y}) = \{x^{(i)}, y^{(i)} = g(x^{(i)})\}_{i=1}^n$ is the dataset (e.g. the training/validation set).

Definition 24. *The **information matrix** is defined as:*

$$\boldsymbol{M} = \{\boldsymbol{M}_{ij} := \Psi_j(x^{(i)}), i = 1, \cdots, n, j = 1, \cdots, \mathrm{card}(\mathcal{A})\} \tag{2.52}$$

The solution of the least squares problem is analytical:

$$\mathcal{C} = \left(\mathbf{M}^T \mathbf{M}\right)^{-1} \mathbf{M}^T \mathcal{Y} \tag{2.53}$$

Remark 35 (Sample and coefficients)**.** *The advantage of a method such as the one presented is that the sampling can also be extended without re-running the previous simulations. In addition, the points of the training set can be chosen arbitrarily. Therefore, sampling strategies such as Latin Hypercube sampling or quasi-random sequences can be exploited for an efficient investigation of the input space.*

UQ applications

The truncated expansion $\hat{Y} = \sum_{\alpha \in \mathcal{A}} \hat{c}_\alpha \Psi_\alpha(X)$, with $\mathcal{A}$ the set of multi-indices and $\hat{c}_\alpha$ the approximated coefficient, contains the information about the random output $Y = g(X)$. Therefore, analytical formulas can be derived for calculating the mean, variance and Sobol' indices of Y.

The formula for the mean and variance is derived from the orthonormality of the polynomial basis:

$$\begin{aligned} \mathbb{E}[\hat{Y}] &= \mathbb{E}\left[\sum_{\alpha \in \mathcal{A}} \hat{c}_\alpha \Psi_\alpha(X)\right] = \hat{c}_0 \\ \mathrm{Var}[\hat{Y}] &= \mathbb{E}\left[\left(\hat{Y} - \hat{c}_0\right)^2\right] = \sum_{\alpha \neq 0, \alpha \in \mathcal{A}} \hat{c}_\alpha^2 \end{aligned} \tag{2.54}$$

The Sobol' index attached to each subset of variables $A := \{i_1, \cdots, i_s\} \subseteq \{1, \cdots, d\}$ is defined as $S_A = V_A/V$ where $V = \mathrm{Var}[Y]$ is the variance of the output and $V_A = \mathrm{Var}[g_A(X_A)]$ is the variance of the output given by the variables X_i s.t. $i \in A$. For more details on Sobol' indices, see Section 2.3. Let consider the set of multivariate polynomials Ψ_α which depend only on the subset of variables A:

$$\mathcal{A}_A := \{\alpha \in A : \alpha_k \neq 0 \iff k \in A\}$$

due to the orthogonality of the PC basis [40]:

$$V_A = \sum_{\alpha \in \mathcal{A}_A} \hat{c}_\alpha^2$$

and therefore

$$S_A = \frac{\sum_{\alpha \in \mathcal{A}_A} \hat{c}_\alpha^2}{\sum_{\alpha \neq 0, \alpha \in \mathcal{A}} \hat{c}_\alpha^2}$$

The confidence intervals for Sobol' indices can not be derived from the asymptotic distribution of the estimators of the indices, but they can still be assessed without performing further simulations through a resampling method, the bootstrap [144, 144].
The main idea is to create a few artificial datasets of different sizes by sampling with replacements the individual elements of the original training one. These artificial datasets are then used to calculate the Sobol' indices (using the PCE method introduced above), thus obtaining an empirical distribution of the indices quantifying the stability of the results with respect to a variation of the input dataset.

Definition 25. *The* α***-percentile bootstrap interval*** *is defined as:*

$$[S_{i[\alpha/2]}, S_{i[1-\alpha/2]}]$$

where $S_{i[\alpha/2]}$ *and* $S_{i[1-\alpha/2]}$ *are the* $\alpha/2$ *and the* $1-\alpha/2$ *empirical quantiles of the i-th Sobol' index distribution [145].*

This interval does not require hypotheses about the S_i distributions (compared to standard intervals which assume normality [145]) but it needs many resamplings to estimate them accurately.

2.4.4 Gaussian Process Regression - Kriging

Gaussian Process (GP) Regression, also known as Kriging or Wiener Kolmogorov prediction, it is a powerful metamodel techniques which interpolates the data using a Gaussian Process instead of a polynomial expansion. The theory behind GPs dates back to 1940, with the works of Wiener [146] and Kolmogorov [126], while it was introduced in the context of global SA in the early 90s by Welch et al. [127], and further explored by Oakley and O'Hagan [147], and Marrel et al. [148].

GP main advantages include a closed form to compute Sobol' indices with the corresponding confidence intervals, making possible to perform global SA using a limited number of evaluations. Furthermore, GP admits a sequential sampling strategy that can be used to extend efficiently the training set with a reduced number of elements. Compared to other metamodelling techniques, GP perform particularly well for extremely small designs and it is comparable with PCE in a broad range of applications [125].

Gaussian Process

The theoretical background for introducing Kriging starts with the definition of a Gaussian process.

Definition 26. *Given a probability space* $(\Omega_Z, \mathcal{F}_Z, \mathbb{P}_Z)$*, a measurable space* $(\mathcal{S}, \mathcal{B}(\mathcal{S}))$ *and a set* $\mathbb{X}$*, a stochastic process* $\{Z(x),\ x \in \mathbb{X}\}$ *is Gaussian if and only if for every finite set* $\{x^{(1)}, \cdots, x^{(k)}\} \subset \mathbb{X}$*,* $Z_{x^{(1)},\cdots,x^{(k)}} := (Z_{x^{(1)}}, \cdots, Z_{x^{(k)}})$ *is a multivariate Gaussian random variable.*

In the UQ framework, the input space is $\mathbb{X} = \mathbb{R}^d$ and the QoI space is $\mathcal{S} = \mathbb{R}$.

A Gaussian Process (GP) $Z(x)$ is uniquely identified by its mean and covariance functions, defined as:

$$\begin{aligned} m(x) &= \mathbb{E}[Z(x)] \\ k(x, x') &= \mathrm{cov}(Z(x), Z(x')) = \mathbb{E}[(Z(x) - m(x))(Z(x') - m(x'))] \end{aligned} \tag{2.55}$$

and therefore can be denoted as:

$$Z(x) \sim \mathcal{GP}(m(x), k(x, x'))$$

The mean and covariance functions are not uniquely determined. Each family of functions has its own properties that strongly alter the underlying GP.A correct choice of these functions can greatly affect the ability of the metamodel to approximate the original model.

Mean function

The mean function $m(x)$ of the GP $Z(x)$ can leads to different predictions of the model. It is common but by no means necessary to consider GPs with a zero

mean function. As a remark, the posterior distribution obtained by conditioning $Z(x)$ to the training dataset can have a non-zero mean even with the zero mean assumption on the prior distribution. Therefore, the obtained posterior mean is not confined to be zero independently on the choice of $m(x)$ [149].

Common choices for $m(x)$ include: stationarity of the first moment over the domain (i.e. $\mathbb{E}[Z(x)] = constant$, simple Kriging), assuming constant unknown over the search neighborhood of x (ordinary Kriging), or assume a general polynomial trend model (universal Kriging).

Covariance function

Definition 27. *The covariance function is a positive definite kernel, i.e. a general function $k : \mathbb{X} \times \mathbb{X} \to \mathbb{R}$ such that*

$$\sum_{i=1}^{m}\sum_{j=1}^{m} c_i c_j \; k(x^{(i)}, x^{(j)}) > 0$$

holds for any $x^{(1)}, \cdots, x^{(m)} \in X$, given $m \in \mathbb{N}$ and $c_1, \cdots, c_m \in \mathbb{R}$.

For a stochastic process $Z(x)$, a covariance function $k(x, x')$ gives the covariance of the values of the random field at the two locations x and x'. The covariance function used in several practical application are stationary.

Definition 28. *A kernel it is called stationary if it is a function of the distance $x - x'$, i.e. $k(x, x') = f(x - x')$, is thus invariant with respect to translation in the input space.*

Describing a GP means making a choice, based on the available information, of the mean and covariance function and identifying their optimal parameters. Indeed, different choices of the kernel can potentially lead to totally different metamodel solutions. Commonly used covariance functions for input domain subset of the vector space $\mathbb{R}^D$ include:

- Constant covariance:
$$k(x, x') = constant$$
- Linear covariance:
$$k(x, x') = x^T x'$$
- Squared exponential (SE) covariance:
$$k(x, x') = \sigma^2 \exp\left(-\frac{1}{2\theta^2}\|x - x'\|^2\right)$$
parametrized by θ (correlation length) and the variance parameter σ^2. The latter is a common stationary choice in Kriging, with $m(x)$ that is intuitively the trend around which the realizations vary, θ the oscillation frequencies, and σ^2 the range of variations.

The SE covariance function is the most frequently used in practical applications. However, it is known that its strong assumptions of regularity can lead to unrealistic results [150].

GP regression

Once the prior GP $Z(x)$ with its own mean function $m(x)$ and covariance function $k(x, x')$ and given a training dataset $(\mathcal{X}, \mathcal{Y}) = \{x^{(i)}, y^{(i)})\}_{i=1}^{n}$ have been defined, regression consists of describing the posterior probability of an unknown output y^* for an input x^*. For the properties of the GP, it holds:

$$\begin{bmatrix} \mathcal{Y} \\ y^* \end{bmatrix} \sim \mathcal{N}\left(\begin{bmatrix} m(\mathcal{X}) \\ m(x^*) \end{bmatrix}, \begin{bmatrix} k(\mathcal{X}, \mathcal{X}) & k(\mathcal{X}, x^*) \\ k(x^*, \mathcal{X}) & k(x^*, x^*) \end{bmatrix} \right) \tag{2.56}$$

The distribution of the predicted output y^* conditioned to the known data (intuitively, generate functions from the prior, and reject the ones that disagree with the observations, see Figure 2.8) can be calculated as follows:

$$\begin{aligned} (y^*|_{x^*,\mathcal{X},\mathcal{Y}}) &\sim \mathcal{N}(\tilde{m}(x^*), \tilde{k}(x^*, x^*)) \\ \tilde{m}(x^*) &:= m(x^*) + k(x^*, \mathcal{X})k(\mathcal{X}, \mathcal{X})^{-1}(\mathcal{Y} - m(\mathcal{X}) \\ k_n(x^*, x^*) &:= k(x^*, x^*) - k(x^*, \mathcal{X})k(\mathcal{X}, \mathcal{X})^{-1}k(\mathcal{X}, x^*) \end{aligned} \tag{2.57}$$

Therefore, given a new input value x^*, an estimate of the output can be obtained from the prior $Z(x)$ in terms of: *predicted mean* $\tilde{m}(x^*)$ and *predicted variance* $\tilde{k}(x^*, x^*)$.

The *predicted mean* is the main result of the regression through GP. It is a linear weighted combinations of the training data, where the output-independent weights are based on the covariance distance between the x^* and $\mathcal{X}$. As a remark, the choice of a prior $m(x) = 0$ still allows to obtain a posterior mean $\tilde{m}(x) \neq 0$. The *predicted variance* represents the posterior variability in the prediction. $\tilde{k}(x^*, x^*)$ is in fact the model mean-square error. This value can be used as an accuracy estimate and exploited to decide where to enrich the training dataset (sequential design), see Figure 2.8.

In most applications, the result must be a point estimate (e.g. the result of a regression). For this purpose, it is necessary to define a *loss function* $\mathcal{L}(y_{true}, y^*)$. Not having y_{true}, the point estimate is obtained by minimising the average expected loss:

$$y^*_{optimal}|x^* = \text{argmin}_{y^*} \int \mathcal{L}(y', y^*)p(y'|x^*, \mathcal{X}, \mathcal{Y})dy' \tag{2.58}$$

In general the value that minimizes the risk is the median. However, when the predictive distribution is Gaussian, the mean and the median coincide, and indeed for any symmetric loss function and symmetric predictive distribution we always get y^* as the mean of the predictive distribution [149]. As a remark, the posterior distribution is computed without the use of the loss function which is used to captures the consequences of making a specific choice, given an actual true state.

Remark 36 (Noisy data)**.** *In case of noisy data the previous formulation can be modified to take into account noise properties. More details are reported both by Rasmussen [149] and Sudret [125].*

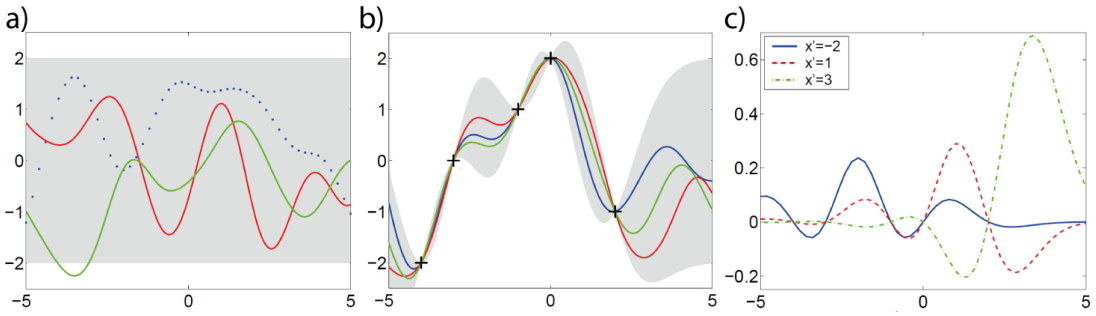

Figure 2.8: Panel a) shows the prior GP $Z(x)$ and three functions drawn at random from it. Panel b) instead describes the posterior GP $\mathcal{GP}(\tilde{m}(x), \tilde{k}(x, x'))$, with three random functions drawn from it. The posterior is obtained by conditioning the prior GP on the five observations indicated. In both plots the shaded area represents the pointwise mean plus and minus two times the standard deviation for each input value (corresponding to the 95% confidence region). The grey area is dependent on the estimated posterior variance at that point, and therefore it is linked with the approximation error of the model itself. Sequential strategy can sample new points to reduce this amount of error (intuitively, choose x as the one with the widest gray region). Panel c) shows the covariance $\tilde{k}(x, x')$ for three different choices of x'. Note, that the covariance is zero at the training points (where there is no variance, since it is a noise-free process) [149]

Sequential design

A crucial feature of GP regression is that the model itself provide an estimate of its performance through the predicted variance $\tilde{k}(x^*, x^*)$, which is the model mean-square error. Therefore, if the model predictions are not sufficiently accurate, new points can be added to the training set. The most common strategy is to select the new points as the ones with the highest predicted $\tilde{k}(x^*, x^*)$, see Figure 2.8c). However, exist several more efficient criteria which can be found in Bates et al. [151]; van Beers and Kleijnen [152]; Le Gratiet and Cannamela [153].

One of the modern applications of Kriging with sequential design is Bayesian optimisation [154, 155]. Consider a complex machine learning problem with hundreds of inputs that has to be solved using an artificial neural network (e.g. image classification). This problem cannot be addressed with UQ methodologies due to the dimensionality of the space being too high. However, the optimal network to be trained depends on certain hyper-parameters (such as the number of nodes, convolutional layers, activation function characteristics). Kriging therefore applies to the relationship between hyperparameters and model accuracy. This technique therefore not only selects the optimal hyperparameters but, in addition, guides subsequent evaluations so as to minimise the number of model trainings required for optimisation.

GP as surrogate model

The GP inference described allows to obtain a prediction of the output starting from a prior GP $Z(x)$ and a training dataset. However, to apply the method to SA problem, it is useful to give a different interpretation based on surrogate models [125].

In this fashion we can see the problem as follow. We have a prior GP $Z(x)$ with a proper choice of mean $m(x)$ and covariance $k(x, x')$ functions. We want to integrate this prior with the known information (e.g. the training dataset $(\mathcal{X}, \mathcal{Y}) = \{x^{(i)}, y^{(i)}\}_{i=1}^n$) to derive a new Gaussian process $\mathcal{GP}(\tilde{m}(x), \tilde{k}(x, x')$ which approximates the original problem. This GP is the surrogate model.

To compute the parameters of the surrogate mode (e.g. $\tilde{m}(x)$ and $\tilde{k}(x, x')$) we can describe the original mean and covariance functions with the following parameterization:

$$\begin{aligned} m(x) &= f^T(x)\beta \\ k(x, x') &= \sigma^2 r(x, x', \theta) \end{aligned} \tag{2.59}$$

where $f^T(x)$ is a vector of prescribed functions and θ are the covariance parameters. The hyperparameters σ^2, θ and β all requires a proper calibration.

Given a training dataset $(\mathcal{X}, \mathcal{Y}) = \{x^{(i)}, y^{(i)}\}_{i=1}^n$, $x^{(i)} \in \mathbb{R}^d$, the metamodel parameters can be calculated as:

$$\begin{aligned} \tilde{m}(x) &= f^T(x)\overline{\beta} + r^T(x)R^{-1}(\mathcal{Y} - F\overline{\beta}) \\ \tilde{k}(x, x') &= \sigma^2 \left(1 - \begin{pmatrix} f(x) \\ r(x) \end{pmatrix}^T \begin{pmatrix} 0 & F^T \\ F & R \end{pmatrix} \begin{pmatrix} f(x') \\ r(x') \end{pmatrix}\right) \end{aligned} \tag{2.60}$$

where

$$\begin{aligned} \overline{\beta} &= (F^T R^{-1} F)^{-1} F^T R^{-1} \mathcal{Y} \\ R &= (r(x^{(i)}, x^{(j)}, \theta))_{i,j=1}^n \\ r(x) &= (r(x, x^{(i)}, \theta))_{i=1}^n \\ F &= (f^T(x^{(i)}))_{i=1}^n \end{aligned} \tag{2.61}$$

This estimation for the mean is the same as in equation (2.57). However, instead of directly providing a predicted variance for the distribution, the entire covariance function is given, uniquely characterising the surrogate model. This characterization, while less intuitive in term of posterior distribution, leads to useful properties for SA.

Remark 37 (Hyperparameters calibration)**.** *While the hyperparameter β admits an analytical formula for its approximation, σ^2 and θ parameters require ad-hoc numerical strategy to find them. Similarly, the choice of the best $f^T(x)$ and $r(x, x'\theta)$ must be based on the training dataset properties. These hyperparameters can be estimated with the maximum likelihood method [156, 157], using gradient methods [158], or with a cross-validation strategy [159]*

GP main effects

A quantity often computed during UQ analysis is the main effect (the effect of one independent variable on the dependent variable) [147] of the model g. The main effect of the group of input variables x_A, $A \subseteq \{1, \cdots, d\}$ is defined by $\mathbb{E}[g(x)|x_A]$.

To compute the main effect we substitute $G(X)$ with its surrogate $\mathcal{GP}(x) := \mathcal{GP}(\tilde{m}(x), \tilde{k}(x, x'))$. Since $\mathcal{E}[\mathcal{GP}(x)|x_A]$ it is a linear transformation of the Gaussian process $\mathcal{GP}$, it is also a Gaussian process, therefore it holds the following formula:

$$\mathbb{E}[\mathcal{GP}(\tilde{m}(x), \tilde{k}(x, x'))|x_A] \sim \mathcal{GP}(\mathbb{E}[\tilde{m}(x)|x_A], \mathbb{E}[\mathbb{E}[\tilde{k}(x, x')|x_A]|x'_A]) \tag{2.62}$$

Where the mean $\mathbb{E}[\tilde{m}(x)|x_A]$ represents the approximation of the main effect and the covariance $\mathbb{E}[\mathbb{E}[\tilde{k}(x, x')|x_A]|x'_A]$ is the mean-square error on the main effects due to the metamodel approximation.

GP Sobol' indices

The Sobol' indices are one of the most popular measure in SA because can be interpreted as the part of the total variance due to a group of variables. They are defined as the normalized variance of the main effect:

$$S_A := \frac{\mathrm{Var}\left(\mathbb{E}[\mathcal{GP}(\tilde{m}(x), \tilde{k}(x, x'))|x_A]\right)}{\mathrm{Var}\left(\mathbb{E}[\mathcal{GP}(\tilde{m}(x), \tilde{k}(x, x'))]\right)} \tag{2.63}$$

Remark 38. *This transformation is not linear and therefore does not exist a closed formula as the one for the main effect.*

To obtain an estimate for the Sobol' indices we can use the methodologies presented for the general case (e.g. Saltelli's algorithm) substituting the original model with its surrogate.

However, the GP regression allows to get a sample $\{S_{A,i}\}_{i=1}^m$ from S_A which, being obtained by substitution of the original model $g(x)$ with its GP surrogate, it is a random variable. The realizations of S_A can be obtained generating a sample on $(x^{(i)}, x^{(i),A})_{i=1}^m$ (is a sample from the random variable $(x, x^{\tilde{A}})$) of the GP $\mathcal{GP}(\tilde{m}(x), \tilde{k}(x, x'))$ and using Sobol' pick-freeze [100] formula:

$$S_A \approx \frac{\frac{1}{n}\sum_{i=1}^n \mathcal{GP}(x^{(i)})\mathcal{GP}(x^{(i),A}) - \left(\frac{1}{22}\sum_{i=1}^2 \left(\mathcal{GP}(x^{(i)}) + \mathcal{GP}(x^{(i),A})\right)\right)^2}{\frac{1}{n}\sum_{i=1}^n \mathcal{GP}(x^{(i)})^2 - \left(\frac{1}{2n}\sum_{i=1}^n \left(\mathcal{GP}(x^{(i)}) + \mathcal{GP}(x^{(i),A})\right)\right)^2} \tag{2.64}$$

Remark 39 (Sample from GP)**.** *GP can be sampled using several other techniques including: Cholesky decomposition [149] and Fourier spectral decomposition [150].*

Once obtained the sample, the following unbiased estimate of S_A can be deduced:

$$\hat{S}_A = \frac{1}{m}\sum_{i=1}^{m} S_{A,i} \quad ; \quad \hat{\sigma}^2_{\hat{S}_A} = \frac{1}{m-1}\sum_{i=1}^{m}\left(S_{A,i} - \hat{S}_A\right)^2 \tag{2.65}$$

The term $\hat{\sigma}_{\hat{S}_A}$ represents the uncertainty on the estimate due to the metamodel approximation [160].

Chapter 3

Sensitivity analysis of an electrophysiology model for the left ventricle

Giulio Del Corso, Roberto Verzicco and Francesco Viola
Journal of the Royal Society Interface 17.171 (2020): 20200532

Abstract

Modeling the cardiac electrophysiology entails dealing with the uncertainties related to the input parameters such as the heart geometry and the electrical conductivities of the tissues, thus calling for an uncertainty quantification (UQ) of the results.

Since the chambers of the heart have different shapes and tissues, in order to make the problem affordable, here we focus on the left ventricle with the aim of identifying which of the uncertain inputs mostly affect its electrophysiology. In a first phase, the uncertainty of the input parameters is evaluated using data available from the literature and the output quantities of interest (QoIs) of the problem are defined. According to the polynomial chaos expansion, a training data–set is then created by sampling the parameter space using a quasi Monte Carlo method whereas a smaller independent data–set is used for the validation of the resulting metamodel. The latter is exploited to run a global sensitivity analysis with non–linear variance–based indices and thus reduce the input parameter space accordingly.

Thereafter, the uncertainty probability distribution of the QoIs are evaluated using a direct UQ strategy on a larger data–set and the results discussed in the light of the medical knowledge.

3.1 Introduction

Advances in computational science have enabled the development of digital twins of biological systems of which a popular application is in cardiology and, more in general, in cardiovascular medicine. This approach not only allows to improve the predicting capabilities of diagnostic tools and to get more insight into patients pathologies, but also provides a numerical framework to test innovative medical devices and to refine them before running further in vivo experiments on animals or humans. Predictive mathematical models imply a physical basis and the quantities of interest (QoIs) have to be obtained by solving the governing equations for the system under investigation.

In particular, modeling the human heart functioning entails reproducing the complex electrical activation triggering the muscular contraction, which includes a conductive network that propagates the local transmembrane potential of the myocytes from the sinoatrial node (SA-node) to the atrial and the ventricular muscles. As visible in figure 3.1(a), the local myocytes depolarization originates in the SA-node that is located in the right atrium close to the entrance of the superior vena cava [161], and then propagates across the right atrium and reaches the atrioventricular node (AV-node). After the transmembrane depolarization front leaves the AV-node, it spreads towards the ventricles passing through the His bundle that bifurcates into a set of bundles that conducts the signal to a fast conduction system (the Purkinje network), thus allowing for a more uniform signal propagation in the ventricular myocardium and for a subsequent simultaneous muscular activation and an efficient blood pumping towards the circulatory system. As the transmembrane depolarization front reaches a certain location in the myocardium the local transmembrane potential of the myocytes rapidly changes from the negative potential (of about -85mV) to a positive value (of about 20mV) before returning to the resting negative potential after about 300ms, as indicated in figure 3.1(b). This transient depolarization of the cardiomyocytes (*action potential*) yields the release of cytosolic calcium from the sarcoplasmic reticulum that originate a contractile force within the cardiac muscle cells (the sarcomers), thus causing the myocardium to contract. The contraction of the muscular fibers can be detected placing electrodes on the patient's limbs and chest as done in electrocardiography (ECG), where the P wave represents the depolarization of the atria, the QRS complex corresponds to the depolarization of the ventricles and the T wave indicates the ventricles repolarization, see figure 3.1(c) for a typical healthy ECG patterns. Variations of the normal ECG pattern and duration are usually ascribed to cardiac pathologies and abnormalities, such as atrial fibrillation and ventricular tachycardia.

This electrical activation of the heart has been studied using different approaches depending on the application. In the interconnected cable method [162, 163] the cardiac tissue is modeled as a connected network of discrete cables representing muscle cardiac fibers. This approach is broadly used because accurately describes the fibers electrical activation at a lower computational cost

compared to other methods and can be efficiently parallelized [164]. Starting from the cable equation, a fractional Laplacian formulation can be used to model the cardiac tissue including the macroscopic effects of structural heterogeneity on impulse propagation [165] or to incorporate more complex conduction structures, such as cardiomyocytic fibers orientation and the His-Purkinje activation network [166]. The propagation of the cellular depolarization front can be also modeled by an eikonal approach, where the excitation time defined at each point mesh as the time instant at which the transmembrane potential crosses the value midway between its resting and plateau potentials is solved [167]. On the other hand, the bidomain model called in this way because the conductive myocardium is modeled as an intracellular and an extracellular overlapping continuum media separated by the myocytes membranes, computes the electrical cardiac activity by solving the quasi steady electric equations [168, 169]. The resulting system of reaction–diffusion partial differential equations governs the electrical propagation across the myocytes and is coupled with a set of ordinary differential equations (the cellular ionic model) describing the current flow through the ion channels, see § 3.2. In the case that the extracellular and intracellular conductivity tensors are parallel to each other, the bidomain equations can be simplified as a single governing equation for the transmembrane potential, the monodomain system, which is computationally cheaper not only because the number of degrees–of–freedom is reduced but also because the equations are more stable numerically [170]. Differences in the electrical propagation and intra/extracellular potentials between monodomain and bidomain are typically very small unless complex activation patterns are applied, as in the case of pacing or defibrillation, where a monodomain approach is generally deprecated [171]. The bidomain model is hence the stat–of–the–art mathematical model for reproducing the electrical activation of the heart chambers in healthy and pathological conditions [170, 172] and the propagation of the myocytes depolarization over the cardiac tissue (see [173, 172] among others). Furthermore, this model is seen to reproduce cardiac phenomena including ischemic events and defibrillation [174] and it has been validated through animal experiments [175, 176]. More recently, the bidomain model has been coupled with a fluid–structure solver to build a multiphysics model for the left heart including the mitral and aortic valves with the aim of using computer simulations to evaluate medical quantities that would be exceedingly difficult or impossible to be measured in vivo or in vitro [177].

Although the bidomain model is nowadays a well-established tool to study cardiac electrophysiology, several quantities have to be provided as input parameters such as the chambers geometry, the orientation of the muscular fibers, the mechanical properties of the biological tissues (whose behaviour is nonlinear and orthotropic) along with the conduction velocities within the electrical network, just to cite a few. Only some of these quantities can be estimated in vivo through the scanning methods (e.g. echocardiography, MRI and CT-scan) and a significant variability among individuals is known to exist [178]. Calibrating the computational models is of crucial for the personalization of the therapies and, as an examples, for the prediction acute hemodynamic changes associated

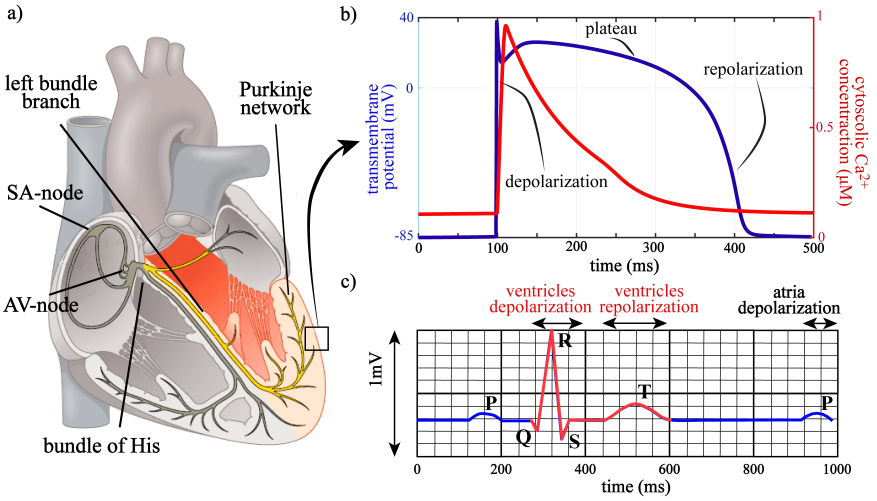

Figure 3.1: (a) Sketch of the electrical network of the heart adapted from [16], with highlighted atrial components. b) Typical depolarization/polarization cycle of a cardiac myocytes (action potential and intracellular calcium profiles), which triggers the muscular active tension. c) ECG pattern in a healthy subject, the ventricular depolarization (QRS complex) and repolarization (T wave) patterns are indicated by the red line.

with cardiac resynchronisation therapy (CRT) [179]. However, the sparsity and the noise of the clinical data used to calibrate the model parameters have a major impact on the model results including the transmembrane potential propagation in the cardiac tissue [180]. In this framework, several computational techniques for the model calibration have been introduced, such as variational approaches based on the constraint optimization [181, 182], data assimilation methods [183] or even patient–specific Bayesian inference strategies using polynomial chaos expansion [184]. The uncertainty on the input parameters hence opens the question about the reliability of the model results, thus calling for a rigorous uncertainty quantification (UQ) analysis. The latter provides a set of mathematical methods to study the uncertainty propagation of the input parameters of an electrophysiology model for heart on the model results, by combining the deterministic approach used to solve the PDEs of the physical model with a probabilistic framework to handle the uncertainties of input parameters and QoIs.

In this work, we apply the UQ analysis to an electrophysiology computational model based on the bidomain equations. Considering the whole heart electrophysiology would require, however, to deal simultaneously with the uncertainties of the fast conductivity bundles (e.g. internodal pathways, His Bundle, left-right posterior-anterior bundles), of the complex geometry of the heart chambers and of the heterogeneous properties of the cellular model through the myocardyum. Hence, the high number of the uncertain parameters along with the computational cost of a single electrophysiology simulation of the full heart would make the UQ analysis very demanding and it should be tackled by successive steps.

With this goal in mind, we have decided to focus here on the UQ analysis of the left ventricle (LV) electrophysiology, which is of paramount importance since the LV is the heart chamber with the thicker muscular myocardium that pumps oxygenated blood to the global body circulation and, as a consequence, is the one that more frequently get diseases with important practical and clinical implications. Furthermore, simulating the left ventricle electrophysiology allows to consider many of the relevant electrophysiology features such as the fibers orientations, the velocity of the electrical conduction over the myocardium, the geometry variability of the chambers and the properties of the cellular model. Although we mainly consider here QoIs relative to the wavefront propagation in a healthy ventricle that could have been investigated with a simplified and computationally cheaper propagation model (e.g. eikonal or cable models), a bidomain approach has been adopted so that the present analysis can be extended to the case of cardiac pacing, defibrillation and arrhythmia using the same UQ methodology.

In the preliminary phase of this UQ analysis the probability distribution functions (PDFs) corresponding to the uncertainty of these input parameters are determined. However, a main difficulty arises here since no data from the literature are available to estimate their PDFs of the cellular model input. For this reason, the UQ analysis has been divided in two parts by studying separately the effect on the LV electrical activation (i) of the geometrical chamber parameters and of the electrical conductivities, whose uncertainty could be estimated by experimental measures reported in the literature, and (ii) of the cellular model inputs, whose PDFs are unknown.

Specifically, in section § 3.3.3 a global sensitivity analysis [185] about the effects of the ventricular geometry and of the electrical conductivities on the myocardium depolarization is carried out. In this analysis the uncertain geometrical and electrical input parameters of the model are identified and their PDFs are estimated from available data from the literature. The sensitivity analysis is carried out using both a direct approach (QMC sampling to compute Sobol' indices using Saltelli's algorithm) and a metamodel one (adaptive polynomial chaos expansion, PCE), which has been also used to run a forward sensitivity analysis to produce the PDFs of the QoIs. Owing to the great computational advantage of using a smaller dataset than direct strategies, the PCE is becoming a common tool in electrophysiological UQ [186, 187] and can be applied to estimate the effect of uncertainty on different QoIs (such as steady state activation/inactivation and current density in ionic channel models [187]), or to speed up the computation eikonal models using a Bayesian multifidelity approach by integrating the electrophysiology solver with a metamodel to achieve near real–time UQ analyses [29].

The second analysis reported in § 3.4.3, aims at understanding the role of the input parameters of the ten Tusscher–Panfilov cellular model [188] governing the electrical current in the ionic channels of the myocytes on the action potential profile as well as on the ventricular electrical activation. The effect of the input electrical conductivities and ions concentration is rationalized through a local

sensitivity analysis (as defined in [87, 85]) using a metamodel technique based on an adaptive sparse PCE. This analysis allows to identify the most relevant input quantities of the cellular model, thus allowing for a significative model reduction of the uncertain input parameter space and suggesting a control strategy to adapt the cellular model to pathological cases. Conclusions and perspectives for future works are then given in § 3.5.

3.2 Problem configuration and numerical method

The electrophysiology model and the numerical method used in this study are thoroughly described in [177] and, therefore, only the main features are summarised here. The bidomain equations governing the depolarization of the ventricular myocardium read:

$$\begin{aligned} \chi\left(C_m\frac{\partial v}{\partial t}+I_{ion}(v,s)+I_s\right) &= \nabla\cdot(\mathcal{M}_{int}\nabla v)+\nabla\cdot(\mathcal{M}_{int}\nabla v_{ext}),\\ 0 &= \nabla\cdot(\mathcal{M}_{int}\nabla v+(\mathcal{M}_{int}+\mathcal{M}_{ext})\nabla v_{ext}),\\ \frac{\partial s}{\partial t} &= F(v,s) \end{aligned} \tag{3.1}$$

where v and v_{ext} are the unknown transmembrane and extracellular potential (expressed in mV) while the surface–to–volume ratio of cells, $\chi = 1400$ cm^{-1} along with the membrane capacitance $C_m = 1\mu$F cm^{-2} are set as in [189]. The symbols $\nabla\bullet$ and $\nabla\cdot\bullet$ indicate the gradient and divergence operators, respectively, whereas $\partial\bullet/\partial t$, indicates the partial derivative with respect to time. $\mathcal{M}_{int}$ and $\mathcal{M}_{ext}$ are the conductivity tensors of the intracellular and extracellular media that depend on the local fiber orientation with a faster propagation velocity along the fiber direction than in the normal ones. These tensors are diagonal when expressed in the local coordinates (i.e. fiber, sheet and sheet–normal directions):

$$\mathcal{M}^*_{ext}=\begin{bmatrix} M^{\parallel}_{ext} & 0 & 0\\ 0 & M^{\perp}_{ext} & 0\\ 0 & 0 & M^{\times}_{ext}\end{bmatrix},\quad \mathcal{M}^*_{int}=\begin{bmatrix} M^{\parallel}_{int} & 0 & 0\\ 0 & M^{\perp}_{int} & 0\\ 0 & 0 & M^{\times}_{int}\end{bmatrix}, \tag{3.2}$$

and the corresponding global conductivity tensors are given by $\mathcal{M}_{ext} = A\mathcal{M}^*_{ext}A^T$ and $\mathcal{M}_{int} = \mathcal{A}\mathcal{M}^*_{int}\mathcal{A}^T$, where $\mathcal{A}$ is the rotation matrix containing column–wise the components of fiber, sheet and sheet–normal unit vectors and $\mathcal{A}^T$ is its transpose [170]. The last of equations (3.1) indicates a cellular model governing the transmembrane ionic currents along with ionic concentrations and ion channel kinetics. The state vector s couples the cellular model with the bidomain equations through the ionic current per unit cell membrane I_{ion} (measured in μAcm^{-2}). Among the several models that exist to represent the cellular-scale dynamics in the bidomain equations, the ten Tusscher–Panfilov cellular model is used, which is seen to correctly reproduce the action potential within ventricular myocytes with physiological detail [188]. The model includes all the major ion channels as

well as intracellular calcium dynamics and it consists of a nonlinear system of 19 ordinary differential equations (ODEs), which are not reported here for the sake of brevity and that are indicated in compact form in the last equation of the system (3.1). Hence, the ionic current, I_s corresponds to the electrical stimulus applied at the bundle of His location initiating the electrical propagation and triggering the ventricular depolarization.

The set of equations (3.1) are discretized on a triangular mesh with Lagrangian finite elements using the electrophysiology library cbcbeat [190], based on the FEniCS FEM library [191, 192], which provides an efficient framework to solve electrophysiology models over arbitrary computational domains (see also [177] where further verification and validation tests are reported). The bidomain equations are marched in time through a second-order Strang splitting method where a step accounting only for the ionic and the external currents and another one involving only the right–hand–side of equation (3.2) are solved sequentially [170]. A Rush-Larsen scheme for the ODEs of the cellular model is combined with a $\theta = 1/2$ second order Crank-Nicholson scheme for the integration of the PDE step. The resulting average CPU time cost to solve a complete depolarization/repolarization cycle of the ventricle on a grid of 4'311 cells (corresponding to 45'885 degrees of freedom including the ones of the cellular model) and using a time step of $dt = 10^{-2}$ ms is 50 CPU-minutes (defined as the time it takes to run the program on a 1GHz reference processor). The computational resources used for the analysis comprise an Intel Xeon Processors with 16 cores (E5-2620 v3 - 15M Cache, 2.40 GHz) that allow to run the same number of simulations simultaneously. Figure 3.2 shows the electrical activation of the left ventricle at several instants within a heart beat. Initially, all the cells are relaxed with a negative transmembrane potential of about -85 mV and, at a given initial time, an electrical impulse originated at the His bundle propagates in the ventricular muscle causing the cells to locally change the transmembrane potential. As a consequence, a rapid flux of positive ions through the cell membrane occurs, and the transmembrane potential raises to positive values, as visible from the isocontours of the transmembrane potential reported in figure 3.2(a). This local depolarization results in a propagating wavefront that travels across the myocardium (see figure 3.2(b) and (c) activating the whole ventricle as visible in figure 3.2(d). As a remark, the myocardium is simplified by considering it as a uniform two–dimensional conductive medium and the bidomain equations are formulated as surface PDEs with anisotropy present only in the tangent plane. Although this approach ignores the transmural anistropy and corresponds to an overestimation of the transmural speed of depolarization, the surface bidomain model is seen to provide the correct depolarization timings of the ventricles as also observed for the atria in previous works [193, 194]. The lack of the fast conductivity fibers has been accounted by scaling the electrical conductivities by a fixed parameter (equal to 4.99, which has been obtain through an optimization procedure based on the Brent's method) so that the computational model reproduces the benchmark timings of ventricular depolarization [16].

The resulting time evolution of the transmembrane potential for one represen-

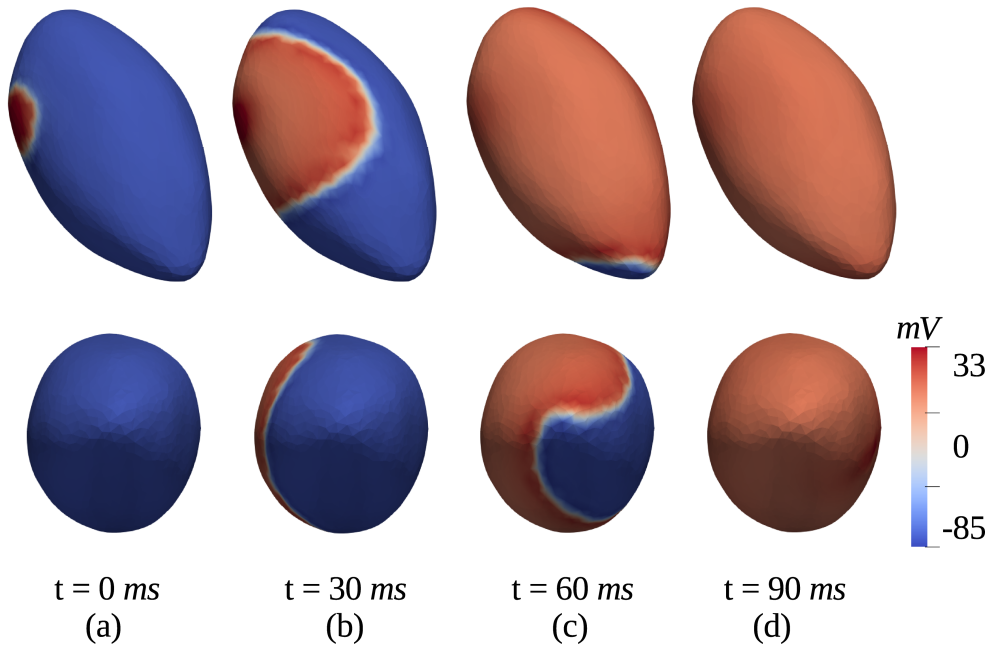

Figure 3.2: Snapshots of the transmembrane potential as a function of time showing the left ventricle depolarization. Top row: perspective side view. Bottom row: view from the ventricle apex.

tative point was reported in figure 3.1(b) together with the intracellular calcium profile triggering muscular contraction. In particular, when the cell is excited by an electrical stimulus over a threshold potential (of about -70 mV), ionic channels at the membrane open and close in a coordinated manner causing the transmembrane potential to raise from its resting negative value to positive values of about 40 mV. This cell depolarization phenomenon is very fast (≈ 2 ms) and is followed by a spike (phase 1) and a relatively long plateau (or dome, phase 2) lasting about 200–300 ms, which ends with a repolarization (phase 3) to the rest potential (phase 4).

The electrical stimulus initiating the ventricular depolarization is given by $I_s = \tilde{I}_s e^{-\|\mathbf{x}-\mathbf{x}_0\|^2/\sigma_{I_s}^2}$ where the current amplitude is equal to $\tilde{I}_s = 25\ \mu A/\text{cm}^2$ if the simulation time within a heart beat is less than the temporal duration of the stimulus (5 ms) and null otherwise. The parameter $\sigma_{I_s}^2 = 0.5\ \text{cm}^2$ concentrates the stimulus around the position $\mathbf{x}_0$ so that the stimulus is only active in the spatial locations $\mathbf{x}$ close to it. The centre of the electrical stimulus, $\mathbf{x}_0$ is thus placed at the bundle of His position, see figure 3.4(a), where the electrical impulses from the atria are transmitted to the ventricles and which also corresponds to the location where the pacemaker are often implanted (the so called His-bundle pacing [195]).

3.3 UQ analysis 1: sensitivity of the electrical activation of the left ventricle on the chamber geometry and electrical conductivities.

In this analysis we investigate the effect of the left ventricle geometry and of the myocardial electrical conductivities on the ventricular depolarization.

3.3.1 Input parameters and their PDFs calibrations

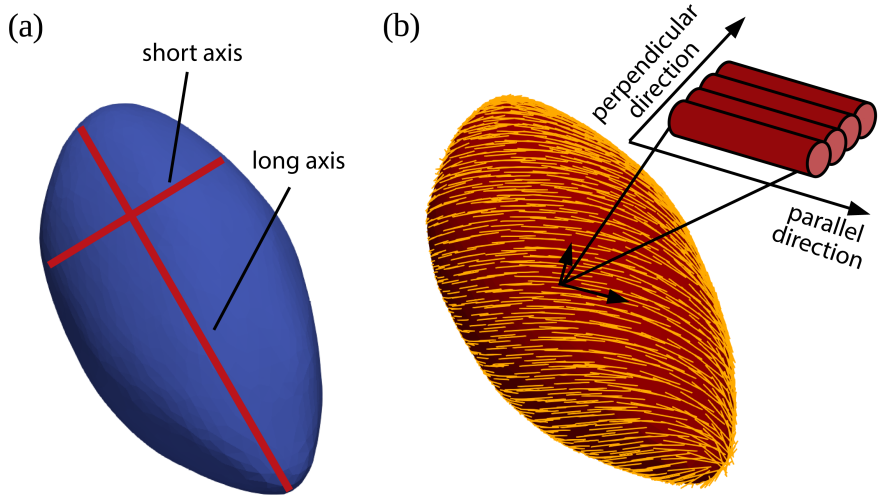

Figure 3.3: (a) Graphical representation of long and short axes of the left ventricle. (b) Local fibers orientation in the ventricular myocardium, the inset indicates the conduction directions parallel and perpendicular to the fibers.

The shape of the heart chambers as well as the electrical conductivities are known to vary among individuals and we consider here the effect of the following six input parameters on the ventricular depolarization (figure 3.3): the long axis of the ventricle L, the sphericity index SI defined as the short to long axis ratio, the intracellular $\mathcal{M}_{int}$ (parallel and perpendicular) and extracellular $\mathcal{M}_{ext}$ (parallel and perpendicular) conductivity tensor that depend on the local fiber orientation according to equation (3.2). However, before investigating the sensitivity and the uncertainty of the model results, the uncertainty PDFs of the input parameters have to be known. In [196] the ventricular end diastolic long and short axes (defined as the distance from the apex to the mid-point of the mitral valve and as the length of the segment that perpendicularly intersects the mid-point of the long axis) have been measured using transthoracic endocardiography for a group of 26 men and 26 women with a mean age of 43 ± 14 years for a total of 52 healthy subjects. The resulting distributions of L and SI were observed to follow the normal distributions reported in table 3.1, which are used here to define the uncertainty PDF of these input parameters of the electrophys-

iology model.

input parameters	normal $\mu \pm sd$	truncation bounds	truncation probability
long axis (mm)	80 ± 9	$[\mu/1.3 = 61.53, \mu \times 1.3 = 104.00]$	0.024
SI (sphericity index)	0.52 ± 0.06	$[\mu/1.3 = 0.400, \mu \times 1.3 = 0.676]$	0.027
$M_{int}^{\parallel}$	0.268 ± 0.081	$[\mu/5 = 0.134, \mu \times 5 = 0.536]$	0.0496
$M_{int}^{\perp}$	0.031 ± 0.0168	$[\mu/5 = 0.0062, \mu \times 5 = 0.155]$	0.070
$M_{ext}^{\parallel}$	0.292 ± 0.194	$[\mu/5 = 0.058, \mu \times 5 = 1.46]$	0.1145
$M_{ext}^{\perp}$	0.141 ± 0.0687	$[\mu/5 = 0.028, \mu \times 5 = 0.705]$	0.050

Table 3.1: Input Gaussian distributions of the model parameter given as mean and standard deviation. For each parameter the truncation bounds to avoid unrealistic shapes and conductivities is also reported, whereas the truncation probability (i.e. the probability of the truncated tails) is reported in the last column.

On the other hand, fewer data on the electrical properties of human myocardium exist owing to the difficulty to measure these quantities in vivo and they are insufficient to accurately estimate a PDF for the uncertain conductivities ($M_{int}^{\parallel}$, $M_{int}^{\perp}$, $M_{ext}^{\parallel}$, $M_{ext}^{\perp}$). A possible UQ strategy that is adopted when data on the input parameters are missing, consists of estimating an initial PDF using the few data available and then refine it through a Bayesian inverse calibration [197]. Also this method, however, relies on an iterative minimization method based on well–known experimental observables, which are usually lacking in the electrophysiology of the human heart. Nevertheless, more biological data on the intracellular and extracellular conductivities have been acquired in the case of animal myocardium in terms of the first two statistical moments, i.e. mean and variance [198]. Although the mean values and the standard deviations of the PDFs can vary among different mammalians, we assume human electrical conductivities to be Gaussian distributed and use the few data available from the literature (reported in table 3.2) to fit these PDFs. In particular, according to the Kolmogorov-Smirnov test [199] the uncertainty of the intracellular and extracellular conductivities corresponds to the normal distributions reported in table 3.1 (all the p-values are greater than 0.5). Furthermore, in order to avoid unphysical ventricular shapes and conductivity values, the PDF of the input parameters have been truncated (see table 3.1) according to the following method. Given a random variable X with PDF $f(X)$ and CDF (cumulative distribution function) $F(X)$, the PDF support is reduced to the range $[a, b]$ by calculating the conditional distribution $g(x) := f(x|a \leq X \leq b) = 1_{[a,b]} f(X)/(F(b) - F(a))$ where $1_{[a,b]}$ is the indicator function and $g(X)$ is the truncated PDF. In the case f(x) is the PDF a Gaussian distribution $\mathcal{N}(\mu, \sigma)$, the corresponding truncated distribution is given by the analytical formula $g(x, \mu, \sigma, a, b) = I_{[a,b]} \frac{1}{\sigma} \frac{\phi\left(\frac{x-\mu}{\sigma}\right)}{\Phi\left(\frac{b-\mu}{\sigma}\right) - \Phi\left(\frac{a-\mu}{\sigma}\right)}$, where ϕ and Φ are the PDF and CDF of the normal distribution $\mathcal{N}(0, 1)$. Adding a truncation bound to the input distributions is important in order to avoid un-

physical configurations in the dataset, which could yield numerical instabilities while its effect on the UQ analysis is expected to be negligible as the Sobol' indices are integral quantities that are not sensitive to few tail elements.

Although other kind of distributions with bounded support could be considered to fit the discrete distribution of the experimental data available, such as the von Mises or the Beta distributions, we have used a truncated Gaussian because it corresponds to the least informative setting as it maximizes the entropy for a fixed mean and variance, with the random variate constrained to be in the interval [51]. Additionally, truncated Gaussians could also account for asymmetries in the PDF shape.

conductivity [mS/mm]	Clerc [200]	Robert et al. [201]	Robert and Scher [202]	Roth [203]	Roth [204]
$M_{int}^{\parallel}$	0.17	0.28	0.34	0.35	0.2
$M_{int}^{\perp}$, $M_{int}^{\times}$	0.019	0.026	0.06	0.03	0.02
$M_{ext}^{\parallel}$	0.62	0.22	0.12	0.30	0.2
$M_{ext}^{\perp}$, $M_{ext}^{\times}$	0.24	0.13	0.08	0.18	0.08

Table 3.2: Available data from the literature on human electrical conductivities.

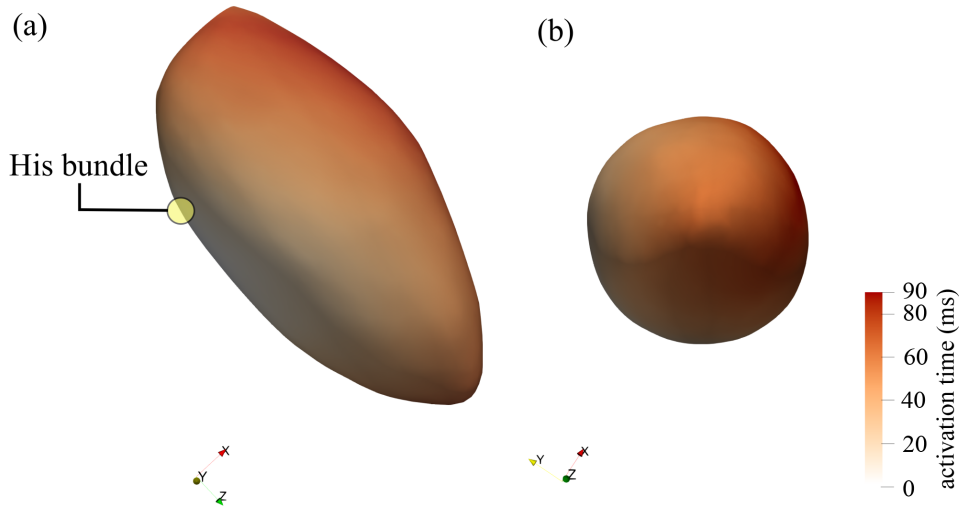

Figure 3.4: (a) Side and (b) bottom view of the ventricular activation map $t_a(\mathbf{x})$, corresponding to the first activation time t at any location $\mathbf{x}$. The yellow dot indicate the the stimulus position corresponding to the location of the bundle of His.

3.3.2 QoIs

At this stage the QoIs of the problem are identified by translating clinically relevant quantities measured in vivo into outputs of the computational model.

The QoIs investigated in this analysis are the *depolarization time* of the left ventricle (DT hereafter, that is expected to be correlated to the conduction velocity) and the *depolarization uniformity* (DU), which are relevant for the patient's health because they are known to be associated with the efficiency of the ventricular pumping during systole [16]. Indeed, only a physiological DT and DU determine a timely and almost simultaneous contraction of the muscular fibers of the myocardium, which is needed to effectively propel oxygenated blood from the left ventricle towards the aorta during systole [177]. Given the activation map $t_a(\mathbf{x})$ of the ventricle, which stores the first activation time at each point $\mathbf{x}$ (computed when the transmembrane potential overcomes a threshold of 0 mV, see figure 3.4), the DT of the ventricular myocardium is defined as:

$$\text{depolarization time } = \max\{t_a(\mathbf{x})\}, \tag{3.3}$$

and the DU reads

$$\text{depolarization uniformity } = \text{std}\{t_a(\mathbf{x})\}, \tag{3.4}$$

with both quantities measured in ms and the operators max and std indicating the maximum and the standard deviation of their argument. Note that according to equation (3.4) a higher (lower) value of the second QoI corresponds to a less (more) uniform and synchronized ventricular depolarization. In particular, a non null value of the time uniformity is expected since a value close to zero would mean an instantaneous depolarization through the whole ventricular myocardium that is unrealistic since a time lag of few milliseconds is known to occur between the activation of septal and apical myocytes.

3.3.3 Model reduction through sensitivity analysis

In this section we aim at understanding how sensitive the QoIs introduced above are on the model input parameters and detecting the most relevant ones. The dimension of the input parameter space will be then reduced through a variance based analysis [205] using the first and total order Sobol' indices as sensitivity indices [101]. The choice to use Sobol' indices is determined by the fact that the scatter plots in figure 3.5 do not exhibit a clear linear nor monotonic relation between the input and the QoIs, as also revealed by the low values of Pearson and Spearman coefficients [92] reported in table 3.3. Nevertheless, we anticipate that the Spearman coefficients will result to be a good predictor for the Sobol' indices ranking.

Given the computational cost of the electrophysiology model and the available computational resources, the number of possible model evaluations is more than what typically used to train a metamodel (dataset of the order of tens of samples), but anyway smaller than what would be needed for a direct strategy (dataset made by tens of thousands of samples). Therefore, we have decided to build a training and a testing dataset of a few hundred samples and train/test not one but a family of metamodels by varying the polynomial degree (ranging

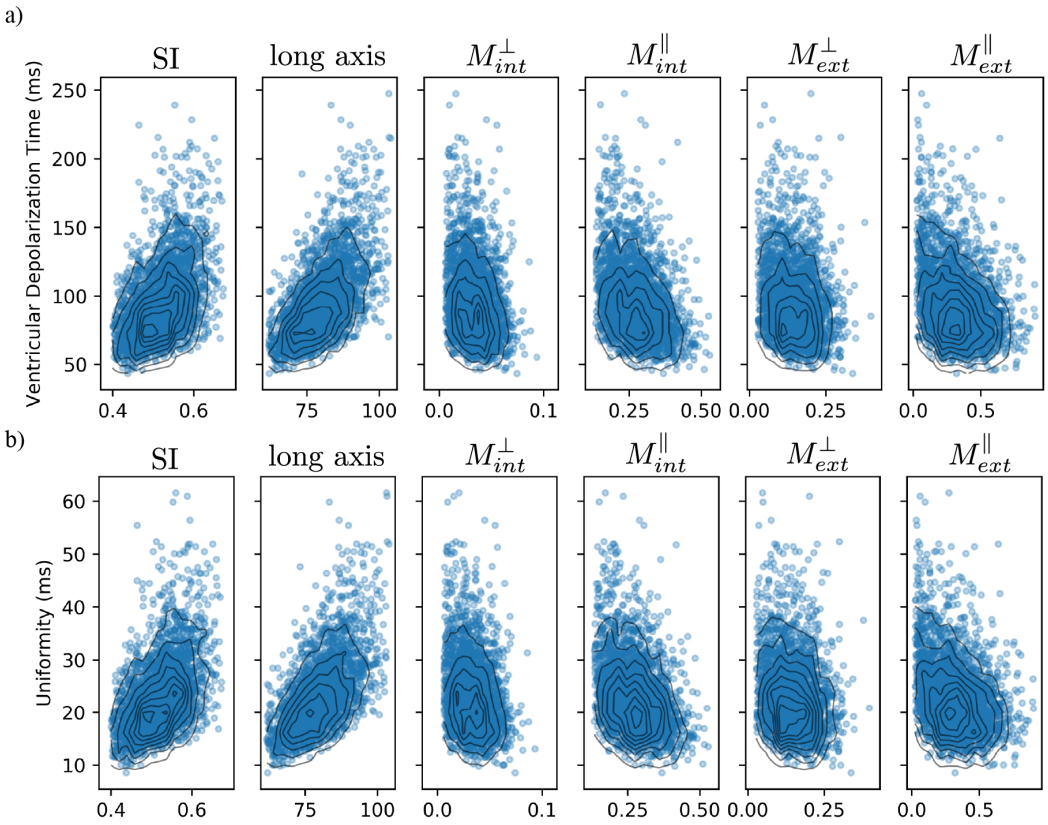

Figure 3.5: Scatter plots of the ventricular depolarization (a) time and (b) uniformity against the 6 input variables computed using the 2'500 independent samples of the 20'000 Saltelli's dataset.

	Pearson		Spearman	
input parameter	time	uniformity	time	uniformity
long axis	0.57	0.50	0.60	0.60
(SI) sphericity index	0.44	0.39	0.46	0.48
$M_{int}^{\parallel}$	-0.33	-0.29	-0.35	-0.35
$M_{int}^{\perp}$	-0.24	-0.20	-0.26	-0.24
$M_{ext}^{\parallel}$	-0.35	-0.31	0.34	-0.33
$M_{ext}^{\perp}$	-0.22	-0.20	-0.22	-0.22

Table 3.3: Pearson and Spearman coefficients for both time and uniformity computed employing the 2'500 independent samples of the 20'000 Saltelli's dataset.

from 1 to 16), by using two different enumeration rules (linear and hyperbolic) and by adopting two different selection strategies (fixed and sequential). All the resulting $16 \times 2 \times 2 = 64$ metamodels are trained and validated against the corresponding dataset. The optimal one is selected among the family according to the

method detailed below and sketched in figure 3.6. A different metamodel is obtained for each of the QoIs so that the trained metamodels are not only surrogate models of the initial complex electrophysiology system but, more importantly, are UQ tools for computing the corresponding global sensitivity indices needed to designing a model reduction strategy. Furthermore, the computational cost of training another metamodel for a different QoI is negligible compared to the cost of building the dataset itself (see Appendix 3.6) and the UQ procedure allows for a quick training of another metamodel in the case different QoIs are defined (in the order of a minute CPU time).

The first step is to produce a training dataset of 400 samples using a quasi Monte Carlo method (QMC - Sobol' sequence) so as to maximize the information contained and avoid samples clustering within the dataset [206]. The Sobol' sequence is used to generate the corresponding low discrepancy sequence of the samples [207]. The QMC has, indeed, a faster converge rate for low number of parameters, $\mathcal{O}\left(\frac{\log(N)^s}{N}\right)$ where s is the input dimension, compared to the standard MC, $\mathcal{O}\left(\frac{1}{\sqrt{N}}\right)$, [30]. Consequently, another 100 samples dataset independent of the training set is produced using a pure MC strategy, which will be used as a validation dataset. The cost of producing the whole dataset for the metamodel approach is of about 17 CPU-days, where one CPU-day is defined as one day of computation done on a 1GHz reference processor.

Since truncated Gaussian distributions, as the ones used to model the input parameters, do not allow for analytical orthogonal polynomials with the respect to the norm weighted by the input PDFs, a family of orthogonal polynomials is produced numerically through the three terms recurrence [208]. It should be noted that, although the data from the literature allow to estimate the uncertainty PDFs of the input parameters, their statistical dependence/independence can not be determined. Hence, the input parameters are treated here as statistically independent and the multidimensional basis for the input space is then given by the product of the mono-dimensional basis of each input parameter. Given a computational model $G : \mathcal{D}_X \subset \mathbb{R}^d \to \mathbb{R}$, suppose that the uncertainty in the input parameters is modeled by a random vector X with prescribed joint probability density function $f_X(x)$ [133]. The resulting quantity of interest $Y = G(X)$ is obtained by propagating the uncertainty on X through G and, assuming that the input variables are statistically independent, the joint PDF is the product of the d marginal distributions $f_X(x) = \prod_{i=1}^{d} f_{X_i}(x_i)$ for each $\mathcal{D}_{X_i}$. For each single variable X_i and any two functions $\phi_1, \phi_2 : \mathcal{D}_{X_i} \to \mathbb{R}$ we can define the inner product as: $\langle \phi_1, \phi_2 \rangle := \int_{D_{X_i}} \phi_1(x)\phi_2(x) f_{X_i}(x)dx$ and use it to define an orthonormal family of polynomials $\{P_k^{(i)}, k \in \mathbb{N}\}$. This set of univariate orthonormal polynomials can be used to define a family of multivariate ones. In fact, given a multi-index $\alpha = (\alpha_1, \cdots, \alpha_d), \alpha_i \in \mathbb{N}$, the associated multivariate polynomial can be defined as $\Psi_\alpha(x) := \prod_{i=1}^{d} P_{\alpha_i}^{(i)}(x_i)$. The set of all multivariate polynomials in the input random vector X forms a basis of the Hilbert space

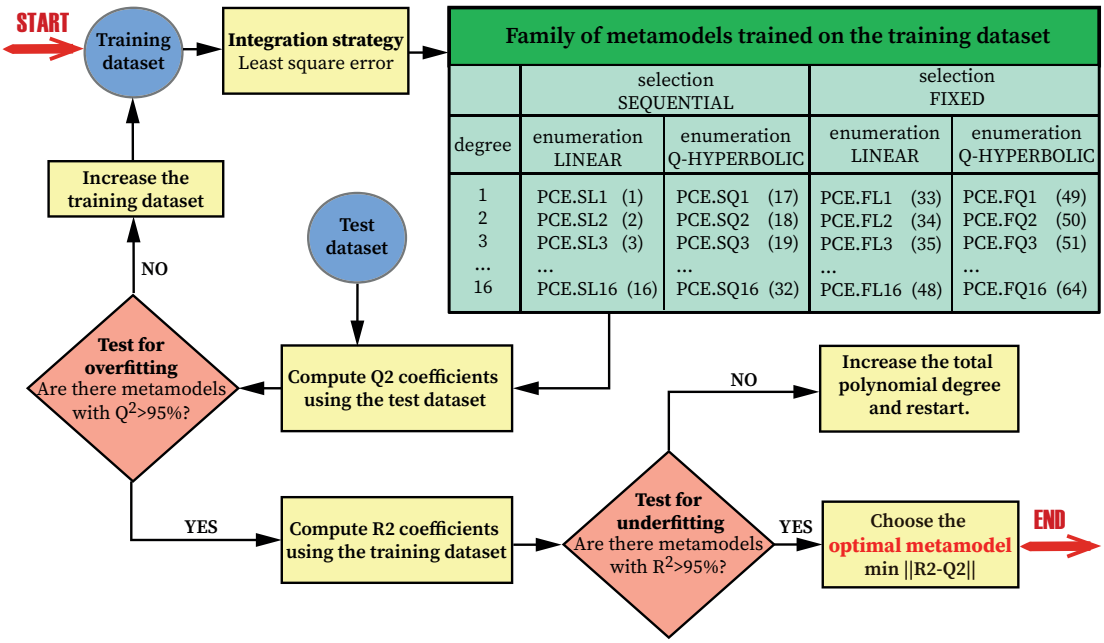

Figure 3.6: Graphical scheme of the adaptive strategy used to train and validate the optimal meta-model. Starting from the training dataset and using a least squares error integration strategy, 64 metamodels are produced accordingly to a sequential/fixed selections strategy coupled with a linear/q-hyperbolic enumeration one and varying the polynomial degree from 1 to 16. To avoid overfitting, Q^2 indices are computed on an external independent test dataset and there are not any metamodels satisfying $Q^2 > 95\%$ the training dataset is increased, otherwise the R^2 coefficients of each metamodel passing the previous test is computed. Among the metamodel that also satisfy the underfitting test ($R^2 > 95\%$), the optimal metamodel is selected as the one minimizing $||R^2 - Q^2||$. If the case any metamodels do not satisfy this last condition the maximum total degree of the metamodel is increased and the procedure is restarted.

[136], in which $Y = G(X)$ is given by the so called polynomial chaos expansion:

$$Y = \sum_{\alpha \in \mathbb{N}^d} y_\alpha \Psi_\alpha(X) \tag{3.5}$$

This infinite series has to be truncated in order to get a finite one approximating $Y = G(X)$ and different truncation strategies are possible depending (i) on how to enumerate the element of the multivariate basis and (ii) on how many terms of the basis have to be retained. We can define the standard, or linear enumeration strategy, based on the standard total degree of a multivariate polynomial Ψ_α, defined as $\|\Psi_\alpha\| := \sum_{i=1}^{d} \alpha_i$, that is the lexicographical order with a constraint of increasing total degree (e.g. for a two dimensional multi-index $(0,0) < (0,1) < (1,0) < (2,0) < (1,1,) < \cdots$).

However, the use of a standard enumeration is usually deprecated for biological applications because it yields oversized family of high order interactions

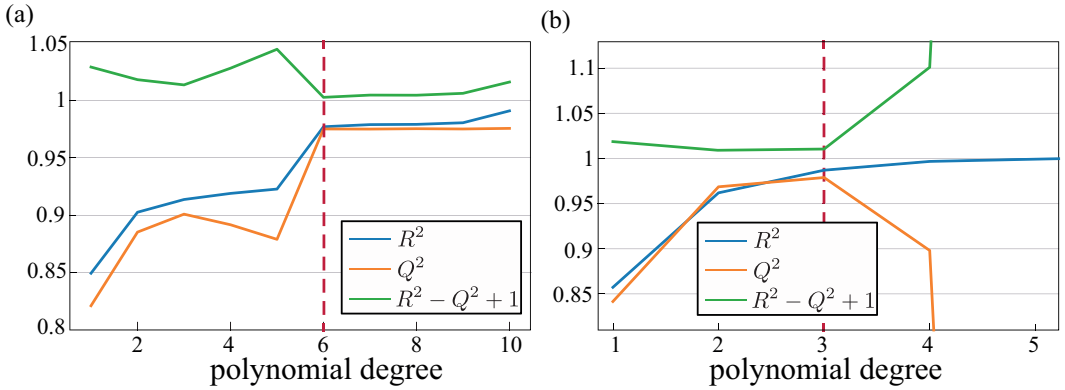

Figure 3.7: R^2 (blue line) and Q^2 (orange line) coefficients as a function of the polynomial degree according to a hyperbolic enumeration for (a) the depolarization time with sequential truncation strategy and for (b) the depolarization uniformity with fixed truncation strategy. The vertical dashed lines indicate the total degree of the optimal metamodels that minimize the norm of $R^2 - Q^2$ (green lines, increased by a unit for visualization purposes).

coefficients that are not observed in such cases [209]. A polynomial expansion coefficient is called a high-order interaction term when it is associated with a polynomial with high degree in more than one variable [210]. As physical phenomena are typically described by low-order interactions, an enumeration rule favoring low-order interactions rather than high order ones is generally preferred [211]. With this motivation, as an alternative to the linear enumeration we have used a q-hyperbolic strategy that is based on the definition of a semi-norm characterizing each coefficient of the polynomial: given a real number $q \in (0, 1)$, the q-hyperbolic quasi-norm of a multi-index α is defined as $\|\alpha\|_q = \left(\sum_{i=1}^{d} \alpha_i^q\right)^{\frac{1}{q}}$ and the space of the coefficients is explored (i.e. numerated) by increasing the value of the norm and selecting all the coefficients with a multi-index lower than the one selected. Smaller q yields a sharper hyperbolic selection and less high order interactions (in terms of high degrees mixed coefficients of the PCE) for a fixed p.

Furthermore, two selection strategies have been selected: a *fixed strategy* where the total degree p is fixed and all the coefficients with norms (depending on the enumeration strategy) smaller or equal to p are retained, and the *sequential strategy* [211] that selects the most relevant coefficients in such a way to maximize the number of null coefficients.

For each metamodel corresponding to a different polynomial degree, truncation strategy and enumeration rule, the training dataset is used to evaluate its coefficients. The standard approach is to use high order Gaussian quadrature rules providing the higher accuracy for a given number of samples [212], but this most accurate strategy has the drawback that the computational model has to be evaluated at the Gaussian integration points that depend on the accuracy of the integration formula. Moreover, in case the metamodel needs to be refined,

the previous simulations can not be used and another data set has to be produced from scratch. In order to circumvent these issues, the metamodel is fitted in a more flexible way using a least squares error minimization of the coefficients [213] using the training dataset (400 samples).

In summary, we used a truncated PCE to approximate the model response. Firstly, a certain polynomial degree family (ranging from 1 to 16) is chosen, then the PCEs are truncated by using two different enumeration strategies alternatively (linear and q-hyperbolic). Lastly, only a subset of the terms of each polynomial is retained according to the fixed or sequential truncation strategy for a total of $16 \cdot 2 \cdot 2 = 64$ possible metamodels that are trained on the given training dataset by minimizing the least squares error. It should be noted that a linear enumeration coupled with a fixed truncation rule corresponds to a dimension of the basis with cardinality $\binom{d+p}{p}$, with p the polynomial degree and d the size of the input space [133].

Given this family of metamodels, the best one in terms of database fitting is then selected as follows. The risk of under/over fitting of the metamodels is assessed through a validation strategy commonly used in regression analysis, which is based on the coefficients R^2 and Q^2 [129]. The dataset is split into a training set that is used to calculate the index R^2 measuring the underfitting, and a validation set used to compute the index Q^2 measuring the overfitting. Given the training (testing) dataset of size n, described by the couples $(\mathbf{x}_i, y_i)_{i=1}^n$ (where y_i is one of the QoIs corresponding to the set of input $\mathbf{x}_i$) and the prediction of the metamodel f for the same input dataset $(\mathbf{x}_i, \hat{y}_i := f(\mathbf{x}_i))_{i=1}^n$, the coefficient of determination is defined as $R^2(Q^2) := 1 - \frac{SS_r}{SS_t} =$, where $SS_r := \sum_{i=1}^n$ is the residual sum square normalized for the total sum of squares $SS_t := \sum_{i=1}^n (y_i - \hat{y}_i)^2$ with $\overline{y} = \frac{1}{n}\sum_{i=1}^n y_i$. The R^2 index is used in regression analysis to evaluate the goodness of the fit on the training dataset and a value close to 1 means that the metamodel correctly reproduces the variability within the training dataset whereas a lower R^2 index is a typical symptom of underfitting. On the other hand, a low Q^2 and high R^2 would correspond to an overfitting condition [129]. Importantly, the R^2 index does not measure the behaviour of the metamodel outside the training set and PCE is typically used in UQ analyses with few samples where all samples are used in the training set so that to avoid poor metamodelling [214]. As a consequence, the prediction error of the metamodel is typically evaluated through a one-leave-out cross-validation [132] that, however, does not provide such a consistent measure of the overfitting as done by the $R^2 - Q^2$ criterion used here [214]. The latter criterion, indeed, both quantifies the under and over fitting with a large difference between $R^2 \approx 1$ and $Q^2 \ll 1$ implying that the metamodel has been over-adapted to the training dataset (overfitting) [128]. Hence, the optimal metamodel is chosen as the one minimizing the difference between these two coefficients, $\min ||R^2 - Q^2||$ with the constraint that both parameters have to be larger than $\alpha = 95\%$, see figure 3.7(a) and (b) for the two QoIs of the first analysis. In the case none of the trained metamodels satisfies $R^2 > \alpha$, implying the polynomial family is not able to well approximate

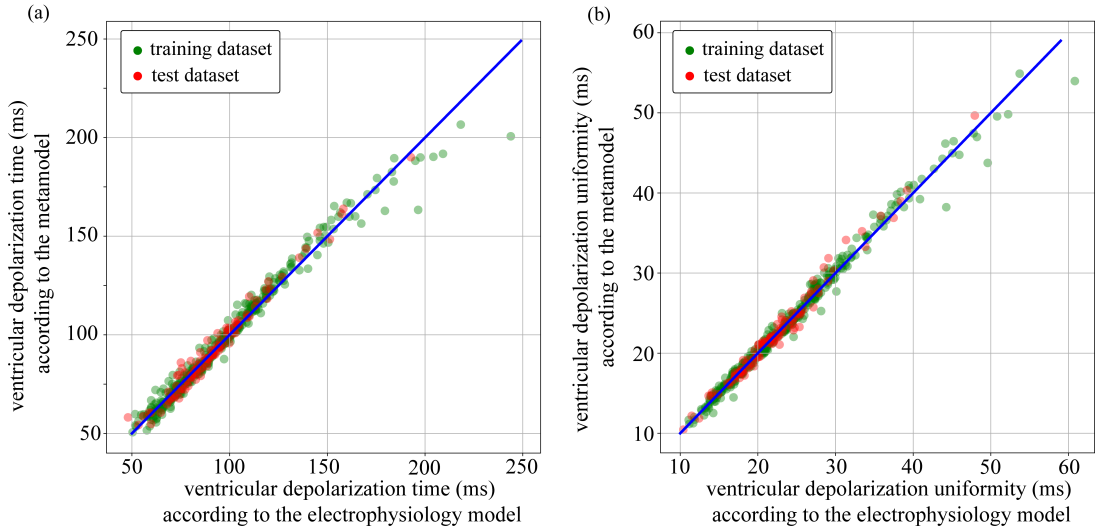

Figure 3.8: Metamodel validation plot for the ventricular depolarization (a) time and (b) uniformity. Each point represents the QoI value computed using the electrophysiology model (abscissa) against the one evaluated by the metamodel (ordinata) for a given set of input values. The green dots correspond to the output values of the training dataset (400 samples) while the red ones correspond to the results of the test dataset (100 samples). The solid blue line indicate an ideal perfect agreement between the metamodel and the full electrophysiology model.

the training set (underfitting) and other metamodels with a higher number of coefficients should be trained. Conversely, if $Q^2 < \alpha$ for every metamodel it means that the validation set is poorly reproduced and the size training dataset has to be increased by adding samples. Importantly, the least squares approximation of the PCE allows to increase the dataset at any time, whereas a projection based PCE needs to rebuild another dataset from scratch when a different size of the dataset is needed [40]).

It turns out that the metamodels built using a sequential strategy are preferred to the ones corresponding to the fixed one, unless the total degree of the polynomial is low and the two selection strategies become equivalent selecting the same coefficients (and providing the same values for them). In this last case, we indicate the optimal model as resulting from a fixed strategy to stress that all the coefficients have been selected. Hence, it turns out that the optimal metamodel depends on the specific QoI: a sequential truncation strategy with a total degree of 6 according to a hyperbolic enumeration ($q = 0.4$) is found for the ventricular DT with $R^2 = 0.9769$ and $Q^2 = 0.97502$, whereas a fixed strategy with total degree 3 and hyperbolic enumeration ($q = 0.4$) is the selected metamodel for the DU with $R^2 = 0.987$, $Q^2 = 0.979$. The corresponding fitting graph validating the optimal metamodel against the full electrophysiology model for the training (green dots) and test (red dots) datasets is reported in figure 3.8 for DT (a) and DU (b).

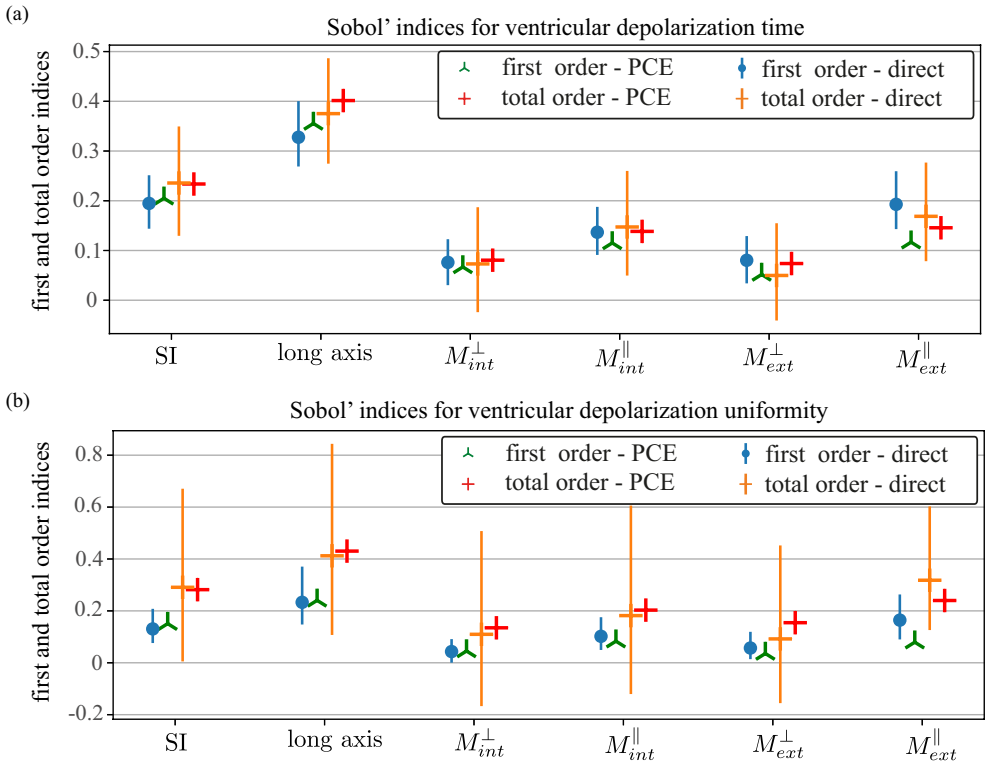

Figure 3.9: First and total order Sobol' indices for ventricular depolarization (a) time and (b) uniformity. Each index is computed using both a PCE strategy (sample size 400+100) and a direct one (sample size 20'000). The direct strategy allows to compute also the 95% Sobol' indices intervals here reported as error bars.

The metamodels can be now exploited to evaluate how sensitive is the variance (Sobol' indices) of the QoIs to the input variables. Figure 3.9(a) indicates that the shape parameters L and SI influence more than the 60% the Sobol' indices of the ventricular DT, whereas the perpendicular conductivities of the fibers have a cumulative influence smaller than 15%. Note that as the ventricular shape parameters can be easily measured in vivo, this is not the case for the electrical conductivities that are hardly measurable with common scanning techniques and, relying on the results of the sensitivity analysis, the system can be reduced by fixing the two less relevant inputs (i.e. the intracellular and extracellular perpendicular conductivities) to their nominal values, thus decreasing the size of the input parameter space from 6 to 4. The same model reduction also applies to the ventricular DU, which exhibits a similar hierarchy of Sobol' indices in figure 3.9(b) and depends on the DT according to a linear law (Spearman coefficient of 0.998 and a Pearson coefficient of 0.992). We refer to Appendix 3.6 for a convergence analysis of the Sobol' indices with respect to the size of the training dataset of the metamodel.

Before moving to the forward UQ analysis, a direct sampling approach, similar to the one proposed in [187], is used to validate the adaptive metamodel strat-

egy. To this aim, a dataset (larger and independent of the 400+100 samples used for the metamodel approach) is built according to Saltelli's method [103, 124] to compute the Sobol' indices (first and total order) using a pure MC sampling strategy [215]. The size of the dataset $N_{ds} = 20'000$ (instead of the $10'000$ proposed in [187]) is chosen accordingly with the Saltelli size $N_{ds} = N \cdot (d + 2)$, where d is the number of parameters and N the number of independent entry, here $d = 6$ and N =2'500. This dataset requires a total of about 691 CPU-days to be produced. It should be remarked that the computational cost to produce the training+test dataset for the metamodel is about 2.5% of that needed for a direct strategy, while the cost to train the metamodel itself using the given methodology is of the order of 1 CPU-hour, therefore negligible compared to the dataset production. Figure 3.9 reports first and total order Sobol' indices obtained by the direct sampling technique superimposed to the ones evaluated by the metamodel. The comparison between the metamodel (trained on a 400+100 samples) and the direct validation strategy (calculated on 20'000 samples) shows as the metamodel predicts both the ranking of the first order indices and their magnitude with a good accuracy (exception made for $M_e^{||}$ for which the metamodel tends to underestimate the index). As expected, the direct approach appears to be less accurate on the total order, on which the confidence interval are large (in particular for the DU) but, also in this case, the metamodel correctly identifies the relative order and approximates the indices well. On the other hand, the smaller confidence interval for the importance measures obtained from the asymptotic distribution of the Saltelli statistic, is a good indicator of the convergence of the algorithm. This comparison should be considered, we recall, only as a further check of the accuracy of the metamodels, as satisfying the $R^2 - Q^2$ criterion a sufficient validation. As a remark, the agreement between the two UQ techniques can be probably ascribed to the low-order non linearity of the problem that can be readily sampled by a small dataset.

3.3.4 Forward analysis

Once performed the sensitivity analysis, we can turn to the statistical characterization of the QoIs and evaluate their PDF using a direct UQ strategy. The sampling strategy is the QMC with Sobol's low discrepancy sequence (as detailed in the previous section) with a dataset made by 20'000 samples ($\approx$ 691 CPU-days to be produced). Note that a direct strategy is the most robust method to evaluate the QoIs PDFs but, when this is not affordable owing to the large computational cost, the trained and validated metamodel is also used to produce the PDF best–fitting the data of the training set (see the analysis 2 in section 3.4).

The computed stochastic moments are reported in table 3.4 showing for both QoIs a similar distribution shapes (also according to the skewness and the kurtosis) and a narrow 95% confidence interval on the mean. The corresponding PDFs of the QoIs are shown in figure 3.10(a,b) as histograms (using Sylvester's rule for bandwidth [216]) with superimposed an approximated lognormal distribution. The PDF of the ventricular DT in figure 3.10 (a) can be read in the light

	depolarization time	depolarization uniformity
Mean	94.178 ms	22.90
Mean 95%-confidence interval	[93.85,94.51] ms	[22.82,22.98] ms
Standard deviation	23.86 ms	6.10 ms
Skewness	1.14	1.01
Kurtosis	5.28	5.04

Table 3.4: Statistical moments of the two QoIs according to the forward UQ analysis using the direct QMC sampling strategy (20'000 samples) on the reduced model.

of the medical knowledge about the ventricular DT that is measured in vivo through electrocardiogram by monitoring the QRS complex (see figure 3.1(c) and is considered normal as its value does not exceeds 100 ms [16]. The UQ analysis predicts that, for input data corresponding to an healthy subject, the event of a normal DT happens with a probability of 65.8%, whereas a DT between 100 and 130 ms that is considered intermediate or slightly prolonged has a probability of 26.2%. Furthermore, a pathological DT longer than 130 ms has probability 8% to happen. Vice–versa the probability to obtain a DT shorter than 40 ms is lower than 10^{-6} because limited by the maximum speed of the electrical front propagation within the myocardium. The lognormal shape of the PDF for DT is probably related to the non–linear relationship between the electrical conductivities and the conduction velocity and it was also obtained by Quaglino et al [29] for the atrial myocardium by randomly perturbing both fibers orientation and local conductivities using a Bayesian multifidelity approach.

Owing to the quasi–linear relation between the two QoIs, the PDF of the DU (see figure 3.10b) has a similar shape as that of the DT with a mean value of 6.10 ms. For this PDF, the probability of a variation of ± 10 ms with respect the mean value results to be equal to 8.1%, whereas it is very rare to observe a halving or doubling of the uniformity (still respect to its mean value) corresponding to a probability of 0.72%. This last result has important medical implications since a larger value of this QoI (as defined in (3.4)) corresponds to a less uniform ventricular depolarization and, as a consequence, a less effective blood ejection into the aorta during systole.

3.4 UQ analysis 2: sensitivity of the electrical activation of the left ventricle on the cellular model parameters

We now turn to investigate the UQ properties of the cellular model that determines the ionic current through the membrane channels and which is coupled

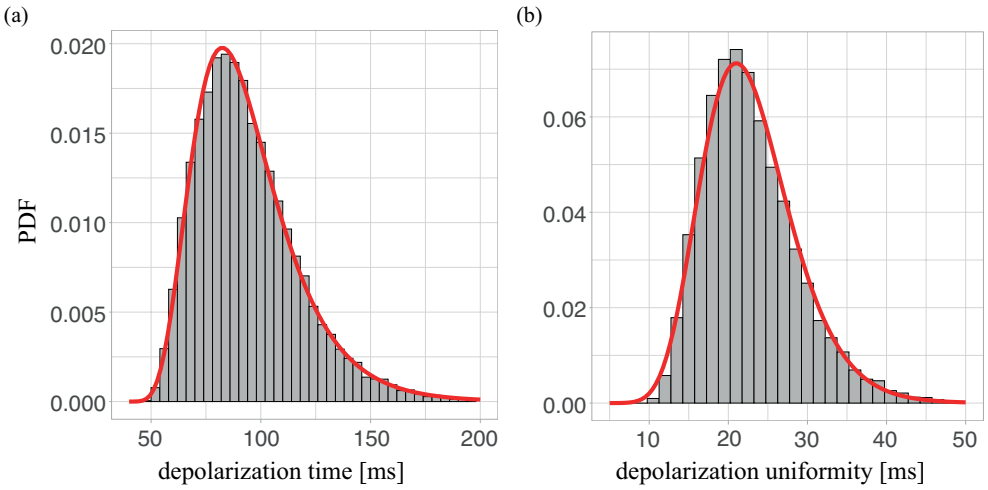

Figure 3.10: PDF of the depolarization (a) time and (b) uniformity according to the forward analysis with QMC strategy on 20'000 cases. The grey histograms correspond to the computed model outputs (using Sylvester's bandwidth), whereas the red continuous distributions are lognormals (with parameters $\mu\log = 4.05, \sigma\log = 0.374, \gamma\,\text{shift} = 32.23$ for (a) and $\mu\log = 3.25, \sigma\log = 0.221, \gamma\,\text{shift} = -3.67$) for (b).

with the governing equations via the term I_{ion} in equations (3.1). With this analysis, we aim at investigating not only the sensitivity of the ventricular depolarization but also of the action potential profile on the input parameters of the ten Tusscher–Panfilov cellular model [188] and determine which of them are the most relevant. The ten Tusscher–Panfilov model, indeed, has been seen to well reproduce the ions kinematics and the corresponding action potential profile (see figure 3.1b), but its input parameters are usually taken equal to their nominal value by the user without exploring their sensitivity on the electrophysiology results, which is going to be studied in this section. Furthermore, we aim at understanding what parameters have to be varied in order to specialize the ten Tusscher–Panfilov equations to reproduce the action potential profile in pathological conditions or to model the myocardial depolarization in the heart chambers other than the left ventricle (i.e. the atria and the right ventricle).

As motivated in the introduction, we recall that this UQ analysis has been run separately with respect to the former one (see section 3.3) due to the lack of knowledge about the PDFs of the input parameters of the cellular model, which does not allow to perform a proper global sensitivity analysis [85] Investigating simultaneously all the inputs would have polluted the resulting PDFs of the QoIs and, for this reason, two separated UQ analyses are considered rather than a single one on a larger input parameter space grouping the cellular model parameters with the geometrical and electrical input parameters. In this analysis, hence, the input parameters PDF are unknown and the UQ methodology is exploited to get some more insight on the cellular model.

A possible approach to deal with input parameters with an unknown uncer-

tainty, would be to run a one-at-time sensitivity (OAT) analysis where each parameter p is varied around its mean μ within a range $\pm\alpha\mu$ in order to measure the sensitivity index $\frac{f[\mu(1+\alpha)]}{f[\mu(1-\alpha)]}$. The OAT analysis, however, has the main drawback that interactions among parameters would be neglected owing to the local variation of the parameters about their nominal values [87]. This approach has been here extended to run a semi–local analysis by varying each parameter uniformly across the entire range $[\mu(1-\alpha),\ \mu(1+\alpha)]$ and using the dataset so produced to calculate the Sobol' indices, which consider the parameters interactions. Being this analysis a generalization of the OAT sensitivity measure, it is natural to vary the inputs uniformly around their mean rather than using a tentative Gaussian distribution, which could yield an ill-posed global sensitivity analysis [92].

3.4.1 Input

Input parameter	Definition	Nominal value
G_{K_1}	maximal IK1 conductance	5.405 nS/pF
G_{K_r}	maximal IKr conductance	0.153 nS/pF
G_{K_s}	maximal IKs conductance	0.392 nS/pF
G_{Na}	maximal INa conductance	14.838 nS/pF
G_{bNa}	maximal IbNa conductance	2.9e-04 nS/pF
G_{CaL}	maximal ICal conductance	3.983e-05 nS/pF
G_{bCa}	maximal IbCa conductance	5.92e-04 nS/pF
G_{to}	epicardial Ito conductance	0.294 nS/pF
G_{pCa}	maximal IpCa conductance	0.1238 nS/pF
G_{pK}	maximal IpK conductance	0.0146 nS/pF
Ca_o	extracellular Ca concentration	2 mM
Na_o	extracellular Na concentration	140 mM
K_o	extracellular K concentration	5.4 mM

Table 3.5: List of the input parameter of the cellular model considered in this analysis. Their nominal values are taken as in [188].

The ten Tusscher–Panfilov cellular model represents the cellular–scale dynamics in the monodomain and bidomain equations and includes all the major ion channels as well as intracellular calcium dynamics. The resulting system of equations is made of 19 ordinary differential equations (not reported here for the sake of brevity) that depend on 53 input parameters. Some of these input quantities, however, are constants, such as the gas and the Faraday constants, and some others are well controlled and measurable, such as the temperature and the surface to volume ratio of the cells. On the other hand, some other parameters are difficult to be measured both in–vivo and ex–vivo and, despite a significant variability among individuals is expected to happen, no data from the literature

are available to estimate their PDFs. Therefore, among the 53 input parameters of the ten Tusscher–Panfilov cellular model, we focus here on the influence of the 10 ions conductances and 3 ions concentrations, which are modeled as aleatory variables uniformly distributed in a range of ±30% around the nominal values reported in table 3.5. This variation range of the input parameters is larger than the one used in other parametric studies, where the effect of more parameters but varying in a smaller range was investigated [217].

3.4.2 QoIs

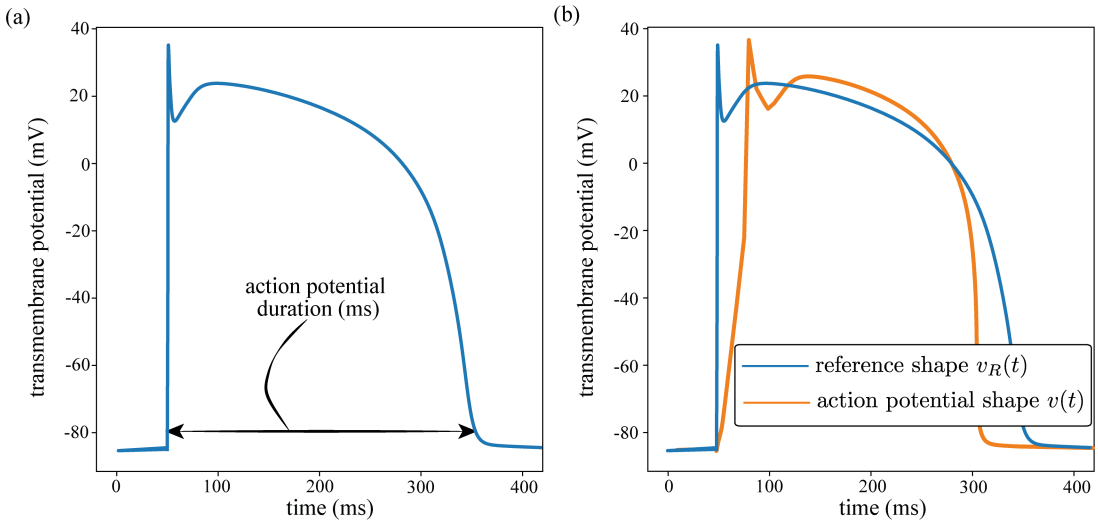

Figure 3.11: QoIs for the analysis 2. (a) The action potential duration (APD) is the time in milliseconds occurring between the fast depolarization and the end of the repolarization phase. (b) Reference action potential (blue line) and a generic action potential (orange line) used to compute the shape similarity index.

Along with the QoIs introduced in section 3.3.2, i.e. the DT and DU, two more QoIs related to the action potential profile are considered here. The first one is the *action potential duration* (APD) defined as the time needed for a myocytes to return to the resting state and be reactive to another electrical stimulus. This quantity corresponds to the time interval occurring between the fast depolarization and the end of the slow repolarization of the myocytes (see figure 3.11(a) and is measured in the numerical model as the time lag between the instant at which the cell reaches an active potential higher than -70 mV and the one at which the signal decreases lower than -80 mV (so to avoid possible spurious depolarization signal triggered by small perturbations). The APD is measured using a fixed threshold instead of the APD_{90} (the time for 90% repolarization from maximum voltage), because the latter is defined using the action potential amplitude (APA), which is sensitive to the variation of the input parameters and could yield anomalous evaluation of the APD (see [217] and figure 3.16b-d).

As sketched in figure 3.11(b), the second additional QoI is the *shape similarity index* that measures the deviation of the action potential, $v(t)$, from the reference profile, $v_R(t)$, corresponding to the input parameters set to their nominal values (as reported in table 3.5). This QoI is defined as the maximum of the cross-correlation [218] between the action potential profile and the reference one normalized by the auto-correlation of $v_R^*(t)$ (i.e. the cross correlation of the reference profile with itself with time lag $\tau = 0$):

$$\text{shape similarity index}(v(t)) = \frac{\max_\tau \int_t v^*(t) v_R^*(t+\tau) \mathrm{d}t}{\int_t v_R^*(t) v_R^*(t) \mathrm{d}t}, \tag{3.6}$$

where $v^*(t) = v^*(t) + v_0$ and $v_R^*(t) = v_R^*(t) + v_0$ are the action potential profiles increased by the resting potential, v_0=-85 mV. This definition of shape similarity index is commonly used in signal analysis to identify the starting point of a signal, even in the presence of noise [219]. Note that the formula (3.6) generally provides a shape similarity index less than one if $v(t)$ differs from the reference $v_R(t)$ with the two functions having a similar amplitude, whereas values greater than one occur when $v(t)$ has an amplitude larger than that of $v_R(t)$.

In order to compute the APD and the shape similarity index, we monitor the action potential at a sample node of the mesh that has to be far enough from the input signal in order to avoid an extra potential at the beginning of the electrical stimulus [170]. Since in a dedicated preliminary analysis the APD and the shape similarity index were seen to be independent on the monitored myocardial location, without loss of generality both QoIs are here evaluated at the apex of the ventricle. These two additional QoIs investigated in this second analysis were not considered in section 3 as a preliminary one-at-a-time (OAT) investigation (not reported here for the sake of brevity) revealed that they are weakly sensitive on the electrical conductivities and on the ventricular geometry.

3.4.3 Parametric study through sensitivity analysis

Owing to the large number of the input parameters, the QMC has an asymptotic slower convergence rate than the standard MC and about 10^4 samples are needed for the QMC to perform better than the MC with 13 input variables. For both the sampling methods, a direct strategy is not affordable in this case and the metamodel strategy introduced in section 3.3 is applied by training the adaptive sparse PCE against a sample dataset of 1'800 numerical simulations built using a Latin Hypercube. An independent dataset of 200 samples is then created with a pure MC strategy to test the trained metamodels. The adaptive strategy described in section 3.3 yields the metamodels reported in table 3.6. The cost of producing the entire dataset for training the metamodels is of about 70 CPU-days, whereas the cost of a direct approach similar to the one used in the previous section would be about 3.5 CPU-years (with a Saltelli dimension of $2'500 \cdot (13 + 2) = 37'500$ samples).

The resulting scatter plots comparing the inputs variable and the corresponding QoIs are reported in figure 3.12 for some relevant cases: although, a clear

		total degree	enumeration strategy	truncation strategy	R^2	Q^2
QoI1	ventricular depolarization time	3	hyperbolic ($q = 0.4$)	fixed	0.995	0.995
QoI2	ventricular depolarization uniformity	10	hyperbolic ($q = 0.4$)	sequential	0.999	0.999
QoI3	action potential duration	12	hyperbolic ($q = 0.4$)	fixed	0.999	0.999
QoI4	action potential shape similarity index	7	hyperbolic ($q = 0.4$)	fixed	0.998	0.995

Table 3.6: Selected metamodels for evaluating the different QoIs of analysis 2.

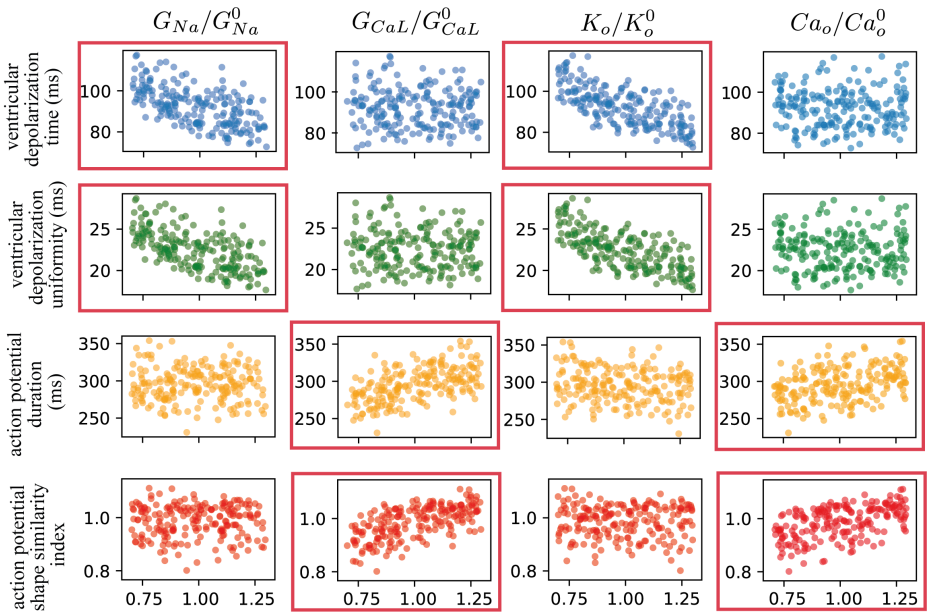

Figure 3.12: Typical scatterplots of the 4 QoIs against some of the inputs parameters normalized by their nominal value reported in table 3.5 using the training dataset of the PCE (400 samples). The red boxes highlight possible input–QoIs relation that will be eventually confirmed through a Sobol' indices analysis.

input–QoIs correlation is not visible in all panels, some monotonic trends can be observed such as the maximal ICaL conductance, G_{CaL}, influencing the APD and the action potential shape similarity index or the maximal INa conductance, G_{Na}, and extracellular K concentration, K_o, affecting the ventricular DT and DU.

This monotonic behaviour is confirmed by the Spearman coefficients, which are good predictors for low order interactions between inputs and outputs and are reported in figure 3.13 for the four QoIs against each input parameter. It can be noted that the DT and DU of the ventricle have a monotonic dependence on the maximal IbNa conductance, G_{bNa}, and extracellular K concentration, K_o, whereas the APD and the shape similarity index of the action potential manifest

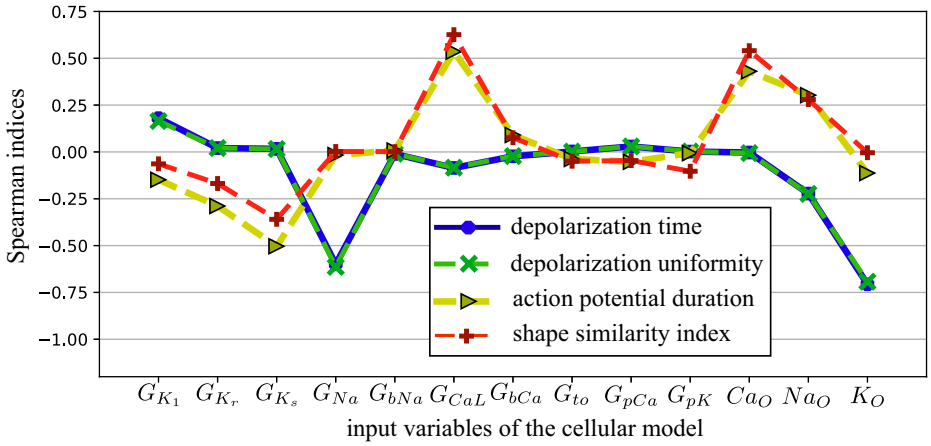

Figure 3.13: Spearman indices of analysis 2 computed using the training dataset (400 samples).

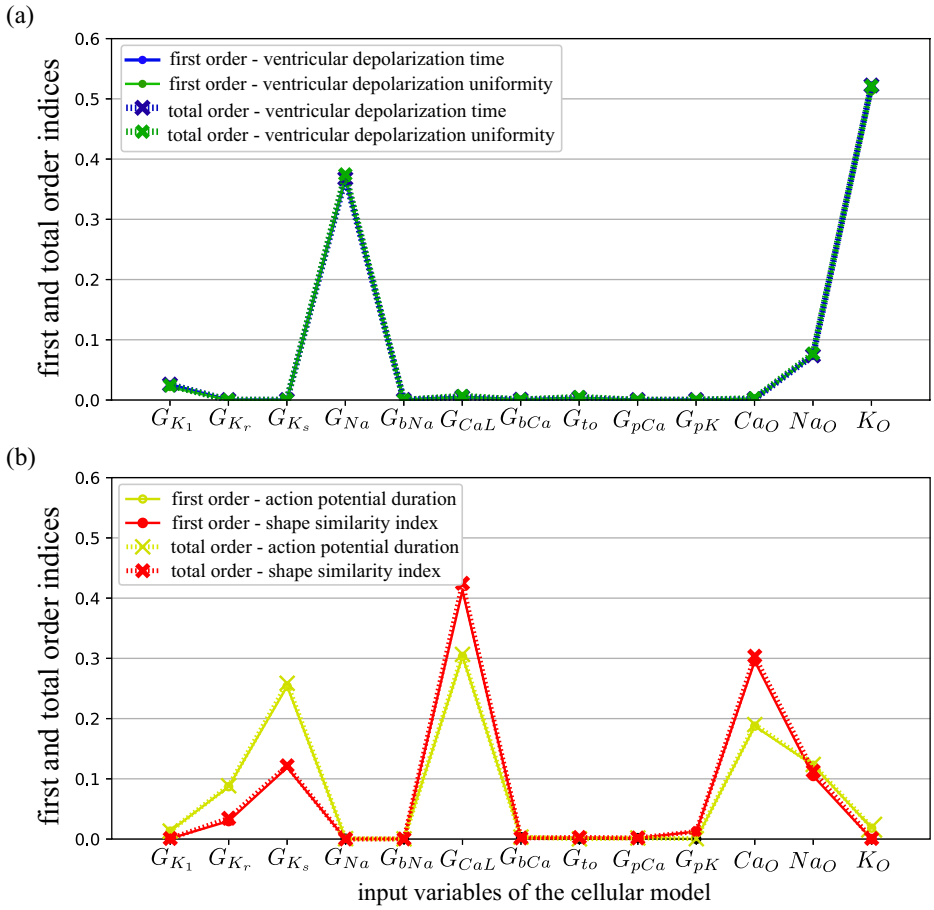

Figure 3.14: First and total order Sobol' indices computed using the adaptive PCE strategy on a dataset of 400+100 samples for (a) ventricular depolarization time and uniformity and (b) the APD and shape similarity index of the action potential.

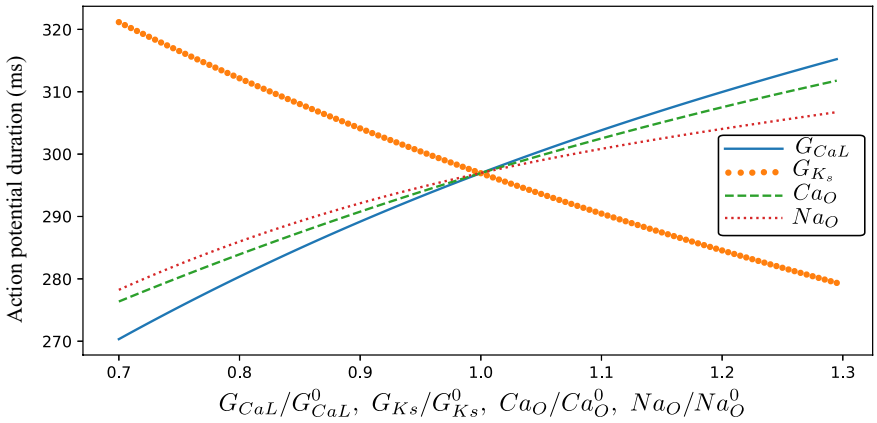

Figure 3.15: Approximated polynomial response of the APD as a function of the four most relevant inputs (see text). The input parameter in abscissa have been normalized by the nominal value from the literature [188], which is indicated by the superscript ^{0}.

a monotonic dependence on the maximal IKs and ICal conductances along with the extracellular K concentration, G_{Ks}, G_{CaL} and K_o respectively. This preliminary statistical test thus confirms the low order input–output interactions that were suggested by the scatter plots in figure 3.12. Nevertheless, higher order interaction among variables may be present as well and they need to be investigated before reducing the input parameters space. To this aim, the importance measures and the Sobol' indices of the 13 input parameters of the cellular model are computed using the trained metamodels for each QoI. Figure 3.14(a) shows that only the maximal INa conductance, G_{Na}, the extracellular Na concentration, Na_o and the extracellular K concentration, K_o, influence the variance of the DT and DU, while these two QoIs are almost insensitive to the remaining 10 parameters, which have a total influence of less than 5% on the variance. Both these QoIs manifest a similar hierarchy of Sobol' indices that can be rationalized by computing their Pearson and Spearman coefficients that are both equal to 0.999. On the other hand, the importance measures and Sobol' indices of the other two QoIs (i.e. APD and shape similarity index) in figure 3.14(b) indicate that the most influent input parameters are the maximal IKr, IKs and ICal conductances (G_{K_r}, G_{K_s} and G_{CaL}) along with the extracellular Ca and Na concentration (Ca_o, Na_o). Again, these two QoIs share the same behaviour of Sobol' indices with a Pearson and Spearman coefficients of 0.940 and 0.947, respectively.

For a complete model reduction, the whole set of 4 QoIs must be taken into account noticing that 6 input parameters have a weak influence on any QoIs (namely G_{K_1}, G_{bNa}, G_{bCa}, G_{to}, G_{pCa}, G_{pK} and G_{K_r}) and the number of input variables can then be reduced from 13 to 7. A further reduction can then be done if only certain QoIs are chosen (e.g. the time and uniformity or shape and APD) as suggested by the Sobol' indices in figure 3.14.

In this analysis the difference between first order and total order indices is very

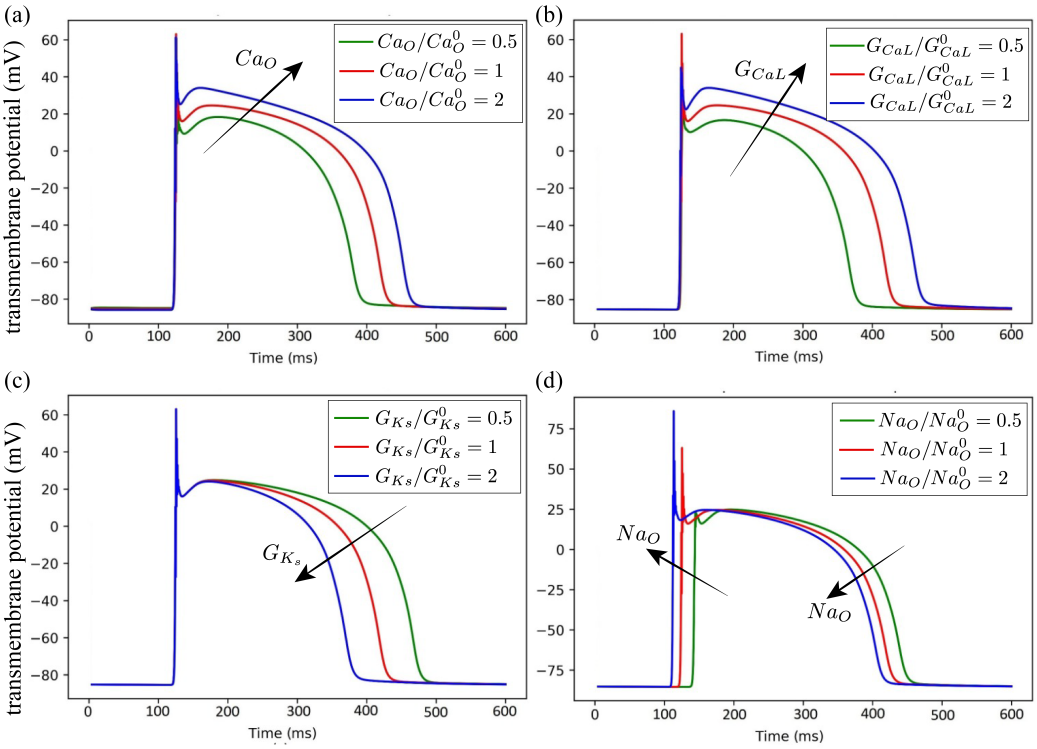

Figure 3.16: Variation of the action potential corresponding to doubling and halving the most sensitive input parameter according to the sensitivity analysis: (a) Ca_o, (b) G_{CaL}, (c) G_{Ks} and (d) Na_o.

little (in the order of 10^{-3}), which is in–line with the choice of a hyperbolic enumeration strategy that neglects high terms interaction, and allows a substantial reduction of the dimension of the samples needed to train the PCE. Furthermore, this low interaction among the input and the output variables permits to use low order polynomials to better approximate (with a least squares error of 10^{-4}) the QoI curves that are obtained by varying only one input parameter at the time while fixing the others to their nominal value, as shown in figure 3.15.

The sensitivity analysis carried out here thus provides the functional dependence between a local perturbation of the input parameter and the corresponding variation of the QoIs. This result can be applied to predict how the input parameters have to be set in such a way to reproduce action potential profiles occurring in pathological conditions or in the heart chambers other than the left ventricle. For instance, Sobol' indices suggest that the most effective parameters to increase or decrease the APD are G_{CaL}, G_{Ks}, Ca_o, Na_o and, as an example, these parameters have been varied in figure 3.16 showing how these values can be opportunely tuned to effectively modify and adapt the shape of the action potential. Vice–versa a major modification of the other conductances and ions concentrations that are found to be irrelevant according to the sensitivity analysis do not yield a significant variation of the action potential (not reported in

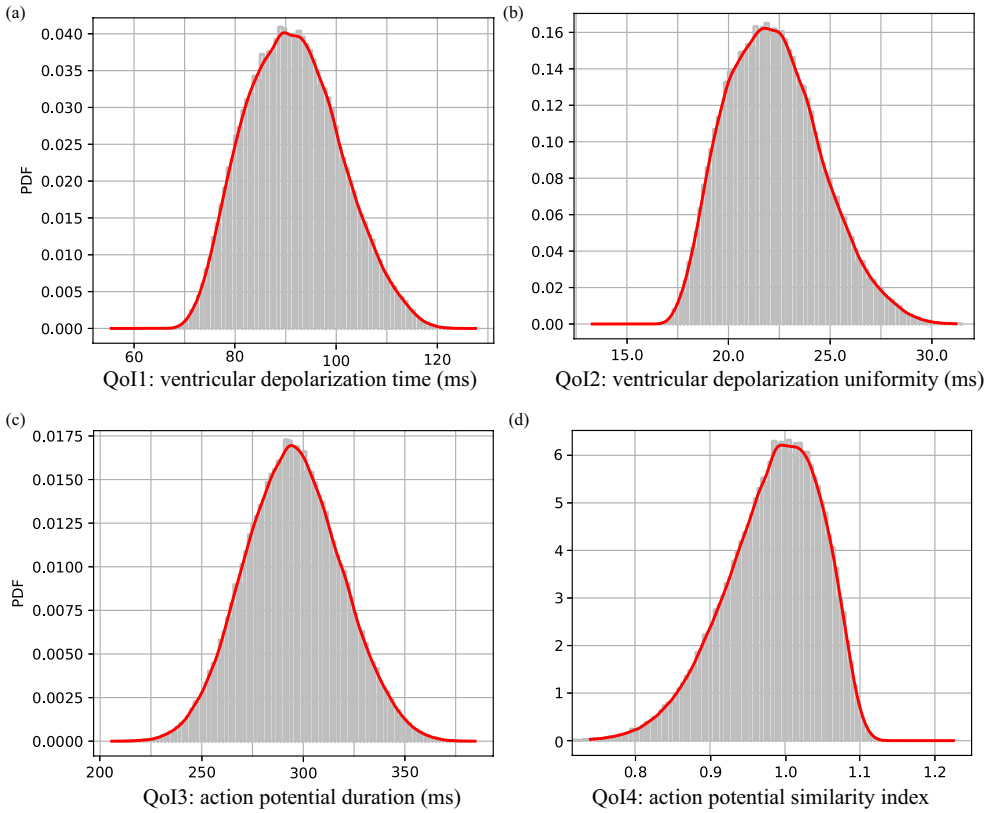

Figure 3.17: PDF of the depolarization (a) time and (b) uniformity, (c) APD and (d) shape similarity index of the action potential according to the forward analysis. The grey histograms correspond to the computed metamodel outputs.

the figure).

3.4.4 Forward analysis

Although the lack of knowledge of the input PDFs makes the forward UQ not data based, the metamodels trained as in the previous subsection are here used to carry out a forward analysis by producing a large dataset (10^6 samples according to a pure MC scheme) that is used to evaluate the QoIs uncertainty. The computational cost of the forward analysis using a trained metamodel is negligible once the training is complete as the 20'000 metamodel evaluations needed for the UQ analysis are only obtained in about 1 CPU-minute, rather than 1.9 CPU-years as in the case of running the full computational model. The resulting PDFs are reported in figure 3.17 as histograms superimposed with the best–fitting distributions (obtained using the Kernel smoothing method). It results that varying the cellular model parameters within a range of $\pm 30\%$ over their nominal values does not produce pathological DTs since the standard deviation of its PDF is 9.2 ms and the probability for a DT greater than 120 ms or smaller than 60 ms are less than $10^{-2}\%$ and $10^{-10}\%$, respectively. Owing to the quasi–linear relation among the DT and DU observed in section 3.3.3,

also the distribution of the ventricular DU is concentrated about its mean value with a standard deviation equal to 2.31 ms and a probability to experience a DU shifted by more than 5 ms from its mean below 2.5%. Interestingly, the asymmetric distribution of the DT and DU reported in figure 3.17 a) and b) is due to the non linear influence of the cellular model on the conduction velocity that has a superlinear (sublinear) dependence on the electrical conductivities for small (large) values of the electrical conductivities themselves.

On the other hand, the APD exhibits a more symmetric PDF (skewness 0.05) with a mean of 295.8 ms and a standard deviation equal to 23.4 ms, see figure 3.17 c). The probability of a APD 30 ms larger than the mean value, corresponding to a longer inability of the muscular fiber to contract, is equal to 20.8%. Lastly, the PDF of the action potential similarity index has an average of 0.98 and a standard deviation of $4 \cdot 10^{-3}$ where, we recall, the unitary value corresponds to the reference action potential shape. The asymmetric distribution with a skewness of -0.58 and the absence of a right tail means that the main effect on the action potential shape is a modification with respect to the reference profile (yielding indeed a cross–correlation less than one according to the equation (3.6)), rather than a variation of its amplitude corresponding to a shape similarity index greater than one.

3.5 Conclusions

In this work, the UQ analysis for an electrophysiology model of the human left ventricle has been performed. The first analysis is focused on the effect of the ventricular geometry and electrical conductivities (input parameters) on the effectiveness of ventricular contraction during the systolic phase that is known to be correlated with (i) the time needed to depolarize the whole myocardium and (ii) the spatial uniformity of the depolarization front (QoIs). The uncertain PDFs of the shape parameters are taken from available data in the literature acquired with cardiac–echography, whereas the electrical conductivities are known to be distributed as Gaussians for mammalians and the few available measurements for humans are used to calibrate Gaussian PDFs. Thereafter, a sensitivity analysis has been carried out using an adaptive strategy based on a training dataset (400 samples) produced using a QMC strategy (with Sobol' low discrepancy sequence) and an independent test dataset (100 samples) obtained using a pure MC strategy. A family of metamodels (PCE based on orthogonal polynomials recovered using a three terms recursion) has been built by using (i) two different selection strategies of their coefficients (fixed or sequential), (ii) two enumeration rules (linear or hyperbolic) and varying (iii) the total maximum degree of the expansion from 1 to 16. Each of the 64 resulting metamodels is trained against the training dataset and the optimal one is selected as the one minimizing the distance between the R^2 index (evaluated on the training dataset) and the Q^2 index (evaluated on the test dataset), with the constraint $R^2,\ Q^2 > 95\%$. The optimal metamodel is then used to compute the first and total Sobol' indices to determine

the QoI sensitivities on the input parameters. In order to validate the sensitivity analysis, a direct *brute force* approach has been also applied on an independent QMC dataset of 20'000 samples to produce Sobol' indices using Saltelli's algorithm that well agree with the one obtained using the metamodelling approach. PCE metamodels, indeed, are seen to fit well several electrophysiology models and to provide sensitivity results in line with direct strategy approaches but using smaller datasets than the ones needed for a direct UQ analysis (see figure 3.9 for an example) [187]. This high prediction ability, combined with the stability of electrophysiology models at small perturbations, places PCE strategies among the gold standards techniques for electrophysiological UQ [217].

The analysis reveals that ventricular depolarization is very sensitive to the geometrical parameters (with an influence greater than 60%), while the parallel and perpendicular conductivities have a total influence of about 25% and 15% respectively. This result thus suggests to reduce the model by neglecting the perpendicular conductivities and decrease the size of the input parameter space from 6 to 4. Interestingly, a strong linear correlation between the DT and DU is observed (Pearson index 0.992 and Spearman index 0.998) implying that the same model reduction applies to both QoIs. The reduced model is then used to run a forward analysis (QMC dataset with Sobol' low discrepancy sequence) and obtain the uncertainty PDFs that are seen to be in–line with clinical observations exhibiting a non–pathologic DT with a probability of 80%, whereas a slow DT longer than 130 ms has a probability of about 8%. On the other hand, the probability of unphysically low DT (i.e. ¡40 ms) is smaller than 10^{-6}.

We then turned our attention to investigate the role of the input parameters of the ten Tusscher–Panfilov cellular model on the DT and DU of the left ventricle along with two more QoIs related to the active potential profile: the APD and the shape similarity index (the latter defined with respect to the reference case corresponding to the input parameters set to their nominal values). This second analysis has been run separately from the first one since no data from the literature are available to estimate the input uncertainties, which have been modeled as independent uniform distributions with values ranging from 0.7 to 1.3 times the nominal value. In this parametric study, a direct UQ strategy is unaffordable owing to the large number of parameters involved (10 conductances plus the 3 ions concentrations), and the adaptive metamodel strategy used in the first analysis has been adapted to this case to run a sensitivity analysis. The resulting Sobol' indices show that the DT and DU only depend on the maximal INa conductance, G_{Na}, extracellular Na concentration, Na_o, and extracellular K concentration, K_0, whereas the other 10 input parameters have a total influence of less than 5% on the variance. The action potential QoIs (i.e. APD and shape similarity index) are sensitive to the maximal conductances G_{CaL}, G_{K_s} and G_{K_r} along with the extracellular Ca and Na concentrations N_{aO} and G_{K_r}, with a total influence exceeding 95%. This result naturally suggests a model reduction from 12 to 5 input variables, namely G_{CaL}, G_{K_s}, C_{aO}, N_{aO},G_{K_r}.

A similar strategy for the model reduction was obtained by Hurtado et al. [186] where a PCE approach based on the R^2 validation index, similar to the

one adopted in our analysis, is used. Although these authors considered different cellular models compared to ours (the Nash-Panfilov and the Rice models) and a smaller dimension of the input parameters space (5 independent inputs, rather than 12 ones investigated here), the same order of importance for the 4 common input parameters on the APD is observed (namely G_{CaL}, G_{K_s}, G_{K_r} and G_{Na} with a negligible effect of the latter one on the APD). Furthermore, the sign of the APD sensitivity on each input parameter reported in Hurtado et al. corresponds to those computed here using the Spearman's indices, see figure 3.13. The sensitivity analysis and the corresponding model reduction relative to the APD is also confirmed by Pathmanathan and Cordeiro [217, 220], where a parametric study with normal input distributions was carried out using a direct UQ approach on several QoIs. Also in their work G_{K_ℓ}, G_{Kr} and G_{Cal} result to be the relevant input parameters on the APD that, instead, is less sensitive on G_{K_1}, G_{Na} and G_{to}.

On the other hand, if the whole set of 4 QoIs is considered, 6 variables among 13 are seen to have a weak influence on any QoI and they can be neglected with the aim of reducing the model complexity. Importantly, the difference between first and total order indices is small (in the order of 10^{-3}) thus meaning that the cellular model inputs could be varied separately to modify the QoIs. This result has then been exploited to successfully control the APD of the cellular model by perturbing the sensitive input parameters detected by the sensitivity analysis. This analysis thus provides a deeper insight on the effects of the input parameters on the action potential shape and the sensitive input parameters can be used in future studies to reproduce the transmembrane action potential heterogeneity in the heart chambers and/or reproduce the action potential profiles observed in pathological conditions.

A main limitation of this work, however, is that the electrophysiology model solves for the left ventricle as uncoupled from the rest of the heart chambers by setting an initial electrical stimulus at the location of the bundle of His, thus neglecting the electrical depolarization of the atria that is initiated in the sino–atrial node. Furthermore, the electrical system of fast conduction of the heart including the highly conductive bundles and the Purkinje network are also neglected and a more evolute and accurate electrophysiology model is needed to account for these limitations.

Nevertheless this work represents a starting point to detect the key input parameters influencing the electrical activation of the ventricular myocardium, to quantify the uncertainty on the depolarization pattern and to reduce the input parameter space. This last aspect is of paramount importance when the computational cost of the model is further increased as in the case of multi–physics models for the heart where such an electrophysiology model is coupled with the structural dynamics of the myocardium (electro-mechanical interaction) and the mechanical stresses influence the conductivity properties of cardiac tissue through a generalised reaction-diffusion-mechanics model [221, 222]. Such refined computational models introduce additional input parameters and QoIs, thus calling for further UQ analyses. Future UQ analyses could be thus car-

ried out by considering other relevant quantities to describe critical features in the cardiac dynamics such as the electrical conduction velocity or, in the case of electro-fluid-structure interaction (FSEI [177]), fluid-dynamics QoIs such as recirculation zones, flow patterns or the cardiac output. The size of the input parameter space could also be increased by including the uncertainty of the fibers orientation, of the specific membrane capacitance C_m and of the surface-to volume ratio of cells χ as well as by considering different positions and patterns of the stimulus I_s. Indeed, at higher stimulation frequencies, other ionic parameters can become relevant [223, 224] and *ad hoc* QoIs characterizing the action potential patterns can be introduced [225].

As a final note, we wish to remark that the accuracy of the UQ analyses proposed here as further development of this work depend on the uncertainty PDFs of the input parameters that need to be retrieved from real data through dedicated in-vitro and in-vivo laboratory experiments.

3.6 Appendix: Convergence analyses

3.6.1 Convergence check of the electrophysiology model

The transmembrane potential averaged over the ventricular domain as a function of time is shown in figure 3.18(a). Each solid curve corresponds to a different simulation of the bidomain equations with the ten Tusscher-Panfilov model on a different grid (with cells number varying from 2'000 to 68'000), where the electrical conductivities are scaled by a fixed parameter equal to 3.0 to account the lack of the fast conductivity fibers (see section 2). The resulting transient dynamics of the average transmembrane potential evolves in a similar fashion to a typical action potential profile with a steep depolarization front and a smoother repolarization one occurring after about 300 ms (see figure 3.1b). Qualitative differences of this quantity are visible when the number of cells is below 3'000 cells, whereas the results become insensitive on the grid resolution for number of cells larger than 50'000. Such a resolution, however, would require a CPU time exceeding 20'000 days to built a dataset as large as the one used for the direct UQ analysis in section 3 (20'000 samples), thus calling for a massively parallel CPU infrastructure. According to dedicated numerical tests, the computational cost to solve a single time step of the bidomain model is found to increase linearly with the number of mesh cells and, at the same time, the largest timestep ensuring numerical stability is seen to decrease about with the same scaling. As a result, the total computational cost has a quadratic dependence on the number of mesh cells as shown in figure 3.18(b). In order to reduce the computational cost to match the computational resources available, we have conveniently used the mesh with 4'311 cells and scaled the electrical conductivities by a fixed parameter equal to 4.99 accounting both for the lack of the fast conductivity fibers and for the correction of the conduction velocities to mesh size effects. This method is commonly used in modomain/bidomain modeling [226, 227, 228] as

it allows to capture a more accurate approximation of the conductive velocity (see the dashed line in figure 3.18a) and, consequently, to build a 20'000 samples dataset with a CPU cost of 691 days.

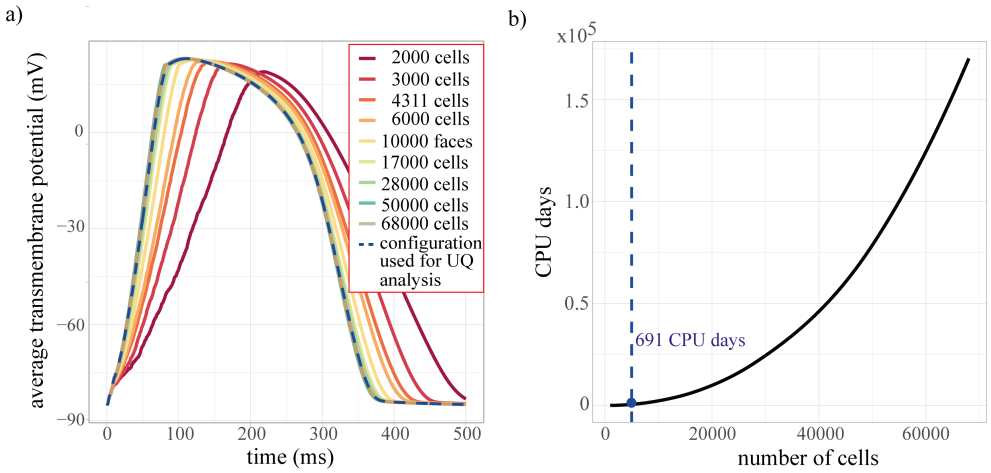

Figure 3.18: a) Time behaviour of the average transmembrane potential in the left ventricle with electrical conductivities scaled by a fixed parameter equal to 3. The dashed line indicates the configuration used for the UQ analysis, corresponding to the 4'311 cells grid with electrical conductivities scaled by a factor 4.99. b) Computational cost in CPU days of producing a dataset of 20'000 samples (as large as the one used for the direct UQ analysis in section 3) as a function of the mesh cells number. The vertical dashed line indicates the computational cost corresponding to the configuration used to the UQ analyses in section 3 and 4.

3.6.2 Convergence check of the metamodel UQ method

The accuracy of both the metamodel and the direct UQ approaches has been already shown by the crossed–validation test reported in section 3c, where the first and total order Sobol' indices obtained with the two techniques well agree each other, see figure 3.9. A convergence study of the metamodel approach is carried out here by varying the size of the training dataset. To this aim, smaller training datasets are obtained by extracting a subset of the training dataset used in section 3c containing from 50 to 400 samples with step of 50 (in the last case the subset corresponds to the whole training dataset) and for each case a different metamodel is trained using the same adaptive technique introduced above. Figure 3.19 shows the first order Sobol' indices as a function of the number of samples of the dataset used to train the metamodel: as the dataset is larger than 200 samples (i.e. half of the dataset used for training the metamodel in section 3c), the measures of importance are almost stable thus guaranteeing the convergence of the method. It should be noted that this good behavior of the metamodel is also attributable to the sampling procedure (Quasi Monte Carlo), which maps the input space effectively identifying the average properties with few samples.

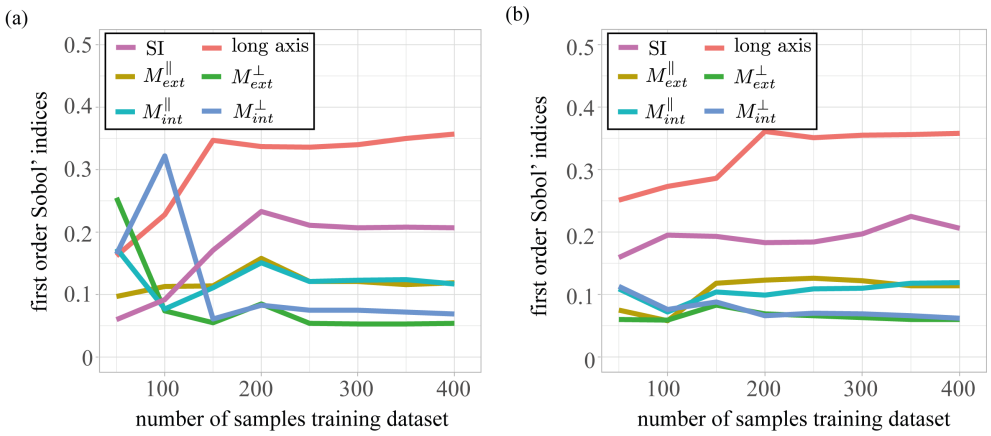

Figure 3.19: Convergence analysis for the metamodel training procedure. First order Sobol' indices of analysis 1 (see section 3) as a function of the size of the training dataset for (a) DT and (b) DU.

3.6.3 Convergence check of the direct UQ method

The convergence of the direct quasi Monte Carlo method is tested by applying the same quasi Monte Carlo UQ procedure used for analysis 1 in section 3c to an independent and smaller Saltelli dataset of size 4′000 samples. Figure 3.20 shows that the first order Sobol' indices computed using the two datasets reasonably agree each other and, importantly, manifest the same order of importance (except for the SI and $M_{ext}^{\parallel}$ on the DU) despite this second dataset is five times smaller than the one used in section 3c. Furthermore, the importance measures of DT result to be within the confidence intervals calculated on the larger Saltelli dataset of 20′000 samples.

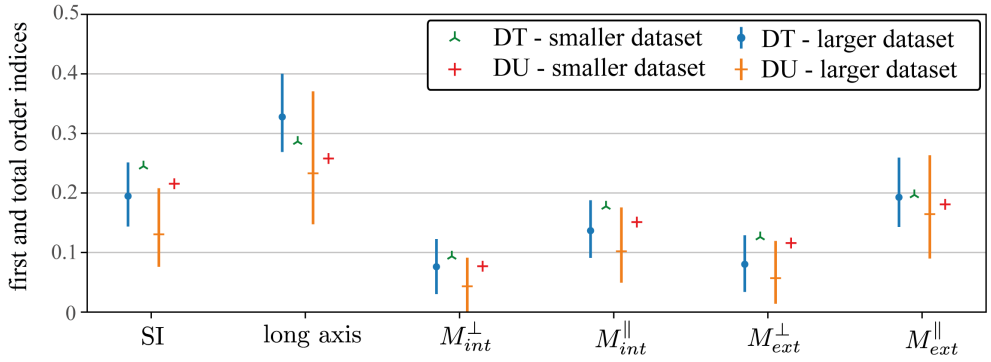

Figure 3.20: Convergence analysis for the direct UQ procedure. First order Sobol' indices of analysis 1 (see section 3) using the smaller (4'000 samples) and larger (20'000 samples) datasets.

Funding

This work has been partly supported with the 865 Grant 2017A889FP 'Fluid dynamics of hearts at risk of failure: towards methods for the prediction of disease progressions' funded by the Italian Ministry of Education and University.

Author Contributions

G.D.C., R.V., F.V. designed the research. G.D.C. carried out the numerical simulations and the UQ analysis. G.D.C. and F.V. wrote the paper with inputs from R.V.

Chapter 4

A fast computational model for the electrophysiology of the whole human heart

Giulio Del Corso, Roberto Verzicco and Francesco Viola
Journal of computational physics 457 (2022): 111084

Abstract

In this study we present a novel computational model for unprecedented simulations of the whole cardiac electrophysiology. According to the heterogeneous electrophysiologic properties of the heart, the whole cardiac geometry is decomposed into a set of coupled conductive media having different topology and electrical conductivities: (i) a network of slender bundles comprising a fast conduction atrial network, the AV–node and the ventricular bundles; (ii) the Purkinje network; and (iii) the atrial and ventricular myocardium. The propagation of the action potential in these conductive media is governed by the bidomain/monodomain equations, which are discretized in space using an in–house finite volume method and coupled to three different cell models, the Courtemanche model [229] for the atrial myocytes, the Stewart model [230] for the Purkinje Network and the ten Tusscher–Panfilov model [188] for the ventricular myocytes. The developed numerical model correctly reproduces the cardiac electrophysiology of the whole human heart in healthy and pathological conditions and it can be tailored to study and optimize resynchronization therapies or invasive surgical procedures. Importantly, the whole solver is GPU–accelerated using CUDA Fortran providing an unprecedented speedup, thus opening the way for systematic parametric studies and uncertainty quantification analyses.

4.1 Introduction

Owing to the development of accurate mathematical models capable of virtually replicating biological systems and to the growing availability of computational resources to solve them, medical research is increasingly integrated with computational engineering [231]. In particular, the correct modelling of the heart functioning in healthy and pathological conditions – such in the case of *ischemic* events (reduced blood supply to a portion of the myocardium leading to dysfunction and, possibly, to the necrosis of the tissue) or of *bundle branch block* (delay or blockage along the heart electrical pathway) – entails reproducing the highly cooperative and interconnected dynamics of the heart, including its complex electrical activation.

The latter involves many embedded conductive structures with different biological properties so as to rapidly propagate the electrical activation of atria and ventricles in order to achieve an efficient muscular contraction propelling the blood into the circulatory system. As shown in Figure 4.1 a), the cardiac electrical depolarization, corresponding to a rise in the electrical potential across the cellular membrane owing to the transmembrane flux of ions, is initiated close to the entrance of the superior vena cava at the sinoatrial node (SA–node). Within the SA–node, some specialized pacemaker cells spontaneously produce a periodic electrical impulse, the *action potential*, which propagates across the right atrium through three high speed conductivity bundles – namely the Thorel's pathway/posterior internodal tract, the Wenckebach's middle internodal tract and the anterior internodal tract – that wrap the right atrial chamber to assure a uniform activation. A branch bifurcating from the latter bundle then penetrates into the internal muscle of the left atrium (Bachmann's bundle), thus initiating the depolarization also of this chamber. Since the propagation speed of the action potential within the fast internodal bundles is of about 1–2 m/s (significantly larger than the one observed in the atrial muscle of about 0.3–0.5 m/s [16, 22, 232]), after 30 ms the depolarization front reaches the atrioventricular node (AV–node) which is the electrical gate connecting the atrial with the ventricular electrophysiology system, see Figure 4.1(b). In the AV–node, specialized cells slow down the propagation of the transmembrane potential by about 100 ms in order to allow both atria to contract before the activation wave reaches the ventricles; this avoids the simultaneous contraction of the whole organ which would produce inefficient filling/emptying of the four chambers and impaired pumping [233]. Once beyond the AV–node, the signal propagates through the His bundle, which forks into the right and left bundle branch that, in turn, progressively divide into a plethora of thin, tightly woven specialized cells named the Purkinje network, where the propagation speed of the action potential is in the range 1.5-4 m/s, corresponding to six times the propagation speed in the ventricular muscle [16]. This fast conduction system quickly propagates the electrical signal within the ventricular myocardium (about 30 ms to reach the terminations of the Purkinje fibers) to provide an almost simultaneous contraction of

the ventricular muscle. In addition, the Purkinje network also assures the timely activation of the papillary muscles, which stretch the *chordae tendineae* so to prevent the eversion of the mitral and tricuspid valve leaflets by pulling down their free margins during early systole [234]. Although the precise morphology and orientation of the Purkinje network can not be measured in–vivo, a significant variability among individuals is known to exist [235], also depending on the positions of the papillary muscles which also varies among the population [28]. Furthermore, its smaller fibers are randomly oriented in the subendocardium with a penetration length in the myocardium of about $0.5 - 100\ \mu m$ and with an average distance among them of about 0.1 mm [236, 237]. The Purkinje fibers are electrically isolated from the myocardial muscle, except at their endpoints called *PMJs* (Purkinje Muscle Junctions), where the electrical signal can propagate from the Purkinje fibers to the ventricular myocardium with a delay ranging from to 5 to 15 ms (*orthodromic* propagation) and vice–versa from the myocardium to Purkinje with a delay of 2-3 ms (*antidromic* propagation) [238].

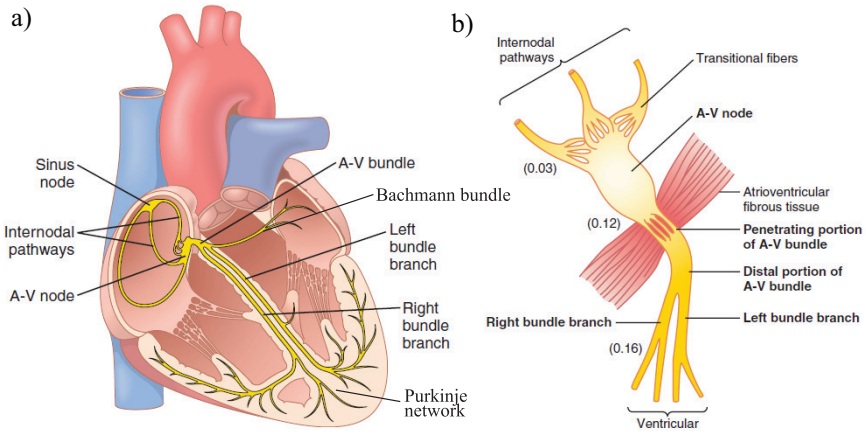

Figure 4.1: Sketch of the electrophysiology system of the heart [16]. a) Fast conduction networks of bundles and Purkinje. b) Detail of the AV bundle with the corresponding activation times (in seconds) showing the propagation delay happening in the AV–node.

Both the fast bundles and the Purkinje networks electrically activate the muscular myocardium in terms of action potential, which then propagates in the thick muscular myocardium at a lower speed that depends on the local fiber orientation. The myocardium is, indeed, an orthotropic medium [239] made of oriented myocytes that enable a faster transmission of electrical impulses in the fiber direction than in the orthogonal one and this tissue heterogeneity, playing a role in the atrial [240] and ventricular [241, 242] depolarization, should be accounted for in cardiac numerical models. According to the model proposed by Buckberg et al. [243] the muscular fibers have a dual-orientation, with directions ranging approximately from $+60°$ to $-60°$ across the ventricular wall [244] and this structure has been confirmed by accurate imaging analysis of mammalians heart [245]. An additional cause of inhomogeneity is that the ventricular myocytes

have different electrical properties from the atrial ones, thus resulting in a different electrical conductivity (yielding a different propagation speed) and different ionic fluxes across the myocytes membrane, which entail a different contraction pattern of atrial and ventricular chambers.

In the last decades few mathematical models for solving the cardiac electrophysiology have been proposed. The eikonal approach solves directly the electrical depolarization of the cardiac tissue by taking as input the propagation speed within the media [167], whereas the interconnected cable methods solve the propagation of an electrical stimulus thorough a connected network of discrete cables representing the myocardium [162, 163]. These methodologies have a limited computational cost and have been used to model the cardiac tissue including the macroscopic effects of structural heterogeneity on impulse propagation [165] and to incorporate more complex conduction structures, such as cardiomyocytic fibers orientation and the His–Purkinje activation network [166]. On the other hand, leveraging on the continuum hypothesis the cardiac tissue can be modeled as an intracellular and an extracellular overlapping conductive media separated by the cell membrane. The resulting bidomain model [168, 169] thus consists of the coupling between a system of reaction–diffusion partial differential equations (PDEs, governing the potential propagation in the media) and a set of ordinary differential equations (ODEs) for the cellular ionic model describing the current flow through ion channels. The bidomain model is the state–of–the–art mathematical model for reproducing the cardiac electrophysiology at a continuum level [170, 172], it has been validated against several experiments on animals [175, 176] and it is currently adopted to solve the action potential propagation in healthy and pathological conditions including ischemic events and fibrillation [173, 174, 172]. In the case the extracellular conductivity tensor is proportional to the intracellular one, the bidomain equations can be simplified into a single governing equation for the transmembrane potential, the monodomain system, which is computationally cheaper than the bidomain counterpart as the number of degrees–of–freedom (dofs of the system of PDEs) is halved [170]. Unless complex pacing patterns or fibrillation are present, the monodomain equation can be conveniently used to approximate the bidomain solution also in the case the conductivity tensors are not proportional [171] by setting the components of the monodomain conductivity tensor to half the harmonic mean of the corresponding extracellular and intracellular components [170].

The bidomain/monodomain electrophysiology model has been widely used to study different components of the cardiac electrical network such as the atrial depolarization also including pathological atrial fibrillation [246, 240] or to model the AV–node depolarization [247, 248]. The depolarization in the ventricular myocardium has been investigated in a series of works [241, 249, 250, 177] also including the fast conduction Purkinje network [238, 245, 251], which is needed to reproduce a realistic ventricular depolarization, especially in the presence of infarction [252] or reentry initiation of arrhythmias [253, 254, 255]. In these works, the geometry of the Purkinje network is generally obtained by applying a *growing* algorithm to a one–dimensional (1D) network of fibers, which

has to be sufficiently dense in order to correctly activate the 3D myocardium [256, 257, 258].

Although some studies are very advanced in solving the bidomain/monodomain equations in a portion of the cardiac electrical network [259, 260, 261, 222, 262], a comprehensive computational framework, solving simultaneously the fast conduction electrophysiology networks and the four–chambers muscular myocardium, is still missing. Such a computational model for the whole cardiac electrophysiology would entail, indeed, the solution of a large dynamical system, thus calling for efficient code parallelization with an effective use of the computational resources. This work aims at building an accurate computational framework for solving the whole cardiac electrophysiology accounting for: (i) the fast conductivity structures of the atria and ventricles including the internodal pathways, branch bifurcations, and the AV–node; (ii) the Purkinje network immersed in the ventricular myocardium, which activates the ventricular muscle at the PMJs; (iii) the thick atrial and ventricular myocardium with their muscular fibers orientation yielding electrical anisotropy. These three electrical components of the system have different electrophysiology properties and are modelled using a hierarchy of interconnected geometries having different topological dimension and cell models. The bidomain/monodomain equations are discretized in space using an in–house finite volume method that allows for tackling complex geometries, also deforming in time, and the whole model has been ported to CUDA to run on GPU architectures thus providing unprecedented speedups [263, 231]. The resulting computational model is then applied to solve the cardiac electrophysiology in healthy and pathological conditions with the aim of assessing the model performance and validating its results.

The paper is organized as follows. After the introduction of the cardiac geometry used throughout the work in § 4.2, the governing equations and the GPU–accelerated numerical methods are detailed in § 4.3. The convergence analysis of the code and validations against benchmarks results from the literature are reported in § 4.4. In § 4.5 the electrophysiology activation of the whole human heart is studied in healthy and pathologicalal conditions, including bundle branch blocks and the implant of artificial cardiac pacemakers. Conclusions and further research directions including possible uncertainty quantification analyses are outlined in § 4.6.

4.2 Computational domain: splitting the electrophysiology system

As anticipated above, the cardiac electrophysiology system is made of a (i) fast conduction network of bundles, (ii) a Purkinje network for the ventricular activation and (iii) the massive conductive myocardium contracting as the myocytes depolarize. Our computational approach is based on intrinsic connections among different conductive media and pathways, and the complex electrophysiology sys-

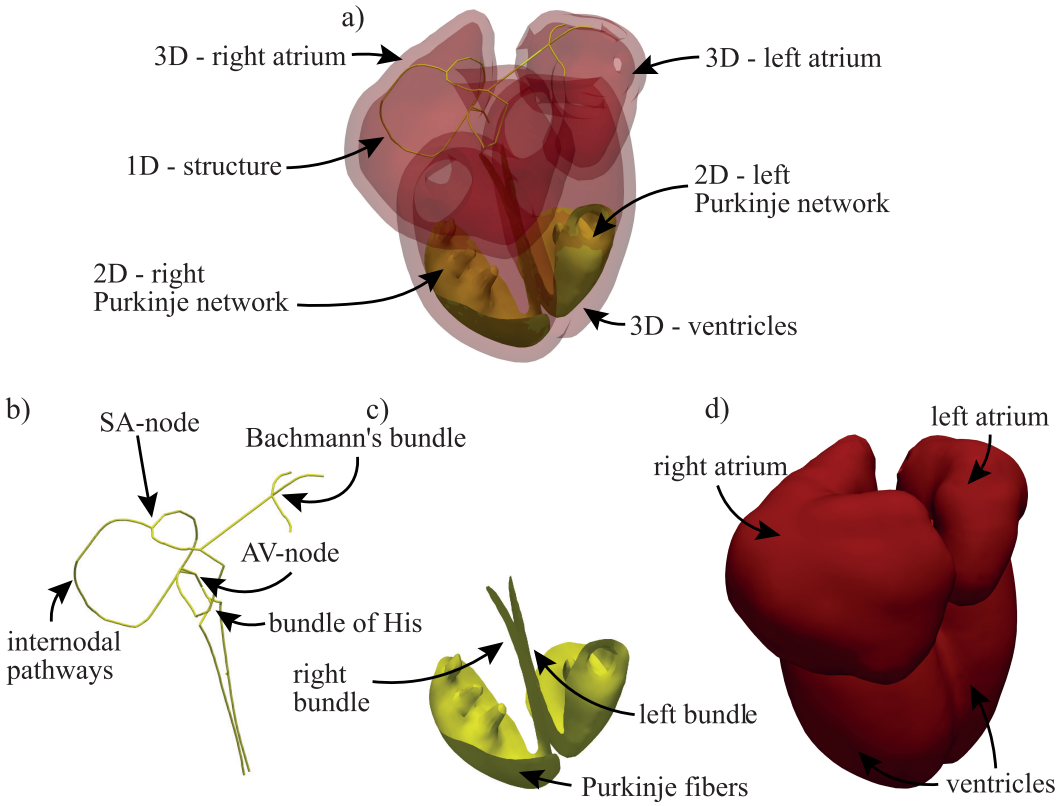

Figure 4.2: The a) whole cardiac electrophysiology system is split in: b) 1D network of fast conduction bundles, c) 2D Purkinje network and d) 3D myocardium.

tem is thus split in several interconnected subdomains with different dimensional topology (see Figure 4.2), namely a one–dimensional graph (1D) modelling the fast conduction bundles (panel 4.2 b); a two–dimensional (2D) surface approximating the dense Purkinje network (panel 4.2 c); three-dimensional (3D) media for the atrial and ventricular muscles (panel 4.2 d). The solution of the complete system, shown in panel 4.2a, is thus obtained by the coupled solutions of these three distinct components which are detailed in the following.

4.2.1 One dimensional fast conduction network of bundles

Owing to its slenderness, the fast conductivity structures conveying the electrical signal through the 3D myocardium has been modelled as a 1D fast conduction pathway with space–varying electrophysiology properties (see Figure 4.3). The network originates from the SA–node and branches into the three internodal pathways reaching the AV–node with one of them (the anterior internodal pathway) further branching and connecting the right atrium to the left one through the Bachmann's bundle. The terminations of the internodal pathways reach the AV–node (in two locations) connecting the atrial fast conduction network with

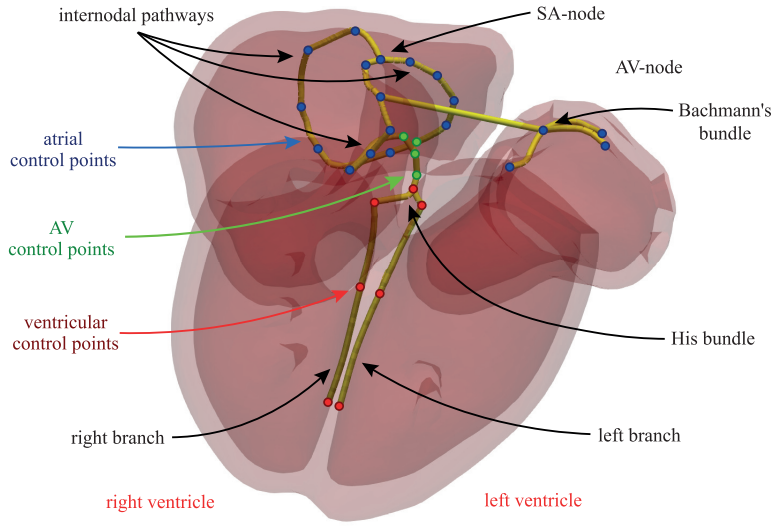

Figure 4.3: Fast conduction network of bundles. The circles indicate the geometrical control points of the atrial network (blue), AV–node (green) and ventricular network (red).

the ventricular through the bundle of His, which then splits into two distinct branches, one immersed in the right ventricle and the other in the left one.

In order to eventually adapt the fast conduction network to different patient geometries, the entire graph is generated through a set of control points whose coordinates can be arbitrarily set so to easily reproduce a given cardiac geometry following the adaptive procedure. Specifically, 19 control points are distributed among the SA–node and the atrial bundles (indicated by blue bullets in Figure 4.3), 4 control points are used for the AV–node and its connection with the bundle of His (green bullets in Figure 4.3) and 7 more control points are used for the ventricular bundles (red bullets Figure 4.3). The pathways connecting the control points are built using a piecewise linear interpolation which are then projected over the atrial and ventricular endocardium, whereas the portions of the 1D graph lying within the ventricular septum, such as the AV–node, are immersed in the 3D mesh volume. The 1D graph is then meshed uniformly with linear elements of a given grid size (much finer than the distance between two adjacent bullets). The whole procedure runs in few CPU–minutes, thus providing the correct positioning of a realistic 1D conduction network within the 3D mesh, with multiples bundles branching/joining the same nodes, as shown in Figure 4.3.

4.2.2 Two dimensional fast conduction Purkinje

The Purkinje network in humans and other mammals is distributed in a layer within the subendocardium, which is thin with respect to the myocardium thickness (of the order of 0.5–100 μm [264] compared to an average thickness of

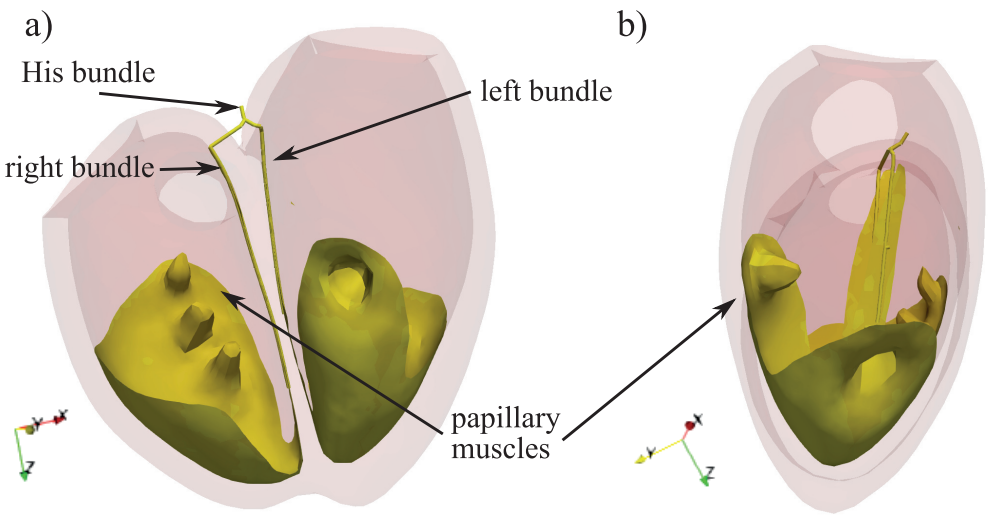

Figure 4.4: Ventricular bundles and Purkinje network, which cover the papillary muscles.

7±1 and 15.4±2.3 mm for the right and left ventricles, respectively [265]) and is made of thicker fibers with a branching distance of the order of 2 mm [266] which bifurcate multiple times until forming a dense plethora of thinner fibers [256, 267]. This dense network of fibers is typically mimicked in computational models through the growth of a fractal structure by defining a set of generating rules and an initial topology (in a similar fashion to the growing models for plant branches) with the smallest branching structure in the order of 100 μm [256, 236, 237]. As an alternative approach to the growth of a fractal 1D network, the dense fiber distribution of the Purkinje network is here merged into a continuum 2D isotropic conductive medium wrapping the endocardium. Such approach is motivated by the uncertainty on the precise arrangement of Purkinje fibers and the great variability among individuals, which make it difficult to develop an accurate fractal rule for the network growth. Furthermore, a high fiber density (more than 2000 branches and 300 PMJs for the major bundles [268] and an even smaller branching distance of 0.1–2 mm for thinner branches [266, 256]) is required to adequately model the Purkinje and correctly activate the myocardium both in healthy [257] and pathological [252] cases. Figure (4.4) shows as the 2D Purkinje network develops from the His bundle and extends parallel to the left and right bundles until reaching the apex of the heart and then raises up upon two third of the ventricles height, completely covering the papillary muscles in order to timely activate their contraction at early systole. The right and left sides of the Purkinje complex do not have a direct electrical connection since they are separated by the thickness of the interventricular septum.

4.2.3 Three dimensional excitable myocardium

The 3D myocardium is made of three excitable and conductive media, namely two for the left and right atria and another for the ventricles (see Figure 4.2d), which has been built using modeling software so as to reproduce high–resolution clinical images and medical atlas. This splitting of the myocardium is inspired by the cardiac electrophysiology as the heart septum between the atria and the ventricles (the fibrous trine plane) acts as an electrical insulator, thus decoupling the atrial and the ventricular electrophysiology. The transmembrane depolarization front, indeed, only propagates from the atria to the ventricles through the AV–node that is part of the 1D network of bundles (see § 4.2.1). Similarly, the atria are electrically insulated by the atrial septum and they can thus be modelled as two disjoint electrical domains. On the other hand, the ventricular myocardium cannot be further subdivided into two independent meshes as, we anticipate, the ventricular endocardium is made by the same muscular fibers wrapped around the ventricles which are thus electrically connected [170].

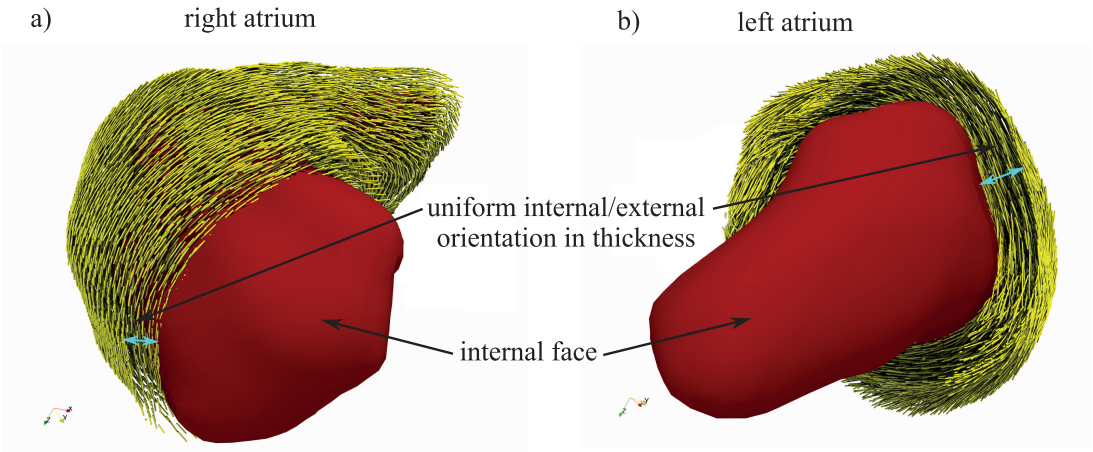

Figure 4.5: Fibers orientation in the a) right and b) left atrium. The red surface indicate the internal endocardium.

Figure 4.5 shows the muscular fibers orientation within the (a) right and (b) left atrial wall, with the fibers wrapping around the main atrial axes as observed in–vivo by diffusion tensor magnetic resonance [233]. Since the atrial fiber orientation is uniform within the myocardium thickness (of about 4 mm), this is first defined on the atrial endocardium (red surfaces in Figure 4.5) and, then replicated, at each cell across the 3D myocardium thickness. Different or patient–specific fiber orientation in healthy and pathological conditions can be included as well in the geometrical description of the 3D media.

The ventricular myocardium is modelled as a single 3D mesh for both the left and right ventricles and includes the papillary muscles, whose location corresponds to the most recurrent one observed in a population study [269, 270]. The main reason for creating a single mesh (instead of two as in the modelling of the atria) is that the external part of the ventricular myocardium wrapping

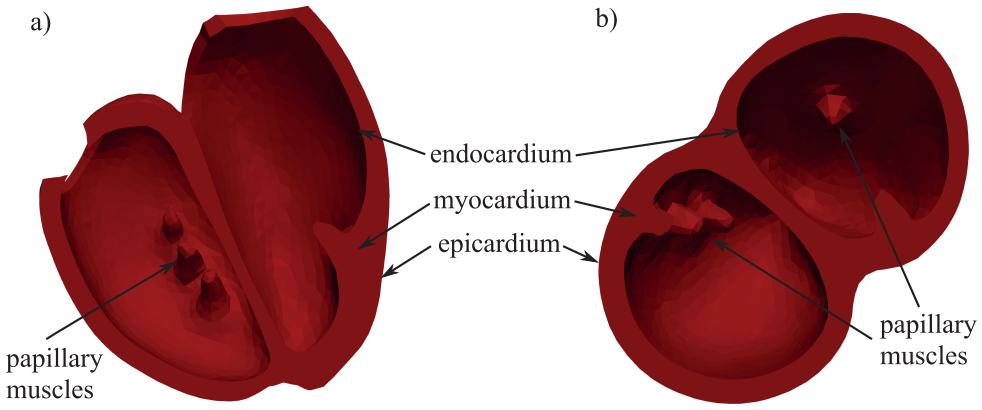

Figure 4.6: a) Front and b) top view of the ventricular myocardium incorporating the papillary muscles.

the whole heart (often described as a *scarf* [243]) is electrically connected and allows for a slow propagation of the depolarization front from one ventricle to the other, which is not observed in healthy cases as the two ventricles are simultaneously activated by the right and left fast conduction branches but it may occur in pathological cases as studied in the next section.

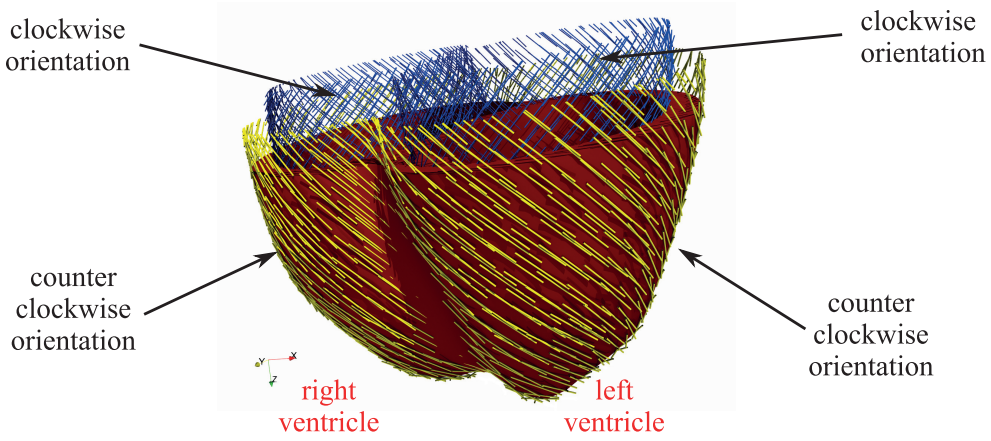

Figure 4.7: Fibers orientation in the ventricular myocardium. The external (yellow) epicardial muscular fibers are oriented in opposite direction compared with the internal endocardial one (blue).

Although the orientation of the muscle fibers shows some variability among individuals, it is known to vary across the myocardium wall from $\alpha_{epi} = 60°$ at the endocardium to $\alpha_{endo} = -60°$ at the epicardium with respect to the ventricles major axis [244, 271, 21]. The vector field, corresponding to the fibers orientation at each cell of the 3D mesh, is thus defined as $\alpha = \alpha_{endo} \cdot d + \alpha_{epi} \cdot (1 - d)$, where d is the cell transmural distance from the endocardium normalized by the myocadium thickness (of about 8 mm on average), yielding the typical counter-

clockwise (clockwise) fiber orientation over the epicardium (endocadium) shown in Figure 4.7.

4.3 Governing equations and numerical method

4.3.1 The bidomain model

The electric wave propagating across the cardiac tissue is governed by the bidomain model that is made by the following system of two reaction–diffusion PDEs, coupled with a set of nonlinear ODEs corresponding to the cell model:

$$\begin{aligned} \chi\left(C_m\frac{\partial v}{\partial t}+I^{ion}(v,\mathbf{s})+I^s\right) &= \nabla\cdot(M^{int}\nabla v)+\nabla\cdot(M^{int}\nabla v^{ext}),\\ 0 &= \nabla\cdot(M^{int}\nabla v+(M^{int}+M^{ext})\nabla v^{ext}),\\ \frac{\mathrm{d}\mathbf{s}}{\mathrm{d}t} &= F(v,\mathbf{s}). \end{aligned} \tag{4.1}$$

Here, v and v^{ext} are the unknown transmembrane and extracellular potential (expressed in mV), whereas the surface–to–volume ratio of cells $\chi = 140$ mm^{-1} and the specific membrane capacitance $C_m = 0.01\mu$F mm^{-2} are set as in [189]. M^{int} and M^{ext} are the conductivity tensors of the intracellular and extracellular media that depend on the local fiber orientation with a faster propagation velocity along the fiber than in the orthogonal directions. In the case of a 3D conductive media as the myocardium these tensors have rank three and are diagonal when expressed in the fiber ($\parallel$), sheet–fiber ($/$) and cross–fiber ($\perp$) directions [170], see Figure 4.7:

$$\hat{M}^{ext}=\begin{bmatrix} m_{\parallel}^{ext} & 0 & 0\\ 0 & m_{/}^{ext} & 0\\ 0 & 0 & m_{\perp}^{ext}\end{bmatrix},\qquad \hat{M}^{int}=\begin{bmatrix} m_{\parallel}^{int} & 0 & 0\\ 0 & m_{/}^{int} & 0\\ 0 & 0 & m_{\perp}^{int}\end{bmatrix}. \tag{4.2}$$

The conductivity tensor in the global coordinate system are thus obtained by the transformations

$$M^{ext}=\mathcal{A}\hat{M}^{ext}\mathcal{A}^T,\qquad M^{int}=\mathcal{A}\hat{M}^{int}\mathcal{A}^T, \tag{4.3}$$

where $\mathcal{A}$ is the rotation matrix containing column–wise the components of fiber, sheet–fiber and cross–fiber normal unit vectors. On the other hand, for 2D electrical media as the Purkinje model, the transmembrane potential depolarization can only propagate in the fiber and sheet–fiber directions corresponding to the principal conductivities $m_{\parallel}^{ext,int}$ and $m_{/}^{ext,int}$. Lastly, in the case of 1D conductive media as the fast conduction network of bundles, the conduction properties are only given by the fiber conductivity $m_{\parallel}^{ext,int}$.

The last of equations (4.1) indicates a set of nonlinear ordinary differential equations (ODEs) governing the cellular-scale dynamics in the bidomain equations. Its complexity depends on the physiological details of the model and the

unknown state vector, $\mathbf{s}$, couples the cell model with the bidomain equations through the ionic current per unit cell membrane area I^{ion}. Since the various components of the cardiac electrophysiology system have different cellular properties yielding different ionic fluxes and, consequently, different action potential profile, we adopt a Courtemanche cell model [229] for the atrial myocytes (and the corresponding internodal pathways), a Stewart model [230] for the Purkinje network and a ten Tusscher–Panfilov model [188] for the ventricular myocytes. These cell models are made by a system of 21, 20 and 19 ODEs, respectively, which are not reported here for the sake of brevity.

The ionic current, I^s gives to a periodic electrical stimulus concentrated in time and space at the SA–node triggering the electrical stimulus to the ventricular myocardium, thus initiating the electrical depolarization throughout the heart:

$$I^s = S_a(\mathcal{H}[t] - \mathcal{H}[t - S_d]), \tag{4.4}$$

where $S_a = 1\ mA/mm^2$ and $S_d = 2.5\ ms$ are the stimulus amplitude and duration, t is the time within a heart beat and $\mathcal{H}[\cdot]$ the Heaviside function. In a previous work, we have verified through an uncertainty quantification analysis that the values of the amplitude and duration of the stimulus do not significantly impact the subsequent depolarization of the fast conducting bundles, as far as they vary in physiological ranges [23].

4.3.2 Numerical method

The set of governing equations (4.1) is solved using an in–house finite volume (FV) library, which provides a suitable approach for solving the electrophysiology equation in complex geometries. As introduced above, the cardiac electrophysiology media is split in a 1D graph for the fast conduction bundles, a 2D shell for the fast conduction Purkinje and 3D media for the atrial and ventricular myocardium, which are respectively segmented with linear, triangular and tetrahedral elements.

Using the divergence theorem, the bidomain equations (4.1) can be rewritten in conservative form on each grid cell, Ω_i,

$$\begin{aligned}
\int_{\Omega_i} \chi \left(C_m \frac{\partial v}{\partial t} + I^{ion} + I^s \right) \mathrm{d}\Omega &= \int_{\partial\Omega_i} (M^{int} \nabla v) \cdot \mathbf{n} \mathrm{d}\gamma + \int_{\partial\Omega_i} (M^{int} \nabla v^{ext}) \cdot \mathbf{n} \mathrm{d}\gamma, \\
0 &= \int_{\partial\Omega_i} [M^{int} \nabla v] \cdot \mathbf{n} \mathrm{d}\gamma + \int_{\partial\Omega_i} [(M^{int} + M^{ext}) \nabla v^{ext})] \cdot \mathbf{n} \mathrm{d}\gamma,
\end{aligned} \tag{4.5}$$

where $\mathbf{n}$ is the normal unit vector of the cell boundary, $\partial\Omega_i$.

In the case of the 3D myocardium, the domain is discretized through a tetra-

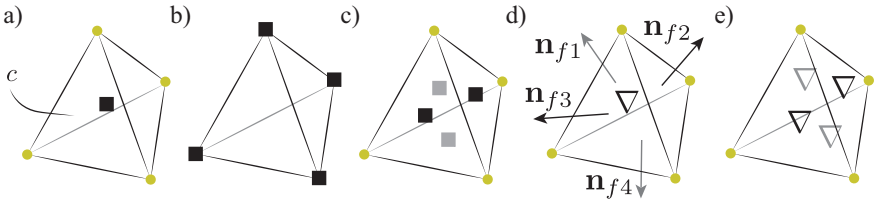

Figure 4.8: Graphical scheme of the procedure to evaluate the gradient at the cell faces of a 3D media. a) The cell—based v_c is interpolated to obtain b) the node–based v_n, which is then used to estimate the same quantity at c) the midpoint of the tetrahedrons faces, v_f. The latter is used to determine d) ∇v_c on the cell center using the Gauss–Green theorem and is successively interpolated to evaluate the e) gradient at the mesh faces ∇v_f.

hedral mesh and equation (4.5) for a cell based FV method reads

$$\begin{aligned} &\chi\left(C_m\frac{\partial v_c}{\partial t}+I_c^{ion}+I_c^s\right)V_c=\sum_{j=1}^{4}A_{fj}[M_{fj}^{int}(\nabla v_{fj}+\nabla v_{fj}^{ext})]\cdot\mathbf{n}_{fj},\\ &\sum_{j=1}^{4}A_{fj}[M_{fj}^{int}\nabla v_{fj}]\cdot\mathbf{n}_{fj}+\sum_{j=1}^{4}A_{fj}[(M_{fj}^{int}+M_{fj}^{ext})\nabla v_{fj}^{ext}]\cdot\mathbf{n}_{fj}=0, \end{aligned} \tag{4.6}$$

where the subscript c indicates that the quantities are evaluated at the cell center whereas the subscript fj denotes the $j-th$ face of the cell c. In the case the external and the internal conductivity tensors are parallel $M^{ext}=\lambda M^{int}$ the bidomain model (4.6) reduces to the monodomain equation (4.6):

$$\chi\left(C_m\frac{\partial v_c}{\partial t}+I_{ion,c}+I_{s,c}\right)V_c=\sum_{j=1}^{4}A_{fj}[M_{fj}\nabla v_{fj}]\cdot\mathbf{n}_{fj}, \tag{4.7}$$

where $M=\lambda M^{int}/(1+\lambda)$.

The fluxes over the tetrahedron cell faces are evaluated as indicated in reference [2] and summarized in Figure 4.8. Firstly, the transmembrane potential at the vertex nodes v_n (see panel 4.8 b) is computed by using the weighted average of the potential within the cells surrounding that node, v_k, yielding $v_n=\sum_{k=1}^{Nc_n}v_k d_k^{-1}/\sum_{k=1}^{Nc_n}d_k^{-1}$, where N_{c_n} is the number of cells sharing the node and d_k is the distance between the node and the k–th cell center. Once the values v_n are found, the values of the transmembrane potential at the faces centroids v_f (see panel 4.8 c) are calculated by averaging the three nodal values at the triangle vertices. According the Gauss–Green formula (panel 4.8 d), the gradient of the transmembrane potential ∇v_c is related to the flux of the same quantity through the cell faces and, using a second order accurate mid-point integration rule to evaluate these fluxes, we get $\nabla v_c=\frac{1}{V_c}\sum_{j=1}^{4}v_{fj}S_{fj}\mathbf{n}_{fj}$, where V_c is the volume of the cell and v_{fj}, S_{fj}, $\mathbf{n}_{fj}$, are the transmembrane potential, area and the normal vector at j–th face. The gradient at the mesh faces is then obtained as the weighted average of the cell gradients defined at the cells c_1 and c_2 sharing the

face f, $\overline{\nabla v}_f = \alpha_{c_1} \nabla v_{c_1} + \alpha_{c_2} \nabla v_{c_2}$, where α_{c_1} and α_{c_2} are the linear interpolation weights defined on the position of the face f with respect to the centers of the two cells ($\alpha_{c_1} + \alpha_{c_2} = 1$). The resulting face gradient $\overline{\nabla v}_f$ is computed not only using the two transmembrane potential values defined at the two cells sharing the face, but also using the cell values of all the cells sharing the nodes of the two cells c_1 and c_2, thus enlarging the stencil of the formula. The 3D face gradient $\overline{\nabla v}_f$, can be modified in such a way to include the low–stencil directional derivative

$$\nabla v_f = \overline{\nabla v}_f + \left[\frac{v_{c_1} - v_{c_2}}{d_{c_1 c_2}} - (\overline{\nabla v}_f \cdot \mathbf{e}_{c_1 c_2}) \right] \mathbf{e}_{c_1 c_2}, \tag{4.8}$$

where $\mathbf{e}_{c1c2}$ is the unity vector in the direction joining the centroid of the two cells c_1 and c_2 straddling the face. Such treatment of the cross diffusion term of the face gradient (which is often used to improve the stability of the method in the case of implicit schemes through a deferred correction [2]) reduces to the second–order difference quotient between c_1 and c_2 when $\mathbf{e}_{c1c2}$ is parallel to the face normal vector, $\mathbf{n}_f$; as is the case for orthogonal or locally orthogonal grids. The face gradient (4.8) (corresponding to the last panel in Figure 4.8) can be then directly used to compute the fluxes in the conservative equation (4.1) and obtain the spatially discretized bidomain equations in the 3D myocardium. A similar FV approach is used to discretize the bidomain/monodomain equations over 1D and 2D media (in order to model the bundles and Purkinje network, respectively) with the only exception that a vertex–based FV is used in the 1D case so to better handling multiple bundles branching from the same grid node, as happening at the internodal pathway and at the Bachmann's bundle (see Figure 4.3).

This FV approach thus provides an effective spatial discretization of the bidomain equations over complex geometries and is second–order accurate in space provided the grid is sufficiently regular (see the convergence analysis in section 4.4). Importantly, as typical in FV methods the mass matrix is diagonal, thus meaning that in the case of an explicit time scheme, the discretized unsteady bidomain equation for v (as well as the monodomain one) can be marched in time simply correcting the transmembrane potential at the previous timestep by summing an incremental vector. Although an explicit temporal scheme needs a timestep small enough to prevent numerical instabilities, still the overall computational cost is smaller than that of an implicit scheme which requires the solution of a nonlinear system at each mesh element and any timestep owing to the nonlinearity of the cell model. However, the cell models are extremely stiff, due to the significant variables variations over short timescales of the spike–and–dome of the action potential and of the so–called gating variables (describing the opening and closing dynamics of ion channels) and require prohibitively small timesteps to assure numerical stability. This difficulty can be circumvented by noting that the ODEs governing the gating variables are quasi-linear and can be solved analytically within a timestep if the transmembrane potential v is held constant, whereas an explicit method is used to integrate the remaining nonlinear ones. This semi–analytical approach is known as the Rush–Larsen scheme

[272, 273] and it has been successfully applied to the three cell models adopted here: the Courtemanche model with 15 gating variables out of 21 state variables, the Stewart model with 13 gating variables out of 20 state variables and the ten Tusscher–Panfilov models with 13 gating variables out of 19 state variables. The enhanced stability properties of the method thus allow for an integration timestep more than one order of magnitude larger than the one used with a standard explicit time scheme.

On the other hand, owing to the first order accuracy of the Rush–Larsen solution, the non–gating variables of the cell model (typically describing the variations of intracellular ions concentrations) and the spatially discretized bidomain equations (4.6) are integrated in time using a forward Euler method [273] and at each timestep the updated transmembrane potential $v(t^{n+1})$ is thus obtained as an explicit function of v, v^{ext}, I^{ion} and I^s previously computed at time t^n and, similarly, the updated state vector of the cell model $\mathbf{s}^{n+1}$ is computed using $\mathbf{s}^n$. As the numerical converge analysis (see section 4.4) reveals that the error of the numerical solution is more sensitive to the spatial rather than to the temporal refinement, the Rush–Larsen method with its remarkable stability properties is thus a convenient temporal scheme for the bidomain/monodomain model, although first order accurate. Furthermore, in the perspective of multiphysics heart simulations including the coupled structural and blood dynamics, the timestep will be limited to few μs by the fluid–structure–interaction [177] and a first order temporal scheme for the electrophysiology system entails a numerical precision of the solution with such a small timestep. In the case of bidomain model, once $v(t^{n+1})$ is solved, the external potential $v^{ext}(t^{n+1})$, is obtained by solving the linear system given by the second equation of the system (4.6) through an iterative GMRES method with restart [274] using the external potential computed at previous time, $v^{ext}(t^n)$, as first estimate for the unknown field $v^{ext}(t^{n+1})$.

The FV library has been GPU accelerated using CUDA Fortran [275] which extends Fortran by allowing the programmer to define Fortran functions, called kernels, which when called are executed N times in parallel by N different CUDA threads, as opposed to the serial nature of the regular Fortran functions, thus greatly improving the performance. Furthermore, CUDA provides CUF kernel directories which automatically run single and nested loops on the GPU device without neither modifying the original CPU code nor writing a dedicated GPU subroutine. Specifically, the electrophysiology solver results in a sequence of loops on the mesh cells and on the mesh faces, which are GPU accelerated simply wrapping the original CPU code in the CUF kernel directive.

4.3.3 Subsystems coupling

The topological splitting of the cardiac electrophysiology network requires a coupling mechanisms to connect electrically the various subdomains. In particular, three two–way couplings are needed: (i) a first one between the 1D bundles and the 2D Purkinje networks, (ii) another between the 1D network of bundles and the 3D atrial myocardium and (iii) a last one between the 2D Purkinje and

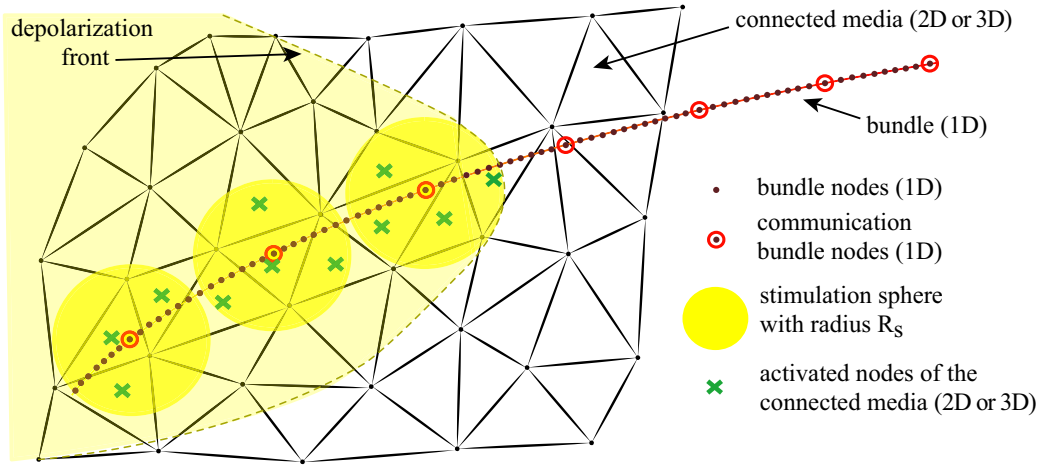

Figure 4.9: Sketch of electrical coupling between the 1D fast conduction bundles and the surrounding 2D (or 3D) mesh. The wave front of the electric potential propagates across 1D mesh causing the threshold values of the communication nodes to be exceeded, thus activating the 2D (or 3D) cells within a radius R_s.

the 3D ventricular myocardium.

As sketched in Figure 4.9, the communication between the 1D mesh and the underlying 2D (or 3D) counterpart occurs through some communication nodes (CNs, indicated by red circles) which are defined in the preprocessing phase as a subset of the bundle grid nodes (black dots). In particular, as the transmembrane potential at a CN exceeds a certain threshold (here set to 0 mV), an external localized stimulus I^s (with $S_a = 1\ mA/mm^2$ and $S_d = 0.5\ ms$, see equation (4.4)) is applied to the underlying 2D (or 3D) mesh cells within a distance R_S from the CN, thus initiating a depolarization front in the 2D (or 3D) media. Specifically, since the 1D domain represents the network of internodal pathways that are some millimeters thick in the atrial myocardium [232], the communication range for the coupling between the 1D and the 3D atrial mesh is taken equal to $R_S = 1$ mm, whereas any CNs between the 1D and the 3D ventricular mesh are not present since the bundles do not directly excite the ventricular myocardium (they are isolated by fibrous sheaths) but they only transfer the propagation front to the Purkinje network [276]. Hence, the depolarization of the Purkinje mesh is initiated by the CNs between the 1D and the 2D domains having a smaller communication range of $R_S = 0.1$ mm, scaling as the local Purkinje thickness. Although all bundle nodes (black dots in Figure 4.9) can be taken as CNs, only a subset of them is used in order to reduce the computational cost of the coupling since at any timestep the local transmembrane potential at the CNs should be monitored for eventually applying a localized electrical stimulus. In this work, the CNs are equally distributed over the 1D network with a relative distance among them of $\varsigma \cdot \tau \approx 1$ mm, where $\varsigma = 2$ m/s is the typical internodal pathways propagation speed and $\tau = 0.5$ ms is the maximum time delay in the activation between two consecutive CNs, which is found to trigger correctly the depolariza-

tion of the Purkinje network as later shown in section 4.5.1. On the other hand, a shorter τ would correspond to a denser distribution of the CNs and vice–versa.

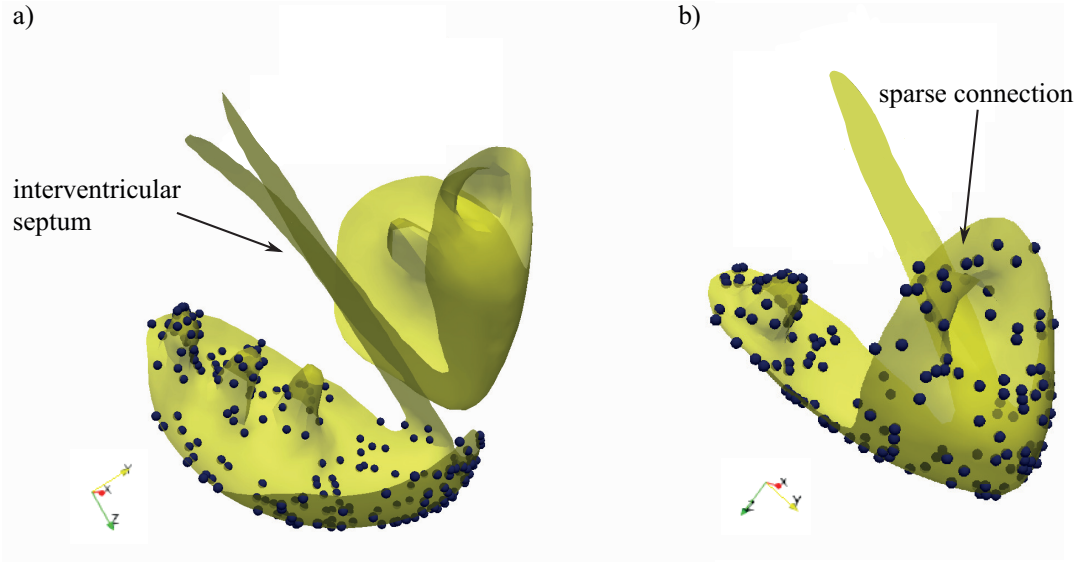

Figure 4.10: Distribution of the communication nodes (CNs) between the 2D Purkinje and the 3D ventricular myocardium, corresponding to the Purkinje muscle junctions (PMJs).

Figure 4.10 show the distribution of the CNs between the 2D and the 3D ventricular media ($R_S = 0.1$ mm), which allow the Purkinje network to activate the ventricular myocardium with an orthodromic delay of 5 milliseconds [238]. The density and the positions of these CNs is user–defined and it has been set so to reproduce the ones of the Purkinje muscle junctions (PMJ) [268, 277]. In this work 300 CNs equally distributed among the left and right ventricles [278] have been considered with their distribution corresponding to the one of the PMJ with no CNs present in the interventricular septum as the Purkinje network is insulated by fibrous sheaths in that region [279, 276] (Figure 4.10 a).

In the case of healthy cardiac electrophysiology, the electrical coupling through the CNs is *one–way*, meaning that only the lower topological domain triggers an electrical stimulus on the higher one, e.g. the 1D bundle excites the 3D myocardium but not vice–versa. On the other hand, in some pathological cases such as nodal re-entry tachycardia [280] or antidromic propagation (re–enter of the signal in the Purkinje network from the myocardium) [238], the coupling is *two–way* and the 3D myocardium can eventually excite back the 1D bundles and the 2D Purkinje, as shown in § 4.5.

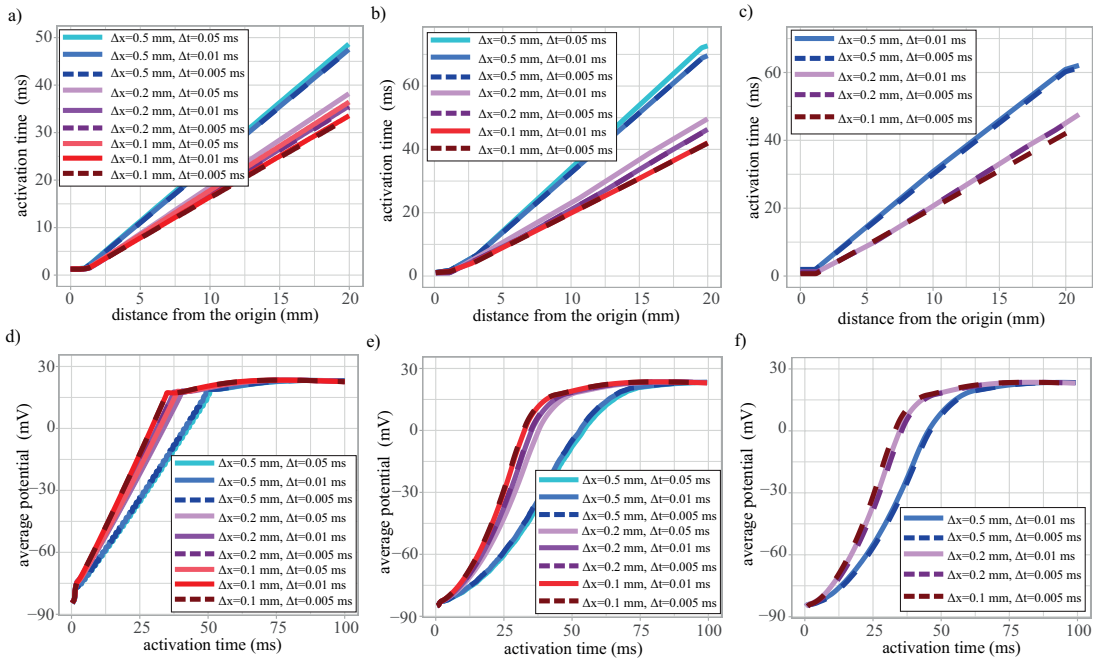

Figure 4.11: Activation time along the main diagonal in the a) 1D, b) 2D and c) 3D domain according to the monodomain model for various temporal and spatial resolutions (Δx is the grid spacing the x direction in 1D, x, y in 2D and x, y, z in 3D). The corresponding average transmembrane potential is reported in d), e) and f), respectively.

4.4 Numerical convergence and validations

The convergence of the numerical method is investigated using a procedure similar to the one reported in the benchmark paper [189] by solving the monodomain and the bidomain equations over a 3D Cartesian domain of size $20\times7\times3$ mm^3 coupled with the ten Tusscher–Panfilov cell model [188]. In order to validate the 2D and 1D solvers, a similar test–case is also run on a rectangular 2D domain (20×7 mm^2) and on a straight linear domain (of length 20 mm). In all cases, the Cartesian domain is discretized by a structured grid with a minimum grid size of 0.5, 0.2 and 0.1 mm in each direction (x in the 1D, x, y in the 2D and x, y, z in the 3D), and three different timesteps have been used, namely 0.05, 0.01 and 0.005 ms. The muscle fibers are taken aligned with the long axis direction (20 mm in 2D and 3D) and the electrophysiology parameters, including the initial state variables of the cell model, are set as in [189]. The initial stimulus is applied within a line/square/cube of side 1.5 mm placed in the corner closer to the origin.

In the case of the monodomain solver, Figure 4.11 reports the activation time (defined as the instant when the transmembrane potential exceeds 0 mV) along the diagonal of the domain departing from the corner where the stimulus is applied for the (a) 1D (b) 2D and (c) 3D domains. The corresponding trans-

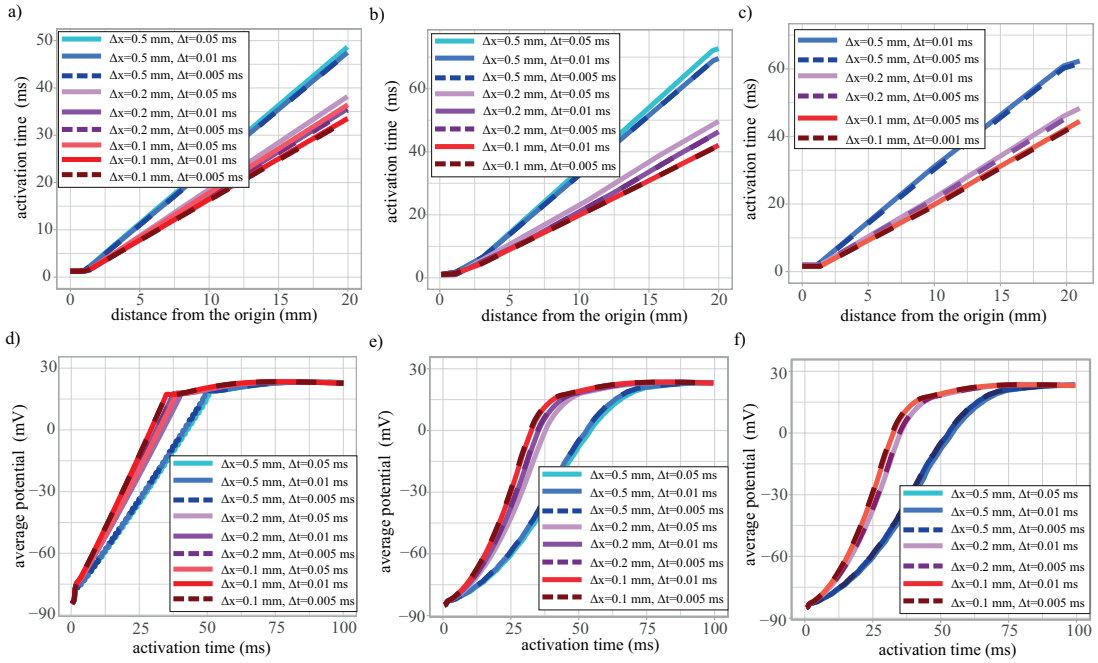

Figure 4.12: Same as Figure 4.11 but solving the bidomain electrophysiology model.

membrane potential averaged in the domain volume V, $\overline{v}(t) = \int_V v(\mathbf{x}, t) dV/V$ are reported as a function of time in Figure 4.11(d,e,f), showing that, as the spatial grid is refined, the propagation speed of the depolarization front increases until convergence is attained for the more refined grid spacing with a timestep equal–smaller than $\Delta t = 0.01$ ms. The corresponding convergence curve for the bidomain model are given in Figure 4.12 for each topological dimension of the conductive media, thus showing similar results for the same grid spacing and timestep.

In the 3D case, the numerical solution of the monodomain and bidomain equations can be validated against previous results from the literature. The former is validated against the benchmark paper of Niederer et al. 2011 [189] where 11 different numerical codes (either based on finite elements or finite differences) have been used and the resulting average activation time along the diagonal of the cubic domain (blue solid line) and standard deviation (blue shaded region) are reported in Figure 4.13 (a). Moreover, the solution of the bidomain equations is validated against the results of Cuccuru et al. [282], which is reported in Figure 4.13 (b) for different spatial steps and different polynomial degrees, see [282] for further details on their numerical method. Both the monodomain and the bidomain results obtained with our numerical solver fit well those reported in the literature.

The corresponding convergence curves are reported in Figure 4.14 in the case of the 1D, 2D and 3D monodomain model. Figure 4.14(a) indicates the second order spatial accuracy of the FV method by showing the error on the average

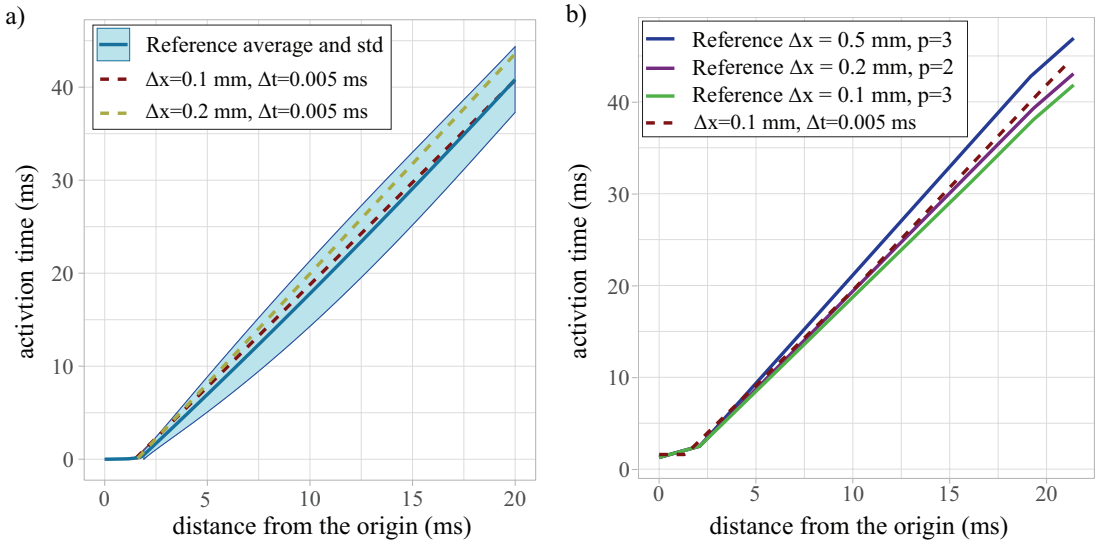

Figure 4.13: Average transmembrane potential in the 3D domain according to a) the monodomain and b) the bidomain electrophysiology model. a) Our numerical results (yellow dashed line for $\Delta x = 0.2$ mm and red dashed one for $\Delta x = 0.1$ mm) are compared against the average results (blue solid line) of the benchmark paper [281], where the shaded area indicates the corresponding standard deviation. In panel b) our code is validated against the results reported [282].

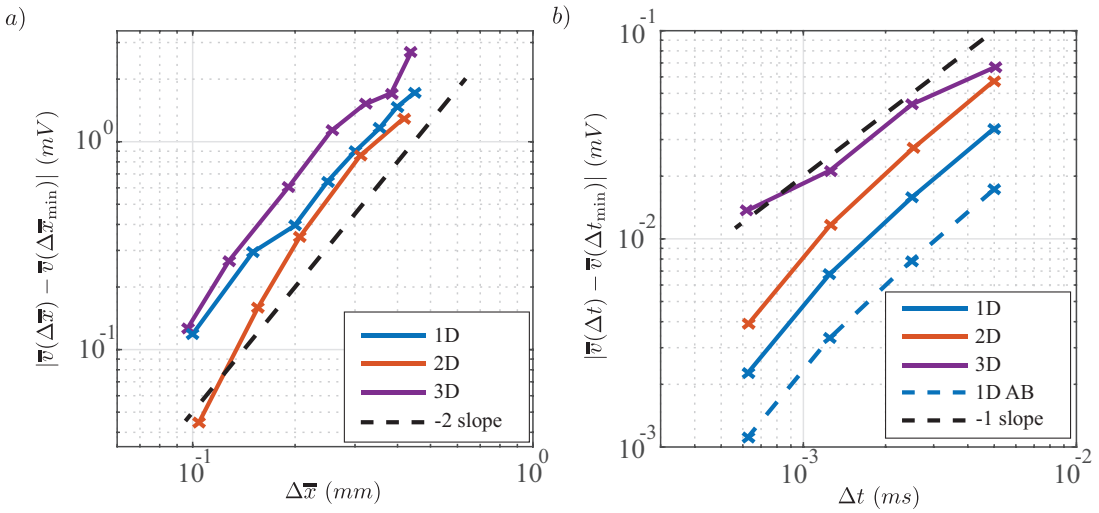

Figure 4.14: (a) Spatial and (b) temporal convergence curves of the 1D, 2D, and 3D monodomain solver. In (a) the error on the average transmembrane potential (computed at time $t = 50$ ms for $\Delta t = 0.005$ ms) is shown as a function of the mean grid size, $\overline{\Delta x}$. In (b) the same quantity (at time $t = 50$ ms for $\overline{\Delta x} = 0.31$ mm) is reported as a function of the timestep, Δt.

transmembrane potential over the domain at time $t = 50$ ms (and timestep set to $\Delta t = 0.005$ ms) as a function of the average grid size, $\overline{\Delta x}$. On the other hand, Figure 4.14(b) reports the same quantity (evaluated with $\overline{\Delta x} = 0.31$ mm) as a function of the timestep Δt, thus retrieving the first order temporal accuracy of the Rush–Larsen temporal integration scheme, where the non–gating variables are solved using forward Euler. The numerical error could be reduced by adopting a second–order Adams–Bashforth scheme for the non–gating variables (dashed blue line for the 1D case), although a modified second order Rush–Larsen scheme [283] would be needed to attain a second order accuracy.

Grid Δx, cells	**CPU** bidomain	**GPU** bidomain	**speedup** bidomain	**CPU** monod.	**GPU** monod.	**speedup** monod.
0.5 mm, 20'160	0.027 s	0.0015 s	18	0.018 s	0.0002 s	90
0.2 mm, 315'000	0.45 s	0.017 s	27	0.20 s	0.0013 s	154
0.1 mm, 2'520'000	3.7 s	0.09 s	41	1.6 s	0.009 s	177

Table 4.1: Wall–clock time for integrating a single bidomain and monodomain time step for the three Cartesian grids considered in Figures 4.11–4.13. The CPU time is obtained using a single core Intel(R) Xeon(R) Gold 6230 with 2.10GHz, whereas the GPU time corresponds to a Tesla V100 from Nvidia.

Table 4.1 reports the wall–clock time for solving a single bidomain and monodomain timestep on the benchmark Cartesian domain using a single CPU core or GPU device. Running the GPU version of the code yields a significant speedup in all cases, which increases as the grid gets more refined owing to the better balance of workload across the GPU threads running in parallel. It can be observed, that the speedup is larger in the case of monodomain computations with respect to the bidomain counterpart because the Arnoldi iteration and the solution of the corresponding Hessenberg system in the GMRES algorithm are based on the Lapack library running on the CPU.

The convergence of the numerical solution over the cardiac domains used in sections 4.2 and 4.5 for the electrical conductivities reported in Table 4.2 is assessed by monitoring the average transmembrane potential as a function of time, $\overline{v}(t)$. Figure 4.15(a) shows $\overline{v}(t)$ solved over the 1D network of fast conduction bundles using the monodomain model coupled with the Courtemanche cell model with a timestep equal to $\Delta t = 0.001$ ms, thus showing good convergence for a spatial discretization finer than $\Delta x = 0.25$ mm (corresponding to a number of cells equal to $2'000$). On the other hand, the monodomain equations over the right Purkinje 2D media coupled with the Stewart cell model are at convergence for the number of triangles of about 54'000 (i.e. $\Delta x = 0.45$ mm). The bidomain solution over the 3D left atrium becomes grid independent for a number of cells around 5'500'000 ($\Delta x = 0.31$ mm), but a coarser grid with 1'500'000 cells (corresponding to $\Delta x = 0.53$ mm) yields a slower propagation of the depolarization front corresponding to a time delay of the electrical activation of the chamber be-

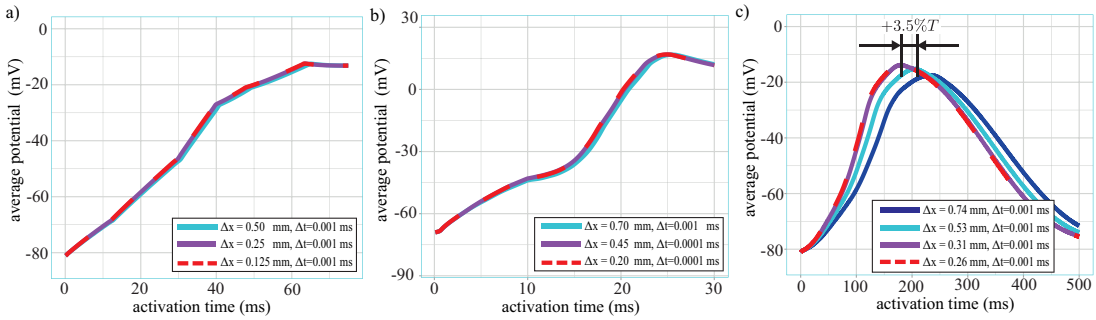

Figure 4.15: Average transmembrane potential for different temporal and spatial resolutions over the a) the internodal pathways, b) the right Purkinje network and c) the left atrium. In the 3D case, a spatial resolution of $\Delta x = 0.53$ mm corresponds to a delay in the chamber activation below $3.5\%T$, where T is the heart beating period which is equal to 750 ms for a heart rate of 80 b.p.m..

low 3.5% the heart beating period (equal to 750 ms for a heart rate of 80 b.p.m.). Based on these results, a 1D grid made of 2'500 linear elements and a 2D grid of 108'000 triangles have been used to discretize the fast conduction and the Purkinje networks with a timestep of 0.0001 ms. Hence, the electrophysiology of the 3D myocardium is integrated with a timestep of $\Delta t = 0.005$ ms using using 1'500'000, 2'500'000 and 5'500'000 tetrahedra for the left atrium, right atrium and ventricles, respectively. The electrophysiology of each 3D chamber is integrated using a dedicated GPU card Tesla V100 from Nvidia and the wall–clock time to run a single heart beat is thus given by that of solving the ventricular electrophysiology, which is equal to 7.9 hours (corresponding to a speedup of 60 times with respect to the serial CPU version of the code). Remarkably, since the computational cost is dominated by the 3D solution of the bidomain equations, it can be greatly reduced by using a monodomain approach as it avoids solving a large linear system for v^{ext}, thus obtaining a wall–clock time of 1.4 hours per heart beat.

4.5 Results: electrophysiology of the whole heart

The electrophysiology of the whole heart is solved using the cardiac configuration introduced in § 4.2 (Figure 4.2), which is composed of a 1D network of bundles, a 2D surface to mimic the Purkinje placed at the ventricular endocardium and 3D media for atrial and ventricular myocardium. In order to better account for their heterogeneous electrophysiology properties three different cell models are adopted (Figure 4.16). In particular, the Courtemanche model [229] is used for the atrial bundles and myocardium, which has a resting potential of -80 mV and is characterized by rapid repolarization occurring in about 200 ms. On the other hand, the high peak of depolarization followed by a stable plateau

phase of about 250 ms observed in the Purkinje cells is modelled through the Stewart cell model [230], whereas the ionic fluxes across the ventricular myocytes are governed by the ten Tusscher–Panfilov cell model [188] exhibiting a resting potential of about −85 mV and a longer depolarization plateau of about 300 ms which is related to a longer muscular contraction of the fibers. Furthermore,

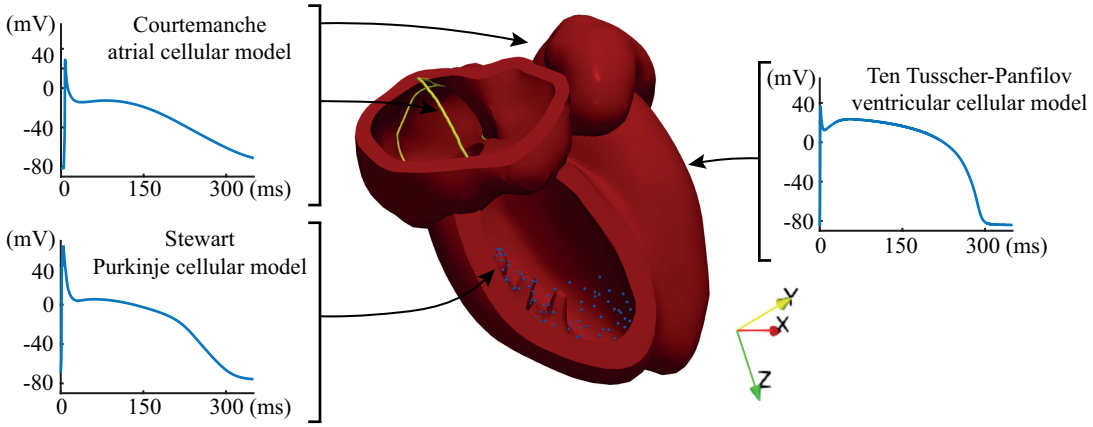

Figure 4.16: Action potential at different cardiac locations. a) The Courtemanche cell model [229] is used in the 1D atrial bundles and in the 3D atrial myocardium, b) the Stewart model [230] is adopted for the Purkinje network and c) the ten Tusscher-Panfilov model [188] governs the action potential in the 3D ventricular myocardium.

the depolarization front propagates at different velocity through these media according to different electrical conductivities, which have been set in the electrophysiology model as summarized in Table 4.2. Since the monodomain and bidomain models are equivalent in the case of a 1D domain, only a single electrical conductivity has been set so to reproduce the propagation velocity reported in the literature [16]. Owing to the high density of the Purkinje fibers and their heterogeneous intracellular and extracellular orientation, the Purkinje network is modelled as a uniform media governed by the monodomain equation with an isotropic conductivity tensor with its components set to reproduce a propagation velocity of 4 m/s [23, 24, 22]. The intracelluar and extracellular electrical heterogeneity in the 3D ventricular myocardium is accounted by setting an anisotropic conductivity tensor in the bidomain equations as reported in the literature [189] (Table 4.2). Owing to the lack of data on the atrial myocardium conductivity, the same conductivity tensors as in the ventricles have been used but rescaled by a factor to match the propagation velocity measured experimentally.

4.5.1 Healthy electrophysiology

We can now analyze the whole cardiac electrical activation in a healthy heart. Figure 4.17 shows the depolarization of the fast conduction atrial bundles (panels a,b,c) and of the 3D atrial myocardium (panels d,e,f) at three different time

heart component	cell/PDE model	conductivity (mS/mm)	reference
1D internodal bundles	Courtemanche, isotropic monodomain	$m_{\parallel} = 1.29$	corresponding to a velocity 1.54 m/s [22, 24, 23]
2D Purkinje network	Stewart, isotropic monodomain	$m_{\parallel} = m_{/} = 3.95$	corresponding to a velocity 4.0 m/s [16]
3D ventricles	ten Tusscher–Panfilov, bidomain	$m_{\parallel}^{ext} = 0.62$ $m_{\perp}^{ext} = m_{/}^{ext} = 0.24$ $m_{\parallel}^{int} = 0.17$ $m_{\perp}^{int} = m_{/}^{int} = 0.019$	data from [189]
3D atria	Courtemanche, bidomain	same as ventricles but rescaled by a factor 1.05	corresponding to a longitudinal velocity 0.5 m/s [16, 22]

Table 4.2: Monodomain and bidomain electrical conductivities of the various cardiac components, as defined in section 4.3.2.

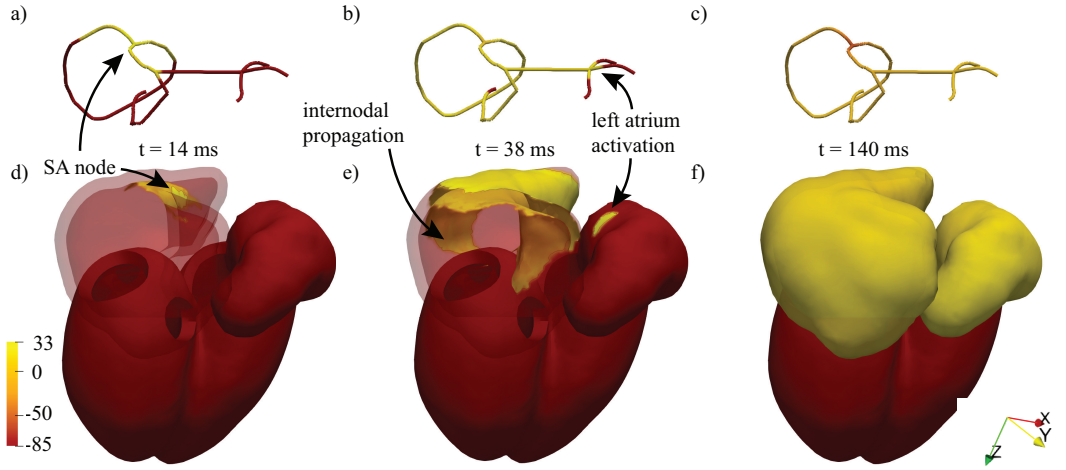

Figure 4.17: Atrial depolarization. Transmembrane potential in the fast conduction atrial bundles at a) $t = 14$ ms b) $t = 38$ ms and c) $t = 140$ ms, whereas the corresponding depolarization of the 3D myocardium is shown in d), e) and f), respectively. In (a,d) the depolarization front has just been initiated in the SA–node, in (b,e) most of 3D right atrium is depolarized and the depolarization front just reached the left atrium through the 1D bundles. In c) both atria are depolarized and the right one starts the repolarize.

instants, with t defined as the time lag with respect to the SA–node activation (corresponding to $t = 0$). In both 1D and 3D media, the transmembrane potential, v, has an initial resting value of -80 mV (red isolevel) and transiently reaches a positive value (yellow isolevel) as the depolarization front advances. The latter

originates at the SA–node, where the effect of the pace–maker cells translates into an initial electrical stimulus (4.4) activating the SA–node (Figure 4.17 a), which then advances simultaneously into the three internodal pathways, namely the Thorel's posterior internodal tract, the Wenckebach's bundle-middle internodal tract and the anterior internodal tract that further bifurcates in the Bachmann's bundle towards the left atrium (Figure 4.17 b). The propagation fronts in these three internodal pathways then recollect at the bottom of the atrial network into the AV–node (see Figure 4.17 b) after about 25-40 ms from the SA–node activation, first throughout the anterior and middle bundle and later throughout the posterior one. In the meantime the depolarization front propagates in the 1D network of bundles, it activates the surrounding atrial myocardium through the CNs, thus triggering another depolarization front in the 3D media, as shown by the incipient myocardial activation near by the SA–node in Figure 4.17(d). Although the conduction speed in the 3D myocardium is anisotropic and the transmembrane depolarization advances faster in the directions aligned with the muscular fibers (owing to a larger electrical conductivity), the myocardium depolarization is about three times slower than the one in the bundles. This leads to a complete activation of both 3D atrial chambers after about 140 ms, as visible in Figure 4.17 (f). Interestingly, the endocardial and epicardial depolarization fronts in Figure 4.17 (e), reveal that the epicardium depolarizes with few milliseconds delay with respect to the endocadium, which corresponds to the time lag needed by the 3D depolarization front (originated at the bundles placed within the endocardium) to propagate across the atrial wall in the cross–fiber directions.

In non–pathological profiles, as is the case here, the signal carried into the AV–node by the internodal pathways propagates from the left atrium to the ventricles only through the AV–node itself. In the AV–node, the propagation speed of the depolarization front greatly reduces, yielding a delay of about 100 ms between the atrial and the subsequent ventricular depolarization (Figure 4.18 a). After the depolarization front swept the AV–node, it reaches the bundle of His before propagating in the two ventricular chambers through left bundle and right bundles (Figure 4.18 a), which, in turn, are electrically connected to the Purkinje network. The latter carry the depolarization front in both ventricular chambers with a propagation speed of about 4 m/s (roughly ten times the surrounding myocardial tissue), first activating the lower part of the ventricle (Figure 4.18 d,e) and then the upper part (Figure 4.18 e,f). As visible in the same panels, the activation of the 2D Purkinje network precedes the surrounding 3D ventricular activation, thus yielding a more synchronous depolarization of the 3D media. As visible in the upper panels of Figure 4.18, the 3D myocardium is electrically activated by the 2D Purkinje network through the PMJs with an orthodromic delay of 5 ms. Importantly, when the ventricles are almost completely depolarized, the atria are repolarizing (Figure 4.18 e) and, successively, when the ventricles are completely activated, the atria are fully repolarized (Figure 4.18 f).

Figure 4.19 compares the electrical activation at various cardiac locations reported in medical atlas [16] with respect to those obtained by our computational

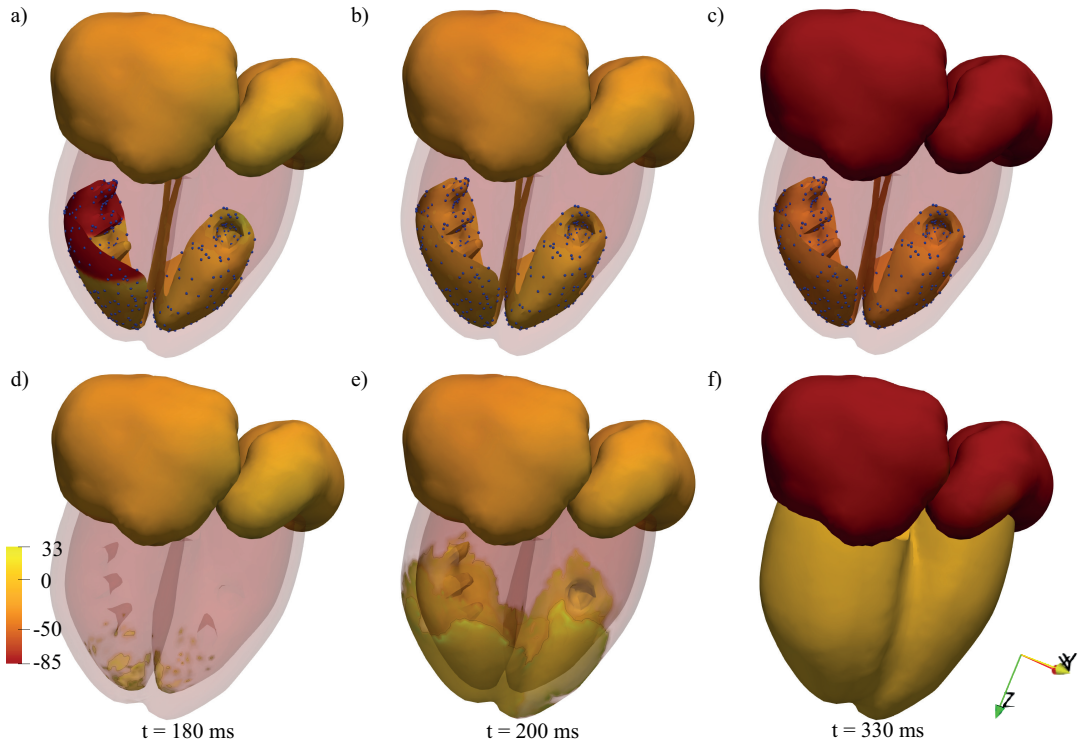

Figure 4.18: Ventricular depolarization. Transmembrane potential at a) $t = 180$ ms b) $t = 200$ ms and c) $t = 330$ ms showing the action potential propagation front in the Purkinje and the locations of the PMJs coupling the Purkinje with the ventricular myocardium. The same data are reported in panels d) e) and f) but using a different transparency so to better visualize the 3D ventricular depolarization. In panels (a,b) both atria have been activated, whereas in panel (c) they are completely depolarized.

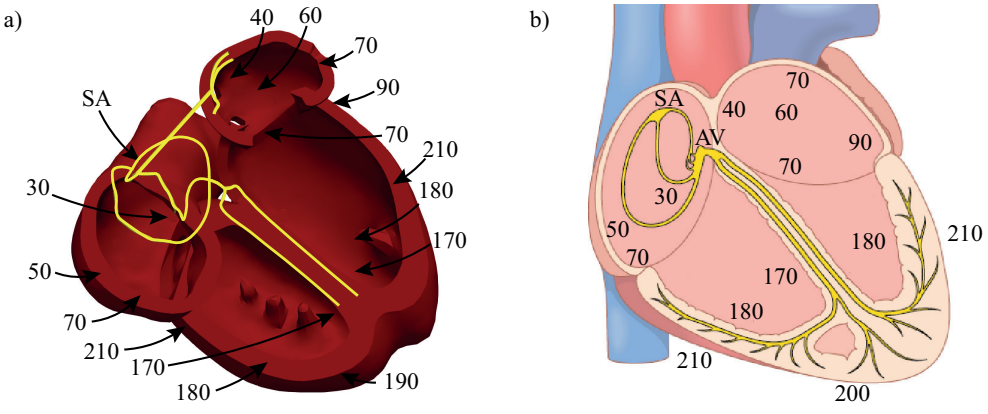

Figure 4.19: Time lag (in ms) of the cardiac depolarization at various heart locations with respect the SA–node stimulus according to a) our numerical model and b) medical atlas [16].

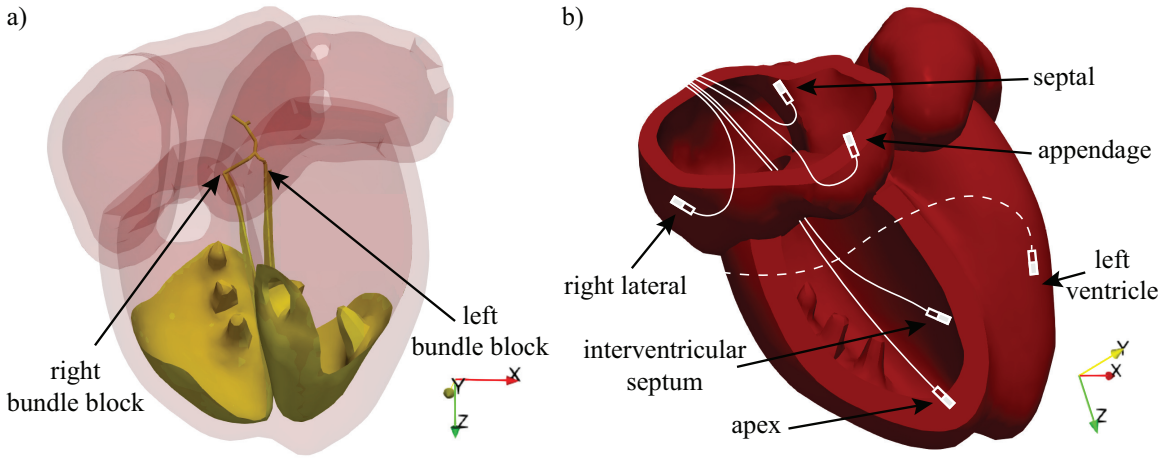

Figure 4.20: a) Positions of the right and left ventricular bundle blocks. b) Most common leads potitioning for atrial and ventricular pacemaking [284].

model, where each number corresponds to the time interval in milliseconds that lapse between the activation of SA–node and that of the location indicated by the number: an overall good agreement can be observed. In particular, the fast atrial 1D conduction system (internodal pathways) correctly ensures the activation of the atrioventricular node after 30 milliseconds from the activation of the SA–node, with a perfect match with what observed in–vivo reality. Furthermore, the slower conduction velocity in the AV–node and the subsequent rapid spreading of the depolarization front in the 2D Purkinje network provide the correct activation of the entire ventricular endocardium, including the papillary muscles.

4.5.2 pathological and aided electrophysiology: bundle branch block and artificial pacing

The present high–fidelity computational framework for the whole heart electrophysiology allows also to model cardiac pathologies and predict the effect of medical devices, such as the artificial pacing applied to a patient affected by a bundle branch block. The latter consists of the delay or blockage of the electrical propagation within a ventricular bundle (see Figure 4.20a), thus implying a delayed activation of some areas of the ventricular myocardium and a consequent anomaly in the activation/contraction profile of the ventricle [285, 286]. Possible causes originating a bundle branch block include heart attacks (myocardial infarction involving the bundles), myocarditis (viral/bacterial infection of the heart muscle), cardiomyopathy (thickened/stiffened or weakened heart muscle), congenital heart abnormality (such as atrial septal defect) or even high blood pressure (hypertension) [287, 288].

The occurrence of this pathology is included in the 1D fast conductivity bundles and in the 2D Purkinje network as a local reduction of the electrical conductivities proportionally to the severity of the bundle branch delay, whereas

a null conductivity tensor is used to simulate a complete block of the bundle. The resulting pathological activation in the case of a right bundle branch block is reported in Figure 4.21 showing that, despite the depolarization of the left ventricular myocardium is correctly initiated after about 180 ms (panel 4.21a), the missing propagation of the depolarization front through the right Purkinje network prevents the normal depolarization of the ventricular myocardium observed in the healthy cases (Figure 4.18 d,e). However, as the left and right ventricular myocardium are a unique 3D excitable media, the right ventricular depolarization is triggered by the surrounding left ventricular one with a delay of about 20 ms and the propagation front then travels throughout the chambers (panel 4.21b). Nevertheless, as the conduction speed in the 3D myocardium is about ten times slower than the one in the Purkinje network, the depolarization of the right chamber results significantly delayed with respect to healthy conditions with an asynchronous depolarization of the apical, equatorial and basal myocytes (Figure 4.21c), which would entail an inefficient systolic contraction [16]. Vice–versa, the presence of a left bundle block, shown in Figure 4.22, yields a delayed activation of the left ventricle owing to the missing propagation in the left ventricular bundle and Purkinje network.

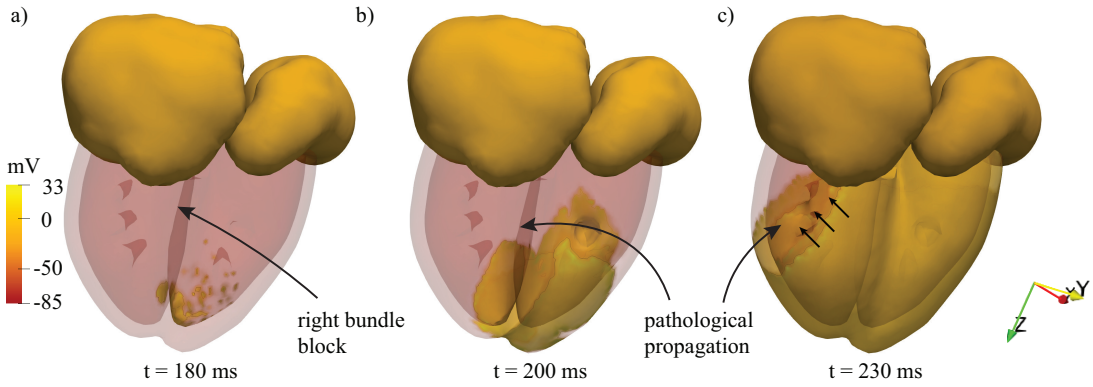

Figure 4.21: pathological ventricular activation in the case of right bundle block at various time instants with respect the SA–node activation. In particular, the time instants of panels (a) and (b) corresponds to the ones for the healthy cases reported in Figure 4.18. The black arrow in panel c) highlights the delayed right ventricle depolarization caused by the disease.

Bundle block pathologies, as well as other cardiac diseases such as sinus node dysfunction and intermittent AV block [289, 290] are often treated with artificial stimulation through the implantation of an artificial cardiac pacemaker [284], which consists of inserting an artificial lead in contact with the internal muscular wall (endocardium) inducing the periodic depolarization of the surrounding tissue. The effect of an implanted pacemaker lead can be accounted for in the model through an additional stimulation current I^s in equation (4.1) acting on the 3D myocardium and localized at the lead position. Among the most common atrial (septal, right lateral, appendage) and ventricular (apex, interventricular

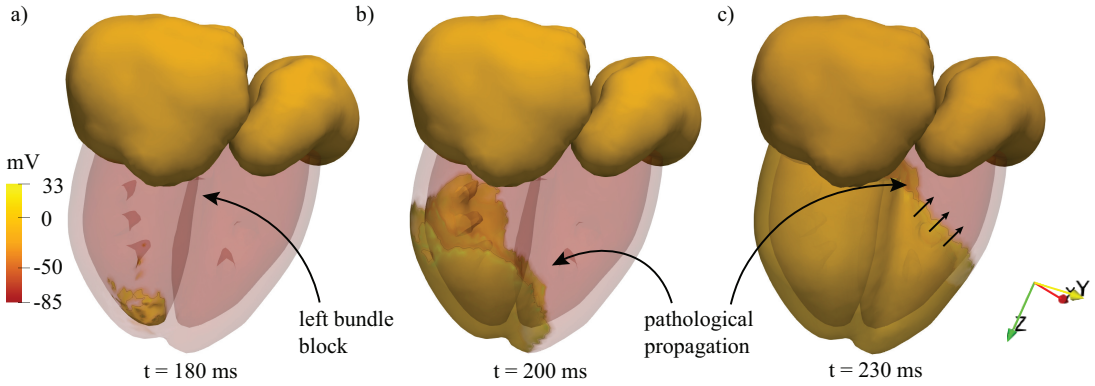

Figure 4.22: pathological ventricular activation in the case of left bundle block at various time instants with respect the SA–node activation. In particular, the time instants of panels (a) and (b) correspond to the ones for the healthy cases reported in Figure 4.18. The black arrow in panel c) highlights the delayed left ventricle depolarization caused by the disease.

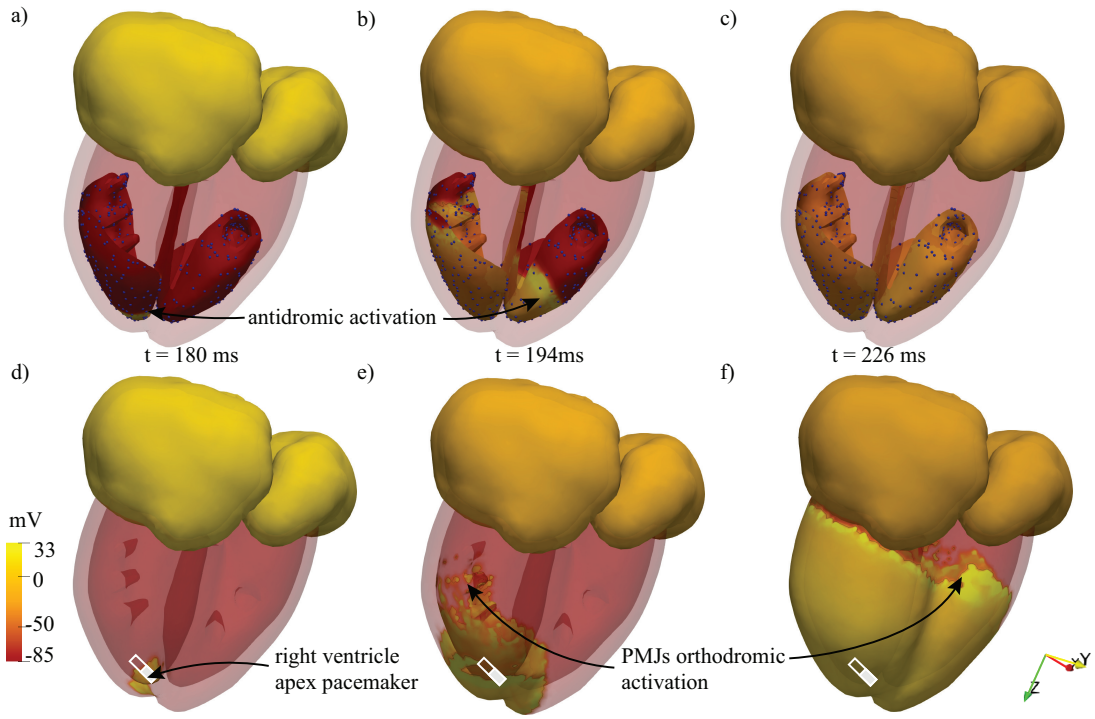

Figure 4.23: Cardiac electrophysiology with an artificial pacing at the ventricular apex, the white symbol indicates the lead location. Panels (a,b,c) show the action potential front in the Purkinje network while panels (d,e,f) describe corresponding depolarization of the surrounding 3D myocardium. The AV–node communication is interrupted (AV block).

septum, left ventricle) leads implantation sites reported in Figure 4.20(b), here we consider a ventricular apex pacing to mitigate a pathological atrioventricu-

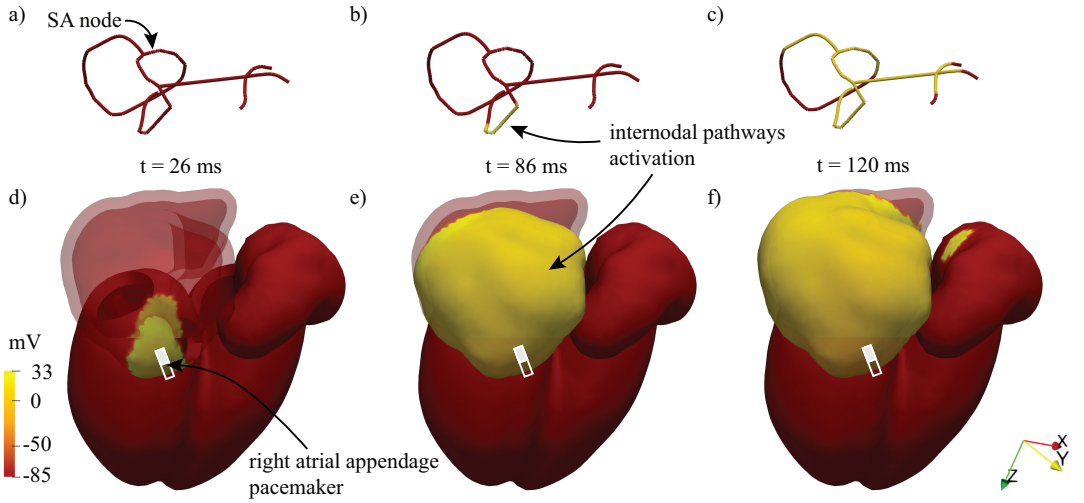

Figure 4.24: Cardiac electrophysiology with an artificial pacing at the atrial appendage, the white symbol indicates the lead location. Panels (a,b,c) show the action potential depolarization front within the internodal pathways, whereas panels (d,e,f) indicate the corresponding 3D myocardium.

lar block (inability of the signal to cross the AV–node) simulated by setting the conductivity of the AV–node to zero. As shown in Figure 4.23(a), although the ventricular myocardium is not activated by the fast conduction Purkinje complex, as in healthy conditions, the pacing lead implanted within the apical tissue of the right ventricle induces an electrical stimulus with a delay of 160 seconds with respect to the SA–node. In particular, the depolarization front propagates from the 3D myocardium activated by the lead to the Purkinje network through the PMJs (with an antidromic delay of 3 ms, see Figure 4.23 b,e), and then rapidly propagates through the rest of the Purkinje network which, in turn, triggers the depolarization of the underlying 3D myocardial tissue through the downstream PMJs (with an orthodromic communication delay, see Figure 4.23 e). Hence, in agreement with the medical evidence, the presence of an artificial stimulation through an implanted lead manages to activate the Purkinje network downstream the bundle block and to recover an effective depolarization of the ventricular myocardium in a similar fashion as the healthy depolarization pattern studied above and reported in Figure 4.18.

In addition, Figure 4.24 shows the cardiac electrophysiology corresponding to an atrial pacemaking, where the lead is positioned in the right atrial appendage [291], one of the most frequent implantation sites for an atrial lead [284]. Initially, the electrical stimulus provided by the lead only depolarizes a surrounding piece of the 3D atrial myocardium (panel 4.24 d), whereas the atrial 1D bundles are not directly activated by the lead (panel 4.24 a). The electrical depolarization front propagates in the 3D myocardium until reaching and, consequently, activating the fast conduction bundles (see panel 4.24 b), which then rapidly propagates the depolarization front in the whole 1D network, including the left

atrial network (panel 4.24 c). The combined effect of slow (3D) and fast (1D) depolarization fronts induced by the atrial lead thus yields a homogeneous activation of the left atrium. Nevertheless, compared to healthy propagation shown in Figure 4.17 b), the atrial depolarization occurs with a delay of approximately 95 ms.

4.6 Discussion

In this work, a numerical framework for solving the cardiac electrophysiology of the whole human heart in healthy and pathological conditions has been proposed. According to the complex spatial distribution of the electrophysiology properties of the heart, the whole cardiac geometry is decomposed into a set of coupled conductive media of different topology, namely (i) a 1D network of bundles comprising a fast conduction atrial network, the AV–node and the ventricular bundles; (ii) a 2D Purkinje network; and (iii) the 3D atrial and ventricular myocardium. These overlapping subdomains are two–way electrically coupled and the advancing depolarization front can propagate from one media to another, as happens in physiological conditions. Specifically, in a healthy heart, the fast conduction atrial network activates the 3D atrial myocardium and the AV–node which, in turn, activates the ventricular bundles transmitting the depolarization front to the Purkinje network which rapidly activates the 3D ventricular myocardium through the PMJs. Nevertheless, different activation patterns, also including backward activation from the 3D myocardium to the bundles and/or to the Purkinje, may occur in pathological conditions as observed in section 4.5.2. Although the propagation of the depolarization front in all these conductive media is governed by the bidomain/monodomain equations, the heterogeneity of the cardiac electrophysiology properties at the cellular scale corresponds to different electrical conductivities and ionic currents across the myocytes membrane at the continuum scale, which has been accounted in the numerical model through non–uniform conductivity tensors which depend on the local fiber orientation and using three different cell models. Specifically, the Courtemanche cell model [229] is used for the atrial myocytes (and the corresponding internodal pathways), the Stewart cell model [230] is adopted for the Purkinje Network, whereas the transmembrane ionic fluxes in the ventricular myocytes are solved through the ten Tusscher–Panfilov cell model [188], which correctly reproduces the action potential within ventricular myocytes. These models are coupled with the bidomain/monodomain equations, which are discretized in space using an in–house finite–volume method tailored for 1D, 2D and 3D complex geometries and the explicit Rush–Larsen temporal integration scheme guarantees enhanced stability properties. The numerical solver has been thoroughly validated with available benchmark results from the literature [189, 282] and the resulting depolarization within the whole heart well agrees with in–vivo observations [16].

The whole solver is GPU–accelerated using CUDA Fortran with the extensive use of kernel loop directives (CUF kernels) providing an unprecedented speedup,

thus allowing to solve a complete heartbeat in less than 8 wall–clock hours using Tesla V100 GPU devices. It should be noted that such computational cost could be further reduced either resorting to a monodomain model for the 3D myocardium corresponding to a 1.5 wall–clock hours per heartbeat, or using the next generation Tesla A100 GPU devices which are expected to provide a further acceleration of about four times while keeping the same code [41].

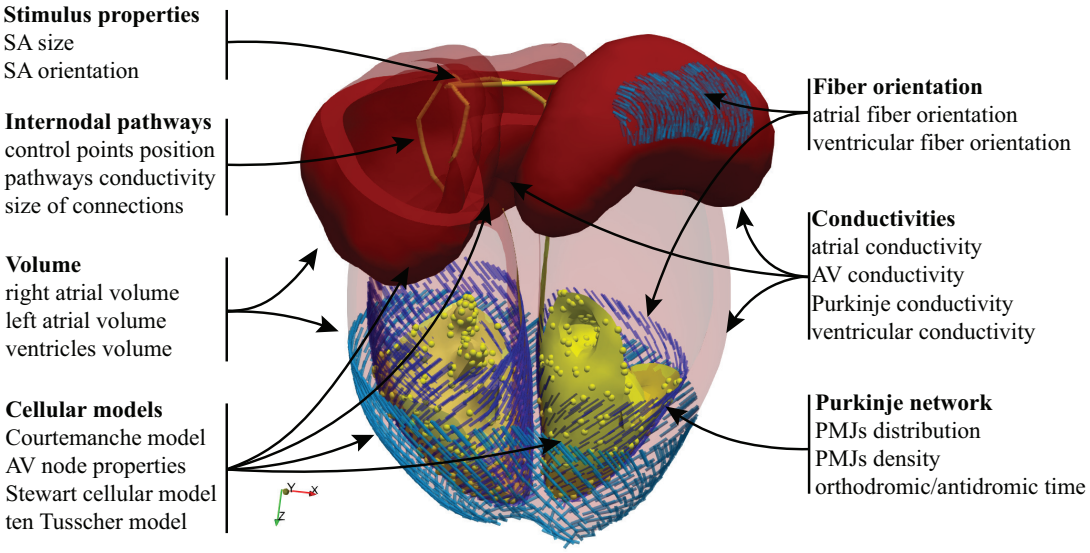

Figure 4.25: Summary of the electrophysiology components having a high variability among individuals and which may be studied systematically with the proposed numerical model through an UQ analysis.

The resulting digital twin of the human cardiac electrophysiology could be applied to study spatiotemporal alternans patterns within ventricles and assess the role of the Purkinje network in the initiation/suppression of arrhythmia, also through the use of appropriate spatiotemporal correlation indices [225]. A natural development of the model is the integration of the corresponding electrocardiogram profile (ECG) either using a pseudo-ECG formulation [292] or a more realistic torso model with a detailed body surface potential analysis [293]. The latter would allow not only to directly compute the ECG problems of a given cardiac configuration, but also to determine in a reverse fashion the electrophysiology network corresponding to an observed pathological ECG [294].

Importantly, the computational high–performance of the solver and its versatility in controlling the geometrical and electrical properties of the whole cardiac electrophysiology open the way for systematic uncertainty quantification (UQ) analyses. The human electrophysiology system, indeed, presents high variability in the several of its components such as the fiber orientations, conductivity tensors, chambers volume, internodal pathways positions and the density of PMJs, and our numerical framework is designed to easily control and vary all these relevant quantities summarized in Figure 4.25. The splitting of the cardiac electrophysiology system in a set of interconnected conductive media not only

reduces the computational cost, but also provides an ideal framework for investigating the effect of an electrical or geometrical modification of the fast conduction network (bundles and/or Purkinje) on the cardiac depolarization, thus allowing to optimize cardiac resynchronization therapies or invasive surgical procedures [295, 296, 297]. Furthermore, the computational bottleneck given by the 3D bidomain simulations can be circumvented by exploiting appropriate multi–fidelity strategies [298, 299, 300]. On the other hand, a monodomain inverse conductivity problem (MICP) [181, 301] can be solved for the fast conduction network of bundles to calibrate the electrical conductivities of monodomain model in order to match medical data acquired in–vivo. As a last comment, the relationship between the cardiac valves functioning [302, 303, 234] and the geometry of the Purkinje network, papillary muscles and chordae tendinae could be investigated by integrating our electrophysiology model within a fluid–structure solver [177], so to also account for the cardiac hemodynamics and tissues kinematics in the UQ analysis.

Acknowledgements

This work has been partly supported by grant no. 2017A889FP 'Fluid dynamics of hearts at risk of failure: towards methods for the prediction of disease progressions' funded by the Italian Ministry of Education and University.

Author Contributions

G.D.C., R.V., F.V. designed the research. G.D.C. developed the model and the corresponding coupling. FV implemented the GPU-acceleration of the electrophysiology finite element library. GDC and FV performed numerical simulations and validations. G.D.C. and F.V. wrote the paper with inputs from R.V.

Chapter 5

On the electrophysiology of the atrial fast conduction system: model validation and UQ analysis

Giulio Del Corso, Roberto Verzicco and Francesco Viola
Acta Mechanica Sinica (2021): 1

Abstract

Cardiac modeling entails the epistemic uncertainty of the input parameters, such as bundles and chambers geometry, electrical conductivities and cell parameters, thus calling for an uncertainty quantification (UQ) analysis. Since the cardiac activation and the subsequent muscular contraction is provided by a complex electrophysiology system made of interconnected conductive media, we focus here on the fast conductivity structures of the atria (internodal pathways) with the aim of identifying which of the uncertain inputs mostly influence the propagation of the depolarization front.

Firstly, the distributions of the input parameters are calibrated using data available from the literature taking into account gender differences. The output quantities of interest (QoIs) of medical relevance are defined and a set of metamodels (one for each QoI) is then trained according to a polynomial chaos expansion (PCE) in order to run a global sensitivity analysis with non–linear variance–based Sobol' indices with confidence intervals evaluated through the bootstrap method. The most sensitive parameters on each QoI are then identified for both genders showing the same order of importance of the model inputs on the electrical activation. Lastly, the probability distributions of the QoIs are obtained through a forward sensitivity analysis using the same trained meta-

models. It results that several input parameters – including the position of the internodal pathways and the electrical impulse applied at the sinoatrial node – have a little influence on the QoIs studied. Vice–versa the electrical activation of the atrial fast conduction system is sensitive on the bundles geometry and electrical conductivities that need to be carefully measured or calibrated in order for the electrophysiology model to be accurate and predictive.

5.1 Introduction

At each heartbeat the synchronized contraction of the cardiac chambers is originated by the timely electrical activation of the myocytes that are integrated in a sophisticated and robust electrical network. As sketched in Figure 5.1(a), the local myocytes depolarization starts from the sinoatrial node (SA-node hereafter), which is located in the right atrium at the junction of the crista terminalis close to the entrance of the superior vena cava, and then propagates across the atria. When a myocyte is reached by the electrical propagation front, the local transmembrane potential rapidly changes from the negative potential (of about -85mV) to a positive value (of about 20mV) before returning to the resting negative potential after about 300 ms, see Figure 5.1(b). The propagation of the electrical depolarization front is affected by the strong heterogeneity of the cardiac tissue, with an average conduction velocity of about 0.3-0.5 m/s in the atrial fibers that reaches 1.5-2 m/s in specialized high conductivity structures, the so-called internodal pathways [16, 22]. These (i) anterior internodal, (ii) middle (Wenckbach) and (iii) posterior (Thorel) bundles connect the SA-node to the left atrium (through the Bachmann's bundle) and to the atrioventricular node (AV-node hereafter), thus ensuring a rapid and smooth conduction across the whole heart. The AV-node connects the atrial to the ventricular electrical network and is made by specialized cardiac cells designed to slow down the electrical propagation by an AV-delay of about 90 ms [16], which plays a crucial role for the cardiac dynamics as it ensures a timely atrial contraction before the ventricular one. The AV-node is thus the electrical connection between the atrial and the ventricular bundle network: the propagation front travelling across the AV-node to the bundle of His further propagates through the Purkinje network at a higher conduction speed of about 4 m/s [16], thus allowing for an almost simultaneous activation of the ventricular muscle.

The state–of–the–art model for simulate and study the electrical activation within the heart chambers in healthy and pathological conditions is the bidomain model [170, 172], which is called in this way because the conductive myocardium is modeled as an intracellular and an extracellular overlapping continuum media separated by the myocytes membranes [168]. The resulting system of reaction–diffusion partial differential equations governs the electrical propagation across the myocytes and is coupled with the cellular ionic model (given by a set of ordinary differential equations) describing the current flows through the ion channels. In the case the extracellular and intracellular conductivity tensors are parallel

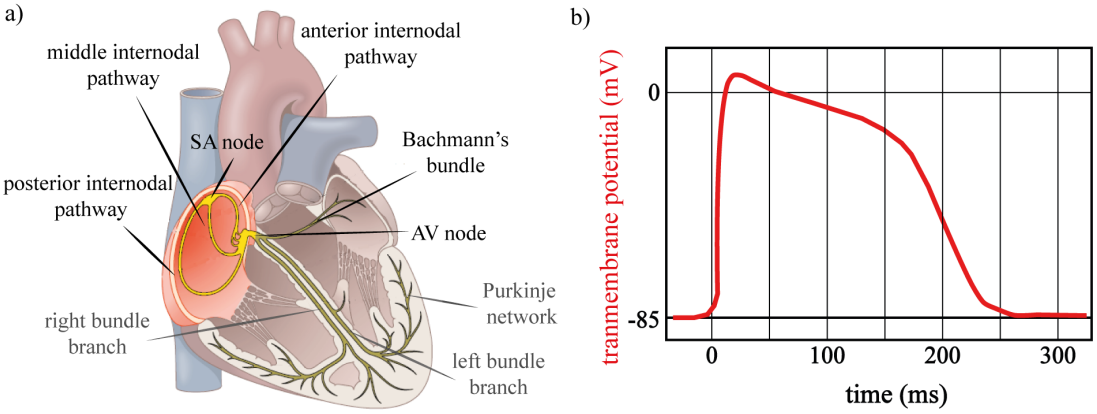

Figure 5.1: a) Sketch of the electrical network of the heart adapted from [16], with highlighted the atrial components. b) Sketch of a typical depolarization/polarization cycle (action potential) of an atrial myocyte [16].

to each other, as is always the case in monodimensional domains, the bidomain equations can be simplified as a single governing equation for the transmembrane potential, the monodomain system. The latter is computationally cheaper not only because the number of degrees–of–freedom is reduced but also because the equations are more stable numerically [170]. In contrast with computationally cheaper electrophysiology models such as the eikonal [167] method that correctly solve the electrical propagation through the medium, the monodomain/bidomain model is also seen to accurately reproduce cardiac phenomena including ischemic events and defibrillation.

Cardiac modelling, however, entails a high epistemic uncertainty for the geometrical and electrical input parameters entering in the governing equations as only some of these quantities can be measured in–vivo. The calibration of electrical input parameters for monodomain equations based on available medical data is typically solved in the framework of monodomain inverse conductivity problem (MICP). Multiple techniques, including variational data assimilation procedure [181] and proper generalized decomposition (PGD) [301], were used to derive space-dependent conductivity for 2D and 3D media. The input parameters variability among individuals can be rigorously accounted for through an uncertainty quantification (UQ) approach, where the input parameters are treated as aleatory variables with an uncertainty probability distribution function (PDF). Consequently, not a single simulation but a set of simulations is run in order to determine the sensitivity of some quantities of interest (QoIs) on the input parameters (and their PDFs) as well as the PDFs of the QoIs. This statistical approach has been recently used by the authors to investigate the propagation of uncertainties in an electrophysiology model for the electrical activation of the left ventricular myocardium [304].

In this work we study the global sensitivity of the electrical activation within the atrial fast conduction network on the geometry and on the electrical properties of the system. The aim is to isolate which of the model parameters,

either geometrical or electrical, have a greater impact on the atrial depolarization dynamics and, through the atrioventricular node, on the ventricular one. The identification of the most sensitive parameters would not only increase our comprehension of the electrophysiology phenomena, but it would also allow to improve existing computational models. Furthermore, determining what parameters influence the initial cardiac activation through sensitive analysis, as done here, is a first step towards reduced order models and the design of effective inverse calibration for patient–specific applications.

The paper is organized as follows. The computational model for the fast conduction atrial bundles based on the monodomain equations coupled with the ten Tusscher–Panfilov cellular model is detailed in (§ 5.2.1). The uncertainty PDFs of the input parameter space owing to the variability among individuals is calibrated in § 5.2.2 using available experimental data from the literature, while the QoIs of the study are defined in § 5.2.3. The UQ analysis is based on a metamodelling technique (polynomial chaos expansion [212, 40]) with a quasi Monte Carlo Sobol' low discrepancy sampling strategy so that to minimize the size of the dataset. The metamodel performance in reproducing the QoIs as obtained by the full electrophysiology model is verified through a cross validation strategy and the confidence intervals of the sensitivity indices are calculated using the bootstrap method as detailed in § 5.3. Section § 5.4.1 reports the sensitivity analysis of the selected QoIs on the input parameter space using the Sobol' sensitivity index, whereas the corresponding forward analysis, still obtained by the PCE, is reported in § 5.4.2. A final discussion of the UQ results and future developments of the work are proposed in § 5.5.

5.2 Electrophysiology problem, input parameter and quantities of interest

5.2.1 Bidomain/monodomain equations for the fast conductive bundles

The computational domain consists of four bundles, with three of them (the posterior internodal pathway, the middle internodal pathway, the anterior internodal pathway) originating from the SA-node, while the fourth one, the Bachmann's bundle, connects the right and left atrium among them and bifurcated into three small bundles within the left atrium, see Figure 5.2. The bundles are immersed in the atrial endocardium through some control points and, consequently, any modification of the atrial geometry studied in the UQ analysis (e.g. owing to a different volume of the cardiac chambers) directly affects the bundles geometry, which move so that to follow the location of the atrial control points. For any configuration of the atrial network, the bundles are automatically re–meshed in order to have the same spatial discretization for all UQ samples, see appendix 5.6 for more details about the convergence of the numerical method.

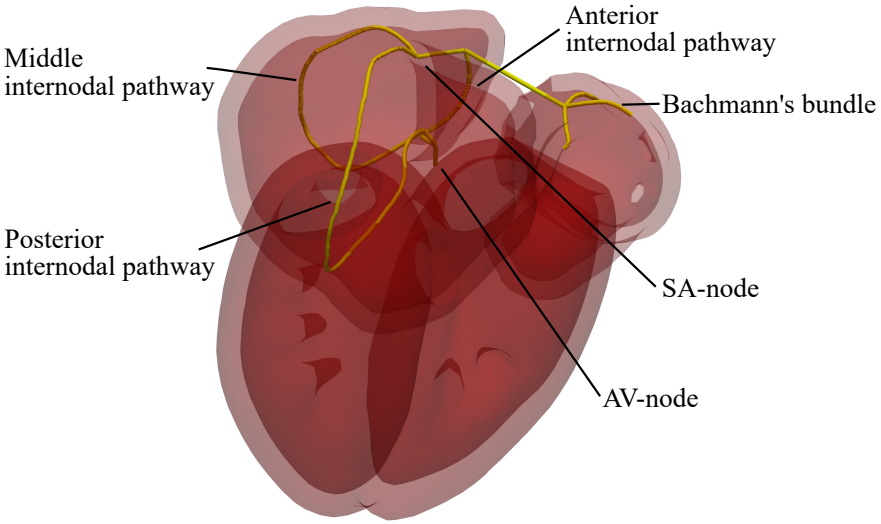

Figure 5.2: Computational domain of the atrial fast conduction network (yellow) and the surrounding myocardium (red).

The propagation of the electrical front through the myocardium is governed by the bidomain equations where the conductive tissue is modelled as an interior and exterior media [170]. Owing to the slenderness of the fast conduction bundles they can be considered as a network of one dimensional fibers that bifurcate and intersect at the network nodes and, as a consequence, the bidomain equations are equivalent to the monodomain equations as the intracellular and extracellular electrical conductivities reduce to scalar quantities necessarily proportional one each other:

$$C_m \frac{\partial v}{\partial t} + I_{ion}(v, \xi) + I_s = \chi^{-1} \frac{\partial}{\partial s} \left(M \frac{\partial v}{\partial s} \right), \qquad \frac{\partial \xi}{\partial t} = F(v, \xi). \tag{5.1}$$

Here v is the unknown transmembrane potential, $\chi = 140$ mm^{-1} and $C_m = 0.01 \mu$F mm^{-2} are the surface–to–volume ratio and the membrane capacitance of the cells [189]. The effective conductivity M is assumed to be uniform over the computational domain and is equal to half the harmonic mean of the intracellular and extracellular conductivities $M = \frac{M_{int} M_{ext}}{M_{int} + M_{ext}}$. The quantity I_{ion} is the net ionic current across the cell membrane and it is determined using the the ten Tusscher–Panfilov cellular model [188], which is indicated in compact form in the second equation (5.1). The solver imposes homogeneous Neumann boundary conditions on the transmembrane potential, whereas the network nodes are automatically handled by the FEM library as internal dofs and branching conditions do not need to be imposed. For each tissue location, the cellular model is given by a set of nonlinear ordinary differential equations (19 in our case that are not reported here for the sake of brevity) that is two–way coupled to the monodomain equation through the cell model state vector ξ and the transmembrane potential v. The current I_s corresponds to the electrical stimulus applied at SA-node location (see

Figure 5.3) where the electrical propagation originates:

$$I_s = S_a(\mathcal{H}[t] - \mathcal{H}[t - S_d]), \tag{5.2}$$

with S_a and S_d being the stimulus amplitude and duration, t the time within a heart beat and $\mathcal{H}[\cdot]$ the Heaviside function.

The governing equations (5.1) are discretized on a one-dimensional domain immersed in the atrial endocardium using the electrophysiology library cbcbeat [190], which is based on the finite element library FEniCS [191].The monodomain equation (5.1) is integrated in time using a fractional step method based on the Crank-Nicholson scheme and the cellular model is solved in each mesh cell using a Rush-Larsen integration scheme, see [177, 304]. The resulting average CPU time cost to solve a complete activation of the fast conduction bundles until reaching the AV-node on a reference grid of 2'397 linear elements (corresponding to 47'940 degrees of freedom including the ones of the cell model) and using a time step of $dt = 5 \cdot 10^{-3}$ ms is of about 30 CPU-minutes (defined as the time it takes to run the program on a 1 GHz reference processor). The computational resources used for the analysis comprise an Intel Xeon Processors with 16 cores (E5-2620 v3 - 15M Cache, 2.40 GHz) that allow to run the same number of simulations simultaneously.

5.2.2 Input parameters

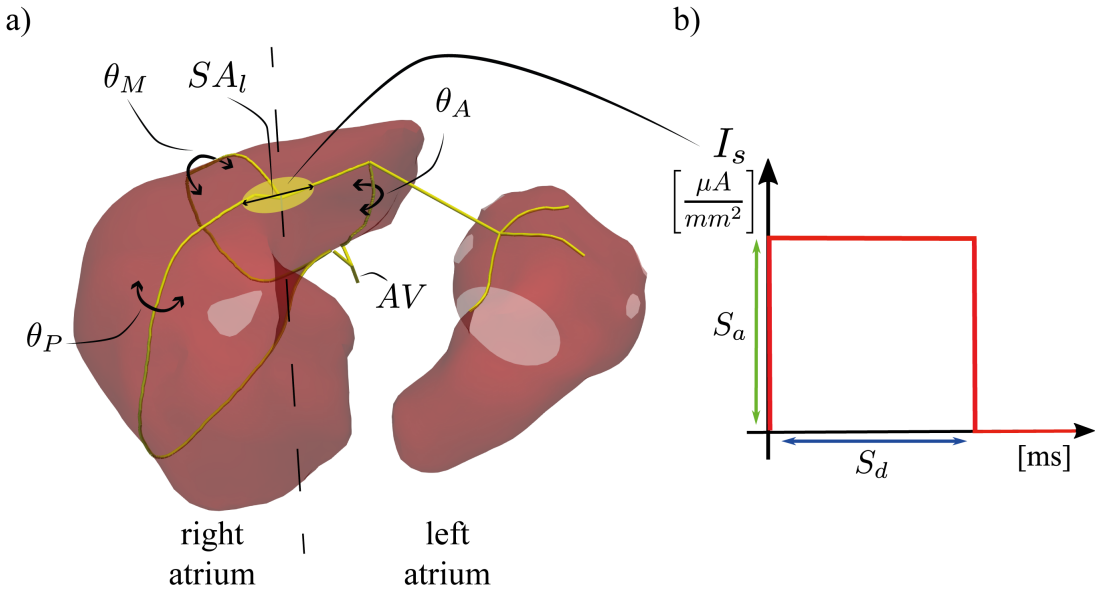

Figure 5.3: (a) Atrial electrical pathways with sketched the angle parameters θ_A, θ_M, and θ_P along with the size of the sinoatrial node SA_L. (b) Stimulus current as a function of time, the parameters S_a and S_d indicate the amplitude and duration of the stimulus.

In order to run a global sensitivity analysis of the fast bundles electrical activation on the model input parameters, their uncertainty PDFs have to be determined from the in-vitro an in-vivo data reported in the literature. Unfortunately, these input PDFs are usually not available and even when systematic measurements of clinical quantities on a large population are carried out (e.g. the volume of the heart chambers) only the first (the mean μ) or the first and second (the mean μ and standard deviation σ) statistical moments of the PDF are reported in the literature. In such cases, in information theory, the PDF shape matching the statistical moments available is typically selected as the one maximizing the Shannon entropy (or its continuous extension) [52] as done here. In particular, in the case the PDF is known to be bounded in the interval $[a, b]$, the corresponding PDF maximizing the entropy is the uniform random variable $\mathcal{U}[a, b]$. On the other hand, if also the experimental mean value μ and standard deviation σ are available, a truncated normal distribution $\mathcal{N}_{[a,b]}(\mu_T, \sigma_T)$ should be considered. With formalism $\mathcal{N}_{[a,b]}(\mu_T, \sigma_T)$ we indicate the truncated normal distribution with mean $\mu_T = \mu$ and variance $\sigma_T = \sigma$, which is the maximum entropy distribution for fixed mean, variance and support.

The left atrium volume can be measured using several non-invasive techniques such echocardiography and magnetic resonance imaging (MRI) and a significant statistical difference between male and female atrial size is observed whereas the patient age weakly influences the atrial volume change for healthy subjects [26]. The mean and standard deviation of the left atrial volume measured on a population of 45 females and 63 males is equal to $(41, 11)$ ml and $(46, 14)$ ml, respectively. These results were obtained throughout a CMR (cardiovascular magnetic resonance imaging) procedure [27], with lower and upper bounds of $(20, 120)$ ml measured on a larger population using MRI (including both genders) [305]. It should be noted that although both CMR and echocardiography can provide high resolution data, the volume chamber is typically evaluated by a human operator that necessarily introduces an additional source of uncertainty [27]. It is not possible, however, to distinguish the impact of the human operator on the measure of the volume chamber and the variability of this geometrical parameter is here ascribed to the individual variability only. According to the principle of maximum entropy mentioned above, the left ventricle volume for males (V_m) and females (V_f) is modelled as two random variables distributed according to the truncated Gaussian distributions $\mathcal{N}_{[20\text{ml},120\text{ml}]}(\mu_T = 46\text{ml}, \sigma_T = 14\text{ml})$ and $\mathcal{N}_{[20\text{ml},120\text{ml}]}(\mu_T = 41\text{ml}, \sigma_T = 11\text{ml})$.

In the UQ analysis, left and right atrial volume are assumed to be correlated and the same random variable (V_m for male and V_f for female population) is used to vary the volume of both chambers. The one–dimensional bundle geometry lies within the atrial myocardium with a nominal orientation of bundles as reported in Figure 5.3(a). The internodal angles are varied over their nominal orientation by an angular rotation around the vertical axis passing by the SA-node (dashed line) of size θ_A for the anterior, θ_M for the middle (Wenckebach) and θ_P for the posterior (Thorel) bundle, which are modeled as uniform distributions with amplitude $\pm\pi/7$ so that to vary significantly the bundles orientation but avoiding

variable	symbol	nominal value	distribution
volume males	V_m	46 ml	$\mathcal{N}_{[20,120]}(\mu_T = 46, \sigma_T = 14)$
volume females	V_f	41 ml	$\mathcal{N}_{[20,120]}(\mu_T = 41, \sigma_T = 11)$
anterior internodal	θ_A	0	$\mathcal{U}[-\pi/7, \pi/7]$
middle internodal	θ_M	0	$\mathcal{U}[-\pi/7, \pi/7]$
posterior internodal	θ_P	0	$\mathcal{U}[-\pi/7, \pi/7]$
electrical conduction	M	0.87 mS/mm	$\mathcal{U}[0.33, 1.41]$
SA stimulus duration	S_d	2.5 ms	$\mathcal{U}[0.5, 5.5]$
SA stimulus amplitude	S_a	1 mA/mm^2	$\mathcal{U}[0.5, 1.5]$
SA size	SA_l	6.85 mm	$\mathcal{U}[5.2, 8.5]$
Extra AV time	AV_d	90 ms	$\mathcal{U}[80, 100]$
maximal I_{Na} conductance	G_{Na}	14.838 nS/pF	$\mathcal{U}[11.870, 17.805]$
extracellular Na concentration	Na_O	140 mM	$\mathcal{U}[112, 168]$
extracellular K concentration	K_O	5.4 mM	$\mathcal{U}[4.32, 6.48]$

Table 5.1: Input parameters for the sensitivity analysis. The bounds, mean and standard deviation of the PDFs reported in the last column have the same physical dimensions of the corresponding nominal value.

to overlaps and cross intersections among them.

Regarding the electrical properties of the fast conduction network, the input parameter space includes the electrical conductivity M influencing the conduction velocity of the fibers (see the monodomain equations (5.1)). The uncertainty PDF of the electrical conductivity is obtained in a reversed engineering fashion from the conduction velocity that is indicated to be of about 1-1.1 m/s [16, 24] and in general below 2 m/s [22]. Hence, we have considered the conduction velocity to be bounded within the interval 1-2 m/s (in agreement with the velocity range measured in the canine atrial pathways, 0.88-1.66 m/s [306]), which corresponds to an electrical conductivity range of $M = 0.33 - 1.41$ S/mm according to the deterministic relation between the conduction velocity and electrical conductivity reported in appendix 5.8. As only the mean value and the bounds for the electrical conductivity are known, a uniform distribution is considered as reported in Table 5.1.

Furthermore, the sensitivity of the bundles electrical activation on the duration S_d and amplitude S_a of the stimulus in the SA-node, along with extension of the SA is studied. The input current stimulus, see Figure 5.3(a), is modelled as a rectangular function with duration and amplitude equal to S_d and S_a whose uncertainty is modeled as uniform distributions containing the values used in the literature to activate the wavefront propagation [307]. On the other hand, the length of the SA is known to vary between 5.2 and 8.5 mm [308], and these values have been used as bounds for the spatial extension of the stimulus applied

in the SA-node. Additionally, the variability of the time delay in the propagation of the electrical signal occurring the AV-node, AV_d, is considered as a uniform PDF with mean value 90 ms and bounds equal to ± 10 the mean value [16].

The effect of the input parameters of the ten Tusscher–Panfilov cellular model on the electrical activation is studied by accounting for variability of the maximal I_{Na} conductance, G_{Na}, of the extracellular Na concentration, Na_O, and of the extracellular K concentration, K_O, that were seen to be the most relevant parameters in previous analyses [186, 304]. A uniform uncertainty of $\pm 20\%$ the nominal value around the nominal value itself is considered.

The dimension of the input parameter space is thus equal to $d = 12$ and the corresponding PDFs are reported in Table 5.1. As the relationships between these input random variables are unknown, they are modeled as independent random variables.

5.2.3 Quantities of interest

As the main objective of the analysis is to investigate the effect of the model input parameters introduced above on the propagation of the electrical wavefront through the atrial pathways, the quantities of interest (QoIs) of the UQ analysis are defined as the activation times of the network nodes. Referring to Figure 5.4, the UQ analysis monitors the time needed to reach the two junctions of the AV-node (t_1, t_2), along with the activation times of the tips of the Bachmann's bundle (t_3, t_4, t_5). Additionally, two further QoIs are defined as the activation time of the upstream $t^* = \min(t_1, t_2)$ and downstream t_{AV} tip of the AV. We recall that the downstream tip of the AV-node transmits the electrical propagation front to the ventricular fast conduction system (not included in this UQ analysis). A last QoI is given by the conduction velocity v_c of the propagation of the depolarization front, which is uniform across the bundles since the electrical conductivity and the cell model properties are uniform in the domain. Without loss of generality the conduction velocity is thus measured at the middle internodal pathway.

5.3 UQ methods

5.3.1 Polynomial chaos expansion

The sensitivity of the QoIs on the input parameters is investigated through a variance-based global sensitivity analysis using first (also called importance measures) and total order Sobol' indices [309]. These quantities are defined as the influence of input parameters on the variance of the QoIs and are able to describe the combined effects of multiple input variables, thus providing a deeper understanding of the physical system at study. Computing the Sobol' indices using a direct approach can be computationally expensive because the QoIs dependence on the input variables is obtained by solving the full system (the monodomain model here). As an example, given d input parameters, the computational cost

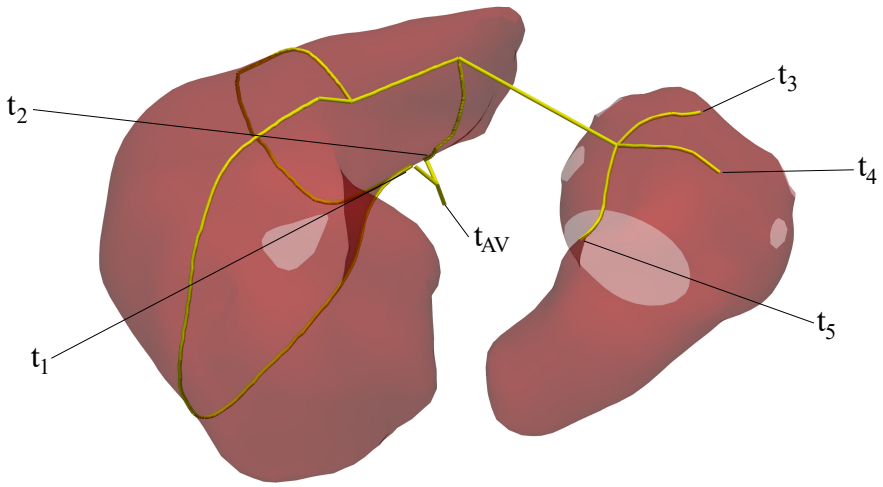

Figure 5.4: Activation time at the AV bundle (t_1, t_2), at the end of the Bachmann's bundle (t_3, t_4, t_5) and at the downstream tip of the AV-node t_{AV}.

for evaluating the first order Sobol' indices is $\mathcal{O}(dN^2)$ using a a standard Monte Carlo (MC) approach or $\mathcal{O}((d+2)N)$ applying the Saltelli's algorithm, with $N \approx 10^3$ the size of the samples needed to approximate one of the input variables. In order to reduce the computational cost of the UQ analysis, a polynomial chaos expansion (PCE) approach is adopted [40], which belongs to the family of the metamodelling techniques where the sensitivity indices are evaluated using a simplified model rather than the whole physical system as done in the direct methods. The adaptive procedure for the PCE calibration used here has been previously validated in the case of the electrical depolarization of the ventricular myocardium [304]. All of the details of the algorithms, the validations and the convergence checks can be found in the above reference; only the main features are summarized here. The metamodel is built so that to reproduce/approximate the input–output relation of the governing equations using a training and a testing dataset.

In particular, given a computational model, $G : \mathcal{D}_X \subset \mathbb{R}^d \to \mathbb{R}$, the uncertainty of the input parameters is modeled by a random vector X prescribed by joint probability density function $f_X(x)$ [133] and the QoI $Y = G(X)$ is obtained by propagating the uncertainty on X through G. Assuming that the input variables are statistically independent, the joint PDF is the product of the d marginal distributions $f_X(x) = \prod_{i=1}^{d} f_{X_i}(x_i)$ for each $\mathcal{D}_{X_i}$ and we can define the inner product for each single variable X_i and for any two functions $\phi_1, \phi_2 : \mathcal{D}_{X_i} \to \mathbb{R}$ as: $\langle \phi_1, \phi_2 \rangle := \int_{D_{X_i}} \phi_1(x)\phi_2(x) f_{X_i}(x) dx$ and use it to define an orthonormal family of polynomials $\{P_k^{(i)}, k \in \mathbb{N}\}$. This set of univariate orthonormal polynomials can be used to define a family of multivariate ones. In fact, given a multi-index $\alpha = (\alpha_1, \cdots, \alpha_d), \alpha_i \in \mathbb{N}$, the associated multivariate polynomial can be defined

as $\Psi_\alpha(x) := \prod_{i=1}^{d} P_{\alpha_i}^{(i)}(x_i)$. The set of all multivariate polynomials in the input random vector X forms a basis of the Hilbert space, in which $Y = G(X)$ is given by the so called polynomial chaos expansion:

$$Y = \sum_{\alpha \in \mathbb{N}^d} y_\alpha \Psi_\alpha(X) \tag{5.3}$$

This infinite series has to be truncated in order to get a finite one approximating $Y = G(X)$ and different truncation strategies are possible depending (i) on how to enumerate the element of the multivariate basis and (ii) on how many terms of the basis have to be retained. The standard (linear) enumeration strategy is based on the total degree of a multivariate polynomial Ψ_α (with $\|\Psi_\alpha\| := \sum_{i=1}^{d} \alpha_i$) and is defined as the lexicographical order with a constraint of increasing total degree (e.g. for a two dimensional multi-index $(0,0) < (0,1) < (1,0) < (2,0) < (1,1,) < \cdots$). The chosen selection strategy is a fixed one, in which the total degree p is fixed and all the coefficients with total degree smaller or equal to p are retained. It should be noted that a linear enumeration coupled with a fixed truncation rule corresponds to a dimension of the basis with cardinality $\binom{d+p}{p}$, with p the polynomial degree and d the size of the input space [133]. The optimal hyper-parameter for each metamodel (i.e. the total degree) is calculated using an adaptive strategy [304].

The PCE coefficients are chosen using a least squares strategy (LQS hereafter), which minimizes the least squares error of the metamodel response on the training set. The main advantage of using an LQS is the fact that the training dataset can be extended if needed, whereas the use of integration rules based on Gaussian point can not. A training dataset of 2'000 samples is here built using a quasi Monte Carlo method (QMC) with low discrepancy Sobol' sequence in order to maximize the information contained and avoid clustering phenomena within the dataset [309]. The QMC has, indeed, a faster asymptotic converge rate for low number of parameters, $\mathcal{O}\left(\frac{\log(N)^d}{N}\right)$ where d is the input dimension, compared to the standard MC, $\mathcal{O}\left(\frac{1}{\sqrt{N}}\right)$, [30].

5.3.2 Metamodel validation and confidence intervals

Metamodelling techniques require a validation protocol to verify their ability to reproduce the results of the original physical system. In this analysis the risk of underfitting and overfitting is measured by evaluating the coefficients R^2 and Q^2. To this aim, a testing dataset of 200 samples (independent from the ones of the training dataset) is produced according to a pure MC strategy and used to validate the metamodel. Given the training (testing) dataset of size n, described by the couples $(\mathbf{x}_i, y_i)_{i=1}^n$ with y_i the QoIs corresponding to the set of input $\mathbf{x}_i$, and the prediction of the metamodel f for the same input dataset $(\mathbf{x}_i, \hat{y}_i := f(\mathbf{x}_i))_{i=1}^n$, the coefficient of determination is defined as $R^2(Q^2) := 1 - \frac{SS_r}{SS_t}$, where $SS_r := \sum_{i=1}^{n}(y_i - \hat{y}_i)^2$ is the residual sum square normalized for the total sum of squares $SS_t := \sum_{i=1}^{n}(y_i - \overline{y})^2$ with $\overline{y} = \frac{1}{n}\sum_{i=1}^{n} y_i$. The R^2 index is commonly used

in regression analysis to measure the metamodel performance in reproducing the variability within the training dataset with values close to one implying that the metamodel is well–trained, whereas low Q^2 and a high R^2 would correspond to an overfitting condition [128].

In contrast with a direct approach such as Saltelli's algorithm, the confidence intervals for Sobol' indices can not be derived from the asymptotic distribution of the estimators of the indices, but they can still be assessed without performing further simulations through a resampling method, the bootstrap [144]. The main idea is to create a few artificial datasets of different sizes by sampling with replacements the individual elements of the original training one. These artificial datasets are then used to calculate the Sobol' indices (using the PCE method introduced above), thus obtaining an empirical distribution of the indices quantifying the stability of the results with respect to a variation of the input dataset. The α-percentile bootstrap interval is defined as: $[S_{i[\alpha/2]}, S_{i[1-\alpha/2]}]$ where $S_{i[\alpha/2]}$ and $S_{i[1-\alpha/2]}$ are the $\alpha/2$ and the $1-\alpha/2$ empirical quantiles of the i-th Sobol' index distribution [145]. This interval does not require hypotheses about the S_i distributions (compared to standard intervals which assume normality [145]) but it needs many resamplings to estimate them accurately.

5.4 Results

5.4.1 Sensitivity analysis

An optimal PCE is trained and validated as detailed in the previous section for each QoI and the resulting hyper-parameters are summarized in Table 5.2. Although the resulting total polynomial degree is relatively low (equal to to 3) for each QoI the metamodels are able to describe over 99% the output variance, as visible by the R^2 coefficients reported in Table 5.2. Furthermore, the non-zero coefficients of the PCEs, are related to the interactions of single variables, which implies that the PCEs neglect high order interactions (i.e. associated with a polynomial with high degree in more than one variable [210]) and that the Sobol' total order are expected to be similar to the corresponding importance measure. The cost of producing the entire dataset for the metamodel approach is approximately 42 CPU-days, where a CPU-day is defined as a compute day run on a 1 GHz reference processor, while the metamodel is trained in about 1 CPU-minute.

As the input uncertainty of the atrial volume is different for male and female population, see (§ 5.2.2), two different sensitivity analyses are carried out for each QoI that are depicted by the blue and pink histograms in Figure 5.5. The small error bars on top of the histograms (corresponding the 95%-confidence interval computed using the bootstrap method with 500 resamplings) indicate that the training dataset is sufficiently large to accurately evaluate the Sobol' indices, see appendix 5.7 for a convergence analysis of the PCE method. We anticipate that, as the sensitivity results of t_1, t_2 (t_3, t_5) are similar to the ones of t^* (t_4) their

Sobol' indices are not reported in the figure.

QoI	enumeration strategy	truncation strategy	p	PCE cardinality	R^2/Q^2
Female t_4	linear	fixed degree	3	364	0.991/0.986
Female t_4	linear	fixed degree	3	364	0.999/0.998
Male t^*	linear	fixed degree	3	364	0.992/0.987
Male t^*	linear	fixed degree	3	364	0.999/0.999
Female t_{AV}	linear	fixed degree	3	455	0.995/0.990
Male t_{AV}	linear	fixed degree	3	455	0.995/0.990
v_c	linear	fixed degree	2	78	0.999/0.999

Table 5.2: Optimal metamodels selected by the adaptive PCE methodology.

As visible in Figure 5.5(a,b) both t^* and t_4 are sensitive on the electrical conductivity (with an importance of about 80%) and on the size of the atrial chambers (with a lower importance of about 20%). The sensitivities presented in Figure 5.5 are described in terms of both first order Sobol' indices (importance measure, defined for females and males as female importance and male importance) and total order (defined for females and males as female total and male total). Additionally, the cell model parameter G_{Na} has a minor effect (with about 5%) importance, whereas the rest of the input parameter space, including the duration and amplitude of the electrical stimulus along with the length of the SA-node, have a negligible effect on the QoI. A similar weak influence on the QoIs is observed for the angle perturbation of the bundles with the only exception of θ_A that slightly influences t^* because the anterior internodal pathway is the shortest path connecting the SA-node to the AV-node and a variation of its length owing to the angular variation (we recall that the bundle is constraint on the atrial endocardium) affect the time at which the AV-node is reached by the electrical propagation front. Importantly, males and females population manifest similar sensitivities of t_4 and t^* on the input parameters with a relatively larger sensitivity of the female population on the electrical conductivity and a relatively smaller one on the atrial volume.

Conversely, the activation time of the lower tip of the AV-node (the one towards the ventricular network), t_{AV}, is not only sensitive to the electrical conductivity (importance of about 45%) but is also affected by the time delay occurring in the AV-node AV_d (importance of about 35-40%). It should be noted that even the small percentage variation of the AV_d considered here (about $\pm 11\%$ of the mean value, see Table 5.1) has a relevant effect on t_{AV} and a larger variation of AV_d would further increase the time needed to fully activate the AV-node. Furthermore, the AV_d is slightly more important in female hearts with respect to the male population (one tailed t-test with $N = 500$ refusing the hypothesis that male AV_d is lower the female AV_d at a level $\alpha = 10^{-3}$ for both importance measure and total order) as the volume variation for females has a lower standard variation (11 ml against 14 ml for males), thus naturally increasing the

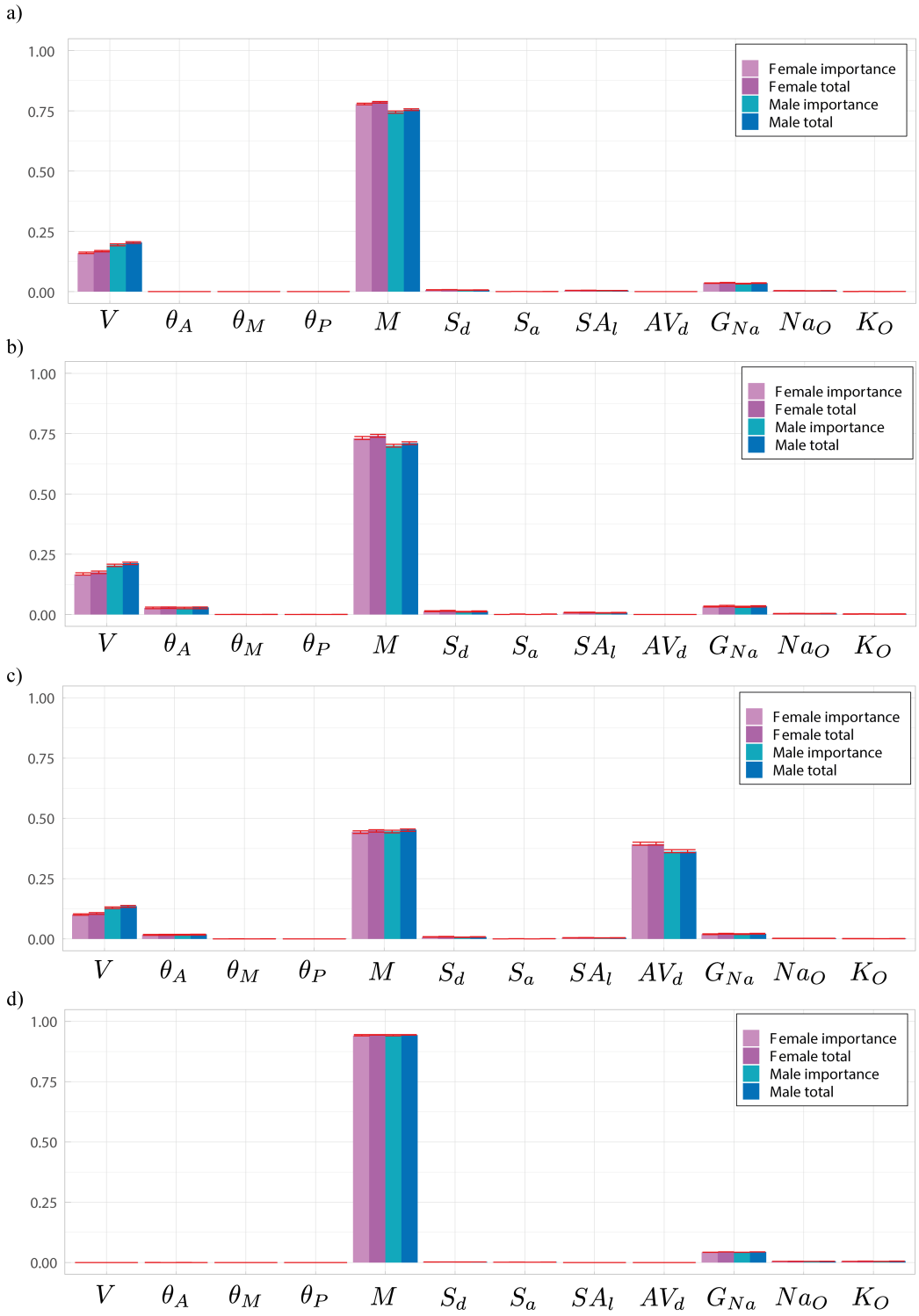

Figure 5.5: Importance measures (e.g. female/male importance) and Sobol' total order indices (female/male total) for (a) t_4 (b) t^* (c) t_{AV} and (d) v_c. Females (males) population is indicated by the pink (blue) histograms, whereas the errorbars indicate the confidence intervals of the metamodels.

sensitivity of the other parameters. Regarding the other parameters, the t_{AV} is seen to also depend on the atrial volume, on G_{Na} and on θ_A, whereas the other angular perturbations and the current stimulus parameters (S_a, S_d and S_l) have a negligible effect on the QoI.

As expected in diffusion dominated problems, the conduction velocity v_c is greatly sensitive on the electrical conductivity M with an importance exceeding 90 %, see 5.5(d). The complementary part of the importance indices is shared among the three input parameters of the cell model with a major influence of G_{Na}. This result differs from what observed in the two–dimensional solution of the bidomain equations where the Na_O and K_O were seen to influence the ventricular activation time more than G_{Na} [304].

5.4.2 Forward analysis

Let now turn to evaluate the PDFs of the QoIs through a direct UQ strategy using the trained metamodel (see Table 5.2), rather than the full monodomain system. The metamodels, one for each QoI, are applied on a very large input dataset (10^6 samples) sampled using a Latin hypercube strategy to avoid clustering phenomena, and the corresponding output dataset is used to approximate the PDFs of the QoIs that are reported in Figure 5.6. The computational cost of this forward analysis using the metamodel trained for the sensitivity analysis is negligible (of the order of CPU-minutes), whereas the same forward direct analysis would have required 57 CPU-years using the initial electrophysiology equations (5.1).

Table 5.3: Statistical moments for t^*, t_4, t_{AV} and v_c. The means and standard deviations of the times are expressed in ms, the velocity in m/s.

	female t^*	female t_4	female t_{AV}	Male t^*	Male t_4	Male t_{AV}	v_c
mean	32.19	41.2	122.19	33.55	43.62	123.54	1.62
std	7.13	9.12	9.15	7.62	9.72	9.54	0.31
skewness	0.74	0.73	0.34	0.73	0.73	0.37	-0.14
kurtosis	3.13	3.00	2.85	3.16	3.05	2.90	1.96

The PDFs of the activation times t^* and t_4 have a similar skewness and kurtosis for both, male and female population but with a larger mean value, respectively of 6.4% and 5.8%, for the former, see Table 5.3. On average, t^* corresponds to what observed in–vivo (about 30 ms [16]), even if the high standard deviations resulting from our forward analysis implies that it is not uncommon to have longer activation times. According to the PDFs, the probability of a normal/physiological activation time of the AV-node corresponding to a t^* comprises between 20 and 50 ms is equal to 97.6% for females and 96.3% for males, where in both cases the positive skewness of the PDFs favors longer activation time with respect to the mean t^* rather than shorter ones. Specifically, the probability of

experiencing an AV activation time shorter than 10 ms is about 0, whereas a t^* shorter than 20 ms has a probability to occur of 0.7% and 0.5% for females and males, respectively. On the other hand, the probability of having an AV activation time greater than 50 ms is larger for the males population (3.2% probability) than for females (1.6% probability).

The PDF of the activation time at the downstream tip of the AV-node t_{AV}, is shown in Figure 5.6(c), while the statistical moments are reported in Table 5.3. As could be inferred from the Sobol' indices, the sensitivity of t_{AV} on the time delay in the AV, AV_d, reduces the differences between the PDFs of males and females with relative difference of the mean values of about 1.1%. Furthermore, the statistical dispersion for t_{AV} (evaluated by variation coefficient σ/μ), is also reduced (-7.4% for females and -7.7% for males) with respect to the one observed in t^* (-22.1% and -22.7 %) The PDF for the t_{AV} results in line with the medical knowledge, with an about null probability of activation time higher than 150 ms that would compromise a timely ventricular contraction. [16].

As it could have been anticipated by noting that the Sobol' index corresponding to the volume parameter is about null, no differences are present among the PDFs of the v_c for the males and females population shown in Figure 5.6(d). Moreover, the PDF skewness is a consequence of the nonlinear relation between the conduction velocity and the electrical conductivity documented in appendix 5.8. Specifically, as a symmetric PDF around its mean has been considered to model the uncertainty of the electrical conduction, the probability of v_c to be slower (faster) than the physiological lower (upper) bound of 1 m/s (2 m/s) is below 0.5% (13%).

5.5 Discussion and future developments

In this work, we have investigated the global sensitivity analysis of the electrical activation of the atrial fast conduction network on the geometrical and electrical input parameters of the electrophysiology model. The network has been modelled as four mono–dimensional bundles, with three of them connecting the SA-node to the AV-node whereas the last one joins the right with the left atrium. The propagation of the electrical depolarization front through the myocardium is governed by the bidomain equations, which, in the case of a one-dimensional domain, are equivalent to the monodomain model. The uncertainty PDFs of these input parameters have been taken from the experimental data available and the gender difference has been accounted for in the UQ analysis by considering two different PDFs for the atrial volume of the females and males population. Moreover, the PDF of the electrical conduction has been obtained through an inverse calibration of the conduction velocity data from the literature. The UQ analysis is based on the PCE method with a different metamodel trained for each QoI on a training dataset, which is built running the full monodomain model. The risk of overfitting has been assessed by testing the metamodels performances against a testing dataset, which is independent of the training one,

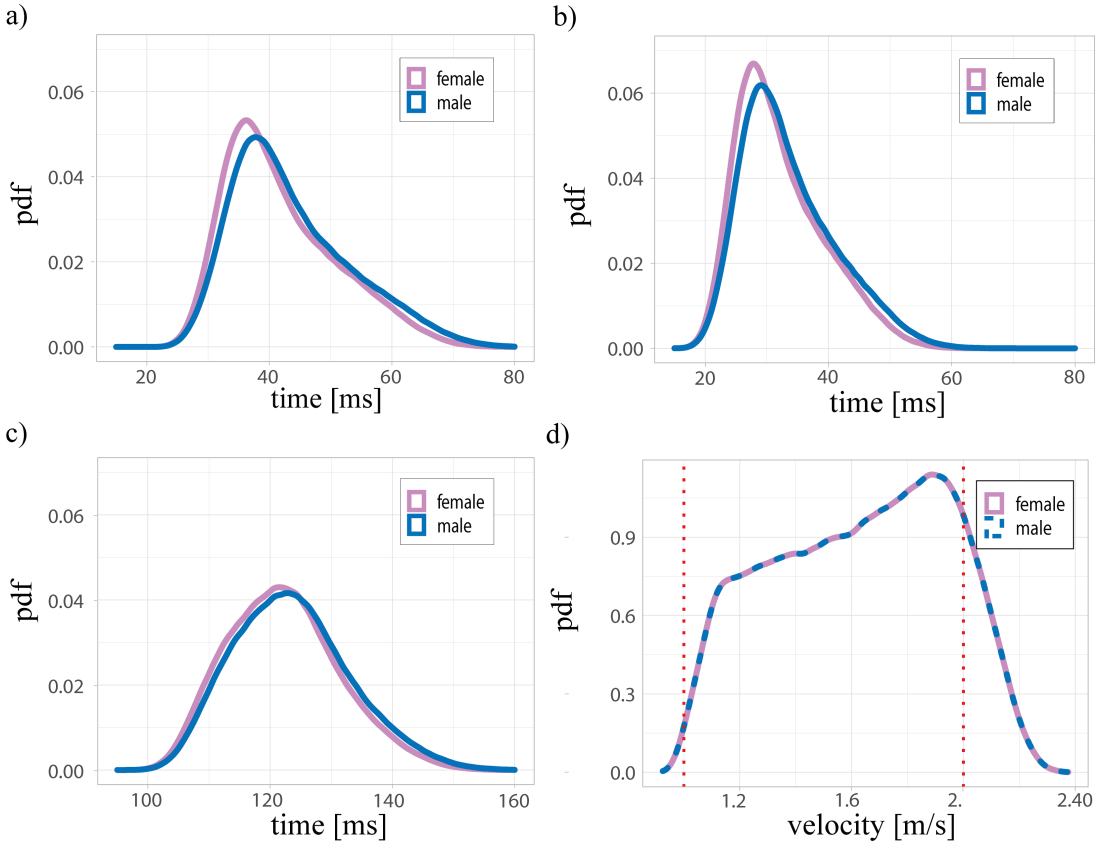

Figure 5.6: PDF of the QoIs obtained using 10^6 samples evaluated through the optimal metamodel: (a) t_4, (b) t^*, (c) t_{AV} and (d) v_c.

whereas the confidence intervals of the Sobol' indices, computed using the bootstrap technique, indicate that the sensitivity results are converged with respect to the size of the dataset used to train the metamodel.

For both the female and male population, the activation times of the atrial fast conduction network, t_4, t^* and t_{AV}, are seen to be sensitive to the electrical conductivity M, the atrial volume V and the temporal delay in the AV AV_d with a total effect on their variance exceeding 95 %. Importantly, the relative positions of the internodal pathways that, to the authors' knowledge, can be hardly measured in–vivo and are not sufficiently documented in the literature only play a marginal role in the activation of the atrioventricular node according to the Sobol' indices (total effect on the QoI variance below 5 %). According to our results, these geometrical input parameters could be disregarded in future UQ analyses. The smaller atrial volume (on average) of the female population leads to a reduced effect of this input parameter on the variance of the QoIs compared to the males population, in particular the Sobol' total order of V reduces from 0.21 to 0.17 for t^* and from 0.20 to 0.16 for t_4 . Consequently, the other inputs have a larger effects on the QoIs in the female population, as an example, the sensitivity of t^* (t_4) on M and G_{Na} increases from 0.71 and 0.034 (0.75 and

0.0351) in the male population to 0.74 and 0.035 (0.78 and 0.0354) in female one.

On the other hand, the conduction velocity is only sensitive to the electrical conduction (with an effect of about 95%) and to the maximal I_{Na} conductance (G_{Na}, with an effect of about 5%) while the other ten input parameters, including the extracellular Na concentration, Na_O, and the extracellular K concentration, K_O, have a negligible effect on the QoIs variance. This result differs from what observed in the solution of the bidomain equations in a multi–dimensional domain where both the extracellular Na concentration, Na_O, and the extracellular K concentration, K_O, were seen to have a greater effect on v_c with respect to G_{Na} [217, 304]. As a consequence, isolating the internodal pathways from the surrounding three–dimensional myocardium yields to a smaller input parameter space and, consequently, to a reduced computational cost for future UQ studies.

It should be noted that both the electrical activation of the network and the conduction velocity are insensitive to the parameters of the electrical stimulation (stimulus intensity S_d, stimulus amplitude S_a and size of the SA-node SA_l) and any simulation protocol able to originate the depolarization front is suitable in such electrophysiology models. Further studies, however, could assess the possible differences in the electrical activation of the electrical pathways if the SA-node is modeled using a three–dimensional geometry integrated in the electrical network rather than as a localized in put current as done in this work [310, 311].

The same metamodels used in the sensitivity analysis have been then used to determine the uncertainty PDF of the QoIs (forward UQ analysis) by producing a large dataset of 10^6 elements. The PDFs of the activation times are characterized by a positive skewness (i.e. with a longer right tail with respect to the left one) while the conduction velocity has a negative one. The PDFs of t_4 and t^* have a high statistical dispersion equal to $\sigma/\mu \approx 20\%$, while t_{AV} has a smaller dispersion (about 7.5%) owing to the higher sensitivity on the AV-delay, AV_d. The PDF of the activation times well agrees with the medical knowledge [16] with a probability for the AV-node to be reached by the electrical stimulus (t^*) in less than 20ms or more than 50 ms below 0.7% and 3.2%, respectively (for both males and females population), while t_{AV} has an almost zero probability of being higher than 150 ms. We recall that the activation time of the ventricular tip of the AV-node t_{AV} plays a major role in the synchronization of atrial–ventricular contraction and if t_{AV} is not sufficiently long the ventricles would start contracting before the end of atrial systole, thus yielding to an inefficient blood pumping. Although the activation time of the whole atrial myocardium is known from the clinical evidence to have an average depolarization time of 148.8 ms with a standard deviation of 18.9 ms [312], these data can only be considered as an upper bound with respect to the activation time of the fast conduction bundles that is studied here. Indeed, the high conductivity structures should be fully activated before the surrounding myocardium depolarizes, which is in line with our UQ analysis where the average time needed for the electrical signal to reach the AV-node, t^*, results equal to 32.19 ms (33.55 ms) for the females (males) population. More-

over, for both genders t^* is less than the lower bound of the activation time of the three–dimensional myocardium reported in the literature (defined as the mean value minus three times the standard deviation $148.8\text{ ms} - 3 \cdot 18.9\text{ ms} = 92.1\text{ ms}$) with a probability exceeding 99%.

The uncertainty PDFs of the conduction velocity v_c is seen to be skewed towards the high velocity range as it has been previously observed in the case of electrical conduction within the atrial myocardium by randomly perturbing both fibers orientation and local conductivities [29]. This result can be probably explained by the non-linear relationship between the electrical conductivity and the conduction velocity reported in appendix 5.8, which means that considering a symmetric PDF of the electrical conductivity automatically introduces a skewness in the conduction velocity distribution and, eventually, in the PDFs of the other QoIs. Alternatively, considering a symmetric uncertainty PDF for the conduction velocity, it would greatly reduce the marked skewness phenomenon in the forward analysis, thus suggesting to use the conduction velocity as input parameter rather than the electric conduction. Nevertheless, proper calibration of the electric conduction could solve the problem of considering uniformly varied inputs with the consequent output asymmetry, and the model reduction carried out here offers a starting point for a Bayesian inverse calibration of the electrical conduction–conduction velocity from the available experimental measurements of the AV-activation time t^*. The sensitivity analysis, indeed, shows that the time needed for the depolarization front to reach the AV, t^*, basically only depends on M and V (with a reduced influence of G_{Na}) and all these quantities but M can be measured through non-invasive medical procedures such as MRI for the atrial volume [305] and ECG for t^* [312]). This is the optimal context for Bayesian inverse calibration where only an input parameter is unknown, which can be retrieved knowing the PDFs of the other physical quantities at play [313, 314]. Similar techniques used in the framework of MICP (monodomain inverse conductivity problem) to calibrate space-dependent conductivity for two-dimensional [181] and three-dimensional [301] models can be adapted to the one-dimensional problem proposed here. Even the presence of local perturbations of conductivity can be taken into account both in the direct and inverse problem, possibly exploiting a multi-fidelity method applied using the monodomain as a high fidelity model and a simplified alternative (e.g. eikonal) as a low fidelity one [29].

A natural extension of the present UQ analysis would be to include the effect of the fast conduction bundles on the three–dimensional myocardial tissue surrounding them, thus allowing to investigate further QoIs commonly used in the medical field, such as the atrial activation time (that is expected to depend on the stimulus location [315]), the uniformity of the depolarization front propagation and the action potential duration [316, 217], which are known to be relevant for the patient's health as they influence the efficiency of the atrial systole [16]. Given the proposed decomposition between the fast structures and the underlying three-dimensional fiber, the model to be used. The anisotropic and heterogeneous myocardium could also be modelled using the new fractional models [165, 317], which show promising results in cardiac dynamics and can naturally integrate

techniques for the calibration of the model parameters [182]. Furthermore, in addition to the healthy myocardium [318, 319, 240, 245] the effect of pathologies can be included in the UQ analysis by accounting for modified electrical properties of the conductive medium [320, 321, 322]. As the electrical signal travels from the atria to the ventricles passing through the AV, this analysis could be also extended by adding the ventricular fast conduction bundles (including the Purkinje network) to investigate how sensitive is the ventricular activation to atrial dysfunctions such as atrial fibrillation [323]. A further open question calling for dedicated UQ studies, is the effect of the stimulation frequency on the action potential duration and the depolarization front propagation and, interestingly, the most relevant input parameters of the cellular model are expected to strongly depend on the stimulation frequency itself [223, 224, 303].

5.6 Appendix: Convergence of the electrophysiology model

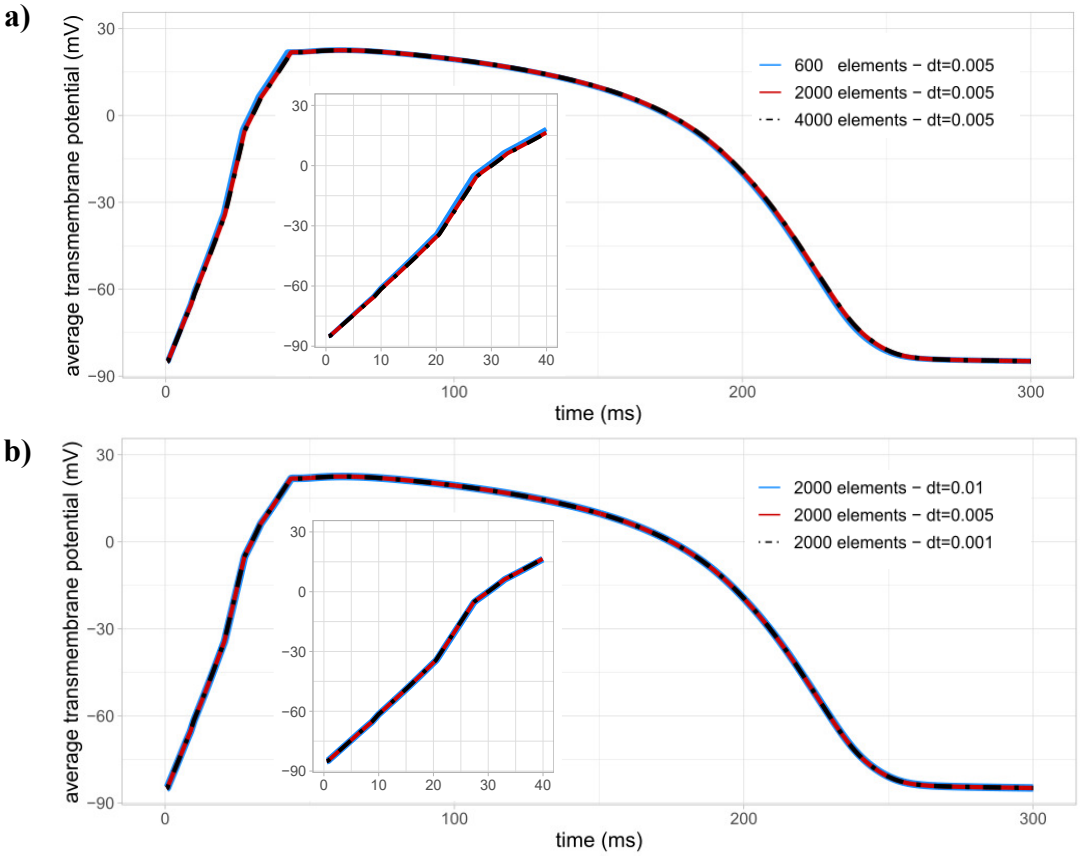

Figure 5.7: Time behaviour of the average transmembrane potential in the atrial fast conduction network by refining a) the spatial and b) the temporal resolution. The insets show the same quantity within the initial fast depolarization phase.

The transmembrane potential averaged over the ventricular domain as a function of time is shown in Figure 5.7. Each solid curve corresponds to a different simulation of the monodomain equations with the ten Tusscher-Panfilov model on a different grid with elements number varying from 600 to 4'000 and different time step sizes. [189]. The averaged transmembrane potential becomes basically grid independent for mesh resolution exceeding 2'000 elements and, based on this result, a mesh with 2'397 elements (corresponding to a $\Delta_x = 0.25$ mm) and $\Delta t = 0.005$ ms is used for the UQ analysis. The corresponding computational cost to run a single simulation is of about 30 CPU-minutes and, consequently, the cost to build the UQ datasets is of about 42 CPU-days. The numerical simulation have been run on an Intel Xeon Processors [E5-2620 v3 - 15M Cache, 2.40 GHz], with 16 CPUs.

5.7 Appendix: Convergence of the PCE analysis

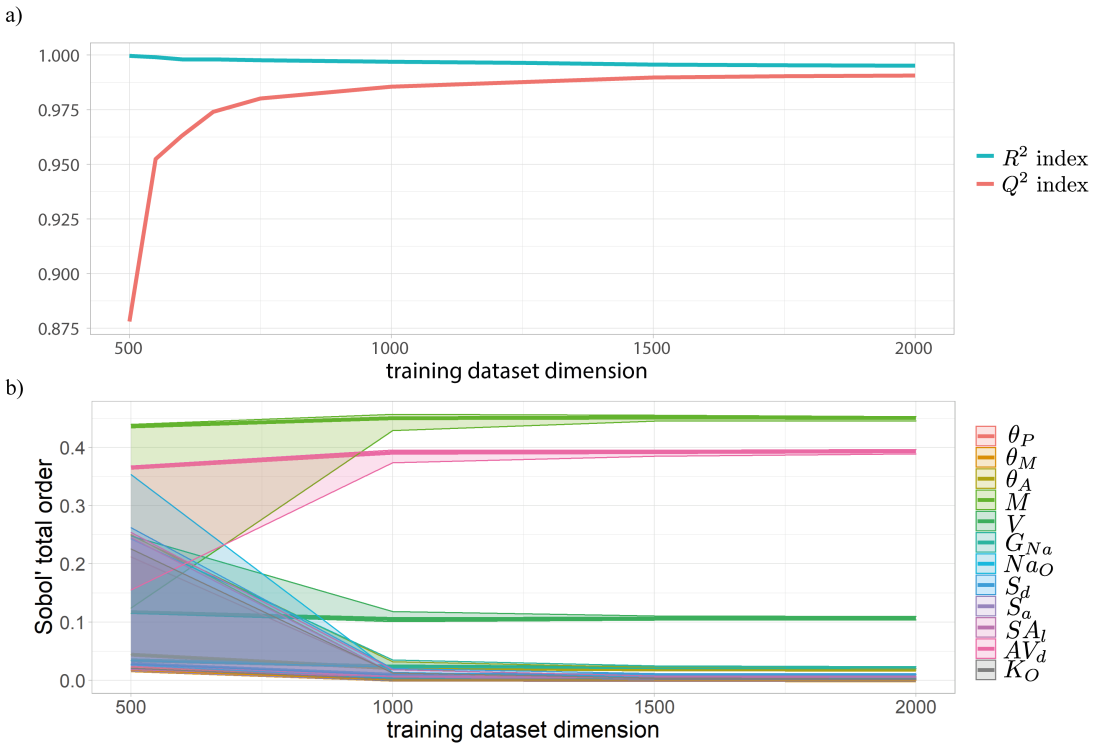

Figure 5.8: (a) R^2 and Q^2 indices for t_{AV} of the female dataset. Indices are reported for an increasing size of the training dataset and a fixed testing dataset of size 200 is used to compute the corresponding Q^2 index. (b) Stability analysis of Sobol' indices for t_{AV} on the female dataset with 5-percentile confidence intervals calculated using a bootstrap methodology.

Figure 5.8(a) shows the coefficient R^2 and Q^2 introduced in section 5.2 for the

case of t_{AV} in the female population as a function of the training dataset size. The optimal metamodel (see Table 5.2) is trained each time using a different training dataset with size ranging from 500 to 2'000 and tested against the same testing dataset made of 200 samples. The R^2 index is stable with respect to the training data set size as the number of samples is larger than 500, which means that the variety of the metamodel is sufficient to describe the physical phenomenon at study. Conversely, lower size of the training dataset lead to a suboptimal value of the index Q^2, which corresponds to a reduced ability of the metamodel to predict values outside the training sample. Hence, the convergence of the difference R^2–Q^2 indicates that the metamodel can be considered stable when the size of the training metamodel exceeds 1'000 cases. Similar results are obtained for the other QoIs and the males population (not reported here for the sake of brevity).

Another approach for testing the metamodel performance consists of evaluating its stability to a perturbation of the training dataset. Specifically, the results of the UQ analysis are shown as a function of the dataset size thus determining for what size they become stable, as shown in Figure 5.8(b) where the Sobol' indices are seen to be stable for dataset size larger than 1'000. The figure also reports the 5-percentile confidence intervals calculated using a bootstrap method on the training dataset.

5.8 Appendix: Electrical conductivity vs conduction velocity

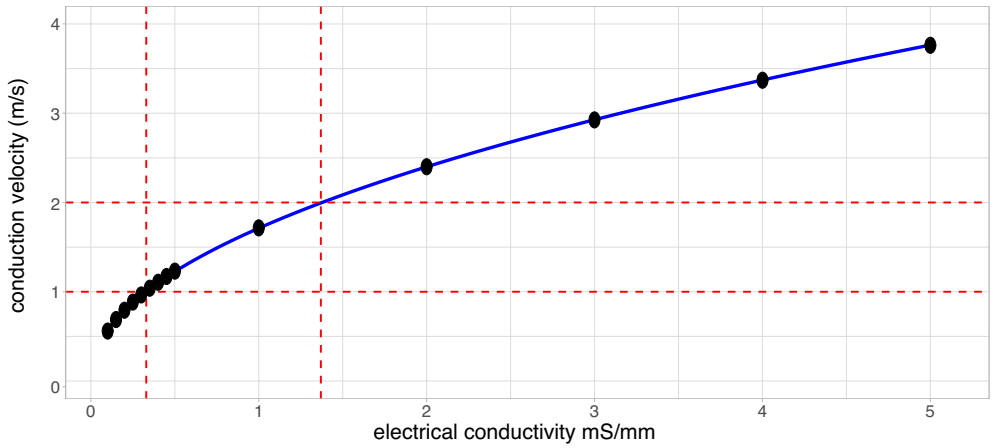

Figure 5.9: Conduction velocity as a function of the electrical conductivity (black dots) with superimposed a square root interpolation function (blue line). The straight red lines indicate the ranges of the electrical conductivity and of the conduction velocity studied in the UQ analysis.

The electrical conductivity M is an important input parameter of the electrophysiology model. However, most of the available measurements in the liter-

ature refer to the conduction velocity rather than to the electrical conductivity [16, 22, 24, 306]. For this reason, an inverse calibration has to be preformed to determine the electrical conductivities corresponding to the conduction velocities measured experimentally. In order to determine such relation between the electrical conductivity and the conduction velocity, the monodomain equations have been solved over a one–dimensional straight domain of length 100 mm for several electrical conductivity values. The corresponding conduction velocity is measured by selecting two points 50 mm apart each other inside the domain and monitoring their activation time (defined as the instant when the transmembrane potential exceeds -70 mV). The conduction velocity is thus measured as the ratio between the distance between the monitoring points and the time interval among their activation and is reported in Figure 5.9 for spatial and temporal discretization of $\Delta x = 0.25$ mm and $\Delta t = 1 \cdot 10^{-3}$ ms and current stimulus applied at one tip of the domain as defined in equation (5.2) with S_d =2.5 ms, S_a =1 mA/mm^2 and $SA_l = 6.85$ mm.

Acknowledgements

This study has been performed with support of the Grant 2017A889FP 'Fluid dynamics of hearts at risk of failure: towards methods for the prediction of disease progressions' funded by the Italian Ministry of Education and University.

Author Contributions

G.D.C., R.V., F.V. designed the research. G.D.C. carried out the numerical simulations and the UQ analysis. G.D.C. and F.V. wrote the paper with inputs from R.V.

Chapter 6

GPU accelerated digital twins of the human heart open new routes for cardiovascular research

Francesco Viola, Giulio Del Corso, Ruggero De Paulis, and Roberto Verzicco

manuscript in preparation

Abstract

The recruitment of patients for rare or complex cardiovascular diseases is a bottleneck for clinical trials and digital twins of the human heart have recently been proposed as a viable alternative. In this paper we present an unprecedented cardiovascular computer model which, relying on the latest GPU–acceleration technologies, replicates the full cardiac dynamics within a few hours. This opens the way to extensive simulation campaigns to study the response of synthetic cohorts of patients to cardiovascular disorders, novel prosthetic devices or surgical procedures. As a proof–of–concept we show the results obtained for left bundle branch block disorder and the subsequent cardiac resynchronization obtained by pacemaker implantation. The in–silico results closely match those obtained in clinical practice, confirming the reliability of the method. This innovative approach makes possible a systematic use of digital twins in cardiovascular research, thus reducing the need of real patients with their economical and ethical implications. This study is a major step towards in–silico clinical trials in the era of digital medicine.

After the initial phase of research and development, the standard route for the transfer of a novel treatment to clinical practice is through randomised trials. In fact, every human is one of a kind and the efficacy of a new therapy can

be assessed only via statistical analyses on large cohorts of patients. These are collected into randomised homogeneous groups and subjected to different treatments to compare the outcome of the new therapy with the established ones.

However, recruiting enough participants for trials on rare or complex diseases could be very challenging while biased and incomplete cohorts yield inconclusive or misleading results. Paradoxically, clinical trials can thus become a barrier preventing some patients from accessing innovative treatments (not to mention the ethical question associated with sub–optimal or placebo therapies applied to some trial control groups).

The generation of synthetic data by high–fidelity computer models might be an effective strategy to mitigate the above issues and this is one of the main aims of digital medicine.

In fact, these models are referred to as digital twins and, when provided with appropriate input parameters, they can be used to surrogate real patients with 'on demand' features. In this way, the completion of thorough and cost effective clinical trials could be possible even in those cases in which enrolling a patients cohort would be challenging.

The advantages of digital twins are huge since not only they can produce specific data but, in principle, they can anticipate the outcome of a surgical procedure, the progression of a disease or the performance of an implanted device thus shifting the medical paradigm from decisions based on past experience to predictions guided by virtual models.

Considerable efforts have been made in the last decade to produce digital twins for clinical applications and cardiac modelling has been among the fastest growing fields. Leaving aside the wealth of literature dealing with individual parts of the heart, recent examples include the computational investigation of electromechanical features [324, 325], the influence of cardiac contraction on the electrocardiogram (ECG)[326] and of the heart rate variability [327]; the recent review Sung et al. [328] gives a detailed account of whole–heart electromechanical models.

Models including the hemodynamics are more scarce and the flow is often parametrised by simplified laws, as by considering only the blood pressure within each heart chamber while all valves are reduced to viscous resistances[329] or by introducing a more realistic hemodynamics within a bi–ventricular configuration with simple lumped models for the heart valves[330]. More recently, an accurate model which includes the atria and the hemodynamics has been proposed [331], although only the systolic function is considered and, therefore, the sealed atrio–ventricular valves are modelled as impermeable plane disks while the fully open semilunar ones as circular holes.

From the above literature review, it appears that implementing a truly digital twin for the whole heart, capable of simulating all the features throughout the heartbeat is a formidable task which has not been fully accomplished yet. Furthermore, in order for a digital twin to be reliable and predictive, it must reproduce all the relevant dynamical details of the real counterpart thus requiring hundreds of million degrees of freedom. Even on modern supercomputers, such

models entail simulation times of weeks or months and this prevents their routine clinical use: overcoming such limitation has huge cardiovascular potential and this has motivated the present work.

In this paper we present a groundbreaking virtual heart model coping with all the main features of the cardiovascular function: it accounts of the dynamics of the complex biological tissues both, active myocardium and passive valves, the transitional and turbulent hemodynamics, the myocardium electrophysiology and their strongly coupled interactions. The complete computer model uses up to one billion of spatial degrees of freedom and half a million time steps per heartbeat to capture with uncompromised accuracy the complex heart dynamics. The resulting huge computational burden is tackled by the latest graphics processing units (GPU) technologies which reduce the time–to–solution from months to hours [332].

In the following we show first some results for a healthy heart with a physiologic function then, by disconnecting the electrical conduction between the atrio–ventricular node and the left bundled branch, we induce its block and observe a deterioration of several cardiovascular indicators similarly to the clinical experience. Starting from this impaired configuration, cardiac resynchronization is simulated by pacemaker therapy and a small clinical trial is generated by varying the position of the implanted lead within the left ventricle. The outcome of the various virtual treatments is discussed in the light of the clinical experience (of one of the authors) and perspectives for future work are finally given.

Results

The quantities of interest, used to monitor the heart function and their dynamics, are obtained by our computer model whose details are given in the section *Methods*. Here we add that the heart, including the four cardiac valves and main arteries/vessels, is properly located in a human torso (see Fig. 6.1a-d) and, during the simulations the electrical signals reaching the skin surface are detected to produce synthetic ECGs.

In fact, in addition to the composite heart elastomechanics and hemodynamics [333], the model accounts also for the complex, hierarchical structure of the electrophysiologic system [334], therefore it produces a realistic source of electric potential which propagates throughout the body.

Owing to the inherent human variability, defining a representative geometry of a heart is a problem in itself and two opposite directions can be taken: *i*) replicating the heart of a particular individual (patient–specific model) or *ii*) modelling a 'normal' organ with average properties. In this case the latter approach was pursued with the shape of each chamber, the local thickness of the tissues and their fiber directions obtained by surgical atlases [335] or measurements whose means and standard deviations are reported in Table 6.1. It is worth mentioning that the heart resulting from these parameters does not belong to any specific individual but it rather exemplifies a standard configuration representative of

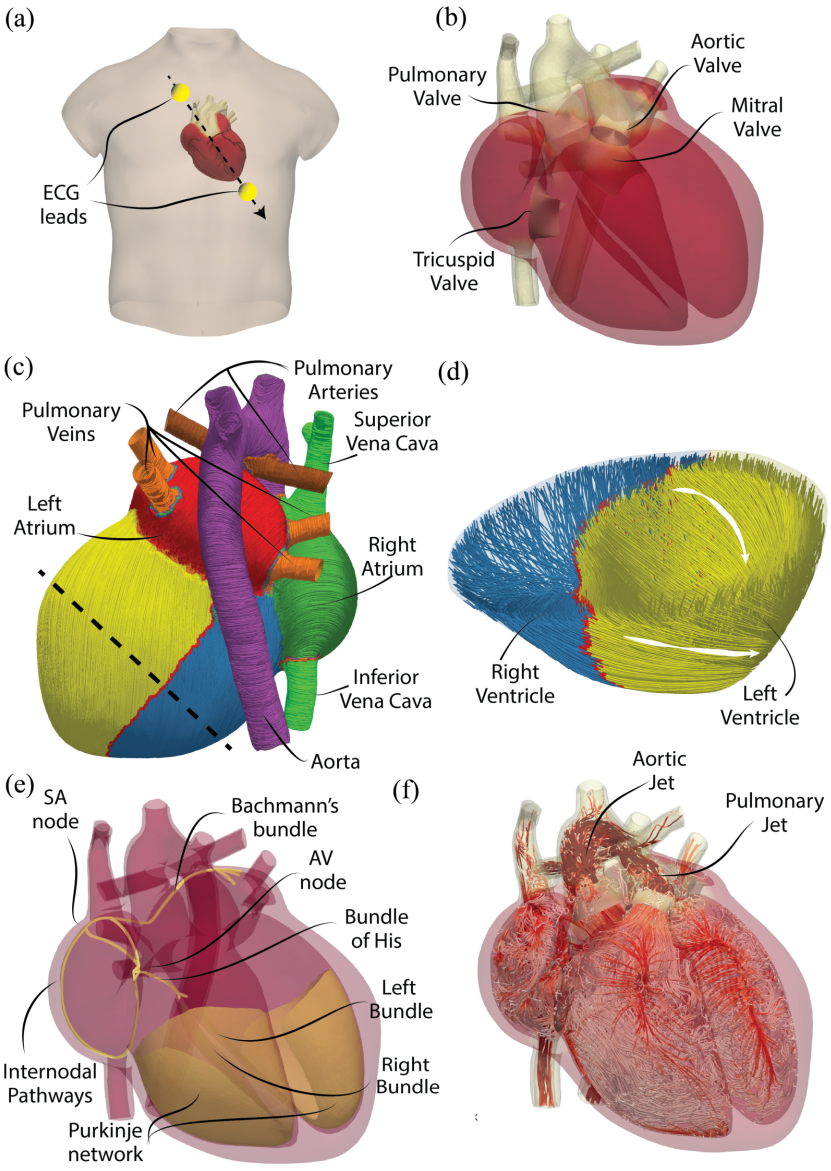

Figure 6.1: **Geometrical and topological features of the cardiac digital twin.** **a,** Location of the heart model in a human torso and position of two virtual electrodes with which the ECG is computed. **b,** Geometrical assembly of the heart model with the main elements, including veins and arteries. **c,** Zonal separation of the heart with the external fibers orientation; the black dashed line is the trace of the cutting plane of panel d. The active and passive mechanical properties of the tissues are specific of each heart structure. **d,** Plane section through the apical region of the ventricles to show the fibers orientation across the myocardium thickness. Note that the active contraction of the myocardium occurs along these directions thus yielding anisotropic and inhomogeneous features. **e,** Hierarchical structures of the electrophysiological system: the conduction velocity of the electrical signal is position dependent. **f,** Instantaneous snapshot of the flow streamlines coloured with the velocity magnitude (0 m/s white, 1.5 m/s dark red); the clustering of lines in the ventricles evidences a swirling motion while the dark regions in veins and arteries show intense flows.

the heart of adult humans.

A typical run consists of a couple of initial heartbeats, during which the transient is accommodated, followed by ten cycles which are used to extract phase averaged quantities and statistics; each simulation lasts ≈ 12 hours per heartbeat on 8xA100 Nvidia cards and produces a database of ≈ 8 Tbytes to be analysed by successive postprocessing.

Physiologic conditions. The reference healthy case is generated by running the model under nominal conditions and some representative results are given in the figures respectively for the electrophysiology, hemodynamics and the tissue mechanics.

Fig. 6.2 shows the depolarization pattern which starts from the sino–atrial node and quickly proceeds through the atria via the fast conducting bundles. The signal then slows down in the atrio–ventricular node for about 100 ms to allow the fully contracted atria to complete the filling of the relaxed ventricles. A quick propagation follows along the His bundle and the Purkinje fibers to depolarize the ventricles and lead to their strong (almost) synchronous contraction.

The electrically driven contraction and relaxation of the tissues squeezes the blood from atria to ventricles and then to veins and arteries following precise directions which are ensured by the passive opening and closing of the heart valves. Fig. 6.3 shows the flow structure during several instants of the heartbeat and, since a single planar section cannot describe the complex structure of the heart, the flow on two different planes for the left and right heart is shown.

For the sake of completeness, in Fig. 6.4, the intensity of the tissue contraction is visualised through tension stress along the tissue fibers with results which are complementary to the activation potential of Fig. 6.2 and the produced hemodynamics of Fig. 6.3.

Although a high–fidelity digital model makes easily accessible the complex three–dimensional dynamics of the various heart systems the same is not true in the routine clinical practice which, instead, relies on simpler quantities that can be directly measured or inferred through standard analyses. Examples are the pressure variations during a heartbeat, the volume of the left ventricle and the ejection fraction or the ECG as shown at the bottom of Fig. 6.4.

The values obtained for the healthy configuration are 127/76 mmHg for systolic/diastolic pressure, $\approx 50.5\%$ for the ejection fraction and an ECG trace showing the appropriate duration of the QRS complex and T wave.

We wish to stress that all these quantities have obtained as part of the model results without additional inputs other than the electro–mechanical properties of the system thus providing evidence of its predictive capability.

Pathological left bundle block. A further step forward for the model assessment is to show that not only it behaves correctly in healthy physiologic cases (for which it has been designed) but it also reproduces the pathological conditions of a specific induced disfunction. In order to accomplish this goal, we have disconnected the electrical conduction between the atrio–ventricular node and the left His bundle (Fig. 6.5c) thus causing a left bundle block disorder.

The immediate consequence is that the tissue depolarization proceeds quickly

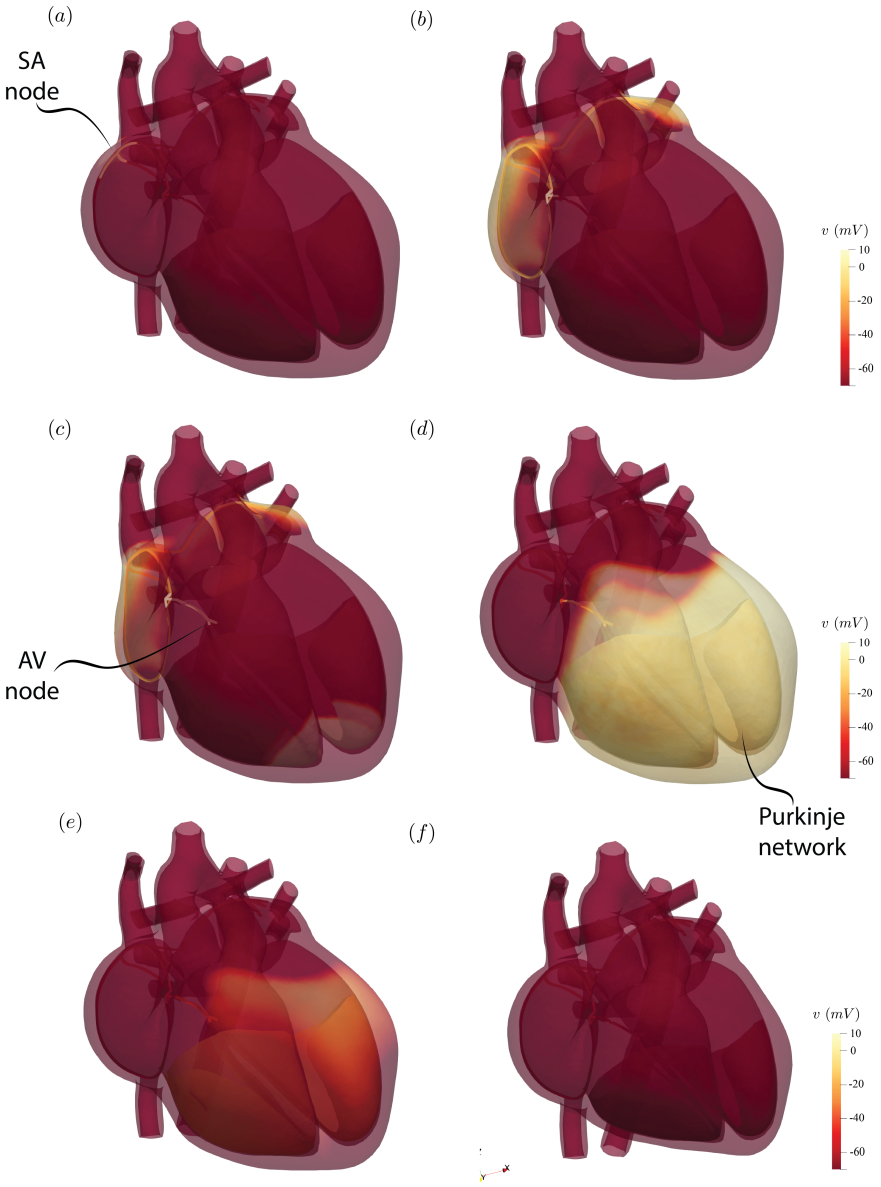

Figure 6.2: Instantaneous snapshots of the activation potential during the heartbeat: **a,** the sino–atrial node 'sparks' the initial triggering signal ($t \simeq 0$ s); **b,** The electrical signal spreads quickly, via the internodal pathway, across the atrial tissue and depolarises them ($t = 160$ms); **c,** The signal reaches the atrio–ventricular node where it is delayed by ≈ 100 ms by the very small conduction velocity of the signal in that region ($t = 190$ms); **d,** At $t = 395$ms, the activation potential has spread through the bundle of His, the Purkinje fibres and the myocardial tissue of the ventricles; **e,** While the myocardium repolarises a vigorous contraction starts ($t = 460$ms); **f,** The ventricles attain the strongest contraction at $t = 560$ms, a long relaxation period follows until the beginning of the next heartbeat.

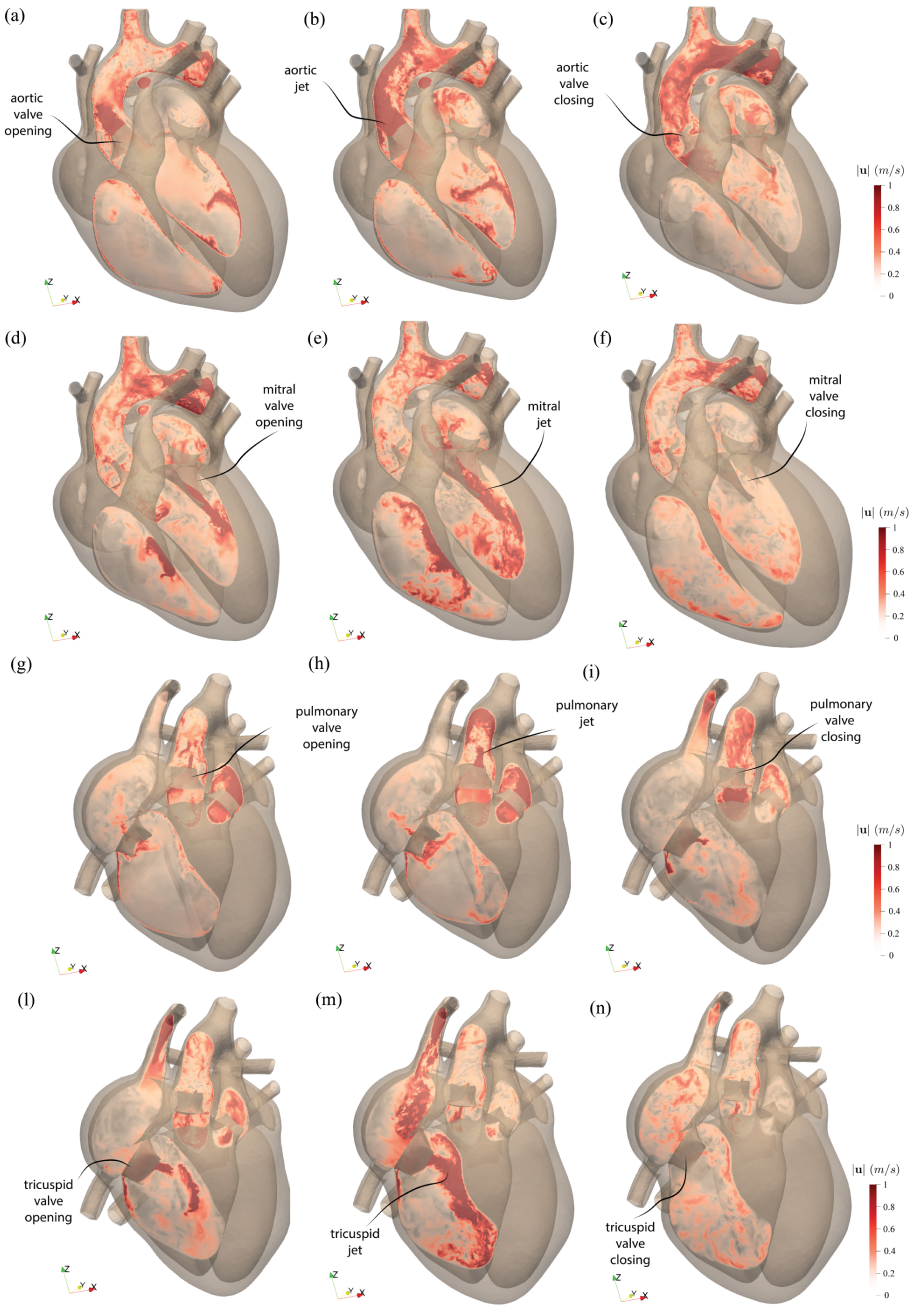

Figure 6.3: Instantaneous snapshots of the blood velocity magnitude over plane sections crossing the left (**a,**–**f,**) and right (**g,**–**l,**) parts of the heart. The left plane position is such to cross in the middle the mitral and aortic valves. Similarly, the right plane crosses the pulmonary and tricuspid valve. **a,** and **g,** $t = 500$ms, **b,** and **h,** $t = 540$ms, **c,** and **i,** $t = 600$ms, **d,** and **j,** $t = 620$ms, **e,** and **k,** $t = 680$ms, **f,** and **l,** $t = 780$ms.

Parameter	Source	Population (female)	Normal range	Digital heart
LV end diastolic volume (ml)	[336]	800(462)	75-211	176
LV end systolic volume (ml)	[336]	800(462)	37-101	86
LV stroke volume (ml)	[336]	800(462)	56-136	90
LV ejection fraction (%)	[336]	800(462)	48-68	51
RV end diastolic volume (ml)	[336]	800(462)	110-254	189
RV end systolic volume (ml)	[336]	800(462)	41-129	98
RV stroke volume (ml)	[336]	800(462)	77-117	91
RV ejection fraction (%)	[336]	800(462)	42-66	48
LA max volume (ml)	[336]	795(462)	28-104	75
LA stroke volume (ml)	[336]	795(432)	18-62	38
LA ejection fraction (%)	[336]	795(432)	46-74	51
RA max volume (ml)	[336]	795(432)	30-130	84
RA stroke volume (ml)	[336]	795(432)	9-61	35
RA ejection fraction (%)	[336]	795(432)	24-64	42
LV long axis diastole (mm)	[196]	52(26)	62-98	92
LV short axis diastole(mm)	[196]	52(26)	36-48	50
LV sphericity index diastole	[196]	52(26)	0.40-0.64	0.54
RV long axis diastole (mm)	[337]	41(21)	71.0-81.0	79
RV short axis diastole (mm)	[337]	41(21)	27.0-33.0	32
Aortic annulus diameter (mm)	[338]	3370(1156)	17.4-27.1	23
Pulmonary annulus diameter (mm)	[338]	3997(1408)	19.5-30.8	22
Mitral annulus area (mm^2)	[339]	211(114)	460-1220	800
Tricuspid annulus area (mm^2)	[340]	209(116)	460-1260	800

Table 6.1: Normal ranges of cardiac parameters in healthy adults calculated as the mean value ± the standard deviation and corresponding parameters of the digital twin (normal electrophysiology case)

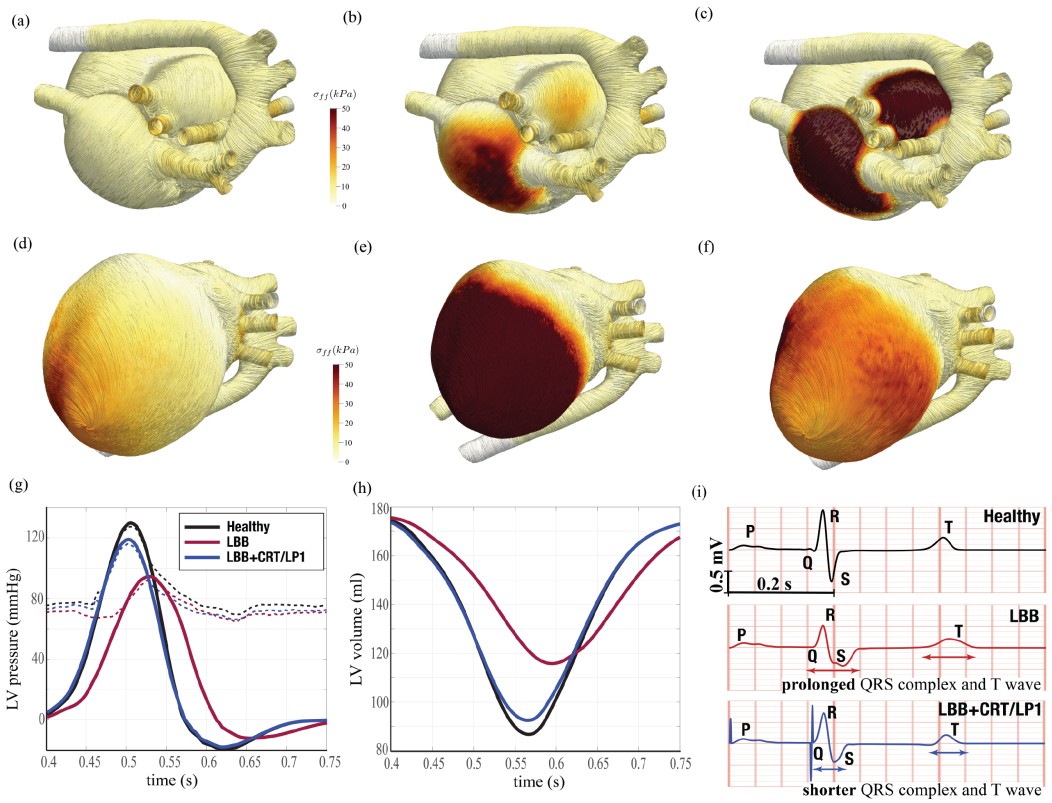

Figure 6.4: **a**–**f** Instantaneous surface distribution of the tension along the fibres axes (force per unit area) during a heartbeat; during diastole, when atria contract, the heart is viewed from above (panels **a**–**c**), during systole (**d**–**f**) the viewpoint is from below to evidence ventricles contraction. **a,** $t = 20$ms, **b,** $t = 120$ms, **c,** $t = 260$ms, **d,** $t = 460$ms, **e,** $t = 560$ms, **f,** $t = 640$ms. **g,** Time evolution of the left ventricle blood pressure during systole: black solid line for a healthy heart; red solid line for the impaired heart with a left bundle block; blue solid line for the impaired heart after resynchronization. The dashed lines have the same meaning as before but for the aortic pressure. **h,** Time evolution of the left ventricle volume during systole, the colour code is the same as in panel **g**. **i** ECG trace from the two sensors as in Fig. 6.1a), the colour code is the same as in panel **g**.

in the right ventricle along the Purkinje fibers but it is much delayed on the left counterpart as the activation potential can propagate only through the slow conducting myocardium: this is evident in Fig. 6.6b showing the largely polarized (not contracted) posterior region of the left ventricle compared with the fully contracted myocardium of the healthy case (Figs. 6.6a,g). The hemodynamics produced by the impaired left ventricle function yields a weak aortic jet evidenced by Fig. 6.6e. Also the myocardium contraction is consistent with the above picture and Fig. 6.6h confirms that the left ventricle fails to reach the same contraction strength as the right part.

Concerning the classical clinical indicators, we see that the peak left ventricle and aortic systolic pressures drop by about 30% (95/69 mmHg) and the systole duration is extended in the cycle. The ejection fraction decreases to a value of 34% with the ECG trace evidencing slower repolarization, prolonged QRS duration and QT interval which are all common indicators of the left bundle block disorder.

Effect of cardiac resynchronization therapy. Cardiac resynchronization therapy (CRT) is indicated in patients with heart failure evidenced by depressed ejection fraction and wide QRS complex in the ECG trace. In short, CRT consists of the implantation of a pacemaker which using artificial electrical signals restores the coordination of ventricles contraction. A common device is the biventricular pacemaker which has three leads implanted, respectively, in the upper part of the right atrium, in the apex of the right ventricle and in the posterior wall of the left ventricle. The leads are inserted via the upper vena cava and the left ventricle is reached passing through the coronary sinus; as a consequence, it can be implanted only in the regions crossed by its main tributary veins (Fig. 6.5a). On the other hand, the most appropriate positioning would be the latest depolarized point of the left ventricle whose position neither is known precisely nor is necessarily reached by a main vein. In Fig. 6.5d,e we show the optimum implantation point (hereafter indicates as LP1– *lead position one*), according to the above criteria, with the lead activation time tuned so to yield the maximum cardiac output. Fig. 6.6 show the activation potential, the hemodynamics and tissue contraction after the resyncrhonization therapy which exhibit features similar to the physiologic case. Further quantitative confirmation comes from the standard clinical indicators of Fig. 6.4g–i whose values and time evolution closely match those of the healthy reference case. In particular blood pressure values recover to 118/72 mmHg while the ejection fraction raises to 48% with the ECG trace which regains the physiologic timings.

Sub–optimal left–ventricle lead implantation. For real patients, instantaneous maps of the activation potential such as that of Fig. 6.5d are not available and the exact location of the latest depolarised left–ventricle region is not known a–priori. Furthermore, the main myocardium veins form a very sparse network thus the left–ventricle lead is unlikely to be implanted in the best possible position and the initial sub–optimal outcome is usually improved by successive tuning of timings and delays among the atrial and ventricular leads.

Nevertheless, depending on the particular lead position, the cardiac function improves only up to a given threshold and in Fig. 6.7 we report the results of a simulation campaign, in which the left ventricle lead has been implanted in five possible alternative positions. For each case, denoted by LP2–6, the activation time of the left ventricle lead has been tuned, by complementary simulations, so to obtain the best cardiac output similarly to the procedure following real implantation surgery. The data are presented in the same form as for the previous cases and, in the sake of conciseness, we avoid to show all the maps of activation potential blood flow and active tension distribution over the tissue; the emerging picture from the results of Figs. 6.7d–e is that the cardiac function improved in all cases although the recovery is the smaller the farther is the implantation point from the optimal position identified by the LP1 case. Similar indication comes from the ECG traces of Fig. 6.7f when comparing the duration of the QRS complex and the repolarization time delay with the values of the healthy reference case.

More quantitative data about the efficacy of the resynchronization procedure is summarised in Table 6.2 in which volumes, pressures and derived quantities are computed for all the simulated cases. As the position of the left ventricular lead is moved from the optimal position LP1 to the suboptimals ones LP2-6, the end systolic volume increases, thus corresponding to a decrease of the stroke volume, of the ejection fraction and of the peak systolic pressure.

Discussion

In this paper we have presented a proof–of–concept for the use of a human heart digital twin to study specific features of the cardiac function; the model has reproduced the physiologic behaviour when run in healthy conditions while pathological alterations have emerged after having induced a disorder. Finally, the same model has predicted the outcome of a resynchronization treatment aimed at restoring the cardiac function; in order to account for the inherent uncertainties related to the clinical procedure, different positions of the left ventricle pacemaker lead have been tested and the results have yielded the whole range of possible outcomes, from full recovery to marginal improvements.

The complete set of simulations presented in this paper can therefore be regarded as a proof–of–concept for a small clinical trial aimed at assessing the effect of uncertainty in the positioning of the ventricular lead of a pacemaker device. In real clinical practice this would be achieved by collecting data from different patients and performing a retrospective statistical analysis. However, each patient is different from the others, therefore when comparing different outcomes it is practically impossible to separate the effects of the surgical procedure from the epistemic variability of each individual.

In contrast, the present model produces different cases simply by changing one or more input parameters which, therefore, can be assigned to form a representative cohort of patients in clean, repeatable and controllable conditions.

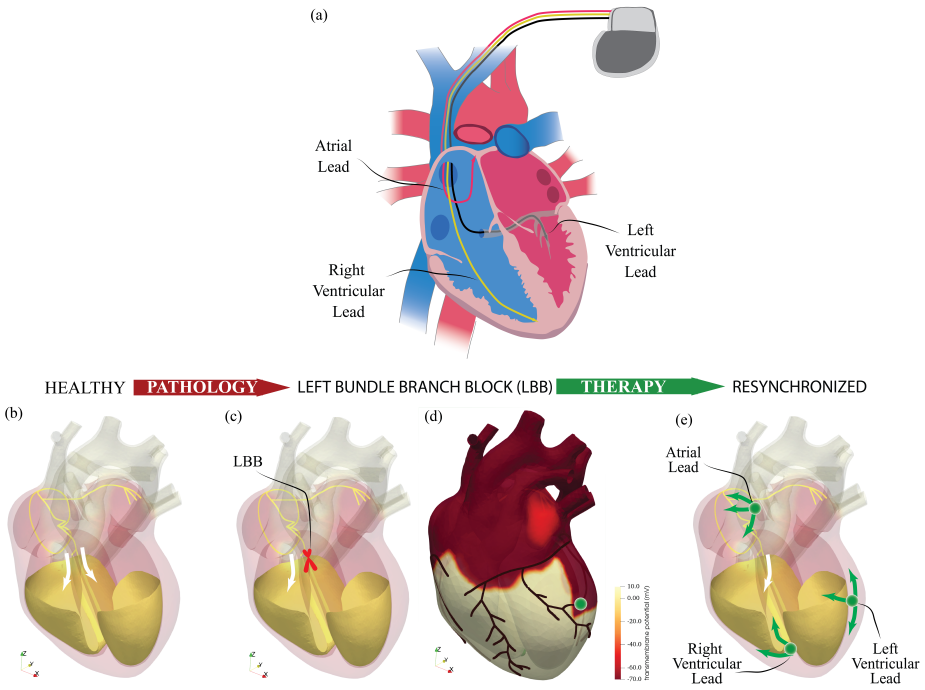

Figure 6.5: **a,** Sketch of the biventricular pacemaker device with the atrial lead (in red), right ventricular lead (in yellow) and left ventricular lead (in green). **b,** Arrangement of the fast conducting structures of the electrical signal in the heart. The two white arrows evidence the branching of the signal in the Bundle of His, after the Atrio–Ventricular node. **c,** The same as **a,** but with a red cross indicating the point where the electrical connection for the left side has been interrupted. **d,** Surface distribution of the activation potential in the myocardium (at $t = 316$ms) for a configuration as in panel **b,** with overlapped the position of the main veins; the green bullet indicates the optimal point for the lead implantation as it can be reached via the coronary vein and is located within the polarised portion of the tissue. **e,** Same configuration as in panel **b,** with the position of the three pacemaker leads. Note that in this configuration the atrial and right ventricle leads operate only as sensors since only the left ventricle lead is allowed to issue triggering signals.

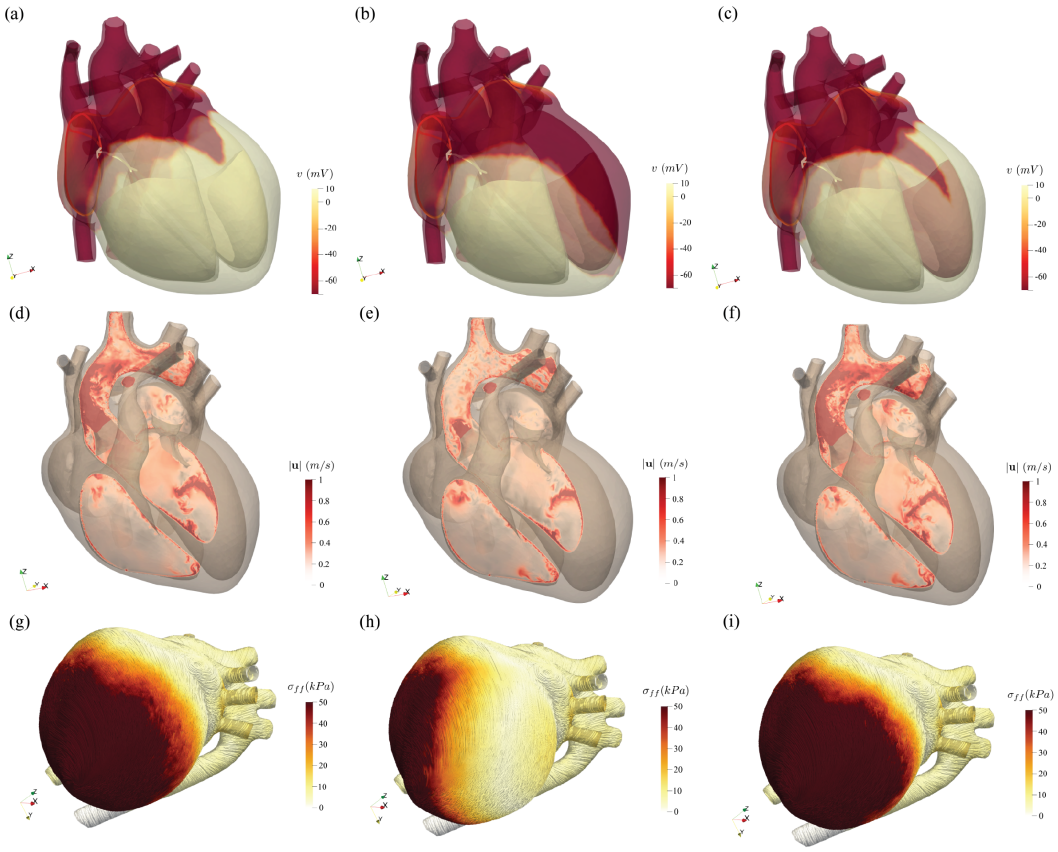

Figure 6.6: Comparison of different quantities for healthy (**a**, **d**, **g**), impaired (**b**, **e**, **h**) and resynchronized (**c**, **f**, **i**) hearts during systole. **a**–**c,** Instantaneous surface distribution of the activation potential ($t = 252$ms). **d**–**f,** Blood velocity distribution on a planar section cutting the left heart at peak systole ($t = 520$ms). **g**–**i,** Surface distribution of the tension along the fibres axes at peak systole (force per unit area, $t = 520$ms).

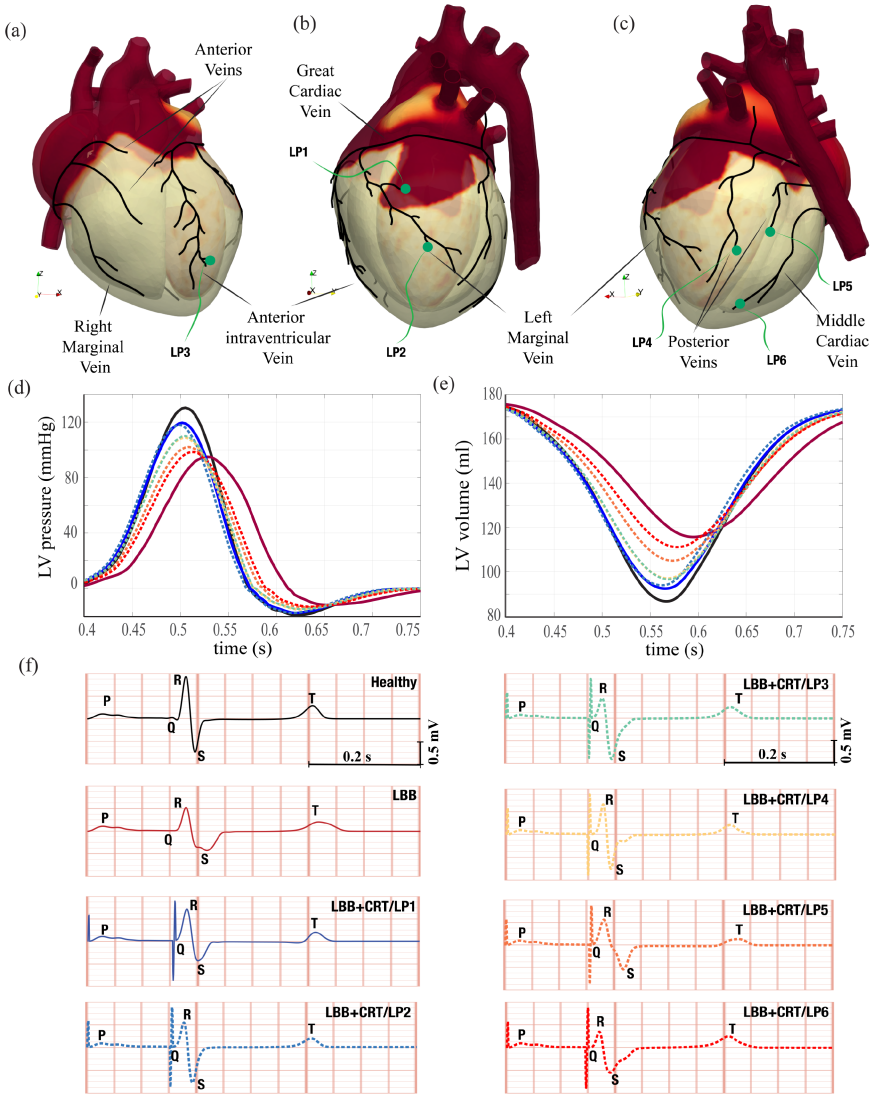

Figure 6.7: **a**–**c,** Views of the different possible positions for the left ventricular lead with a sketch of the main veins arrangement. **d,** Time evolution of the left ventricle blood pressure during systole: black solid line for healthy, red solid for impaired and blue solid for the heart after optimal resynchronization. The dashed lines represent the other resynchronization cases for different lead positions as detailed in panels **a**–**c**. **e,** Time evolution of the left ventricle volume during systole, the colour code is the same as in panel **d**. **f,** ECG trace from the two sensors as in Fig. 6.1a), the colour code and labels are the same as in previous panels.

Parameter	Healthy	LBB	LBB+CRT LP1	LBB+CRT LP2	LBB+CRT LP3	LBB+CRT LP4	LBB+CRT LP5	LBB+CRT LP6
LV end diastolic volume (ml)	176	176	176	176	176	176	176	176
LV end systolic volume (ml)	86	116	92	94	97	97	105	111
LV stroke volume (ml)	90	60	84	82	79	79	71	65
LV ejection fraction (%)	51	34	48	47	45	45	40	37
max LV pressure (mmHg)	130	95	120	118	110	109	102	98

Table 6.2: Main cardiac parameters as obtained from the model for the various healthy, pathological and treated cases. The labeling of the cases is the same as in figure 6.7.

In fact, clinical trials infer the quantities of interest (QoIs) by comparing the outcome of alternative treatments on different cohorts of homogeneous patients. These should include a number of individuals large enough to properly represent the statistics of the population in turn entailing a random sampling. This is equivalent to a Monte Carlo analysis (MC), which gauges the size N of the cohort needed to compute the statistics; since the error in estimating statistical moments [30] decays as $\sim 1/\sqrt{N}$, a cohort of about $N = 400$ patients is needed to reduce the uncertainty below 5% while it ramps up to $N = 10000$ for a threshold of 1%.

When resorting to in–silico trials, however, the features of virtual patients can be defined on demand and this allows the use of more efficient sampling strategies which ensure a faster convergence than MC. For example, using a variance reduction technique (such as the Latin Hypercube sampling [69]), the error decreases as $\sim C/N^{1/2}$, with the constant $C \leq 1$ [30]. The converge of the QoIs statistic can be further improved considering the so called quasi–random sampling strategies, such as the Sobol' low discrepancy sequence [207]. In this case the error decays as $1/N^{\alpha}$, with the exponent α in the range $[1/2, 1]$ [74].

It appears that combining a quasi–random method with a moderate variance reduction technique entails a significant reduction of the number of samples and, consequently, the size of the virtual patients cohort. For example, with $\alpha = 0.7$ and $C = 0.08$, an in–silico study would need $N = 50$ ($N = 500$) samples to estimate QoIs within 5% (1%), rather than $N = 400$ ($N = 10000$) of a standard MC method routinely employed in the clinical practice.

Before concluding this section we wish to point out that the advantages associated with in–silico trials and the optimal sampling techniques are even larger when the analysis is focused on rare diseases. In fact, estimating events with low probability ($p \ll 1$) yields a prohibitively slow convergence rate ($\sim 1/\sqrt{pN}$ for standard MC methods while, using a method like the Subset Simulation [32], which sequentially samples the distribution tails, the error decays as $\sqrt{(\log(p^{-1})^2/N}$ [66]. This implies that, for an uncertainty threshold of $\approx 10\%$, an event of probability $p = 10^-2$ needs a cohort of 10'000 patients for MC sampling and only about 400 with a Subset Simulation approach.

Methods

Cardiac geometry. The 3D heart geometry including the four cardiac valves and the main vessels has been built using modeling softwares (*Rhinocad, Blender, MeshMixer, Meshlab*) so as to reproduce high-resolution clinical images and medical atlas, where the corresponding lengths and thicknesses are within the normal ranges reported in Table 6.1. In the left part of the heart, the left atrium (red chamber in Fig. 6.1c) receives oxygenated blood via the pulmonary veins (orange veins in the same figure) and is connected to the left ventricle through the mitral valve which has two leaflets, an anterior next to the aortic valve and the other posterior close to the lateral myocardium (see Fig. 6.1b). The left ventricle (yellow chamber) pumps blood through the aorta causing the three-leaflets aortic valve (see Fig. 6.1b) to open during systole and to close during diastole. On the other hand, the right atrium (green chamber in Fig. 6.1c) receives deoxygenated blood from the superior and inferior vena cava (green veins) and is connected to the right ventricle through the tricuspid valve that has three leaflets (see Fig. 6.1b). The right ventricle (blue chamber) pumps blood through the three-leaflets pulmonary valve (see Fig. 6.1b) towards the pulmonary artery (brown artery in Fig. 6.1c). The heart tissues are made of fibers which make their electrical conductivities and elastic properties orthotropic. In particular, the muscular fibers of the ventricular myocardium have a dual-orientation[243, 341], with directions ranging approximately from +60° to -60° across the ventricular wall [244] whereas atrial fiber orientation is uniform within the myocardium thickness [233], see Figure 6.1c,d.

The Lagrangian mesh used for the structural and electrophysiology solver of the heart is described by $\sim 5 \times 10^5$ cells including the four cardiac valves. The heart geometry is *immerse* in a computational box for the hemodynamics of $L_x \times L_y \times L_z = 10 \times 10 \times 14$ cm^3 that is discretized, with an Eulerian mesh of $531 \times 531 \times 751$ nodes corresponding to a grid spacing ≤ 190 μm, which is needed to correctly solve the hemodynamics. A small time step of about $2\mu s$ is needed to advance a single heart beat, which corresponds to 500'000 time steps with a heart rate HR = 60 bpm.

Fluid-Structure-Electrophysiology interaction (FSEI). The digital twin of the human heart is based on a multi-physics computational model tailored to accurately solve cardiovascular flows, which can cope with the electrophysiology of the myocardium, its active contraction and passive relaxation, the dynamics of the valves and the hemodynamics within the heart chambers and arteries. These models are three-way coupled with each other, thus capturing the fully synergistic physics of the heart functioning and the resulting FSEI is here summarized.

Structural solver. The dynamics of the deformable heart tissues is solved using a spring–network structural model based on the Fedosov's interaction potential approach [342]. A 3D solver is used for the ventricular and atrial myocardium

that are discretized using a tetrahedral mesh, with the endocardium wet by the blood corresponding to a triangular inner surface. On the other hand, thin membranes as the valve leaflets are discretized through 2D triangulated surfaces. The orthotropic and hyperelastic nature of biological cardiac tissues is modelled by a larger elastic stiffness in the fiber direction, $\hat{\mathbf{e}}_f$, than in the sheet, $\hat{\mathbf{e}}_s$, and sheet–normal, $\hat{\mathbf{e}}_n$, directions and by a nonlinear strain–stress behaviour according to a Fung–type constitutive relation, where the strain energy density reads $W_e = \frac{c}{2}(e^Q - 1)$, with $Q = \alpha_f \epsilon_{ff}^2 + \alpha_s \epsilon_{ss}^2 + \alpha_n \epsilon_{nn}^2$ being a combination of the Green strain tensor components in the fiber, ϵ_{ff}, sheet, ϵ_{ss}, and sheet–normal ϵ_{nn} directions. The coefficients c, α_f, α_s, α_n have been set so as to reproduce the stress-strain curves in the fiber and cross-fiber direction measured ex-vivo in different portions of the cardiac tissue [343, 344, 345, 346, 347, 348, 349, 350, 351, 352, 333].

Electrophysiology solver. The heterogeneous properties of the electrophysiology network are captured by resorting to a state-of-the-art electrical model of the whole heart [334]. Specifically, the cardiac geometry is decomposed into a set of coupled conductive media having different topology and electrical conductivities: (i) a network of slender *bundles* comprising a fast conduction atrial network, the *AV–node* and the ventricular bundles; (ii) the *Purkinje network*; and (iii) the atrial and ventricular myocardium (see Figure 6.1e). The propagation of the cellular *action potential* in these conductive media is governed by bidomain equations:

$$\begin{aligned}
\chi\left(C_m \frac{\partial v}{\partial t} + I_{ion}(\mathbf{s}) + I_s\right) = \\
\nabla \cdot (\mathcal{M}^{int} \nabla v) + \nabla \cdot (\mathcal{M}^{int} \nabla v_{ext}), \\
0 = \nabla \cdot (\mathcal{M}^{int} \nabla v + (\mathcal{M}^{int} + \mathcal{M}^{ext}) \nabla v_{ext}), \\
\frac{\mathrm{d}\mathbf{s}}{\mathrm{d}t} = F(\mathbf{s}, v, t),
\end{aligned}$$

where v and v_{ext} are the transmembrane and extracellular potential, χ and C_m are the surface–to–volume ratio of cells and the membrane capacitance and I_s is the external triggering stimulus initiating the myocardial depolarization placed in the sino–atrial node. The intracellular, $\mathcal{M}^{int}$, and extracellular, $\mathcal{M}^{ext}$, conductivity tensors are set to reflect the orthotropic myocardium electrical properties [334] and thus depend both on the conductive media and on the local fiber orientation (Figure 6.1c,d). The set of bidomain equations is solved using an in–house finite volume library, which provides a suitable approach for solving the electrophysiology equations in complex geometries [334], and it is coupled through the ionic current per unit cell membrane I_{ion} to three different *cellular models* (indicated by the last equation): the Courtemanche model [229] for the atrial myocytes, the Stewart model [230] for the Purkinje Network and the ten Tusscher–Panfilov model [188] for the ventricular myocytes. The active muscular tension $\mathbf{F}_n^{act}$ at the mesh cell is then obtained as a function of the transmembrane potential v

through the model equation proposed by Nash and Panfilov [353].

Fluid solver. The blood velocity $\mathbf{u}$ and pressure p are governed by the incompressible Navier–Stokes and continuity equations that in non–dimensional form read:

$$\frac{\partial \mathbf{u}}{\partial t} + \nabla \cdot (\mathbf{u}\mathbf{u}) = -\nabla p + \nabla \cdot \boldsymbol{\tau} + \mathbf{f}, \quad \nabla \cdot \mathbf{u} = 0. \tag{6.1}$$

In the case of a Newtonian fluid, the viscous stress tensor is given by $\boldsymbol{\tau} = \mathrm{Re}^{-1}(\nabla + \nabla^T)\mathbf{u}$ with Re the Reynolds number, whereas non-Newtonian fluids call for more complex constitutive relations. Blood is a concentrated suspension of cells, in a Newtonian liquid, the plasma, therefore its overall behaviour is that of a non–Newtonian fluid owing to the surface tension of the cell membranes on the Newtonian matrix. In order to account also for this behavior, a non-Newtonian (shear-thinning, Carreau–Yasuda [354]) blood model has been implemented in the flow solver even if it has been shown that the non-Newtonian blood features become relevant only in vessels of sub-millimeter diameter while in the ventricular flow they produce only minor effects. The governing equations (6.1) are solved over Cartesian meshes using central second–order finite–differences discretized on staggered grids, whereas the equations are marched in time using a fractional step with an explicit Adams–Bashforth method for the nonlinear convective term and an implicit Crank-Nicolson method for the viscous terms[333, 332]. The no–slip condition on the moving wet heart tissues is imposed through the instantaneous forcing $\mathbf{f}$ using an *immersed boundary technique* based on the moving least square (MLS) approach [355]. In order to provide the hydrodynamic loads as input to the structural solver for fluid–structure coupling, the pressure and the viscous stresses are evaluated at the Lagrangian markers laying on the immersed body surface as $\mathbf{F}_f^{ext} = [-p_f \mathbf{n}_f + \boldsymbol{\tau} \cdot \mathbf{n}_f]A_f$, being A_f the area of the triangular face and $\mathbf{n}$ its normal direction. The hydrodynamic loads evaluated at the wet faces are then transferred to the wet nodes thus obtaining, $\mathbf{F}_n^{ext}$, used in the Newton's equation in the next paragraph. In the case of the valve leaflets, both sides of the tissues are wet by the fluid and the local hydrodynamic force at the wet triangular surface $\mathbf{F}_f^{ext}$ is computed over both the positive $\mathbf{n}^+$ and negative $\mathbf{n}^- = -\mathbf{n}^+$ normal directions: $\mathbf{F}_f^{ext} = [-(p_f^+ - p_f^-)\mathbf{n}_f^+ + (\boldsymbol{\tau}_f^+ - \boldsymbol{\tau}_f^-) \cdot \mathbf{n}_f^+]A_f$, where A_f is the area of the triangular face. On the other hand, for closed surfaces, like the ventricle, aorta and atrium, hydrodynamic loads are only computed over the inner surface.

Coupling and boundary conditions. The contraction and relaxation of the heart chambers along with the passive motion of the aorta and valve leaflets result from the dynamic balance among the inertia of the tissues, the external hydrodynamic forces given by the fluid solver $\mathbf{F}_n^{ext}$, the internal passive forces coming from the structural solver $\mathbf{F}_n^{int}$ and the active tension computed by the electrophysiology solver $\mathbf{F}_n^{act}$: $m_n \frac{\mathrm{d}^2 \mathbf{x}_n}{\mathrm{d}t^2} = \mathbf{F}_n^{ext} + \mathbf{F}_n^{int} + \mathbf{F}_n^{act}$, where m_n is the tissue mass associated with the $n^{th}-$Lagrangian mesh node and $\mathbf{x}_n$ its (instantaneous) position. The hydrodynamics force is non–zero only on the mesh nodes belonging to the wet surfaces (namely the valve leaflets and the inner wall of the

heart chambers), whereas the active tension can be non–zero only for the nodes belonging to the muscular myocardium, i.e. ventricles and atria. Both a strong and loose coupling approaches have been implemented in the code[333, 332] .

As it happens in IB methods, the heart is immersed in the fluid domain (Eulerian grid) without crossing its boundaries and during the cardiac dynamics blood can be sucked from the outer volume through the inlets of the pulmonary veins and superior/inferior vena cava or propelled towards the same outer volume through the aorta and the pulmonary arteries. However, the heart is just a portion of the whole circulatory system and since the 3D modelling will be limited to the heart and to the initial tracts of the main vessels, boundary conditions must be applied at the inlets and outlets of the model, so to account for the resistive, elastic and inertial features of the missing vascular network. These features are represented into a lumped parameter network whose description requires inexpensive ordinary differential equations (analogous to those of electrical circuits) [356]. We use a *Windkessel* with 3 elements to reproduce the dynamics of the missing parts of circulatory system. and matching its physiologic impedance.

Synthetic ECG. The heart model has been enclosed in the idealized torso geometry shown in Figure 6.1a, which also indicates the surface locations used to calculate the ECG. The difference between these two leads examines the cardiac depolarization along the junction between atria and ventricles (heart vertical axis), with negative electrical potentials corresponding to electrical wavefronts moving towards the apex of the heart. The surface potential at the ECG leads, V_s, can be obtained by solving the electrical potential within the torso coupled with the cardiac electrophysiology system [357]. Alternatively, in the assumption of isotropic electrical conductivity in the torso, V_s at a surface position $\mathbf{x}_s$ and time t is given by [358]:

$$V_s(\mathbf{x}_s, t) = -\int_{\Omega_{heart}} \nabla v(\mathbf{x}, t) \cdot \nabla \left(\frac{1}{||\mathbf{x}_s - \mathbf{x}||} \right) \mathrm{d}\mathbf{x},$$

where Ω_{heart} indicates the cardiac domain where the electrophysiology bidomain equations are solved and $v(\mathbf{x})$ is the transmembrane potential at the cardiac location $\mathbf{x}$. A spike signal before the P wave and the QRS complex has been added to the ECG profile to indicate the activation of the atrial and ventricular leads, respectively.

GPU acceleration. A drawback of the FSEI is that it requires a large computational power implying long time to obtain results. GPUs, however, have emerged as a convenient platform for high performance computing as they allow for unprecedented speed-ups and, consequently, considerable reductions of the time-to-solution. To this aim, the code has been ported to CUDA-Fortran [332] and the GPU-accelerated FSEI algorithm can now tackle complex cardiac simulations with $\sim$1 billion dofs (including the demanding solution of the Navier-Stokes equations) within a few hours, thus allowing for running in–silico clinical trials.

Author Contributions

F.V., G.D.C, R.D.P., and R.V. conceived the research, F.V. and G.D.C. carried out the numerical simulations and data analysis. R.V. and F.V. wrote the paper with inputs from G.D.C. and R.D.P.

Chapter 7

A Monte Carlo approach to evaluate correlation test in case of measurements errors

Giulio Del Corso, Roberto Verzicco and Francesco Viola
manuscript in preparation

Abstract

Correlation analyzes are a cornerstone of applied statistics, providing a powerful and intuitive tool for investigating the relationship between variables. The study of the correlation index and its statistical significance is strongly influenced by the error measurements on such variables, which are unavoidable in experimental settings, including social and medical studies. The canonical approach to mitigate measurement errors is to increase the correlation index on the basis of the error distribution, which may lead to spurious correlations, especially when working with small data sets. A novel approach is presented here to determine how robust the analyzed sample is to errors, both in the case that their distribution is known to the experimenter (forward perturbation index) and in the more common case of exploratory analyses (inverse perturbation index). Accordingly, two perturbation indices are defined along with an algorithmic methodology necessary for their calculation, which is based on the propagation of uncertainties using the Monte Carlo method. The python code used for numerical validations of the method has been open-sourced.

7.1 Introduction

In applied statistics and particularly in medical sciences, the study of correlation among variables retains a crucial role for the correct interpretation of the results. As an example, identifying a strong correlation between two variables where one is more easier to be measured than the other, would allow to use the former as a predictor for the latter (see [359, 360, 361]. On a more fundamental level, determining a proper correlation index (as the Pearson correlation coefficient, defined as the ratio of the covariance among two variables and the product of their standard deviations) is a preliminary step of more complex analysis and multivariate methods (such as General Linear Models, Principal Component Analysis [362], Partial Least Squares regression and Canonical Correlation Analysis [363]). Furthermore, when modeling the joint probability of the parameters of a numerical model, the presence of correlations between variables must be entered by defining an appropriate copula that takes this phenomenon into account [44, 43], whereas neglecting this dependence can lead to unpredictable results in subsequent analyzes.

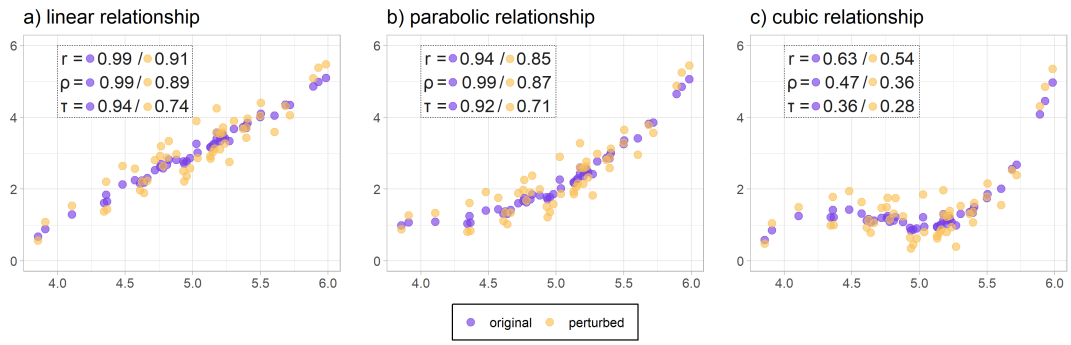

Figure 7.1: Effects of perturbation (orange) on a standard dataset (purple) for Pearson (r), Spearman (ρ) and Kendall (τ) correlation indices. Panels a), b), c) show an original linear, parabolic and cubic relationship respectively. In all the cases described, the attenuation of the index calculated in the presence of an error can be noted (e.g., Panel a), Spearman ρ decreasing from 0.99 to 0.89 after the perturbation).

However, in most of the applications, researchers have to deal with data affected by measurement errors, which is intrinsic to every experimental technique and measurement methodologies, can pollutes the corresponding statistical analyzes. When the dependent variable is affected by error, a reduction in the statistical power of correlation tests is observed [364]. Viceversa, measurement errors of the independent variable can lead to different coefficients in regression models, see [365, 366]. The most marked effect of the presence of measurement errors in the datasets under consideration results in a bias of the calculated correlation coefficient [367, 368, 369], which is known since the pioneer work of Spearman [370]. In particular, a low estimation of the measuring instruments

reliability [367, 371, 372, 373] or an error on both variables [374, 375, 364, 373] attenuates the calculated correlation index (as shown in Figure 7.1 for Pearson, Spearman and Kendall correlation indices).

A peculiarity of correlation analyzes in medical practice and human sciences is the presence of high measurement errors combined with low sample sizes (often less than $n = 100$) [376, 377, 378]. These errors, although often neglected in studies [379], can lead to erroneously different conclusions between studies analyzing (different) small datasets [380].

A methodology to correct the attenuation in the correlation index has already been addressed by Spearman and Rosner for uncorrelated errors [370, 381, 382] making assumptions on the error distribution and modifying the formula for calculating the correlation indices so as to enforce an increase in the correlation value obtained to balance the presence of errors. In more recent times, extensions to cases with more complex (correlated) errors have been proposed [374]. These methodologies, however, lend themselves to a fictitious increase in the calculated index, with values that may exceed 1 [383, 384, 385], and may create spurious correlations, especially when working on small datasets (e.g. $n \sim 20$) [373]. Therefore, when insufficient information about the error is known, a cautious approach must be applied when using correlation index corrections [367]. A different methodological approach is based on the introduction of confidence sets obtained through Monte Carlo methodologies [384]. These intervals, calculated using several numerical repetitions, can be used to compare the results of different analyses using corrective indices and, thus, to make inferences. This method is of considerable interest but still little used as it is more difficult to interpret than corrected indices [386]. Again in a perspective based on the use of simulations, recent bootstrap-based methods have been developed to determine a deattenuated correlation with the corresponding confidence intervals [386].

In this work we presents an approach based on Monte Carlo simulations in line with modern works on de-attenuated correlation indices [384, 387, 386] but, instead of looking for a method to correct the index once the error is known, a perturbation index to describe the stability of the analysis results with respect to the presence of an error on the dataset is introduced. This index is based on the need to provide a conservative tool, in particular for very small datasets (e.g. $n < 50$), which allows to understand whether the correlation analysis performed is stable in the presence of errors and, therefore, it is not possible to use corrective methods [367]. The index, is defined by setting the problem as a forward analysis of uncertainty quantification. Its purpose is to provide easy-to-read information to determine if the presence of possible measurement errors can alter the correlation analysis made and it can be calculated a posteriori. Section 7.2 describes the most common types of errors in datasets and their modeling based on the complete work of [374]. Section 7.3 describes the methodology for integrating the errors previously described in the calculation of the correlation value. A formal definition of the correlation perturbation index is then provided. Contextually, an inverse measure is introduced in order to use a variant of the index even if the information on the errors is not known to the investigator. Section 7.4 presents

numerical simulations to experimentally verify the index's ability to strengthen a pre-existing correlation analysis. In particular, the effectiveness of the variation of the sample size, the α level and the type of error considered are discussed. In Section 7.5 are the discussions with the consequent conclusions.

7.2 Definition of the errors types

Let us consider two correlated random variables $\tilde{X}$ and $\tilde{Y}$, and let us introduce a non-reproducible component called the error component (or uncertainty/noise) that can alter their values. This error can be modeled as a random variable that will act on the $\tilde{X}$ and $\tilde{Y}$ values in an additive, proportional, or combined (realistic) way. In this section, we introduce three models of error in uncorrelated and correlated cases in line with Saccenti, Carroll, Rocke and Buonaccorsi's full discussions [374, 364, 388, 389]. A short section is therefore proposed that summarizes the commonly used distributions to be used to model the error.

7.2.1 Uncorrelated errors

The most simple models for the error are called additive and proportional (or multiplicative). The additive model defines the error as the difference between the measurements and the true value, while the proportional one defines the error as the ratio between the two. Additive errors can be found in relationships that range from birth infants weight [390] to soil-plant [391] or even in control engineering [392], whereas proportional error models are instead common in daily precipitations measurements [393], animals detection [394] or economy [395, 396]. If the measurement process leads to both additive and proportional errors, the error generated is said to be realistic. Examples of additive, proportional and real errors are reported in Figure 7.2, where these models are applied to a database with a strong linear correlation. The proportional error affects more the higher scores by causing a pronounced spread between the values and a consequent reduction in the correlation determined between the variables. The models for the univariate random variables affected by errors therefore lead to consider the data as a combination between the original random variables $(\tilde{X}, \tilde{Y})$ unaffected by errors and the errors $\mathcal{E}$ itself. To apply correction of the correlation index, the error must fulfil additional conditions, e.g. be normally distributed around zero [374] despite most of the error distributions are non-normal. The proposed discussion is, therefore, not limited to normally distributed error models. [394, 397, 393].

7.2.2 Correlated errors

Although often simplified to allow for systematic treatment, the measurement errors found in the real world are often correlated. The correlation between two variables is common in clinical measurements [398], examples are the indicator

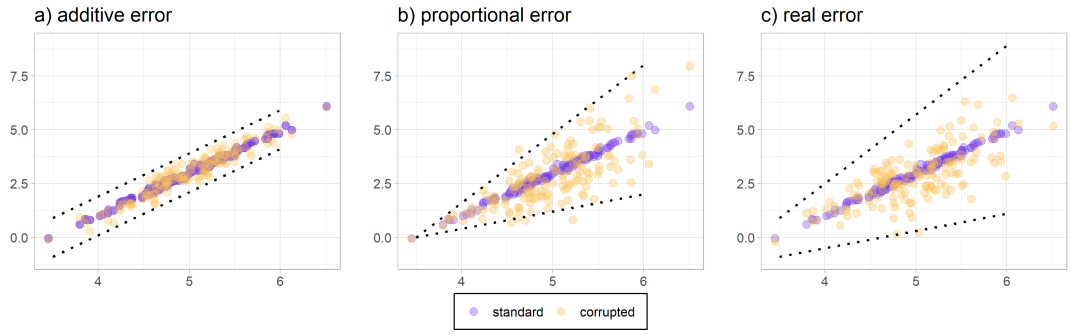

Figure 7.2: Effect of additive (panel a), proportional (panel b) and real error (panel c) on the variable $\tilde{Y}$ of a dataset characterized by a strong linear correlation (reported in purple). While the additive error acts uniformly on the values, the proportional and real errors affect the higher values more.

dilution technique for the estimation of cardiac output [399, 400], metabolic analyzes [401], or studies of epidemiology [402]. More generally, the correlation among errors occurs every time the data is treated similarly, measured with similar tools or, more commonly, the data are repeated measurements of the same dataset. [403].

7.2.3 Error notation

Considering both the correlated/uncorrelated errors and the proportional and additive cases, we obtain the general realistic error presented by Saccenti et al. [374] based on the uncorrelated realistic error discussed by Rocke et al. [388]:

$$\begin{cases} X = \tilde{X} \cdot (1 + \mathcal{E}_X^P + \mathcal{E}_{X,C}^P) + \mathcal{E}_X^A + \mathcal{E}_{X,C}^A \\ Y = \tilde{Y} \cdot (1 + \mathcal{E}_Y^P \pm \mathcal{E}_{Y,C}^P) + \mathcal{E}_Y^A \pm \mathcal{E}_{Y,C}^A \end{cases}$$

where all errors are assumed to be independent of each other (proportional rispetto ad additive) and independent of the original values ($\tilde{X}$ and $\tilde{Y}$). $\mathcal{E}_X^P, \mathcal{E}_Y^P$ are the uncorrelated proportional errors for the variables $\tilde{X}$ and $\tilde{Y}$, while $\mathcal{E}_X^A, \mathcal{E}_Y^A$ are the uncorrelated additive ones. The correlated errors $\mathcal{E}_{X,C}^P, \mathcal{E}_{Y,C}^P, \mathcal{E}_{X,C}^A, \mathcal{E}_{Y,C}^A$ are the correlated errors, with, the $\pm$ symbol modelling the sign of errors correlation.

In this study, we investigate the (unknown) error-free variables, which, based on the equation above, are denoted as follows:

$$\begin{cases} \tilde{X} = (X - \mathcal{E}_X^A - \mathcal{E}_{X,C}^A)/(1 + \mathcal{E}_X^P + \mathcal{E}_{X,C}^P) \\ \tilde{Y} = (Y - \mathcal{E}_Y^A \mp \mathcal{E}_{Y,C}^A)/(1 + \mathcal{E}_Y^P \pm \mathcal{E}_{Y,C}^P) \end{cases} \tag{7.1}$$

Specifically, given a study dataset $\{(x_i, y_i)\}_{i=1}^n$ affected by errors $\{(\varepsilon_x^i, \varepsilon_y^i)\}_{i=1}^n$, we would like to study the dataset without the errors $\{(\tilde{x}_i, \tilde{y}_i)\}_{i=1}^n$. Not knowing ε^i this can only be done in an approximate manner, hence the need to introduce the perturbation index.

7.2.4 Errors distribution based on maximum entropy principle

Using modified indices to account for the presence of errors that pollute the measurements requires very strong assumptions about the distribution of these errors (i.e., they are typically considered normal errors with zero mean). In clinical and applicative practice, these assumptions are often missing, as errors have non-standard distributions [373]. Unfortunately, these input PDFs are usually not available and they must be reconstructed on the basis of known information [404, 23]. In such cases, in information theory, the PDF shape matching the statistical moments available is typically selected as the one maximizing the Shannon entropy (or its continuous extension) [51, 52].

knowledge	**maximum entropy distribution**	**notation**
support $[a, b]$	Uniform	$\mathcal{U}([a, b])$
support $[0, 2\pi)$ [periodic] mean μ variance σ^2	Von Mises	$VonMises(\mu, k = h(\sigma))$
support $(-\infty, \infty)$ mean μ variance σ^2	Normal	$\mathcal{N}(\mu, \sigma^2)$
support $(0, \infty)$ [positive] mean μ variance σ^2	LogNormal	$Lognormal(\mu, \sigma^2)$

Table 7.1: Table describing the four most common maximum entropy distributions in practical applications as experimenter knowledge varies. Where $k = h(\sigma)$ is the solution of the equation $\sigma = 1 - \frac{\int_0^{2\pi} e^{ix} f(x|\mu,k)dx}{\int_0^{2\pi} f(x|\mu,k)dx}$ where $f(\cdot)$ is the density function of the Von Mises distribution.

Table 7.1 shows the 4 most common distributions used in statistical applications. If only the support is known and is limited between a and b, the maximum entropy distribution is the uniform one $\mathcal{U}([a, b])$. If the support is periodic (e.g. $[0, 2\pi)$), once the mean and the variance is known, the Von Mises distribution is the least-informative default. If the support is unbounded and both the mean μ and the variance σ^2 is known, the maximum entropy distribution is the normal one $\mathcal{N}(\mu, \sigma^2)$. Viceversa, if the support is positive (e.g. $(0, \infty)$), the Log-Normal distribution is the maximum entropy one. It should be emphasized that in several applicative settings, particularly in medical and human science fields, the only known information regards the boundaries of the support (e.g. many accuracy ranges of measuring instruments are provided in the form of maximum/minimum accuracy calculated in the evaluation), and therefore the corresponding optimal distribution according to the maximum entropy principle is the uniform distribution and not the normal one.

7.3 Perturbation indices

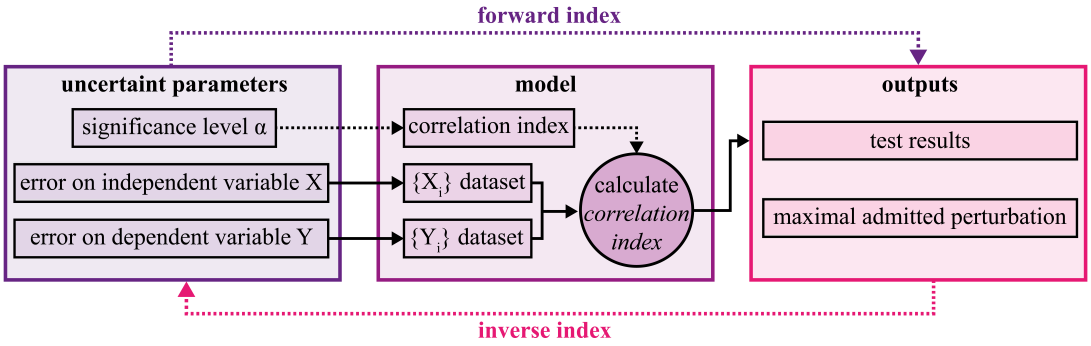

Figure 7.3: Scheme of the definition of the forward and inverse perturbation indices. The problem is seen as a forward/inverse analysis of uncertainty quantification, for which the uncertain parameters are the significance level α, the error on the dependent variable and the error on the independent variable. These uncertain parameters are applied to the datasets $\{(x_i, y_i)\}_{i=1}^n$ (defined a priori) on which the correlation analysis is performed. Using a Monte Carlo methodology, this uncertainty is propagated and an appropriate perturbation index is defined based on the correlation tests passed/failed at the α level.

In this section we define the forward and inverse perturbation indices, where the latter are obtained by structuring the problem as an uncertainty quantification analysis, see Figure 7.3. The uncertain parameters of the problem are the level of significance of the correlation test *alpha*, along with the type and the amount of estimated error present on the datasets under consideration. These uncertain parameters affect the model, which consists of the two (fixed) datasets, the correlation index chosen and the test applied to determine the presence or absence of a statistically significant correlation. It should be noted that the uncertainty does not lie in the datasets, but in the amount and types of error that are supposed to corrupt the data available.

The output of the problem is the result of the correlation test at a significance level α (positive if the correlation test detects statistical significance of the presence of correlation at the level α on the datasets $\{(x_i, y_i)\}_{i=1}^n$ for the defined error). Based on the relationship between the amount of perturbation and the test results, the forward perturbation index and the corresponding inverse index can be defined.

The forward index is the probability that the dataset perturbed with the given error distribution satisfies the test at the α level. The inverse index is the minimum amount of error that can be applied to the dataset, such that the probability that the dataset perturbed with the given error distribution pass the test at the α level becomes less or equal to a threshold β.

7.3.1 Forward index definition

Given the random variables affected by the errors that we are studying (X, Y) and the corresponding sample $\{(x_i, y_i)\}_{i=1}^n$, a canonical analysis of correlation aims to test a null hypothesis (i.e. there is no monotone correlation, Spearman $\rho = 0$) for a given significance level α. The correlation between two variables can be investigated using different correlation indices, like the Pearson r, the Spearman ρ, and the Kendall τ. However, each of the corresponding tests requires different assumptions on the distribution of (X, Y). In particular, to test the presence of linear correlation (Pearson), (X, Y) has to follow a bivariate normal distribution. This assumption is often violated with low sample numbers, also because the error (both actually present and modeled) does not follow a normal distribution [373]. It should be emphasized that the (normal) distribution of the sample after applying a proportional or realistic error loses its normality even in the case of normal errors [405, 374]. Consequently, although the methodology does not depend on the chosen correlation index, the analysis is set up using only the Spearman index, which does not require the normality of (X, Y) [406]. Furthermore, the Spearman index is a good candidate as it is more inferentially robust than Pearson r [407], and also applicable to non-continuous ordinal data (common in psychology and human sciences [408, 409]

Given a dataset $\{(x_i, y_i)\}_{i=1}^n$ and a significance level α we want to define the forward perturbation index for a given error distribution. The latter is a multivariate distribution $\mathcal{E}^* := (\mathcal{E}_X^A, \mathcal{E}_X^P, \mathcal{E}_Y^A, \mathcal{E}_Y^P, \mathcal{E}_{C,X}^A, \mathcal{E}_{C,X}^P, \mathcal{E}_{C,Y}^A, \mathcal{E}_{C,Y}^P)$ as described in Section 7.2, which admits a probability density function $\varphi_{\mathcal{E}}(\varepsilon)$. The index is defined as the probability that the correlation test is passed (at level α) considering the error distribution on each element of the dataset. Therefore, we can introduce the multivariate random variable $(\mathcal{E}^*)^n := (\mathcal{E}^*, \cdots, \mathcal{E}^*)$, whereas each entry is independent from the others and describes the error on the i^{th} element of the dataset. This variable admits a density $\varphi_{\mathcal{E}}^*(\varepsilon_1, \cdots, \varepsilon_n)$ and the perturbation index is defined as:

$$I_\alpha(\{(x_i, y_i)\}_{i=1}^n, \mathcal{E}^*) := \iint \text{Test}_\rho(\{(\tilde{x}_i, \tilde{y}_i)\}_{i=1}^n, \alpha)\varphi_{\mathcal{E}}^*(\varepsilon_1, \cdots, \varepsilon_n)\, d\varepsilon_1^* \cdots \varepsilon_n^*$$

where the dataset $\{(\tilde{x}_i, \tilde{y}_i)\}_{i=1}^n$ is defined as a possible original dataset without the errors realization $(\varepsilon_1^*, \cdots, \varepsilon_n^*)$ (as described in Section 7.2); and $\text{Test}_\rho(\cdot, \alpha)$ is the test, which can return values 1 (the null hypothesis of no monotonic correlation is rejected) or 0 (the null hypothesis cannot be rejected) at a significance level α the Spearman's rank correlation coefficient.

Increasing the amount of errors affects the original dataset leading to a reduction in the value of the correlation coefficient and, therefore, of the ability of the test to detect an actual correlation (the so-called attenuation phenomenon [370, 381, 382]). However, the decay rate of the correlation index is strongly influenced by the distribution of the variables (X, Y), the sample size N and the type and distribution of the error. Therefore, some datasets will be more robust to the presence of errors while others will lead to marked changes in the perturbation index $I_\alpha(\{(x_i, y_i)\}_{i=1}^n, \mathcal{E}^*)$ for smaller perturbations of the available data.

The index, expressed as a percentage, is thus an indicator of the robustness of the original correlation analysis carried out.

As an example, given a sample $\{(x_i, y_i)\}_{i=1}^n$ with a statistically significant monotone correlation index $\rho = 0.84$ at a level $\alpha = 0.2$. Given a uniform proportional error of 10 % on both variables (e.g., $\mathcal{E}_X^P = \mathcal{E}_Y^P = \mathcal{U}([-0.1, 0.1])$): an index $I_{0.2} = 100\%$ implies that the amount of error considered is unable to invalidate the statistical analysis performed. On the contrary, $I_{0.2} = 15\%$ means that the error considered significantly modifies the tests (e.g. in 85% of the perturbed cases, the correlation test leads to a negative result). The value thus calculated depends on the significance level chosen. A result ($\rho = 0.82$ significant at $\alpha = 0.2$, $I_{0.2} = 74\%$ while $I_{0.5} = 98\%$) can be read as data showing a strong monotonous reaction, not excessively stable to perturbations but which, by accepting a lower significance in order to understand the $\mathcal{E}^*$ errors in the analysis, is nevertheless shown to be present.

Algorithm 1: Forward perturbation index algorithm

Result: Forward perturbation index I_α
Given the datasets $\{(x_i, y_i)\}_{i=1}^n$;
Define error distribution $\mathcal{E}^*$;
Choose the significance level α ;
Define the maximum iteration M ;
Initialize test_passed = 0 ;
while *(converged == FALSE* ***and*** *j ¡M)* **do**
  # Sample L times the n-dimensional space of the error:
  $\{(\varepsilon_i^*)_{i=1}^n\}_{k=1}^L \in (\mathcal{E}^*)^n$;
  for *k=1:L* **do**
    for *i=1:n* **do**
      # Define the new dataset:
      $\tilde{x}_i = (x_i - \varepsilon_{X,k,i}^A - \varepsilon_{X,C,k,i}^A)/(1 + \varepsilon_{X,k,i}^P + \varepsilon_{X,C,k,i}^P)$;
      $\tilde{y}_i = (y_i - \varepsilon_{Y,k,i}^A - \varepsilon_{Y,C,k,i}^A)/(1 + \varepsilon_{Y,k,i}^P + \varepsilon_{Y,C,k,i}^P)$;
    end
    if *correlation_test*$(\{\tilde{x}_i\}_{i=1}^n, \{\tilde{y}_i\}_{i=1}^n, \alpha)$*==TRUE* **then**
      test_passed++ ;
    end
    j++ ;
  end
  I_α = test_passed/j ;
  converged = *convergence_test*(I_α);
end

Algorithm 1 details the procedure to calculate the forward perturbation index $I_\alpha(\cdot)$. Given the dataset formed by the two samples $\{x_i\}_{i=1}^n$ and $\{y_i\}_{i=1}^n$ whose index is to be evaluated, the distributions of the errors are defined as described in Section 7.2: $\mathcal{E}^* := (\mathcal{E}_X^A, \mathcal{E}_X^P, \mathcal{E}_Y^A, \mathcal{E}_Y^P, \mathcal{E}_{C,X}^A, \mathcal{E}_{C,X}^P, \mathcal{E}_{C,Y}^A, \mathcal{E}_{C,Y}^P)$. Where the distri-

bution could include only the additive or proportional error on one or both the variables. The α significance level is then fixed for the analysis (e.g. coinciding with the α level used in the correlation test used in the canonical correlation analysis), as well as M (the maximum number of iterations of the algorithm). Each step of the algorithm involves sampling the error space $\{(\varepsilon^*_{k,i})_{i=1}^n\}_{k=1}^L \in (\mathcal{E}^*)^n$ L-times, and as described by Equation (7.1), the error defined above is then removed from the dataset $\{(x_i, y_i)\}_{i=1}^n$, resulting in the new dataset $\{(\tilde{x}_i, \tilde{y}_i)\}_{i=1}^n$. The correlation test is then carried out between the two datasets $\{\tilde{x}_i\}_{i=1}^n$, $\{\tilde{y}_i\}_{i=1}^n$ of significance level α. If the test is passed, it means that the amount of error considered in step k^{th} is not such as to invalidate the statistical significance of the correlation determined and the counter *test_passed*, which is the number of times that the test is passed, is incremented. Otherwise, the dataset has remained stable. After performing this procedure L times, the index I_α is calculated as the ratio between the number of times the test is passed and the total number of simulations. This approach is a Monte Carlo integration of the probability of passing the test with respect to the space of possible perturbations (errors) of the data set. At the same time, the reliability of the result obtained is determined (e.g., if the method has reached convergence/the estimator of the index is reliable) as described in the next section. If the method is convergent, the perturbation index is returned. Otherwise the error space is sampled another L times and the procedure is iterated until the maximum M.

Assessing the convergence of the sampling methodology and defining a proper stopping criterion is essential for the algorithm because the ability to halt the simulations when sufficient accuracy has been attained permits reducing the computational burden of Monte Carlo. A method that works for crude MC is a sampling-splitting bootstrap methodology [73] that can be used to assess convergence for the mean value of a function of the sampled data which, in our case, it is exactly the perturbation index evaluated by the Algorithm 1. The accuracy indicator is the standard deviation of the estimated perturbation I_α, which after n sampling steps is randomly split in m-groups. The perturbation indices are calculated for every group leading to m values $\{I_\alpha(\cdot)_i\}_{i=1}^m$. The internal single-$n$-run-set based accuracy indicator for $I_\alpha(\cdot)$ is [410, 70]:

$$std(I_\alpha(\cdot)) = \frac{std_m\left(\{I_\alpha(\cdot)_1, \cdots, I_\alpha(\cdot)_m\}\right)}{\sqrt{m}} \tag{7.2}$$

where std_m is the standard deviation of these m values. The algorithm is therefore iterated until the convergence test (i.e. $std(I_\alpha(\cdot)) <$ fixed threshold) is passed. The result is then collected without evaluating other samples. The value of m influences directly the computational cost. Lower value of m requires less simulation. While higher values of m are advocated in literature [69, 387] even smaller values of $m \sim 5$ can lead to accurate results [73].

7.3.2 Inverse perturbation index

In practical applications the probability distribution of the errors is not available to and it is not possible to define the forward index as above. We therefore propose the definition of an inverse perturbation index which is based on modeled error family, such as Gaussian, uniform, additive, or proportional

Given the dataset $\{(x_i, y_i)\}_{i=1}^n$ and the significance level α of the correlation test, we first introduce the maximum admitted perturbation $\beta \in [0, 1]$. The latter is the maximum permissible perturbation value (given by the forward index introduced) on the test value (i.e. the QoI). A value of $\beta = 100\%$ means that all tests must be passed, while a value of $\beta = 90\%$ implies that up to 10% of failed tests are considered acceptable. The range of possible standard deviations of the errors $[0, \sigma_{max}]$ is then defined (i.e. the maximum error expected on the dataset), where $\sigma_{max} = 0$ describers a dataset with no error, while a higher σ_{max} leads to more perturbed dataset. The error distribution over the dataset (dependent on its standard deviation) is reported as $\mathcal{E}(\sigma)$ and the inverse perturbation index is defined as:

$$\mathcal{I}_{\alpha,\beta}(\{(x_i, y_i)\}_{i=1}^n) := \max\left(\sigma \in [0, \sigma_{max}] : I_\alpha\left(\{(x_i, y_i)\}_{i=1}^n, \mathcal{E}(\sigma)\right) \geq \beta\right)$$

Intuitively, the inverse perturbation index is the amount of error (expressed by its standard deviation σ) admissible before the number of times the correlation test at α level fails falls below the β threshold (the maximum admissible perturbation). The error $\mathcal{E}(\sigma)$ can be either additive or proportional and it is applied to a single variable (X or Y). This choice leads to an error which is dependent on only one parameter (σ), and therefore it is easier to define the inverse perturbation index. As a remark, it is known from the literature that an increase in the amount error leads to a reduction in the estimated correlation [370, 364, 374]. As a consequence, the index I_α is monotonic to the respect of σ from which follows the choice of defining the inverse index as a maximum.

It should be noted that a choice of $\beta = 100\%$ means that the index is the minimum σ such that there is at least one perturbation in the data set that leads to a negative correlation test. Therefore, it can also be interpreted as the maximum amount of perturbation before the correlation vanishes. To further improve the interpretability of the index, the error distribution can be chosen as uniform.

Several strategies can be used to calculate the inverse perturbation index. However, for each candidate σ, the evaluation of the function

$$I_\alpha\left(\{(x_i, y_i)\}_{i=1}^n, \mathcal{E}(\sigma)\right)$$

is computationally very expensive (it is the calculation of a direct index). Instead of using a brute force approach (i.e., subdividing the interval $[0, \sigma_{max}]$ and evaluate the function $I_\alpha(\cdot)$ several hundred times), this problem can be rewritten as a root-finding problem, introducing the function:

$$g(\sigma) = I_\alpha\left(\{(x_i, y_i)\}_{i=1}^n, \mathcal{E}(\sigma)\right) - \beta$$

which can be solved by using one of the classical iterative methods (e.g. Newton, bisection, secant, etc.) to reduce the amount of calculation compared to the brute-force approach. In this work we used the Brent's method, which is a hybrid root-finding algorithm that requires only very few evaluations of $g(\sigma)$.

The Brent method can be adapted to the particular structure of this problem by using it first with a low-fidelity version of the forward index and then by refining the result with the high-fidelity one (multilevel Brent's method). Indeed, by setting a less restrictive condition on the adaptive convergence parameter, each evaluation required by Brent's method is much less computationally expensive (requiring less simulation to reach convergence). This low fidelity method can be applied to obtain a first rough estimate of the root/inverse index root_{LF} and the high-fidelity version of the method itself (i.e., the one with no downgrade on the adaptive convergence parameter) can be sequentially applied using as a starting interval $[((1-s)\cdot \text{root}_{LF}), s\cdot\sigma_{max} + (1-s)\cdot \text{root}_{LF})]$ where s is a chosen scaling parameter. When the root is close enough, Brent's method no longer exploits bisection method but the secant one to approximate the result with great speed. Furthermore, obtaining the first estimate of the root root_{LF} can be computationally less onerous than one single evaluation of the direct method without the adaptive parameter downgrading.

7.4 Results

These methodologies have been tested on some artificial dataset to better control the performance of the index. The code is written in Python 3.6.7 [411, 412] and released under the MIT license, available at GitHub repository:

https://github.com/GDelCorso/PerturbedCorrelationIndex.git

The simulations are performed on a single processor (Intel(R) Pentium(R) Silver N5000 1.1GHz) and the computing time reported here are therefore indicative of a common laptop so to underline as the method proposed is fast to be run event without recurrign to high performance computing.

As shown in Figure 7.4a), dataset (C1) (*correlated-large*) represents two correlated variables (Spearman index $r = 0.93$, $p = 3.8\cdot 10^{-9}$) with medium-high sample size (20). Dataset C2 (*correlated-small*) is a subset of the previous one (10 elements), the correlation is therefore always present but statistically less relevant (Spearman index $r = 0.91$, $p = 2.0\cdot 10^{-4}$). Viceversa, dataset C3 (*uncorrelated-large*) is a set of 40 samples whose variables are linked by a hyperbolic relationship (therefore not monotone). However, with a more permissive threshold it is possible to determine an apparent monotonous relationship between the variables (Spearman index $r = 0.33$, $p = 3.6\cdot 10^{-2}$): this dataset therefore allows to assess the method in the presence of fictitious correlations.

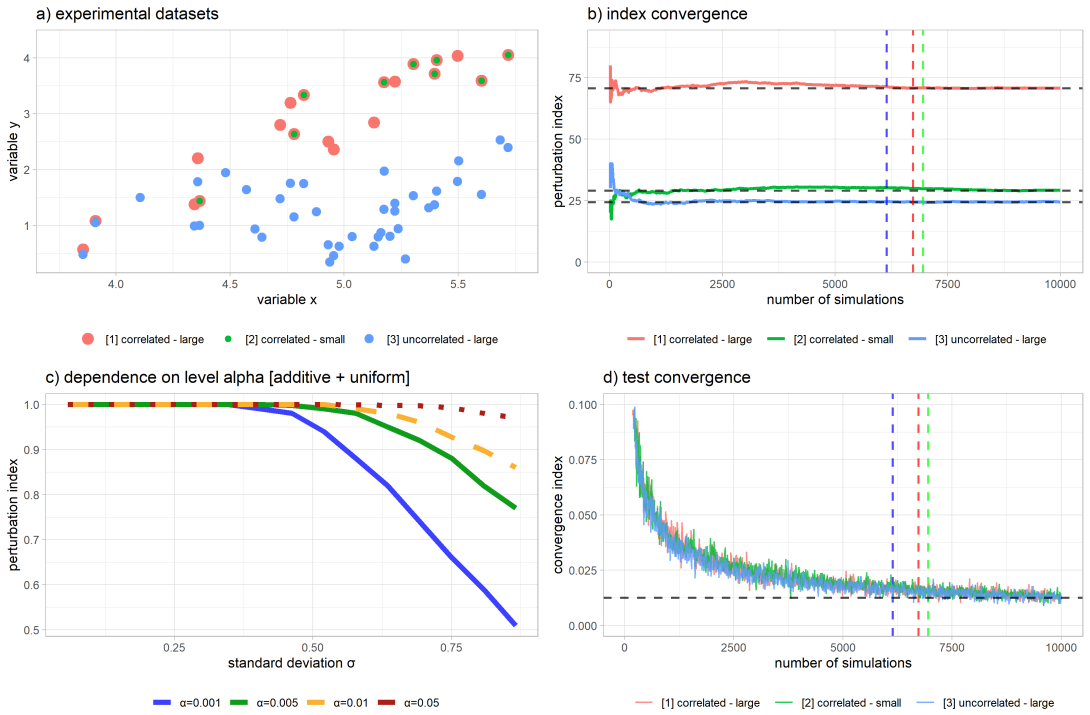

Figure 7.4: Panel a) shows the three different datasets: (1) *correlated-large* (red), (2) *correlated-small* (green), and (3) *uncorrelated-large* (blue). Index convergence, plotted against a reference solution calculated with 60000 simulations, is shown in panel b). Panel d) shows the corresponding values of the convergence index, highlighting the stopping threshold (0.0125) for the three datasets. Panel c) underlines the dependence on the α significance level of the forward index. The perturbation is applied on the Y variable of the (1) correlated-large dataset and the error is additive and uniform.

7.4.1 Forward algorithm convergence

The forward methodology involves the execution of several thousand simulations to obtain an estimate of the proposed index. Given the low speed of convergence of the Monte Carlo methods for the approximation of integral quantities (order $\mathcal{O}(1/\sqrt{n})$), Figure 7.4b shows the forward indices as the number of simulations increases. The simulations are performed by applying a Gaussian proportional error without bias $\mathcal{N}(0, 0.5)$ to the three datasets and the horizontal reference consists of the solution calculated with 60000 iterations. As can be seen from the figure, after a first transient of the order of a few thousand cases, the solution approaches the limit value. In accordance with the convergence theorems, for over 10000 simulations, the values are approximated with an accuracy of less than 1%. Given a negligible code initialization cost, 10000 simulations take 46 seconds on the smallest dataset and 55 seconds on the largest.

Figure 7.4d) shows the corresponding values of the adaptive convergence index as the number of simulations increases, where the convergence index is calculated

on $M = 10$ subsets per $M_{mean} = 5$ times and making the average to reduce the presence of fluctuations that can lead to an early stop. The graph also highlights the number of simulations required to bring the index below a threshold of 0.0125. The comparison of these data with Figure 7.4b), shows that even with a small number of simulations the results are significant.

Given the definition of the index, it is expected that as the α level of the test decreases (i.e., requiring stronger statistical evidence for the presence of correlation) the index will be more sensitive to perturbations. The same behavior occurred for all the simulations carried out, as reported for example for dataset 1 by applying a uniform additive error $\mathcal{U}(\cdot, \cdot)$ in Figure 7.4c): as the α level is reduced, the index become unstable. A minor perturbation is therefore sufficient to lower the index below 100 % ($\sigma = 0.75$ for $\alpha = 0.05$ while $\sigma = 0.35$ for $\alpha = 0.001$).

7.4.2 Forward perturbation index

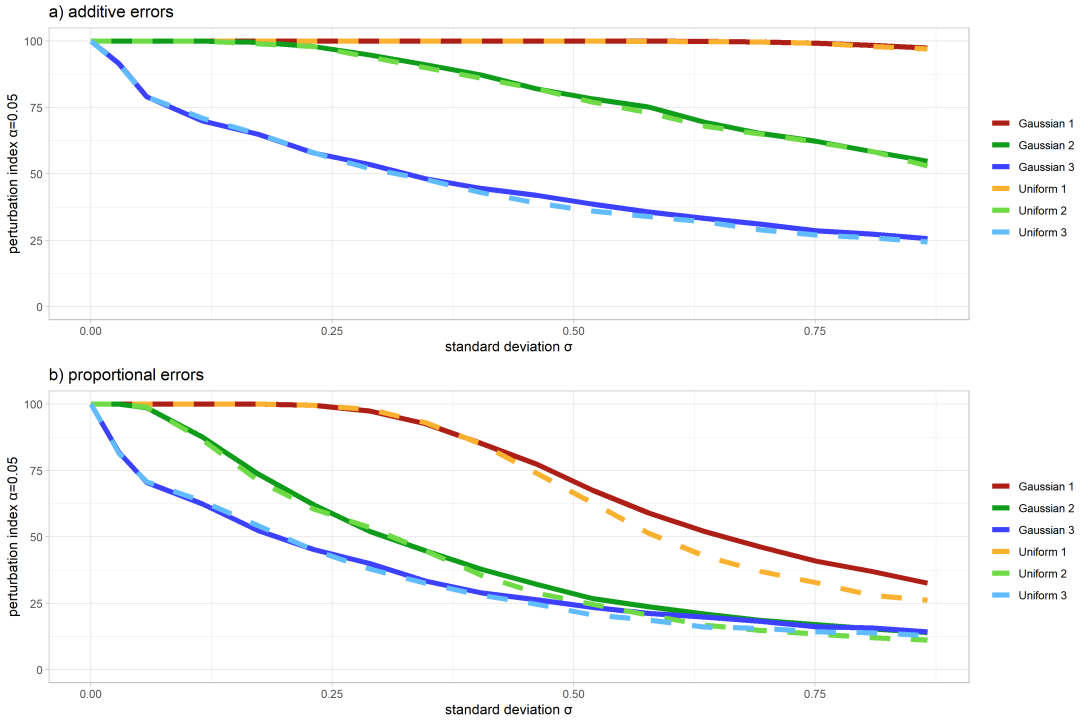

Figure 7.5: Forward perturbation index ($\alpha = 0.05$) for different error distributions (Gaussian, Uniform), error type (additive in panel a and proportional in panel b), and datasets ((1) correlated-large in red, (2) correlated-small in green, and (3) uncorrelated-large in blue) by varying the standard deviation of the error (σ). The error is applied to the dataset variable Y.

Figure 7.5a shows the experiments ($\alpha = 0.05$) for additive errors on the forward perturbation index at varying Y error (Gaussian, Uniform) and dataset type

((C1) correlated-large, (C2) correlated-small, (C3) uncorrelated-large), whereas the same analysis for proportional errors is reported in panel b). For both additive/proportional errors, it can be verified that the stable datasets (red and green) are less affected by perturbations. The proportional error has a greater impact on the dynamics which is not surprising since the datasets are values of the order of a few units (Figure 7.4a)), the absolute value of the proportional error is much greater than the additive error. As a remark, there is a minor difference in the effect of the type of distribution (uniform or Gaussian): for higher values of the perturbation ($\sigma > 0.5$, panel b) the uniform variable has a greater impact on the dynamics than the Gaussian one (lower index value), especially for stable datasets (red and green). It is interesting to observe how, for both panels, the index remains stably at 100% for stable datasets (red and green) while at the slightest disturbance the dataset with the fictitious correlation (blue), the value falls well below 95%. In particular, for the dataset with strong correlation and fairly high numerosity (red), the additive perturbations up to $\sigma = 0.75$ or proportional up to $\sigma = 0.25$ do not lead to any variation. The choice of determining the maximum admissible perturbation such as to keep the forward index equal to 100% is therefore interesting (inverse analysis, $\beta = 100\%$).

7.4.3 Inverse perturbation index

case	index	case	index
[C1] correlated - large $\sigma_{max} = 0.2$ $\mathcal{E}_Y^P = \mathcal{U}(\cdot,\cdot)$	-	[C2] correlated - small $\sigma_{max} = 1$ $\mathcal{E}_Y^A = \mathcal{N}(0,\cdot)$	$\mathcal{I}_{\alpha=0.05,\beta=0.99} = 0.20$
[C1] correlated - large $\sigma_{max} = 1$ $\mathcal{E}_Y^P = \mathcal{U}(\cdot,\cdot)$	$\mathcal{I}_{\alpha=0.05,\beta=0.99} = 0.26$	[C2] correlated - small $\sigma_{max} = 1$ $\mathcal{E}_Y^A = \mathcal{U}(\cdot,\cdot)$	$\mathcal{I}_{\alpha=0.05,\beta=0.99} = 0.21$
[C1] correlated - large $\sigma_{max} = 2$ $\mathcal{E}_Y^P = \mathcal{U}(\cdot,\cdot)$	$\mathcal{I}_{\alpha=0.05,\beta=0.99} = 0.26$	[C2] correlated - small $\sigma_{max} = 1$ $\mathcal{E}_X^A = \mathcal{N}(0,\cdot)$	$\mathcal{I}_{\alpha=0.05,\beta=0.95} = 0.27$
[C1] correlated - large $\sigma_{max} = 2$ $\mathcal{E}_Y^P = \mathcal{U}(\cdot,\cdot)$	$\mathcal{I}_{\alpha=0.05,\beta=0.95} = 0.33$	[C2] correlated - small $\sigma_{max} = 1$ $\mathcal{E}_X^P = \mathcal{N}(0,\cdot)$	$\mathcal{I}_{\alpha=0.05,\beta=0.95} = 0.05$
[C1] correlated - large $\sigma_{max} = 2$ $\mathcal{E}_Y^P = \mathcal{U}(\cdot,\cdot)$	$\mathcal{I}_{\alpha=0.05,\beta=0.90} = 0.37$	[C3] uncorrelated - large $\sigma_{max} = 1$ $\mathcal{E}_X^P = \mathcal{U}(\cdot,\cdot)$	$\mathcal{I}_{\alpha=0.10,\beta=0.95} = 0.02$
[C1] correlated - large $\sigma_{max} = 2$ $\mathcal{E}_Y^P = \mathcal{U}(\cdot,\cdot)$	$\mathcal{I}_{\alpha=0.05,\beta=0.80} = 0.43$	[C3] uncorrelated - large $\sigma_{max} = 1$ $\mathcal{E}_Y^A = \mathcal{N}(0,\cdot)$	$\mathcal{I}_{\alpha=0.10,\beta=0.95} = 0.10$

Table 7.2: Table of inverse indices calculated on different datasets and with different parameters $(\alpha, \beta, \sigma_{max})$. The error type is described using the previously introduced formalism $\mathcal{E}_X^P, \mathcal{E}_Y^A$ are a proportional error on X and an additive error on Y respectively.

The results of the simulations for the inverse indices using the same datasets

(C1 correlated - large, C2 correlated - small, and C3 uncorrelated - large) are shown in Table 7.2 for different choices of σ_{max} and error type and distribution. The simulations are carried out using a first low-fidelity run with maximum number of simulations 1500 and adaptive parameter 0.01. The high-fidelity simulations are instead carried out with maximum number of simulations equal to 60000, the adaptive parameter set as 0.001, on the interval reduced by a factor of 80% centered around the low fidelity result. The median of the number of low-fidelity runs performed is 14, while the median of the high-fidelity ones is 8. The CPU time of the entire low fidelity procedure is less than the execution time of a single high-fidelity run and the average execution time of the entire procedure is approximately 20 minutes. The first three simulations (column 1, lines 1-3) show the effect of the interval to be explored on the index obtained. In the first case the maximum interval $[0, \sigma_{max}]$ is not wide enough to identify a sufficient perturbation and therefore the result is null. The second and third simulations return the same value, as for the definition of the index, a greater extension of the σ explored must not lead to a different result. The remaining three simulations (column 1, lines 4-6) show the behavior of the index as the β threshold decreases (95%, 90% and 80% respectively). Reducing the β value means determining the perturbation such as to induce a variation in $(1 - \beta)$ cases. Therefore decreasing β values require an ever greater value of σ before inducing a sufficient effect on the ensemble (0.33, 0.37, 0.43 respectively). The difference in the form of the error distribution is appreciable in simulations 1 and 2 of the second column, where the same maximum $\sigma = 1$ and type of error (additive error on Y) is considered, but in the first case the variable is Gaussian while in the second it is uniform. This leads for the first case to an inverse index of 0.20, while in the second one it is 0.21. Simulations 3 and 4 of column 2 show the difference in the impact of an additive variable (index 0.27) compared to a proportional, where already a value $\sigma = 0.05$ brings the forward index below the threshold of 0.95. Finally, the latest simulations (5 and 6 of column 2) show the ability of the inverse index to determine the instability of a set with low correlation. Indeed, even selecting a much more permissive alpha ($\alpha = 0.10$), the minimum perturbation (only 0.02 for the proportional uniform case and 0.10 for the Gaussian additive case) leads to a marked variation .

We observe that for an exploratory analysis of the dataset reduced fidelity simulations can be performed in a very short time ($N \approx 10000$, adaptive parameter ≈ 0.01).

7.5 Discussion and conclusion

A methodology based on direct error propagation using Monte Carlo strategies was presented in order to integrate possible measurement errors (either additive, proportional, or real) in a correlation study. The method yields to a forward and an inverse perturbation indices, with the first index evaluating the impact of a known error distribution on the correlation of a dataset, whereas the second

one allows to estimate the stability of the dataset (with respect to a correlation analysis) when the amount of the error is not known but only its distribution. It should be noted that the proposed perturbation indices complement the well-established Spearman ρ as they increase the strength of a previously performed analysis by assessing the stability of the correlation analysis to perturbations. The proposed algorithm to compute these indices is based on a sampling mechanism to minimize the number of computing steps and an adaptive method to evaluate the convergence of the procedure. The indices were tested numerically on some representative problems and the corresponding code was made as open source.

This work is therefore to be considered as an integration of an already flourishing literature on the analysis of measurement errors (and their calibration [413, 414]), corrections to classical indices [374, 382, 386] and Monte Carlo methods for probability and UQ estimation [404, 23, 415]. While corrective methods infer the exact value of the correlation index by increasing the one obtained taking into account errors, our method conservatively proposes to determine the effective stability of the correlation analysis carried out. On the other hand, when the investigator can structure a two-step analysis to both accurately estimate the error and then assess the correlation, other more advanced methodologies are preferable [416, 417, 418, 419, 415, 420]. Furthermore, in the event that the population under examination follows particular distributions (e.g. Gaussian) and has a high sample size, it is possible to determine analytical formulations of the proposed indices, making the introduced Monte Carlo methodology superfluous. Finally, it should be noted that the proposed indices are conservative and therefore have more the purpose of confirming a correlation highlighted on a small sample than to hypothesize a correlation present [382, 374].

The natural development of this work concerns a systematic application of the indices to application contexts in which the presence of an error is known (e.g., social sciences, exploratory analyzes with a reduced number of data, correlation between scores and psychological tests). Having defined the algorithmic procedure for the determination of the indices also allows to structure a complete analysis of uncertainty quantification to determine how the sample size, the family and the entity of the errors and the distributions of the data can alter a correlation study (global sensitivity analysis using Sobol' indices [205, 309]). The inverse index should be extended to the case that both variables are affected by error. Furthermore, in some practical applications the interest is not related to the presence of correlation (i.e., correlation test $H_0 : r = 0$) but rather whether the correlation is greater than a certain threshold (i.e., correlation test $H_0 : r \leq r_0$) [421, 422].

Author Contributions

G.D.C. designed the research. G.D.C. defined the method and implemented the corresponding software. G.D.C. and F.V. wrote the paper with inputs from R.V.

Chapter 8

A robustness index for sensitivity analysis

Giulio Del Corso, Roberto Verzicco and Francesco Viola

manuscript in preparation

Abstract

The application of in silico models to real problems is often limited by the presence of uncertainties. Differences induced by individual variability or the presence of random phenomena intrinsic to the model must be properly investigated by means of an uncertainty quantification analysis. The main purpose of most uncertainty quantification applications is to perform a sensitivity analysis, i.e. to determine which of them has the greatest impact on the model. However, a sensitivity analysis is only accurate when the sources of uncertainty are estimated correctly. This assumption, however, is often unfulfilled in practical applications, where only partial information about these distributions is available. In this paper, we present an index to assess the robustness of the sensitivity analysis on a perturbation of the input uncertainties, which is expressed in terms of the statistical moments of the uncertainty distributions. A direct algorithmic procedure (nested Sensitivity Analysis) for calculating this robustness sensitivity index, along with an alternative approach based on metamodelling that is more suitable for uncertainty quantification analyses on computationally expensive models.

8.1 Introduction

The evolution of mathematical modeling associated with an increase in computational power has made possible to study how model uncertainties affect the model reults. Indeed, all models used as *digital twins* of reality contain uncertainties relating to unknown properties of the parameters (epistemic uncertainties), or quantities which by their nature are intrinsically random (aleatoric uncertainties). The corresponding research branch is called uncertainty quantification (UQ) and deals with two main issues: how to interpret a non-deterministic analysis (e.g. containing uncertain or random elements) and how to do it in a computationally efficient way. The related UQ strategy depends on the problem at study which may include calibrating the uncertain parameters of a model (uncertainty inverse calibration), determining the propagation of the uncertainties on the model results (uncertainty propagation) or, even more, determining what are the most relevant parameters (sensitivity analysis).

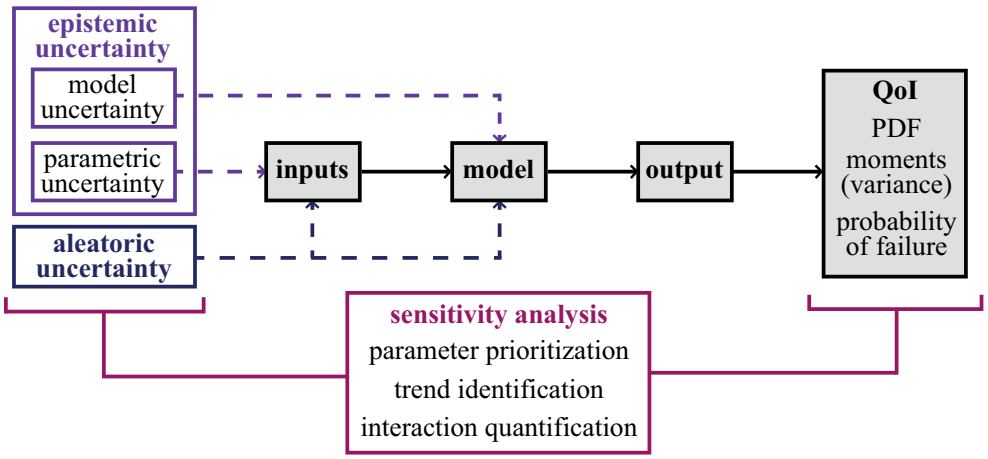

Figure 8.1: Sketch of a sensitivity analysis. Uncertainties (epistemic and aleatoric) both affect the inputs and the model itself. Appropriate quantities of interest (QoI), extracted from the output, are then used to study the effect of uncertainties. In particular, it is determined which of the parameters most influences the output.

Referring to Figure 8.1, in a sensitivity analysis the model is described by a family of uncertain inputs (which are influenced by both random and parametric uncertainties) and a numerical model, whose parameters are also affected by uncertainties. The output of the model is used to define some experimental quantities of interest (QoI), whose probability distribution (PDF), moments or probability of failure are studied. Sensitivity analysis studies the relationship between uncertainties and the QoIs [102]. This relationship can serve several purposes: parameter prioritization (i.e., identify the input parameters that can most influence QoI [423]), trend identification (i.e., whether an increase/decrease in a parameter leads to an increase/decrease in QoI [424]) and interaction quantification (i.e., understand if the variation of the QoI is the direct sum of the

individual effects of the variations in the parameters [92]). The central objective of the sensitivity analysis remains, however, the subdivision of the inputs into two families, those whose uncertainty influences the result (QoI) from those that can be neglected in subsequent analyses (model reduction).

In recent times, an extensive literature has developed on various indices for sensitivity analyses, raging from the elementary One-at-a-time Sensitivity Index [87] to the most complex variance based sensitivity indices like the Sobol' indices [85, 100]. It is important to emphasise that the optimal index to be used depends on the problem at study [87]. In particular, in order to reduce the computational cost of sensitivity analyses, which can often be prohibitive [425], the use of metamodels that approximate the real problem at a lower cost has become increasingly popular, allowing the analysis to be carried out with fewer simulations. A metamodel, also called surrogate model, is a simplified numerical duplicate that emulates the input quantity relation of interest of the original problem. Examples are Kriging (or Gaussian modelling) [39], polynomial regression, Multivariate Adaptive Regression Splines [426] or Polynomial Chaos expansion [139].

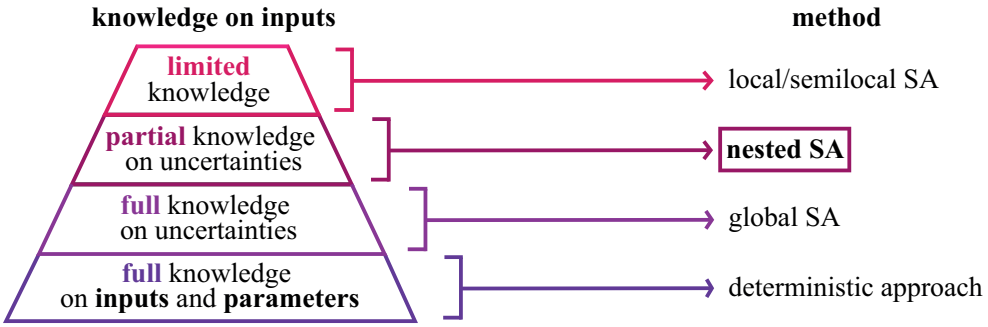

Figure 8.2: Scheme of the relationship between the knowledge available about the uncertainty of the inputs and the method of analysis to be used. This study focuses on when knowledge is partial (i.e., error distributions are known but are approximate or cannot be guaranteed to be accurately estimated) and proposes an analysis technique called Nested Sensitivity Analysis.

Despite the presence of increasingly sophisticated techniques to reduce the amount of data needed for a proper sensitivity analysis, the quality of information on uncertainties available to the investigator remains a fundamental prerequisite for obtaining reliable results. According to Figure 8.2, the amount of knowledge on inputs influences the choice of technique to be used. When only the reference values of uncertain quantities (i.e., minimal knowledge) are known, the model parameters can be only varied *locally*, i.e. close to their nominal value, such as in One-at-Time (OAT) local analyses [87] or in the adjoint method [427]. Detailed information on the distributions of uncertainties allows to explore the problem in more detail (global sensitivity analysis, [85]) by analyzing the interactions between variables and their effect on the QoI.

However, in many cases there is a lack of knowledge on the uncertainty distri-

butions, such as in several biomedical and engineering applications where only the range of variation of a parameter is known (e.g. tolerance range provided by the manufacturer) or only mean and standard deviation of the PDF are reported [26, 27, 305]. This inaccuracy in the definition of uncertain quantities can alter the results of the sensitivity analysis and it is thus important to assess the robustness of the sensitivity analysis to a modification of the input uncertainties.

In this work, an algorithmic non-intrusive approach (Nested Sensitivity Analysis) is proposed to define a robustness index for global sensitivity analysis in order to check whether the uncertainty on the input distributions can alter the result of a canonical sensitivity analysis. In Section 8.2 the standard sensitivity analysis and its corresponding notation is presented. Section 8.3 describes the perturbations of the most common distributions used to model error uncertainties, and the corresponding nested sensitivity analysis methodology used to define the robustness index. To reduce the computational burden of the analysis, an approach based on the use of surrogate models is presented in Section 8.4, along with the definition of an appropriate minimal extended training space (founded on the effect of perturbations on input quantities). The applicability of the method and future research directions are discussed in Section 8.5. The appendix contains details on the perturbed distributions (i.e. tilted uniform distribution) and on the algorithm to calculate the sorting cost.

8.2 Standard sensitivity analysis

An uncertainty quantification analysis seeks to understand how uncertainties in the model inputs and parameters, $\mathbf{X}$, propagate through the model G to the output $\mathbf{Y} = G(\mathbf{X})$ or, more in general, to some quantities of interest which depend on the output, $QoI = f(\mathbf{Y}) = f(G(\mathbf{X}))$, see Figure 8.3.

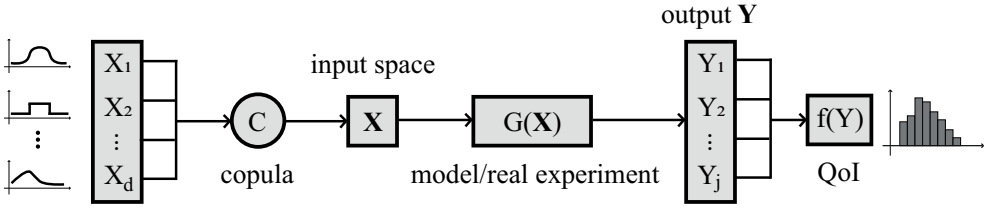

Figure 8.3: Sketch of a standard sensitivity analysis. The input space $\mathbf{X}$ is described by the d variables X_i and a suitable copula C. A sample of this input (the inputs/parameters) is passed to the model/experiment G obtaining result $\mathbf{Y}$, which is used to extract a scalar function $f(\mathbf{Y})$, called quantity of interest (QoI), whose empirical distribution is calculated based on the values assumed by the model.

The input random vector $\mathbf{X}$ is affected by uncertainties and is made of d independent variables $\{\mathbf{X}_i\}_{i=1}^{d}$. However, it is possible to exploit Sklar's theorem to generalize the space to non-independent variables [428]. Some uncertainty

quantification techniques assume the hypothesis of independence of variables (e.g. standard Polynomial Chaos Expansion) but can be generalized (through decorrelation methodologies or directly use of Gram-Schmidt orthogonalization) to be integrated with the copula formalism described above for working with dependent variables [429, 430]. In the manuscript we will deal with independent variables for simplicity but the whole methodology can be generalized for dependent variables using the copula formalism. Therefore, hereafter we consider an input vector $\mathbf{X} = (X_1, \cdots, X_d)$ for which the variables X_i are independent.

These inputs are sampled according to a suitable ssampling strategy (crude Monte Carlo, Latin Hypercube Sampling, quasi Monte Carlo [30]) and the corresponding output $\mathbf{Y} = G(\mathbf{X})$ and $QoI = f(\mathbf{Y})$ are computed. Model G can be an experiment or a numerical simulation and it is often the bottleneck of the whole analysis, unless metamodels are used. An example can be a model describing the electrical signal propagation in human ventricular chambers, a family of inputs describing the conductivity properties and the underlying cellular models, an output that is the cardiac activation profile, and scalar QoIs of medical interest such as the signal propagation speed or the activation time of the entire chamber [23, 404, 431].

Importantly, the sensitivity analysis allows to determine what are the most sensitive parameters in the model and, vice–versa, the ones less affecting the QoIs, which can be set tot their nominal value in subsequent analysis in a model reduction fashion. The effect of an input variable on the QoI is quantified thorough a sensitivity index, such as the Sobol index (first order/importance measure and total order) [92], which belongs to the broader family of variance-based sensitivity indices. Other examples which are computationally cheaper (but neglect the nonlinear interaction between the variables) include: correlation coefficients, standardized rank correlation coefficients, partial rank correlation coefficients [85], or the Shapley effect [432, 433]. Since the proposed methodology is independent of the measure, the term sensitivity index is going to be used in the rest of the manuscript.

Algorithm 2: Standard sensitivity analysis

Result: Sorting vector v_0
Define the input vector $\mathbf{X} = (X_i)_{i=1}^d$;
Choose the sensitivity index for the analysis ;
Standard sensitivity analysis:
  Sample the input distribution and get $\{x^{(i)}\}_{i=1}^n$;
  Evaluate the sample $\{y^{(i)}\}_{i=1}^n = G(\{x^{(i)}\}_{i=1}^n)$;
  Evaluate the corresponding quantities of interest $f(\{y^{(i)}\}_{i=1}^n)$;
  Calculate the vector of the sensitivity indices $(s_j)_{j=1}^d$;
  Define the (reference) sorting vector v_0 ;

On the basis of the chosen sensitivity index, a standard global sensitivity analysis can be performed. The result of this analysis consists of a vector $(s_j)_{j=1}^d$ with s_j the sensitivity index of the j^{th} input variable on the QoI (i.e. the relative order of importance of each input) and is the reference value to investigate the

robustness of the SA, as described in Algorithm 2. Once the sensitivity indices have been computed, one can define a sorting vector v_0, labelling the most relevant input with 1, the second most relevant one with 2 and so on, thus defining a hierarchy of importance of the model parameters. As an example $v_0 = (3\ 1\ 4\ 2)$ indicates that the variable with the greatest effect is X_3, the second one is X_1 and so on. This vector, commonly used in model reduction to select which variables to keep in the model, will be used to define the nested SA analysis in the next section.

8.3 Nested SA

The proposed methodology to evaluate the impact of an imperfect knowledge of uncertainties on the model parameters is reported in Algorithm 3.

Algorithm 3: Nested sensitivity analysis steps

Result: robustness index I and perturbation map M
Define the perturbations $\mathbf{P} = (P_i)_{i=1}^d$ of the inputs $\mathbf{X} = (X_i)_{i=1}^d$;
Nested UQ analysis:
  Define the new problem:
    The new inputs are the perturbations $\mathbf{P} = (P_i)_{i=1}^d$;
    The new QoI is the sorting cost $s(\cdot)$;
    The new model is $G^{2nd}(\mathbf{P}) = s(v(\mathbf{P}), v_0)$
  Sample from perturbation distribution ;
  (IF G is costly) Surrogate model:
    Define the extended input vector $\overline{\mathbf{X}}$;
    Sample from $\overline{\mathbf{X}}$ distribution ;
    Calculate $f(G(\overline{\mathbf{X}}))$;
    Train a surrogate model S to approximate $\left(\overline{\mathbf{X}}, f(G(\overline{\mathbf{X}}))\right)$;
  for *each element* $p = (p_i)_{i=1}^d$ *of the sample* **do**
    Define the perturbed input $\mathbf{X}(p)$;
    Calculate the new sorting vector $v(\mathbf{X}(p))$ using $f(G)$ or S;
    Calculate the sorting cost $s(v(\mathbf{X}(p)), v_0)$;
  end
  Define the robustness index I and the perturbation map M ;

8.3.1 Define the perturbations:

The distributions of the uncertain inputs are perturbed by modifying their principal moments. Formally, the perturbation of the i^{th} input is a random vector $P_i = (H_1^{(i)}, \cdots, H_\ell^{(i)})$ such that $H_1^{(i)}$ is the distribution of the (perturbed) mean, $H_2^{(i)}$ the (perturbed) variance distribution, $H_3^{(i)}$ the (perturbed) skewness and $H_4^{(i)}$ the (perturbed) kurtosis. As an example, given a random input $X_2 \sim \mathcal{U}(3, 5)$, which has a mean 4 and variance 1/3, a possible perturbation can be $P_2 = (H_1^{(2)}, 0)$ with $H_1^{(2)} \sim \mathcal{U}(3.8, 4.2)$ corresponding to an uniform uncer-

tainty of $\pm 5\%$ of the original mean. Another example is $P_2 = (H_1^{(2)}, H_2^{(2)})$ with $H_1^{(2)} \sim \mathcal{N}(1/3, 0.2)$ which also adds a Gaussian uncertainties on the variance.

Once that the perturbation $\mathbf{P} = (P_i)_{i=1}^d$ is defined, the relationship between a value p_i (sampled from P_i) and the change in the variable $X_i(p_i)$ has to be investigated. Indeed, most commonly used distributions (such as Uniform, Gaussian, LogNormal) are uniquely determined by the values of mean, variance, skewness and kurtosis. By emulating the method of moments [434], the corresponding perturbed distribution (see Table 8.1) is therefore defined for each assignment in the ranges of mean, variance and skewness obtained as a value p_i of the perturbation P_i. Table 8.1 is to be considered as non-exhaustive since, analytically or numerically, a much larger family of distributions can be determined by setting their stochastic moments.

input distribution	**perturbation** $p = (h_1, \cdots, h_\ell)$	**corresponding parameters**
Uniform $\mathcal{U}([a,b])$	$h_1 = \frac{(b+a)}{2}$ $h_2 = \frac{(b-a)^2}{12}$	$a = h_1 - \sqrt{3}\sqrt{h_2}$ $b = h_1 + \sqrt{3}\sqrt{h_2}$
Normal $N(\mu, \sigma^2)$	$h_1 = \mu$ $h_2 = \sigma^2$	$\mu = h_1$ $\sigma^2 = h_2$
Log-normal $LogNor(m, s^2)$	$h_1 = e^{\left(m + \frac{s^2}{2}\right)}$ $h_2 = (e^{(s^2)-1})e^{(2m+s^2)}$	$m = log\left(\frac{h_1^2}{\sqrt{h_1^2+h_2}}\right)$ $s^2 = log\left(\frac{h_2}{h_1^2}+1\right)$
Exponential $Exponential(\lambda)$	$h_1 = \frac{1}{\lambda}$	$\lambda = \frac{1}{h_1}$
Laplace $Laplace(\mu, b)$	$h_1 = \mu$ $h_2 = 2b^2$	$\mu = h_1$ $b = \sqrt{\frac{\lvert h_2 \rvert}{2}}$
Exponentially modified Gaussian $EMG(m, s^2, \lambda)$	$h_1 = m + \frac{1}{\lambda}$ $h_2 = s^2 + \frac{1}{\lambda^2}$ $h_3 = \frac{2}{s^3\lambda^3}\left(1 + \frac{1}{s^2\lambda^2}\right)^{-3/2}$	$m = h_1 - \sqrt{h_2}\left(\frac{h_3}{2}\right)^{1/3}$ $s^2 = h_2\left[1 - \left(\frac{h_3}{2}\right)^{2/3}\right]$ $\lambda = \frac{1}{\sqrt{h_2}\left(\frac{h_3}{2}\right)^{1/3}}$
Tilted uniform $\mathcal{T}(M, A, \alpha)$	$h_1 = M + \frac{A\alpha}{6}$ $h_2 = A^2\left(\frac{3-\alpha^2}{36}\right)$ $h_3 = z(\alpha) = \frac{2}{5}\frac{\alpha\left(5\alpha^2-9\right)}{(3-\alpha^2)^{3/2}}$	$M = h_1 - \sqrt{\frac{h_2}{3-z^{-1}(h_3)^2}}z^{-1}(h_3)$ $A = 6\sqrt{\frac{h_2}{3-z^{-1}(h_3)^2}}$ $\alpha = z^{-1}(h_3)$

Table 8.1: Where $\{h_i\}_{i=1}^3$ act, respectively, on the mean ($\mu = h_1$), the variance ($\sigma^2 = h_2$) and the skewness ($\tilde{\mu}_3 = h_3$) of the given input distribution. The function z^{-1} is discussed in the appendix.

The perturbations that can be defined are limited by the input distribution. Although a Gaussian or Uniform distribution would only allow for a perturbation of the first two moments, the effect of a skewness perturbation can be included in the analysis, by extending these distributions to the Tilted uniform distribution and modified Gaussian distribution (see Table 8.1 and Appendix 1).

8.3.2 Nested SA model:

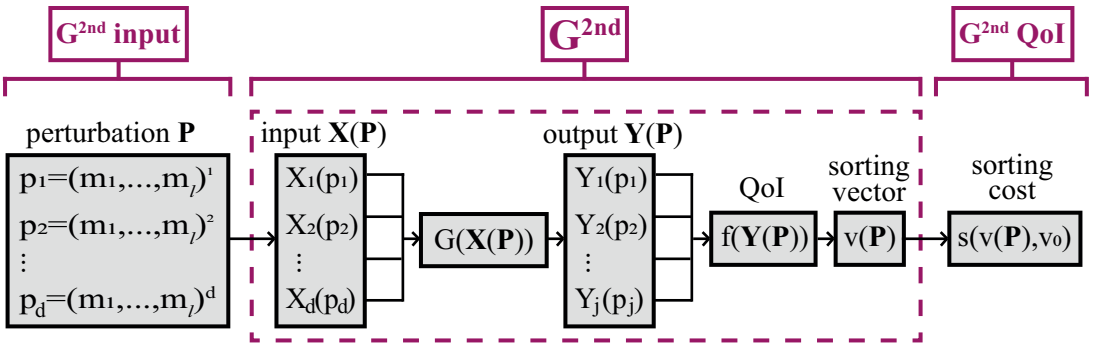

Figure 8.4: Sketch of the nested sensitivity analysis, which can be seen as a new problem that has the perturbations vector $\mathbf{P}$ as input, for each sampled value p it defines a perturbed input vector of the original problem $\mathbf{X}(p)$ and calculates the new sorting vector $v(\mathbf{X}(p))$. The QoI of the new nested problem is the sorting cost $s(v(\mathbf{X}(p)), v_0)$.

The graphic scheme of the nested sensitivity analysis is shown in Figure 8.4. To evaluate the perturbation robustness of the SA analysis on the uncertainties of the inputs, we set up an extended UQ problem which has as input the perturbations defined above, while the G^{2nd} model consists of the entire standard sensitivity analysis described in § 2 but having as input the perturbed one $\mathbf{X}(p)$.

The perturbation of the inputs $\mathbf{X}$ can modify the QoI $f(G(\mathbf{X}))$ under examination. As a result, the relative order of the relevant variables may change, leading to a new ordering vector different from the original v_0. The quantity of interest of the new problem G^{2nd} is therefore a measure of similarity between the (reference) sorting vector v_o and the perturbed one $v(\mathbf{X}(p))$, this quantity is called sorting cost and is denoted by $s(v(\mathbf{X}(p)), v_0)$ which is detailed in the next section.

8.3.3 Sorting cost:

Given a value p of the perturbation $\mathbf{P}$, an ordering of the input variables $(X_1, \cdots, X_d)$ is obtained with respect to the sensitivity index chosen. A method to represent the order of variables $(X_1, \cdots, X_d)$ with respect to the sensitivity index is by means of a *sorting vector* of length d where the i^{th} cell contains j if the variable X_j is the ith in order of importance. The sorting vector obtained for p must be compared with the original ordering v_0 to evaluate the effective impact of the different configuration of the input. Given two integers vectors $v_1, v_2 \in \mathbb{N}^d$, the **sorting cost** $s(v_1, v_2)$ is defined as the minimum number of adjacent swapping necessary to sort v_2 respect to v_1 (e.g. $v_1 = (1, 3, 5)$ and $v_2 = (3, 1, 5)$ have a sorting cost of 1). The choice of using adjacent swaps to calculate the sorting cost is dictated by the fact that the usual application of sensitivity analyzes is to obtain a model reduction which is, indeed, based on ranking the parameters by

their sensitivity on the QoI. Intuitively, the impact of the perturbation is greater in the case of a switch between the first and last sensitive parameters (cost $d-1$) with respect to the case of a switch between the first and second ones (cost 1).

To simplify the reordering algorithm, a preliminary step is performed by defining the vector v_2^*, where its i^{th} element is the v_1-index of the entry v_2. As an example given $v_1 = (1, 3, 4, 2)$ and $v_2 = (3, 4, 1, 2)$, then $v_2^* = (2, 3, 1, 4)$. Hence, owing to this replacement the problem of determining the sorting cost of v_2 with respect to v_1 becomes the problem of calculating the sorting cost of v_2^* with respect to vector $(1, 2, \cdots, d)$. The overall complexity of Algorithm 4 is $\mathcal{O}(d^2)$.

Algorithm 4: Compute sorting cost

```
Result: Sorting cost s
Given the vector v_2^* ∈ N^d;
s = 0 ;
for i = 1 : d do
    # Find the position of the ith element:
    for j=i:d do
        if v_2^*[j] = i then
            element_position = j ;
        end
        # Move the element i to the right position:
        temporary =v_2^*[element_position] ;
        v_2^*[(i+1):element_position] = v_2^*[i:(element_position-1)] ;
        v_2^*[element_position] = temp ;
        v_2^*[i] = temp ;
        # This can be done with (element_position-i) adjacent swap:
        s = s + (element_position-i) ;
    end
end
```

In most of the model reductions we are only interested in how the k most important parameters behave. In this framework, the proposed analysis approach could only focus on the relative orderings of the k most important values (and neglect the remaining $d-k$ less sensitive parameters). Given two integers vectors $v_1, v_2 \in \mathbb{N}^d$, the **$k$-sorting cost** $\overline{s}_k$ is defined as the minimum number of adjacent swapping necessary to sort the first k elements of v_1 in the vector v_2 (e.g. $v_1 = (1, 2, 3, 4, 5)$ and $v_2 = (2, 3, 1, 5, 4)$ have a 2-sorting cost of 1 of 2). Algorithm 4 can be adapted to calculate the k-sorting cost by replacing the outer **for** loop with: **for** $i = 1 : k$ **do**. The choice of the value k, as long as the sorting vector is stored as the perturbations vary, can be carried out without having to repeat the analysis.

8.3.4 Robustness index and perturbation map

Given the perturbation $\mathbf{P}$ and the nested problem G^{2nd}, a forward analysis provides the empirical distribution function of the QoI (the sorting cost c), which

reads:

$$CDF_s(y) = \mathbb{P}(s(G^{2nd}(X)) \leq y)$$
$$C\hat{D}F_s(y) = \frac{1}{n}\sum_{i=1}^{n} \mathbb{1}_{s(G^{2nd}(\mathbf{P},X))\leq y}$$

with $\mathbb{1}_A$ the indicator function of the event A and $s(G^{2nd}(\mathbf{P}, X))$ the sorting cost of the perturbations. The robustness index of the problem is defined as:

$$I_{\mathbf{P},\alpha} = \beta \text{ such that: } \left[CDF_s(\beta) \approx C\hat{D}F_s(\beta) = 1-\alpha\right] \tag{8.1}$$

where α is a parameter fixed by the user.

The index thus defines the maximum number of exchanges (in the importance order of the input variables) expected in the $1-\alpha$ of the perturbations of the result. It should be emphasized that the sorting cost is a positive defined value and, therefore, the index represents the minimum β such that $\mathbb{P}(s \in [0, \beta]) > 1-\alpha$. As an example, a robustness index $I_{\mathbf{P},0.01} = 2$ means that 99 % of the perturbations results in a number of adjacent changes ≤ 2 in the order of the sorting vector, and therefore the problem is very stable to perturbations. Conversely, an index $I_{\mathbf{P},0.4} = 6$ means that in 40% of cases the number of permutations obtained exceeds 6 and that therefore the perturbations have a greater impact on the dynamics.

To consider the k-sorting cost $\overline{s}_k$ defined on the first k values of the sorting vector, the index can be adapted as follow:

$$I_{\mathbf{P},\alpha,k} = \beta \text{ such that: } [CDF_{\overline{s}_k} = 1-\alpha] \tag{8.2}$$

As an example $I_{\mathbf{P},0.2,k=5} = 3$ with an input $\mathbf{X}$ of dimension 12 means that 80% of the perturbations lead to a number of changes of the first 5 elements less than or equal to 3 and does not consider any changes in the order of the remaining 7 parameters less relevant in the sorting vector v_0.

In order to identify what kind of perturbation have larger effect on the SA results we introduce the perturbation map. Indeed, having defined the nested problem as a new UQ analysis, the information on how the perturbations affect the result can be seen as a new sensitivity analysis with as input the perturbations $\mathbf{P}$ and as QoI the sorting cost c. The perturbation map M_P is the matrix of the Sobol' indices [102] corresponding to the given perturbations $\mathbf{P}$:

$$M_P = \begin{pmatrix} \text{Sobol}_1^{(1)} & \cdots & \text{Sobol}_\ell^{(1)} \\ \vdots & & \vdots \\ \text{Sobol}_1^{(d)} & \cdots & \text{Sobol}_\ell^{(d)} \end{pmatrix} \tag{8.3}$$

where $\text{Sobol}_j^{(i)}$ is the Sobol' index of the j^{th} perturbation of the i^{th} random input variable X_i. The latter can be calculated using standard techniques (such as Saltelli's algorithm) or using a metamodel approach (PCE, Kriging) to reduce the computational load.

8.4 Direct sampling, extended space and metamodelling

Once the index has been defined, it is necessary to introduce an efficient methodology to calculate it. This section presents a direct sampling method (Monte Carlo) and the identification of an appropriate extended space to train a metamodel.

The calculation of the index can be done by direct Monte Carlo simulations by sampling from the space of perturbations $\mathbf{P}$ in order to obtain the parameters that perturb the space of inputs X. For the obtained realization $\mathbf{p}$ of $\mathbf{P}$, we sample from the perturbed space $X(\mathbf{P})$ in order to obtain the perturbed inputs. This double sampling (first from the perturbations and then from the corresponding inputs) gives the method its name (nested) and can be effectively applied when the model evaluation requires only few minutes/seconds.

A direct double sampling approach can be computationally expensive and overwhelm available computational power even by using efficient sampling methodology (like a Latin Hypercube sampling or a Sobol' low discrepancy sequence [30]). In addition, most of the perturbation does not significantly vary the inputs and, therefore, it is convenient to use an appropriate methodology to take this into account.

8.4.1 Extended space

To reduce the computational cost of the nested analysis when necessary (e.g. computationally expensive model) we define an extended space, sample from it and use the sample as a training set for a metamodel which approximate the original problem G.

The extended input vector $\overline{\mathbf{X}}$ can be defined as the set of the input values to be analyzed in the nested analysis (weighted by the probability to be effectively used during the analysis). As an example, consider a problem for which the input variable X_1 is a uniform random variable $\mathcal{U}[(2,3)]$. In the nested analysis, we can add a perturbation P_1 that alters the inputs, such as an uncertainty of 10 % in the correct amplitude of the uniform variable. During the nested analysis, therefore, values of variable X_1 between 1.9 and 3.1 must be sampled, which is the extended input.

Given the input $\mathbf{X}$ with marginals $\{X_i\}_{i=1}^d$ with densities $\{\varphi_i\}_{i=1}^d$, and the perturbation vector $\mathbf{P} = (P_1, \cdots, P_d)$, the extended marginals $\overline{X}_i$ densities (assumed independent) are defined as

$$\overline{\varphi}_i(x) = \int \varphi_i(x, p_i)\varphi_{P_i}(p_i)dp_i$$

where $\varphi_i(x, p_i)$ is the density φ_i after a perturbation p_i, and φ_{P_i} is the density of the perturbation P_i. The extended input vector $\overline{\mathbf{X}}$ is defined as a random vector which distribution is derived by the original Copula C and the extended

marginals $\overline{X}_i$. In practical applications the extended space is very similar to the original one. Consequently, the sample size to be obtained as a training set is comparable to that of a normal SA, and the nested analysis does not amplify the computational cost of the nominal sensitivity analysis. For example, any symmetrical perturbation of the skewness of a uniform distribution leaves the extended space coincident with the original.

The extended space, being the set of input parameters admissible in the course of the nested analysis, weighted for the probability of each perturbation (e.g. for the distribution of perturbations), is the ideal space for training a metamodel/surrogate model S that approximates $f(G)$ on the entire spectrum of the possible values of the perturbed X_i.

Sampling from extended space:

When the density of the marginals of the extended space can be calculated explicitly, standard sampling techniques (Monte Carlo, Quasi Monte Carlo, stratified sampling) can be adopted. Nevertheless, it may be convenient to sample from the extended space without computing such marginals distribution explicitly. In this case, the extended space can be sampled using a two-step procedure: first, a perturbation $\mathbf{p} = (p_i)_{i=1^d}$ is obtained on the basis of its distribution, and then the perturbed density of the marginals is defined $(\varphi_i(p_i))_{i=1}^d$ and one sample from the extended space can be obtained from this distribution. By iterating this two steps procedure n times, a full sample can be obtained.

8.4.2 Metamodel

Direct methods to calculate the robustness index can be computationally burdensome. An alternative is the use of a S metamodel which, if properly trained and validated, can reduce the number of simulations to be performed. The use of a metamodel is therefore particularly advantageous in the case of analyses that are computationally burdensome or for which it is already known that a metamodel approximates the problem well.

Once a suitable surrogate model S approximating $S(x) \approx f(G(\mathbf{x}))$ has been chosen, it is trained and validated on the entire extended space. This surrogate model is capable of predicting the output of the original model for all those inputs values obtainable by perturbing the original inputs. Indeed, by considering a choice of the perturbation parameters during the nested analysis $\mathbf{p} \in \mathbf{P}$, to this choice corresponds a variation of the marginal densities $\varphi_i(p_i)$ characterizing the input vector $\mathbf{X}$. To study the effect of perturbations it is necessary to sample from the new perturbed densities and perform a new first order analysis. This computationally burdensome step can be avoided by using the surrogate model S by observing that the values assumed by the samples belong to the extended space on which this latter has been trained.

As a remark, the choice of the right metamodel S and the corresponding training and validation methodology depends on the problem under examina-

tion. Possible choices are polynomial models, artificial neural networks (ANN), Kriging, and so on. It is important to underline that the choice of surrogate models with specific advantages for the UQ (e.g. the Polynomial Chaos Expansion) is not necessarily advantageous as the training of the model on the extended space is necessary only for the subsequent evaluation of the input and perturbed variables.

8.5 Discussion and conclusion

In this paper, a robustness index was presented to determine the robustness of a global sensitivity analysis to a perturbation of the model uncertainty distributions. In particular, the relationship between the perturbations of the moments of an input distribution and the corresponding perturbed one was defined. On the basis of these perturbations, an index was defined which identifies whether the sensitivity analysis is affected by the presence of these alterations. To ease the computational cost necessary for this analysis in the case of expensive models, a method for calculating the index based on the use of metamodels was also proposed. In addition, the theoretical derivation of the sorting cost used to define the index was discussed in the appendix and the normal Skew distribution was briefly presented.

The proposed robustness index, therefore, extends a global sensitivity analyses in case of a lack of knowledge on the uncertainty distribution of the model inputs. In particular, the definition of the index is not linked to a specific sensitivity index and can be integrated with the different sensitivity indices commonly used in uncertainty quantification, such as Sobol' indices [100], entropy-based sensitivity indices [435], or distribution based ones [436].

The main limitation of this method is that further simulations in addition to those used for the nominal SA analysis are required and is therefore better suited to analyses with a low computational model cost. The proposed use of extended space and metamodels, as verified on test cases, presents the usual problems of metamodelling. In particular, the choice of the correct metamodel, its validation, and the ability of the metamodel to analyse particularly non-linear phenomena.

In future works the proposed index will be applied to real world problems to extensively verify its predictive ability. In addition, we want to study a more general formulation of the perturbations defined on moments to include arbitrary input distributions and not be limited to the most common ones. Similarly, being able to extend the perturbations also to the copula and describe the relationship between variables would increase the applicability of the method [437]. Finally, given the high use of sensitivity screening techniques, it is interesting to extend the definition of the index to different methods such as the Morris method [35, 112] or the Radial design. [438].

8.6 Appendix: Tilted uniform distribution

The family of uniform distributions does not allow for non zero skewness. In order to analyze the impact of the skewness in the proposed second order analysis, it is necessary to extend the family of uniform distributions to admit non zero skewness. A family of distributions is therefore presented, called tilted uniform distribution, which admits non-zero skewness and such that it has the uniform distribution as its specific case. This tilted distribution is a specific case of the extended family of distributions introduced by Kotz and van Dorp [439] based on Topp and Leone's work [440] and it is covered here in detail for second order analysis. This family is different from other skew-symmetric distributions which extend of the uniform distribution [441, 442, 443], indeed it maintains an intuitive geometric meaning of the parameters that control it.

A tilted uniform $X \sim \mathcal{T}(M, A, \alpha)$ with parameters $(M, A, \alpha) \in \mathbb{R} \times (0, \infty) \times [-1, 1]$ (respectively the center, the amplitude and the shape parameter) is the continuous random variable with density:

$$\varphi_{[M,A,\alpha]}(x) = \mathbb{1}_{[M-A/2, M+A/2]}(x) \left[\frac{2\alpha}{A^2} \left(x - \left(M - \frac{A}{2} \right) \right) + \frac{(1-\alpha)}{A} \right] \tag{8.4}$$

where $\mathbb{1}$ is the indicator function. This density is reported in Figure 8.5 and shows how given the effects of the 3 parameters on the shape of this latter. The distribution $X \sim \mathcal{T}(M, A, \alpha)$ is a generalization of the uniform distribution, indeed

$$\mathcal{T}(M, A, 0) = \mathcal{U}([M - A/2, M + A/2])$$

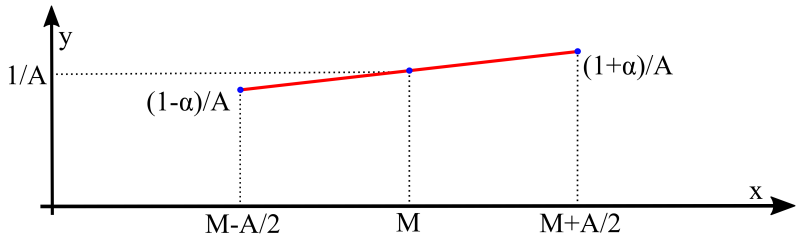

Figure 8.5: Reference density $\varphi_{[M,A,\alpha]}$. This density is uniquely determined by 3 parameters: the position of the center M, the width A of the support and the variation of the height of the extremes $(1 - \alpha)$

$f_{[M,A,\alpha]}(x)$ is a density for every values of $[M, A, \alpha] \in \mathbb{R} \times (0, \infty) \times [-1, 1]$. $f_{[M,A,\alpha]}(x)$ is a product of an indicator function (i.e. 1 in $[M - A/2, M - A/2]$) and a function that is positive in the interval $[M - A/2, \infty)$, indeed:

$$\frac{2\alpha}{A^2} \left(x - \left(M - \frac{A}{2} \right) \right) + \frac{(1-\alpha)}{A} > 0 \iff \left(x - \left(M - \frac{A}{2} \right) \right) > -\frac{A}{2\alpha}(1-\alpha)$$
$$\iff x > M - \frac{A}{2} - \frac{A}{2\alpha}(1-\alpha) > M - \frac{A}{2}$$

The function $\varphi_{[M,A,\alpha]}(x)$ is the product of an indicator function of closed interval and a linear function on a finite support, therefore is Lebesgue integrable. Furthermore:

$$\begin{aligned}
&\int_{M-\frac{A}{2}}^{M+\frac{A}{2}} \frac{2\alpha}{A^2}\left(x-\left(M-\frac{A}{2}\right)\right)+\frac{(1-\alpha)}{A}dx = \\
&= \frac{2\alpha}{A^2}\int_{M-\frac{A}{2}}^{M+\frac{A}{2}} xdx - \frac{2\alpha}{A^2}\left(M-\frac{A}{2}\right)\int_{M-\frac{A}{2}}^{M+\frac{A}{2}} dx + \frac{(1-\alpha)}{A}\int_{M-\frac{A}{2}}^{M+\frac{A}{2}} dx \\
&= \frac{2\alpha}{A^2}\frac{((M+\frac{A}{2})^2-(M-\frac{A}{2})^2)}{2} - \frac{2\alpha}{A}\left(M-\frac{A}{2}\right)+1-\alpha \\
&= \frac{2M\alpha-2(M-A/2)\alpha}{A}+1-\alpha = \alpha\frac{A}{A}+1-\alpha = 1
\end{aligned}$$

Therefore $\varphi_{[M,A,\alpha]}(x)$ is a probability density function and the continuous random variable X is uniquely determined.

Given the tilted uniform $X \sim \mathcal{T}(M, A, \alpha)$, it allows for an analytical CDF:

$$F_X(x) := \begin{cases} 0 & x \leq M-\frac{A}{2} \\ \frac{\alpha x^2}{A^2}+\frac{A-2\alpha M}{A^2}x+\frac{(M-\frac{A}{2})}{A^2}\left(\alpha M - A\left(1-\frac{\alpha}{2}\right)\right) & x \in \left[M-\frac{A}{2}, M-\frac{A}{2}\right] \\ 1 & x \geq M+\frac{A}{2} \end{cases} \tag{8.5}$$

Using the location-scale transformation we can write $X = c + dX_0$ where $c = M - A/2$ is the location parameter, $d = A$ the scale parameter and $X_0 \sim \mathcal{T}(0.5, 1, \alpha)$ the **standard tilted uniform distribution** that has density:

$$\varphi_{X_0}(x) = \mathbb{1}_{[0,1]}(x)\left[2\alpha x + (1-\alpha)\right]$$

which admits an explicit formula for the moments:

$$\mathbb{E}[X_0] = \frac{3+\alpha}{6} \;;\; \mathbb{E}[X_0^2] = \frac{2+\alpha}{6} \;;\; \mathbb{E}[X_0^3] = \frac{5+3\alpha}{20}$$

and therefore for the mean, the variance and the skewness:

$$\begin{aligned}
\mathbb{E}[X_0] &= \frac{3+\alpha}{6} \\
Var[X_0] &= \frac{3-\alpha^2}{36} \\
Skewness[X_0] &= \frac{2}{5}\frac{\alpha\left(5\alpha^2-9\right)}{(3-\alpha^2)^{3/2}}
\end{aligned}$$

With this choice of c and d it holds that $X \sim \mathcal{T}(M, A, \alpha)$. We must prove that $\varphi_{[A,M,\alpha]}(x) = \frac{1}{|d|}\varphi_{X_0[A,M,\alpha]}\left(\frac{x-c}{d}\right)$:

$$\begin{aligned}
\frac{\varphi_{X_0[A,M,\alpha]}\left(\frac{x-c}{d}\right)}{|d|} &= \mathbb{1}_{[0,1]}\left(\frac{x-c}{d}\right)\left[\frac{1}{d}\left(2\alpha\frac{x-c}{d} + (1-\alpha)\right)\right] \\
&= \mathbb{1}_{[c,c+d]}\left(x\right)\left[2\alpha\frac{x-c}{d^2} + \frac{(1-\alpha)}{d}\right] \\
&= \mathbb{1}_{[M-A/2,M+A/2]}\left(x\right)\left[\frac{2\alpha}{A^2}\left(x - \left(M - \frac{A}{2}\right)\right) + \frac{(1-\alpha)}{A}\right] \\
&= \varphi_{[A,M,\alpha]}(x)
\end{aligned}$$

Using the location-scale transformation we can compute the mean, the variance and the skewness of the tilted uniform distribution $X \sim \mathcal{T}[A, M, \alpha]$:

$$\begin{aligned}
\mathbb{E}[X] &= (M - A/2) + A\left(\frac{3+\alpha}{6}\right) \\
Var[X] &= A^2\left(\frac{3-\alpha^2}{36}\right) \\
Skewness[X] &= \frac{2}{5}\frac{\alpha\left(5\alpha^2 - 9\right)}{(3-\alpha^2)^{3/2}}
\end{aligned}$$

where the skewness is calculated using that if $c \in \mathbb{R}$ and $d \in \mathbb{R} \setminus \{0\}$:

$$\begin{cases}
Skewness[X = c + dX_0] = Skewness[X_0] & d > 0 \\
Skewness[X = c + dX_0] = -Skewness[X_0] & d < 0
\end{cases}$$

Sample generation through inverse transform sampling:

The density family described in the article requires a method for generating the sample. Since the CDF (8.5) is strictly monotone in the support $[M - A/2, M + A/2]$, it admits an inverse function $F_X^{-1}(\cdot)$. This latter can be applied to use the inverse transform sampling to generate a sample from X. That is, given a sample $\{u\}_{i=1}^N$ sampled from the uniform distribution $\mathcal{U}([0,1])$, the corresponding element sampled for the trapezoidal distribution can be computed as $\{F_X^{-1}(u_i)\}_{i=1}^N$. For $\alpha \in [-1,1] \neq 0$ this corresponds to the quantile function:

$$F_X^{-1}(u) = \frac{-A + 2\alpha M + A\sqrt{\frac{(A-2\alpha M)^2}{A^2} - 4\alpha\left(\frac{(M-\frac{A}{2})}{A^2}\left(\alpha M - A\left(1 - \frac{\alpha}{2}\right)\right) - u\right)}}{2\alpha}$$

While if $\alpha = 0$ the inverse function is:

$$F_X^{-1}(u) = Au + \left(M - \frac{A}{2}\right)$$

Define the perturbation:

To apply the perturbation of the mean, variance and skewness defined in Section 8.3.1 we have to solve the following non-linear system:

$$\begin{cases} h_1 = M + \left(\frac{A\alpha}{6}\right) \\ h_2 = A^2\left(\frac{3-\alpha^2}{36}\right) \\ h_3 = z(\alpha) = \frac{2}{5}\frac{\alpha\left(5\alpha^2-9\right)}{(3-\alpha^2)^{3/2}} \end{cases} \implies \begin{cases} M = h_1 - \sqrt{\frac{h_2}{3-z^{-1}(h_3)^2}}z^{-1}(h_3) \\ A = 6\sqrt{\frac{h_2}{3-z^{-1}(h_3)^2}} \\ \alpha = z^{-1}(h_3) \end{cases}$$

where the function $z(\alpha)$ admits derivative

$$z'(\alpha) = \frac{54(x^2-1)}{5(3-x^2)^{5/2}}$$

which is negative for $\alpha \in [-1, 1]$, therefore it admits an inverse function $z^{-1}(h_3)$ for $h_3 \in \left[-\frac{2\sqrt{2}}{5}, \frac{2\sqrt{2}}{5}\right]$ that can be calculated numerically.

Author Contributions

G.D.C. and F.V. designed the research. G.D.C. defined the UQ method and implemented the corresponding software. G.D.C. and F.V. wrote the paper with inputs from R.V.

Chapter 9

Improving pediatric/neonatology residents' newborn resuscitation skills with a digital serious game: DIANA

Giulio Del Corso & Serena Bardelli, Massimiliano Ciantelli, Marta Del Pistoia, Francesca Lorenzoni, Nicoletta Fossati, Rosa T. Scaramuzzo, and Armando Cuttano

Frontiers in pediatrics 10 (2022)

Abstract

Serious games, and especially Digital Game Based Learning (DGBL) methodologies, have the potential to strengthen classic learning methodology in all medical procedures characterized by a flowchart (e.g., neonatal resuscitation algorithm). However, few studies have compared short- and long-term knowledge retention in DGBL methodologies with a control group undergoing specialist training led by experienced operators. In particular, resident doctors' learning still has limited representation in simulation-based education literature.

A serious computer game DIANA (DIgital Application in Newborn Assessment) was developed, according to newborn resuscitation algorithm, to train pediatric/neonatology residents in neonatal resuscitation algorithm knowledge and implementation (from procedure knowledge to ventilation/chest compressions rate). We analyzed user learning curves after each session and compared knowledge retention against a classic theoretical teaching session.

Pediatric/neonatology residents of the Azienda Ospedaliera Universitaria Pisana (AOUP) were invited to take part in the study and were split into a

game group or a control group; both groups were homogeneous in terms of previous training and baseline scores. The control group attended a classic 80-minute teaching session with a neonatal trainer, while game group participants played four 20-minute sessions over four different days. Three written tests (pre/immediately post-training and at 28 days) were used to evaluate and compare the two groups' performances.

48 pediatric/neonatology residents participated in the study. While classic training by a neonatal trainer demonstrated an excellent effectiveness in short/long-term knowledge retention, DGBL methodology proved to be equivalent or better. Furthermore, after each game session, DGBL score improved for both procedure knowledge and ventilation/chest compressions rate.

In this study, DGBL was as effective as classic specialist training for neonatal resuscitation in term of both algorithm memorization and knowledge retention. User appreciation for the methodology and ease of administration, including remotely, support the use of DGBL methodologies for pediatric/neonatology residents education.

9.1 Introduction

Globally, an estimated 2.5 million newborns die each year worldwide from childbirth asphyxia (defined as a failure to initiate or sustain spontaneous breathing at birth) [444] as approximately 15% of full term births require effective resuscitation [445]. Correctly performed neonatal resuscitation can save around 700000 lives worldwide every year (SIN (Società Italiana di Neonatologia - Italian Neonatology Society) Survey on the organization of care in the delivery room, 2020). However, resuscitation guidelines are not adhered in more than 90% of cases [446].

Digital Game Based Learning (DGBL) methodologies have proved effective in multiple medical contexts [447, 448, 449] by integrating the advantages of the classic teaching process with the possibilities offered by the use of simulations (replicability, standardized teaching environment, user adaptability of the procedure). They can be applied to most flowchart-based medical procedures and, crucially, their high repeatability and the possibility of dividing a each session into several parts can stimulate procedural memory [450, 451]. Further advantages of DGBL methodologies include the provision of an optimal context for user result analysis (every action performed by the learner is stored) and a higher attention/appreciation rate by users.

While it is questioned whether DGBL approach can fully replace classic teaching methodologies [452, 453, 454, 455], DGBL methods are known to be effective in checking what was learned and reinforcing motivation to enhance adult learning in medical education [456] and, more in general, in higher education [457]. With particular regard to medical practice [457, 458, 459], and especially neonatal resuscitation [452, 460, 461, 462], numerous existing studies demonstrate the effectiveness of DGBL/simulation methods in stimulating better learning. How-

ever, many of these studies lack a scoring baseline (pre-test), a subsequent follow up to evaluate knowledge retention and/or a homogeneous and independent control group.

DGBL methodologies can be applied to most flowchart-based medical procedures. In this study, we implemented a new ad hoc digital serious game **DIANA** (**DI**gital **A**pplication in **N**ewborn **A**ssessment) and we developed it for neonatal resuscitation teaching. Rather than focusing on a single skill (e.g., endotracheal intubation) this computer game aims to teach the entire neonatal resuscitation algorithm. Unlike most published studies, which involved medical students [452, 463, 464] and expert neonatal professionals [460, 465] as learners, we tested it on a group of resident students of varying experience, using a randomized control study design with the primary goal of testing short- and medium-/long-term knowledge retention [primary endpoint: compare knowledge retention of DGBL and classical training]. The analysis is done by comparing the DGBL group with an independent group undergoing classic training (e.g., 80 minutes' theoretical teaching session provided by an expert neonatal trainer). Indeed, despite an autonomous training using didactic material [452], the choice of a guided approach provides a more controlled training path [453]. In addition, several other secondary endpoints were tested to evaluate the performance obtain from DGBL recording scores: knowledge scores, time decision, ventilation/chest compression rate, and user acceptance of this new training methodology.

9.2 Material and methods

9.2.1 Software description

The DIANA software was developed according to newborn resuscitation flow chart to verify DGBL methodology for training. The DIANA software code was implemented with the real-time development platform Unity. The video game was divided into four sessions (i.e., distributed study) with an inter-study interval (ISI) of 48 hours, to consolidate information memory through repetition [447]. Each game session consisted of a theoretical and an interactive part. The interactive part started with one minute of equipment check. The interactive part simulated a clinical case, where the user would choose how to proceed from one of four options provided. A virtual assistant would intervene in case of errors, and provide detailed instructions to enhance learning without diminishing the gaming experience [466]. In the theoretical part the same virtual assistant, with a human voice, would give a theoretical tutorial using videos to demonstrate technical skills. The first session included an interactive game and complete theoretical teaching about the whole neonatal resuscitation procedure. In the second session, the theoretical part addressed equipment check, neonatal care, and assisted ventilation. The interactive part of the video game followed on from the first session, with successful resuscitation after correctly assisted ventilation. In the third session, the theoretical part dealt with endotracheal intubation skills,

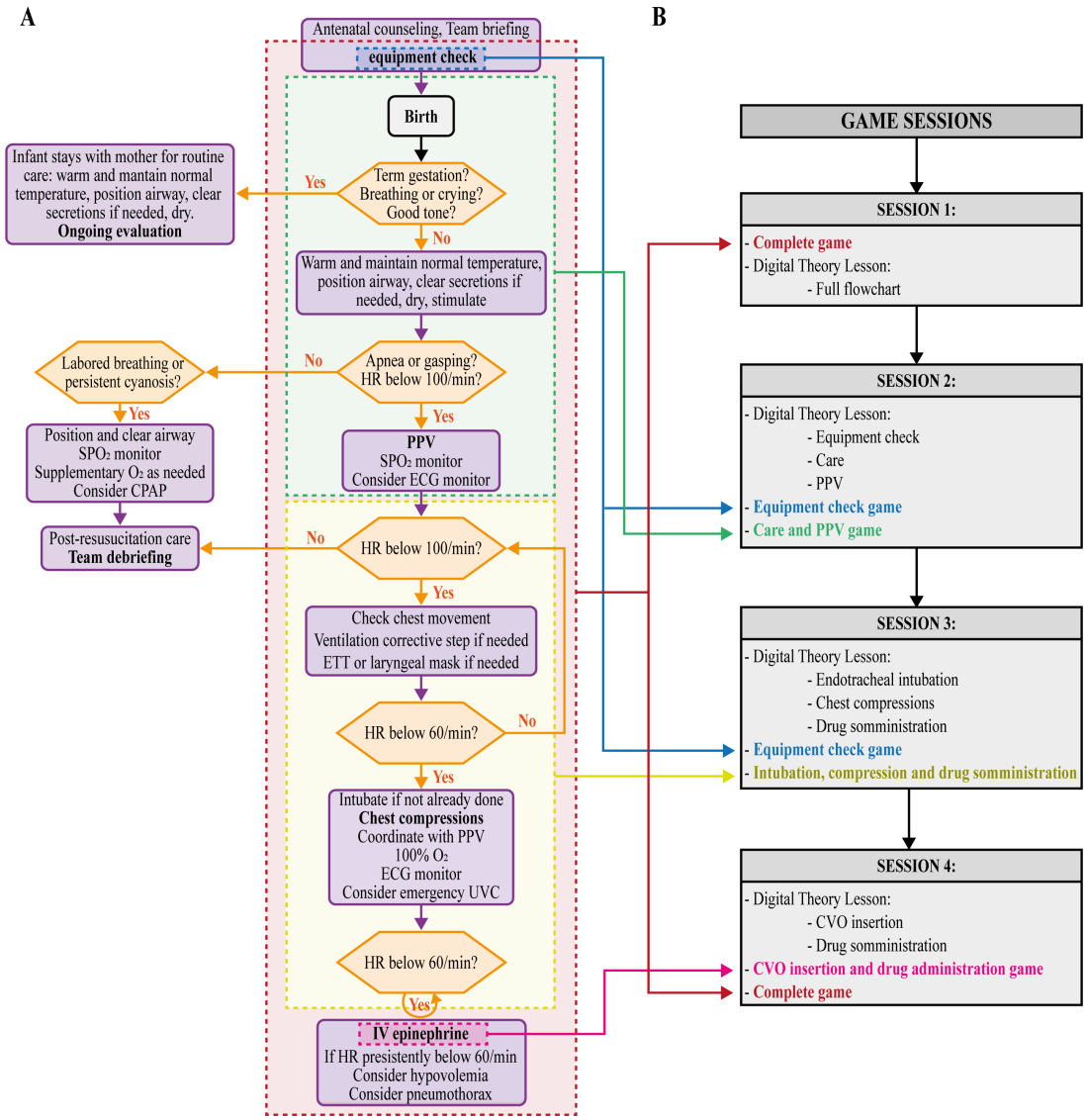

Figure 9.1: Panel **A** - Newborn resuscitation flow chart showing corresponding sections in the DIANA game (Equipment check, Neonatal care and PPV, Intubation, Chest compression and Drug administration, umbilical vein catheterization (UVC, CVO in italian and consequently in this game version) and drug administration, and Complete). Panel **B** - details of the game sessions (1,2,3,4).

chest compressions, and drug delivery, with the interactive part of the video game ending after the execution of chest compressions. Lastly, the fourth session consisted of three activities: a tutorial on venous umbilical catheter insertion, a mini game related to the procedure, and the full execution of resuscitation simulation as in the first session (Figure 9.1). To the aim of the present study, residents did not have free access to the software except for sessions scheduled on the basis of the time intervals described in the study. In this work we scheduled the DIANA

sessions to ensure the same time practice between residents. However, for future practical uses of DIANA to support classical training, this fixed schedule is not imposed by the software. Indeed, DIANA does not impose on the user the sequential use of the game levels (e.g., a practitioner can freely select one of the four sessions). This allows the end user to freely practice on a single flowchart topic or to assess their knowledge of the entire algorithm. The only limitation is that the user within the session will be guided to follow the theoretical part first and then the practical part.

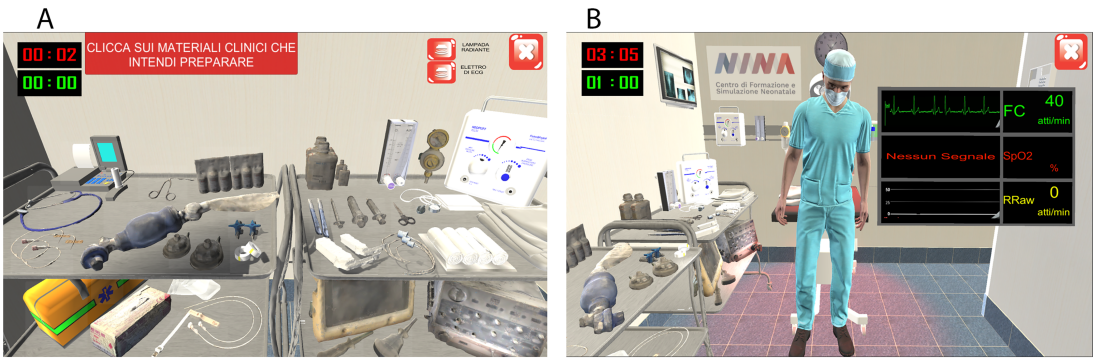

Figure 9.2: Software screenshots: equipment check (panel **A**) and dynamic curves of the simulated newborn's main vital signs (panel **B**). In equipment check (panel **A**) the user follow the instruction of the game in the red box in the left corner (in English: "click on the materials you want to check").

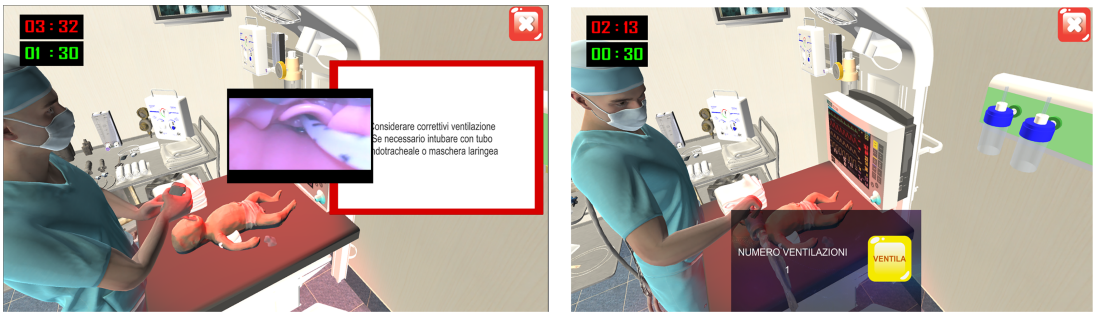

Figure 9.3: Software screenshots: execution of endotracheal intubation and assisted ventilations by the virtual assistant.During the execution by virtual assistant the user can read some useful advice as you can see in the white panel where you can read "consider the corrective actions of ventilation as endotracheal intubation or insertion of the laryngeal mask". During the execution of assisted ventilation the virtual assistant execute the compression of Ambu when the users click on button identify as VENTILA (translate as "act ventilation"). The number of ventilation acts performed is showed next to VENTILA button.

Within the interactive video game, the user had one minute to select the es-

sential tools (Figure 9.2A), categorized as totally correct, partially correct, and incorrect; Depending on the tool, size and setting selection would be required. After one minute, the chosen tools would appear in a box, checked in green ("selection made") or red ("missing" equipment). When assessing the clinical state of the patient, a monitor would show dynamic curves and heart rate, respiratory rate, and oxygen saturation (Figure 9.2B). Practical procedures were performed by the virtual assistant (Figure 9.3). During ventilation execution, the user defined the timing of the ventilation by selecting a "Ventilation" button. The game was designed to last 30 seconds, during which, every 10 seconds, the assistant's voice would reassuringly provide feedback to the user, e.g., advising them to increase or reduce the rhythm or complimenting him/her for maintaining an optimal respiratory rate in assisted ventilation. Importantly, chest compressions execution would imply cooperation between user and virtual assistant: the former would perform the required three chest compressions, following one assisted breath by the latter.

9.2.2 Study design and procedure

Study participants filled a questionnaire to assess their previous knowledge and experience (Figure 9.4). Based on questionnaire results, two homogeneous groups (Stratified random sampling, similar to other DGBL studies [467, 455]) were randomized to either the classic teaching process (frontal teaching session) or the one based on digital simulations (DGBL), respectively.

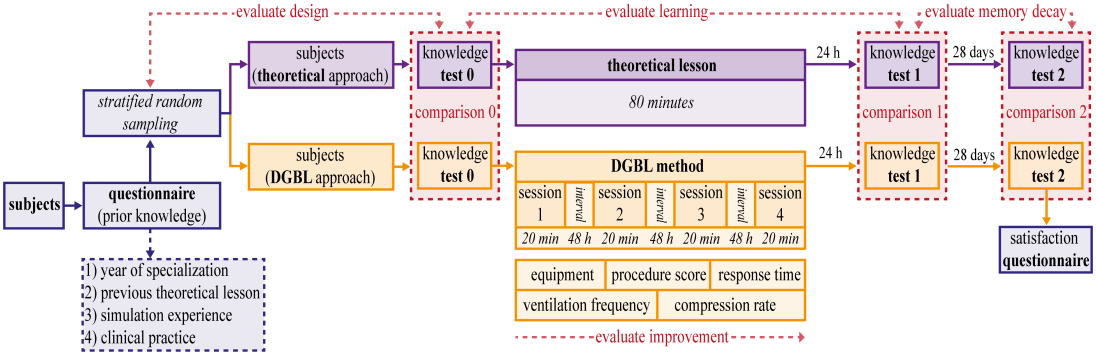

Figure 9.4: Study analysis scheme. Subjects are divided using a stratified random sampling into two homogeneous and independent groups, based on the score in a prior knowledge questionnaire. The first group (theoretical lesson) is trained by an expert neonatal trainer for 80 minutes. The second group (DGBL method) is trained using DIANA for the same length of time on 4 different sessions. Three written tests (0 pre-test, 1 post-test, 2 follow-up) are used to compare the methodologies (comparisons 0,1,2) and to evaluate learning and memory decay. The knowledge test 0 is used to evaluate the stratified random sampling.

The theoretical teaching session (Figure 9.4, in purple) was given in person by an expert neonatal trainer, with no more than 10 medical residents for each

group, which allowed them to take a very interactive lesson. After finishing the theoretical part, residents practiced the technical skills of PPV, chest compression and endotracheal intubation on a medium fidelity mannequin (Newborne ANNE, https://laerdal.com/it/doc/222/Newborn-Anne). Neither in the theory lesson nor in the software a specific (limited) clinical case was presented and discussed. On the contrary, in both training residents were asked to perform the whole resuscitation algorithm.

The DGBL group training methodology is based on the use of DIANA software. The software guided the user through the entire resuscitation flowchart divided into four phases. Indeed, starting from the promising results obtained even with a single session of a serious game approach [452, 465, 460], DGBL group (Figure 9.4, in orange) training was based on the natural subdivision allowed by a digital game: four sessions of 20 minutes each, separated by a 48-hour break; knowledge tests began 24 hours after the last session, with the same evaluation process as for the classic training group.

Both the groups (Figure 9.4, in purple) underwent three knowledge tests about neonatal resuscitation algorithm and equipment check. The test was administered at three different times: immediately before the tutorial (pre-test 0), at 24 hours (post-test 1) and at 28 days (follow-up test 2) after training ending; the questions and answers remained the same, while their order was randomly altered. Specific time intervals between assessments were chosen to capture actual knowledge retention. A 24-hour post-training time interval was specifically chosen to filter out the positive effects of short-term memory on scores [468]. The 28-day interval to evaluate of memory decay has been widely used in DGBL [469]. Unlike a much longer interval adopted by other Authors [452, 460], it minimizes the high risk of study drop out within a medical resident population, or the confounding effect of further training. Similarly, candidates were not made aware of our study's assessment methods and timings, including the 28-day delayed test, in order to prevent skewed outcomes. The three scores for either learning method were compared to evaluate the two methodologies, their strengths and limitations (comparisons 0,1,2 in red in Figure 9.4). Knowledge test 0 was also used to evaluate the design.

Furthermore, in DGBL group, user improvement was evaluated as the sessions progressed by recording any change in individual tests' numerical values (equipment score, procedure score, response time, ventilation frequency, compression rate) as common in DGBL methodologies [470]. At the end of data collection, a user satisfaction questionnaire was administered to DGBL group, to integrate subsequent versions of the software with user suggestions.

9.2.3 Measures

The primary endpoint of this study is to compare the effectiveness between DGBL (DIANA) and classic learning methodology on knowledge retention based on knowledge questionnaire performance. The several secondary endpoints regarding the evaluation of the effectiveness of the DGBL methodologies on the

user's performance during the gaming sessions and the satisfactions evaluation of this new methodology are summarized in Table 9.1 and described below ("Knowledge test scores" and "DGBL scores").

Comparison	**Feature observed**	**Comparison Tool**	**Question to answer**
DGBL and classic learning methodology	knowledge retention and equipment checklist	knowledge tests (pre-training, 1 day post, and 28 days post training)	Did the DGBL training methodology prove as effective as theoretical teaching session in knowledge retention?
DGBL games performance	knowledge retention	performance of different session game scores	Was the DGBL training methodology effective to learn a flowchart reducing decision time and increasing scores results?
	equipment checklist		Was the DGBL training methodology effective to learn the equipment checklist?
	ventilation rate		Was the DIANA ventilation game effective to learn the correct ventilation rate to perform during a PPV procedure?
	chest compression rate		Was the DIANA chest compression game effective to learn the correct rate to perform during a newborn resuscitation?
	satisfaction of new methodology	satisfaction questionnaire	Has the DGBL methodology been considered useful and effective by users?

Table 9.1: Description of the variables observed during the study divided between primary endpoints (evaluate the effectiveness of DGBL and classic learning methodology on knowledge retention) and secondary endpoints (evaluate the effectiveness on user's performance during the gaming sessions).

Knowledge test scores

Knowledge tests are used in DGBL analysis to evaluate performance [464]. The test used in this work was written by neonatal resuscitation trainers accredited by SIN, and consisted of 21 questions (each with 1 correct and 5 incorrect answers) related to the correct resuscitation procedure and a list of 40 items (21

correct, 6 partially correct and 13 incorrect) to check. The knowledge test score was calculated by allocating 1 point for each correct answer, 0 for null, and -0.2 for incorrect ones, so that the average score could be assumed to be zero in case of randomly selected answers. The result was then normalized by the number of questions. The equipment score, on the other hand, consisted of the number of correct instruments (21) selected from the list of 40 items.

DGBL scores

During the execution of DIANA game the following parameters were recorded: decision-making/response time, answer correctness from the multiple options included in the simulation, choice of equipment before each simulation, uniformity and correctness of ventilations/compressions timing. A positive score was assigned for a correct answer, a negative value for an incorrect selection and a neutral (null) score for selecting the *"Get help"* option, available for every question to cover the operator's inability to make a decision. Choosing this option was followed by a detailed explanation of the correct decision by the virtual assistant, to stimulate learning and improve subsequent sessions' performance. Knowledge score was calculated as the number of correct answers normalized by the number of questions for each session. The equipment score consisted of the number of correct instruments selected from a list of 40 items (21 correct, 6 partially correct and 13 incorrect). As some game sessions covered only part of the resuscitation procedure (Figure 9.1), the knowledge score was calculated on three question subsets: on care and assisted ventilation (PPV) (sessions 1-2-3-4); on intubation and compressions (sessions 1-3-4), and those on drug administration (session 1-4), respectively. For each answer, the response time (i.e., the time elapsed between the question administration and the execution of the action) was also calculated.

Compression and ventilation scores

In the games involving compressions and ventilations, choosing a score that rewarded maintenance of a correct frequency and penalized frequency fluctuations was essential. The number of acts per minute is not necessarily a reliable parameter to tell an excellent performance (i.e., correct and uniform rate) from a sub-optimal one, such as correct but non-uniform rate with marked variations in frequency. With reference to Figure 9.5, we defined the sequence of acts $1, \cdots, n$ and the corresponding $\Delta_i := t_i - t_{i-1}$ as the difference between the time of act i and the time of the previous act $i-1$. The correct timing intervals are then defined $[min_{freq}, max_{freq}]$ (40-60 ventilations per minute and 80-100 [+30] compressions per minute, where +30 represents the ventilations performed alternately by the virtual assistant). These ranges represent the reference values that the user must maintain, and correspond to an interval $[min_{timing}, max_{timing}] = [1/max_{freq}, 1/min_{freq}]$ between the minimum and maximum of the time interval allowed to perform a correct number of acts per

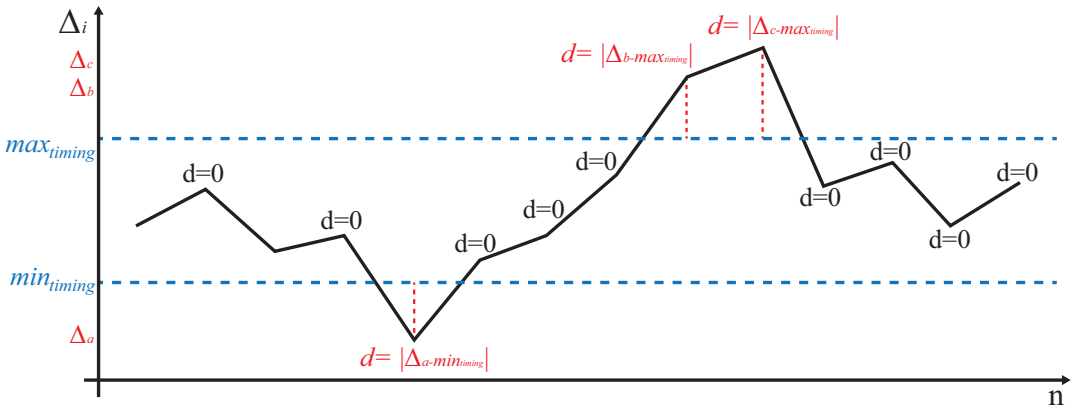

Figure 9.5: Example of a possible of ventilation/compression pattern (black). If the Δ_i between two consecutive acts is correct it falls between the horizontal dashed lines $y = min_{timing}$ and $y = max_{timing}$, in this case the value is considered perfectly correct (e.g. $d = 0$). Excessively irregular patterns lead to a positive value of d (red).

minute. Therefore, the correctness value of the i-th act is defined as follows:

$$d_i := \begin{cases} 0 & \text{if } \Delta_i \in [min_{timing}, max_{timing}] \\ max\left(\left|\Delta_i - min_{timing}\right|, \left|\Delta_i - max_{timing}\right|\right) & \text{otherwise} \end{cases}$$

With reference to Figure 9.5, every act falling within the correct ranges is rated as zero, while any variation outside the range (in red in the figure) increases the score in proportion to how much it deviates from the reference values. The first score is defined as the average of the $\{d_i\}_{i=1}^n$ (e.g. $score_{mean} = mean_{i=1}^n(d_i)$. A null score represents a candidate who has always maintained an optimal frequency of acts while a higher score identifies any deviation from the correct execution. The second score is based on the standard deviation of the $\{d_i\}_{i=1}^n$ (e.g. $score_{std} = std_{i=1}^n(d_i)$. This score characterizes the irregularity of the values and is, therefore, indicative of maintaining a non-homogeneous timing during the test.

9.2.4 Statistical Analysis

The study design is based on a stratified random sampling to control the nuisance factors. The strata are designed on the basis of a score extrapolated from a questionnaire of previous theoretical/clinical/practical experience. This score was used to create four levels of competence (0 no experience, 1 - one of the three experiences, 2 - two experiences, up to 3 for those who participated in all simulation, theory and practice experiences), then used in the study design to divide the candidates of the two groups. The uniformity of the knowledge test

0 score distributions of the two groups' clinical experience, was tested using a Kolmogorov-Smirnov (KS) two-sided test. A further indicator of uniformity is the amount of times a random sampling could have produced a better subdivision than the chosen design. This estimate was achieved by using a Monte Carlo method for probability estimation: 100000 times the group of all candidates (associated with their respective knowledge test score 0) is randomly divided into two groups (27 and 21 respectively). This (artificial) subdivision represents a possible result of a random fully experimental design. Then, the Kolmogorov-Smirnov distance D between the two sets is calculated and compared with that obtained in the stratified random sampling. The knowledge test scores calculated before learning, at the end of learning and 28 days later, were evaluated by comparing the means, variances and distributions (KS test). The normality of the scores obtained was tested by Shapiro-Wilk test. Variances were compared by F-test for (independent) groups comparison and by Pitman-Morgan test of variance for paired sample for internal group comparisons. Under the assumptions of normality and homogeneity of variances, the independent t-test was used to compare means. In the absence of these hypotheses, the non-parametric (conservative) Wilcoxon signed-rank test and the Mann-Whitney U test were used. Considering that the scores calculated in the knowledge tests 0, 1 and 2 are repeated measures of the same group and the frequent absence of the hypothesis of normality, the values are preliminary compared using a Friedman test. Post-hoc pairwise analysis through the previously described paired tests are then applied to detect variations of the score. Bonferroni correction is presented to counter the problem of multiple post-hoc analysis. The comparison between independent groups (i.e., DGBL vs theory) pre-training, at 1 day and at 28 days is instead carried out with non-paired tests. To analyze the performance of the individual game sessions, the same tests were applied to learning score procedure, the response times of the questions and the uniformity of the ventilation/compression timing. One-sided versions of the tests were applied to test the monotony of the scores. Statistical analysis was carried out using the software R [4.1.1] [471].

9.2.5 Ethical approval

Users were pediatric/neonatology residents of the Azienda Ospedaliera Universitaria Pisana (AOUP) who consented to the acquisition, processing and dissemination of data in anonymized form. The study was approved by the local Institutional Review Board for Ethic Issues. All analyzed data were anonymized and the entire analysis was blinded.

9.3 Results

9.3.1 Participant characteristics and stratified sampling

63 pediatric/neonatology residents from the Azienda Ospedaliera Universitaria Pisana (AOUP) were recruited for the study, ranging from the first to the fifth specialty year with a high variability in previous training. The level of competence of each resident depends on the experience acquired before the start of the analysis (year of specialty, practice using a simulator, having attended theoretical training, and also real clinical practice with newborns). These nuisance variables (i.e., a variable that may alter the outcome of the study but is of limited interest in the chosen design) were of no interest to the study and had to be controlled to ensure homogeneity of the two groups using the stratified random sampling. By applying the Monte Carlo approach against the Kolmogorov-Smirnov distance calculated with the chosen design (d=0.13), only 8% of the random subdivisions thus generated show a distance $D < d = 0.13$, confirming the validity of the design used.

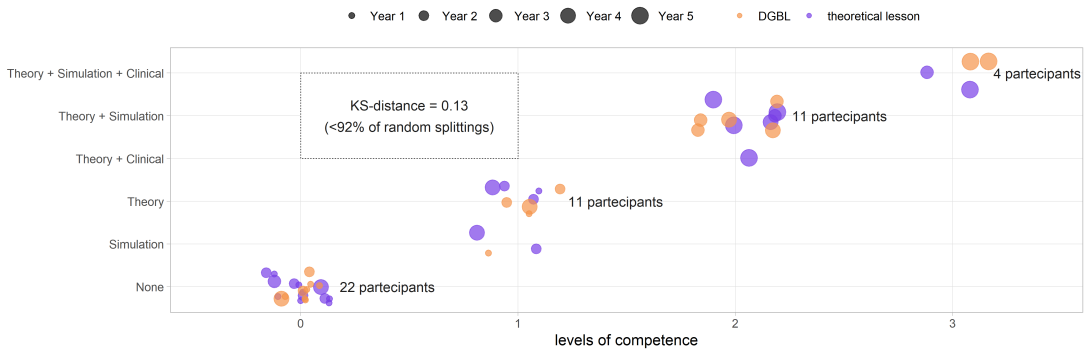

Figure 9.6: Group subdivision based on competence levels for the stratified random sampling (DGBL group in orange, theoretical teaching session group in purple). Using a Monte Carlo approach based on the knowledge test 0 score and the Kolmogorov-Smirnov distance, it can be shown that this subdivision is better than 92% of those artificially obtained through a fully random design.

Furthermore, the validity of the study design was tested also by comparing the knowledge test 0 and the check equipment scores between the two groups: no statistically significant differences were found (two-sided Mann-Whitney U test $p = 0.21 \gg 0.05$ and two-sided independent t-test $p = 0.51 \gg 0.05$ for equipment score). Furthermore, the distributions of both values were also not dissimilar (two-sided Kolmogorov-Smirnov test, $p \gg 0.5$). The experiment design, and the corresponding subdivision of the population in strata, allowed to obtain a homogeneous level of past experience (as shown by the level of competence in Figure 9.6). The two groups were therefore considered uniform in the baseline scores (knowledge test 0) and homogeneously subdivided according to

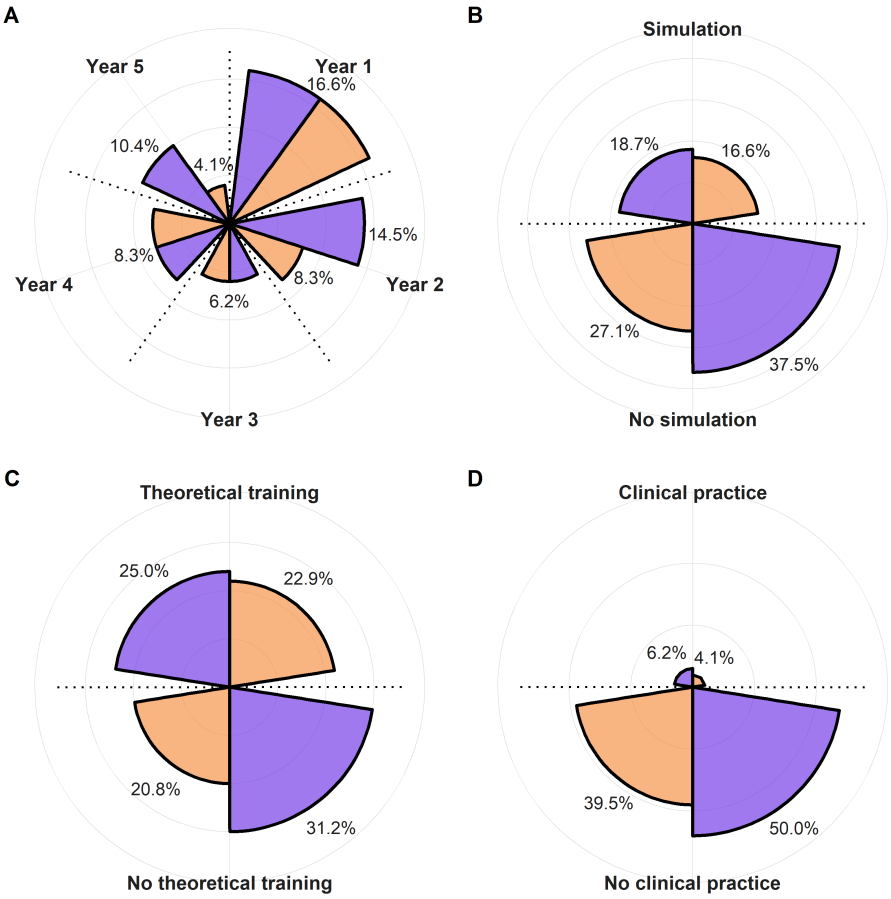

Figure 9.7: Subdivision of the population of the study between DGBL group (in orange) and classic theoretical teaching group (in purple). Panel **A** shows the year of specialty training (not one of the variables considered in the stratified random sampling and is therefore characterized by a higher variability. Panels **B**, **C**, **D** show the percentage of the subjects that had used a newborn clinical simulator, underwent theoretical training in neonatal resuscitation, and practiced in neonatology, respectively.)

the confounding variables.

The design led to two groups uniform in terms of previous experiences (Figure 9.7). Candidates who dropped off for personal reasons, or those failed to meet learning and testing sessions deadlines, were excluded from the study: of a total of 15, the majority affected DGBL group, yielding 27 candidates for the classic learning group and 21 for DGBL group. In the breakdown of the study sample by specialty year, 56% of the residents clustered around first and second year (Figure 9.7A), only 35.3% of the trainees had practiced at the simulator before this study (Figure 9.7B), whereas, 47.9% had already received theoretical training in neonatal resuscitation (Figure 9.7C). User characteristics that could significantly

impact results (e.g., neonatal clinical experience, as shown in Figure 9.7D) were uncommon in this cohort (only 10.3% of candidates); this setting required a proper design in order to prevent concentrating the few candidates with any particular characteristic in only one of the two groups. Consequently, the reference sample can be described as having a dominant component of students of the first years, mostly with no previous experience (45.8%). The older residents were the ones with greater medical experience (clinical/simulation/theoretical), with all fifth-years students having received at least one theoretical teaching session and one practical tutorial at the simulator.

9.3.2 Comparison between DGBL and classic learning

Knowledge retention

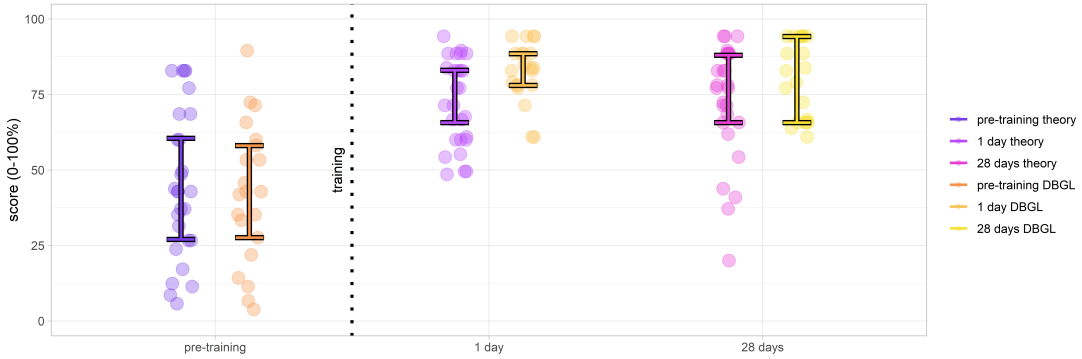

Figure 9.8: Results of knowledge tests evaluated pre-training, 1 day post-training and at 28 days follow-up (score medians and middle 50% interquantile ([0.25,0.75]); theoretical teaching session group scores in purple, DGBL method group scores in orange). Whereas pre-training groups are comparable, post training scores demonstrate the effectiveness of both methodologies, and of DGBL in particular.

The first analysis was based on the scores obtained in the knowledge tests 0,1,2 (respectively pre-training, 1 day post-test and 28 days later follow-up). None of the observed test score distributions could be assumed to be normal except pre-training scores (Shapiro-Wilk test, $\alpha = 0.05$) as shown in Figure 9.8 (purple for classic learning and orange for DGBL approach). After a preliminary Friedman test ($\alpha = 0.05$) that found differences in scores between the knowledge tests 0,1,2 for both the DGBL ($p \ll 0.001$) and the theoretical training ($p \ll 0.001$), we moved on to the post-hoc pairwise analysis. The effectiveness of the theoretical teaching session was proved by an increase in pre-training and post-training tested scores at 1 day, with an increase in median scores from 42.8% to 71.4% (paired one-sided Wilcoxon signed rank test, $p \ll= 0.001$). An even greater increase in scores was found for DGBL training, with median

scores ranging from 42.8% pre-training to 83.8% post-training (paired one-sided Wilcoxon signed rank test, $p \ll 0.001$). There was no statistically significant reduction in scores following the 28-day wait ($\alpha = 0.05$). Even considering a conservative Bonferroni correction factor ($m = 2$) to control the family-wise error rate, the reported results have much lower p-values than the corrected $\tilde{\alpha} = \alpha/m = 0.025$. The initial pre-training scores could be considered coincident both as medians (two-sided Mann-Whitney U test, $p = 0.21 \gg \alpha = 0.05$) and as distributions (two-sided Kolmogorov-Smirnov test, $p = 0.97 \gg \alpha = 0.05$). This allowed to compare the score increases for the two methodologies. Therefore, considering the post/pre-training score differences, DGBL method was statistically not inferior to the classic teaching session (one-sided Mann-Whitney U test, $p = 0.005$). As represented graphically in Figure 9.8 (28 days), score variance decreased between pre-training and post-training (1 day) for both methodologies (one-sided paired Pitman-Morgan test, $p \ll \alpha = 0.001$). There was no statistically significant variance increase 28 days post-learning for DGBL group ($p = 0.07 > \alpha = 0.05$), while variance increased significantly for the classic methodology group ($p = 0.02 < \alpha = 0.05$). Furthermore, the variance at 28 days for the classic learning group was greater than that of DGBL group, with values more distributed over the score range (one-sided F-test, $p = 0.03 < \alpha = 0.05$). The variance of the analyzed scores makes it possible to distinguish between a population with a homogeneous knowledge (low variance) compared to one with marked differences between the scores of the individuals (high variance). For this reason we want to investigate whether following learning there is a simple increase in scores, which is an indication of an effective transmission of knowledge, or even a consequent reduction in the variance of scores, that is representative of uniformity of skills following learning (e.g., we were able to teach them what we wanted to teach them).

Equipment game

Equipment scores were divided into three categories: totally correct, partially correct, incorrect. Learning was considered to be effective if users selected a greater number of correct options and fewer of the incorrect/partially correct ones. The scores evaluated at steps 0,1,2 (respectively pre-training, 1 day post-training, 28 days follow-up) of classic learning (in purple, panel A) and DGBL methodology (in orange, panel B) are shown in Figure 9.9. All the score distributions were non-normal, except scores for the correct tools at the 0 / pre-training evaluation (Shapiro-Wilk, $\alpha = 0.05$). A preliminary Friedman test ($\alpha = 0.05$) is performed to detect if there is a difference among the 3 assessments (knowledge test 0,1,2) for both DGB/classic learning and for the totally/partially correct and incorrect items. A statistical significance of the learning effect is only found for the totally correct items (classical theoretical learning, $p = 0.02$) and for both totally correct ($p \ll 0.001$) and incorrect ($p = 0.007$) items score for the DGBL training. Classic learning (Figure 9.9A) was effective in achieving memorization of totally correct objects (57.1% to 71.4%, paired one-sided Wilcoxon

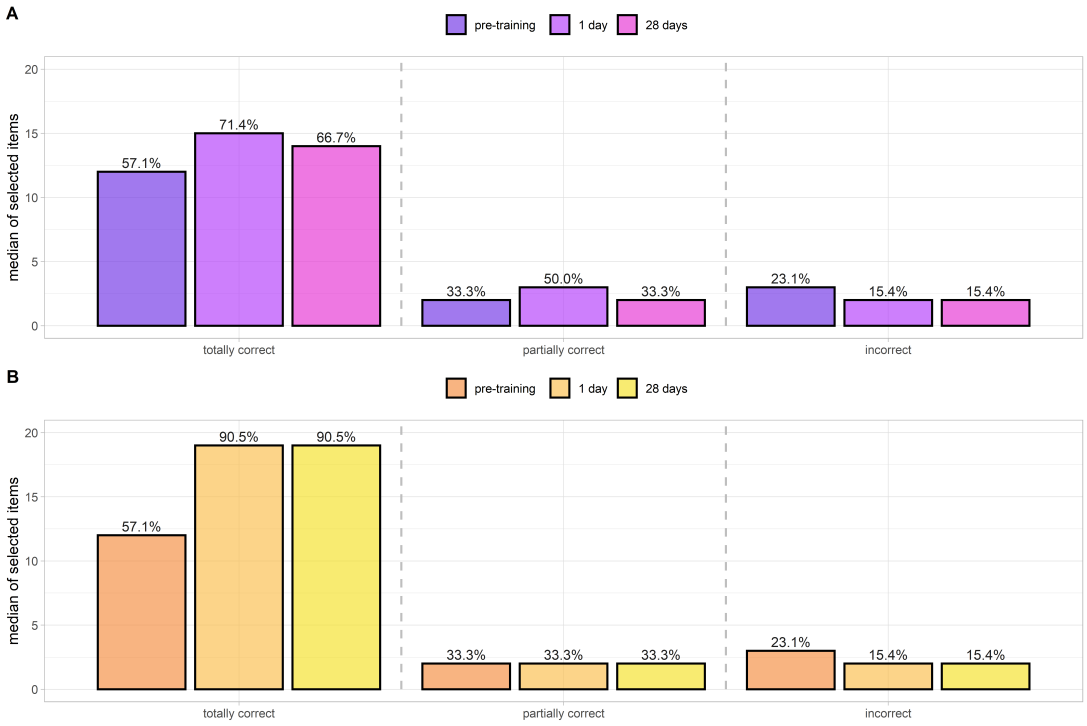

Figure 9.9: Equipment scores of totally correct/partially correct and incorrect items selected by the control group (standard teaching session, panel **A**) and DGBL group (panel **B**). Initial equipment scores for the two methodologies are not statistically different. DGBL methodology leads to a greater increase in correct item selection. It also reduces selection of incorrect/partially correct items, whereas after theoretical teaching no reduction is observed.

signed-rank test con $p \ll 0.001$). No other statistically significant improvement ($\alpha = 0.05$) was noted in any of the other scores, either in relation to the 1-day or 28-day assessment. Conversely, there was an increase in the partially correct objects chosen in Test 1 (33.3% to 50.0%, $p = 0.01$). The DGBL methodology proved more effective (Figure 9.9B), with not only a statistically significant improvement in pre-training/ 1-day scores for correct items (57.1% to 90.5%, paired one-sided Wilcoxon signed-rank test con $p \ll 0.001$), but also with a moderate a reduction of incorrect items (23.1% to 15.4%, $p = 0.03$) which is not statistically relevant for the classical learning method. The initial scores for the correct objects coincide for the two groups for both the median (57.1%, paired two-sided Wilcoxon signed-rank test con $p = 0.72 \gg 0.05$) and the mean values (59.2% theoretical teaching session, 56.7% DGBL, two-sided independent t-test, $p = 0.51 \gg \alpha = 0.05$). As the coinciding baselines allow an analysis of the pre / post-training differences of the two groups, the DGBL methodology led to a significantly greater improvement than the classic learning one (one-sided Mann-Whitney U test, $p = 0.009 < \alpha = 0.05$). We did not carry out the same analysis for partially correct and incorrect objects, as uniformity between the

two strategies cannot be assumed at the $\alpha = 0.05$ level. In this analysis, considering a Bonferroni correction factor ($m = 2$) did not change the result of the effect of training on score of correct items. However, the effect of the reduction of incorrect items for the DGLB group can no longer be considered statistically significant.

Figure 9.10: Number of items selected by users (regardless of learning mode) during the knowledge tests, divided by color into incorrect (red), partially correct (yellow) and totally correct (green). Greater color opacity indicates a greater number of selected items. Selected elements numbers are subdivided as pre-training (inner circle), 1-day post-training (middle circle) and at 28 days follow-up (outer circle). Color opacity shifts highlight the items for which learning has proved particularly effective (e.g. ECG leads that go from 27 pre-training to 38/33 post-training or ET tubes(size 2.5, 3, 3.5) that are reduced from 30 to 19/17), whereas uniformity of color opacity across the concentric circles show the items for which learning has proved ineffective (e.g., Intensive care ventilator, Laryngeal mask airway or Check neonatal incubator).

Item choice in equipment check

With regard to the total number of times that each tool was selected during the knowledge tests (regardless of the learning mode), training methodology can be improved. Indeed, Figure 9.10 highlights the elements for which the methodology worked well (increasing values for totally correct from the center outwards, and decreasing for partially correct/incorrect ones) and those for which it does not (stable scores among the sessions). For almost all totally correct options, learning proved effective with both methodologies; however, some options were too obviously correct, e.g., adrenaline administration (45 to 47/47) or pulse oximeter use (41 to 40/44). The best training effect was seen on discouraging the selection of Endotracheal Tubes (ET) (0,1) (30 to 19/17). For other incorrect items (intensive care ventilator, E.R. Bag, E.T. Tube size) and partially correct ones (laryngeal mask airway (31 to 33/33), check neonatal incubator (37 to 43/43), E.R. bag (20 to 18/15) and Intensive care ventilator (19 to 25/27)), the learning was not effective enough, as users continued to rate them as necessary despite training indicating otherwise. We are planning the implementation of software changes, which will allow to investigate communication effectiveness for these learning objectives. It should be emphasized that some incorrect tools (ultrasound machine, ultrasound probe, LISAcath(R)) proved poor distractors, as users hardly ever selected them. Therefore, future versions of the game will not include those items.

9.3.3 DGBL game performance

Knowledge retention

Figure 9.11A shows the scores and the respective averages of the game sessions (e.g., the number of correct answers) by category and session number (1,2,3,4). The medians response times (seconds) for the entire corresponding series of questions are shown in Figure 9.11B. After three preliminary Friedman tests for scoring (CARE and PPV, intubation and chest compression and drug administration) and three more for answer times ($\alpha = 0.05$), all identifying a statistical difference, we moved on to post-hoc pairwise analysis. Both panels show a strong monotonicity in the functions, with increasing scores (~ 65.3 to 96.7) and decreasing times ($\sim$ 11.9 s to $\sim$ 7.7 s) as the sessions progress (one sided paired Wilcoxon signed-rank test, $\alpha = 0.05$), except for equipment CARE and PPV/intubation and chest compression scores between session 3 and session 4 ($\alpha = 0.05$), which did not show a statistically significant increase (knowledge plateau). After a Bonferroni correction by a factor ($m = 5$) for the CARE and PPV and a factor 3 for intubation and chest compression, the same results remained valid at a level of $\tilde{\alpha} = \alpha/m = 0.01$ except for the CARE and PPV scores between session 2 and 3, whose increase was no longer statistically significant. Test values at sessions 1 and 4 highly correlate ($\rho = 0.84$, Pearson test for linear correlation $p \ll 0.001$) with knowledge test scores 0 and 4. The game scores are therefore predictive of success in the following knowledge test.

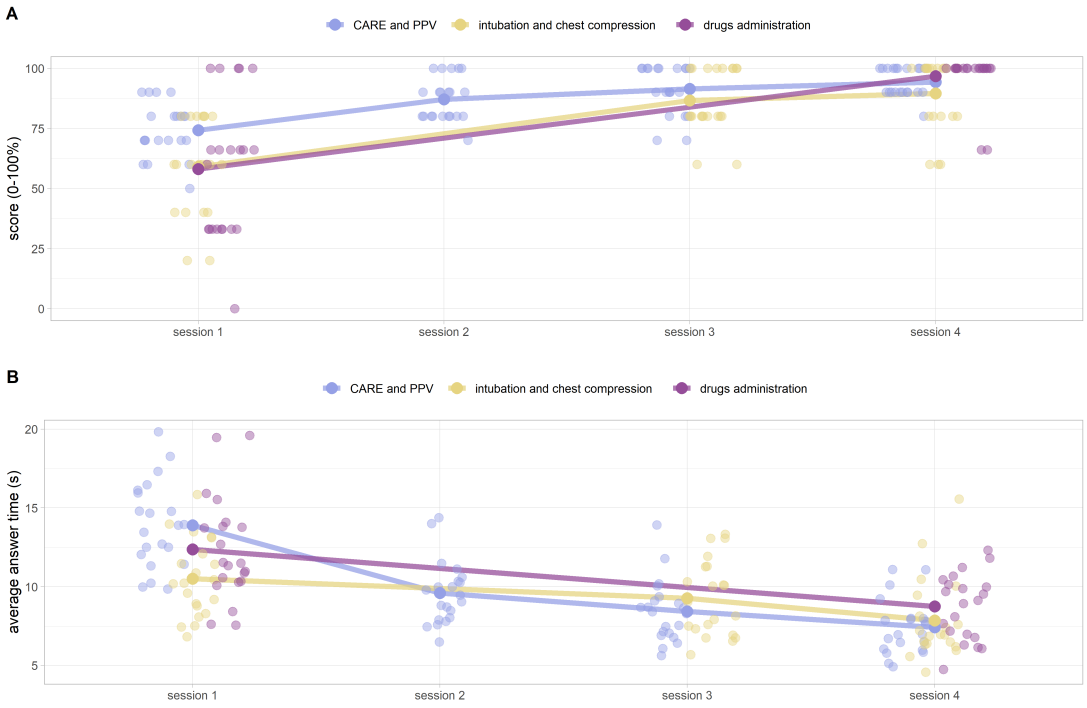

Figure 9.11: Panel **A** - DIANA game scores, and corresponding median values, over the 4 sessions. The scores are subdivided into three categories (CARE and PPV, intubation and chest compressions, drugs administration) for ease of analysis. Panel **B** - corresponding average answer times (in seconds).

Equipment game

As anticipated by knowledge tests (Figure 9.8), the sessions improve users' ability to choose the correct objects. Indeed, the number of totally correct objects selected (Figure 9.12A) and of partially correct/incorrect ones (Figure 9.12B) respectively increased and decreased after each session. Specifically, since all the scores are not normal (Shapiro-Wilk test at the alpha level = 0.05), we proceeded to test the monotony of the score with a non-parametric test (preliminary Friedman test at a level $\alpha = 0.05$ that revealed a statistical difference between the totally correct scores, and post-hoc one-sided paired Wilcoxon signed-rank test, respectively $p \ll 0.001, p = 0.01, p = 0.003$ between sessions 1-2, 2-3 and 3-4). Unlike procedure memorization highlighted by the scores (Figure 9.11), there is still a statistically significant improvement for this game between sessions 3 and 4 ($p = 0.003$). A Bonferroni correction factor $m = 5$, the number of pairwise analysis carried out, can be applied ($\tilde{\alpha} = \alpha/m = 0.01$). Despite the correction, the results presented remain unchanged. Furthermore, candidates made fewer mistakes when the tool name was paired with its picture (medians of 0 for partially correct items and incorrect ones vs 33.3% and 15.4% for the same students during the knowledge test), as shown in Figure 9.12B and Figure 9.9B,

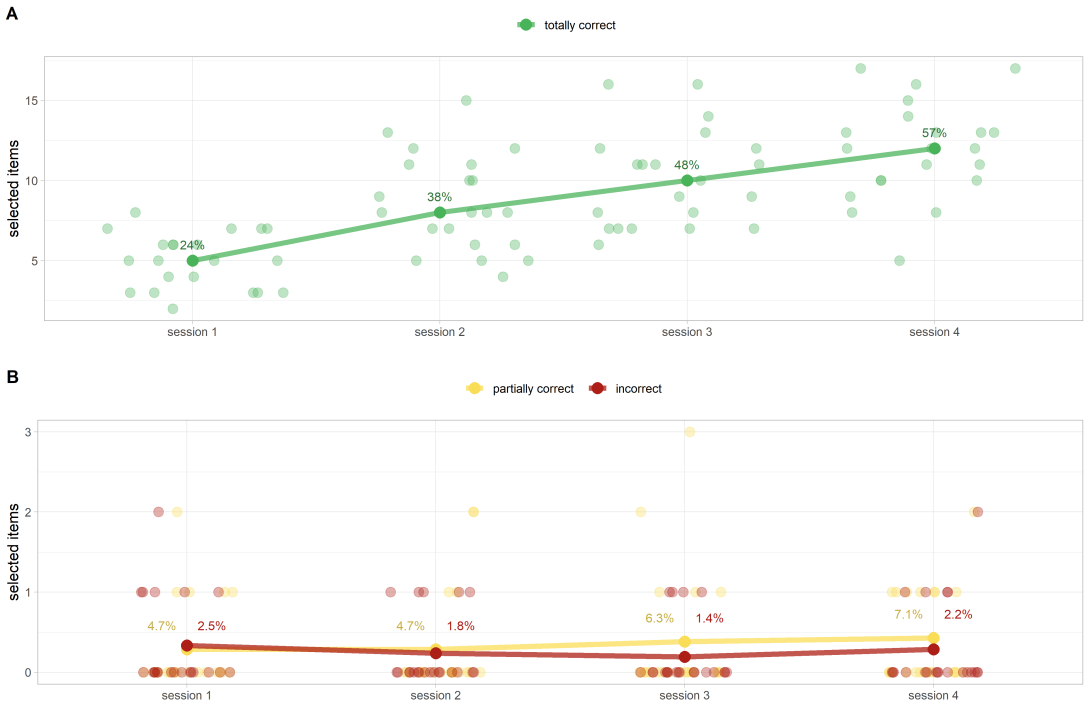

Figure 9.12: DIANA game equipment scores (as selected items and their percentage of the median of total items) for totally correct (panel **A**) and partially correct/incorrect items (panel **B**). Panel **A** shows a monotonous increase of correctly chosen elements (from 24% to 56%). Panel **B** shows extremely low values of partially correct/incorrect scores. This finding reinforces the idea that visual memory plays a pivotal role in memorization. Panel B shows the percentage of the mean values because the corresponding medians are all equal to 0.

respectively.

Ventilation and compression game

Figure 9.13 shows the deviation from the correct ventilation- (40-60 breaths per minute = intervals between 100-150 hundredths of a second) and compression ranges (80-100 breaths per minute = considering 30 alternating breaths per minute, intervals between acts of 46-54 hundredths of a second). The score (Y axis) represents the precision of execution in terms of number of acts, a score of 0 representing a frequency kept within the range. Circle size is the standard deviation (STD) of the uniformity score d. Smaller circles represent greater execution uniformity. Ventilation frequency was not as effectively learned as compression rate, despite the apparent similarity of the games aiming to teach them (Figures 9.13A and B, respectively). From a statistical point of view, the values of the scores and the STDs of the rates all follow non-normal distributions (Shapiro-Wilk test, $p < 0.001$ for scores and $p < 0.01$ for STDs). Regarding the

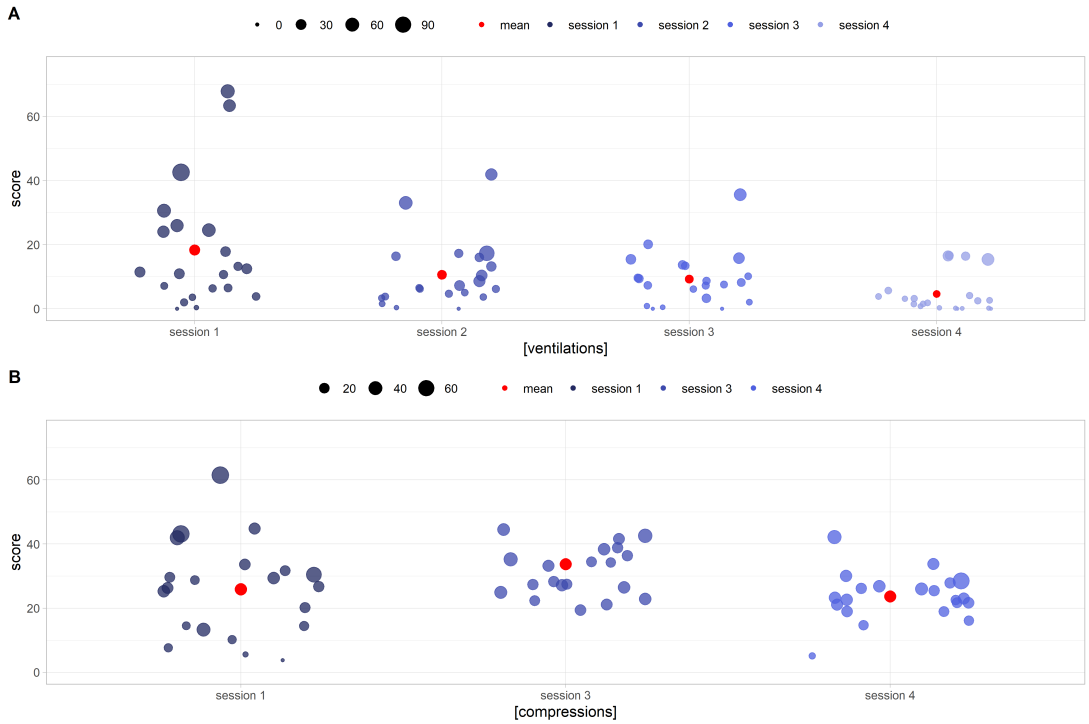

Figure 9.13: DIANA game scores (y axis) and standard deviation (circle size) for ventilation (panel **A**) and chest compression (panel **B**) execution. Low y values imply an execution frequency closer to the correct one, while short circle radii identify smoother acts. Panel **A** shows performance improvement in terms of both correct frequency (decreasing score to 0) and smoothness of execution (small circles radii). Panel **B** shows a less noticeable improvement in performance, with users still unable to execute compressions correctly after the fourth session.

ventilations there is an improvement of both parameters. Score values are decreasing with monotony (one tailed Wilcoxon signed rank test $p < 0.01$). As regards STDs, on the other hand, there is a statistically significant reduction between the first/second session ($p = 0.03$) and the third/fourth session ($p = 0.001$) but not between the second/third. The same tests, applied to compressions, were all statistically inconclusive.

Satisfaction questionnaires

Of the data collected from DGBL user satisfaction questionnaires (20/21), we evaluated perceived utility and enjoyment of the procedure (both using a five-level Likert scale). Ratings were generally positive in terms of perceived utility (40% (5/5) and 60% (4/5)) and procedure agreeableness (40% (5/5) and 60% (4/5)). Suggestions mainly concerned the need to increase available equipment game time, perceived as too short. Positive feedback was given on spreading the game sessions over different days.

9.4 Discussion

This study successfully applied a DGBL-based approach to neonatal resuscitation teaching through the use of a newly developed software (DIANA). DIANA game focused on the entire neonatal resuscitation algorithm (including: equipment check, neonatal care, drug administration, assisted ventilation and chest compressions). The study was aimed at pediatric/neonatology residents (a learners' category considered in few studies as in the mixed study group by [455]); while the majority of previous findings in this field have focused on undergraduate medical students [452, 463, 464], healthcare professionals [454, 465, 455], and experienced neonatal providers [460, 465]. This study's sample size is similar to other DGBL studies in the medical/neonatal field [452, 472, 473, 453, 460]. Learner allocation (Stratified random sampling) to two experience-based groups (year of specialty training, previous theoretical teaching session, simulation experience, clinical practice experience) proved effective in obtaining homogeneous baseline scores (Section 9.3.1). Furthermore, the subdivision obtained was better than 92% of those eventually obtained by applying a completely random method. This study is among the few that: 1) fully exploit the ability of a game to extract user data (e.g., ventilation/compression game scores, response time, etc.), 2) define a treatment group and an independent control group through a baseline score (pre-test), 3) evaluate two follow-ups (short- and long-term knowledge retention). In addition, compared with the majority of published studies, which tested learner months apart [452, 453, 460], we preferred to keep the testing interval shorter (and yet longer than 2 weeks, in line with best practice in assessing DGBL learning [474]); as the studied cohort was recruited among pediatric/neonatology residents, specialty training would invariably continue to provide reinforcement of the skills assessed. It should be noted that 28 days are considered a sufficient timeframe to evaluate memorization of a procedure in the medium- to long term [469].

The DGBL methodology proved to be useful and appreciated by users to teach both neonatal resuscitation algorithm and ventilation execution. Furthermore, it proved to be even more effective than the classic frontal teaching session for both short-term procedure memorization and equipment game score. In particular, the scores related to short-term knowledge retention proved to be higher than those obtained by the theoretical frontal teaching session, in line with the existing literature [453, 463, 464]. Also in line with the limited number of studies with a follow-up at more than 28 days [452, 460, 453], long-term knowledge retention for DGBL group was as good as the control group one. Furthermore, candidates who had received classic training demonstrated a regression to lower scores, unlike DGBL methodology learners. DGBL methodology was particularly effective in the learning of clinical equipment checking. Whereas the classic theory teaching session led to a statistically significant, but moderate increase in the number of correct objects chosen (57.1% to 71.4%), DGBL-based approach led to a much greater improvement (57.1% to 90.5%). Furthermore, while the

classic teaching session had almost no effect on changing the scores for partially correct/incorrect items (33.1% to 50.0% and 23.1% to 15.4%), DIANA game reduced or leave unchanged scores for both partially correct (33.1% to 33.1%) and incorrect tools (23.1% to 15.4%). This score discrepancy is likely due to the difference in the way the learning objective is conveyed: DGBL approach breaks learning into sub-games (one of which is the explicit teaching of which tools should be used), while during a theory teaching session the tools are named progressively at the time of their use. Overall, the DGBL methodology subdivision of learning into multiple sessions was confirmed to be effective for the learning of neonatal resuscitation in line with further previous simulation-based studies [472, 473], especially for the maintenance of the acquired competencies [475]. The information collected in the DGBL sessions allows performance analysis (learning curve) related to flowchart learning, response times, equipment check, and timing of assisted ventilations/chest compressions. Procedure learning was effectively achieved, in line with the existing literature [452, 460, 465]: the first three sessions showed significant improvements in learning, while the fourth highlighted a learning plateau. Of note, there was a constant improvement in response times along the four sessions, with a total reduction of more than 30% of the initial one. Similarly, there was a steady improvement in the correct equipment check score (from 24% to 57%). In the assisted ventilation game, DGBL methodology proved to be effective, as residents responded to the feedback from the game and learned to keep the correct rate independently. However, in the chest compressions game, similar in execution to the assisted ventilation one, we did not observe the same effectiveness; candidates did not improve in either the frequency (remaining outside the required clinical range) or the regularity of compressions. This pattern persisted across all four sessions. The discrepancy between these two results could be induced by the differences between the two games. Indeed, during the compression game, the user must interact with the virtual assistant which performs ventilation. To complete the task before next the ventilation, users' tend to perform excessively clustered and irregular compressions.

The administration of a user satisfaction questionnaire confirmed a greater appreciation for DGBL as a training methodology than the classic frontal theory teaching session, in line with the existing literature [456, 463, 464]. DGBL methodology usability is crucial for future developments, as learners positively disposed to digital tools tend to respond more effectively [470]. Based on the satisfaction questionnaire results, appreciation was lower for the check equipment game compared to the others, despite its effectiveness on improving user scoring.

One of the limitations of this study is the inability of digital software to teach the execution of technical skills. Particularly for complex tasks (also to be combined with another operator), such as chest compressions, this methodology proved ineffective: users' acts remained too frequent, inappropriately clustered and not coordinated with the virtual assistant. Furthermore, the knowledge test does not guarantee that users will apply those skills effectively in a clinical context. Future versions of this software will be developed from the analysis pre-

sented in this study and the suggestions collected through the satisfaction questionnaire. Specifically, we aim to reduce the number of sessions to 3 (learning plateau detected at the fourth one), allow no time limitation for the equipment check game, and exclude from the tool list the obviously incorrect options (poor distractors). To overcome the limitation of learning technical skills in DGBL methodology, future developments may require integration with a physical support structure to allow the candidate to practice clinical tasks. To improve the application of these training methodologies we are developing the online implementation of DIANA (both in Italian and English) to allow the autonomous use of DIANA in further medical realities, as a free tool for training and re-training. Thanks to the online platform we are already extending the same analysis on a wider population. In this way we can use our findings (on both population characteristics and expected scores) to estimate the required sample size to improve future studies. The future development of a hardware device for the execution of practical skills will also allow to overcome a known limitation in simulation field (i.e. by lack of a report on the technical performance of the user with high-fidelity mannequins). A high-fidelity simulator could offer a report on the correct execution of the flowchart, based on human external observation of simulation. However, with a hardware device designed to record the events performed, both in terms of decision-making and practical performance, it will be possible to conduct a more detailed and precise study of the effectiveness of this two training methodologies.

We will also seek to modify the software with/without hardware integration to widen the potential user base, including other clinical specialties and varying levels of experience. In particular, we aim to extend this learning tool to users less accustomed to digital technology to further assess the impact of user mindset on the effectiveness of DGBL methodology [470]. Moreover, as DGBL is unlikely to be adopted as a stand-alone teaching method [454] (especially in higher education [457]), future research may involve using the two methods in sequence, e.g., reinforcing the classic theory teaching session by DGBL, or a simulator-based introduction to a classic teaching session. This blended approach has been already validated for simulations outside neonatology [476]. Considering the positive feedback obtained by remotely testing DGBL in other healthcare education contexts [460], deployment of DGBL to support healthcare education in low-income countries could represent another future development in the use of this learning technology.

9.5 Conclusion

In this study, DGBL methodology for pediatric/neonatology resident training proved to be superior to theoretical teaching session (led by a neonatal expert trainer) on short- and long-term knowledge retention of memorization of the correct equipment to assemble. In addition, DGBL proved to be at least as effective as the teaching lesson for memorization and retention of neonatal resuscitation

algorithm. DIANA game allows individual user session analysis, with an improvement in "session-after-session" scores and a reduction in decision-making times. We propose that DGBL could be a valuable addition to classic learning methodology for all medical procedures involving a procedural algorithm.

Conflict of Interest Statement

The authors declare that the research was conducted in the absence of any commercial or financial relationships that could be construed as a potential conflict of interest.

Author Contributions

S.B. and G.D.C. share co-first authorship. S.B. fully implemented the software DIANA, collected the data, drafted the initial manuscript, reviewed, and revised the manuscript. G.D.C. designed the study and the data collection tools, analyzed the data, carried out statistical analysis, drafted the initial manuscript, reviewed, and revised the manuscript. M.D.P., F.L. collected the data, were involved in the classic training sessions and revised the manuscript. R.T.S., M.C., and A.C. wrote the knowledge test, taught during the classic training sessions, integrated the analysis with the corresponding medical discussion, reviewed, and revised the manuscript. N.F. reviewed, critically analyzed and revised the manuscript including revision of English language.

Chapter 10

Chicago Classification v4.0 Protocol Improves Specificity and Accuracy of Diagnosis of Oesophagogastric Junction Outflow Obstruction

Pierfrancesco Visaggi, Matteo Ghisa, Giulio Del Corso, Federica Baiano Svizzero, Lucia Mariani, Salvatore Tolone; Marzio Frazzoni, Andrea Buda, Massimo Bellini, Vincenzo Savarino, Roberto Penagini, C. Prakash Gyawali, Edoardo V. Savarino and Nicola de Bortoli

Alimentary Pharmacology & Therapeutics (2022)

Summary

Background: Chicago Classification version 4.0 (CCv4.0) introduced stringent diagnostic criteria for oesophagogastric junction outflow obstruction (EGJOO), in order to increase the clinical relevance of the diagnosis, although this has not been demonstrated yet.

Aims & Methods: We aimed to determine the prevalence of EGJOO using CCv4.0 criteria in patients with CCv3.0-based EGJOO, and to assess if provocative maneuvers can predict a conclusive CCv4.0 diagnosis of EGJOO. Clinical presentation, high-resolution manometry (HRM) with rapid drink challenge (RDC), and timed barium oesophagogram (TBE) data were extracted in patients diagnosed with EGJOO as per CCv3.0 between 2018-2020. Patients were then reclassified according to CCv4.0 criteria, using clinically relevant symptoms (dys-

phagia and/or chest pain), and abnormal barium emptying at 5 min on TBE. Receiver operating characteristic (ROC) analyses identified HRM predictors of EGJOO.
Results: Of 2010 HRM studies, 144 (7.2%) fulfilled CCv3.0 criteria for EGJOO (median age 61 years, 56.9% female). Upon applying CCv4.0 criteria, EGJOO prevalence decreased to 1.2%. On ROC analysis, integrated relaxation pressure during RDC (RDC-IRP) was a significant predictor of a conclusive EGJOO diagnosis by CCv4.0 criteria (area under the curve: 96.1%). The optimal RDC-IRP threshold of 16.7 mmHg had 87% sensitivity, 97.1% specificity, 95.7% negative predictive value and 91.3% positive predictive value for a conclusive EGJOO diagnosis; lower thresholds (10 mmHg, 12 mmHg) had better sensitivity but lower specificity.
Conclusion: CCv4.0 criteria reduced the prevalence of EGJOO by 80%, thereby refining the diagnosis and identifying clinically relevant outflow obstruction. Elevated RDC-IRP can predict conclusive EGJOO per CCv4.0.

10.1 Introduction

Oesophagogastric junction outflow obstruction (EGJOO) can manifest as a motor disorder of the oesophagus with incomplete relaxation of the lower oesophageal sphincter (LES) and intact oesophageal body peristalsis on high-resolution manometry (HRM) [477]. However, EGJOO can also occur from structural etiologies, from non-specific mechanisms, and can be an artefact [478]. Clinically, patients with conclusive EGJOO may report dysphagia and/or non-cardiac chest pain (NCCP), while reflux symptoms are less common [478]. Therapeutic strategies include medications and invasive procedures aimed at reducing LES tone [479]. For EGJOO diagnosis, Chicago Classification version 3.0 (CCv3.0) required elevated LES median integrated relaxation pressure (IRP) with preserved oesophageal body peristalsis and no HRM criteria for achalasia4, with prevalence from 5% to 24% among patients undergoing HRM [478]. However, up to 94% of these patients may improve without treatment, raising questions on the significance of the diagnosis [479, 480, 481, 482]. In the recently published CCv4.0 [477], diagnostic criteria for EGJOO were made more clinically relevant, requiring elevated IRP in both supine and upright positions, intact oesophageal body peristalsis, as well as elevated intrabolus pressure (IBP) in $\geq 20\%$ of supine swallows [477, 483]. Additionally, manometric EGJOO is considered clinically inconclusive [478], needing relevant symptoms (i.e., dysphagia and/or chest pain) and supportive non-manometric investigations such as timed barium oesophagogram (TBE) and/or functional lumen imaging probe (FLIP) for a conclusive diagnosis. Oesophageal pressurization during the rapid drink challenge (RDC) provocative test is considered supportive evidence for EGJOO [477]. Although diagnostic criteria for EGJOO are now more stringent, impact on disease prevalence and consequently, relevance to clinical practice are currently unknown. The primary aim of this study was to determine EGJOO prevalence using CCv4.0

criteria among patients with EGJOO according to CCv3.0. The secondary aim was to assess whether RDC could predict EGJOO.

10.2 Materials and methods

10.2.1 Study design and patients

In this multi-center retrospective cohort study, HRM studies in adults >18 years of age from tertiary referral centers in Pisa, Padova, and Feltre between 2018-2020 were retrieved and analyzed using both CCv3.0 and CCv4.0. Further data, including clinical presentation, demographics and barium oesophagograms (when available) were collected in patients meeting CCv3.0 criteria for EGJOO. All patients stopped proton pump inhibitors (PPIs), H2-receptor antagonists (H2RA), opioids or prokinetics at least 3 weeks prior to HRM. Exclusion criteria were evidence of luminal stricture, extraluminal compression, or hiatus hernia on endoscopy; history of foregut surgery; neoplasia; eosinophilic oesophagitis; pregnancy and/or breast feeding. Participants were allowed to take alginates as rescue therapy for controlling heartburn [484]. CCv4.0 criteria were applied to the cohort with CCv3.0 EGJOO diagnosis to determine proportions with a clinically relevant conclusive diagnosis of EGJOO. Prior to the HRM study, all patients underwent a detailed clinical interview, including medical history (with recording of height and weight), current medications, smoking, coffee and alcohol consumption. All patients also completed validated questionnaires evaluating GERD symptoms10 and dysphagia [485]. Patients were further categorized into those with and without clinically relevant symptoms (dysphagia and/or chest pain). A timed barium oesophagogram (TBE) with assessment of barium retention at 5 minutes (TBE5) was recommended to all patients for evaluation of oesophageal emptying when EGJOO was identified as per CCv3.0 criteria on HRM, and those who underwent TBE were classified into those with or without a conclusive CCv4.0 diagnosis of EGJOO. The study was conducted in accordance with the Helsinki Declaration (Sixth revision, Seoul 2008). Because all patients were part of each institution's institutional review board-approved data collection., and only de-identified data were shared across the participating institutions with no links to the original patients, repeat institutional review board approval was not deemed necessary.

10.2.2 High resolution manometry protocol

Oesophageal HRM was performed using a 4.2 mm outer diameter, solid-state catheter assembly with 36 circumferential pressure sensors spaced 1 cm apart (Medtronic Inc, Shoreview, MN, USA) after at least a six-hour fast. The HRM protocol included a 30-second baseline recording, and ten 5-ml water swallows at 20-30 sec interval in the supine position [486, 487]. Three sets of multiple rapid swallows (MRS) were performed, consisting of five consecutive 2 mL swallows

in rapid succession within 10 seconds [486]. The RDC test consisted of rapidly drinking 200 ml of water through a straw in the sitting position. The HRM studies were analyzed using the ManoView^{TM} Analysis Software v3.0 (Medtronic) by experts from each center.

10.2.3 High resolution manometry analysis

For each tracing, EGJ relaxation with integrated relaxation pressure (IRP), EGJ morphology, distal contractile integral (DCI), distal latency (DL), and intrabolus pressure (IBP) were recorded [486, 488]. The IBP was considered elevated when >20mmHg2. The EGJ-CI was calculated as previously reported [489]. For each MRS maneuver, the time to complete the MRS, oesophageal body inhibition, mean IRP of the three MRS (MRS-IRP), and mean DCI of the three MRS (MRS-DCI) were assessed [490]. Oesophageal body inhibition was considered abnormal if there was a contraction segment with isobaric contour >20mmHg and >3cm in length [491], during the MRS course. Deglutitive inhibition of the LES was considered abnormal if the MRS-IRP was >15mmHg. The presence of contraction reserve was assessed using the ratio of MRS DCI to SS DCI, and MRS/SS ratio > 1 indicated preserved contraction reserve. Therefore, an intact MRS response consisted of complete deglutitive inhibition of the oesophageal body and LES during the repetitive swallows, and presence of contraction reserve [477]. Pressurization during MRS (i.e., evidence of pressurization with isobaric contour >20mmHg during the repetitive phase of the MRS) was also recorded. For each RDC test, the time to complete the RDC, post-RDC DCI (RDC-DCI), the IRP of the entire duration of the RDC (RDC-IRP), and the presence of pressurization (i.e., evidence of pressurization with isobaric contour >20mmHg during the repetitive phase of the RDC) were assessed. Finally, the percentage of time with pressure >20mmHg was calculated as the sum of the duration of the pressurizations divided by the time taken to complete the RDC [491].

10.2.4 Timed Barium Oesophagogram

TBE was performed in the upright position within thirty days following HRM. Radiological images were obtained in the upright position after ingestion of 200 mL of low-density barium sulphate; frontal spot films of the oesophagus were obtained at baseline and 5 minutes after ingestion [492]. The height of the barium column was measured vertically from the EGJ using a lead scale placed directly on the patient. Complete emptying was defined as a barium column height of ¡1 cm at 5 minutes.

10.2.5 Conclusive EGJOO Diagnosis according to CCv4.0

A conclusive diagnosis of EGJOO according to CCv4.0 required manometric EGJOO, relevant clinical symptoms, and abnormal TBE5. Only patients with

complete HRM, clinical, and TBE5 data were included in the assessment of EGJOO prevalence using CCv4.0 criteria. Since HRM studies were performed using the CCv3.0 protocol [493], upright single swallows (SS) were not available for assessment.

10.2.6 Statistical analysis

Continuous data are described as median and interquartile range (IQR), and categorical data as counts and percent. Normality was evaluated using Shapiro-Wilk test. Homogeneity of the variances was verified with Fligner-Killeen test. Non-normal continuous variables were evaluated with non-parametric Mann-Whitney U test (one-sided and two-sided), while categorical variables were analyzed using Pearson's χ^2 test (using Yates' correction for continuity). Unless otherwise specified, the continuous variables were found to be non-normal and/or to have a non-uniform variance between the two groups, and therefore the non-parametric U-test was used. Correlation between the non-normal continuous variables was tested using the non-parametric Spearman coefficient. Receiver operating characteristic (ROC) curve analyses were used to assess the performance characteristics of predictors of conclusive EGJOO as per CCv4.0, including area under the curve (AUC), sensitivity, specificity, positive predictive value (PPV), negative predictive value (NPV) with bootstrap 95% confidence intervals (CI) when appropriate. A p-value of < 0.05 was considered statistically significant. The statistical analysis was performed using R-studio version 4.1.2.

10.3 Results

10.3.1 Clinical characteristics

Among 2010 patients undergoing an oesophageal HRM during the study period, 144 (7.2%) were diagnosed as EGJOO using CCv3.0 criteria, and met the inclusion criteria for this study (median age 61 years, 56.9% female). Clinical presentation and demographics of the included patients are described in Table 1. Of these, 54 patients (37.5%) had clinically relevant symptoms of dysphagia and/or chest pain. Demographics, BMI, smoking, coffee and alcohol use were similar between patients with and without clinically relevant symptoms (Table 10.3.1). Proportions with heartburn (31.5% vs. 47.8% respectively, p=0.08) and regurgitation (51.9% vs. 50.0% respectively, p=0.97) were not statistically different.

10.3.2 High resolution manometry findings

Single swallows

Patients with EGJOO with clinically relevant symptoms had higher median IRP ($p < 0.001$), mean DCI (p=0.017), and mean IBP ($p < 0.001$) compared

Clinical variable	All patients with EGJOO according to CCv3.0 *n = 144*	Patients with clinically relevant symptoms *n = 54*	Patients without clinically relevant symptoms *n = 90*	*p*-value
Age (years)	61 (45.0–70.2)	63 (54.0–69.0)	56.5 (42.2–71.0)	0.16
Females	82 (56.9%)	30 (55.5%)	52 (57.7%)	0.93
Males	62 (43.1%)	24 (44.5%)	38 (42.3%)	
BMI	24.2 (21.2–26.8)	24.8 (22.0–27.7)	24.1 (21.0–26.6)	0.25
Smoking	24 (16.7%)	7 (13.0%)	17 (18.9%)	0.49
Coffee ≥1/day	98 (68.0%)	37 (68.5%)	61 (67.7%)	0.58
Alcohol >2 units/day	62 (43.1%)	18 (33.3%)	44 (48.9%)	0.10
Dysphagia	46	46	0	-
Chest pain	28	28	0	-
Heartburn	60 (41.7%)	17 (31.5%)	43 (47.8%)	0.08
Regurgitation	73 (50.7%)	28 (51.9%)	45 (50.0%)	0.97

to those without clinically relevant symptoms (Table 10.3.2). Type 1 EGJ morphology (no hiatus hernia) was significantly more prevalent, in the presence of clinically relevant symptoms (p=0.013). There were no differences in basal EGJ pressure or mean DL between the two groups (Table 10.3.2).

HRM findings	All patients with EGJOO according to CCv3.0 *n = 144*	Patients with clinically relevant symptoms *n = 54*	Patients without clinically relevant symptoms *n = 90*	*p*-value
Single swallows				
Median IRP (mmHg)	19.2 (17.0–22.7)	20.8 (18.5–26.2)	18.4 (16.8–21.8)	**<0.001****
Type 1 EGJ	101 (70.1%)	45 (83.3%)	56 (62.2%)	**0.013**
Type 2 EGJ	43 (29.9%)	9 (16.7%)	34 (37.8%)	
Basal EGJ pressure (mm Hg)	40.2 (31.4–53.5)	41.0 (34.7–56.6)	39.1 (31.0–49.7)	0.13
Mean DCI (mm Hg cm s)	1670 (886–2748)	1909 (1221–2976)	1414 (704–2474]	**0.017**
Mean DL (s)	6.4 (5.7–7.4)	6.3 (5.4–7.8)	6.5 (5.8–7.2)	0.85
Mean IBP (mm Hg)	13.5 (11.1–17.3)	19.1 (14.9–23.5)	12.3 (10.6–14.1)	**<0.001****
Multiple Rapid Swallows				
Mean MRS IRP (mm Hg)	11.6 (9.1–14.6)	16.3 (12.2–23.7)	10.7 (8.8–12.5)	**<0.001****
Contraction reserve	71 (49.3%)	19 (35.2%)	52 (57.8%)	**0.014**
Oesophageal pressurisation	31 (21.5%)	28 (51.9%)	3 (3.3%)	**<0.001****
Rapid drink challenge				
Mean RDC-IRP (mmHg)	9.1 (5.8–14.1)	17.3 (10.2–21.0)	7.8 (5.1–9.9)	**<0.001****
Oesophageal pressurisation (>20% duration)	48 (33.3%)	39 (72.2%)	9 (10.0%)	**<0.001****

Provocative tests

There were significant differences on provocative tests during HRM between EGJOO patients with and without clinically relevant symptoms. With MRS, both mean MRS-IRP ($p < 0.001$) and oesophageal pressurization ($p < 0.001$) were higher in the presence of clinically relevant symptoms, while the proportion with contraction reserve was lower (p=0.014) (Table 10.3.2). Similar findings were noted with RDC, with higher mean RDC-IRP and higher oesophageal pressurization in the presence of clinically relevant symptoms ($p < 0.001$).

10.3.3 Timed barium oesophagogram findings

Although all 144 patients were asked to undergo TBE, only 95 (66.0%) ultimately underwent TBE. Radiographic evidence of EGJOO was noted in 65.7% (23/35) of patients with clinically relevant symptoms, compared to none with no clinically relevant symptoms ($p < 0.001$, Table 10.3.3). Additionally, the mean barium column height at 5 minutes was significantly higher in the presence of clinically relevant symptoms ($p < 0.001$).

TBE5 findings	All patients with EGJOO according to CCv3.0 *n = 144*	Patients with clinically relevant symptoms *n = 54*	Patients without clinically relevant symptoms *n = 90*	*p*-value
Patients with TBE performed	95 (66.0%)	35 (64.8%)	60 (66.7%)	0.96
Radiological signs of obstruction	23/95 (24.2%)	23/35 (65.7%)	0/60 (0%)	<0.001*
Median barium column height at 5 min	0.0 (0.0–0.0)	1.0 (0.0–2.0)	0.0 (0.0–0.0)	<0.001*

10.3.4 Prevalence of EGJOO according to Chicago Classification v4.0

A complete investigation profile (HRM metrics, symptoms, and TBE findings) to determine prevalence of EGJOO according to CCv4.0 criteria were available for 95/144 patients. Accordingly, the CCv4.0 prevalence of EGJOO was calculated out of a total of 1961 patients, and was 1.2% (23/1961, 95% CI 0.7%-1.6%), significantly lower than the CCv3.0 prevalence of 7.2% (144/2010, 95% CI 6.0%-8.3%). Among patients with clinically relevant symptoms, 23 of 35 patients (65.7%) with a complete investigation profile fulfilled CCv4.0 criteria for EGJOO. In contrast, none of patients with other foregut symptoms had barium retention on TBE5 ($p < 0.001$, Table 10.3.3).

10.3.5 Predictors of EGJOO

Median RDC-IRP in patients with a conclusive diagnosis of EGJOO as defined by CCv4.0 (21.4 mmHg, IQR 19.5-25.0 mmHg) were higher compared to those of patients without a conclusive EGJOO diagnosis (6.9 mmHg, IQR 5.3-9.9 mmHg, $p < 0.001$). On ROC analysis, RDC-IRP predicted a conclusive diagnosis of EGJOO as defined by CCv4.0 with an AUC of 96.1% (95% CI 91.5%-100%). (Figure 10.1). The optimal RDC-IRP cut-off, selected to maximize the sum of specificity and sensitivity, was 16.7 mmHg, with a sensitivity of 87.0% (95% CI 73.9%-100.0%), specificity of 97.1% (95% CI 92.6%-100.0%), NPV of 95.7%, (95% CI 91.3%-100%) and PPV of 91.3% (95% CI 78.6%-100%). Two additional thresholds were evaluated as predictors of conclusive EGJOO. The RDC-IRP threshold of 12 mmHg, corresponding to the upright IRP threshold proposed by CCv4.01, had 87% sensitivity (95% CI 73.9%-100%), 88.2% specificity (95% CI 80.8%-95.6%), 95.3% NPV (95% CI 90.3%-100%), and 71.7% PPV (95% CI 58.8%-87.0%) for a conclusive CCv4.0 diagnosis of EGJOO. The RDC-IRP

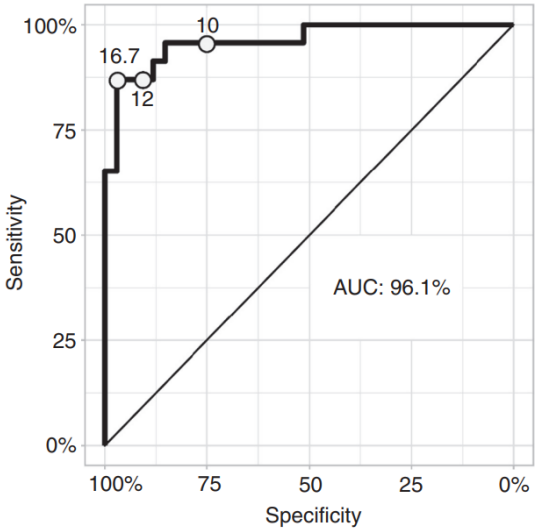

Figure 10.1: Receiver operating characteristic (ROC) analysis of the performance of integrated relaxation pressure (IRP) during rapid drink challenge (RDC) in predicting a conclusive diagnosis of oesophagogastric junction outflow obstruction (EGJOO) according to Chicago Classification version 4.0, with radiographic evidence of barium column >1 cm at 5 minutes on a timed upright oesophagram. The performance characteristics were most optimal at RDC-IRP threshold of 16.7 mmHg, with sensitivity of 87.0%, specificity of 97.1%, negative predictive value of 95.7% and positive predictive value of 91.3%. Area under the curve (AUC) was 96.1%.

threshold of 10.0 mmHg, reported to predict abnormal TBE in treated achalasia19, had 95.7% sensitivity (95% CI 87.0%-100%), 75.0% specificity (95% CI 64.7%-85.3%), 98.1% NPV (95% CI 94.2%-100%), 56.4% PPV (95% CI 47.7%-67.7%) for a conclusive CCv4.0 diagnosis of EGJOO. When considering patients with a complete clinical, HRM, and TBE profile, 95.7% (22/23) with a conclusive CCv4.0 diagnosis of EGJOO had RDC-IRP above all three thresholds studied (>10.0 mmHg, >12 mmHg and >16.7 mmHg), and 100% (23/23) had oesophageal pressurization for ≥20% of the duration of the RDC. On the other hand, 23.6% (17/72), 11.1% (8/72) and 2.7% (2/72) of those without a conclusive diagnosis of EGJOO had RDC-IRP above the three thresholds, respectively, and 11.8% (8/68) had ≥20% oesophageal pressurization during RDC (Figure 10.2). There was a strong correlation between RDC-IRP and oesophageal pressurization ($\rho = 0.61$, $\rho < 0.001$) with higher RDC-IRP values corresponding to higher HRM metrics, and between RDC-IRP and barium column height at 5 minutes ($\rho = 0.71$, $\rho < 0.001$).

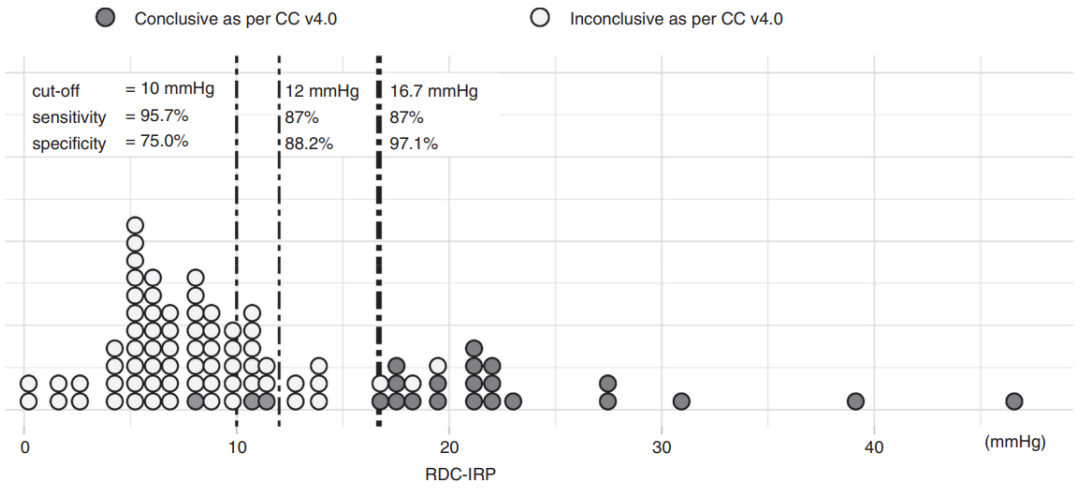

Figure 10.2: Scatter-graph showing integrated relaxation pressure (IRP) values during rapid drink challenge (RDC) in patients with a conclusive diagnosis of oesophagogastric junction outflow obstruction (EGJOO) according to Chicago Classification version 4.0 criteria (black circles) and inconclusive EGJOO (fulfilling Chicago Classification version 3.0 criteria but not 4.0 criteria) (grey circles). Performance characteristics were most optimal for RDC-IRP threshold of 16.7 mmHg; sensitivity was higher at a 10.0 mmHg threshold, at the expense of specificity. Only 3 patients (13.0%) had RDC-IRP $<$ 16.7 mmHg, and 1 patient (4.3%) had RDC-IRP$<$ 10.0 mmHg.

10.4 Discussion

The clinical relevance of an EGJOO diagnosis using CCv3.0 has been questioned, with patients likely to undergo unnecessary additional testing and invasive treatments that may not change prognosis, since a large proportion improve with non-specific measures or no therapy [479, 494, 495, 496]. With this background, the recently published CCv4.0 updated diagnostic criteria strived to make EGJOO a more clinically relevant diagnosis1, requiring symptoms of dysphagia and/or chest pain, and mandating supportive findings on complementary tests for a conclusive diagnosis. In this retrospective study we estimated the prevalence of conclusive EGJOO among diagnosis made using CCv3.0, which was expected to decline with use of stringent CCv4.0 criteria [478]. We demonstrate a 6-fold reduction in prevalence of EGJOO, declining from 7.2% using CCv3.0 to 1.2% using CCv4.0 criteria, particularly by selecting out patients with clinically relevant symptoms, and by use of RDC. Our findings further support use of provocative maneuvers, especially RDC during HRM, as conclusive EGJOO confirmed by oesophageal barium retention on TBE could be predicted with impressive performance characteristics using RDC metrics, obviating need for adjunctive confirmatory testing when abnormal RDC metrics are found. Additionally, these findings lend further support for the expansion of the HRM test

protocol recommended by CCv4.0. In the years since EGJOO has been clinically recognized, it has become increasingly evident that this manometric pattern is a clinical conundrum. While a small proportion of patients with EGJOO based solely on an abnormal median supine IRP have true motor obstruction that responds to achalasia like treatments, the majority require no therapy or non-specific medical approaches [482, 497]. Therefore, a singular management approach does not apply to all EGJOO patients. The new CCv4.0 criteria attempts to circumvent the clinical conundrum by requiring not just relevant symptoms, but also confirmation of outflow obstruction using TBE or FLIP [477, 478]. Using these criteria as a gold standard, we show that the expanded CCv4.0 HRM protocol is indeed able to identify conclusive EGJOO with a high degree of accuracy, especially using RDC during HRM. Although CCv4.0 criteria suggest that abnormal provocative maneuver findings are supportive, our findings suggest that these findings add additional confidence for a conclusive EGJOO diagnosis, and might obviate need for additional testing. Several of the steps recommended by CCv4.0 were factored into the current study. The first step involved identification of patients with clinically relevant symptoms of dysphagia and chest pain. When segregated by clinically relevant symptoms, reflux symptoms were reported less often, albeit not statistically significant. Median IRP during single swallows, MRS and RDC, as well as IBP were significantly higher when symptoms were clinically relevant, supporting obstructive pathophysiology. When applying the gold standard of abnormal TBE5, 65.7% with clinically relevant symptoms had radiographic EGJOO, and these patients fulfilled conclusive EGJOO criteria by CCv4.0. In contrast, none of the patients with other upper gastrointestinal symptoms had radiographic obstruction on TBE5. On the other hand, ten patients who reported dysphagia and/or chest pain in the context of an elevated supine median IRP did not have obstruction on TBE5, which is consistent with previous reports where primary EGJOO was associated with normal TBE5 [498, 499]. Although upright swallows were not performed, RDC was effective in identification of patients with radiographic obstruction on TBE. Obstruction during RDC has been associated with abnormal TBE findings, with published evidence supporting its value in confirming latent obstructive processes1. Woodland et al. reported that an elevated RDC-IRP correlates with obstructive symptoms (as measured by the Eckardt score) and was the best predictor of EGJ obstruction on TBE5 [500]. Penagini et al. [501] also demonstrated that RDC-IRP strongly correlates with TBE5, with RDC-IRP >10 mmHg providing excellent discrimination between complete from incomplete barium emptying in treated achalasia patients, leading the authors to speculate that RDC-IRP could be discriminative in identifying any obstructive oesophageal syndrome. Our findings support the value of RDC in patients with clinically relevant symptoms, where an RDC-IRP of 10 mmHg had 95.7% sensitivity, 75.0% specificity, 98.1% NPV, and 56.4% PPV in identifying conclusive EGJOO according to CCv4.0. Higher RDC-IRP thresholds had even better performance characteristics, and a threshold of 16.7 mmHg had the best performance characteristics, with sensitivity of 87.0%, specificity of 97.1%, NPV of 95.7%, and PPV of 91.3%. Oesophageal

pressurization during RDC is a surrogate for elevated RDC-IRP, as all patients with elevated RDC-IRP also demonstrated pressurization of ≥20% during RDC. Our findings thus confirm that RDC is a valuable addition to the HRM protocol, and that higher RDC-IRP values strongly predict radiographic EGJOO, making RDC findings potentially conclusive for EGJOO diagnosed using CCv4.0 without need for supplementary investigation. Our retrospective cohort study has a few limitations that need to be considered. First, HRM were performed using the CCv3.0 protocol [493]; while provocative maneuvers were performed, upright swallows were not part of the protocol and were not available for comparison. Data from Triggs et al. shows that radiographic EGJOO associates with higher median upright IRP, and dysphagia and upright IRP predict barium retention on TBE5 in patients with a CCv3.0 diagnosis of EGJOO [502]. In addition, Misselwitz et al. showed that patients with EGJOO or achalasia in single swallows in both supine and upright positions, had RDC-IRP >12mmHg in 75% of cases [503]. In addition, upright and supine IRP correlated with RDC-IRP. Although upright swallows were not performed in this study, RDC-IRP predicted a clinically relevant EGJOO as defined by CCv4.0 with an AUC of 96.1%. Taken together, these findings add confidence to the fact that an elevated upright IRP would have likely been abnormal in patients with conclusive EGJOO by CCv4.0 criteria in our study, although we could not provide conclusive evidence for this. Second, although CCv4.0 proposes that TBE should preferably be performed in conjunction with a barium tablet swallow, TBEs were performed with 200 mL of low-density barium sulphate alone in this study. Third, 19/54 patients with clinically relevant symptoms in the context of EGJOO according to CCv3.0 did not undergo radiographic evaluation, and had to be excluded from evaluation of CCv4.0 EGJOO prevalence to avoid potential bias. Fourth, FLIP and some of the additional provocative tests, including solid test meal or pharmacologic provocation of the EGJ, were not performed in this study. Finally, this study only evaluated diagnosis of EGJOO and management was not addressed. Therefore, the impact of conclusive vs. inconclusive CCv4.0 EGJOO diagnosis on treatment response could not be evaluated. However, other studies have shown that provocative testing during HRM, including RDC and MRS, have high sensitivity in identifying clinically relevant EGJOO that will respond to an EGJ-directed treatment [504, 505]. Further prospective studies are needed to address the impact of CCv4.0 criteria on management outcome of EGJOO diagnoses. In summary, the more stringent CCv4.0 criteria have significantly reduced the prevalence of EGJOO compared to CCv3.0, allowing identification of clinically relevant radiographically confirmed outflow obstruction. The expansion of the HRM testing protocol to include provocative testing augments the diagnostic yield of conclusive EGJOO, and use of abnormal RDC-IRP may obviate the need for radiographic confirmation of EGJOO. The impact of the new EGJOO criteria on the therapeutic management of the disease remains to be investigated.

10.5 Author contributions

P.V. and N.d.B. conceived and drafted the study. P.V., R.P., C.P.G., E.V.S., N.d.B. drafted the manuscript. P.V., G.D.C., C.P.G., and N.d.B. analyzed all data. All authors commented on drafts of the paper. All authors have approved the final draft of the manuscript.

Chapter 11

Efficacy of Second PPI Course Following Steroid-Induced Remission in Eosinophilic Esophagitis Refractory to Initial PPI Therapy

Pierfrancesco Visaggi, Federica Baiano Svizzero, Giulio Del Corso, Massimo Bellini, Edoardo Savarino, Nicola de Bortoli

American Journal of Gastroenterology (2022)

Abstract

Background and Aims: Eosinophilic esophagitis (EoE) requires maintenance therapy to avoid recurrence. We investigated the efficacy of a second course of proton pump inhibitors (scPPIs) to maintain steroid-induced histological remission (HR) in EoE patients who had previously failed induction of remission with PPIs.

Methods: We retrospectively included 18 patients who achieved HR with topical steroids (TS) but could not be maintained on long-term TS. Treatment outcomes were assessed after 12 weeks of scPPIs.

Results: Most patients (67%) maintained HR with high-dose PPIs monotherapy at week 12.

Conclusion: scPPIs might work as maintenance strategy in primary PPIs non-responder EoE patients.

11.1 Brief communication

Eosinophilic esophagitis is a chronic disorder of the esophagus characterized by symptoms of esophageal dysfunction and eosinophil-predominant inflammation, in the absence of secondary causes of eosinophilia [506]. Adult often complain of dysphagia, bolus impaction, and chest pain, but less specific symptoms are common in childhood [506]. The diagnosis requires at least 15 eosinophils/high power field (eos/hpf) in at least one esophageal biopsy [507]. On endoscopy, disease activity is assessed based on the EoE endoscopic reference score (EREFS) [508]. Improvement of histology, endoscopic findings, and symptoms all represent treatment endpoints [509]. Therapeutic options include proton pump inhibitors (PPIs), topical steroids, elimination dietary regimens (ED), and dilation of strictures, all of which can be considered as first line treatment [510]. Only recently, the FDA approved the use of dupilumab, a monoclonal antibody against interleukin-4 receptor alpha, for EoE patients of 12 years or older. Other novel treatment strategies are increasingly being investigated in randomized controlled trials (RCT), although most are not routinely available in clinical practice [511]. In this regard, when standard pharmacological treatments fail to induce remission or are poorly tolerated, and patients refuse dietary regimens [512], the management of EoE may become challenging. Thus, we retrospectively investigated if EoE patients who had not responded to a first course of PPIs and had achieved histological remission with subsequent topical steroid treatment could be maintained in histological remission with scPPIs monotherapy.

We included EoE patients who did not respond histologically (i.e., $\geq$ 15 eos/hpf) to a 12-week course of high-dose PPIs who subsequently achieved histological remission following 12 weeks of second line therapy with topical steroids between January 2020 – March 2022. Among topical steroid responders (TSR), those who were intolerant to or concerned of long-term treatment with steroids or complained of any steroid-related adverse event after a minimum of 12 weeks of treatment were offered a therapeutic switch to either ED or scPPIs. TSR patients who declined ED and opted for a therapeutic switch to scPPIs were then evaluated histologically with at least 4 esophageal biopsies after 12 weeks of scPPIs monotherapy. We only included patients for which all the following information were available: sex; age; age at diagnosis; voluptuary habits history (alcohol, smoking, coffee); history of upper gastrointestinal symptoms (dysphagia, chest pain, heartburn, regurgitation, history of bolus impaction); history of allergic comorbidities including asthma, nasal polyposis, and food allergy; EREFS score and peak eosinophil count (PEC) at specific timepoints (before and after first PPIs course, after topical steroids, after scPPIs); type and dose of PPI and topical steroid used. We excluded patients taking systemic steroids or who had esophageal dilation. Continuous variables were analysed using a two-sided Mann-Whitney U test, while a two-sided Fisher's exact test was used for categorical variables. Significance level was set at $p \leq 0.05$.

We found that 98 primary PPIs non-responders who were TSR had complete

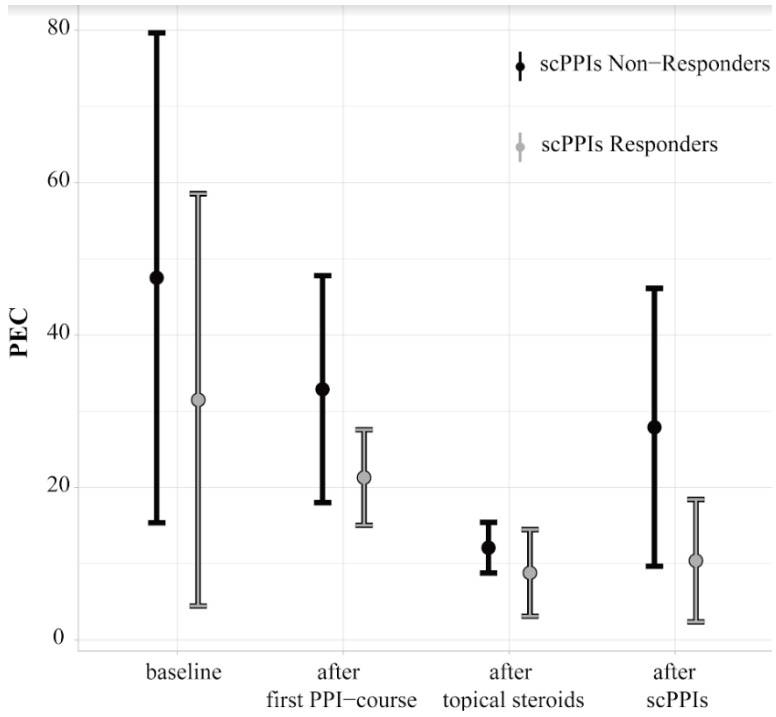

Figure 11.1: The plot shows mean values and 95% confidence intervals of peak eosinophil counts at each treatment efficacy assessment

	scPPIs Responders (n=12)	scPPIs Non-Responders (n=6)	*p-value*
Demographics			
Males/Females	10/2	4/2	0.57
Age	34.3±13.8	36.8±13.4	0.77
Age at diagnosis	30.6±12.1	32.8±12.8	0.76
Alcohol > 2 units/day	1	4	**0.02***
Smokers	3	2	1
Coffee >1/day	11	5	1
Clinical History			
Dysphagia	12	6	1
Previous bolus impaction	1	4	**0.02***
Chest pain	1	3	0.08
Heartburn/Regurgitation	4	2	1
Food allergy	1	2	0.24
Asthma	3	2	1
Nasal polyposis	1	5	**0.004***
Symptoms			
Dysphagia after first PPI-course /topical steroids/scPPIs	12/2/0	6/1/2	1/1/0.33
Bolus impaction after first PPI-course/topical steroids/scPPIs	0/0/0	1/0/1	0.33/1/0.33
Chest pain after first PPI-course/topical steroids/scPPIs	1/0/0	3/1/2	0.08/0.33/0.1
Heartburn/Regurgitation after first PPI-course/topical steroids/scPPIs	4/2/2	2/2/2	1/0.57/0.57
Endoscopy			
EREFS score baseline	3.5±2.8	3.2±2.6	0.83
EREFS score after first PPI-course	3±1.9	3.2±2.9	0.86
EREFS score after topical steroids	1.5±0.9	1.9±1.1	0.42
EREFS score after scPPIs	1.3±0.6	3.1±2.4	**0.02***
Histology			
PEC baseline	31.5±13.8	47.5±16.4	**0.04***
PEC after first PPI-course	21.3±3.2	32.9±7.6	**<0.001***
PEC after topical steroids	8.8±2.9	12.1±1.7	**0.02***
PEC after scPPIs	10.4±4.1	27.9±9.3	**<0.0001***

Figure 11.2: Differences and similarities between scPPIs responders and non-responders.

data and could be evaluated. Of these, 18 (14 males; 35.1 ± 13yrs) opted for scPPIs following withdrawal of topical steroid treatment because of treatment concerns (n=7), intolerance (n=6), or adverse events (oral candidiasis n=4; fatigue n=1). All patients received esomeprazole 40mg twice daily for both courses of PPIs. All patients received topical steroids via a multi-dose inhaler (n=15 budesonide 2mg daily, n=3 fluticasone propionate 1750mcg daily). Based on endoscopy with biopsies, 12 patients (66.7%) (10 males, 34.3 ± 13.8yrs) were scPPIs responders (scPPIs-R, i.e., eos/HPF > 15), and 6 (33.3%) (4 males, 36.8 ± 13.4yrs) were scPPIs non-responders (scPPIs-NR, i.e., eos/HPF > 15). ScPPIs-NR were more frequently drinkers of more than 2 units of alcohol per day. Significantly more scPPIs-NR patients reported history of bolus impaction (scPPIs- NR=67% vs scPPIs-R=8% p=0.02) or had nasal polyposis (scPPIs-NR=83% vs scPPIs-R=8%, p=0.004). Symptoms improved following topical steroids and remained stable during scPPIs in both cohorts. PEC was higher in scPPIs-NR at each histologic evaluation timepoint ($p \leq 0.05$) (Figure 11.1). The EREFS score improved in both groups following topical steroids but worsened after scPPIs in scPPIs-NR patients (Table 11.2).

Our findings allow to speculate that a scPPIs, at least in the short-term, might work as a maintenance strategy in primary PPI non-responders who achieved histological remission with topical steroids. In this setting, a clinical history of previous bolus impaction, nasal polyposis, and higher PEC may help to identify patients less likely to maintain histological remission after a scPPIs.

This study has limitations that should be considered. First, this was a retrospective study and there was no control group taking placebo instead of scPPIs. Second, the study cohort was small because only patients who could not be maintained on long-term topical steroids who had refused ED were offered a scPPIs. Finally, the follow-up was limited to 12 weeks and symptoms were not evaluated with validated questionnaires. Although it could be argued that steroids were responsible for the maintenance of histology remission at week 12 following scPPIs, a recent RCT [513] showed that, when treatment with topical budesonide is withdrawn following induction of histological remission, 86.4% of patients show active inflammation on histology (i.e., > 15 eos/hpf) when assessed at week 12 regardless of symptoms. In contrast, in this study, 67.7% of patients maintained histological remission under scPPIs after 12 weeks from topical steroids withdrawal. In addition, although symptoms were not statistically different between cohorts during scPPIs treatment, scPPIs-NR showed a trend towards symptoms recurrence. In this regard, EoE is a complex disease with different histological, endoscopic, and clinical markers of disease activity and there may be modest correlation across different outcome measures, possibly due to coexisting psychological distress or esophageal dysmotility [514, 515] . Moreover, a recent RCT also showed that the median time to symptoms recurrence following steroid discontinuation exceeds 12 weeks [516] . Therefore, although we showed that scPPIs have maintained histology and endoscopy improvements in scPPIs-R patients, we were less precise in estimating the efficacy on EoE symptoms.

In conclusion, scPPIs could represent a maintenance treatment strategy in

primary PPIs refractory patients. The efficacy of a scPPIs should be confirmed prospectively in a RCT as PPIs could represent the least expensive maintenance treatment worthwhile considering in clinical practice.

Author Contributions

P.V., E.S., and N.d.B. conceived and drafted the manuscript. P.V., F.B.S., E.S., N.d.B. collected all data. P.V., F.B.S., G.D.C., N.d.B. analyzed all data. All authors commented on drafts of the paper.

Chapter 12

Conclusions

This manuscript deals with the development and validation of an in-silico duplicate of human cardiac electrophysiology and associated uncertainty quantification analyses. Indeed, the overwhelming individual variety in terms of form and characteristics makes canonical validation methodologies inadequate. Analyses were therefore performed using uncertainty quantification (UQ) techniques to understand how variability propagates over quantities of medical interest (forward analysis) and which of the uncertain variables impact most the dynamics (global sensitivity analysis). The application of these methodologies led to the subsequent development of original UQ techniques for contexts with partial information on individual variability.

With reference to Figure 12.1a), starting with a model of the ventricle, simplified but already with a very good match with reality, a detailed UQ analysis was carried out. The latter investigated which of the geometric, conductivity or cellular pattern uncertainties played a decisive role in the fast, correct, and uniform activation of the heart. In the case of healthy hearts, it was evident that the dominant components were the macroscopic ones: muscle fibers orientation, geometry and, above all, the conduction velocity of the Purkinje network.

On the basis of these results, a complete cardiac electrophysiology model was therefore developed from scratch, incorporating the description of the four atrial and ventricular chambers, a realistic orientation of the muscle fibers and, above all, the presence of the fast conduction structures (Purkinje network, internodal bundles, Bachmann's bundle, etc.), see Figure 12.1b. The model so defined is also fully parametric: the features are described by individual scalar values which alter the macroscopic structure (e.g. the orientation of the ventricular fibres depends on three angles, three electrical conduction values describe the Purkinje network, two parameters its extension, etc.). This characterisation therefore makes the model ideal for carrying out structured uncertainty quantification analysis. In addition to healthy cardiac activation, some pathologies related to the detailed electrophysiological structure implemented were investigated. In particular, heart stroke, bundle branch blocks and artificial pacemaking have

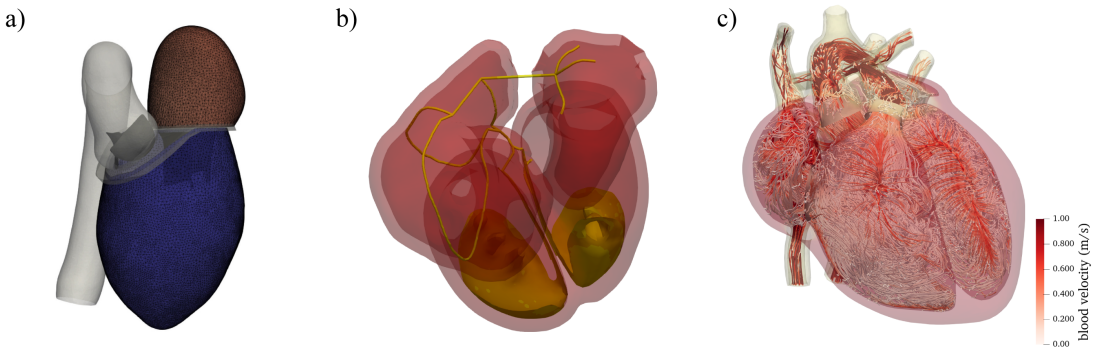

Figure 12.1: Evolution of the cardiac model. Panel a) shows the original [177] model, comprising an atrial chamber, a ventricular chamber, and a simplified electrophysiology model (monodomain on 2D domain approximating 3D tissue). Panel b) shows the advanced electrophysiology model. In this second version, atrial internodal pathways, ventricular conduction fibres, the AV-node and the Purkinje network are added. The cellular models were then differentiated between atrial and ventricular chambers, providing a different shape of the action potential. Finally, the two-dimensional simplification of the myocardium was eliminated in favour of a three-dimensional model incorporating a complex geometry of muscle fibres. Panel c) shows the final cardiac model, which includes the four heart valves (Aortic, Mitral, Pulmonary and Tricuspid), the principal veins, and the main arteries. The geometry was modified to obtain an average heart in line with a large body of literature. The electrophysiological model was then coupled with the original fluid structure solver, resulting in one of the first fully parametric complete human heart models.

been discussed.

This novel model was therefore used to analyse which parameters of atrial dynamics most affect ventricular activation, distinguishing between male and female hearts. The analysis reveals that electrical conduction and fast conduction fibers control more than 90% of the dynamics of a healthy heart. The electrophysiology model has been then integrated with a fluid-structure solver developed by out group, thus obtaining an electro-fluid-structure digital heart, see Figure 12.1c.

The latter provides the optimal starting point for structuring an extensive body of research in three major branches.

- In order to improve medical and didactic applicability, it is possible to define a simulated ECG to further investigate the properties of the model and to provide medical students with an unprecedented learning technique. Indeed, as it is possible to manipulate the cardiac model parameters as required, it is possible to generate pathological situations/rare events and provide the students with both the full three-dimensional visualisation of cardiac dynamics and the corresponding ECG. Incorporating medical expertise, it is also possible to further refine the model by integrating the

atrial and ventricular trabeculae, acting on the local wall thicknesses and performing a precise adjustment of the cell model parameters.

- A second research strand is based on the modelling of further pathological phenomena to be integrated into the model. In addition to heart stroke and artificial pacemaking, it is indeed possible to introduce cardiac ablations, the effect of temperature on cardiac dynamics, and arrhythmias.

- Given the high parameterisability and low computational cost of the model, the most important future developments concern uncertainty quantification applications. Using adaptive sampling techniques (based on Kriging) combined with the pre-analysis performed on atrial important variables, it is possible to perform a sensitivity analysis of the entire human heart with quantities of medical interest. Furthermore, the modular nature of the human heart combined with the possibility of defining low fidelity models (i.e., by reducing the grain of the mesh) is the optimal context for performing multi-fidelity analyses.

Throughout the entire manuscript, the pivotal importance of using the correct input distributions was emphasised. In view of the great variety of medical data and the dependence of both additional characteristics (gender, age, training status, etc.) and investigative techniques (MRI, echography, etc.) an important step towards the standardisation of UQ-analysis consists in the creation of a selected bibliographic database. The latter, integrated into an online platform, would allow not only the sharing of data on which to carry out UQ analyses, but also a more precise comparison of the results obtained.

The flexibility of the uncertainty quantification methodologies made it possible to conduct research projects with several different groups. In particular, the collaboration with the "Centro di Formazione e Simulazione Neonatale NINA" resulted in the development of UQ methodologies for medical application. Indeed, unlike in-silico models, individual variability and low control over confounding factors prevent the use of most canonical UQ techniques. While developing software to teach neonatal resuscitation procedure to medical residents, an adaptive splitting procedure was therefore introduced. The latter integrates forward UQ methodologies with the medical need for a simple tool to achieve optimal splitting of study populations. The collaboration with the Gastroenterology Unit, Department of Translational Research and New Technologies in Medicine and Surgery of the University of Pisa led instead to the application of standard statistical techniques integrated with predictive metamodels for the study of esophagitis. In addition, a methodology integrating forward analysis with the study of correlation indices was developed in order to reduce errors in medical analyses.

However, the combined experience of cardiac UQ and medical applications has demonstrated a fundamental problem that taints much of UQ analysis: the information available to the investigator is almost always inadequate. A key development of the work begun in this thesis is therefore the development of appropriate indices to assess whether the resulting analyses are valid even in the

presence of incomplete information (Nested Sensitivity Analysis). The techniques presented in this thesis, their flexibility, and their numerous applications, confirm that nowadays a deterministic numerical approach must be supplemented with a shrewd study of uncertainties to fully describe the complexity of real phenomena.

Bibliography

[1] T.-P. Fries, T. Belytschko, The extended/generalized finite element method: an overview of the method and its applications, International journal for numerical methods in engineering 84 (3) (2010) 253–304.

[2] F. Moukalled, L. Mangani, M. Darwish, The finite volume method, in: The finite volume method in computational fluid dynamics, Springer, 2016, pp. 103–135.

[3] B. Sudret, S. Marelli, J. Wiart, Surrogate models for uncertainty quantification: An overview, in: 2017 11th European conference on antennas and propagation (EUCAP), IEEE, 2017, pp. 793–797.

[4] E. Mollick, Establishing moore's law, IEEE Annals of the History of Computing 28 (3) (2006) 62–75.

[5] G. Taylor, The next decade of computing, in: AIP Conference Proceedings, Vol. 1456, American Institute of Physics, 2012, pp. 55–61.

[6] A. Koutsoudis, B. Vidmar, G. Ioannakis, F. Arnaoutoglou, G. Pavlidis, C. Chamzas, Multi-image 3d reconstruction data evaluation, Journal of cultural heritage 15 (1) (2014) 73–79.

[7] S. Oh, B. Lee, H. Park, H. Choi, S.-T. Kim, A numerical and theoretical study of the aerodynamic performance of a hovering rhinoceros beetle (trypoxylus dichotomus), Journal of Fluid Mechanics 885 (2020).

[8] A. Blass, X. Zhu, R. Verzicco, D. Lohse, R. J. Stevens, Flow organization and heat transfer in turbulent wall sheared thermal convection, Journal of fluid mechanics 897 (2020).

[9] Z. Wei, Y. Jia, Non-hydrostatic finite element model for coastal wave processes, Coastal engineering 92 (2014) 31–47.

[10] A. Posa, R. Broglia, E. Balaras, The wake structure of a propeller operating upstream of a hydrofoil, Journal of Fluid Mechanics 904 (2020).

[11] B. J. Doyle, P. E. Norman, Computational biomechanics in thoracic aortic dissection: today's approaches and tomorrow's opportunities, Annals of biomedical engineering 44 (1) (2016) 71–83.

[12] R. Gruetter, E. R. Seaquist, K. Ugurbil, A mathematical model of compartmentalized neurotransmitter metabolism in the human brain, American Journal of Physiology-Endocrinology And Metabolism 281 (1) (2001) E100–E112.

[13] J. Sanz-Herrera, J. Garcia-Aznar, M. Doblare, A mathematical model for bone tissue regeneration inside a specific type of scaffold, Biomechanics and modeling in mechanobiology 7 (5) (2008) 355–366.

[14] L. G. de Pillis, A. E. Radunskaya, C. L. Wiseman, A validated mathematical model of cell-mediated immune response to tumor growth, Cancer research 65 (17) (2005) 7950–7958.

[15] J. B. Partridge, M. H. Smerup, S. E. Petersen, P. F. Niederer, R. H. Anderson, Linking left ventricular function and mural architecture: what does the clinician need to know?, Heart 100 (16) (2014) 1289–1298.

[16] J. E. Hall, Guyton and Hall textbook of medical physiology e-Book, Elsevier Health Sciences, 2015.

[17] E. Clarke, Aristotelian concepts of the form and function of the brain, Bulletin of the History of Medicine 37 (1) (1963) 1–14.

[18] W. Pagel, Galen and the usefulness of the parts of the body, translated from the greek with an introduction and commentary by margaret tallmadge may, ithaca, new york, cornell university press1968, 2 vols., pp. xv, 802, $25 (238s.)., Medical History 14 (4) (1970) 406–408.

[19] M. M. Shoja, P. S. Agutter, M. Loukas, B. Benninger, G. Shokouhi, H. Namdar, K. Ghabili, M. Khalili, R. S. Tubbs, Leonardo da vinci's studies of the heart, International journal of cardiology 167 (4) (2013) 1126–1133.

[20] W. Harvey, The circulation of the blood, no. 262, Dent, 1923.

[21] R. Greenbaum, S. Y. Ho, D. Gibson, A. Becker, R. Anderson, Left ventricular fibre architecture in man., Heart 45 (3) (1981) 248–263.

[22] D. M. Harrild, C. S. Henriquez, A computer model of normal conduction in the human atria, Circulation research 87 (7) (2000) e25–e36.

[23] G. Del Corso, R. Verzicco, F. Viola, On the electrophysiology of the atrial fast conduction system: model validation and uq analysis, Acta Mechanica Sinica (2021) 1.

[24] O. Dössel, M. W. Krueger, F. M. Weber, M. Wilhelms, G. Seemann, Computational modeling of the human atrial anatomy and electrophysiology, Medical & biological engineering & computing 50 (8) (2012) 773–799.

[25] H. J. Levine, et al., Rest heart rate and life expectancy, Journal of the American College of Cardiology 30 (4) (1997) 1104–1106.

[26] A. M. Maceira, J. Cosín-Sales, M. Roughton, S. K. Prasad, D. J. Pennell, Reference left atrial dimensions and volumes by steady state free precession cardiovascular magnetic resonance, Journal of cardiovascular magnetic resonance 12 (1) (2010) 65.

[27] L. E. Hudsmith, S. E. Petersen, J. M. Francis, M. D. Robson, S. Neubauer, Normal human left and right ventricular and left atrial dimensions using steady state free precession magnetic resonance imaging, Journal of cardiovascular magnetic resonance 7 (5) (2005) 775–782.

[28] A. Saha, S. Roy, Papillary muscles of right ventricle - morphological variations and its clinical relevance, Cardiovascular Pathology 34 (2018) 22–27.

[29] A. Quaglino, S. Pezzuto, P.-S. Koutsourelakis, A. Auricchio, R. Krause, Fast uncertainty quantification of activation sequences in patient-specific cardiac electrophysiology meeting clinical time constraints, International journal for numerical methods in biomedical engineering 34 (7) (2018) e2985.

[30] R. E. Caflisch, Monte carlo and quasi-monte carlo methods, Acta numerica 7 (1998) 1–49.

[31] S.-K. Au, J. L. Beck, Estimation of small failure probabilities in high dimensions by subset simulation, Probabilistic engineering mechanics 16 (4) (2001) 263–277.

[32] I. Papaioannou, W. Betz, K. Zwirglmaier, D. Straub, Mcmc algorithms for subset simulation, Probabilistic Engineering Mechanics 41 (2015) 89–103.

[33] C. Bucher, Asymptotic sampling for high-dimensional reliability analysis, Probabilistic Engineering Mechanics 24 (4) (2009) 504–510.

[34] J. B. Nagel, B. Sudret, Bayesian multilevel model calibration for inverse problems under uncertainty with perfect data, Journal of Aerospace Information Systems 12 (1) (2015) 97–113.

[35] M. D. Morris, Factorial sampling plans for preliminary computational experiments, Technometrics 33 (2) (1991) 161–174.

[36] A. Saltelli, P. Annoni, I. Azzini, F. Campolongo, M. Ratto, S. Tarantola, Variance based sensitivity analysis of model output. design and estimator for the total sensitivity index, Computer physics communications 181 (2) (2010) 259–270.

[37] G. Glen, K. Isaacs, Estimating sobol sensitivity indices using correlations, Environmental Modelling & Software 37 (2012) 157–166.

[38] A. Saltelli, K. Aleksankina, W. Becker, P. Fennell, F. Ferretti, N. Holst, S. Li, Q. Wu, Why so many published sensitivity analyses are false: A systematic review of sensitivity analysis practices, Environmental modelling & software 114 (2019) 29–39.

[39] J. P. Kleijnen, Kriging metamodeling in simulation: A review, European journal of operational research 192 (3) (2009) 707–716.

[40] B. Sudret, Global sensitivity analysis using polynomial chaos expansions, Reliability engineering & system safety 93 (7) (2008) 964–979.

[41] F. Viola, V. Spandan, V. Meschini, J. Romero, M. Fatica, M. D. de Tullio, R. Verzicco, Fsei-gpu: Gpu accelerated simulations of the fluid-structure-electrophysiology interaction in the left heart, arXiv preprint arXiv:2103.15187 (2021).

[42] T. J. Sullivan, Introduction to uncertainty quantification, Vol. 63, Springer, 2015.

[43] P. Embrechts, F. Lindskog, A. McNeil, Modelling dependence with copulas, Rapport technique, Département de mathématiques, Institut Fédéral de Technologie de Zurich, Zurich 14 (2001) 1–50.

[44] R. B. Nelsen, An introduction to copulas, Springer Science & Business Media, 2007.

[45] A. Nataf, Determination des distribution don't les marges sont donnees, Comptes rendus de l'Académie des Sciences 225 (1962) 42–43.

[46] R. Lebrun, A. Dutfoy, An innovating analysis of the nataf transformation from the copula viewpoint, Probabilistic Engineering Mechanics 24 (3) (2009) 312–320.

[47] C. Genest, K. Ghoudi, L.-P. Rivest, A semiparametric estimation procedure of dependence parameters in multivariate families of distributions, Biometrika 82 (3) (1995) 543–552.

[48] R. d. S. Silva, H. F. Lopes, Copula, marginal distributions and model selection: a bayesian note, Statistics and Computing 18 (3) (2008) 313–320.

[49] D. Huard, G. Evin, A.-C. Favre, Bayesian copula selection, Computational Statistics & Data Analysis 51 (2) (2006) 809–822.

[50] R. Lebrun, A. Dutfoy, A generalization of the nataf transformation to distributions with elliptical copula, Probabilistic Engineering Mechanics 24 (2) (2009) 172–178.

[51] D. Dowson, A. Wragg, Maximum-entropy distributions having prescribed first and second moments (corresp.), IEEE Transactions on Information Theory 19 (5) (1973) 689–693.

[52] J.-L. Muñoz-Cobo, R. Mendizábal, A. Miquel, C. Berna, A. Escrivá, Use of the principles of maximum entropy and maximum relative entropy for the determination of uncertain parameter distributions in engineering applications, Entropy 19 (9) (2017) 486.

[53] B. Liquet, Y. Nazarathy, A dynamic view to moment matching of truncated distributions, Statistics & Probability Letters 104 (2015) 87–93.

[54] R. M. Neal, Slice sampling, The annals of statistics 31 (3) (2003) 705–767.

[55] J. E. Gentle, Random number generation and Monte Carlo methods, Vol. 381, Springer, 2003.

[56] N. Metropolis, A. W. Rosenbluth, M. N. Rosenbluth, A. H. Teller, E. Teller, Equation of state calculations by fast computing machines, The journal of chemical physics 21 (6) (1953) 1087–1092.

[57] H. Tanizaki, Computational methods in statistics and econometrics, CRC Press, 2004.

[58] D. S. Wilks, Statistical methods in the atmospheric sciences, Vol. 100, Academic press, 2011.

[59] S. Olver, A. Townsend, Fast inverse transform sampling in one and two dimensions, arXiv preprint arXiv:1307.1223 (2013).

[60] L. N. Trefethen, Approximation Theory and Approximation Practice, Extended Edition, SIAM, 2019.

[61] B. D. Flury, Acceptance–rejection sampling made easy, SIAM Review 32 (3) (1990) 474–476.

[62] G. Casella, C. P. Robert, M. T. Wells, et al., Generalized accept-reject sampling schemes, in: A Festschrift for Herman Rubin, Institute of Mathematical Statistics, 2004, pp. 342–347.

[63] K. Sigman, Acceptance-rejection method, Columbia University (2007).

[64] J. K. Blitzstein, J. Hwang, Introduction to probability, Crc Press Boca Raton, FL, 2015.

[65] C. P. Robert, G. Casella, G. Casella, Monte Carlo statistical methods, Vol. 2, Springer, 1999.

[66] J. L. Beck, K. M. Zuev, Rare event simulation, arXiv preprint arXiv:1508.05047 (2015).

[67] J. C. Helton, F. J. Davis, Latin hypercube sampling and the propagation of uncertainty in analyses of complex systems, Reliability Engineering & System Safety 81 (1) (2003) 23–69.

[68] M. D. McKay, R. J. Beckman, W. J. Conover, A comparison of three methods for selecting values of input variables in the analysis of output from a computer code, Technometrics 42 (1) (2000) 55–61.

[69] P. J. Bickel, F. Götze, W. R. van Zwet, Resampling fewer than n observations: gains, losses, and remedies for losses, in: Selected works of Willem van Zwet, Springer, 2012, pp. 267–297.

[70] M. D. McKay, Evaluating prediction uncertainty, Tech. rep., Nuclear Regulatory Commission (1995).

[71] M. J. Gilman, A brief survey of stopping rules in monte carlo simulations, Tech. rep., Institute of Electrical and Electronics Engineers (IEEE) (1968).

[72] B. Efron, R. Tibshirani, Bootstrap methods for standard errors, confidence intervals, and other measures of statistical accuracy, Statistical science (1986) 54–75.

[73] H. Janssen, Monte-carlo based uncertainty analysis: Sampling efficiency and sampling convergence, Reliability Engineering & System Safety 109 (2013) 123–132.

[74] S. Kucherenko, D. Albrecht, A. Saltelli, Exploring multi-dimensional spaces: A comparison of latin hypercube and quasi monte carlo sampling techniques, arXiv preprint arXiv:1505.02350 (2015).

[75] H. Kahn, A. W. Marshall, Methods of reducing sample size in monte carlo computations, Journal of the Operations Research Society of America 1 (5) (1953) 263–278.

[76] O. Ditlevsen, H. O. Madsen, Structural reliability methods, Vol. 178, Wiley New York, 1996.

[77] P.-S. Koutsourelakis, H. J. Pradlwarter, G. I. Schueller, Reliability of structures in high dimensions, part i: algorithms and applications, Probabilistic Engineering Mechanics 19 (4) (2004) 409–417.

[78] K. Zuev, Subset simulation method for rare event estimation: an introduction, arXiv preprint arXiv:1505.03506 (2015).

[79] C. J. Geyer, Practical markov chain monte carlo, Statistical science (1992) 473–483.

[80] S.-K. Au, Y. Wang, Engineering risk assessment with subset simulation, John Wiley & Sons, 2014.

[81] K. Breitung, The geometry of limit state function graphs and subset simulation: Counterexamples, Reliability Engineering & System Safety 182 (2019) 98–106.

[82] J. Beck, S. Au, Reliability of dynamic systems using stochastic simulation (2005).

[83] A. Saltelli, Sensitivity analysis for importance assessment, Risk analysis 22 (3) (2002) 579–590.

[84] E. de Rocquigny, N. Devictor, S. Tarantola, Uncertainty in industrial practice: a guide to quantitative uncertainty management, John Wiley & Sons, 2008.

[85] B. Iooss, P. Lemaître, A review on global sensitivity analysis methods, in: Uncertainty management in simulation-optimization of complex systems, Springer, 2015, pp. 101–122.

[86] D. Kurowicka, R. M. Cooke, Uncertainty analysis with high dimensional dependence modelling, John Wiley & Sons, 2006.

[87] D. Hamby, A comparison of sensitivity analysis techniques, Health physics 68 (2) (1995) 195–204.

[88] Y. Cao, S. Li, L. Petzold, R. Serban, Adjoint sensitivity analysis for differential-algebraic equations: The adjoint dae system and its numerical solution, SIAM journal on scientific computing 24 (3) (2003) 1076–1089.

[89] A. Saltelli, M. Ratto, S. Tarantola, F. Campolongo, et al., Sensitivity analysis practices: Strategies for model-based inference, Reliability Engineering & System Safety 91 (10-11) (2006) 1109–1125.

[90] A. Saltelli, P. Annoni, How to avoid a perfunctory sensitivity analysis, Environmental Modelling & Software 25 (12) (2010) 1508–1517.

[91] A. Saltelli, K. Chan, E. Scott, Wiley series in probability and statistics, Sensitivity analysis (2000).

[92] A. Saltelli, K. Chan, M. Scott, et al., Sensitivity analysis. probability and statistics series, John and Wiley & Sons, New York (2000).

[93] A. Saltelli, J. Marivoet, Non-parametric statistics in sensitivity analysis for model output: a comparison of selected techniques, Reliability Engineering & System Safety 28 (2) (1990) 229–253.

[94] J. C. Helton, J. D. Johnson, C. J. Sallaberry, C. B. Storlie, Survey of sampling-based methods for uncertainty and sensitivity analysis, Reliability Engineering & System Safety 91 (10-11) (2006) 1175–1209.

[95] R. L. Iman, J. C. Helton, J. E. Campbell, Risk methodology for geologic disposal of radioactive waste: Sensitivity analysis techniques, Tech. rep., Sandia Labs., Albuquerque, NM (USA) (1978).

[96] W. J. Conover, Practical nonparametric statistics, Vol. 350, john wiley & sons, 1999.

[97] W. Hoeffding, A class of statistics with asymptotically normal distribution, in: Breakthroughs in Statistics, Springer, 1992, pp. 308–334.

[98] I. M. Sobol', On sensitivity estimation for nonlinear mathematical models, Matematicheskoe modelirovanie 2 (1) (1990) 112–118.

[99] B. Efron, C. Stein, The jackknife estimate of variance, The Annals of Statistics (1981) 586–596.

[100] I. M. Sobol, Sensitivity analysis for non-linear mathematical models, Mathematical modelling and computational experiment 1 (1993) 407–414.

[101] T. Homma, A. Saltelli, Importance measures in global sensitivity analysis of nonlinear models, Reliability Engineering & System Safety 52 (1) (1996) 1–17.

[102] A. Saltelli, M. Ratto, T. Andres, F. Campolongo, J. Cariboni, D. Gatelli, M. Saisana, S. Tarantola, Global sensitivity analysis: the primer, John Wiley & Sons, 2008.

[103] A. Saltelli, Making best use of model evaluations to compute sensitivity indices, Computer physics communications 145 (2) (2002) 280–297.

[104] A. Janon, T. Klein, A. Lagnoux, M. Nodet, C. Prieur, Asymptotic normality and efficiency of two sobol index estimators, ESAIM: Probability and Statistics 18 (2014) 342–364.

[105] B. Iooss, F. Van Dorpe, N. Devictor, Response surfaces and sensitivity analyses for an environmental model of dose calculations, Reliability Engineering & System Safety 91 (10-11) (2006) 1241–1251.

[106] G. Archer, A. Saltelli, I. M. Sobol, Sensitivity measures, anova-like techniques and the use of bootstrap, Journal of Statistical Computation and Simulation 58 (2) (1997) 99–120.

[107] S. Kucherenko, B. Feil, N. Shah, W. Mauntz, The identification of model effective dimensions using global sensitivity analysis, Reliability Engineering & System Safety 96 (4) (2011) 440–449.

[108] M. J. Jansen, Analysis of variance designs for model output, Computer Physics Communications 117 (1-2) (1999) 35–43.

[109] R. Cukier, H. Levine, K. Shuler, Nonlinear sensitivity analysis of multiparameter model systems, Journal of computational physics 26 (1) (1978) 1–42.

[110] A. Saltelli, S. Tarantola, K.-S. Chan, A quantitative model-independent method for global sensitivity analysis of model output, Technometrics 41 (1) (1999) 39–56.

[111] J. Tissot, C. Prieur, A bias correction method for the estimation of sensitivity indices based on random balance designs, 2011.

[112] F. Campolongo, J. Cariboni, A. Saltelli, W. Schoutens, Enhancing the morris method, Sensitivity Analysis of Model Output (2005) 369–379.

[113] A. Saltelli, S. Tarantola, F. Campolongo, M. Ratto, Sensitivity analysis in practice: a guide to assessing scientific models, Vol. 1, Wiley Online Library, 2004.

[114] D. C. Montgomery, Design and analysis of experiments, John wiley & sons, 2017.

[115] D. K. Lin, A new class of supersaturated designs, Technometrics 35 (1) (1993) 28–31.

[116] B. Bettonvil, J. P. Kleijnen, Searching for important factors in simulation models with many factors: Sequential bifurcation, European Journal of Operational Research 96 (1) (1997) 180–194.

[117] A. Dean, S. Lewis, Screening: methods for experimentation in industry, drug discovery, and genetics, Springer Science & Business Media, 2006.

[118] G. A. Seber, A. J. Lee, Linear regression analysis, John Wiley & Sons, 2012.

[119] K. A. McNeil, I. Newman, F. J. Kelly, Testing research hypotheses with the general linear model, SIU Press, 1996.

[120] G. F. Glonek, P. McCullagh, Multivariate logistic models, Journal of the Royal Statistical Society: Series B (Methodological) 57 (3) (1995) 533–546.

[121] M. H. Hassoun, et al., Fundamentals of artificial neural networks, MIT press, 1995.

[122] D. J. MacKay, Bayesian neural networks and density networks, Nuclear Instruments and Methods in Physics Research Section A: Accelerators, Spectrometers, Detectors and Associated Equipment 354 (1) (1995) 73–80.

[123] D. P. Kingma, M. Welling, Auto-encoding variational bayes, arXiv preprint arXiv:1312.6114 (2013).

[124] R. C. Smith, Uncertainty quantification: theory, implementation, and applications, Vol. 12, Siam, 2013.

[125] L. Le Gratiet, S. Marelli, B. Sudret, Metamodel-based sensitivity analysis: polynomial chaos expansions and gaussian processes, in: Handbook of uncertainty quantification, Springer, 2017, pp. 1289–1325.

[126] A. Kolmogoroff, Interpolation und extrapolation von stationaren zufalligen folgen, Izvestiya Rossiiskoi Akademii Nauk. Seriya Matematicheskaya 5 (1) (1941) 3–14.

[127] W. J. Welch, R. J. Buck, J. Sacks, H. P. Wynn, T. J. Mitchell, M. D. Morris, Screening, predicting, and computer experiments, Technometrics 34 (1) (1992) 15–25.

[128] M. Mohri, A. Rostamizadeh, A. Talwalkar, Foundations of machine learning, MIT press, 2018.

[129] V. Consonni, D. Ballabio, R. Todeschini, Evaluation of model predictive ability by external validation techniques, Journal of chemometrics 24 (3-4) (2010) 194–201.

[130] G. Blatman, Adaptive sparse polynomial chaos expansions for uncertainty propagation and sensitivity analysis, Ph.D. thesis, Clermont-Ferrand 2 (2009).

[131] T. Fushiki, Estimation of prediction error by using k-fold cross-validation, Statistics and Computing 21 (2) (2011) 137–146.

[132] C.-F. J. Wu, et al., Jackknife, bootstrap and other resampling methods in regression analysis, the Annals of Statistics 14 (4) (1986) 1261–1295.

[133] L. L. Gratiet, S. Marelli, B. Sudret, Metamodel-based sensitivity analysis: polynomial chaos expansions and gaussian processes, Handbook of Uncertainty Quantification (2016) 1–37.

[134] R. G. Ghanem, P. D. Spanos, Spectral stochastic finite-element formulation for reliability analysis, Journal of Engineering Mechanics 117 (10) (1991) 2351–2372.

[135] D. Xiu, G. E. Karniadakis, The wiener–askey polynomial chaos for stochastic differential equations, SIAM journal on scientific computing 24 (2) (2002) 619–644.

[136] C. Soize, R. Ghanem, Physical systems with random uncertainties: chaos representations with arbitrary probability measure, SIAM Journal on Scientific Computing 26 (2) (2004) 395–410.

[137] D. A. Bini, M. Capovani, O. Menchi, Metodi numerici per l'algebra lineare (1988).

[138] B. Sudret, Uncertainty propagation and sensitivity analysis in mechanical models–contributions to structural reliability and stochastic spectral methods, Habilitationa diriger des recherches, Université Blaise Pascal, Clermont-Ferrand, France 147 (2007) 53.

[139] G. Blatman, B. Sudret, Adaptive sparse polynomial chaos expansion based on least angle regression, Journal of computational Physics 230 (6) (2011) 2345–2367.

[140] M. Bieri, C. Schwab, Sparse high order fem for elliptic spdes, Computer Methods in Applied Mechanics and Engineering 198 (13-14) (2009) 1149–1170.

[141] R. G. Ghanem, P. D. Spanos, Stochastic finite elements: a spectral approach, Courier Corporation, 2003.

[142] M. Berveiller, B. Sudret, M. Lemaire, Presentation of two methods for computing the response coefficients in stochastic finite element analysis, in: Proc. 9th ASCE Specialty Conference on Probabilistic Mechanics and Structural Reliability, Albuquerque, USA, 2004.

[143] M. Berveiller, B. Sudret, M. Lemaire, Stochastic finite element: a non intrusive approach by regression, European Journal of Computational Mechanics/Revue Européenne de Mécanique Numérique 15 (1-3) (2006) 81–92.

[144] G. Rousselet, C. Pernet, R. R. Wilcox, A practical introduction to the bootstrap: a versatile method to make inferences by using data-driven simulations (2019).

[145] S. Dubreuil, M. Berveiller, F. Petitjean, M. Salaün, Construction of bootstrap confidence intervals on sensitivity indices computed by polynomial chaos expansion, Reliability Engineering & System Safety 121 (2014) 263–275.

[146] N. Wiener, N. Wiener, C. Mathematician, N. Wiener, N. Wiener, C. Mathématicien, Extrapolation, interpolation, and smoothing of stationary time series: with engineering applications, Vol. 113, MIT press Cambridge, MA, 1949.

[147] J. E. Oakley, A. O'Hagan, Probabilistic sensitivity analysis of complex models: a bayesian approach, Journal of the Royal Statistical Society: Series B (Statistical Methodology) 66 (3) (2004) 751–769.

[148] A. Marrel, B. Iooss, B. Laurent, O. Roustant, Calculations of sobol indices for the gaussian process metamodel, Reliability Engineering & System Safety 94 (3) (2009) 742–751.

[149] C. E. Rasmussen, Gaussian processes in machine learning, in: Summer school on machine learning, Springer, 2003, pp. 63–71.

[150] M. L. Stein, Interpolation of spatial data: some theory for kriging, Springer Science & Business Media, 1999.

[151] R. Bates, R. Buck, E. Riccomagno, H. Wynn, Experimental design and observation for large systems, Journal of the Royal Statistical Society: Series B (Methodological) 58 (1) (1996) 77–94.

[152] W. C. Van Beers, J. P. Kleijnen, Customized sequential designs for random simulation experiments: Kriging metamodeling and bootstrapping, European journal of operational research 186 (3) (2008) 1099–1113.

[153] L. Le Gratiet, C. Cannamela, Cokriging-based sequential design strategies using fast cross-validation techniques for multi-fidelity computer codes, Technometrics 57 (3) (2015) 418–427.

[154] B. Betrò, Bayesian methods in global optimization, Journal of Global Optimization 1 (1) (1991) 1–14.

[155] B. Shahriari, K. Swersky, Z. Wang, R. P. Adams, N. De Freitas, Taking the human out of the loop: A review of bayesian optimization, Proceedings of the IEEE 104 (1) (2015) 148–175.

[156] D. A. Harville, Maximum likelihood approaches to variance component estimation and to related problems, Journal of the American statistical association 72 (358) (1977) 320–338.

[157] T. J. Santner, B. J. Williams, W. I. Notz, B. J. Williams, The design and analysis of computer experiments, Vol. 1, Springer, 2003.

[158] C. E. Rasmussen, C. K. Williams, Model selection and adaptation of hyperparameters, in: Gaussian processes for machine learning, MIT Press, 2005, pp. 105–128.

[159] F. Bachoc, Cross validation and maximum likelihood estimations of hyperparameters of gaussian processes with model misspecification, Computational Statistics & Data Analysis 66 (2013) 55–69.

[160] L. Le Gratiet, C. Cannamela, B. Iooss, A bayesian approach for global sensitivity analysis of (multifidelity) computer codes, SIAM/ASA Journal on Uncertainty Quantification 2 (1) (2014) 336–363.

[161] K. R. Anderson, S. Y. Ho, R. H. Anderson, Location and vascular supply of sinus node in human heart., Heart 41 (1) (1979) 28–32.

[162] J. J. B. Jack, D. Noble, R. W. Tsien, Electric current flow in excitable cells, Clarendon Press Oxford, 1975.

[163] L. Leon, F. Roberge, Directional characteristics of action potential propagation in cardiac muscle. a model study., Circulation research 69 (2) (1991) 378–395.

[164] E. J. Vigmond, M. Hughes, G. Plank, L. J. Leon, Computational tools for modeling electrical activity in cardiac tissue, Journal of electrocardiology 36 (2003) 69–74.

[165] A. Bueno-Orovio, D. Kay, V. Grau, B. Rodriguez, K. Burrage, Fractional diffusion models of cardiac electrical propagation: role of structural heterogeneity in dispersion of repolarization, Journal of the Royal Society Interface 11 (97) (2014) 20140352.

[166] D. E. Hurtado, S. Castro, A. Gizzi, Computational modeling of non-linear diffusion in cardiac electrophysiology: A novel porous-medium approach, Computer Methods in Applied Mechanics and Engineering 300 (2016) 70–83.

[167] A. J. Pullan, K. A. Tomlinson, P. J. Hunter, A finite element method for an eikonal equation model of myocardial excitation wavefront propagation, SIAM Journal on Applied Mathematics 63 (1) (2002) 324–350.

[168] N. G. Sepulveda, B. J. Roth, J. P. Wikswo Jr, Current injection into a two-dimensional anisotropic bidomain., Biophysical journal 55 (5) (1989) 987.

[169] L. Tung, A bi-domain model for describing ischemic myocardial dc potentials., MIT, USA, 1978.

[170] J. Sundnes, G. T. Lines, X. Cai, B. F. Nielsen, K.-A. Mardal, A. Tveito, Computing the electrical activity in the heart, Vol. 1, Springer Science & Business Media, 2007.

[171] M. Potse, B. Dubé, J. Richer, A. Vinet, R. M. Gulrajani, A comparison of monodomain and bidomain reaction-diffusion models for action potential propagation in the human heart, IEEE Transactions on Biomedical Engineering 53 (12) (2006) 2425–2435.

[172] E. Vigmond, R. W. Dos Santos, A. Prassl, M. Deo, G. Plank, Solvers for the cardiac bidomain equations, Progress in biophysics and molecular biology 96 (1-3) (2008) 3–18.

[173] B. J. Roth, Meandering of spiral waves in anisotropic cardiac tissue, Physica D: Nonlinear Phenomena 150 (1-2) (2001) 127–136.

[174] N. Trayanova, Defibrillation of the heart: insights into mechanisms from modelling studies, Experimental physiology 91 (2) (2006) 323–337.

[175] J. P. Wikswo Jr, S.-F. Lin, R. A. Abbas, Virtual electrodes in cardiac tissue: a common mechanism for anodal and cathodal stimulation, Biophysical journal 69 (6) (1995) 2195–2210.

[176] A. Muzikant, C. Henriquez, Validation of three-dimensional conduction models using experimental mapping: are we getting closer?, Progress in biophysics and molecular biology 69 (2-3) (1998) 205–223.

[177] F. Viola, V. Meschini, R. Verzicco, Fluid–structure-electrophysiology interaction (fsei) in the left-heart: A multi-way coupled computational model, European Journal of Mechanics-B/Fluids 79 (2020) 212–232.

[178] O. J. Britton, A. Bueno-Orovio, K. Van Ammel, H. R. Lu, R. Towart, D. J. Gallacher, B. Rodriguez, Experimentally calibrated population of models predicts and explains intersubject variability in cardiac cellular electrophysiology, Proceedings of the National Academy of Sciences 110 (23) (2013) E2098–E2105.

[179] M. Sermesant, R. Chabiniok, P. Chinchapatnam, T. Mansi, F. Billet, P. Moireau, J.-M. Peyrat, K. Wong, J. Relan, K. Rhode, et al., Patient-specific electromechanical models of the heart for the prediction of pacing acute effects in crt: a preliminary clinical validation, Medical image analysis 16 (1) (2012) 201–215.

[180] P. R. Johnston, A sensitivity study of conductivity values in the passive bidomain equation, Mathematical biosciences 232 (2) (2011) 142–150.

[181] A. Barone, A. Gizzi, F. Fenton, S. Filippi, A. Veneziani, Experimental validation of a variational data assimilation procedure for estimating space-dependent cardiac conductivities, Computer Methods in Applied Mechanics and Engineering 358 (2020) 112615.

[182] N. Cusimano, A. Gizzi, F. Fenton, S. Filippi, L. Gerardo-Giorda, Key aspects for effective mathematical modelling of fractional-diffusion in cardiac electrophysiology: A quantitative study, Communications in Nonlinear Science and Numerical Simulation 84 (2020) 105152.

[183] H. Yang, A. Veneziani, Estimation of cardiac conductivities in ventricular tissue by a variational approach, Inverse Problems 31 (11) (2015) 115001.

[184] E. Konukoglu, J. Relan, U. Cilingir, B. H. Menze, P. Chinchapatnam, A. Jadidi, H. Cochet, M. Hocini, H. Delingette, P. Jaïs, et al., Efficient

probabilistic model personalization integrating uncertainty on data and parameters: Application to eikonal-diffusion models in cardiac electrophysiology, Progress in biophysics and molecular biology 107 (1) (2011) 134–146.

[185] K. Chan, A. Saltelli, S. Tarantola, Sensitivity analysis of model output: variance-based methods make the difference, in: Proceedings of the 29th conference on Winter simulation, 1997, pp. 261–268.

[186] D. E. Hurtado, S. Castro, P. Madrid, Uncertainty quantification of 2 models of cardiac electromechanics, International journal for numerical methods in biomedical engineering 33 (12) (2017) e2894.

[187] Z. Hu, D. Du, Y. Du, Generalized polynomial chaos-based uncertainty quantification and propagation in multi-scale modeling of cardiac electrophysiology, Computers in biology and medicine 102 (2018) 57–74.

[188] K. Ten Tusscher, A. Panfilov, Cell model for efficient simulation of wave propagation in human ventricular tissue under normal and pathological conditions, Physics in Medicine & Biology 51 (23) (2006) 6141.

[189] S. A. Niederer, E. Kerfoot, A. P. Benson, M. O. Bernabeu, O. Bernus, C. Bradley, E. M. Cherry, R. Clayton, F. H. Fenton, A. Garny, et al., Verification of cardiac tissue electrophysiology simulators using an n-version benchmark, Philosophical Transactions of the Royal Society A: Mathematical, Physical and Engineering Sciences 369 (1954) (2011) 4331–4351.

[190] M. E Rognes, P. E Farrell, S. W Funke, J. E Hake, M. MC Maleckar, cbcbeat: an adjoint-enabled framework for computational cardiac electrophysiology, The Journal of Open Source Software 2 (2017).

[191] M. S. Alnæs, J. Blechta, J. Hake, A. Johansson, B. Kehlet, A. Logg, C. Richardson, J. Ring, M. E. Rognes, G. N. Wells, The fenics project version 1.5, Archive of Numerical Software 3 (100) (2015).

[192] A. Logg, K.-A. Mardal, G. N. Wells, et al., Automated Solution of Differential Equations by the Finite Element Method, Springer, 2012.

[193] D. Chapelle, A. Collin, J.-F. Gerbeau, A surface-based electrophysiology model relying on asymptotic analysis and motivated by cardiac atria modeling, Mathematical Models and Methods in Applied Sciences 23 (14) (2013) 2749–2776.

[194] A. Collin, J.-F. Gerbeau, M. Hocini, M. Haïssaguerre, D. Chapelle, Surface-based electrophysiology modeling and assessment of physiological simulations in atria, in: International Conference on Functional Imaging and Modeling of the Heart, Springer, 2013, pp. 352–359.

[195] P. Deshmukh, D. A. Casavant, M. Romanyshyn, K. Anderson, Permanent, direct his-bundle pacing: a novel approach to cardiac pacing in patients with normal his-purkinje activation, Circulation 101 (8) (2000) 869–877.

[196] M. Di Donato, P. Dabic, S. Castelvecchio, C. Santambrogio, J. Brankovic, L. Collarini, T. Joussef, A. Frigiola, G. Buckberg, L. Menicanti, et al., Left ventricular geometry in normal and post-anterior myocardial infarction patients: sphericity index and new conicity index comparisons, European journal of cardio-thoracic surgery 29 (Supplement_1) (2006) S225–S230.

[197] A. Tarantola, Inverse problem theory and methods for model parameter estimation, Vol. 89, siam, 2005.

[198] J. Greiner, A. C. Sankarankutty, G. Seemann, T. Seidel, F. B. Sachse, Confocal microscopy-based estimation of parameters for computational modeling of electrical conduction in the normal and infarcted heart, Frontiers in physiology 9 (2018) 239.

[199] F. J. Massey Jr, The kolmogorov-smirnov test for goodness of fit, Journal of the American statistical Association 46 (253) (1951) 68–78.

[200] L. Clerc, Directional differences of impulse spread in trabecular muscle from mammalian heart., The Journal of physiology 255 (2) (1976) 335–346.

[201] D. E. Roberts, A. M. Scher, Effect of tissue anisotropy on extracellular potential fields in canine myocardium in situ., Circulation Research 50 (3) (1982) 342–351.

[202] D. E. Roberts, L. T. Hersh, A. M. Scher, Influence of cardiac fiber orientation on wavefront voltage, conduction velocity, and tissue resistivity in the dog., Circulation research 44 (5) (1979) 701–712.

[203] B. J. Roth, The electrical potential produced by a strand of cardiac muscle: a bidomain analysis, Annals of biomedical engineering 16 (6) (1988) 609–637.

[204] B. J. Roth, Nonsustained reentry following successive stimulation of cardiac tissue through a unipolar electrode, Journal of Cardiovascular Electrophysiology 8 (7) (1997) 768–778.

[205] K. Chan, S. Tarantola, A. Saltelli, I. M. Sobol, Variance-based methods, Sensitivity analysis 45 (2000) 167–197.

[206] A. B. Owen, Monte carlo, quasi-monte carlo, and randomized quasi-monte carlo, in: Monte-Carlo and Quasi-Monte Carlo Methods 1998, Springer, 2000, pp. 86–97.

[207] I. M. Sobol', On the distribution of points in a cube and the approximate evaluation of integrals, Zhurnal Vychislitel'noi Matematiki i Matematicheskoi Fiziki 7 (4) (1967) 784–802.

[208] W. Gautschi, Orthogonal polynomials, Oxford university press Oxford, 2004.

[209] D. C Montgomery, Montgomery design and analysis of experiments (1997).

[210] G. Blatman, B. Sudret, Efficient computation of global sensitivity indices using sparse polynomial chaos expansions, Reliability Engineering & System Safety 95 (11) (2010) 1216–1229.

[211] B. Sudret, Global sensitivity analysis using polynomial chaos expansions, Reliability engineering & system safety 93 (7) (2008) 964–979.

[212] M. Eldred, J. Burkardt, Comparison of non-intrusive polynomial chaos and stochastic collocation methods for uncertainty quantification, in: 47th AIAA aerospace sciences meeting including the new horizons forum and aerospace exposition, 2009, p. 976.

[213] K. Levenberg, A method for the solution of certain non-linear problems in least squares, Quarterly of applied mathematics 2 (2) (1944) 164–168.

[214] E. Anderssen, K. Dyrstad, F. Westad, H. Martens, Reducing over-optimism in variable selection by cross-model validation, Chemometrics and intelligent laboratory systems 84 (1-2) (2006) 69–74.

[215] N. Metropolis, S. Ulam, The monte carlo method, Journal of the American statistical association 44 (247) (1949) 335–341.

[216] D. W. Scott, Multivariate density estimation: theory, practice, and visualization, John Wiley & Sons, 2015.

[217] P. Pathmanathan, J. M. Cordeiro, R. A. Gray, Comprehensive uncertainty quantification and sensitivity analysis for cardiac action potential models, Frontiers in physiology 10 (2019) 721.

[218] J. Martin, J. L. Crowley, Comparison of correlation techniques, in: Intelligent Autonomous Systems, 1995, pp. 86–93.

[219] K. J. Coakley, P. Hale, Alignment of noisy signals, IEEE Transactions on Instrumentation and Measurement 50 (1) (2001) 141–149.

[220] P. Pathmanathan, M. S. Shotwell, D. J. Gavaghan, J. M. Cordeiro, R. A. Gray, Uncertainty quantification of fast sodium current steady-state inactivation for multi-scale models of cardiac electrophysiology, Progress in biophysics and molecular biology 117 (1) (2015) 4–18.

[221] C. Cherubini, S. Filippi, A. Gizzi, R. Ruiz-Baier, A note on stress-driven anisotropic diffusion and its role in active deformable media, Journal of Theoretical Biology 430 (2017) 221–228.

[222] A. Loppini, A. Gizzi, R. Ruiz-Baier, C. Cherubini, F. H. Fenton, S. Filippi, Competing mechanisms of stress-assisted diffusivity and stretch-activated currents in cardiac electromechanics, Frontiers in Physiology 9 (2018) 1714.

[223] A. Gizzi, E. Cherry, R. F. Gilmour Jr, S. Luther, S. Filippi, F. H. Fenton, Effects of pacing site and stimulation history on alternans dynamics and the development of complex spatiotemporal patterns in cardiac tissue, Frontiers in physiology 4 (2013) 71.

[224] E. M. Cherry, F. H. Fenton, Suppression of alternans and conduction blocks despite steep apd restitution: electrotonic, memory, and conduction velocity restitution effects, American Journal of Physiology-Heart and Circulatory Physiology 286 (6) (2004) H2332–H2341.

[225] A. Loppini, A. Gizzi, C. Cherubini, E. M. Cherry, F. H. Fenton, S. Filippi, Spatiotemporal correlation uncovers characteristic lengths in cardiac tissue, Physical Review E 100 (2) (2019) 020201.

[226] A. Quarteroni, T. Lassila, S. Rossi, R. Ruiz-Baier, Integrated heart—coupling multiscale and multiphysics models for the simulation of the cardiac function, Computer Methods in Applied Mechanics and Engineering 314 (2017) 345–407.

[227] S. Krishnamoorthi, M. Sarkar, W. S. Klug, Numerical quadrature and operator splitting in finite element methods for cardiac electrophysiology, International journal for numerical methods in biomedical engineering 29 (11) (2013) 1243–1266.

[228] N. Virag, V. Jacquemet, C. Henriquez, S. Zozor, O. Blanc, J.-M. Vesin, E. Pruvot, L. Kappenberger, Study of atrial arrhythmias in a computer model based on magnetic resonance images of human atria, Chaos: An Interdisciplinary Journal of Nonlinear Science 12 (3) (2002) 754–763.

[229] M. Courtemanche, R. J. Ramirez, S. Nattel, Ionic mechanisms underlying human atrial action potential properties: insights from a mathematical model, American Journal of Physiology-Heart and Circulatory Physiology 275 (1) (1998) H301–H321.

[230] P. Stewart, O. V. Aslanidi, D. Noble, P. J. Noble, M. R. Boyett, H. Zhang, Mathematical models of the electrical action potential of purkinje fibre cells, Philosophical Transactions of the Royal Society A: Mathematical, Physical and Engineering Sciences 367 (1896) (2009) 2225–2255.

[231] A. Kaboudian, E. M. Cherry, F. H. Fenton, Real-time interactive simulations of large-scale systems on personal computers and cell phones: Toward patient-specific heart modeling and other applications, Science advances 5 (3) (2019) eaav6019.

[232] T. N. James, The internodal pathways of the human heart, Progress in cardiovascular diseases 43 (6) (2001) 495–535.

[233] F. Pashakhanloo, D. A. Herzka, H. Ashikaga, S. Mori, N. Gai, D. A. Bluemke, N. A. Trayanova, E. R. McVeigh, Myofiber architecture of the human atria as revealed by submillimeter diffusion tensor imaging, Circulation: arrhythmia and electrophysiology 9 (4) (2016) e004133.

[234] S. Karas Jr, R. C. Elkins, Mechanism of function of the mitral valve leaflets, chordae tendineae and left ventricular papillary muscles in dogs, Circulation research 26 (6) (1970) 689–696.

[235] R. Bordas, V. Grau, R. Burton, P. Hales, J. Schneider, D. Gavaghan, P. Kohl, B. Rodriguez, Integrated approach for the study of anatomical variability in the cardiac purkinje system: from high resolution mri to electrophysiology simulation, in: 2010 Annual International Conference of the IEEE Engineering in Medicine and Biology, IEEE, 2010, pp. 6793–6796.

[236] R. A. Bergman, A. K. Afifi, et al., Atlas of microscopic anatomy (1974).

[237] J. Tranum-Jensen, A. Wilde, J. T. Vermeulen, M. J. Janse, Morphology of electrophysiologically identified junctions between purkinje fibers and ventricular muscle in rabbit and pig hearts., Circulation research 69 (2) (1991) 429–437.

[238] O. Berenfeld, J. Jalife, Purkinje-muscle reentry as a mechanism of polymorphic ventricular arrhythmias in a 3-dimensional model of the ventricles, Circulation Research 82 (10) (1998) 1063–1077.

[239] G. A. Holzapfel, R. W. Ogden, Constitutive modelling of passive myocardium: a structurally based framework for material characterization, Philosophical Transactions of the Royal Society A: Mathematical, Physical and Engineering Sciences 367 (1902) (2009) 3445–3475.

[240] G. Seemann, C. Höper, F. B. Sachse, O. Dössel, A. V. Holden, H. Zhang, Heterogeneous three-dimensional anatomical and electrophysiological model of human atria, Philosophical Transactions of the Royal Society A: Mathematical, Physical and Engineering Sciences 364 (1843) (2006) 1465–1481.

[241] D. Nickerson, N. Smith, P. Hunter, New developments in a strongly coupled cardiac electromechanical model, EP Europace 7 (s2) (2005) S118–S127.

[242] S. G. Campbell, E. Howard, J. Aguado-Sierra, B. A. Coppola, J. H. Omens, L. J. Mulligan, A. D. McCulloch, R. C. Kerckhoffs, Effect of transmurally heterogeneous myocyte excitation–contraction coupling on canine left ventricular electromechanics, Experimental physiology 94 (5) (2009) 541–552.

[243] G. Buckberg, A. Mahajan, S. Saleh, J. I. Hoffman, C. Coghlan, Structure and function relationships of the helical ventricular myocardial band, The Journal of thoracic and cardiovascular surgery 136 (3) (2008) 578–589.

[244] R. Doste, D. Soto-Iglesias, G. Bernardino, A. Alcaine, R. Sebastian, S. Giffard-Roisin, M. Sermesant, A. Berruezo, D. Sanchez-Quintana, O. Camara, A rule-based method to model myocardial fiber orientation in cardiac biventricular geometries with outflow tracts, International journal for numerical methods in biomedical engineering 35 (4) (2019) e3185.

[245] N. A. Trayanova, Whole-heart modeling: applications to cardiac electrophysiology and electromechanics, Circulation research 108 (1) (2011) 113–128.

[246] M. Wilhelms, H. Hettmann, M. M. C. Maleckar, J. T. Koivumäki, O. Dössel, G. Seemann, Benchmarking electrophysiological models of human atrial myocytes, Frontiers in physiology 3 (2013) 487.

[247] S. Inada, J. Hancox, H. Zhang, M. Boyett, One-dimensional mathematical model of the atrioventricular node including atrio-nodal, nodal, and nodal-his cells, Biophysical journal 97 (8) (2009) 2117–2127.

[248] V. D. Corino, F. Sandberg, L. T. Mainardi, L. Sornmo, An atrioventricular node model for analysis of the ventricular response during atrial fibrillation, IEEE transactions on biomedical engineering 58 (12) (2011) 3386–3395.

[249] B. Baillargeon, N. Rebelo, D. D. Fox, R. L. Taylor, E. Kuhl, The living heart project: a robust and integrative simulator for human heart function, European Journal of Mechanics-A/Solids 48 (2014) 38–47.

[250] S. Sugiura, T. Washio, A. Hatano, J. Okada, H. Watanabe, T. Hisada, Multi-scale simulations of cardiac electrophysiology and mechanics using the university of tokyo heart simulator, Progress in biophysics and molecular biology 110 (2-3) (2012) 380–389.

[251] E. J. Vigmond, C. Clements, Construction of a computer model to investigate sawtooth effects in the purkinje system, IEEE transactions on biomedical engineering 54 (3) (2007) 389–399.

[252] T. Lassila, M. Lange, A. R. P. Perez, K. Lekadir, X. Albà, G. Piella, A. F. Frangi, Electrophysiology model for a human heart with ischemic scar and realistic purkinje network, in: Statistical Atlases and Computational Models of the Heart, Springer, 2015, pp. 90–97.

[253] M. Deo, P. Boyle, G. Plank, E. Vigmond, Arrhythmogenic mechanisms of the purkinje system during electric shocks: a modeling study, Heart rhythm 6 (12) (2009) 1782–1789.

[254] M. Deo, P. M. Boyle, A. M. Kim, E. J. Vigmond, Arrhythmogenesis by single ectopic beats originating in the purkinje system, American Journal of Physiology-Heart and Circulatory Physiology 299 (4) (2010) H1002–H1011.

[255] E. Behradfar, A. Nygren, E. J. Vigmond, The role of purkinje-myocardial coupling during ventricular arrhythmia: a modeling study, PloS one 9 (2) (2014).

[256] T. Ijiri, T. Ashihara, T. Yamaguchi, K. Takayama, T. Igarashi, T. Shimada, T. Namba, R. Haraguchi, K. Nakazawa, A procedural method for modeling the purkinje fibers of the heart, The journal of physiological sciences (2008) 0810170079–0810170079.

[257] A. Lopez-Perez, R. Sebastian, J. M. Ferrero, Three-dimensional cardiac computational modelling: methods, features and applications, Biomedical engineering online 14 (1) (2015) 35.

[258] C. Vergara, M. Lange, S. Palamara, T. Lassila, A. F. Frangi, A. Quarteroni, A coupled 3d–1d numerical monodomain solver for cardiac electrical activation in the myocardium with detailed purkinje network, Journal of Computational Physics 308 (2016) 218–238.

[259] P. Pathmanathan, M. O. Bernabeu, R. Bordas, J. Cooper, A. Garny, J. M. Pitt-Francis, J. P. Whiteley, D. J. Gavaghan, A numerical guide to the solution of the bidomain equations of cardiac electrophysiology, Progress in biophysics and molecular biology 102 (2) (2010) 136–155.

[260] N. A. Trayanova, J. Constantino, V. Gurev, Electromechanical models of the ventricles, American Journal of Physiology-Heart and Circulatory Physiology 301 (2) (2011) H279–H286.

[261] J. Cooper, A. Corrias, D. Gavaghan, D. Noble, Considerations for the use of cellular electrophysiology models within cardiac tissue simulations, Progress in biophysics and molecular biology 107 (1) (2011) 74–80.

[262] R. H. Clayton, Y. Aboelkassem, C. D. Cantwell, C. Corrado, T. Delhaas, W. Huberts, C. L. Lei, H. Ni, A. V. Panfilov, C. Roney, et al., An audit of uncertainty in multi-scale cardiac electrophysiology models, Philosophical Transactions of the Royal Society A 378 (2173) (2020) 20190335.

[263] E. C. Vasconcellos, E. W. Clua, F. H. Fenton, M. Zamith, Accelerating simulations of cardiac electrical dynamics through a multi-gpu platform and an optimized data structure, Concurrency and Computation: Practice and Experience 32 (5) (2020) e5528.

[264] E. Koprla, L. Nemeseri, Essential features of endocardial and myocardial morphology: Sem and tem studies., Acta Physiologica Hungarica 64 (1) (1984) 65–79.

[265] G. M. Hutchins, B. H. Bulkley, G. W. Moore, M. A. Piasio, F. T. Lohr, Shape of the human cardiac ventricles, The American journal of cardiology 41 (4) (1978) 646–654.

[266] A. Ansari, S. Yen Ho, R. H. Anderson, Distribution of the purkinje fibres in the sheep heart, The Anatomical Record: An Official Publication of the American Association of Anatomists 254 (1) (1999) 92–97.

[267] T. Shimada, Purkinje fibers of the heart, Shinyaku to Chiryou 42 (1992) 11–13.

[268] C. Vergara, S. Palamara, D. Catanzariti, F. Nobile, E. Faggiano, C. Pangrazzi, M. Centonze, M. Maines, A. Quarteroni, G. Vergara, Patient-specific generation of the purkinje network driven by clinical measurements of a normal propagation, Medical & biological engineering & computing 52 (10) (2014) 813–826.

[269] A. Saha, S. Roy, Papillary muscles of left ventricle - morphological variations and its clinical relevance, Indian heart journal 70 (6) (2018) 894–900.

[270] G. Nigri, L. Di Dio, C. Baptista, Papillary muscles and tendinous cords of the right ventricle of the human heart morphological characteristics, Surgical and Radiologic Anatomy 23 (1) (2001) 45–49.

[271] G. D. Buckberg, Basic science review: the helix and the heart, The Journal of Thoracic and Cardiovascular Surgery 124 (5) (2002) 863–883.

[272] S. Rush, H. Larsen, A practical algorithm for solving dynamic membrane equations, IEEE Transactions on Biomedical Engineering (4) (1978) 389–392.

[273] M. E. Marsh, S. T. Ziaratgahi, R. J. Spiteri, The secrets to the success of the rush–larsen method and its generalizations, IEEE transactions on biomedical engineering 59 (9) (2012) 2506–2515.

[274] L. N. Trefethen, D. Bau III, Numerical linear algebra, Vol. 50, Siam, 1997.

[275] G. Ruetsch, M. Fatica, CUDA Fortran for scientists and engineers: best practices for efficient CUDA Fortran programming, Elsevier, 2013.

[276] R. H. Anderson, S. Mori, D. E. Spicer, D. Sanchez-Quintana, B. Jensen, The anatomy, development, and evolution of the atrioventricular conduction axis, Journal of cardiovascular development and disease 5 (3) (2018) 44.

[277] N. Ono, T. Yamaguchi, H. Ishikawa, M. Arakawa, N. Takahashi, T. Saikawa, T. Shimada, Morphological varieties of the purkinje fiber network in mammalian hearts, as revealed by light and electron microscopy, Archives of histology and cytology 72 (3) (2009) 139–149.

[278] B. R. Liu, E. M. Cherry, Image-based structural modeling of the cardiac purkinje network, BioMed research international 2015 (2015).

[279] S. Tawara, Das Reizleitungssystem des Säugetierherzens: eine anatomisch-histologische Studie über das Atrioventrikularbündel und die Purkinjeschen Fäden, Fischer, 1906.

[280] O. S. Narula, Sinus node re-entry: a mechanism for supraventricular tachycardia, Circulation 50 (6) (1974) 1114–1128.

[281] S. Niederer, L. Mitchell, N. Smith, G. Plank, Simulating human cardiac electrophysiology on clinical time-scales, Frontiers in physiology 2 (2011) 14.

[282] G. Cuccuru, G. Fotia, F. Maggio, J. Southern, Simulating cardiac electrophysiology using unstructured all-hexahedra spectral elements, BioMed research international 2015 (2015).

[283] M. Perego, A. Veneziani, An efficient generalization of the rush-larsen method for solving electro-physiology membrane equations, Electronic Transactions on Numerical Analysis 35 (2009) 234–256.

[284] S. Pakarinen, L. Toivonen, Minimizing ventricular pacing by a novel atrioventricular (av) delay hysteresis algorithm in patients with intact or compromised intrinsic av conduction and different atrial and ventricular lead locations, Annals of medicine 45 (5-6) (2013) 438–445.

[285] A. Takeshita, L. L. Basta, J. M. Kioschos, Effect of intermittent left bundle branch block on left ventricular performance, The American journal of medicine 56 (2) (1974) 251–255.

[286] H. Xiao, C. Lee, D. Gibson, Effect of left bundle branch block on diastolic function in dilated cardiomyopathy., Heart 66 (6) (1991) 443–447.

[287] H. Mahrholdt, A. Wagner, C. C. Deluigi, E. Kispert, S. Hager, G. Meinhardt, H. Vogelsberg, P. Fritz, J. Dippon, C.-T. Bock, et al., Clinical perspective, Circulation 114 (15) (2006) 1581–1590.

[288] B. J. Maron, J. A. Towbin, G. Thiene, C. Antzelevitch, D. Corrado, D. Arnett, A. J. Moss, C. E. Seidman, J. B. Young, Contemporary definitions and classification of the cardiomyopathies: an american heart association scientific statement from the council on clinical cardiology, heart failure and transplantation committee; quality of care and outcomes research and functional genomics and translational biology interdisciplinary working groups;

and council on epidemiology and prevention, Circulation 113 (14) (2006) 1807–1816.

[289] H. C. Strauss, J. Bigger, A. L. Saroff, E.-G. Giardina, Electrophysiologic evaluation of sinus node function in patients with sinus node dysfunction., Circulation 53 (5) (1976) 763–776.

[290] A. M. Gillis, H. Puererfellner, C. W. Israel, H. Sunthorn, S. Kacet, M. Anelli-Monti, F. Tang, M. Young, G. Boriani, M. E. C. S. Investigators, Reducing unnecessary right ventricular pacing with the managed ventricular pacing mode in patients with sinus node disease and av block, Pacing and clinical electrophysiology 29 (7) (2006) 697–705.

[291] J. L. Cox, T. M. Sundt, Operative techniques in cardiac & thoracic surgery: A comparative atlas, Operative Techniques in Cardiac and Thoracic Surgery 1 (1) (1996) 1.

[292] M. Dupraz, S. Filippi, A. Gizzi, A. Quarteroni, R. Ruiz-Baier, Finite element and finite volume-element simulation of pseudo-ecgs and cardiac alternans, Mathematical Methods in the Applied Sciences 38 (6) (2015) 1046–1058.

[293] H. D. Simms Jr, D. B. Geselowitz, Computation of heart surface potentials using the surface source model, Journal of cardiovascular electrophysiology 6 (7) (1995) 522–531.

[294] D. Wang, R. M. Kirby, C. R. Johnson, Resolution strategies for the finite-element-based solution of the ecg inverse problem, IEEE Transactions on biomedical engineering 57 (2) (2009) 220–237.

[295] L. C. Lee, M. Genet, A. B. Dang, L. Ge, J. M. Guccione, M. B. Ratcliffe, Applications of computational modeling in cardiac surgery, Journal of Cardiac Surgery: Including Mechanical and Biological Support for the Heart and Lungs 29 (3) (2014) 293–302.

[296] W. Sun, C. Martin, T. Pham, Computational modeling of cardiac valve function and intervention, Annual review of biomedical engineering 16 (2014) 53–76.

[297] A. W. Lee, C. M. Costa, M. Strocchi, C. A. Rinaldi, S. A. Niederer, Computational modeling for cardiac resynchronization therapy, Journal of cardiovascular translational research 11 (2) (2018) 92–108.

[298] L. W.-T. Ng, M. Eldred, Multifidelity uncertainty quantification using non-intrusive polynomial chaos and stochastic collocation, in: 53rd AIAA/ASME/ASCE/AHS/ASC Structures, Structural Dynamics and Materials Conference, 2012, p. 1852.

[299] R. Molléro, X. Pennec, H. Delingette, A. Garny, N. Ayache, M. Sermesant, Multifidelity-cma: a multifidelity approach for efficient personalisation of 3d cardiac electromechanical models, Biomechanics and modeling in mechanobiology 17 (1) (2018) 285–300.

[300] C. M. Fleeter, G. Geraci, D. E. Schiavazzi, A. M. Kahn, A. L. Marsden, Multilevel and multifidelity uncertainty quantification for cardiovascular hemodynamics, Computer methods in applied mechanics and engineering 365 (2020) 113030.

[301] A. Barone, M. G. Carlino, A. Gizzi, S. Perotto, A. Veneziani, Efficient estimation of cardiac conductivities: A proper generalized decomposition approach, Journal of Computational Physics 423 (2020) 109810.

[302] V. Meschini, M. D. de Tullio, R. Verzicco, Effects of mitral chordae tendineae on the flow in the left heart ventricle., European Physical Journal E–Soft Matter 41 (2) (2018).

[303] V. Meschini, F. Viola, R. Verzicco, Heart rate effects on the ventricular hemodynamics and mitral valve kinematics, Computers & Fluids 197 (2020) 104359.

[304] G. Del Corso, R. Verzicco, F. Viola, Sensitivity analysis of an electrophysiology model for the left ventricle, Journal of the Royal Society Interface 17 (171) (2020) 20200532.

[305] A. Keller, A. Gopal, D. King, Left and right atrial volume by freehand three-dimensional echocardiography: in vivo validation using magnetic resonance imaging, European Journal of Echocardiography 1 (1) (2000) 55–65.

[306] H. Hayashi, R. L. Lux, R. F. Wyatt, M. Burgess, J. Abildskov, Relation of canine atrial activation sequence to anatomic landmarks, American Journal of Physiology-Heart and Circulatory Physiology 242 (3) (1982) H421–H428.

[307] L. Pegolotti, L. Dedè, A. Quarteroni, Isogeometric analysis of the electrophysiology in the human heart: Numerical simulation of the bidomain equations on the atria, Computer Methods in Applied Mechanics and Engineering 343 (2019) 52–73.

[308] R. C. Truex, M. Q. Smythe, Reconstruction of the human atrioventricular node, The Anatomical Record 158 (1) (1967) 11–19.

[309] M. Sobol'Ilya, B. V. Shukhman, et al., On global sensitivity indices: Monte carlo estimates affected by random errors, Monte Carlo Methods and Applications 13 (1) (2007) 89–97.

[310] H. Zhang, A. Holden, I. Kodama, H. Honjo, M. Lei, T. Varghese, M. Boyett, Mathematical models of action potentials in the periphery and center of

the rabbit sinoatrial node, American Journal of Physiology-Heart and Circulatory Physiology 279 (1) (2000) H397–H421.

[311] R. Wilders, H. Jongsma, A. Van Ginneken, Pacemaker activity of the rabbit sinoatrial node. a comparison of mathematical models, Biophysical journal 60 (5) (1991) 1202–1216.

[312] K. L. Merckx, C. B. De Vos, A. Palmans, J. Habets, E. C. Cheriex, H. J. Crijns, R. G. Tieleman, Atrial activation time determined by transthoracic doppler tissue imaging can be used as an estimate of the total duration of atrial electrical activation, Journal of the American Society of Echocardiography 18 (9) (2005) 940–944.

[313] D. Lucor, O. P. Le Maître, Cardiovascular modeling with adapted parametric inference, ESAIM: Proceedings and Surveys 62 (2018) 91–107.

[314] D. G. Whittaker, M. Clerx, C. L. Lei, D. J. Christini, G. R. Mirams, Calibration of ionic and cellular cardiac electrophysiology models, Wiley Interdisciplinary Reviews: Systems Biology and Medicine (2020) e1482.

[315] F. X. Roithinger, M. ABOU-HARB, O. Pachinger, F. Hintringer, The effect of the atrial pacing site on the total atrial activation time, Pacing and Clinical Electrophysiology 24 (3) (2001) 316–322.

[316] R. J. Ramirez, S. Nattel, M. Courtemanche, Mathematical analysis of canine atrial action potentials: rate, regional factors, and electrical remodeling, American Journal of Physiology-Heart and Circulatory Physiology 279 (4) (2000) H1767–H1785.

[317] N. Cusimano, F. del Teso, L. Gerardo-Giorda, G. Pagnini, Discretizations of the spectral fractional laplacian on general domains with dirichlet, neumann, and robin boundary conditions, SIAM Journal on Numerical Analysis 56 (3) (2018) 1243–1272.

[318] A. Nygren, C. Fiset, L. Firek, J. W. Clark, D. S. Lindblad, R. B. Clark, W. R. Giles, Mathematical model of an adult human atrial cell: the role of k+ currents in repolarization, Circulation research 82 (1) (1998) 63–81.

[319] V. Meschini, F. Viola, R. Verzicco, Modeling mitral valve stenosis: A parametric study on the stenosis severity level, Journal of biomechanics 84 (2019) 218–226.

[320] B. Rodriguez, N. Trayanova, D. Noble, Modeling cardiac ischemia, Annals of the New York academy of sciences 1080 (2006) 395.

[321] G. Seemann, P. C. Bustamante, S. Ponto, M. Wilhelms, E. P. Scholz, O. Dössel, Atrial fibrillation-based electrical remodeling in a computer model of the human atrium, in: 2010 Computing in Cardiology, IEEE, 2010, pp. 417–420.

[322] F. Viola, E. Jermyn, J. Warnock, G. Querzoli, R. Verzicco, Left ventricular hemodynamics with an implanted assist device: an in vitro fluid dynamics study, Annals of biomedical engineering 47 (8) (2019) 1799–1814.

[323] J. M. Rawles, A mathematical model of left ventricular function in atrial fibrillation, International journal of bio-medical computing 23 (1-2) (1988) 57–68.

[324] V. Gurev, J. Constantino, N. Trayanova, Distribution of electromechanical delay in the heart: insights from a three-dimensional electromechanical model., Biophysical Journal 99 (2010) 745–754.

[325] C. Augustin, A. Neic, M. Liebmann, A. Prassl, S. Niederer, G. Haase, G. Plank, Anatomically accurate high resolution modeling of human whole heart electromechanics: a strongly scalable algebraic multigrid solver method for nonlinear deformation, Journal of Computational Physics 305 (2016) 622–646.

[326] R. Moss, E. Wulfers, S. Schuler, A. Loewe, G. Seemann, A fully–coupled electro–mechanical whole–heart computational model: Influence of cardiac contraction on the ecg, Frontiers in Physiology 12 (2021) 778872.

[327] A. Elkaranshawy, A. Ali, I. Abdelrazik, An effective heterogeneous whole-heart mathematical model of cardiac induction system with heart rate variability, Proceedings of the Institution of Mechanical Engineers, Part H: Journal of Engineering in Medicine 235 (2021). doi:doi.org/10.1177/0954411920978052.

[328] E. Sung, S. Etoz, Y. Zhang, N. Trayanova, Whole-heart ventricular arrhythmia modeling moving forward: Mechanistic insights and translational applications, Biophysics Reviews 2 (2021). doi:doi.org/10.1063/5.0058050.

[329] B. Baillargeon, N. Rebelo, D. Fox, R. Taylor, E. Kuhl, The living heart project: A robust and integrative simulator for human heart function, European Journal of Mechanics A/solids 48 (2014) 38–47.

[330] A. Quarteroni, T. Lassila, S. Rossi, R. Ruiz-Baier, Integrated heart–coupling multiscale and multiphysics models for the simulation of the cardiac function, Computer Methods in Applied Mechanics and Engineering 314 (2017) 345–407.

[331] A. Santiago, J. Aguado-Sierra, M. Zavala-Akè, R. Doste-Beltran, S. Gómez, R. Arís, J. Cajas, M. Vázquez, Fully coupled fluid–electro–mechanical model of the human heart for supercomputers, International Journal of Numerical Methods for Biomedical Engineering 34 (2018) e3140.

[332] F. Viola, V. Spandan, V. Meschini, J. Romero, M. Fatica, M. de Tullio, R. Verzicco, Fsei–gpu: Gpu accelerated simulations of the fluid–structure–electrophysiology interaction in the left heart, Computer Physics Communications 273 (2022) 108248.

[333] F. Viola, V. Meschini, R. Verzicco, Fluid–structure–electrophysiology interaction (fsei) in the left–heart: A multi–way coupled computational model, European Journal of Mechanics B/fluids 79 (2020) 212–232.

[334] G. Del Corso, R. Verzicco, F. Viola, A fast computational model for the whole human heart, Journal of Computational Physics 457 (2022) 111084.

[335] X. Zhu, Surgical Atlas of Cardiac Anatomy, Sringer, 2015.

[336] S. E. Petersen, N. Aung, M. M. Sanghvi, F. Zemrak, K. Fung, J. M. Paiva, J. M. Francis, M. Y. Khanji, E. Lukaschuk, A. M. Lee, et al., Reference ranges for cardiac structure and function using cardiovascular magnetic resonance (cmr) in caucasians from the uk biobank population cohort, Journal of Cardiovascular Magnetic Resonance 19 (1) (2017) 1–19.

[337] S. Ho, P. Nihoyannopoulos, Anatomy, echocardiography, and normal right ventricular dimensions, Heart 92 (suppl 1) (2006) i2–i13.

[338] S. B. Capps, R. C. Elkins, D. M. Fronk, Body surface area as a predictor of aortic and pulmonary valve diameter, The Journal of thoracic and cardiovascular surgery 119 (5) (2000) 975–982.

[339] S. Mihăilă, D. Muraru, E. Piasentini, M. H. Miglioranza, D. Peluso, U. Cucchini, S. Iliceto, D. Vinereanu, L. P. Badano, Quantitative analysis of mitral annular geometry and function in healthy volunteers using transthoracic three-dimensional echocardiography, Journal of the American Society of Echocardiography 27 (8) (2014) 846–857.

[340] K. Addetia, D. Muraru, F. Veronesi, C. Jenei, G. Cavalli, S. A. Besser, V. Mor-Avi, R. M. Lang, L. P. Badano, 3-dimensional echocardiographic analysis of the tricuspid annulus provides new insights into tricuspid valve geometry and dynamics, JACC: Cardiovascular Imaging 12 (3) (2019) 401–412.

[341] T. Arts, R. S. Reneman, P. C. Veenstra, A model of the mechanics of the left ventricle, Annals of biomedical engineering 7 (3-4) (1979) 299–318.

[342] D. Fedosov, Multiscale modelling of blood flow and soft matter, Ph.D. thesis, Brown University, Providence, United States (2010).

[343] M. S. Sacks, W. D. Merryman, D. E. Schmidt, On the biomechanics of heart valve function, Journal of biomechanics 42 (12) (2009) 1804–1824.

[344] K. May-Newman, F. Yin, A constitutive law for mitral valve tissue (1998).

[345] J. F. Wenk, M. B. Ratcliffe, J. M. Guccione, Finite element modeling of mitral leaflet tissue using a layered shell approximation, Medical & biological engineering & computing 50 (10) (2012) 1071–1079.

[346] E. J. Weinberg, M. R. Kaazempur-Mofrad, On the constitutive models for heart valve leaflet mechanics, Cardiovascular Engineering 5 (1) (2005) 37–43.

[347] T. P. Usyk, I. J. LeGrice, A. D. McCulloch, Computational model of three-dimensional cardiac electromechanics, Computing and visualization in science 4 (4) (2002) 249–257.

[348] J. M. Guccione, A. D. McCulloch, L. Waldman, Passive material properties of intact ventricular myocardium determined from a cylindrical model (1991).

[349] H. Wang, H. Gao, X. Luo, C. Berry, B. Griffith, R. Ogden, T. Wang, Structure-based finite strain modelling of the human left ventricle in diastole, International journal for numerical methods in biomedical engineering 29 (1) (2013) 83–103.

[350] M. R. Labrosse, C. J. Beller, T. Mesana, J. P. Veinot, Mechanical behavior of human aortas: Experiments, material constants and 3-d finite element modeling including residual stress, Journal of biomechanics 42 (8) (2009) 996–1004.

[351] C. Martin, W. Sun, T. Pham, J. Elefteriades, Predictive biomechanical analysis of ascending aortic aneurysm rupture potential, Acta biomaterialia 9 (12) (2013) 9392–9400.

[352] A. Satriano, E. J. Vigmond, D. S. Schwartzman, E. S. Di Martino, Mechano-electric finite element model of the left atrium, Computers in biology and medicine 96 (2018) 24–31.

[353] M. P. Nash, A. V. Panfilov, Electromechanical model of excitable tissue to study reentrant cardiac arrhythmias, Progress in biophysics and molecular biology 85 (2-3) (2004) 501–522.

[354] D. A. Siginer, D. De Kee, R. P. Chhabra, Advances in the flow and Rheology of non-Newtonian fluids, Elsevier, 1999.

[355] M. D. de Tullio, G. Pascazio, A moving least-squares immersed boundary method for simulating the fluid-structure interaction of elastic bodies with arbitrary thickness, Journal of Computational Physics 235 (2016) 201–225.

[356] A. Marsden, Simulation based planning of surgical interventions in pediatric cardiology, Physics of Fluids 25 (2013) 101303.

[357] M. Boulakia, S. Cazeau, M. A. Fernández, J.-F. Gerbeau, N. Zemzemi, Mathematical modeling of electrocardiograms: a numerical study, Annals of biomedical engineering 38 (3) (2010) 1071–1097.

[358] R. Plonsey, R. C. Barr, A. Bioelectricity, Quantitative Approach, Springer, 2007.

[359] S. Vermeire, S. Schreiber, W. J. Sandborn, C. Dubois, P. Rutgeerts, Correlation between the crohn's disease activity and harvey–bradshaw indices in assessing crohn's disease severity, Clinical Gastroenterology and Hepatology 8 (4) (2010) 357–363.

[360] J. F. Colombel, C. A. Solem, W. J. Sandborn, F. Booya, E. V. Loftus, W. S. Harmsen, A. R. Zinsmeister, K. D. Bodily, J. G. Fletcher, Quantitative measurement and visual assessment of ileal crohn's disease activity by computed tomography enterography: correlation with endoscopic severity and c reactive protein, Gut 55 (11) (2006) 1561–1567.

[361] K. J. Mortele, W. Wiesner, L. Intriere, S. Shankar, K. H. Zou, B. N. Kalantari, A. Perez, E. VanSonnenberg, P. R. Ros, P. A. Banks, et al., A modified ct severity index for evaluating acute pancreatitis: improved correlation with patient outcome, American Journal of Roentgenology 183 (5) (2004) 1261–1265.

[362] I. T. Jolliffe, J. Cadima, Principal component analysis: a review and recent developments, Philosophical Transactions of the Royal Society A: Mathematical, Physical and Engineering Sciences 374 (2065) (2016) 20150202.

[363] W. Hardle, Multivariate statistics (2007).

[364] R. J. Carroll, D. Ruppert, L. A. Stefanski, C. M. Crainiceanu, Measurement error in nonlinear models: a modern perspective, Chapman and Hall/CRC, 2006.

[365] S. E. Hobfoll, S. B. Shoham, C. Ritter, Women's satisfaction with social support and their receipt of aid., Journal of Personality and Social Psychology 61 (2) (1991) 332.

[366] S. Thomas, R. L. Williams, Relationships among perceived stress, trait anger, modes of anger expression and health status of college men and women, Resources in Education (1991).

[367] X. Fan, Two approaches for correcting correlation attenuation caused by measurement error: Implications for research practice, Educational and Psychological Measurement 63 (6) (2003) 915–930.

[368] L. Tarkkonen, K. Vehkalahti, Measurement errors in multivariate measurement scales, Journal of Multivariate Analysis 96 (1) (2005) 172–189.

[369] J. You, G. Chen, Estimation of a semiparametric varying-coefficient partially linear errors-in-variables model, Journal of Multivariate Analysis 97 (2) (2006) 324–341.

[370] C. Spearman, The proof and measurement of association between two things, The American journal of psychology 100 (3/4) (1987) 441–471.

[371] K. R. Murphy, Explaining the weak relationship between job performance and ratings of job performance, Industrial and Organizational Psychology 1 (2) (2008) 148–160.

[372] C. Mutch, J. Tisak, Measurement error and the correlation between positive and negative affect: Spearman (1904, 1907) revisited, Psychological reports 96 (1) (2005) 43–46.

[373] D. W. Zimmerman, R. H. Williams, Properties of the spearman correction for attenuation for normal and realistic non-normal distributions, Applied Psychological Measurement 21 (3) (1997) 253–270.

[374] E. Saccenti, M. H. Hendriks, A. K. Smilde, Corruption of the pearson correlation coefficient by measurement error and its estimation, bias, and correction under different error models, Scientific reports 10 (1) (2020) 1–19.

[375] I. K. Spence, J. Spence, Allen, mj, & yen, wm (1979). introduction to measurement theory. monterey, ca: Brooks/cole. alvord, s., adams, w., shaver, g., rosengren, k., garner, b., & barker, r. relationship between relevant wraml and nepsy subtest performance and reading readiness. national acad-emy of neuropsychology annual meeting, san francisco, november, 2001. american educational research association, american psychological association, national council.

[376] A. Covelli, S. Bardelli, R. T. Scaramuzzo, E. Sigali, M. Ciantelli, M. Del Pistoia, A. Longo, S. Tognarelli, A. Menciassi, A. Cuttano, Effectiveness of a new sensorized videolaryngoscope for retraining on neonatal intubation in simulation environment, Italian journal of pediatrics 46 (1) (2020) 1–11.

[377] F. Moscuzza, F. Belcari, V. Nardini, A. Bartoli, C. Domenici, A. Cuttano, P. Ghirri, A. Boldrini, Correlation between placental histopathology and fetal/neonatal outcome: chorioamnionitis and funisitis are associated to intraventricular haemorrage and retinopathy of prematurity in preterm newborns, Gynecological Endocrinology 27 (5) (2011) 319–323.

[378] C. Domenici, A. Cuttano, V. Nardini, L. Varese, P. Ghirri, A. Boldrini, Drug addiction during pregnancy: Correlations between the placental health and the newborn's outcome–elaboration of a predictive score, Gynecological Endocrinology 25 (12) (2009) 786–792.

[379] F. L. Schmidt, J. E. Hunter, Measurement error in psychological research: Lessons from 26 research scenarios., Psychological Methods 1 (2) (1996) 199.

[380] C. E. Lance, B. Dawson, D. Birkelbach, B. J. Hoffman, Method effects, measurement error, and substantive conclusions, Organizational Research Methods 13 (3) (2010) 435–455.

[381] B. Rosner, W. Willett, Interval estimates for correlation coefficients corrected for within-person variation: implications for study design and hypothesis testing, American journal of epidemiology 127 (2) (1988) 377–386.

[382] W. A. Fuller, Measurement error models, Vol. 305, John Wiley & Sons, 2009.

[383] L. Crocker, J. Algina, Introduction to classical and modern test theory., ERIC, 1986.

[384] E. P. Charles, The correction for attenuation due to measurement error: clarifying concepts and creating confidence sets., Psychological methods 10 (2) (2005) 206.

[385] R. H. Thouless, The effects of errors of measurement on correlation coefficients, British Journal of Psychology 29 (4) (1939) 383.

[386] M. A. Padilla, A. Veprinsky, Correlation attenuation due to measurement error: A new approach using the bootstrap procedure, Educational and Psychological Measurement 72 (5) (2012) 827–846.

[387] R. P. Mejias, M. J. Gamero, A. E. González, A monte carlo comparison of three consistent bootstrap procedures, Journal of Statistical Computation and Simulation 79 (4) (2009) 323–334.

[388] D. M. Rocke, S. Lorenzato, A two-component model for measurement error in analytical chemistry, Technometrics 37 (2) (1995) 176–184.

[389] J. P. Buonaccorsi, Measurement error: models, methods, and applications, Chapman and Hall/CRC, 2010.

[390] J. Zhang, Y. Yu, B. Zhou, H. Liang, Nonlinear measurement error models subject to additive distortion, Journal of Statistical Planning and Inference 150 (2014) 49–65.

[391] A. Pollice, G. J. Lasinio, R. Rossi, M. Amato, T. Kneib, S. Lang, Bayesian measurement error correction in structured additive distributional regression with an application to the analysis of sensor data on soil–plant variability, Stochastic Environmental Research and Risk Assessment 33 (3) (2019) 747–763.

[392] L. Yin, H. Gao, Moving horizon estimation for armax processes with additive output noise, Journal of the Franklin Institute 356 (4) (2019) 2090–2110.

[393] Y. Tian, G. J. Huffman, R. F. Adler, L. Tang, M. Sapiano, V. Maggioni, H. Wu, Modeling errors in daily precipitation measurements: Additive or multiplicative?, Geophysical Research Letters 40 (10) (2013) 2060–2065.

[394] T. A. Marques, Predicting and correcting bias caused by measurement error in line transect sampling using multiplicative error models, Biometrics 60 (3) (2004) 757–763.

[395] M. Lanne, A mixture multiplicative error model for realized volatility, Journal of Financial Econometrics 4 (4) (2006) 594–616.

[396] N. Hautsch, Capturing common components in high-frequency financial time series: A multivariate stochastic multiplicative error model, Journal of Economic Dynamics and Control 32 (12) (2008) 3978–4015.

[397] F. Chapeau-Blondeau, Nonlinear test statistic to improve signal detection in non-gaussian noise, IEEE Signal Processing Letters 7 (7) (2000) 205–207.

[398] R. D. Rifkin, Effects of correlated and uncorrelated measurement error on linear regression and correlation in medical method comparison studies, Statistics in medicine 14 (8) (1995) 789–798.

[399] W. Ganz, R. Donoso, H. S. Marcus, J. S. Forrester, H. J. Swan, A new technique for measurement of cardiac output by thermodilution in man, The American journal of cardiology 27 (4) (1971) 392–396.

[400] B. Olsson, J. Pool, P. Vandermoten, E. Varnauskas, R. Wassén, Validity and reproducibility of determination of cardiac output by thermodilution in man, Cardiology 55 (3) (1970) 136–148.

[401] H. N. Moseley, Error analysis and propagation in metabolomics data analysis, Computational and structural biotechnology journal 4 (5) (2013) e201301006.

[402] N. Day, M. Wong, S. Bingham, K. Khaw, R. Luben, K. Michels, A. Welch, N. Wareham, Correlated measurement error—implications for nutritional epidemiology, International Journal of Epidemiology 33 (6) (2004) 1373–1381.

[403] J. A. Wiley, M. G. Wiley, A note on correlated errors in repeated measurements, Sociological Methods & Research 3 (2) (1974) 172–188.

[404] G. Del Corso, R. Verzicco, F. Viola, Sensitivity analysis of an electrophysiology model for the left ventricle, Journal of the Royal Society Interface 17 (171) (2020) 20200532.

[405] L. A. Aroian, V. S. Taneja, L. W. Cornwell, Mathematical forms of the distribution of the product of two normal variables: Mathematical forms of the distribution, Communications in Statistics-Theory and Methods 7 (2) (1978) 165–172.

[406] S. S. Stevens, et al., On the theory of scales of measurement (1946).

[407] J. C. Caruso, N. Cliff, Empirical size, coverage, and power of confidence intervals for spearman's rho, Educational and psychological Measurement 57 (4) (1997) 637–654.

[408] N. Cliff, Ordinal methods for behavioral data analysis. 1–197 (1996).

[409] P. Cohen, S. G. West, L. S. Aiken, Applied multiple regression/correlation analysis for the behavioral sciences, Psychology press, 2014.

[410] R. Iman, Statistical methods for including uncertainties associated with the geologic isolation of radioactive waste which allow for a comparison with licensing criteria, Tech. rep. (1982).

[411] G. Van Rossum, F. L. Drake Jr, Python reference manual, Centrum voor Wiskunde en Informatica Amsterdam, 1995.

[412] G. Van Rossum, F. L. Drake, Python 3 Reference Manual, CreateSpace, Scotts Valley, CA, 2009.

[413] R. J. Moffat, Describing the uncertainties in experimental results, Experimental thermal and fluid science 1 (1) (1988) 3–17.

[414] K. Chatterjee, M. Modarres, A probabilistic approach for estimating defect size and density considering detection uncertainties and measurement errors, Proceedings of the Institution of Mechanical Engineers, Part O: Journal of Risk and Reliability 227 (1) (2013) 28–40.

[415] X. Chen, J. Chang, D. Spiegelman, F. Li, A bayesian approach for estimating the partial potential impact fraction with exposure measurement error under a main study/internal validation design, Statistical Methods in Medical Research (2021) 09622802211060514.

[416] S. L. Zeger, D. Thomas, F. Dominici, J. M. Samet, J. Schwartz, D. Dockery, A. Cohen, Exposure measurement error in time-series studies of air pollution: concepts and consequences., Environmental health perspectives 108 (5) (2000) 419–426.

[417] G. Kerekes, V. Schwieger, Determining variance-covariance matrices for terrestrial laser scans: A case study of the arch dam kops, in: Contributions to International Conferences on Engineering Surveying, Springer, 2021, pp. 57–68.

[418] D. Spiegelman, B. Rosner, R. Logan, Estimation and inference for logistic regression with covariate misclassification and measurement error in main study/validation study designs, Journal of the American Statistical Association 95 (449) (2000) 51–61.

[419] M. S. Hagger, S. R. Smith, J. J. Keech, S. A. Moyers, K. Hamilton, Predicting social distancing intention and behavior during the covid-19 pandemic: An integrated social cognition model, Annals of Behavioral Medicine 54 (10) (2020) 713–727.

[420] D. Spiegelman, B. Rosner, R. Logan, Estimation and inference for logistic regression with covariate misclassification and measurement error in main study/validation study designs, Journal of the American Statistical Association 95 (449) (2000) 51–61. doi:10.1080/01621459.2000.10473898.

[421] B. Schneider, D. Rasch, K. D. Kubinger, T. Yanagida, A sequential triangular test of a correlation coefficient's null-hypothesis, Statistical Papers 56 (3) (2015) 689–699.

[422] K. D. Kubinger, D. Rasch, M. Šimečkova, Testing a correlation coefficient's significance: Using h0: 0¡ is preferable to h0:= 0, Psychology Science 49 (2) (2007) 74–87.

[423] A. Saltelli, S. Tarantola, On the relative importance of input factors in mathematical models: safety assessment for nuclear waste disposal, Journal of the American Statistical Association 97 (459) (2002) 702–709.

[424] E. Borgonovo, X. Lu, E. Plischke, O. Rakovec, M. C. Hill, Making the most out of a hydrological model data set: Sensitivity analyses to open the model black-box, Water Resources Research 53 (9) (2017) 7933–7950.

[425] M. C. Hill, D. Kavetski, M. Clark, M. Ye, M. Arabi, D. Lu, L. Foglia, S. Mehl, Practical use of computationally frugal model analysis methods, Groundwater 54 (2) (2016) 159–170.

[426] J. H. Friedman, Multivariate adaptive regression splines, The annals of statistics 19 (1) (1991) 1–67.

[427] G. Allaire, A review of adjoint methods for sensitivity analysis, uncertainty quantification and optimization in numerical codes, Ingénieurs de l'Automobile 836 (2015) 33–36.

[428] M. Úbeda-Flores, J. Fernández-Sánchez, Sklar's theorem: The cornerstone of the theory of copulas, in: Copulas and Dependence Models with Applications, Springer, 2017, pp. 241–258.

[429] C. Hu, B. D. Youn, Adaptive-sparse polynomial chaos expansion for reliability analysis and design of complex engineering systems, Structural and Multidisciplinary Optimization 43 (3) (2011) 419–442.

[430] E. Torre, S. Marelli, P. Embrechts, B. Sudret, Data-driven polynomial chaos expansion for machine learning regression, Journal of Computational Physics 388 (2019) 601–623.

[431] G. Del Corso, R. Verzicco, F. Viola, A fast computational model for the electrophysiology of the whole human heart, Journal of Computational Physics (2022) 111084.

[432] E. Song, B. L. Nelson, J. Staum, Shapley effects for global sensitivity analysis: Theory and computation, SIAM/ASA Journal on Uncertainty Quantification 4 (1) (2016) 1060–1083.

[433] B. Iooss, C. Prieur, Shapley effects for sensitivity analysis with correlated inputs: comparisons with sobol'indices, numerical estimation and applications, International Journal for Uncertainty Quantification 9 (5) (2019).

[434] A. R. Hall, Generalized method of moments, OUP Oxford, 2004.

[435] B. Auder, B. Iooss, Global sensitivity analysis based on entropy, in: Safety, reliability and risk analysis-Proceedings of the ESREL 2008 Conference, 2008, pp. 2107–2115.

[436] E. Borgonovo, A new uncertainty importance measure, Reliability Engineering & System Safety 92 (6) (2007) 771–784.

[437] R. Mesiar, M. Komorníková, J. Komorník, Perturbation of bivariate copulas, Fuzzy Sets and Systems 268 (2015) 127–140.

[438] F. Campolongo, A. Saltelli, J. Cariboni, From screening to quantitative sensitivity analysis. a unified approach, Computer Physics Communications 182 (4) (2011) 978–988.

[439] S. Kotz, J. R. Van Dorp, Beyond beta: other continuous families of distributions with bounded support and applications, World Scientific, 2004.

[440] C. W. Topp, F. C. Leone, A family of j-shaped frequency functions, Journal of the American Statistical Association 50 (269) (1955) 209–219.

[441] S. Nadarajah, S. Kotz, Skewed distributions generated by the normal kernel, Statistics & probability letters 65 (3) (2003) 269–277.

[442] S. Nadarajah, G. Aryal, On the skew uniform distribution., Random Operators & Stochastic Equations 12 (4) (2004).

[443] A. Azzalini, G. Regoli, Modulation of symmetry for discrete variables and some extensions, Stat 3 (1) (2014) 56–67.

[444] R. Moshiro, P. Mdoe, J. M. Perlman, A global view of neonatal asphyxia and resuscitation, Frontiers in pediatrics 7 (2019) 489. doi:10.3389/fped.2019.00489.
URL https://www.frontiersin.org/articles/10.3389/fped.2019.00489/full

[445] M. H. Wyckoff, J. Wyllie, K. Aziz, M. F. de Almeida, J. Fabres, J. Fawke, R. Guinsburg, S. Hosono, T. Isayama, V. S. Kapadia, et al., Neonatal life support: 2020 international consensus on cardiopulmonary resuscitation and emergency cardiovascular care science with treatment recommendations, Circulation 142 (16_suppl_1) (2020) S185–S221. doi:10.1161/CIR.0000000000000895.

[446] L. K. McCarthy, C. J. Morley, P. G. Davis, C. O. F. Kamlin, C. P. O'Donnell, Timing of interventions in the delivery room: does reality compare with neonatal resuscitation guidelines?, The Journal of pediatrics 163 (6) (2013) 1553–1557. doi:10.1016/j.jpeds.2013.06.007.

[447] D. P. Larsen, A. C. Butler, Roediger 3rd hl. test-enhanced learning in medical education, Med Educ 42 (10) (2008) 959–66. doi:10.1111/j.1365-2923.2008.03124.x.

[448] E. Pesare, T. Roselli, N. Corriero, V. Rossano, Game-based learning and gamification to promote engagement and motivation in medical learning contexts, Smart Learning Environments 3 (1) (2016) 1–21. doi:10.1089/g4h.2015.0026.

[449] A. Sliney, D. Murphy, Jdoc: A serious game for medical learning, in: First International Conference on Advances in Computer-Human Interaction, IEEE, 2008, pp. 131–136. doi:10.1109/ACHI.2008.50.

[450] B. J. Knowlton, A. L. Siegel, T. D. Moody, Procedural learning in humans (2017). doi:10.1016/B978-0-12-809324-5.21085-7.

[451] A. F. Healy, L. E. Bourne, Learning and memory of knowledge and skills, Sage, 1995.

[452] L. Hu, L. Zhang, R. Yin, Z. Li, J. Shen, H. Tan, J. Wu, W. Zhou, Neogames: A serious computer game that improves long-term knowledge retention of neonatal resuscitation in undergraduate medical students, Frontiers in Pediatrics 9 (2021). doi:10.3389/fped.2021.645776.

[453] S. Rondon, F. C. Sassi, C. R. F. de Andrade, Computer game-based and traditional learning method: a comparison regarding students' knowledge retention, BMC medical education 13 (1) (2013) 1–8. doi:10.1186/1472-6920-13-30.

[454] C. L. Yeo, S. K. Y. Ho, V. C. Tagamolila, S. Arunachalam, S. S. Bharadwaj, W. B. Poon, M. G. Tan, P. E. Edison, W. Y. Yip, A. A. A. Haium,

et al., Use of web-based game in neonatal resuscitation-is it effective?, BMC medical education 20 (2020) 1–11. doi:10.1186/s12909-020-02078-5.

[455] E. A. Akl, K. M. Sackett, R. Pretorius, P. S. S. Bhoopathi, R. Mustafa, H. Schünemann, W. S. Erdley, Educational games for health professionals, Cochrane Database of Systematic Reviews (1) (2008). doi:10.1002/14651858.CD006411.pub2.

[456] C. Rutledge, C. M. Walsh, N. Swinger, M. Auerbach, D. Castro, M. Dewan, M. Khattab, A. Rake, I. Harwayne-Gidansky, T. T. Raymond, et al., Gamification in action: theoretical and practical considerations for medical educators, Academic Medicine 93 (7) (2018) 1014–1020. doi:10.1097/ACM.0000000000002183.

[457] C. L. Brown, M. A. Comunale, B. Wigdahl, S. Urdaneta-Hartmann, Current climate for digital game-based learning of science in further and higher education, FEMS microbiology letters 365 (21) (2018) fny237. doi:doi.org/10.1093/femsle/fny237.

[458] W. C. McGaghie, S. B. Issenberg, M. E. R. Cohen, J. H. Barsuk, D. B. Wayne, Does simulation-based medical education with deliberate practice yield better results than traditional clinical education? a meta-analytic comparative review of the evidence, Academic medicine: journal of the Association of American Medical Colleges 86 (6) (2011) 706. doi:10.1097/ACM.0b013e318217e119.

[459] C. M. Harrington, V. Chaitanya, P. Dicker, O. Traynor, D. O. Kavanagh, Playing to your skills: a randomised controlled trial evaluating a dedicated video game for minimally invasive surgery, Surgical endoscopy 32 (9) (2018) 3813–3821. doi:10.1007/s00464-018-6107-2.

[460] S. K. Ghoman, M. Cutumisu, G. M. Schmölzer, Digital simulation improves, maintains, and helps transfer health-care providers' neonatal resuscitation knowledge, Frontiers in pediatrics 8 (2020). doi:10.3389/fped.2020.599638.

[461] S. K. Ghoman, G. M. Schmölzer, The retain simulation-based serious game—a review of the literature, in: Healthcare, Vol. 8, Multidisciplinary Digital Publishing Institute, 2020, p. 3. doi:10.3390/healthcare8010003.

[462] S. K. Ghoman, S. D. Patel, M. Cutumisu, P. von Hauff, T. Jeffery, M. R. Brown, G. M. Schmölzer, Serious games, a game changer in teaching neonatal resuscitation? a review, Archives of Disease in Childhood-Fetal and Neonatal Edition 105 (1) (2020) 98–107. doi:10.1136/archdischild-2019-317011.

[463] N. Swiderska, E. Thomason, A. Hart, B. Shaw, Randomised controlled trial of the use of an educational board game in neonatology, Medical teacher 35 (5) (2013) 413–415. doi:10.3109/0142159X.2013.769679.

[464] M. Boeker, P. Andel, W. Vach, A. Frankenschmidt, Game-based e-learning is more effective than a conventional instructional method: a randomized controlled trial with third-year medical students, PloS one 8 (12) (2013) e82328. doi:10.1371/journal.pone.0082328.

[465] M. Cutumisu, S. D. Patel, M. R. Brown, C. Fray, P. von Hauff, T. Jeffery, G. M. Schmölzer, Retain: a board game that improves neonatal resuscitation knowledge retention, Frontiers in pediatrics 7 (2019) 13. doi:10.3389/fped.2019.00013.

[466] S. Erhel, E. Jamet, Digital game-based learning: Impact of instructions and feedback on motivation and learning effectiveness, Computers & education 67 (2013) 156–167. doi:10.1016/j.compedu.2013.02.019.

[467] A. All, E. P. N. Castellar, J. Van Looy, Assessing the effectiveness of digital game-based learning: Best practices, Computers & Education 92 (2016) 90–103.

[468] J. J. Donovan, D. J. Radosevich, A meta-analytic review of the distribution of practice effect: Now you see it, now you don't., Journal of Applied Psychology 84 (5) (1999) 795. doi:10.1037/0021-9010.84.5.795.

[469] N. J. Cepeda, H. Pashler, E. Vul, J. T. Wixted, D. Rohrer, Distributed practice in verbal recall tasks: A review and quantitative synthesis., Psychological bulletin 132 (3) (2006) 354. doi:10.1037/0033-2909.132.3.354.

[470] M. Cutumisu, S. K. Ghoman, C. Lu, S. D. Patel, C. Garcia-Hidalgo, C. Fray, M. R. Brown, R. Greiner, G. M. Schmölzer, Health care providers' performance, mindset, and attitudes toward a neonatal resuscitation computer-based simulator: Empirical study, JMIR Serious Games 8 (4) (2020) e21855. doi:10.2196/21855.

[471] R Core Team, R: A Language and Environment for Statistical Computing, R Foundation for Statistical Computing, Vienna, Austria (2020).
URL `https://www.R-project.org/`

[472] L. Cordero, B. J. Hart, R. Hardin, J. D. Mahan, C. a. Nankervis, Deliberate practice improves pediatric residents' skills and team behaviors during simulated neonatal resuscitation, Clinical pediatrics 52 (8) (2013) 747–752. doi:10.1177/0009922813488646.

[473] T. Sawyer, A. Sierocka-Castaneda, D. Chan, B. Berg, M. Lustik, M. Thompson, Deliberate practice using simulation improves neonatal resuscitation performance, Simulation in Healthcare 6 (6) (2011) 327–336. doi:10.1097/SIH.0b013e31822b1307.

[474] A. All, E. P. N. Castellar, J. Van Looy, Measuring effectiveness in digital game-based learning: A methodological review., International Journal of Serious Games 1 (2) (2014). doi:https://doi.org/10.17083/ijsg.v1i2.18.

[475] H. H. Matterson, D. Szyld, B. R. Green, H. B. Howell, M. V. Pusic, P. V. Mally, S. M. Bailey, Neonatal resuscitation experience curves: simulation based mastery learning booster sessions and skill decay patterns among pediatric residents, Journal of perinatal medicine 46 (8) (2018) 934–941. doi:10.1515/jpm-2017-0330.

[476] M. T. Bonde, G. Makransky, J. Wandall, M. V. Larsen, M. Morsing, H. Jarmer, M. O. Sommer, Improving biotech education through gamified laboratory simulations, Nature biotechnology 32 (7) (2014) 694–697. doi:10.1038/nbt.2955.

[477] R. Yadlapati, P. J. Kahrilas, M. R. Fox, A. J. Bredenoord, C. Prakash Gyawali, S. Roman, A. Babaei, R. K. Mittal, N. Rommel, E. Savarino, et al., Esophageal motility disorders on high-resolution manometry: Chicago classification version 4.0©, Neurogastroenterology & Motility 33 (1) (2021) e14058.

[478] A. J. Bredenoord, A. Babaei, D. Carlson, T. Omari, J. Akiyama, R. Yadlapati, J. E. Pandolfino, J. Richter, R. Fass, Esophagogastric junction outflow obstruction, Neurogastroenterology & Motility 33 (9) (2021) e14193.

[479] K. Lynch, Y.-X. Yang, D. Metz, G. Falk, Clinical presentation and disease course of patients with esophagogastric junction outflow obstruction, Diseases of the Esophagus 30 (6) (2017) 1–6.

[480] M.-T. Pérez-Fernández, C. Santander, A. Marinero, D. Burgos-Santamaría, C. Chavarría-Herbozo, Characterization and follow-up of esophagogastric junction outflow obstruction detected by high resolution manometry, Neurogastroenterology & Motility 28 (1) (2016) 116–126.

[481] D. Schupack, D. A. Katzka, D. Geno, K. Ravi, The clinical significance of esophagogastric junction outflow obstruction and hypercontractile esophagus in high resolution esophageal manometry, Neurogastroenterology & Motility 29 (10) (2017) 1–9.

[482] F. B. van Hoeij, A. Smout, A. Bredenoord, Characterization of idiopathic esophagogastric junction outflow obstruction, Neurogastroenterology & Motility 27 (9) (2015) 1310–1316.

[483] N. de Bortoli, P. C. Gyawali, S. Roman, S. Tolone, D. Sifrim, R. Tutuian, R. Penagini, J. E. Pandolfino, E. V. Savarino, Hypercontractile esophagus from pathophysiology to management: proceedings of the pisa symposium, Official journal of the American College of Gastroenterology— ACG 116 (2) (2021) 263–273.

[484] E. Savarino, N. De Bortoli, P. Zentilin, I. Martinucci, L. Bruzzone, M. Furnari, S. Marchi, V. Savarino, Alginate controls heartburn in patients

with erosive and nonerosive reflux disease, World journal of gastroenterology: WJG 18 (32) (2012) 4371.

[485] V. F. Eckardt, I. Gockel, G. Bernhard, Pneumatic dilation for achalasia: Late results of a prospective follow-up investigation, Gastroenterology 4 (124) (2003) A237.

[486] E. Savarino, N. De Bortoli, M. Bellini, F. Galeazzi, M. Ribolsi, R. Salvador, V. Savarino, R. Penagini, Practice guidelines on the use of esophageal manometry–a gismad-sige-aigo medical position statement, Digestive and Liver Disease 48 (10) (2016) 1124–1135.

[487] C. P. Gyawali, N. de Bortoli, J. Clarke, C. Marinelli, S. Tolone, S. Roman, E. Savarino, Indications and interpretation of esophageal function testing, Annals of the New York Academy of Sciences 1434 (1) (2018) 239–253.

[488] C. Gyawali, S. Roman, A. Bredenoord, M. Fox, J. Keller, J. Pandolfino, D. Sifrim, R. Tatum, R. Yadlapati, E. Savarino, et al., Classification of esophageal motor findings in gastro-esophageal reflux disease: Conclusions from an international consensus group, Neurogastroenterology & Motility 29 (12) (2017) e13104.

[489] P. Gor, Y. Li, S. Munigala, A. Patel, A. Bolkhir, C. Gyawali, Interrogation of esophagogastric junction barrier function using the esophagogastric junction contractile integral: an observational cohort study, Diseases of the Esophagus 29 (7) (2016) 820–828.

[490] A. Leopold, D. Yu, R. Bhuta, R. Kataria, X. Lu, A. Jehangir, M. Harrison, F. Friedenberg, Z. Malik, R. Schey, et al., Multiple rapid swallows (mrs) complements single-swallow (ss) analysis for high-resolution esophageal manometry (hrem), Digestive diseases and sciences 64 (8) (2019) 2206–2213.

[491] I. Marin, J. Serra, Patterns of esophageal pressure responses to a rapid drink challenge test in patients with esophageal motility disorders, Neurogastroenterology & Motility 28 (4) (2016) 543–553.

[492] C. P. Gyawali, D. A. Carlson, J. W. Chen, A. Patel, R. J. Wong, R. H. Yadlapati, Acg clinical guidelines: clinical use of esophageal physiologic testing, Official journal of the American College of Gastroenterology— ACG 115 (9) (2020) 1412–1428.

[493] P. J. Kahrilas, A. J. Bredenoord, M. Fox, C. P. Gyawali, S. Roman, A. J. Smout, J. E. Pandolfino, I. H. R. M. W. Group, The chicago classification of esophageal motility disorders, v3. 0, Neurogastroenterology & Motility 27 (2) (2015) 160–174.

[494] F. Okeke, S. Raja, K. Lynch, S. Dhalla, M. Nandwani, E. Stein, B. Chander Roland, M. Khashab, P. Saxena, V. Kumbhari, et al., What is the clinical significance of esophagogastric junction outflow obstruction? evaluation of 60 patients at a tertiary referral center, Neurogastroenterology & Motility 29 (6) (2017) e13061.

[495] A. Babaei, S. Shad, A. Szabo, B. T. Massey, Pharmacologic interrogation of patients with esophagogastric junction outflow obstruction using amyl nitrite, Neurogastroenterology & Motility 31 (9) (2019) e13668.

[496] A. Liu, M. Woo, Y. Nasser, M. Gupta, M. C. Buresi, M. Curley, D. Y. Li, L. Wilsack, C. N. Andrews, Esophagogastric junction outflow obstruction on manometry: outcomes and lack of benefit from ct and eus, Neurogastroenterology & Motility 31 (12) (2019) e13712.

[497] D. Biasutto, F. Mion, A. Garros, S. Roman, Rapid drink challenge test during esophageal high resolution manometry in patients with esophagogastric junction outflow obstruction, Neurogastroenterology & Motility 30 (6) (2018) e13293.

[498] S. B. Clayton, R. Patel, J. E. Richter, Functional and anatomic esophagogastic junction outflow obstruction: manometry, timed barium esophagram findings, and treatment outcomes, Clinical Gastroenterology and Hepatology 14 (6) (2016) 907–911.

[499] W. Blonski, A. Kumar, J. Feldman, J. E. Richter, Timed barium swallow: diagnostic role and predictive value in untreated achalasia, esophagogastric junction outflow obstruction, and non-achalasia dysphagia, Official journal of the American College of Gastroenterology— ACG 113 (2) (2018) 196–203.

[500] P. Woodland, S. Gabieta-Sonmez, J. Arguero, J. Ooi, K. Nakagawa, E. Glasinovic, E. Yazaki, D. Sifrim, 200 ml rapid drink challenge during high-resolution manometry best predicts objective esophagogastric junction obstruction and correlates with symptom severity, Journal of Neurogastroenterology and Motility 24 (3) (2018) 410.

[501] R. Penagini, N. de Bortoli, E. Savarino, E. Arsiè, S. Tolone, G. Greenan, P. Visaggi, D. Maniero, A. Mauro, D. Consonni, et al., Rapid drink challenge during high-resolution manometry for evaluation of esophageal emptying in treated achalasia, Clinical Gastroenterology and Hepatology (2022).

[502] J. R. Triggs, D. A. Carlson, C. Beveridge, A. Jain, M. Y. Tye, P. J. Kahrilas, J. E. Pandolfino, Upright integrated relaxation pressure facilitates characterization of esophagogastric junction outflow obstruction, Clinical Gastroenterology and Hepatology 17 (11) (2019) 2218–2226.

[503] B. Misselwitz, M. Hollenstein, S. Bütikofer, D. Ang, H. Heinrich, M. Fox, Prospective serial diagnostic study: the effects of position and provocative tests on the diagnosis of oesophageal motility disorders by high-resolution manometry, Alimentary pharmacology & therapeutics 51 (7) (2020) 706–718.

[504] S. Sanagapalli, J. McGuire, R. W. Leong, K. Patel, A. Raeburn, H. Abdul-Razakq, A. Plumb, M. Banks, R. Haidry, L. Lovat, et al., The clinical relevance of manometric esophagogastric junction outflow obstruction can be determined using rapid drink challenge and solid swallows, Official journal of the American College of Gastroenterology— ACG 116 (2) (2021) 280–288.

[505] Y. T. Wang, L. F. Tai, E. Yazaki, J. Jafari, R. Sweis, E. Tucker, K. Knowles, J. Wright, S. Ahmad, M. Kasi, et al., Investigation of dysphagia after antireflux surgery by high-resolution manometry: impact of multiple water swallows and a solid test meal on diagnosis, management, and clinical outcome, Clinical gastroenterology and hepatology 13 (9) (2015) 1575–1583.

[506] P. Visaggi, E. Savarino, G. Sciume, T. D. Chio, F. Bronzini, S. Tolone, M. Frazzoni, C. Pugno, M. Ghisa, L. Bertani, et al., Eosinophilic esophagitis: clinical, endoscopic, histologic and therapeutic differences and similarities between children and adults, Therapeutic Advances in Gastroenterology 14 (2021) 1756284820980860.

[507] E. S. Dellon, C. A. Liacouras, J. Molina-Infante, G. T. Furuta, J. M. Spergel, N. Zevit, S. J. Spechler, S. E. Attwood, A. Straumann, S. S. Aceves, et al., Updated international consensus diagnostic criteria for eosinophilic esophagitis: proceedings of the agree conference, Gastroenterology 155 (4) (2018) 1022–1033.

[508] I. Hirano, N. Moy, M. G. Heckman, C. S. Thomas, N. Gonsalves, S. R. Achem, Endoscopic assessment of the oesophageal features of eosinophilic oesophagitis: validation of a novel classification and grading system, Gut 62 (4) (2013) 489–495.

[509] E. S. Dellon, S. K. Gupta, A conceptual approach to understanding treatment response in eosinophilic esophagitis, Clinical Gastroenterology and Hepatology 17 (11) (2019) 2149–2160.

[510] I. Hirano, E. S. Chan, M. A. Rank, R. N. Sharaf, N. H. Stollman, D. R. Stukus, K. Wang, M. Greenhawt, Y. T. Falck-Ytter, K. A. Chachu, et al., Aga institute and the joint task force on allergy-immunology practice parameters clinical guidelines for the management of eosinophilic esophagitis, Gastroenterology 158 (6) (2020) 1776–1786.

[511] P. Visaggi, M. Ghisa, B. Barberio, D. Maniero, E. Greco, V. Savarino, C. J. Black, A. C. Ford, N. de Bortoli, E. Savarino, Treatment trends for eosinophilic esophagitis and the other eosinophilic gastrointestinal diseases: Systematic review of clinical trials, Digestive and Liver Disease (2022).

[512] P. Visaggi, L. Mariani, V. Pardi, E. M. Rosi, C. Pugno, M. Bellini, F. Zingone, M. Ghisa, E. Marabotto, E. G. Giannini, et al., Dietary management of eosinophilic esophagitis: tailoring the approach, Nutrients 13 (5) (2021) 1630.

[513] E. S. Dellon, M. H. Collins, D. A. Katzka, V. A. Mukkada, G. W. Falk, R. Morey, B. Goodwin, J. D. Eisner, L. Lan, N. K. Desai, et al., Long-term treatment of eosinophilic esophagitis with budesonide oral suspension, Clinical Gastroenterology and Hepatology 20 (7) (2022) 1488–1498.

[514] T. H. Taft, D. A. Carlson, M. Simons, S. Zavala, I. Hirano, N. Gonsalves, J. E. Pandolfino, Esophageal hypervigilance and symptom-specific anxiety in patients with eosinophilic esophagitis, Gastroenterology 161 (4) (2021) 1133–1144.

[515] P. Visaggi, M. Ghisa, B. Barberio, E. Marabotto, N. de Bortoli, E. Savarino, Systematic review: esophageal motility patterns in patients with eosinophilic esophagitis, Digestive and Liver Disease (2022).

[516] E. S. Dellon, J. T. Woosley, A. Arrington, S. J. McGee, J. Covington, S. E. Moist, J. H. Gebhart, J. A. Galanko, J. A. Baron, N. J. Shaheen, Rapid recurrence of eosinophilic esophagitis activity after successful treatment in the observation phase of a randomized, double-blind, double-dummy trial, Clinical Gastroenterology and Hepatology 18 (7) (2020) 1483–1492.